18th INTERNATIONAL CONFERENCE ON MACHINE DESIGN AND PRODUCTION

CONFERENCE PROCEEDINGS
VOLUME I

Editorial Board
S. Engin KILIÇ
Bahram LOTFISADIGH

umtik 2018

3-6 July 2018
ESKİŞEHİR- TURKEY

MATIMAREN
DEPARTMENT OF MECHANICAL ENGINEERING
MIDDLE EAST TECHNICAL UNIVERSITY
ANKARA-TURKEY

All rights of this book are reserved by the Middle East Technical University.
None of the papers printed in this book may be reproduced without the prior permission, in writing, from the Author(s) of the paper(s) and the editors of the book. The papers can however be cited by giving the source.

This book can be obtained from the following addresses:

UMTIK
Mechanical Engineering Department
Middle East Technical University
06800 Ankara- Turkey

Manufacturing Engineering Department
ATILIM University
06830 Ankara- Turkey

Cover Print:

METU- Ankara

Printing and Binding:

METU- Ankara

Printed by:

Dereağzı Fotokopi

ISBN 978-975-429-380-7

Organizing Committee

Metin AKKÖK	(METU, Dept. of Mechanical Eng.)	akkok@metu.edu.tr
S. Engin KILIÇ	(Atılım, Dept. of Manufacturing Eng.)	engin.kilic@atilim.edu.tr
Abdülkadir ERDEN	(Beytepe Academi)	abdulkadir.erden@beytepeakademi.com
E. İlhan KONUKSEVEN	(METU, Dept. of Mechanical Eng.)	konuk@metu.edu.tr
Cemal ÇAKIR"	(Uludağ, Dept. of Mechanical Eng.)	cemal@uludag.edu.tr
Ulvi ŞEKER	(Gazi, Dept. of Mechanical Eng.)	useker@gazi.edu.tr
Ali ORAL	(Balıkesiri, Dept. of Mechanical Eng.)	alioral@balikesir.edu.tr
Besim BARANOĞLU	(Atılım, Dept. of Manufacturing Eng.)	Besim.baranoglu@atilim.edu.tr
Bahram LOTFISADIGH	(Atılım, Dept. of Manufacturing Eng.)	Bahram.lotfisadigh@atilim.edu.tr
Nuran AY	(Anadolu, Dept. of Mechanical Eng.)	nay@anadolu.edu.tr
Evren YASA	(E.Osmangazi, Dept. of Mechanical Eng.)	ebalyasa@gmail.com

Contact: umtik@metu.edu.tr **Tel:** +90 312 586 8888

International Program Committee

Memiş	ACAR	UNITED KINGDOM
Serpil	ACAR	UNITED KINGDOM
M. Oktay	ALNIAK	TURKEY
Ahmet T.	ALPAS	CANADA
Yusuf	ALTINTAŞ	CANADA
Carla	ANFLOR	BRAZIL
Ömer	ANLAĞAN	TURKEY
Stuart	BARNES	UNITED KINGDOM
Erhan	BUDAK	TURKEY
Fuh-Kuo	CHEN	TAIWAN R.O.C.
Jiun	CHEN	TAIWAN R.O.C.
Tsung Chia	CHEN	TAIWAN R.O.C.
Hugi	CHRISTOPH	SWITZERLAND
Octavian	CIOBANU	ROMANIA
Can	ÇOĞUN	TURKEY
Samad	DADVANDIPOUR	HUNGARY
Saied	DARWISH	SAUDI ARABIA
László	DUDÁS	HUNGARY
Bülent	EKMEKÇİ	TURKEY
Ferenc	ERDELYI	HUNGARY
Kaan	ERKORKMAZ	CANADA
Emmanuel O.	EZUGWU	NIGERIA
Tahir	FIDAN	TURKEY
Necdet	GEREN	TURKEY
Yiğit	KARPAT	TURKEY
A. Sami	KAZI	FINLAND
Adnan I. O. Zaid	KILANI	JORDAN
Z. Murat	KILIC	CANADA
Ismail	LAZOGLU	TURKEY
Božidar	KRIŽAN	CROATIA
Yangmin	LI	MACAU
Ming-Chyuan	LU	TAIWAN R.O.C.
Tzuo Liang	LUO	TAIWAN R.O.C.
Yoshiyuki	MATSUOKA	JAPAN
Christoph	MEIER	SWITZERLAND
Toshimichi	MORIWAKI	JAPAN
Jokin	MUNOA	SPAIN
Samad	NADIMI BAVIL OLIAI	TURKEY
Karoly	NEHEZ	HUNGARY
Tuğrul	ÖZEL	USA
Fahrettin	ÖZTÜRK	TURKEY
Can	SAYGIN	USA
Eiji	SHAMATO	JAPAN
Arzu	(GÖNENÇ) SORGUÇ	TURKEY
Uğur	ŞİMŞİR	TURKEY
Tibor	TOTH	HUNGARY
Ali	ÜNÜVAR	TURKEY
Hakkı Özgür	ÜNVER	TURKEY
Mustafa	UYSAL	TURKEY
Ivica	VEZA	CROTIA
Min	WAN	P.R.C.
Bülent	YILMAZ	TURKEY
Michael	ZAEH	GERMANY

SUPPORTING MUNICIPALITIES AND ASSOCIATIONS

ESKİŞEHİR METROPOLITAN MUNICIPALITY		ESKİŞEHİR ODUNPAZARI MUNICIPALITY	
ESKİŞEHİR TEPEBAŞI MUNICIPALITY		MAKİNA İHRACATÇILARI BİRLİĞİ	
TÜRKİYE'NİN MAKİNECİLERİ		ESKİŞEHİR CHAMBER OF INDUSTRY	
ESKİŞEHİR CHAMBER OF COMMERCE		BURSA, ESKİŞEHİR, BİLECİK DEVELOPMENT AGENCY	
TÜBİTAK			

GOLD SPONSOR

İNFORMATİK

SILVER SPONSORS

	ÖZLER PLASTİK		MVD MAKİNE SANAYİ A.Ş.
	RÖZMAŞ		TEI

BRONZE SPONSORS

	NETMAK		USEL
	UMAR		AUTODESK
	KARCAN		AES
	RITIM		

SEMINAR SPONSORS

anova	ANOVA	BIAS MÜHENDİSLİK	BIAS
ATLAS KBS ENGINEERING	ATLAS KBS	ERMAKSAN METAL FABRICATING MACHINERY innovative technologies.	ERMAKSAN
NETFORM mühendislik • makina • metal	NETFORM	ONATUS öngörü teknolojileri	ONATUS
ON+ www.on.plus	ON.PLUS	IPG PHOTONICS	IPG Photonics

Conference Secretariat

ORIGIN Event Management Company
Çamlık Mahallesi, Dinç sok. Muyar Plaza No: 4 D: 25 P.O. Box: 34774 Ümraniye, İSTANBUL
TEL: +90 216 372 23 30 FAX: +90 216 372 23 31

www.originemc.com.tr
info@originemc.com.tr

Contact Address

http://www.umtik.com
umtik@metu.edu.tr

PREFACE

The world population is still growing although at a decreasing rate. It is expected to continue growing until the next century raising the population from about 7.5 billion of today to about 11billion at the end of this century. This means that the available resources will be getting less and less for the life on Earth, the nature becoming more and more polluted. Besides, the aged population of over 60 years old is expected to be rising from 962 million globally to 3.1 billion in 2100 according to UN reports, meaning that there will be less and less people actively involved in contributing to the world economy and global wealth. People are becoming more demanding in satisfying their diversified needs with high quality, low cost but customized products and services. Need to adapt to these conditions leads to a new era of disruptive innovations for the industry: the fourth industrial revolution, Industry 4.0. The theme of the previous conference UMTIK 2016 in Bursa was “Industry 4.0 and its Implementation”. The requirements in terms of technological and physical infrastructure for the companies to become active players in Industry 4.0 and to implement it were discussed and presented, in the first day panel, keynote sessions, special and regular sessions and in the brokerage event organized during the last day of the conference. All these; however; were quite limited to the success of the industry through scientific and technological research activities to create new products, technologies and processes giving some reference to the essential components of the Industry 4.0, paying little or no attention to the impact of these revolutionary changes to the people’s life.

The theme of this conference is selected to be “Technological developments and innovations in machine design and production for better and sustainable life”. First day of the conference is particularly devoted to this theme focusing particularly the life in Eskişehir. As the Organizing Committee we had several meetings with the Eskişehir Metropolitan and the two local Eskişehir municipalities: Odunpazarı and Tepebaşı, Eskişehir Chamber of Industry, Anadolu and Eskişehir Osmangazi University Rectors, Regional Development Agency and with Eskişehir Governor’s office to shape the First Day’s Program. As an outcome of those meetings, a panel discussion session on “Expectations from technological developments and innovations in machine design and production for better and sustainable life” is organized. The Panel will be moderated by Mr. Murat Yetkin, the editor-in- chief of the Hürriyet Daily News. Panelists are mainly chosen to represent local academia, industry and agencies. Panel members and the moderator are chosen to provoke discussions interactively between the panel and the participants. Three prominent keynote speakers will deliver keynotes on the transformations needed in three main areas for the positive impacts of the technological developments and innovations; namely: “New generation universities focused on societal impact” by Prof. Dr. İhsan Sabuncuoğlu, Rector of Abdullah Gül University, “Innovation dynamics” by Mr. Cengiz Ultav, Chairman of the Executive Board of TTGV, Turkish Technology Development Foundation, “Impact of energy research and technologies on people’s lives” by Prof. Dr. Pınar Mengüç, Director of the Centre for Energy, Environment and Economy (CEEE), Özyeğin

University. After the keynote presentations there will be a session of four papers on “Innovations in design and technology for better life”. Two of the papers are about the implementation of Industry 4.0 for smart manufacturing in Taiwan and in Croatia with pilot and case studies. The other two papers are on the new design concepts to have positive impacts on the lives of elderly and disabled people.

We would like to express our sincere thanks to the Metropolitan Municipality and Odunpazarı and Tepebaşı municipalities for their warm welcome to UMTIK 2018 and their great support. We are quite sure that all the participants will feel the warm and positive atmosphere here in Eskişehir. There will be a full day city tour for the accompanying persons and spouses and a half day tour for the participants arranged by the Eskişehir Metropolitan Municipality.

Use of software packages, especially the integrated ones, are indispensable in solving complex engineering problems. They are also necessary implementing Industry 4.0 to comply with the Industry 4.0 requirements, such as big data management and horizontal and vertical integration and in certain cases industrial internet of things and the cloud. We therefore invited some leading companies to give introductory seminars about software packages less known but with high potential to raise the engineering capabilities of the companies and the university students. Our invitation was accepted by them and a room of 25 person capacity was allocated for those seminars. The seminar program is announced at our web site. Registered participants have the right to enroll any of those seminars free of charge, provided that there are still vacancies in the seminar intended to be enrolled. We thank all the software companies who accepted our invitation and participated in the program.

Additive and hybrid manufacturing is an important component of the Industry 4.0. There will be 4 papers in hybrid manufacturing session and 14 papers in four additive manufacturing sessions. Most of the papers are coming from the industry. This shows that the industrial companies have already started to show a serious attention to additive and hybrid manufacturing and Industry 4.0 applications becoming widespread.

Surface integrity of manufactured components is very important for their use in some critical applications, such as those in aerospace industry. A symposium within UMTIK is organized on surface integrity for the first time. 17 papers were accepted to be presented in the symposium. This shows that the topic is attracting attention from academia and industry.

There will be about 100 papers to be presented in all the regular, special and symposium sessions except for the keynote and invited papers. More than 30% of the papers to be presented in the conference are either outcome of a joint research project between university and industry or of a research project conducted by an industrial company alone. This is a good sign of the growing interest of the industry to the UMTIK conferences.

Special sessions and the regular sessions will be conducted in three parallel sessions. The First Day program, keynote presentations, panels and the sponsor sessions; however, will be organized as

plenary sessions in order that all the participants can attend with one exception of the keynote presentation on the 5th of July. Mini Symposium on Surface Integrity will take place as the third track of the parallel sessions on the 5th of July.

We highly acknowledge the Honorary Chair Persons of the Conference: Presidents of the four universities, Professor Mustafa Verşan Kök of the Middle East Technical University, Professor Yıldırım Üçtuğ of Atılım University, Professor Naci Gündoğan of Anadolu University and Professor İhsan Sabuncuoğlu of Abdullah Gül University for their kind support. We would like to thank all keynote speakers, Professor İhsan Sabuncuoğlu, Mr. Cengiz Ultav, Professor Pınar Mengüç, Professor Yusuf Altıntaş, Professor Carla Tatiana Mota Anflor and Professor Osman Eroğul, First Day Panel Moderator Mr. Murat Yetkin and the panelists, organizers of the Panel on “Additive manufacturing in Turkey: Developments, applications, opportunities and difficulties” and the Mini Symposium on Surface Integrity Professor Oğuzhan Yılmaz and Assoc. Prof. Dr. Yusuf Kaynak, panelists, special session organizers, session chair persons, authors and all participants for their valuable contributions. Asst. Prof. Dr. Bahram Lotfi Sadigh is gratefully acknowledged for the tremendous time and effort he spent in every phase of the conference organization and in the editorial work of the Conference Proceedings and the Abstracts Book.

Last, but not the least, we would also like to thank our golden sponsor Informatics, TUBITAK, “The Scientific and Technological Research Council of Turkey”, Turkish Machinery Exporters Union, silver, bronze, seminar and symposium sponsors, BEBKA, Bursa, Eskişehir, Bilecik Development Agency, ESO, Eskişehir Chamber of Industry, software companies, the International Program Committee Members, our Conference Secretariat, ORIGINEMC, all conference participants and all those who contributed to the success of UMTIK 2018.

We wish all the participants a highly memorable time during their stay in Eskişehir.

The Organizing Committee

UMTIK 2018, 3-6 July 2018

Eskişehir, Turkey

CONTENTS

page

VOLUME I

Innovations In Design and Technology For Better Life

Innovative smart enterprise-case studies 3
Marina CRNJAC, Marko MLADINEO, Ivica VEZA

Elderly and Disabled Centered Design 15
Bülent YILMAZ

Walkmech 2.0: Conceptual Design and Structural Analyses of An Energy-Recycling Transfemoral Prosthesis For Activities of Daily Life 31
Ramazan ÜNAL, Furkan BALTACIOĞLU

Design for Transport Safety I

Impact Performance Evaluation Of A Crash Cushion Design Using Finite Element Simulation And Full-Scale Crash Testing 47
Murat BÜYÜK, Ali Osman ATAHAN, Kenan KURUCUOĞLU

Derivation Of Stiffnesses For Comparison Of Vehicle Performance In Frontal Impacts 61
Selçuk HİMMETOĞLU

Investigating The Effects Of Materials, Geometric Properties And Modifications On The Crashworthiness Of Bumper And Chassis System 81
Batuhan GÜRER, Volkan ESAT

Design for Transport Safety II

Evaluation Of Soil Conditions And Post Embedment Depth On Guardrail Safety Performance 97
Ali Osman ATAHAN, Murat ÖRNEK, Murat BÜYÜK, Ercan EPSİLELİ

Hazard Perception Test Design Suitability For Older Drivers 113
B. Serpil ACAR, Grace SMALLEY

Traffic Safety At Median Ditch: Steel Vs Concrete Barrier Performance Comparison Using Computer Simulation 131
Ayhan Öner YÜCEL, Ali Osman ATAHAN, Turan ARSLAN, Umur Korkut SEVİM

Design for Transport Safety III

Analysis Of A Coach Side Flap Under Cyclic Loads 145
Burkay DEMIR, Zeki Mert BARUT, Umut AKTAŞ

Topology Optimisation Of An Automobile Brake System Component Under Dynamic Loading Conditions 157
Betül S. YILDIZ

Hybrid Manufacturing

Investigating the Effects of Process Parameters on Residual Stress Evolution in Plasma Transfer Arc (PTA) cladding of Ti-6Al-4V 163
Hadi MOZTARZADEH, Sampan SETH, Hoda AMEL, Gregory J. GIBBONS

Additive Manufacturing I

A Technological And Business Perspective Of Additive Manufacturing For Defense Industry 169
Kıvılcım ERSOY, Barış KOÇ, Evren YASA

Effects Of Liquefier Design On Thermal Profile In Fused Filament Fabrication Based Additive Manufacturing Process 185
Chirayu H. SHAH, Harshal N. SHAH, Kaushalendra PATEL, Tuğrul ÖZEL

Design And Fabrication Of Large-Size FFF 3d Printer 199
Gökberk SERİN, Hakkı Özgür ÜNVER

Additive Manufacturing II

Additive manufacturing of the military oriented medical devices with stereolithography method 217
Erdem İnanç BUDAK, Osman EROĞUL

Practice-Oriented Metal AM Process Simulation And Optimization 233
Michel PEREME, Patrick MEHMERT

Effects Of Structural Hybrid Design Of Cocr-Alloy Scaffolds Fabricated By Selective Laser Melting For Biomedical Applications 247
EMRE ÖZEREN, Mihrigül ALTAN

Additive Manufacturing III

Design Of A Quadcopter Arm For Additive Manufacturing Using Optimization And Lattice Structures 261
Recep Muhammet GÖRGÜLÜARSLAN, Şükrü Taha AKSOY, Tarkan TURNACILAR, Aybars Feyzi KÖKSAL

High Vibration Absorptive Body Production For Turning Cutting Tools With Additive Manufacturing Technology 277
U. MALAYOĞLU, Tuğrul SOYUSİNMEZ, Özgücan GÜZELİPEK, Gökçe AKKUŞ

Additive Manufacturing IV

Design And Development Of An Additive Manufacturing System For Metal Printing 285
S. Shahid MUSTAFA, Ismail LAZOĞLU

Using Multi-Axis Additive Manufacturing In Support-Less Part Fabrication 297
Mohammed A. ISA, Ismail LAZOĞLU

Robotic Additive Manufacturing Of Tooling For Composite Structures 309
I. E. YİĞİT, Shaheryar A. KHAN, Ismail LAZOĞLU

Metal Cutting I

Effects of the rotational speed on the dynamics of micro cutting tools 319
Bekir BEDIZ

Efficiency optimization method of stability parameters for thin-walled workpiece milling process 335
Chung-Yu Tai, Ta-Jen Peng, Tzuo-Liang Luo

Investigation of effect of minimum quantity lubrication technique on surface roughness during milling of titanium alloy (Ti-6Al-4V) 345
Khaled Ali OSMAN, Volkan YILMAZ, Hakkı Özgür ÜNVER, Ulvi ŞEKER, S. Engin KILIÇ

Metal Cutting II

Grinding operation of a workpiece with an unknown shape considering tool deflection compensation 355
Abdulhamit DONDER, Masoud LATIFINAVID, E. İlhan KONUKSEVEN

Design for manufacturability: Determination of minimum manufacturable wall and floor thickness of machined parts by utilizing finite element analysis 367
Candaş URUNGA

Investigating the effect of milling parameters on residual stresses of Ti64 375
Ramazan NAMLU, Okan Deniz YILMAZ, Caner SIMSIR

Computational Mechanics

Damage identification in a cantilever beam using modal strain energy 385
Allan DOMINGUES, Tharcísio SANTOS, Carla ANFLOR, Sergio CARNEIRO

Performance Evaluation of Micro-Textured Cutting Tools in Dry Machining of Inconel 718 Using FE Simulation 399
Eren KAYA, İrfan KAYA

Finite elements analyzing of the effect of crack on stress and strain in honeycomb structure from abs polymer materials 415
Bekir YALÇIN, Berkay ERGENE

Industry 4.0 related topics

Literature-based identification of behavioural modules for social robots using design structure matrix 429
İlayda ÖZER, Zühal ERDEN

Aerospace Engineering

Lay-up design optimization for the loaded-carrying tubular structure made of orthotropic composite 441
Sergey SHEVTSOV, Igor ZHILYAEV, Natalia SNEZHINA, Jiing-Kae WU

Numerical simulation of lateral jet in a supersonic missile using computational fluid dynamics 457
Efe C. DAĞLI, M. Halûk AKSEL

Design and cold flow experimental procedure of a pintle injector 469
Berksu ERKAL, Bülent SÜMER, M. Haluk AKSEL

Computational Fluid Dynamics

CFD simulation of train fire in the Istanbul metro tunnel 479
M. İlter BİLGE, Haluk AKSEL

Cartesian mesh generator with adaptation to boundary layer 495
Merve ÖZKAN, Özgür Uğraş BARAN, M. Halûk AKSEL

Experimental and numerical investigation of coaxial pressure swirl injectors 509
Onur BARAN, Yusuf ÖZYÖRÜK

Unsteady solution of 2D converging-diverging nozzle using linearized harmonic method 517
Arash KARSHENASS, O. Uğraş BARAN, M. Haluk AKSEL

VOLUME II

Electrical Discharge Machining

Experimental Investigation of Machining Characteristics for Al2014 Alloy Reinforced with Tib2 Composites in Powder-Mixed EDM 527
Gökhan KÜÇÜKTÜRK, Javad JOUDI, Recep ÇALIN, Ulvi ŞEKER, Hakan GÜRÜN, Omid Farid AHMADINIA

An Investigation of Material Removal Rate and Tool Wear Rate in Powder Mixed EDM Machining Process of Al2014 Alloy Reinforced with B4C Composites 539
Gökhan KÜÇÜKTÜRK, Omid Farid AHMADINIA, Recep ÇALIN, Ulvi ŞEKER, Duran KAYA, Javad JOUDI

Mechanical Design

Analytical method for bending stress of internal asymmetric spur gears 549
Mahir Gökhan ORAK, Metin AKKÖK

2D manufacturing equipment for the glass-mosaic products 557
Murat ŞAHİN, Bülent YILMAZ

Materials Behavior

A comparative study on hydrogen embrittelement mechanisms 569
Burak BAL, Mustafa YERLİTAŞ, Barış ÇETİN, Halim MEÇO

The effect of insert surface roughness on shear strength of inserted metal injection molded components 577
Asghar SAFARIAN, Mehmet SUBAŞI, Çetin KARATAŞ

TÜRKÇE BİLDİRİLER

Talaşlı İmalat

Jant üretimi talaşli imalat prosesinde parametrik programlama 593
Kağan DALAK, Kaan GÜNGÖR, İsmail ÇAKIRGÖZ, Uğur AYBARÇ

GH4169 süperalaşiminin yüksek hizli işlemede testere dişi talaş oluşumunun sayisal simülasyonu 603
Mehmet AYDIN

CFRP/Al istifli yapının geleneksel matkaplarla delinebilirliği 615
Erman AYDIN, Muammer NALBANT

Dövme piston üretiminde süreç geliştirilmesi 633
Ali ÜNÜVAR, Hüseyin SARIKAYA

Çeşitli İmal Usulleri

Kaynak hücrelerinde endüstri 4.0 uygulamaları 653
Gökhan YENİKAYA, Sibel YENİKAYA, Uğur HATİPOĞLU

Otomotiv Mühendisliği

Taşıt elemanlarının optimum yapısal modelinin belirlenmesi 665
Ali Rıza YILDIZ

Yeni nesil yüksek mukavemetli çelikler ile çarpışma performansı yüksek taşıt tampon ve darbe emici geliştirilmesi 673
Ali Rıza YILDIZ, Emre DEMİRCİ

Termoplastik çarpışma kutularında alüminyum köpük takviyesinin çarpışma karakteristiğine etkisi 685
Betül Gülçimen ÇAKAN, Murat REİS, Cihat ENSARİOĞLU, Hüseyin KÖLÜK, Harun YENİ, Agah UĞUZ, Mustafa Cemal ÇAKIR

Malzeme ve Malzeme Mekaniği

Düşük yoğunluklu hafif AZ91 MG alaşımının aşınma davranışının ETİAL 150 AL alaşımı ve FR-4 cam takviyeli epoksi kompoziti ile deneysel karşılaştırılması 695
Bekir YALÇIN, Emre AYKAN

Kompozit sargılı basınçlı kaplarda çatlak analizi 713
Muzaffer ÇETİN, Kemal YAMAN, Bora YILDIRIM

Lazerle Kesme: Tezgah Tasarımı

Kesim kontrolü yapabilen, yüksek proses hızına sahip gelişmiş lazerli saç kesim tezgahının tasarımı 727
Sinan GANDAŞ, Oktay ÇELENK, Feridun AY, Cem SEVİK, Nihan KOSKU PERKGÖZ

Lazer kesim tezgâhı için kompozit Y-eksen köprü imalatı 737
Oktay ÇELENK, Ali DURMUŞ, Kadir ÇAVDAR

MINI SYMPOSIUM ON SURFACE INTEGRITY IN CONVENTIONAL AND NON-CONVENTIONAL MANUFACTURING PROCESSES

Effect of machining parameters on workpiece surface characteristics in electric discharge drilling (EDD) 761
Oğuz ERDEM, Can ÇOĞUN, İbrahim USLAN

Design, manufacturing and evaluation of a DMLS test artifact for surface texture and form characterization 775
Özgür POYRAZ, Ezgi UĞUR SOLAKOĞLU, Güray AKBULUT, Soner ÖREN, Cansinem TÜZEMEN

Ti6Al4V surface modification by hydroxyapatite powder mixed electric discharge machining for medical application 787
Tahsin T. ÖPÖZ, Mark F. MURPHY, Nihal EKMEKCİ, Bülent EKMEKCİ

Powder mixed electrical discharge machining and biocompatibility: a state of the art review 803
Sudi KALAMAN, Hamidullah YAŞAR, Nihal EKMEKCİ, Tahsin T. OPOZ, Bülent EKMEKCİ

ABRASIVE FLOW MACHINING OF AEROSPACE ALLOYS 831
Kürşad GÖV, Ömer EYERCİOĞLU

Effects of electrodes on aerospace alloys in hole-EDM process 843
Ömer EYERCİOĞLU, Kürşad GÖV

An experimental investigation of the ultrasonic-assisted machining of Ti-6Al-4V 855
F. Hayati ÇAKIR, Selim GÜRGEN, Sezan ORAK, M. Cemal KUŞHAN, M. Alper SOFUOĞLU

The effect of processing on the surface and subsurface characteristic of plastic injection mold steel 863
O. Saban KAMBER, Emre TAŞCIOĞLU

MİNİ SEMPOZYUM: GELENEKSEL VE GELENEKSEL OLMAYAN İMALAT SÜREÇLERİNDE YÜZEY BÜTÜNLÜĞÜ (TÜRKÇE BİLDİRİLER)

CNC tel elektro erozyon tezgâhinda tel elektrot özelliklerinin yüzey pürüzlülüğüne etkisinin taguchi yöntemiyle modellenmesi 881
Hüseyin GÜRBÜZ, Şehmus BADAY, İbrahim HAMARAT

AA 7075 YAŞLANDIRILMASINDA FARKLI ÖN GERİNMELERİN MEKANİK ÖZELLİKLERE ETKİLERİNİN İNCELENMESİ 897
Süleyman KILIÇ, İlyas KACAR, Fahrettin ÖZTÜRK, Mevlüt ŞAHİN, Oğuz ERDEM

Uzay ve havacılık alaşımlarının elektriksel erozyonla delinmesi işleminde yüzey bütünlülüğünün incelenmesi 919
Tohid ABBASI, Merve EKİCİ, Oğuzhan YILMAZ

3B yazdırılmış kompozitlerin yazdırma parametrelerinin yüzey pürüzlülüğüne etkisinin deneysel incelenmesi 935
Tuğçe TEZEL, Volkan KOVAN, Eyüp Sabri TOPAL

AISI 316L çeliğinin tornalanmasında kesici takım formlarının yüzey bütünlüğü üzerine etkisi 945
Hüseyin Gürbüz, Ulvi Şeker, Fırat Kafkas

RENE 65 süper alaşiminin delik delme işleminde farkli parametrelerin taguchi yöntemiyle analizi 973
Furkan BİLGİÇ, Ümit ER, Mustafa ULUTAN

Seçici lazerle ergitme yöntemi ile üretilen Inconel 625 alaşımlı parçada yüzey bütünlüğünün incelenmesi 989
Özhan KITAY, Emre TAŞCIOĞLU, Mustafa KAŞ, Şafak NESLİ, Yusuf KAYNAK, Oğuzhan YILMAZ

Şekil hafızalı niti alaşımın kuru, MQL ve kriyojenik koşullarda işlenmesinde kesici takım aşınmasıyla iş parçası yüzey kalitesi arasındaki ilişkinin araştırılması 999
Özhan KITAY, Yusuf KAYNAK

Pirinç malzemelerin delinmesi sürecinde kesici takim yuvarlanma yariçapinin iş parçasi yüzey bütünlüğüne etkisi 1011
Süleyman ÇİÇEK, Kadir İLBAY, Emre TAŞCIOĞLU, Yusuf KAYNAK

PAPERS

INNOVATIVE SMART ENTERPRISE – CASE STUDIES

Marina CRNJAC, *mcrnjac@fesb.hr*, University of Split, 21000, Split, Croatia
Marko MLADINEO, *mmladine@fesb.hr,* University of Split, 21000, Split, Croatia
Ivica VEZA, *iveza@fesb.hr,* University of Split, 21000, Split, Croatia

ABSTRACT

The innovative smart enterprise represents new ways of production and organization within manufacturing company. Digitalization has a big progress and it affects production systems. It changes the way of work in manufacturing companies. The digitalization impacts every step in the production system and brings more flexible manufacturing processes. To introduce digitalization in manufacturing processes, it is necessary to create better conditions for easier and more meaningful implementation. It means that standardized and well organized work is crucial. The lean methodology could be the first step for the innovative smart enterprise. This paper shows Croatian model of innovative smart enterprise that serves companies to find a way for implementation and definition of their own objectives and priorities according to the current state of Croatian industry. Two case studies show that it is possible to improve their work with Croatian model of the innovative smart enterprise.

Keywords: Industry 4.0, Innovative Smart Enterprise, Croatian model (HR-ISE model)

1. INTRODUCTION

Today manufacturing enterprises are under the pressure of the environment. There are advances in technology, customer needs, ecology and legal frameworks. Factory systems and technologies have been evolving in two directions. The first direction shows how they increase the versatility of the allowable products' variety and the second direction is that companies have extended factories like tools and techniques [1]. The first three industrial revolutions came about as a result of mechanization, electricity and IT. The Industry 4.0 is focused on smart manufacturing systems. This new type of industry is based on Smart Factory model, Fig. 1. The Smart Factory has a completely new approach to production. Smart products are uniquely identifiable because they are capable to store data and may be located any time, they know their own history, current status and alternative routes for achieving their target state. New manufacturing systems are vertically networked with business processes within enterprises and horizontally connected to the dispersed value

networks that can be managed in real time [2]. Smart Factories allow individual customer requirements to be met and mean that even one-off items can be manufactured profitably. In Industry 4.0, dynamic business and engineering processes enable last-minute changes. Those kind of processes are able to respond flexibly to disruptions and failures. End-to-end transparency is provided over the whole manufacturing process and decision-making process is based on gathered data. To change manufacturing system in a mentioned way it is necessary to fulfill some requirements characteristic for Industry 4.0. The main areas for action are: horizontal integration through value networks, end-to-end digital integration across the entire value chain, vertical integration of systems at different hierarchical levels, but also vertical integration with networked manufacturing systems. To implement these features, the first step is to implement several lean methods like standardization, 5S method, continuous improvement and then focus on digitalization. Each enterprise should become smart, i.e. Smart Enterprise / Smart Factory. It should incorporate its machinery, production facilities and warehousing systems in the shape of Cyber-Physical System (CPS) [3] (smart machines, storage systems and production facilities capable of autonomously exchanging information, etc).

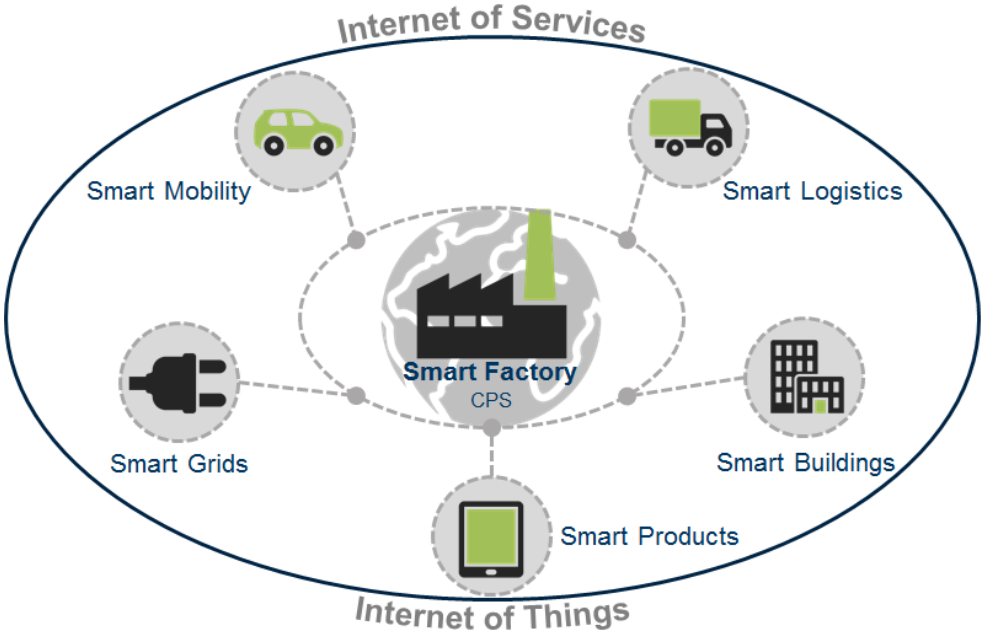


Figure 1. Smart factory and intelligent infrastructure [1]

Global manufacturing enterprises are developing their production system with the selection of lean tools from the palette of proven lean tools. Every global manufacturer has its unique manufacturing system (Toyota, Volvo, Daimler, Bosch, etc.) [4], but also some countries are developing their own unique enterprise model (like Germany – Industry 4.0). Model is aligned with their vision, strategy, values and culture. The problem is that Croatia has not developed

its own model for the enterprise. The model developed in project Innovative Smart Enterprise (INSENT) is the original and unique model for Croatian enterprises (HR-ISE model) and it will be implemented in the economy, especially in small and medium-sized enterprises. This paper presents two case studies which show the implementation of Croatian model of innovative smart enterprise in Croatian enterprises. The Croatian model of the innovative smart enterprise is based on lean methodology and management which are focused on fulfilling customer's satisfaction and creating value through waste reduction [5].

2. INNOVATIVE SMART ENTERPRISE

The idea about innovative smart enterprise for Croatia comes from the current state of Croatian industry. Whole European industry is characterized by a dramatic drop in customer demand leading to reduced working hours, layoffs and idle factories. It is necessary to find new ways of work to survive in a turbulent environment with erratic customer behavior. New objectives should be flexibility, agility and scalability.

The main objective of this project was to develop Croatian model of Innovative Smart Enterprise (HR-ISE model). The aim was to perform model's regional fit, i.e. to harmonize Innovative Smart Enterprise model with a specific regional way of thinking, manufacturing and organizational tradition, specific education and especially to help Croatian enterprises to bridge the gap between their competencies and EU enterprises' competencies and capabilities. Following objectives were crucial to achieve the main objective of this project:

- Objective 1: It was important to perform profound research to describe the current state of Croatian manufacturing enterprise. It was done through questionnaires and interviews with CEOs and technical directors of manufacturing enterprises in Croatia. The aim was to gather the data from as much as possible enterprises. After that, an analysis was done to describe the current state of Croatian manufacturing enterprises. It was the answer on the question: "Where are we now?"
- Objective 2: A synthesis of analysis of Croatian manufacturing enterprises was done through the development of Croatian model of Innovative Smart Enterprise (HR-ISE model). The HR-ISE model is based not just on State-of-the-art theoretical models but also on State-of-the-art practical models like Lean Management philosophy from Toyota Production System. A special effort was made to bridge the cultural and mentality gaps between State-of-the-art models and current Croatian model. It was the answer to the question: "Where do we want to be?"
- Objective 3: A special learning environment is established in one Laboratory during this project. It is a Learning Factory, i.e. simulation of a real factory through specialized equipment (virtual reality gadgets, specialized assembly tables, real products, automatic

assembly station, etc.). The laboratory is organized to simulate factory based on the HR-ISE model. It is a learning environment not just for students but for engineers from manufacturing enterprises. It is a place in which transfer of developed HR-ISE model to the economy subjects is achieved. The Learning factory is still developing and new knowledge is applied. It is the answer to the question: “How can we get there?”

These three objectives were realized through four work packages in the period of four years. The fourth year started with application in production environment.

3. RESEARCH METHODS

The problem was stated and the first phase was determined as a deep search of literature on this specific issue, in order to define basic HR-ISE model. Whole research methodology for this part of the research is shown in figure 2.

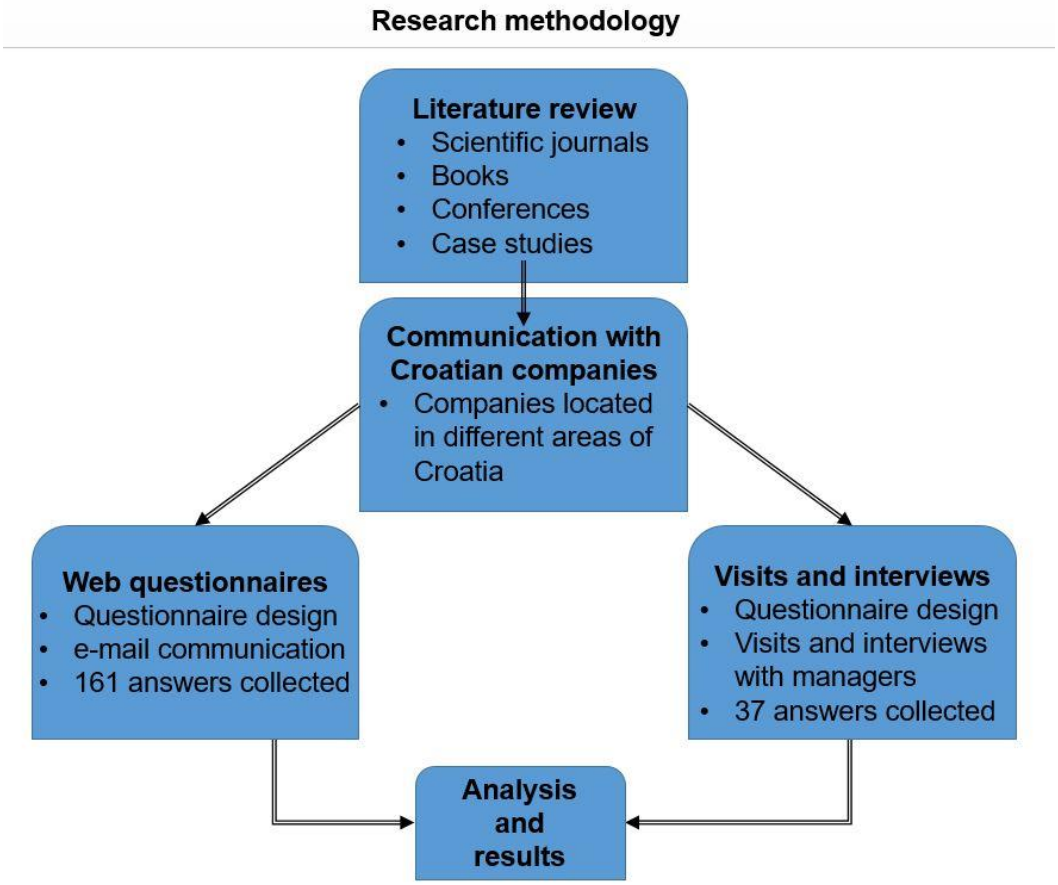


Figure 2. Research methodology for this part of the research

At the beginning of the second phase, the research method for detailed definition of the HR-ISE model was based on questionnaires that were sent to manufacturing enterprises within Croatia, in order to determine what lean principles are currently used and what lean

principles are necessary for their production systems. The HR-ISE model with basic lean tools, which originates from previous research where 161 company participated [6], was presented to 37 enterprises with the aim to collect their opinions about the presented model, Fig. 3. There is unreplaceable part of HR-ISE model and manufacturing enterprises were completing HR-ISE model with their own priorities, objectives and other lean tools (in the cells at the right side of the model) they consider important for their enterprise.



Figure 3. The HR-ISE model with basic lean tools [6]

This research for detailed definition of the HR-ISE model included 37 successful and developed Croatian enterprises from different industrial areas. Most of the enterprises that were surveyed belong to shipbuilding and automotive industry (33% of surveyed enterprises). The survey covered enterprises from all regions in Croatia and some regions in Bosnia and Herzegovina. There are a different number of employees in the surveyed enterprises, Fig. 4. Most of them have over 250 employees.

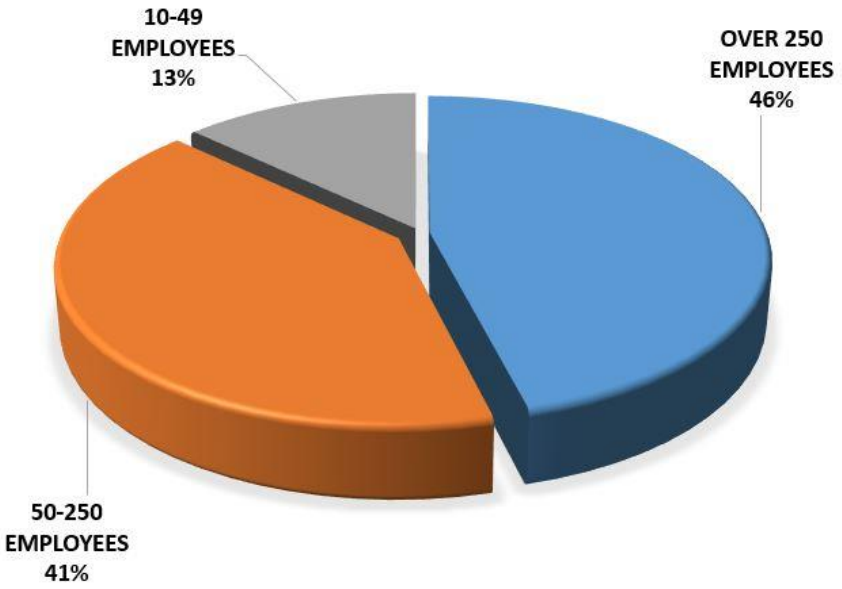


Figure 4. Number of employees in surveyed enterprises

Collected data were analyzed and the new HR-ISE model was created. The HR-ISE model for achieving production improvement offers a potential strategic program with lean principles for companies in Croatia, considering the current state of Croatian industry, Fig. 5. Manufacturing strategy is the foundation of any enterprise. The HR-ISE model should be part of manufacturing strategy. If the enterprise uses few lean principles, the HR-ISE model will complement existing manufacturing strategy. The cost reduction is the fourth important objective so an existing production strategy can only be better with the introduction of the HR-ISE model. At the beginning, it is necessary to find a balance between existing manufacturing strategy and the HR-ISE model, it is possible to influence on a positive thinking about changes through communication about implementation. The first step should be the implementation of lean tools and then is easier to move towards Industry 4.0. Both education and communication are important for successful implementation of the HR-ISE model. The team of experts should be determined and implementation should start with the implementation plan for the enterprise. It should be perfectly clear and understandable to every employee. This implementation should be evaluated every specified period by independent experts. With continuous analysis of the current processes and products, the entire production system can be well organized.



Figure 5. The HR-ISE model [11]

Most surveyed enterprises never had some model that is close to the HR-ISE model and only 15% of surveyed enterprises had already implemented a few lean principles [11]. At the top of the HR-ISE model is main objective customer satisfaction. There are also other objectives but they belong to the foundations of the model. The HR-ISE model represents a model that helps reduce costs what have shown case studies presented in this paper. Developed HR-ISE model is applied in several companies in Croatia and Bosnia and Hercegovina. Two case studies are described below.

4. CASE STUDIES

4.1 Končar Power Transformers - KPT

Production of transformers began in the year 1945, within “Rade Končar” in Zagreb – Croatia. Today Končar-Power Transformers Ltd. (KPT) is a joint venture of Siemens AG and “Končar-Electrical Industry” PLC. Over the last five years, the company KPT generated more than 96% of its revenue by exporting products and services to more than ninety countries in the world [7]. KPT’s production program (Fig. 5) contains:

- generator power transformers,
- large transmission transformers and autotransformers,

- HVDC transformers,
- special transformers and
- customer service.



Figure 5. KPT's production program [8]

The company continuously increases its intellectual capital and develops its ability to respond to all market challenges in a transparent and sustainable way. The main aim is to develop employee's personal skills and knowledge in order to achieve better productivity and efficiency across the entire lifecycle. Challenges in the global market, such as price reduction of transformers, the rise in prices of materials, increased competition and increased workloads are growing. One of the possible answers to sustainability issues is increased efficiency in all company's operations. In 2011, Management board and top management of KPT decided on improvements and changes to existing operations. All employees were included. They were asked to accept and actively support new activities. Special care was focused on behavior changes. The large scale project "SVE5" (System of high efficiency power transformers processes) was started. This project was based on the application of Lean methodology and culture in all existing operations. It included implementation of methods and tools such as value flow analysis, process mapping, implementation of proposed improvements and reward system. Generally, the focus is on people because it is necessary to invest in their knowledge. At the other side, the company invests in a development of product lifecycle management, manufacturing execution systems and also automation software, everything is gathered on the Siemens collaboration platform "Team center". Their Smart factory concept is based on the HR-ISE model. There were several workshops between INSENT research group and KPT employees. KPT implemented lean tools form the HR-ISE model and next step is to introduce digitalization in the production process. The KPT's Smart factory concept is shown in figure 6.

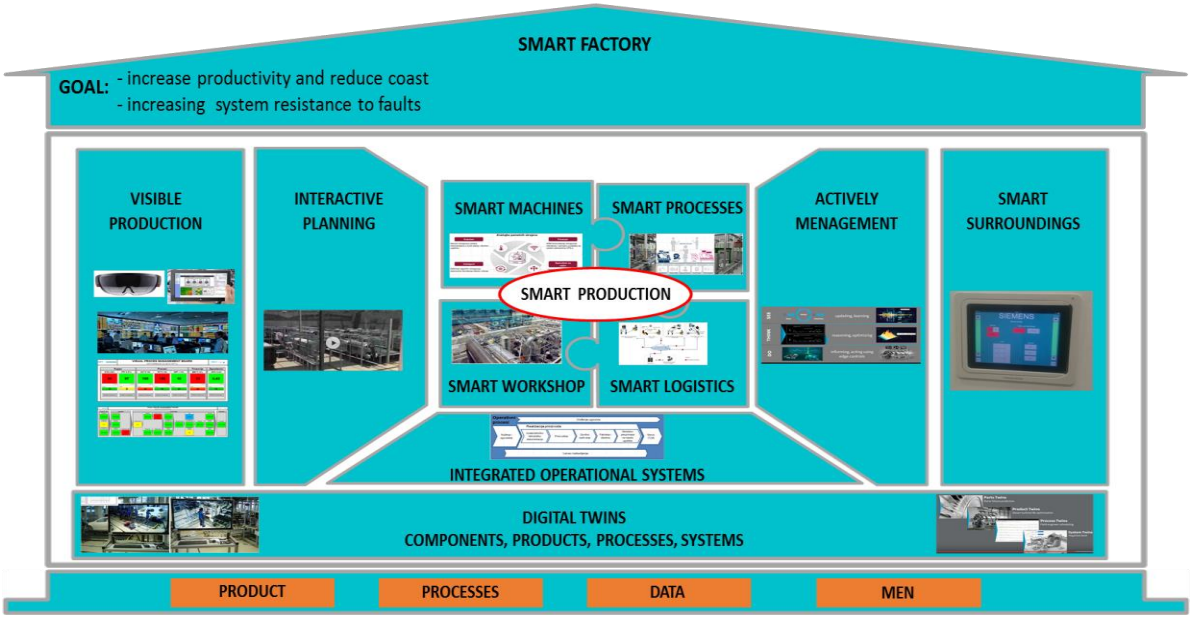


Figure 6. Strategy for creating a smart factory in KPT [9]

The whole process was very successful and today there is a new state with continuous improvement. The implementation of each area is followed by leaders of lean implementation, table 1. shows some examples that are followed and measured in one year according to the previous year.

Table 1. Several activities and measurement to show current state (one period of implementation)

No.	Activity	Measurement unit	Reference point	Long-term goal	Medium-term goal (3years)	Short-term goal (1year)	Current state
1.	Just in time delivery	%	99	99,5	99	98	97,8
2.	Education of employees - Lean	%	100	100	50	30	20
3.	Value stream mapping	%	100	100	90	85	80
4.	Pull system implementation	%	100	80	50	30	20
5.	Production costs reduction	%	90	85	93	97	100

This case study shows an example of a company that moves towards Industry 4.0 through lean implementation which is an excellent base for the introduction of digitalization.

4.2. Oprema

The core business of company Oprema d.d. is the production of refrigeration and ventilation equipment except for households. There are also other products like cooling units with primary production of refrigeration for cooling and dispensing beer, devices for cooling and dispensing soft drinks, water or soda water. The most significant part of the product range, over 75%, is devices for cooling and dispensing beer [10]. Main processes in Oprema d.d. are production, research and development, construction, design, technology development, marketing and sales. Their aim is to have products characterized by high performance, quality and modern design. Main goals are achieved through the attraction of new customers as well as keeping the old ones, which is visible through a constant annual growth of production and sales of about 10%. The company is on a global market for many years and within 5 largest producers of cooling and dispensing drinks in the world. For them is also very important to improve knowledge of all employees [11]. The core priorities of their company are improvements and work on eliminating process losses. Developed model for implementation of lean methodology is shown in Fig. 7.

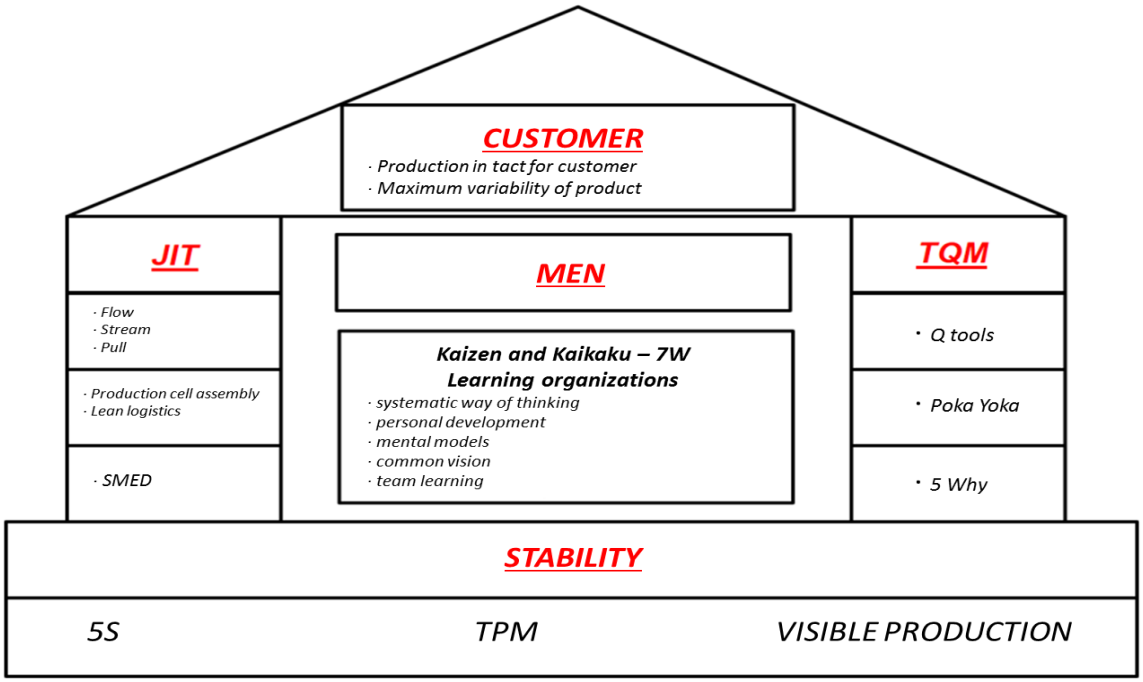


Figure 7. Model for improvement in the company Oprema d.d.

The company focuses on the customer satisfaction through analysis of customer needs and market analysis. It supports innovations especially on the development of a smart and energy-efficient product as well as on Lean implementation in manufacturing processes. The lean implementation started and now it is necessary to measure activities. The

implementation of the HR-ISE model was realized and it is necessary to sustain this model in production but also in other processes in company. Their new plans are focused on digitalization of production line and other movements towards Industry 4.0.

5. CONCLUSION

The HR-ISE model shown in this paper is developed for Croatian industry. It is the result of deep analysis of company attitudes and the literature research. Obviously, Croatian companies are aware of what they have to do in order to achieve their objectives in the future. This paper presents two case studies for companies that are very successful on the global market. These companies want to follow new trends and they make great efforts to move towards Industry 4.0. Whole results that come from INSENT research are defined in accordance with current needs of Croatian manufacturing companies. According to the results of these two case studies, appears conclusion that it is possible to implement the HR-ISE model but it is important to make it sustainable. The best way to do it is to educate people about lean methodology and digitalization skills and create a positive attitude about the whole process. The role of employees is the most important for implementation of the HR-ISE model. Meaningful implementation of the HR-ISE model is a big challenge but if the company insists, it is achievable. After this two case studies, there are some new questions about the HR-ISE model and its connection with production strategy for each company. Also, there are questions about the adaptation of the model to the possibilities of the company. Further research will be focused on the introduction of digitalization process within the HR-ISE model, always in cooperation with companies that need it – Croatian manufacturing companies.

6. ACKNOWLEDGEMENT

This work has been fully supported by Croatian Science Foundation under the project 1353 Innovative Smart Enterprise (INSENT).

REFERENCES

1. **Mourtzis, D., (2016), "**Challenges and future perspectives for the life cycle of manufacturing networks in the mass customization era", Logistics Research, 9(1), 2.

2. **Kagermann H., Wahlster W. and Helbig J., (2013), "**Recommendations for implementing the strategic initiative INDUSTRIE 4.0", Heilmeyer und Sernau, Germany**.**

3. **Lee, J., Bagheri, B. and Kao, H. A., (2015),** "A cyber-physical systems architecture for industry 4.0-based manufacturing systems", Manufacturing Letters, 3, 18-23.

4. **Netland T. H., (2013),** “Company specific production systems: Managing production improvement in global firms, University of Science and Technology Management Department of Industrial Economics and Technology Management”, Trondheim, Norway

5. **Womack, J. P., Jones, D. T. and Roos, D., (2007),** “The machine that changed the world: The story of lean production, Toyota’s secret weapon in the global car wars that is revolutionizing world industry (New Ed.)”. New York.

6. **Veza I., Mladineo M. and Gjeldum N., (2016),** “Selection of the basic lean tools for development of Croatian model of Innovative Smart Enterprise”, Tehnički vjesnik 23.5 (2016): pp. 1317-1324.

7. **Zagorec, I. and Hegedić M. (2016), “**Lean Implementation Status Measurement, LEAN Spring Summit 2016, Lean Management and Industry 4.0 as drivers of the rapid development of Croatian economy and society”, Book of Proceedings Šibenik, pp. 61-71

8. http://kpt.hr/en/, visited 20 January 2018

9. **Pavić, D. and Zagorec, I. (2017),** “Strategy Industry 4.0”, 7. GALP conference, Book of Proceedings, Zagreb, pp. 105-108

10. https://www.oprema.com/, visited 23 January 2018

11. **Crnjac, M., Mladineo, M. and Veža, I. (2017), “**The Croatian model of innovative smart enterprise (HR-ISE model)”, CIM 2017.

ELDERLY AND DISABLED CENTERED DESIGN

Bulent YILMAZ, *bulent.yilmaz@bilecik.edu.tr* Bilecik Seyh Edebali University, Bilecik, Turkey

ABSTRACT

The number of elderly and disabled people in the world population is increasing dramatically. According to the data of United Nations Population Fund, OECD-EU and TUIK-Turkey; nearly 12.3% of the world's population is elderly (60 years and over) and 15% is individuals with disabilities (such as in seeing, hearing, walking, touching, speaking and learning). With this data; it can be concluded that today, approximately 900 million elderly and 1 billion disabled individuals live in the world. In addition, about 200 million of these disabled people are in need of special care. Demographic shows that societies are getting elder and number of the disabled individuals is on increase. For today and future, this is a crucial problem.

Daily routine for elders and disableds is very tough. They can experience hardness on entertainment, education, working life and health. Some scientific and technological disciplines, such as industrial design, industrial engineering, ergonomics, geriatrics, make effort for the needs of these individuals. To increase the quality of life of these people, new products and technologies are being developed.

In this study, we discussed the the needs of the elderly and disabled individuals in the context of the “elderly and disabled centered design”. We hope that this point of view has potential to form a new area in universal design.

Keywords: Elderly and disabled individuals, universal design, elderly and disabled centered design

1. INTRODUCTION

The person’s change over time is the specific characteristic of the elderly and aging comes with the inevitable decline in physical and cognitive function which makes living independently difficult in many ways. The world population is now at least 7.6 billion and the percentage of seniors from the world population has become very high and is predicted to increase even more within dozens of years [United Nations, Department of Economic and Social Affairs, & Population Division]. According to data from World Population Prospects: the 2017 Revision, the number of older persons, those aged 60 years or over, is expected to more

than double by 2050 and to more than triple by 2100, rising from 962 million globally in 2017 to 2.1 billion in 2050 and 3.1 billion in 2100. Globally, population aged 60 or over is growing faster than all younger age groups.

According to a research by European commission, life expectancy of Europeans has increased and people are living longer and healthier. On the other hand, fertility rates are below replacement level and that is causing a decline in population growth, as the postwar baby boomers age in the coming decades. It is predicted that the low fertility rate in the long run will create a gap in working force as the aged population retires without enough replacement [European Commission, 2014]. Aging can be identified as a process that contains some changes in personal appearance, functions and it also shows some differences from one person to another. Older adults are often faced with functional problems that tend to compound with age [Raban, Y. and M. Brynin, 2006, Zimmer, Z. and N. Chappell 1999] leaving them with limited active life choices. Older people need the help of others to manage basic routines in their daily lives [Ahanathapillai et al., 2015]. Carstens [Cartens, 1993] defines that, during the aging process, positive changes appear such as growth and maturity (Table 1).

Table 1. The age-loss continuum [Carstens D. 1993]

Losses: Age	30	40	50	60	70	80	90
Separation of children			x				
Death of peers					x		
Loss of spouse					x		
Motor output deterioration						x	
Sensory acuity losses					x		
Age-related health problems						x	
Reduced physical mobility						x	

The aging process turns up in people’s biophysical, social, and psychological characteristics, as depicted in Figure 1.

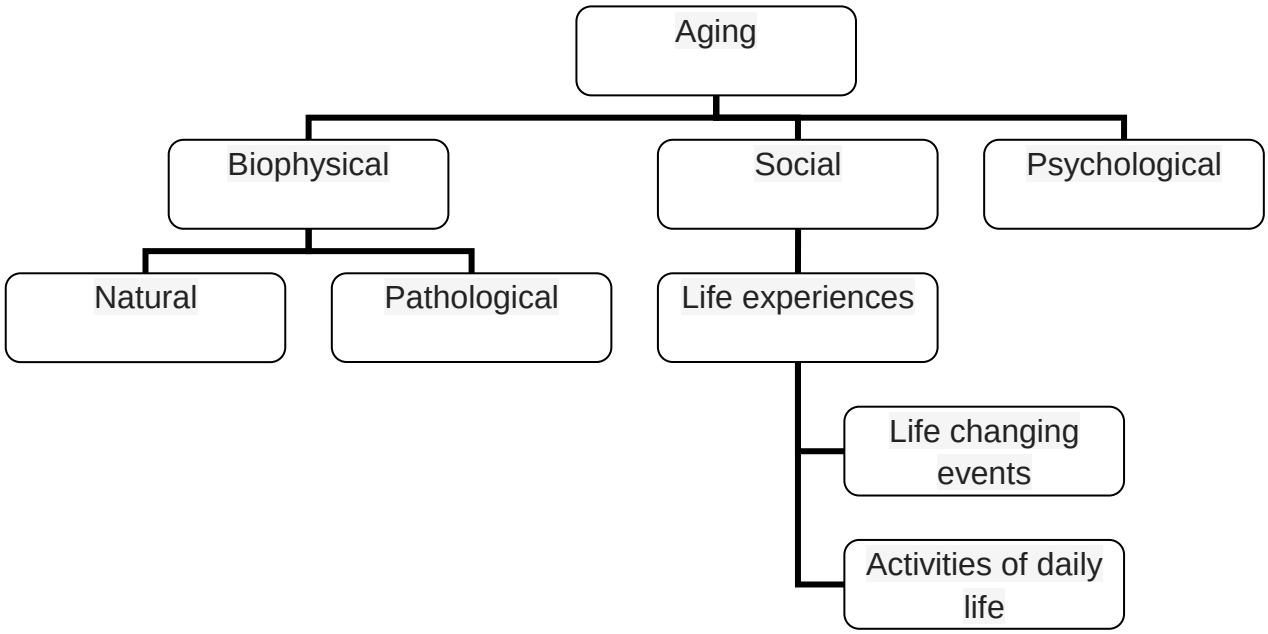


Figure 1. Problems of the aging process

For example, fourty per cent of those aged 65 years and older are limited in physical activity [Tornstam, L., 1996]. Most studies have targeted eight older adults' problems: (1) dependent living, (2) fall risk, (3) chronic disease, (4) dementia, (5) social isolation, (6) depression, (7) poor wellbeing, and (8) poor medication management [Khosravi, P. and A. Ghapanchi, 2016]. However, disability is an impairment that may be cognitive, developmental, intellectual, mental, physical, sensory, or some combination of these. While not all older persons have disabilities, the prevalence of disability is highest amongst this demographic group. The higher life expectancy implies the need for products that support and ease the senior life in both cases. Technology and design can help elder and disabled people to maintain a good quality of life. In other words, assistive technology is the answer to the question. With supporting seniors with products that fit their needs and wants, the quality of life can be maintained as good as possible. The aim of this study is to identify the problems that can occur concerning for disabled and elderly people and to suggest solutions by industrial design science to these problems where possible. In this study, old age and disability were evaluated in the same scope,

2. ASSISTIVE TECHNOLOGY

Today, globally, more than 1 billion people need 1 or more assistive products. ‘‘Using a conservative assumption of 20% of the population aged 60 and older being in need of two assistive devices (AD), each lead to a global estimate of at least 800 million items being in use by older people in the year 2050’’ [Garçon et al. 2016]. Assistive products or technology is an umbrella term covering the systems and services related to the delivery of assistive

products and services. In addition to the term ‘‘assistive technology’’ refers to equipment and services that support and maintain the declined physical and cognitive functions due to age and disability [Reisinger & Ripat, 2014].

and the disabled & elderly ATs provides devices that help to overcome cognitive difficulties, impairments, and disabilities in disabled & geriatric population. Assistive technologies (ATs) are designed to improve the functional capabilities of people with disabilities. Some are relatively low-tech and very familiar, such as such as reading glasses, crutches and hearing aids. Others are more advanced, using cutting-edge science and technology, with future ATs under development that could have a huge impact on all our lives.

World Health Organization (WHO) defines assistive technology as any product that helps maintain or improve an individual function. The idea of assisted technologies (ATs) refers to an innovative concept that integrates technology within elderly and disabled persons in order to maintain and even enhance functional health, security, safety and quality of life of their special life. ATs denote a broad range of devices, services, strategies, and practices that are conceived and applied to ameliorate the problems faced by individuals who have disabilities [Cook, A. and J. Polgar, 2014]. ATs enables people to live healthy, productive, independent, and dignified lives, and to participate in education, the labour market and civic life. Whilst ATs have a role in maintaining the independence and quality of life of both people living with disabilities and their careers, their use have both advantages and disadvantages, can pose challenges for all concerned, and raises ethical dilemmas [Bhattacharyya, S. and S. Benbow, 2015].

Table 2. Classes of AT

Class	**Product examples**
Products for cognitive functions,	Memory devices and pill box reminders,
Products for sensory functions,	Spectacles, software for screen magnification and reading, hearing aids,
Products related to orthotics and prosthetics,	Artificial limbs (prosthesis), spinal orthotics and cervical collar,
Products for personal mobility,	Wheelchairs, canes and crutches,
Products for activities of daily living including personal care and protection,	Toilet chairs, diapers and robots,
Products for communication and skills training,	Voice and speech training devices, Braille apparatus and screen readers,
Products for recreation and sports,	Modified sports equipment,
Products for housing, work and environmental improvement,	Home modification, handrails or grab bar and controlled lighting,

There is a vast range of AT; according to the WHO [WHO Shifting the paradigm, 2014] most of these products can be divided into several classes (Table 2).

People who most need assistive technology include: People with disabilities, elderly people, people with noncommunicable diseases, people with mental health conditions, people with gradual functional decline.

Hearing aids, wheelchairs, communication aids, spectacles, prostheses, pill organizers and memory aids are all examples of assistive products.

Among the most commonly used assistive technology devices; custom made kitchen devices, Bathroom aids, location devices, edication devices, fire and smoke alarms and monitoring and surveillance devices are few examples [Seiler, 2007]. They include but are not limited to mobility aids, vision and hearing aids, furniture or daily living aids, gadgets or small aids, and adaptation to accommodation [McCreadie, C. and A. Tinker, 2005]. Mobility aids enhance the movement of persons with physical disabilities that affect movement. Devices such as various canes, walkers, manual wheelchairs, and power mobility devices help those who can walk some of the time, and whose main mobility problem is one of endurance rather than balance or coordination [Hoenig, H., et al., 2015]. Examples include wheelchairs, scooters, walkers, canes, crutches, prosthetic devices, and orthotic devices, to enhance their mobility.

Furthermore, ‘Smart homes’ that are equipped with assistive devices and systems, that enable frail elderly people to coup with health-related difficulties such as falls, sensory impairment, diminished mobility, medication management and other issues related to diminished cognitive function are being designed and implemented [Demiris & Hensel, 2008].

2.1. Essential tools

AT products; maintain or improve an individual’s functioning and independence, thereby promoting their well-being. Also, AT products; reduces the need for formal health and support services, long-term care and the work of caregivers. This products can have a positive impact on the health and well-being of a person and their family, as well as broader socioeconomic benefits. AT can enable older people to continue to live at home and delay or prevent the need for long-term care [Lansley P, McCreadie C, Tinker A. Age Ageing. 2004]. Proper use of hearing aids by young children leads to improved language skills, without which a person with hearing loss has severely limited opportunities for education and employment Olusanya BO, Newton VE. Lancet. 2007]. Manual wheelchairs increase access to education and employment while reducing healthcare costs due to a reduction in the risk of pressure sores and contractures. Without AT people are often excluded, isolated, and

locked into poverty, thereby increasing the impact of disease and disability on a person, their family, and society. However, only 1 in 10 people in need have access to assistive technology due to high costs and a lack of awareness, availability, trained personnel, policy, and financing. These technologies improve health outcomes, assist in independent living, and reduce healthcare costs by lowering cost given to manual labors in assisting patients. Furthermore, disabled & elderly assistive devices provide devices for the population who are not self-dependent.

In the future, with an aging global population and a rise in noncommunicable diseases, more than 2 billion people will need at least 1 assistive product by 2050, with many older people needing 2 or more, according to a WHO assistive device fact sheet. The market has witnessed tremendous development in the assistive technologies and have evolved in terms of both performance and characteristics. Today, AT products are an important area of product design and development. There is a product list that includes a large number of products and priority in the sector (Table 3).

In adition to, Researches about the assistive technology indicate that people do not like the medical and technical appearance of these products. This shows that they are more in need of industrial design. Industrial design has a unique and professional point of view from which to modify living environments (including the design of products for those environments)

Table 3. Assistive Technology Products and Priority List [World Health Organization 2016]

1. Alarm signallers with light	2. Audioplayers with DAISY	3. Braille displays (note	4. Braille writing equipment/brailers	5. Canes/sticks
6. Chairs for shower, bath, toilet	7. Closed captioning displays	8. Club foot braces	9. Communication boards, boks, cards	10. Communication software
11. Crutches, axillary, elbow	12. Deaf blind communicators	13. Fall detectors	14. Gesture to voice technology	15. Global positioning system (GPS) locators
16. Hand rails, grab bars	17. Hearing aids (digital) and batteries	18. Hearing loops/FM systems	19. Incontinence products, absorbent	20. Keyboard and mouse emulation software
21. Magnifiers, digital hand-held	22. Magnifiers, optical	23. Orthoses, lower limb	24. Orthoses, spinal	25. Orthoses, upper limb
26. Personal digital assistant (PDA)	27. Personal emergency alarm systems	28. Pill organizers	29. Pressure relief cushions	30. Pressure relief mattresses
31. Prostheses, lower limb	32. Ramps, portable	33. Recorders	34. Rollators	35. Screen readers
36. Simplified mobile phones	37. Spectacles; low vision, short distance, long distance, filters and protection	38. Standing frames, adjustable	39. Therapeutic footwear; diabetic, neuropathic, orthopaedic	40. Time management products
41. Travel aids, portable	42. Tricycles	43. Video communication devices	44. Walking frames/walkers	45. Watches, talking/touching
46. Wheelchairs, manual for active use	47. Wheel chairs, manual assistant-controlled	48. Wheel chairs, manual with postural support	49. Wheelchairs, electrically powered	50. White canes

2.2. Accessibility

Globally, more than 1 billion people need one or more assistive products. Examples of the unmet global need for assistive technology include. The World Health Organization (WHO) estimates that 285 million people are visually impaired worldwide.200 million people with low vision who do not have access to glasses or other low-vision devices. 70 million people who need a wheelchair and only 5% to 15% of those in need who have access to one. 360 million people globally have moderate to profound hearing loss. Hearing aid production currently

meets less than 10% of the global need. Huge workforce shortages in assistive technology: over 75% of low-income countries have no prosthetic and orthotics training programmes. The global elderly and disabled assistive devices market was valued at $14 billion in 2015 and is expected to surpass $26 billion by 2024, according to Coherent Market Insights [McCue, T.J., 2017]. There are roughly 13,000 commercially available aids and devices for people with disabilities, but most are only available through occupational therapists, doctors, medical supply houses or specialized mail-order catalogues. It is important for the whole society that all people have access to products, services and environments. Across the globe, many people who need assistive technology do not have access to it. So that older persons and people with disabilities may participate in society on equal terms, it is necessary to improve the accessibility of products, services and environments. The importance of accessibility was recognized when UN member states signed the UN Standard Rules on the Equalization of Opportunities for Persons with Disabilities and the UN Principles for Older Persons. In addition to, the demand for well-designed products for these groups of people can rise.

3. UNIVERSAL DESIGN

Universal design is a relatively new paradigm that emerged from "barrier-free" or "accessible design" and "assistive technology". Universal design is an approach to the design of all products and environments to be as usable as possible by as many people as possible regardless of age, ability, or situation. Barrier free design and assistive technology provide a level of accessibility for people with disabilities.

3.1. The Principles of Universal Design

Equity: Useful and appealing to people with diverse abilities, used in the same or equivalent way by everyone (Figure 1);



Figure 1. Billboard-size captioned video screen at public event allows hearing-impaired attendees to sit anywhere (in Eskişehir/Turkey)

Flexibility: accommodates a range of preferences and abilities, provides choice in method of use, facilitates accuracy and precision, adapts to user constraints and pace (Figure 2);



Figure 2. Adjacent ramp and stairs provide choice of access to building.

Simplicity: Easy or intuitive regardless of experience, knowledge base, language skills, and level of concentration; consistent with users' expectations, eliminates complexity, provides cues, prompts, and feedback (Figure 3);



Figure 3. The Figure on the right illustrates the back of a television with colour-coded plugs and receptacles that simplify installation.

Perceptibility: communicates necessary information regardless of ambient conditions and the expected range of user sensory ability. Redundant modes of presentation through different senses (verbal, written, auditory, tactile), highlights essential information, differentiates elements, maximizes legibility, compatible with glasses, hearing aids, walkers, etc (Figure 4);

Error recovery: Minimizes hazards and unintended actions; useful elements are accessible, hazardous elements are sequestered or eliminated, fail-safe features incorporated, warning signals, not dependent on vigilance (Figure 5);



Figure 4. Dark background on overhead Atatürk airport terminal in İstanbul-Turkey signage contrasts with lighted ceiling.



Figure 5. Clothing iron shuts off automatically after 5 minutes of non-use.

Low effort: can be used comfortably with minimal strain or fatigue; minimizes force or sustained effort, minimizes repetitive actions, requires neutral body positions (Figure 6);



Figure 6. Split, angled keyboard allows computer operator to maintain neutral position from elbow to fingers

Accessibility: Accessible for expected range of body size, posture, or mobility; clear sight lines, comfortable reach, accommodates variations in hand grip or size, minimizes physical barriers (Figure 7);



Figure 7. Wide gate at subway station accommodates wheelchair users as well as commuters with packages or luggage.

4. DESIGN FOR ELDERLY AND DISABLED PERSONS

The importance of designing for elderly and disabled persons becomes more and more obvious. Because, individuals with physical, sensory, or cognitive disabilities have special needs for interacting with their environment. Elderly and disabled person have different preferences with regard to valued attributes than average adults, which have to be considered during product development. In order to appoint elderly and disable persons needs, their characteristics and influence on products has to be clarified.

Designers are used to defining problems. This is the first step in designing any product. Designers understand the interactions among people, products, and environments. They are students of living. The first step, an easy one, is to transfer this knowledge to the special case of older people and the places where they live or would like to live. The best designers never impose a solution upon a problem; rather, they derive a solution from the problem. (Perhaps only the rare genius in invention can engender true solutions outside the context of a given problem). With designers, of course, the solution is almost always a product.

The most recent product design for elder and disabled peoples with disabilities centers on "assistive device technology," making sophisticated electronic aids, computers and other devices more widely available to the people who need them. This influences their wellbeing, related to their outlook on life, their needs and wants and above all their ability to use products. Poorly designed products and environments that may merely inconvenience users normally become insurmountable with such limitations potentially transforming someone’s everyday world into an unsafe and insecure place. Every product is designed for addressing a particular intention. Functional limitations in vision, hearing and mobility interact and often aggravate each other. Development of a new product requires for elder and disabled peoples a study to the possibly involved body functions of eldely and disabled person and their corresponding possible limitations. Products also have certain attributes that can be

considered in product development according to the way older people value. The main reason for a design challenge for a product for this adults is a problem caused by functional limitations. To enumerate there is a number of factors which have to be considered in the design of elderly and disabled person;

- Disabilities that cause the problem,
- Disabilities that influence product use,
- Empathy creation of the target group among developers,
- Consideration of the presence of stigmas,

The design challenge could be the improvement of an existing product (redesign) or the development of a new product.

4.1. Design constraints;

The heterogeneity of the older and disabled causes differences with designing for the normal persons. In comparison with normal persons these differences are in short:

- Elderly and disabled their social position has changed (social)
- Elderly and disabled their well-being and subjective health declines (psychological)
- Elderly and disabled cannot adapt to new products that fast (adoption)
- Elderly have different attitudes to technology, its use is less self-evident (acceptation)
- Elderly are at the last stage of life (life stage)
- Elderly are in an ongoing aging process (limitations)
- Elderly have specific attitudes to innovative products (attitude)

When they don’t want to be associated with elderly stereotypes they don’t use products which refer to them.

4.2. Standards

Older persons and people with disabilities are important user and consumer groups. Standardization greatly influences the design of products and services that are of interest to the consumer and can therefore play an important role in this field. It is recognized that all standards cannot meet the needs of all people with severe and complex disabilities.

5. CONCLUSIONS

The aging population disabled people and is a universal issue and needs a universal perspective. The concept of Universal Design that is suitable for the majority of the elder and disable person is becoming of great importance within the society. As a result of this study, the following findings were obtained;

- There are other large sections of the population that need special design in the society,
- Universal Design is more commonly available related to lower costs than special products,
- Increased numbers of older consumers form a significant buying force in changing market place,
- If products are designed to consider the all people, adaptations for people with disability because of age, physical, sensory, or cognitive ability will be reduced,
- There is an increasing market and demand for products that are designed for all profits all consumers. This explains why universal design is so important,
- Products for elderly people should be performed well, convenient to use and attractive and products in the market should respond the requirements such as accessibility, adaptability, adjustability, and availability,
- Features that make a product accessible to older and disabled people generally allow everyone to use products easily,
- Increasing usability and convenience for the widest range of people spread out the customer base and so expands marketability and reduce costs for assistive technology,
- Disability can be a way into understanding how different bodies use the space around us,
- Improving our understanding of disability and ability is an important step in helping us to take notice and develop approaches to the diverse ways we inhabit the material world.

REFERENCES

1. European commission (2014), Population ageing in Europe: facts, implications and policies,https://ec.europa.eu/research/socialsciences/pdf/policy_reviews/kina26426enc.pdf.
2. Raban, Y. and M. Brynin, (2006), Older people and new technologies. Computers, phones, and the Internet: Domesticating information technology, p. 43-50.
3. Zimmer, Z. and N. (1999), Chappell, Receptivity to new technology among older adults. Disability&Rehabilitation, 21(5-6): p. 222-230.
4. Ahantapillai, Amorb, James (2015), Assistive technology to monitor activity, health and wellbeing in old age: The wrist wearable unit in the USEFIL project, Technology and Disability Journal (27), p17–29.
5. Carstens D., (1993). Site Planning and Design For the Elderly: Issues, Guidelines, and Alternatives, (Van Nostrand Reinhold, New York).
6. Tornstam, L., (1996), Caring for the Elderly. Scandinavian Journal of Caring Sciences, 10(3): p. 144-150.
7. Khosravi, P. and A. Ghapanchi, (2016), investigating the effectiveness of technologies applied to assistseniors: A systematic literature review. International journal of medical informatics, 85(1): p. 17-26.
8. Garçon, Khasnabis, Walker, Nakatani, Lapitan, Borg, Ross, Berumen (2016) Medi-cal and Assistive Health Technology: Meeting the Needs of Aging Populations, Gerontologist, Vol. 56 (2) p293–302.
9. Reisinger & Ripat (2014), Assistive technology provision within the Navajo Nation: user and provider perceptions, Qualitative Health Research vol 24(11):p1501-1517,
10. Cook, A. and J. Polgar, (2014), Assistive technologies: Principles and practice: Elsevier Health Sciences.
11. Bhattacharyya, S. and S. Benbow, (2015),Carers of People with Dementia and the Use of Assistive Technologies. Advanced Technological Solutions for E-Health and Dementia Patient Monitoring, p.12.
12. World Health Organization.(2014), Opening the gate for assistive health technology: Shifting the paradigm. Secondary Opening the gate for assistive health technology: Shifting the paradigm.

13. Seiler (2007), Assistive Technology for Individuals with Cognitive Impairments, http://idahoat.org/Portals/60/Documents/Services/Resources/AT_CognitiveImpairmentsHandbook.pdf,
14. McCreadie, C. and A. Tinker, (2005), The acceptability of assistive technology to older people. Ageing and Society, 25(01): p. 91-110.
15. Hoenig, H., et al., (2015), One Size Does Not Fit All—Mobility Device Type Affects Speed, Collisions, Fatigue, and Pain. Archives of physical medicine and rehabilitation, 96(3): p. 489-497.
16. [Lansley P, McCreadie C, Tinker A. Age Ageing. 2004 Can adapting the homes of older people and providing assistive technology pay its way? Nov;33(6):571-6. Epub 2004 Sep 3].
17. [Olusanya BO, Newton VE. Lancet. 2007 Global burden of childhood hearing impairment and disease control priorities for developing countries. Apr 14;369(9569):1314-7].
18. Demiris & Hensel (2008), Technology for an ageing society: A systematic review of 'smart home' applications, IMIA year book of medical informatics, 4 (suppl 1) p33-40.
19. World Health Organization (2016), Priority Assistive Products List, EQUIPPING, ENABLING AND EMPOWERING.
20. McCue , TJ "Elderly And Disabled Assistive Technology Market To Surpass $26 Billion By 2024, March 21, 2017".

WALKMECH2.0: CONCEPTUAL DESIGN AND STRUCTURAL ANALYSES OF AN ENERGY-RECYCLING TRANSFEMORAL PROSTHESIS FOR ACTIVITIES OF DAILY LIFE

M. Furkan BALTACIOĞLU, *furkan.baltacioglu@agu.edu.tr* Abdullah Gul University, 38080, Kayseri, Turkey

Ramazan ÜNAL, *ramazan.unal@agu.edu.tr* Abdullah Gul University, 38080, Kayseri, Turkey

ABSTRACT

This paper presents the conceptual design of an energy-recycling transfemoral prosthesis providing daily activities, e.g. walking, sit-to-stand and stair climbing. The design is the second phase of a prosthesis called WalkMECH which was designed for providing ankle push-off power during walking by storing and exchanging energy for the ankle and knee joints. In this study we improved the design for providing weight acceptance with a knee flexion, sit-to-stand and stair climbing motions with defining elastic elements according to biomechanical data. Following the CAD model of the conceptual design, we implemented structural analysis for ankle and knee to evaluate the design.

Keywords: Lower-limb prosthetics, Motion Analysis, Design, Biomechanics

1. INTRODUCTION

Transfemoral prostheses are designed to replace knee and ankle joints of individuals who had above-knee amputation. There are varieties of reasons for amputations, however, diabetes, trauma, tumors and infections are considered to be the main reasons [Ertl, 2012]. In Latin America, Asia and Africa, the demand of prosthesis has been increased 25% in four years and reached to 30 millions in 2010 according to World Health Organization [Aleccia, 2010]. This demand has been increased 40% within 20 years only in USA due to increase in diabetes [US-CDC&P, 2016]. With the increased demand and the expectations from users together with the complex nature of human lower limb dynamics brought hard challenges for the design of transfemoral prosthesis that has become interesting subject of robotics field in recent years [Goldfarb, 2013; Johansen, 2016; Gibson, 2015; Hargrove, 2013; Shultz, 2015].

Lower-limb prostheses are categorized in two main groups as passive and active prostheses both in the literature and the market. However, studies in the last decade show that another group called semi-active prostheses has also taken a place in the lower-limb prosthetics field [Lambrecht, 2009; Minerva, 2011; Pfeifer, 2012; Villalpando, 2009; Rouse, 2011]. Passive prostheses do not have external energy input and are exploiting the dynamics of walking with their special kinematics. However, these prostheses have constant characteristics like stiffness, geometry and friction and therefore cannot adapt different conditions or walkin speeds. Furthermore, they cannot perform as its biological counter-part for the activities that requires net positive power like standing-up, stair ascending. Additionally, individuals' walking is far from being natural and their metabolic energy consumption is far more than normal (60-100% extra) [Waters, 1976]. There are also micro-porcessor controlled prostheses that could be considered in the subcategory of passive prostheses, since these devices are inherently passive and their actuators are used only to adapt different walking conditions. The most commonly used micro-processor controlled transfemoral prostheses in the market cause amputees walk without knee flexion during stance phase [van den Bogert, 2012]. However, there is at least 15^{o} of knee flexion in natural walking during this phase. It has also been observed that a healthy individual consumes 25% more metabolic energy while walking without this flexion [Zissimopoulos, 2007]. Even though the device allows this flexion, the reason for the user not doing this flexion would be due to the lack of positive power in the micro-porcessor controlled prostheses [Johansson, 2005; Segal, 2006]. Because, the user must provide the knee extension following this flexion by his/her hip with extra muscular effort and this is undesired situation for an amputee. The same situation applies also for standing up motin and amputee performs this motion by the power form the intact limb due to lack of extension moment in the prosthesis [Highsmith, 2011]. Stair ascending is also demanding high amount of positive work [Wilken, 2011].

On the other hand, it has been observed that cyclic motions like walking, running and sit to stand do not require net positive power from the knee joint [Winter, 1983a; Winter, 1983b], which could be achieved by using energy-store-and-elease systems. In [Zissimopoulos, 2007], the transition of energy storage element between stance and swing phases has been explained. Even though high reduction of metabolic energy consumption by using this system is achieved, the device has not been commercialized. It would be due to the focused design on walking that might not allow other activities and also the fact that the transition mechanism might not be safe enough to prevent knee buckling.

Active, prostheses can provide controllable energy input by means of actuators (pneumatic, hydraulic, DC motor) [Sup, 2008; Popovic, 2000, Bedard, 2003; Kapti, 2006; Geng, 2012; Flowers, 1973]. However, this kind of prostheses still have challenges in energy supply,

weight, price, perception and many other related issues that has yet to be addressed and designing a prosthesis functioning like a biological lower-limb is highly challenging design. With regard to semi-active type of prostheses that have energy storage capacity with elastic elements, some studies on actuator design field show that series elastic actuators (SEA) would reduce the power requirements of actuators [Villalpando, 2009]. Additionally, a combination of an elastic element connected to the motor serially can provide low impedances [Paine, 2014], absorb mechanical impacts, safer interaction with humans and store energy [Hollander, 2005]. Therefore, these actuators would be very useful for prosthetics applications.

In a study that reflects the recent developments in above-knee prostheses, the importance of utilization of elastic elements and re-cycling of mechanical energy have been highlighted [Bayram, 2015]. Also, it has been noted that walking quality, extra metabolic energy consumption of amputees and pain related to use of prosthesis have yet to be addressed despite of technological developments.

Recently, a thorough literature study has shown that there are 21 novel active prostheses study in total and 12 of them are for transfemoral prostheses [Windrich, 2016]. Only one of them has hydraulic and two of them have pneumatic actuators, the rest have electro-mechanical actuators. Additionally, it has been stated that only 2 out of 12 prostheses employ variable stiffness actuator (VSA), while 8 out of 9 studies on ankle prostheses have this type of actuators.

According to the design studies and the limitations of transfemoral prostheses available in the market, challenges like reducing the high metabolic energy consumption, the size of the actuators and the required power from the actuators greatly enhances the importance of a transfemoral prosthesis design that has high mechanical energy efficiency and can provide lower-limb motions by storing, returning and exhanging energy. Accordingly, employing elastic elements in the prosthesis to store energy as much as possible and return it to the joint in need so that the lower limb motions can be carried out naturally and efficiently is considered to be major principle for designing such a prosthesis.

Taking these factors into account, one of the authors in the study has previously designed energy-recycling transfemoral prosthesis [Unal, 2012a; Unal, 2010a; Unal, 2010b; Unal, 2012b]. This prosthesis designed and realized for providing ankle push-off power as in natural walking. Since the design of the elements of the prosthesis is determined according to biomechanical data [Rose, 2005; Winter, 1991], also the amputee gait was close to natural walking in quality. This design has also been further developed with a new design that can change the energy storage capacity to adapt walking at different speeds [Unal, 2014].

Studies have shown that motions other than walking, especially for the knee joint, require external power input [Bayram, 2014; Riener, 1999]. When this energy is not applied to the joint by means of an actuator, the user tries to compensate this energy via the intact limb and remaining hip joint. Considering the goals of energy-efficiency, reducing metabolic energy consumption and increasing walking quality; designing highly efficient transfemoral prosthesis that is based on the power flow on and between the joints and can perform the natural leg functions during daily activities closest to the biological counterpart is the main objective of this study.

2. DATA ANALYSIS

Walking Data for Knee Joint: It was emphasized that the lack of knee flexion and extension in stance phase could lead to back pain due to abnormal pelvic motions. In the first flexion of knee as shown in Fig. 1, between 0-14% of the gait cycle, knee accepts the body weight (weight acceptance-WA) which corresponds to K1 area in power plot of knee joint. K1 is the largest energy storage area during gait. Then knee extends between 14-40% of the gait cycle, to lift the body (Area K2). This extension following the first flexion can be identified as releasing the energy that is stored in the first flexion part around the knee joint. After this, the second flexion occurs (K3) which plays a vital role during gait. It is mainly the preparation of the next step and provides sufficient clearance to prevent the foot to strike the ground prematurely. Around 60% of the gait cycle, toe-off (TO) takes place so the foot leaves the ground completely. Around 72% of the stride the second extension of knee joint takes place (K4). These second flexion and extension correspond to swing phase of gait.

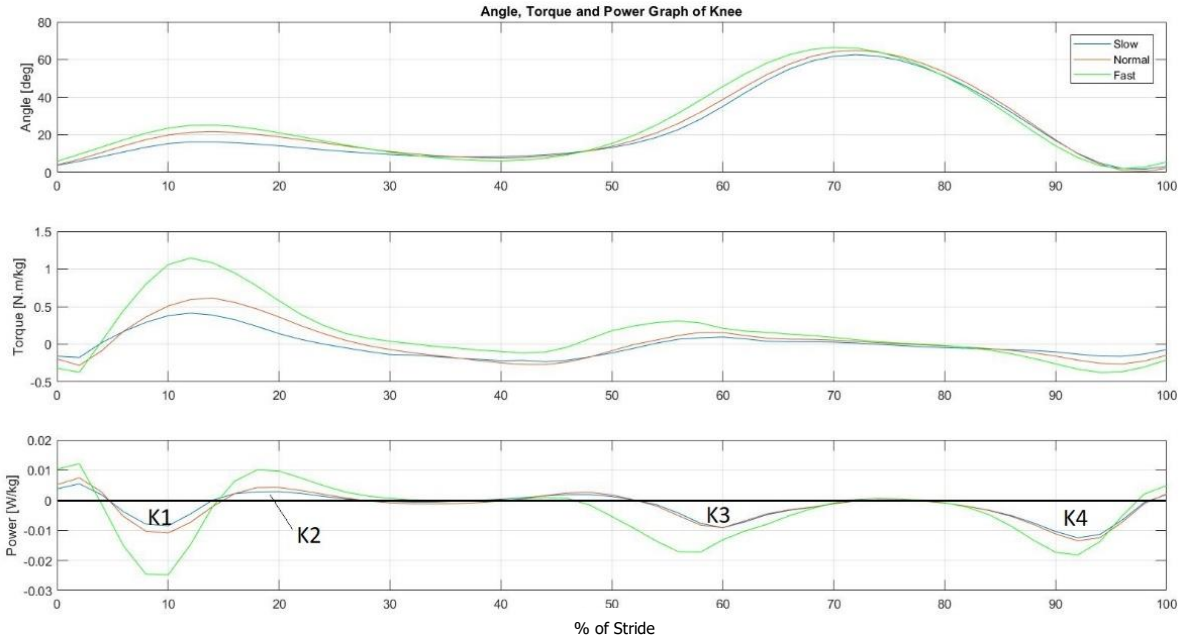


Figure 1 Angle, torque and power flow for natural knee joint in walking [Winter, 1991]

Sit-to-Stand Data for Knee Joint: Sit to stand motion can be described as to raise the body around knee joint. Fig. 2 depicts the torque behavior of knee joint during stand to sit motion. Torque value starts from 0 N-m and it gets higher as the angle of knee joint increases. Even though this relation shows some non-linearity towards the end to avoid the complexity, we approximate this relation with constant spring coefficient.

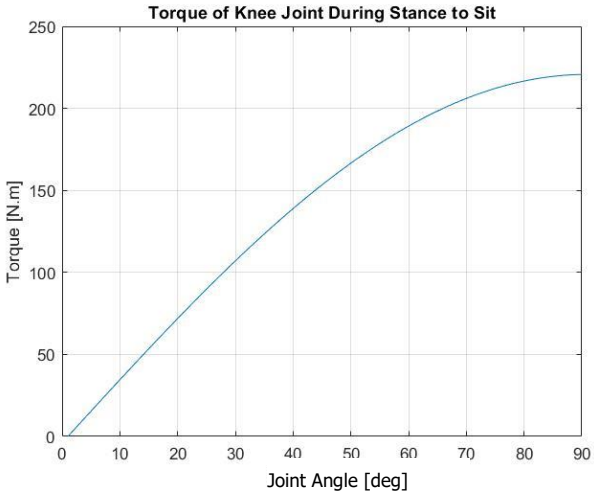


Figure 2 Knee joint torque in stand to sit

Stair Ascending Data for Knee Joint: Knee joint moment during stair ascent motion is depicted in Fig. 3. Knee moment starts from 0 [N.m/kg] and it increases to approximately 1.15 [N-m/kg] because the knee joint is responsible for raising the body on the stair. Then it decreases drastically to about 0 [N-m/kg]. Yet, we can see some fluctuation that is caused by the swing motion of the leg. Knee joint must provide the most of the moment until ∽18% and this moment is decreased linearly until ∽52%. Raising the body by knee corresponds to power generation boost in power plot. During this motion power generation increases from 0 [W/kg] to ∽2.5 [W/kg] and then decreases to 0 [W/kg]. After that, power fluctuates because of the swing motion of leg.

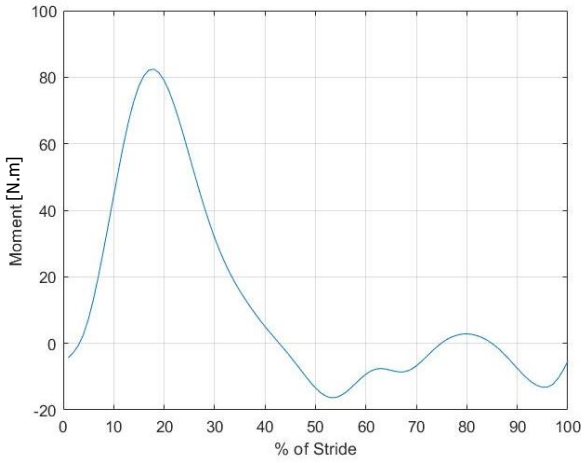


Figure 3 Knee joint moment in stair ascent

3. CONCEPTUAL DESIGN

Design Specifications: The mechanisms involved in the conceptual design in the light of the insight from the literature and the biomechanical data analysis are designed and their working principles are explained in detail in this section on CAD model of the conceptual design, shown in Fig. 4. The CAD model of the conceptual design of the prosthesis has been built according to the specifications of an individual weighing 80 kg and being 1.80 m tall. In summary from the previous sections, it has been understood that a completely passive device can be designed for walking, since the knee joint exhibits very little positive energy generation during walking, and studies have previously been carried out that can perform walking with a passive prosthesis design and provide the required push-off at the ankle [Unal, 2012a; Unal, 2010a; Unal, 2010b; Unal, 2012b]. However, since the stair ascending requires a significant amount of positive energy from the knee joint, the proposed device to perform this movement should have external power input.

In addition to this, the range of motion of the prosthesis is set as 0^o-100^o for the knee joint and 20^o dorsi-flexion and 40^o plantar flexion for the ankle according to biomechanical data.



Figure 4 CAD Model of the conceptual design

Working Principle for Weight Acceptance: Here, the elastic element (green) connects the knee joint to the ankle energetically, the elastic element (red) is employed for energy storage in the ankle during the stance phase, and the elastic element working in catapult principle is assisting to provide effective and sufficient push-off. The elastic element (blue) provides knee flexion and extension during the stance phase. The working principles of these elastic elements for walking are shown in Fig. 5. When the elastic elements are storing energy, it is expressed in red. While green represents energy release and blue stands for unloaded state of the elastic element.



Figure 5 The working principle of the elastic elements during walking - the upper part shows the stance phase and the lower part shows the swing phase.

There is an elastic element employed to mimic the moment behavior caused by weight acceptance while allowing the knee flexion motion in stance phase. This elastic element is engaged only during weight acceptance and it is disengaged with the mechanism shown in Fig.6. The weight acceptance starts with touching the gound of this element with the mechanism shown in Fig.6 (center) and disengagaes the spring when heel is off the ground.



Figure 6 Weigh acceptance function with an elastic element

Working Principle for Sit-to-Stand: As stated in the analyses, it is possible to provide the sit-to-stand motion with a single elasting element. For this function we used the same principle that is used for weight acceptance function. This elestic element is in parallel to the WA elastic element and is designed to store energy up to 100^{o} of flexion by engaging a second elastic element after 20^{o} flexion. The elastic element is locked during seating (Fig.7 center) to prevent returning the energy at an undesired time.

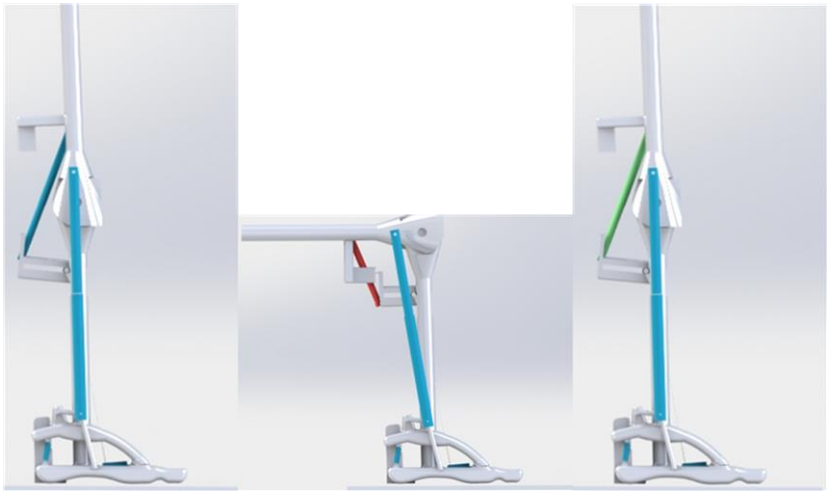


Figure 7 Representation of stand-sit-stand motion with elastic element (blue-unloaded, red-storing and green-releasing energy)

Working Principle for Stair Climbing: As indicated in the previous sections, since the knee must be given a positive power during the stair climbing, we propose a system that the elastic element is compressed by the motor connected to the ball screw mechanism as shown in Fig. 8 for this function.



Figure 8 Ball-screw motor combinantion for stair ascent eleastic element

Since stair climbing cycle has a duration of considerable amount of time compared to other activities, this function can be realized with a low-power motor that stores the extra energy in spring during the cycle when possible. This motor would also be useful in walking to adapt to different speeds and inclinations. The working principle of this system is presented in Fig. 9 on CAD model during stair climbing.



Figure 9 CAD representation of ball-screw mechanism during stair climbing (from left-to-right)

The knee section is designed in geometry to prevent knee hyper-extension and not to be bigger than the biological knee joint as shown in Fig. 10.



Figure 10 CAD model of the knee compartment

Catapult-like ankle-foot compartment of the prosthesis is given in Fig. 11.The sole of the foot part has been modeled by transferring the natural human foot to SolidWorks environment.



Figure 11 CAD model of the ankle-foot compartment

4. STRUCTURAL ANALYSIS

In this section we present the structural analyses for ankle and knee compartments of the prosthesis that have been conducted in ANSYS environment. We select Al7075 as a material candidate for the prototype since it has the good combination of being accessible, low-cost, free-machining material, low-density and high strength.

Ankle-foot Compartment: Initially, we applied body-weight loading to determine the form of the foot compartment. As shown in Fig. 12, we compared the two forms having the same amount and type of material. According to this, we selected the one on the left-side, since the second one had more critical regions, especially on the connection of the upper and bottom parts. Moreover, there is more space for the spring placement in the selected form.

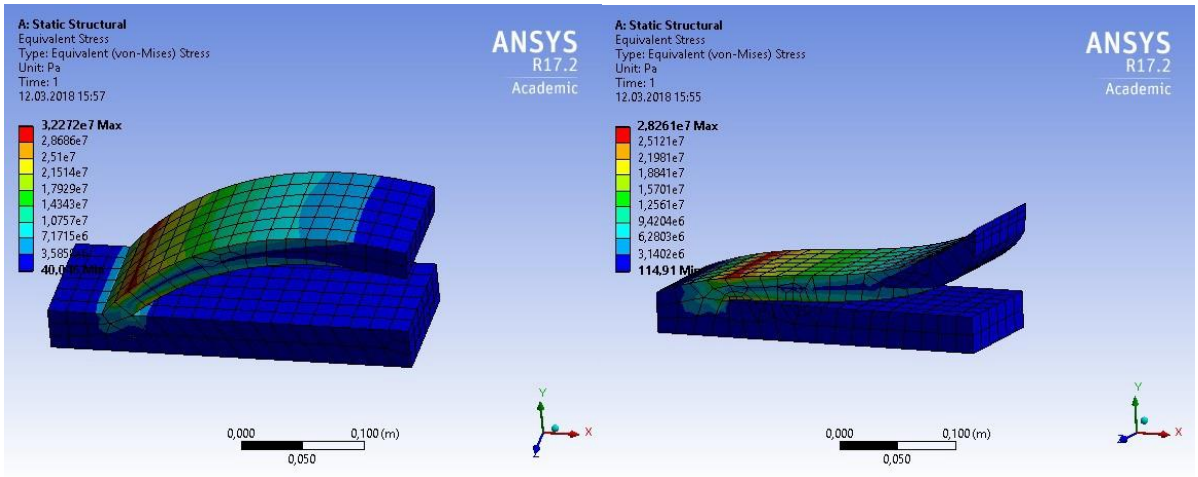


Figure 12 Structural analyses for the two forms of foot compartment

By considering the critical regions of the previous analysis, we modified the design by setting radius on the connection region. Moreover, we finalized the design with consideration of its locking mechanism's place and giving natural foot form at the bottom, as given in Fig. 13. Analysis on this modified design resulted in acceptable strength.

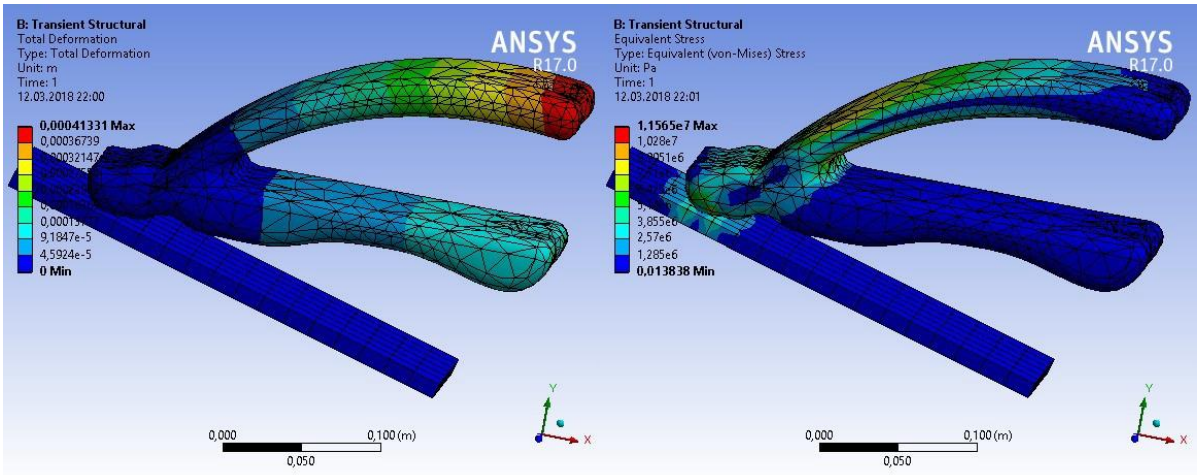


Figure 13 Structural analyses for the re-designed foot compartment

Upper part of the foot has further analyzed under 800 N cyclic-load, as shown in Fig.14, since this part is critical for catapult-like working principle. This load is about 20% bigger than the loading of about 67 kg mass (approx. mass of an 80 kg individual without one leg) and has been selected to be on the safe side for prosthetic application. It has been observed that the stress distribution is more or less symmetrical on the upper and bottom surfaces.

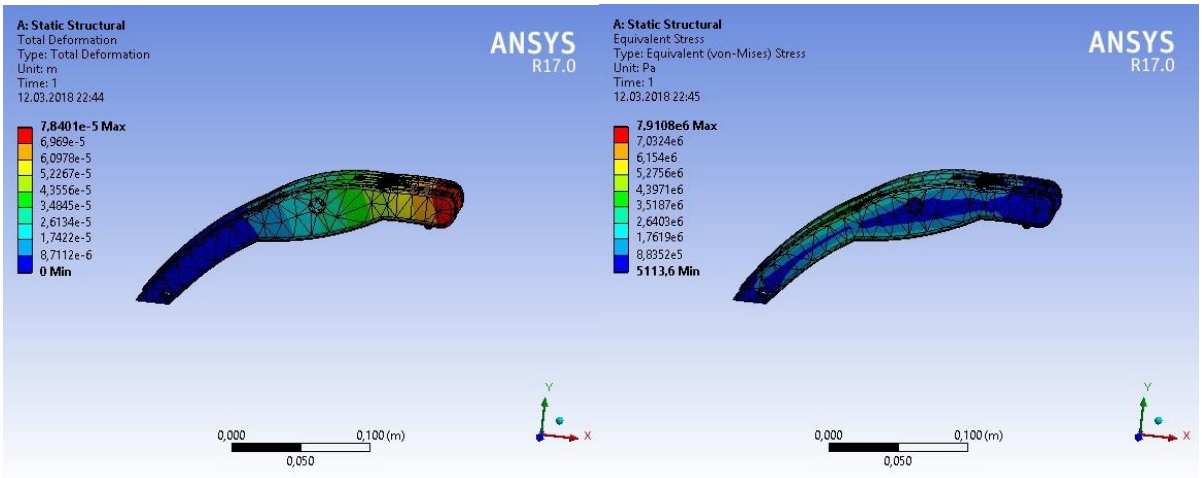


Figure 14 Further structural analyses for the upper part of the foot compartment

Knee Compartment: Initially we implemented the analysis on the upper part of the knee compartment as shown in Fig. 15. Here, we applied the force to generate peak knee torque during stairclimbing, since it is the highest torque for the knee joint in overall motions. It has been observed that at the connection of upper link and knee joint part has critical regions. Moreover, the side surfaces of the knee joint have close to critical regions. To improve this, we increased the thickness and modified the design of the side surfaces and set radius on the connection region. These modifications resulted with acceptable stress levels.

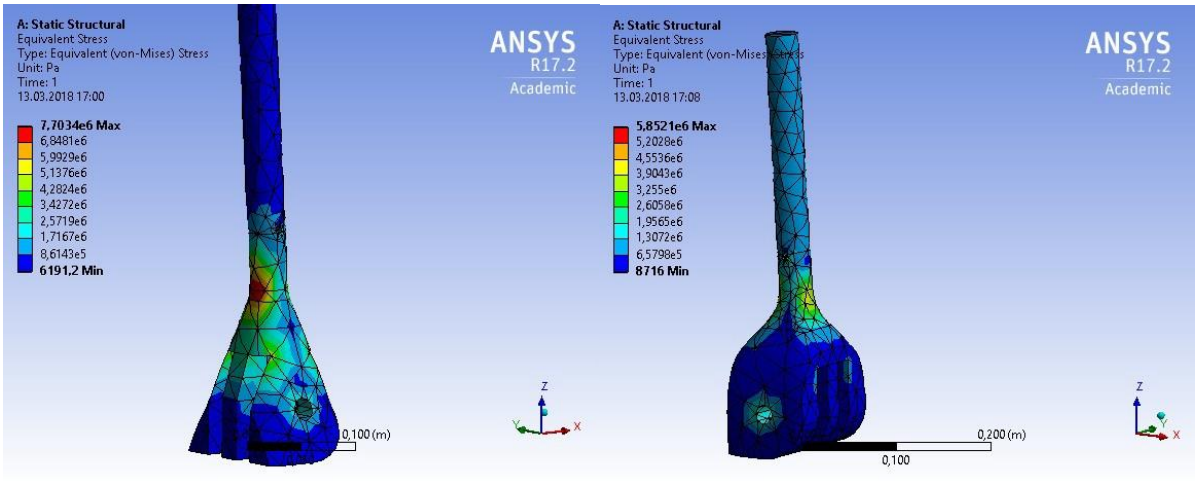


Figure 15 Structural analyses for the upperpart of the knee compartment

Similirlarly, we conducted analysis for the bottom part of the knee compartment. This analysis resulted with safe stress levels, as shown in Fig. 16. Even though the design seemed to have over-safe structure, since this part works together with the upper part and has geometry for hyper-extension we did not apply size changes to this part at this point.

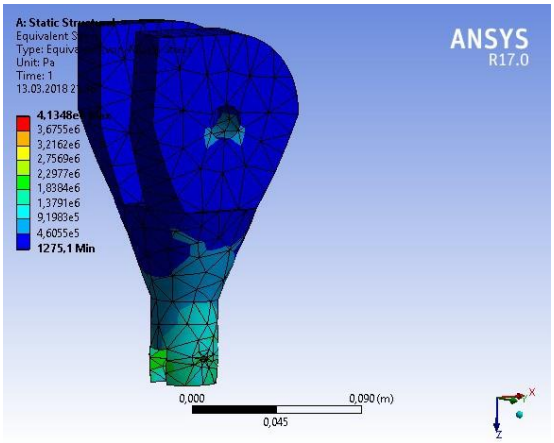


Figure 16 Structural analyses for the bottom part of the knee joint

We also built initial functional protype to evaluate our conceptual design especially in terms of manufacturing, but also to check the functionality of all the elements in related motions. This would give us meaningful insight for further development of the design for the test-prototype. 3D printed of conceptual prototype in half-scale is depicted in Fig.17.



Figure 17 3D printed of conceptual design in half-scale

5. CONCLUSION

In this paper we presented a new conceptual design of WalkMECH that provides weight acceptance, sit-to-stand and stair ascent motions. To be able to do this, first, the biomechanical data of these motions were analyzed. Then, considering these data, we presented the working principles of the elastic elements employed in the conceptual design. Then we implemented structural analysis for the knee ankle compartments to evaluate the design. Currently we are building the test prototype from this conceptual design to test the device first functionally and then on individuals performance evaluation.

6. ACKNOWLEDGEMENT

This research is supported by TUBITAK under the project no: 1109B321600215. Authors also would like to thank Dr. Robert Riener for sharing the data of stair climbing. Authors would also like to thank Dr. Cihan Çiftci and Dr. Hatice S. Şaş Çaycı for their invaluable time and support in this study.

REFERENCES

1. **Ertl, J.P., Ertl, W. and Pritchett J.W., (2012),** "Amputations of the lower extremity workup", eMedicine.

2. **Aleccia, J., (2010),** "Limb loss a grim, growing global crisis". http://haitiamputees.msnbc. msn.com/_news/2010/03/19/4040341-limb-loss-a-grim-growingglobal-crisis.

3. **U.S. Centers for Disease Control and Prevention, (2016),** Age-Adjusted Hospital Discharge Rates for Non-traumatic Lower Extremity Amputation per 1,000 Diabetic Populations, http://www.cdc.gov/ diabetes/statistics.

4. **Goldfarb, M., Lawson, B.E. and Shultz, A.H., (2013)**, "Realizing the promise of robotic leg prostheses", Science Translation Medicine, 5(210): 210-215.

5. **Johansen, D., Cipriani, C., Popovic, D. and Andreasen L., (2016),** "Control of a robotic hand using a tongue control system-a prosthesis application", IEEE Trans. on Biomed. Eng.

6. **Gibson, A. and Artemiadis P., (2015),** "Neural closed-loop control of a hand prosthesis using crossmodal haptic feedback", IEEE Int. Conference on Rehabilitation Robotics.

7. **Hargrove, L.J., Simon, A.M. , Young, A.J. , Lipschutz, L.D., Finucane, S.B., Smith, D.G. and Kuiken, T.A., (2013),** "Robotics leg control with EMG decoding in an amputee with nerve transfers", New England Journal of Medicine, 369(13): 1237-1242.

8. **Shultz., A.H., Lawson, B.E. and Goldfarb, M., (2015),** "Running with a powered knee and ankle prosthesis", IEEE Trans. on Neural Systems & Rehabilitation Eng. 23(3): 403-412.

9. **Lambrecht, B.G.A. and Kazerooni, H., (2009),** "Design of a semi-active knee prosthesis", IEEE International Conference on Robotics and Automation (ICRA), pages 639–45.

10. **Minerva, V.P., Kazerooni, H. and Hurwich, A., (2011),** "Design of a semiactive knee-ankle prosthesis", IEEE Int. Conf. on Robotics and Automation (ICRA), pages 5293–5300.

11. **Pfeifer, R., Riener, R., and Vallery, H., (2012)**, "An actuated transfemoral prosthesis with optimized polycentric knee joint", IEEE Int. Conf. on Biomed. Rob. and Biomechatronics.

12. **Martinez-Villalpando, E.C. and Herr, H., (2009),** "Agonist-antagonist active knee prosthesis: A preliminary study in level-ground walking", J.of Rehab.Res.&Dev.,46(3):361-74.

13. **Rouse, E.J. et al., (2011),** "Design of a semi-active knee-ankle prosthesis", IEEE International Conference on Robotics and Automation (ICRA), pages 5293–5300.

14. **Waters, R. et al., (1976),** "Energy cost of walking amputees: The influence of level of amputation", Journal of Bone & Joint Surgery, 58A:42–46.

15. **Sup, F., Bohara A. and Goldfarb, M., (2008),** "Design and control of a powered transfemoral prosthesis", International Journal of Robotics Research, 27:263–73.

16. **Popovic, D. and Sinkjaer, T., (2000),** "Control of Movement for the Physically Disabled", Springer-Verlag, London, UK.

17. **Bedard, S. and Roy, P., (2003),** "Actuated leg prosthesis for above-knee amputees," U.S. Patent 7314490.

18. **Kapti, A.O. and Yucenur, M.S., (2006),** "Design and control of an active artificial knee joint", Mechanism and Machine Theory, 41:1477–85.

19. **Geng, Y., Yang, P., Xu, X. and Chen, L., (2012),** "Design and simulation of active transfemoral prosthesis", Chinese Control and Decision Conference (CCDC), pp 3724-28.

20. **Flowers, W.C., (1973),** "A man-interactive simulator system for above-knee prosthetics studies", PhD Thesis – MIT, Cambridge, MA, US.

21. **Bayram, H.A., (2015),** "Recent Developments in Above-Knee Prosthetics and the Importance of Energy Recovery in Transfemoral Amputee Gait", Acıbadem Üniversitesi Sağlık Bilimleri Dergisi, 6(2), pp. 61-68.

22. **Windrich, M., Grimmer, M., Christ, O., Rinderknecht S., Beckerle, P., (2016),** "Active lower limb prosthetics: a systematic review of design issues and solutions", BioMed. Eng. OnLine, 15(3):140.

23. **van den Bogert, A.J., Samorezov, S., Davis, B.L., Smith, W.A., (2012),** "Modeling and Optimal Control of an Energy-Storing Prosthetic Knee", ASME J. of Biomech. Eng., 134(5).

24. **Zissimopoulos, A., Fatone, S., and Gard, S.A., (2007),** "Biomechanical and Energetic Effects of a Stance-Control Orthotic Knee Joint," J. Rehabil. Res. Dev., 44(4), pp. 503.

25. **Johansson, J.L., Sherrill, D.M., Riley, P.O., Bonato, P., and Herr, H., (2005),** "A Clinical Comparison of Variable-Damping and Mechanically Passive Prosthetic Knee Devices," Am. J. Phys. Med. Rehabil., 84(8), pp. 563–575.

26. **Segal, A.D., et al, (2006),** “Kinematic and Kinetic Comparisons of Transfemoral Amputee Gait using C-Leg and Mauch SNS Prosthetic Knees,” J. Rehab. Res. Dev., 43, pp. 857-70.

27. **Highsmith, M.J., et al., (2011),** “Kinetic Asymmetry in Transfemoral Amputees While Performing Sit to Stand and Stand to Sit Movements,” Gait and Posture, 34(1), pp. 86–91.

28. **Wilken, J.M., Sinitski, E.H. and Bagg, E.A., (2011),** “The Role of Lower Extremity Joint Powers in Successful Stair Ambulation,” Gait and Posture, 34(1), pp. 142–144.

29. **Winter, D.A., (1983),** “Energy Generation and Absorption at the Ankle and Knee During Fast, Natural, and Slow Cadences,” Clin. Orthop. Rel. Res., 175, pp. 147–154.

30. **Winter, D.A., (1983),** “Moments of Force and Mechanical Power in Jogging,” J. Biomech., 16(1), pp. 91–97.

31. **Paine, N., Oh, S., Sentis, L., (2014),** "Design and control considerations for high-performance series elastic actuators" IEEE/ASME Trans. Mechatronics, 19(3), pp. 1080-91.

32. **Hollander, K. W., Sugar, T.G. and Herring, D.E., (2005),** “Adjustable robotic tendon using a ’jack spring’TM”, IEEE Int. Conference on Rehabilitation Robotics, pages 113-18.

33. **Unal, R. et al., (2012),** “A prosthetic or orthotic device and a method for using such a device. Patent PCT/NL2012/050421.

34. **Unal, R. et al., (2010),** “Conceptual design of an energy efficient transfemoral prosthesis. IEEE/RSJ International Conference on Intelligent Robots and Systems (IROS).

35. **Unal, R. et al., (2010),** “Prototype design and realization of an innovative energy efficient transfemoral prosthesis”, IEEE Int. Conf. on Biomed. Rob. and Biomechatronics (BioRob).

36. **Unal, R. et al., (2012),** “Towards fully passive energy efficient transfemoral prosthesis”, IEEE/RAS-EMBS Int. Conf. on Biomedical Robotics and Biomechatronics (BioRob).

37. **Rose, J. and Gamble, J.G., (2005),** “Human Walking”, Williams & Wilkins.

38. **Winter, D.A., (1991),** “The Biomechanics and Motor Control of Human Gait: Normal, Elderly and Pathological”, University of Waterloo Press, Canada, 2nd edition.

39. **Unal, R. et al., (2012),** “The Control of Recycling Energy Storage Capacity of WalkMECH *adapt*”, IEEE Int. Symp. on Robot and Human Interactive Communication, pp. 720-725.

40. **Bayram, H.A., Chien, C.H. and Davis, B.L., (2014),** “Active functional stiffness of the knee joint during activities of daily living- a parameter for improved design of prosthetic limbs”, Clinical Biomechanics, 29: 1193-99.

41. **Riener, R., Rabuffetti, M. and Frigo, C., (1999),** “Joint powers in stair climbing at different slopes”, Proceedings of the First Joint BMES/EMBS Conference, 1(1):530–35.

IMPACT PERFORMANCE EVALUATION OF A CRASH CUSHION DESIGN USING FINITE ELEMENT SIMULATION AND FULL-SCALE CRASH TESTING

Murat BÜYÜK, *muratbuyuk@sabanciuniv.edu*, Sabanci University, 34956, İstanbul, Turkey

Ali Osman ATAHAN, *atahana@itu.edu.tr*, Istanbul Technical University, 34469, İstanbul, Turkey

Kenan KURUCUOĞLU, *info@ulukur.com*, Ulukur Plastic Traffic Products, 34870, İstanbul, Turkey

ABSTRACT

Crash cushions are designed to gradually absorb kinetic energy of an impacting vehicle and bring it to a controlled stop within an acceptable distance while maintaining a limited amount of deceleration acting on the occupants. These cushions are used to protect errant vehicles from hitting rigid objects, such as poles and barriers located at exit locations on roads. Impact performance evaluation of crash cushions are attained according to EN 1317-3 standard based on various speed limits and impact angles. Crash cushions can be designed to absorb the energy of an impacting vehicle by using different material deformation mechanisms, such as metal plasticity supported by airbag folding or damping.

In this study, a new crash cushion system, called Ulukur Crash Cushion or UCC, is developed by using linear low-density polyethylene (LLDPE) containers supported by embedded plastic energy absorbing tubes as dampers. Steel cables are used to provide anchorage to the design. Crashworthiness of the system was evaluated both numerically and experimentally. Finite element model of the design was developed and solved using LS-DYNA, where the impact performance was evaluated considering the EN 1317 standard. Following the simulations, full scale crash tests were performed to determine the performance of the design in containing and redirecting the impacting vehicle. Both the simulations and crash tests show acceptable agreement. Further crash tests are planned to fully evaluate the crashworthiness of the new crash cushion system.

Keywords: Crash Cushion; Crash Test; Simulation; LS-DYNA; EN 1317; Road Safety; Energy Absorption, Linear Low Density Polyethylene.

1. INTRODUCTION

Traffic and road safety is a serious concern worldwide and multi phased research has been undertaken in recent years. The United Nations General Assembly has made an important initiative to reduce fatality rate in traffic accidents around the world by 50% and provided funds for research. In this context, Turkey has prepared a 10-year vision program covering traffic education and training, safety and enforcement, health and emergency assistance initiatives and finally the improvement of traffic safety with engineering measures [**TRA, 2011, IMM, 2011**]. This program has been implemented step by step by Ministries of Education, Interior, Health and Transportation. It is a fact that since 2010, serious steps have been taken in traffic safety in Turkey. These advances include, speed control using smart detection systems, enforcement of traffic rules through cameras, reducing arrival times of ambulances in an accident site and providing traffic safety culture to students of all ages. Thanks to these undertakings, a significant decrease in fatal accidents in Turkey has occurred, however, according to statistical data the level of achievement is not sufficient. Lack of road restraint system utilization is determined to be one of the areas need improvement [**MM, 2016**].

Crash cushions, are widely used in developed countries to protect vehicles against impacts with fixed, sharp, narrow and rigid objects located at road exit locations, tool booths, workzones, barrier ends and trees [**AASHTO, 2011; FHWA, 2013**]. As shown in **Figure 1**, collision with unprotected objects increase the severity of accidents and result in fatalities. According to predictions by the Turkish Statistics Institute (TUIK) the number of fixed object accidents is on the rise which creates a concern for road safety targets set by Turkish Government [**TUIK, 2016**]. Crash cushions in general are designed to slow down and contain the impacting vehicle in a controlled way by absorbing its kinetic energy. The Istanbul Metropolitan Municipality (IMM), which is responsible from the traffic safety within the city of Istanbul expressed interest in using crash cushions in Istanbul in a very near future [**IMM, 2016**].

The aim of this project is, therefore, to develop a new hybrid crash cushion system, called Ulukur Crash Cushion or UCC, made out of linear low-density polyethylene (LLDPE) containers and steel plates for the IMM. In this respect, UCC will have low initial, maintenance and repair costs with reusable parts. Crashworthiness of the system is evaluated both numerically and experimentally. Finite element model of the UCC is developed and impact performance is analyzed using LS-DYNA in accordance with TS EN 1317 crash testing standard [**CEN, 2010; LSTC, 2017**]. Following the simulations, full scale crash tests were performed to validate the computer simulation results. Both the simulations and crash tests show acceptable agreement. Further crash tests are planned to fully evaluate the crashworthiness of the new crash cushion system.

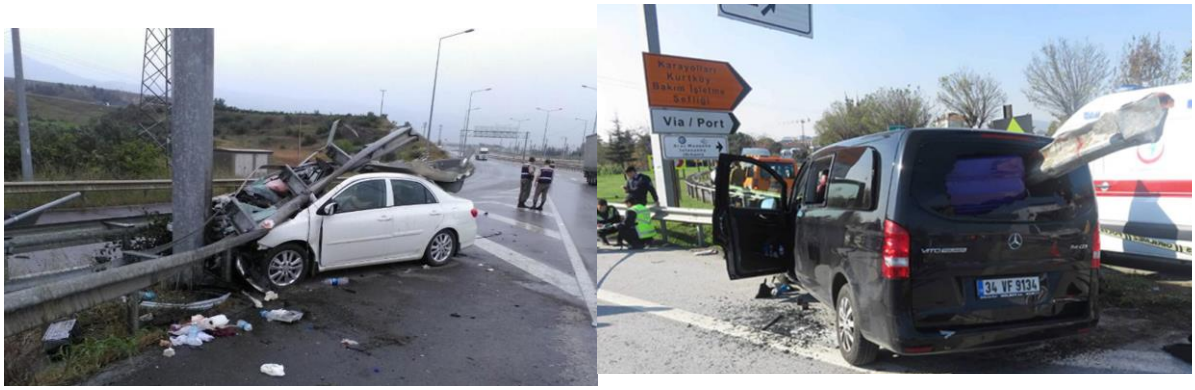


Figure 1. Severity of run of the road accidents with narrow and rigid objects

2. DETAILS OF ULUKUR CRASH CUSHION DEVELOPED

Ulukur Crash Cushion, UCC, design is composed of high Linear Low Density Polyethylene (LLDPE) containers, energy absorbing tubes, steel cables, lower plates and back support plate [**Ulukur, 2016**]. Geometrical details of these materials are provided in **Figure 2**. Containers are produced using LLDPE since it a sustainable and cost-effective material that could sustain large deformations, endure dynamic forces and absorb kinetic energy of the impacting vehicle without crack formation. The measurements for the LLPDE containers are 500 mm long x 800 mm wide x 710 mm tall x 8 mm thick. In addition, 250 mm in diameter, 460 mm long energy absorbing tubes made out of LLPDE are utilized inside the containers to improve the crash performance of the design. 50 mm in diameter holes are provided on tubes to allow controlled air release. The number of tubes varied based on the container type. In other words, as shown in **Figure 2**, the lead container with a shield included 2 tubes, whereas all the other standard containers included 4 tubes. This is intended to provide a soft nose section for vehicles with low energy impacts. As the impact energy increases so do the energy absorption capacities of the UCC design. Material properties of LLPDE are provided in **Table 1**.

The UCC design developed in this study is composed of six containers and a frontal shield. The design is actually intended for 110 kph impacts and so the original design with 6 containers is not altered for 50 kph impact. Total length of the design is 3,700 mm. The measurements of UCC elements are provided in **Figure 2**. This design is intended to provide safe containment and redirection for 50 kph head on and side impacts. Since UCC is a modular nature the design could be easily converted to 80, 100 or 110 kph impacts by adding more containers, tubes and steel members. Thus the length of the system can change based on target design speed. As shown in **Figure 2**, UCC used four 19 mm diameter steel cables, two at the bottom and two at the side and cables are anchored to steel plates at both ends. Bottom cables run between two 650 mm wide x 40 mm wide x 25 mm thick steel plates located under the containers. This allowed controlled deformation of containers during frontal and side vehicle impacts. Two side cables are used to improve lateral stability of the UCC design.

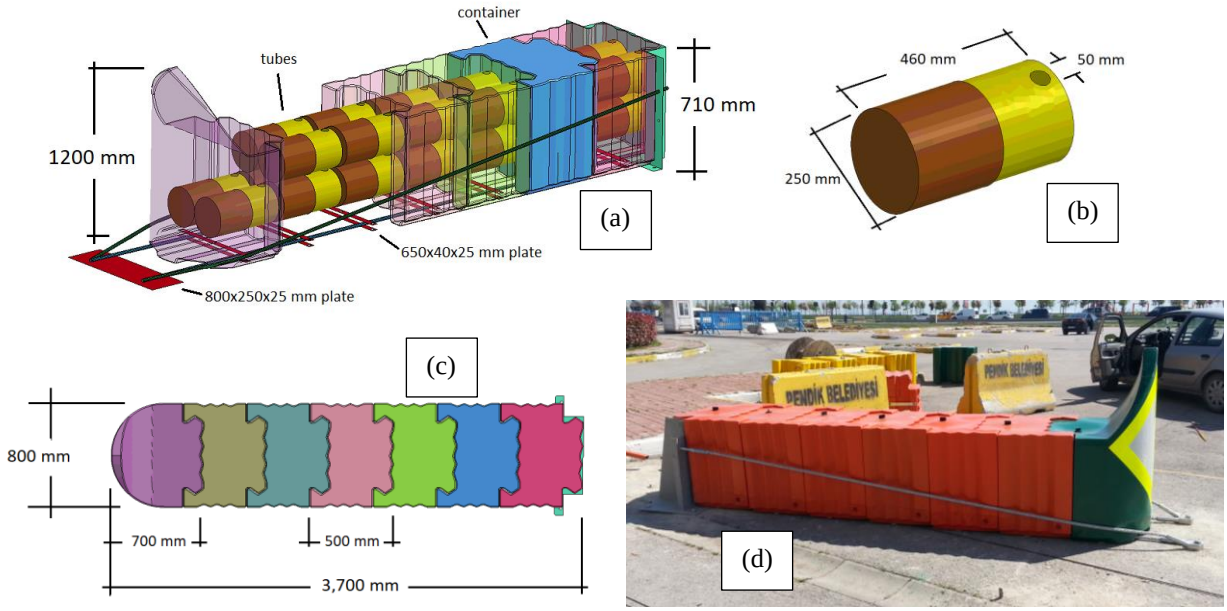


Figure 2. Details of Ulukur Crash Cushion, UCC (a) Internal view, (b) Energy absorbing tube, (c) Top view and (d) Assembled crash cushion [**Ulukur, 2016**]

Table 1. Material properties of LLPDE used in UCC design [**Ulukur, 2017a**]

Property	Value	Test Standard
Density (kg/m^3)	935	ASTM D 1505
Modulus of Elasticity (MPa)	724	ASTM D 790
Toughness	69	ASTM D 2240
Yield Strength (MPa)	18	ASTM D 638
Vicat Softening Temp (^{o}C)	115	ASTM D 1525
Brittleness Temp (^{o}C)	-75	ASTM D 746

3. TS EN1317 CRASH TESTING STANDARD FOR CRASH CUSHION EVALUATION

To assess the performance of crash cushions against vehicle impacts, Part 3 of EN 1317 standard, named “Road restraint systems – Part 3: Performance classes, impact test acceptance criteria and test methods for crash cushions” is followed (**CEN, 2010**). According to this standard, vehicles weighing 900, 1300 or 1500 kg traveling at speeds of 50, 80, 100 or 110 impact crash cushions in 5 different approaches. **Figure 3** shows all possible test combinations described in EN 1317 standard Part 3 (**CEN, 2010**). As shown in **Table 2**, for 50 kph tests there are only two tests, namely TC 1.1.50 and TC 4.2.50, a 900 kg passenger car at impact position 1 and 1300 kg passenger car at impact positon 2, respectively are specified. Both computer simulations and full-scale crash tests on UCC design is performed at

50 kph. In other words, impact performance of the UCC design is evaluated using TC 1.1.50 and TC 4.2.50 crash tests (**CEN, 2010**).

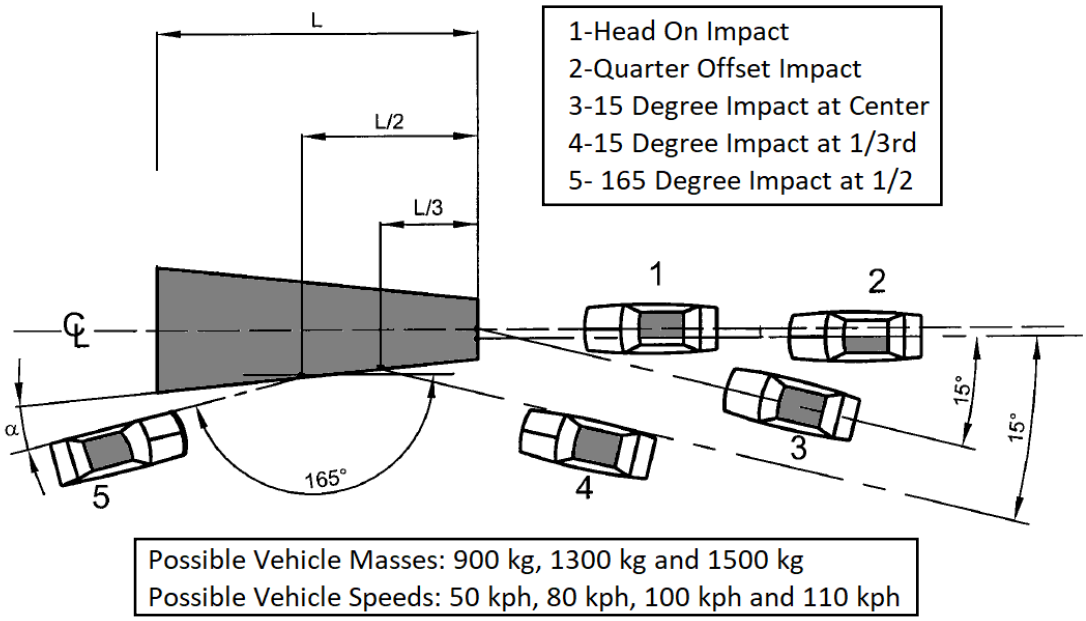


Figure 3. Crash Cushion Test Approaches in EN1317 Standard Part 3 (**CEN, 2010**)

Table 2. Crash Testing Details for Crash Cushions in EN 1317 Part 3 [**CEN, 2010**]

Test Speed (kph)	Acceptance Tests *, **					
50	TC 1.1.50				TC 4.2.50	
80	TC 1.1.80	TC 1.2.80	TC 2.1.80	TC 3.2.80	TC 4.2.80	TC 5.2.80
100	TC 1.1.100	TC 1.2.100	TC 2.1.100	TC 3.2.100	TC 4.2.100	TC 5.2.100
110	TC 1.1.100	TC 1.3.110	TC 2.1.100	TC 3.3.110	TC 4.3.110	TC 5.3.110

* TC 5.3.110 stands for Test Crash Cushion (TC), Approach (5), Vehicle (3) and Speed (110)
** Vehicles 1, 2 and 3 stand for 900 kg, 1,300 kg and 1,500 kg, respectively.

3. COMPUTER SIMULATION OF UCC DESIGN

Before going into a costly full-scale crash testing, a detailed finite element simulation study was performed on UCC design. A highly non-linear and large deformation finite element code LS-DYNA developed by the Livermore Software Technology Corporation (LSTC) was used to model the barrier and simulate the vehicle-barrier impact event [**LSTC, 2017**]. Details of the bridge rail and both vehicle models are explained below.

3.1 Finite Element Model of UCC Design

A finite element model of the UCC was developed to assess the crash test performance of the design. The model as shown in **Figure 4**, consisted of 143,063 nodes, 135,389 shell and 4,264 solid elements. Shell elements represented the LLDPE members and steel plates of the model while solid elements represented the steel cables. The shell elements of the LLPDE containers and internal tubes that are expected to get in direct contact with vehicle and thus experience severe deformations are modeled with full integration formulation to accurately represent the complex interactions and behavior. All steel elements were modeled with default element formulation for computational efficiency.

Since containers is expected to sustain large plastic deformations and possible crushing a piecewise linear plastic material definition is used to model the LLPDE elements [**Vesenjak, 2005, Atahan and Bonin, 2006**]. Since no failure is expected in steel members a rigid material modeling is used to represent plates and cables. Steel cables are firmly attached to steel plates at both ends and steel plates are secured to ground using non failing connections.

In an actual UCC installation, connections between the members, such as lower steel plates and containers and steel plates to ground are established using bolts and nuts. To accurately represent the behavior of these connections during full-scale crash testing CONSTRAINED_SPOTWELD option in LS-DYNA was used [**LSTC, 2017]**. By definition, this option keeps members connected until a certain force criteria is met. Then the connection fails and members allow moving freely. To determine the required force level that fails a connection, a detailed model is constructed using LS-DYNA. The behavior of connection was examined under different loading conditions. A reasonable failure criterion obtained from the component simulation was used in the connection model [**Atahan and Bonin, 2006]**.

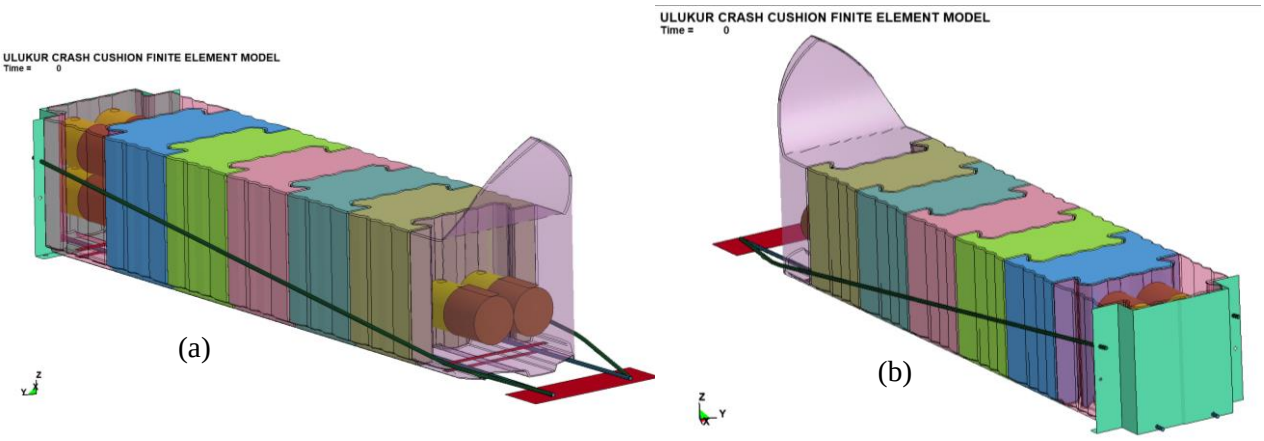


Figure 4. Finite element model of UCC (a) Frontal View and (b) Rear view

3.2 Vehicle Model

After the development of UCC model, a small passenger car model is sought meting the EN 1317 standard requirements to impact the barrier. A 2002 Ford Taurus

vehicle model obtained from the National Crash Analysis Center (NCAC) was used in the study [**FEMA, 2002**]. The mass of the empty vehicle is adjusted to 900 kg and it could be increased to 1300 kg by adding extra mass elements. This particular vehicle model was used in many previous studies with success [**Atahan, 2009**]. A picture of the vehicle is shown in **Figure 5**.

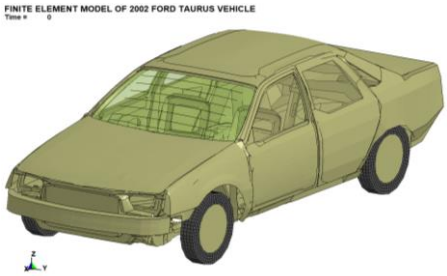


Figure 5. 2002 Ford Taurus vehicle model used in LS-DYNA Impact Simulation

3.3 TC 1.1.50 Simulation

After the final modifications on the vehicle model, the simulation was setup according to TC 1.1.50 conditions specified in EN 1317 Part 3 (**CEN, 2010**). This head on crash test with 900 kg vehicle is performed to evaluate the energy absorption capability of the UCC design and its effectiveness in reducing the velocity of impacting vehicle in a controlled manner thus reducing occupant injury risks. As shown in **Figure 6**, vehicle is positioned in front of the cushion at 0 degrees impact angle. The vehicle speed is 50 kph. In this simulation no dummy is used. Simulation was run about 0.15 sec until the vehicle's kinetic energy is completely dissipated by the crash cushion and vehicle is pushed backwards. As shown in **Figure 7**, vehicle hit the barrier, instantly the front container began to deform and bent towards the impacting vehicle. At 0.06 seconds after the initial impact the kinetic energy of the vehicle significantly reduced and the velocity of the vehicle was approximately 28 km/h. At 0.072 seconds after the initial contact the second container began to deform and absorbed the rest of the kinetic energy of the vehicle. Thus, 0.12 second after the initial impact with the UCC vehicle was brought to a controlled stop. Vehicle left the UCC in a stable and upright position. Energy absorption performance of the UCC was acceptable which resulted low occupant risk values measured inside vehicle. A picture of the deformed shape of the barrier after TC 1.1.50 simulation is shown in **Figure 8**. Based on the simulation predictions, it was determined that UCC design successfully contained and stopped 900 kg vehicle with minimal injury risk to occupants.



Full-Scale Crash Test TC 1.1.50

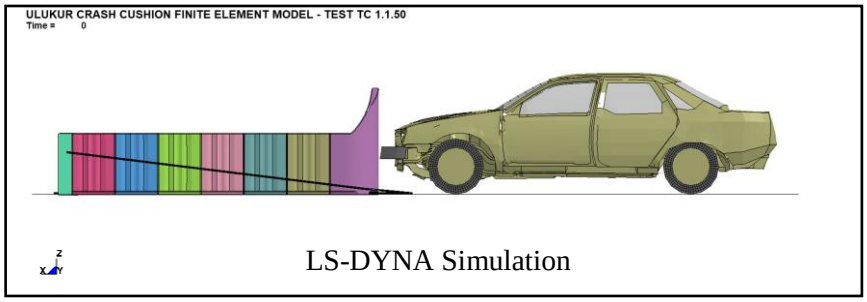
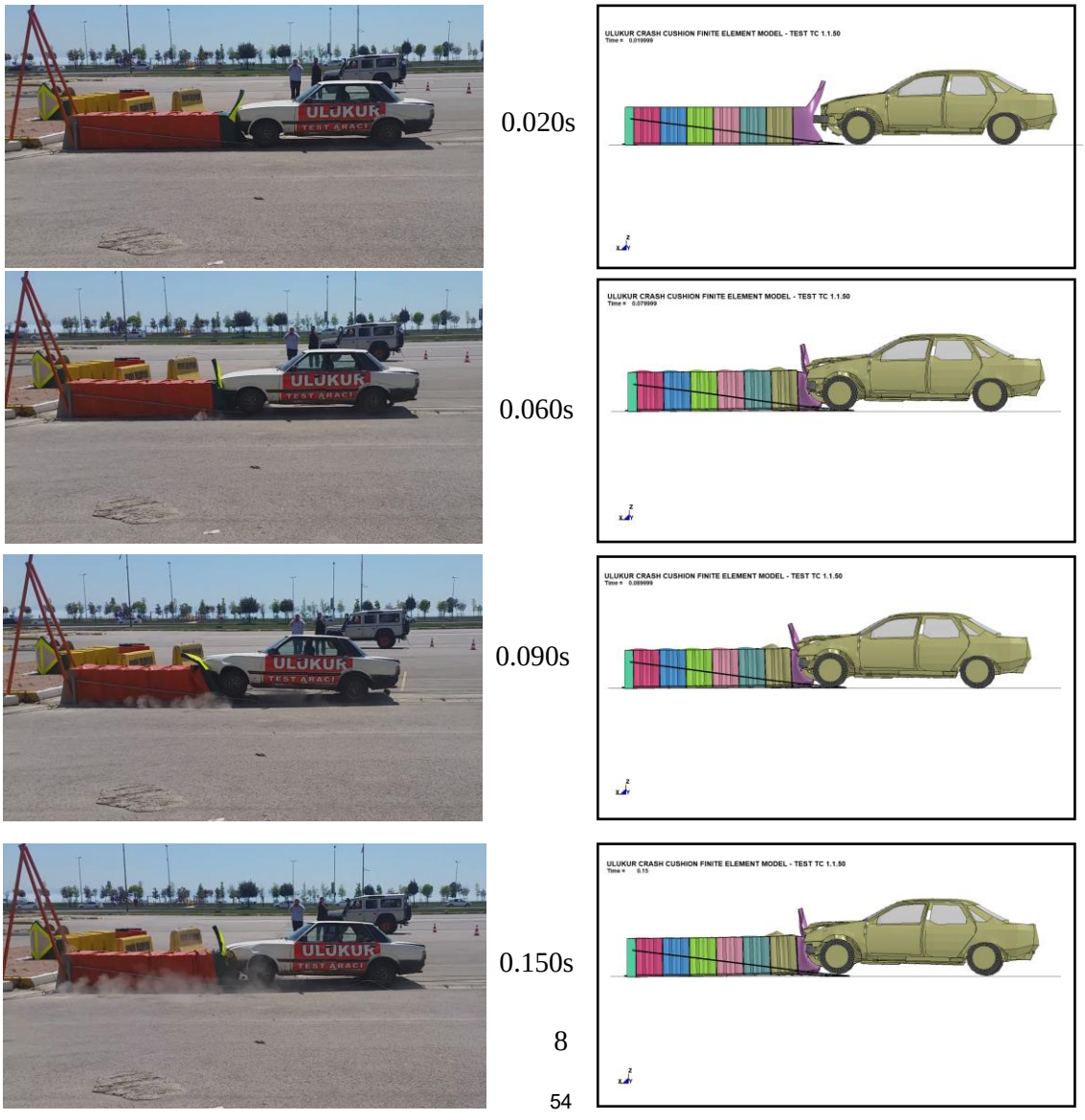


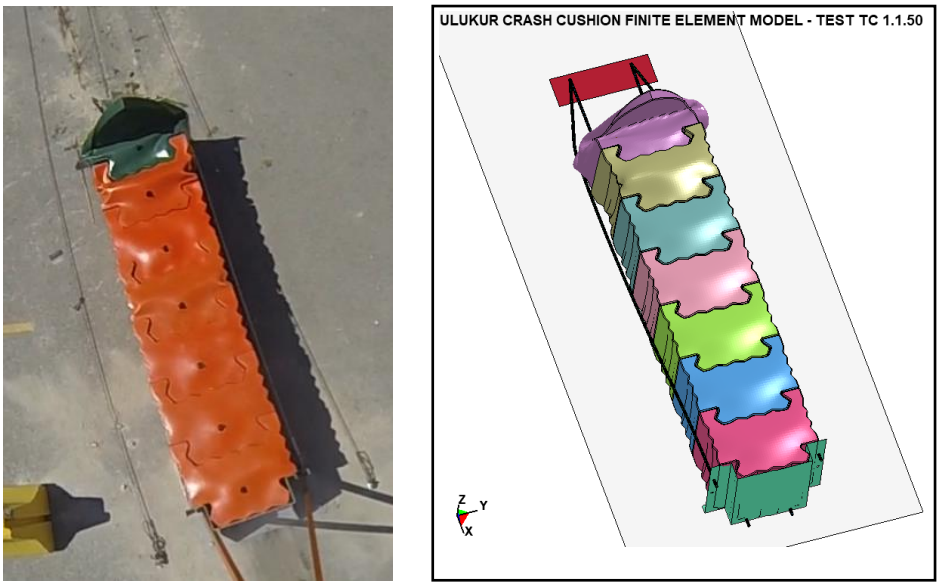
Figure 6. 900 kg car positioned in front of UCC barrier before TC 1.1.50

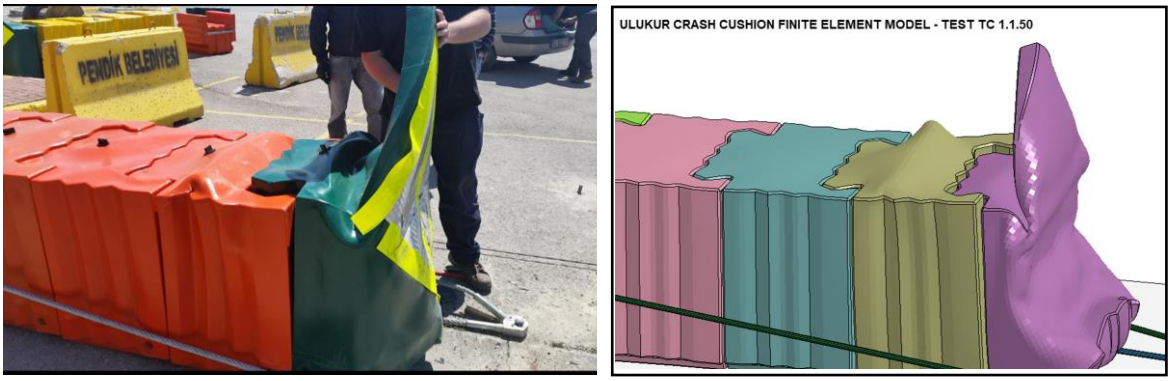


Full-Scale Crash Test TC 1.1.50

LS-DYNA Simulation

Figure 7. Sequential pictures comparison of UCC after TC 1.1.50 crash test and simulation





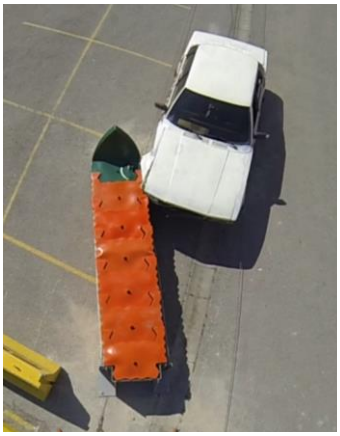
Full-Scale Crash Test TC 1.1.50 LS-DYNA Simulation

Figure 8. Deformed shape comparison of UCC after TC 1.1.50 crash test and simulation

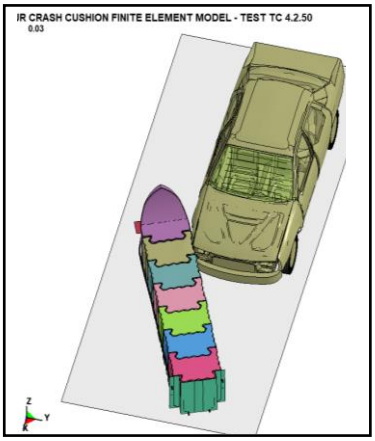
3.4 TC 4.2.50 Simulation

A second simulation study was also performed to evaluate side impact capacity of the UCC design. As described by test TC 4.2.50, a 1,300 kg car model was positioned such that it would impact the cushion 1/3rd of the length (see **Figure 9**). The vehicle contacted the barrier at 15 degrees angle and the velocity of the vehicle just before the impact was 50 kph. Following the initial contact, as shown in **Figure 10** first and second containers began to deform laterally thus absorbing the impact

energy of the vehicle. As vehicle continued to slide on the side of the UCC, it contacted more containers and vehicle speed was further reduced. At 0.1 sec after the initial impact the first 4 containers received moderate damage and vehicle's velocity was almost 28 kph. As shown in sequential pictures in **Figure 10**, 0.2 sec after the initial impact cushion was able to contain and redirect impacting vehicle without any breakage of the elements. Damage to the UCC and vehicle were moderate. Vehicle left the UCC in a stable and upright position. Energy absorption performance of the UCC was acceptable which resulted low occupant risk values measured inside vehicle. A picture of the deformed shape of the barrier after TC 4.2.50 simulation is shown in **Figure 11**. Based on the simulation predictions, it was determined that UCC design has the potential to satisfy 50 kph test requirements described at EN 1317 Part 3.

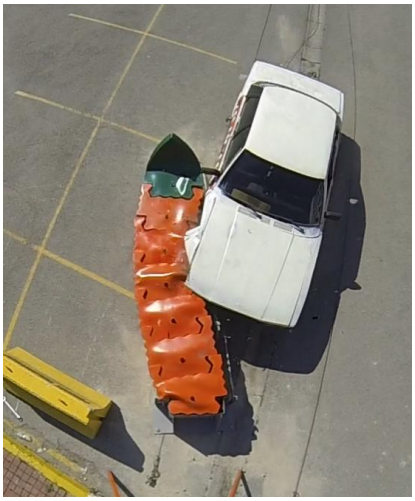


Full-Scale Crash Test TC 4.2.50

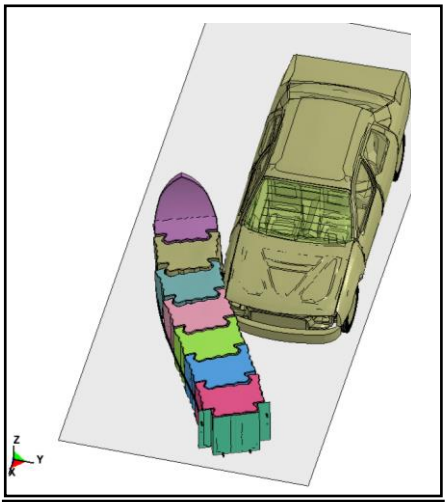


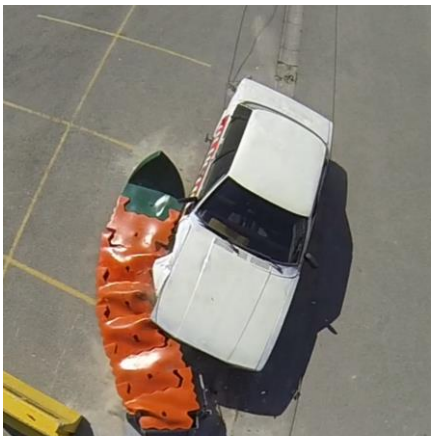
LS-DYNA Simulation

Figure 9. 1,300 kg car positioned in front of UCC barrier before TC 4.2.50



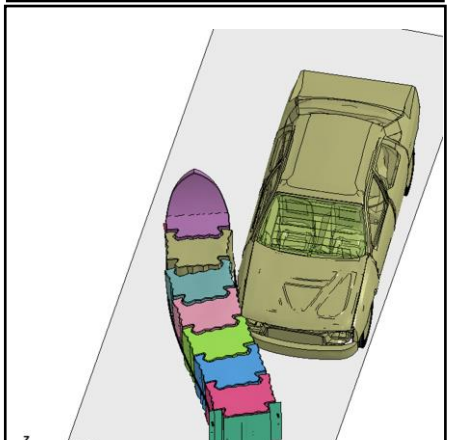
0.070s





10

56



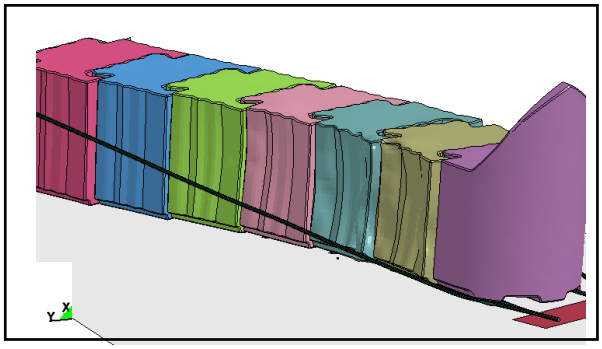
0.120s

Full-Scale Crash Test TC 4.2.50 LS-DYNA Simulation

Figure 10. Sequential pictures comparison of UCC after TC 4.2.50 crash test and simulation



Full-Scale Crash Test TC 4.2.50



LS-DYNA Simulation

Figure 11. Deformed shape comparison of UCC after TC 4.2.50 crash test and simulation

4. Full-Scale Crash Testing

After performing two successful simulation studies for tests TC 1.1.50 and TC 4.2.50, same tests were performed using full scale crash cushion. Crash tests were run in Istanbul during summer of 2016. These tests were intended to both verify the simulation findings and conclusively prove the acceptability of UCC design for 50 kph conditions.

4.1 Crash Test TC 1.1.50

As shown in **Figures 6 and 7**, a full-scale crash test was performed on UCC design according to EN1317 Part 3 TC 1.1.50 conditions [**Ulukur, 2017a**]. UCC design was installed on concrete pavement and the impact point, as described in EN1317 Part 3, was. A 1991 model Ford Taurus was used as the test vehicle. The total mass of the tested vehicle was 900 kg when empty and 1,300 kg with the addition of dummy and measurement devices. Vehicle positioned in the test track, the vehicle accelerated toward the test article at an angle of 0 degrees using a cable pully mechanism and impacted the barrier at 51.5 kph. Behavior of the UCC and the vehicle are illustrated in **Figure 7**. As expected vehicle was not able to damage the cushion significantly. Only the first and second containers compressed and absorbed the kinetic energy of the vehicle. Vehicle slowed down in an acceptable manner and came to a stop. Data

collected from accelerometer installed at vehicle's center of gravity was used to calculate the occupant injury risks. Due to the softened nose design of the barrier and low speed of vehicle occupant injury risk values was determined to be fairly small. Results of TC 1.1.50 crash test showed that the UCC design is soft enough to contain and stop an impacted vehicle in an acceptable manner.

4.2 Crash Test TC 4.2.50

After repairing damaged containers and rotating the cushion 15 degrees, a second crash test was performed on UCC design according to EN1317 Part 3 Test TC 4.2.50 conditions [**Ulukur, 2017b**]. As shown in **Figure 9**, a 1,320 kg Ford Taurus impacted the barrier with a speed of 51 kph and at an angle of 15 degrees. The impact point was 1.5 meters away from the nose which is equal to 1/3rd distance of the UCC. Following the initial contact, as shown in **Figure 10,** first two containers received the impact force began to deform and absorb the initial impact loads. As vehicle continued to slide on the side of the UCC, as in the simulation study, it contacted barrier number 3 and 4 which reduced the vehicle speed further. 0.1 sec after the initial impact the first 4 containers received moderate damage and vehicle's velocity was almost 32 kph. As shown in sequential pictures in **Figure 10**, 0.22 sec after the initial impact cushion was able to contain and redirect impacting vehicle in an acceptable manner. Damage to the UCC and vehicle were moderate. Vehicle left the UCC in a stable and upright position. Energy absorption performance of the UCC was acceptable which resulted low occupant risk values measured inside vehicle. A picture of the deformed shape of the barrier after TC 4.2.50 crash test is shown in **Figure 11**. As predicted by LS-DYNA simulation study, UCC design successfully passed the 50 kph test requirements described at EN 1317 Part 3 [**CEN, 2010**].

5. SUMMARY AND CONCLUSIONS

This paper deals with designing, analyzing and testing a new reusable, low cost and simple crash cushion, called Ulukur Crash Cushion (UCC) for roads with a 50 kph speed limit. UCC design included linear low-density polyethylene (LLDPE) containers with embedded LLPDE energy absorbing tubes as dampers. Design was strengthened by steel cables and steel plates. Crashworthiness of the system was evaluated both numerically and experimentally. Finite element analysis of the UCC design showed that the design is flexible enough to contain and successfully stop a 900 kg car impacting head on while rigid enough to successfully redirect a 15 degrees side impact of a 1,300 kg vehicle at 1/3rd location of the design. Following the promising simulation study, design was installed at a test facility and two full scale crash tests were performed on UCC to conclusively determine its performance under 50 kph vehicle impacts. Both simulation and crash test results agreed well proving the crashworthiness and acceptability of the design at 50 kph. Damage to UCC was moderate and the occupant risk factors were below injury threshold. Since UCC design is composed of modular elements design could be easily repaired and put back to service. Finally, performing further crash tests at higher speeds, such as 80, 100 and 110 kph are recommended to fully assess the acceptability of the new crash cushion system developed.

REFERENCES

AASHTO (2011), Roadside Design Guide, 4th Edition. American Association of State Highways and Transportation Officials, Washington D.C.

Atahan, A.O. (2009), Vehicle crash test simulation of roadside hardware using LS-DYNA: a literature review. International Journal of Heavy Vehicle Systems 17(1), 52-75.

Atahan A.O. and Bonin G. (2006), Numerical analysis of an H4a heavy containment level transition. Int. J. Heavy Vehicle Systems, Inderscience Enterprises, 13(4), 351-365.

CEN (2010), European Committee for Standardization. European Standard EN1317, Road restraint systems - Part 3: Performance classes, impact test acceptance criteria and test methods for crash cushions, Brussels.

FHWA (2013), Online Guide to Crash Cushions. Federal Highway Administration, US Dept of Transportation, https://safety.fhwa.dot.gov/roadwaydept/countermeasure/docs/CrashCushionsNov2013Safelogo.pdf/, Washington, D.C.

FEMA (2002), Finite Element Model Archive, FHWA/NHTSA National Crash Analysis Center, http://www.ncac.gwu.edu/vml/models.html , Virginia.

IMM (2016), Istanbul Traffic Safety Strategic Plan, Technical Report IBB-3-TS04, Istanbul Metropolitan Municipality.

LSTC (2017), LS-DYNA Keyword User's Manual. Livermore Software Technology Corporation, Livermore, California, 2016.

TRA (2011), Traffic Safety Handbook. Turkish Road Association, Department of Transportation, Ankara.

TUİK (2016), Vehicle data on Turkish Highways. Turkish Statistics Organization, Ankara.

Vesenjak M., Borovinsek M. and Ren Z. (2005), Computational and experimental crash analysis of the road safety. Engineering Failure Analysis, 12, 963-973.

Ulukur (2017a), TC 1.1.50 crash tests on UCC crash cushion. Test No. 001/ITU/17, Crash Test Facility, Istanbul.

Ulukur (2017b), TC 4.2.50 crash tests on UCC crash cushion. Test No. 002/ITU/17, Crash Test Facility, Istanbul.

DERIVATION OF STIFFNESSES FOR COMPARISON OF VEHICLE PERFORMANCE IN FRONTAL IMPACTS

Selçuk HİMMETOĞLU, *s.himmetoglu@hacettepe.edu.tr* Hacettepe University, Mechanical Engineering Department, 06800, Ankara, Turkey

ABSTRACT

The stiffnesses of the structural elements of a vehicle plays an important role in the vehicle's crash performance and in the design of restraint systems. In this study, crash test data obtained from US New Car Assessment Program (NCAP) are utilised to derive the overall frontal stiffnesses of selected cars that underwent full-width fixed rigid barrier (FWRB) impact at impact speeds of 40 km/h and 56 km/h. A method to derive the stiffnesses is proposed which is used in conjunction with a generic lumped-mass car model. The presented lumped-mass modelling approach is an efficient tool that can be used in several stages of design for vehicle safety and in accident reconstruction.

Keywords: Vehicle stiffness, Head-on frontal collision, Lumped-mass modelling

1. INTRODUCTION

By law, all new car models have to satisfy safety related legislations before they are sold on the market. In Europe, cars have to meet the legislations described in the regulations of the UN Economic Commission for Europe (ECE). In the United States, the corresponding regulations are the Federal Motor Vehicle Safety Standards (FMVSS). Apart from the legal requirements, there are consumer tests which urge car manufacturers to produce safer cars by exceeding the minimum requirements. The results of consumer tests are made public. The most important consumer tests are the New Car Assessment Programs (NCAP). In Europe, the consumer test is EuroNCAP. In US, the consumer tests are the US NCAP and the Insurance Institute for Highway Safety (IIHS) tests.

The crash test data obtained in US NCAP tests are available for researchers through the website of National Highway Traffic Safety Administration (NHTSA). US NCAP tests include full-width fixed rigid barrier (FWRB) frontal impacts at an impact speed of 56 km/h. In the website of NHTSA, there are also crash test data for FWRB frontal impacts at an impact speed

of 40 km/h for FMVSS 208 compliance testing; however the number of available crash test data at this impact speed are few. The overall frontal stiffnesses of cars can be derived by utilising these crash test data. Apart from the mass of the vehicle, the stiffness and the geometry of the energy-absorbing structures are the key parameters that determine the crash pulse experienced by vehicles in collisions. Therefore, in designing the occupant restraint systems, the stiffness of the energy-absorbing structures needs to be known.

Cars can earn good ratings in consumer crash tests but they may perform poorly in real-world accidents due to a lack of good compatibility with other cars. Load compatibility deals with the differences between colliding vehicles in terms of their respective masses and structural stiffnesses. Typically, a stiffness mismatch occurs between heavier and lighter vehicles. For frontal impact protection, regulatory and consumer crash tests involve a single vehicle and they are conducted at fixed impact speeds hence these tests help to design the vehicle for its self-protection. However, these tests produce stiffer front-end energy-absorbing structures for heavy vehicles since such vehicles must absorb the higher kinetic energy (due to their greater mass) within a limited deformation space. On the other hand, lighter vehicles must manage a lesser amount of kinetic energy thus their front energy-absorbing structures can be less stiff. So a stiffness mismatch can occur between heavier and lighter vehicles. To prevent intrusion in frontal crashes, small light cars can be designed to have stiffer front structures but then occupant deceleration needs to be limited by optimising the restraint systems [Himmetoglu, 2016].

In this study, three different approaches are studied to determine the loading stiffnesses of cars. The derived stiffnesses are used as inputs for a generic lumped-mass car model which is used to simulate the key responses of the actual car that experienced FWRB frontal impact in the US NCAP test. A method to derive the stiffnesses is proposed which produces closely the responses of cars in the US NCAP FWRB tests. The lumped-mass car model is then used to simulate head-on frontal collision of two cars and predict the kinematics and deformations of the cars.

2. US NCAP FULL-WIDTH FIXED RIGID BARRIER (FWRB) FRONTAL IMPACT TEST

In consumer and regulatory frontal impact tests, cars impact a fixed rigid barrier (i.e. fixed rigid wall) with 100% overlap (i.e. full-width) at a fixed impact speed as shown in Figure 1. In US NCAP FWRB test, the cars impact the barrier at a velocity of $V_0 = 56$ km/h. The aim of this test is to obtain information about vehicle crashworthiness and the performance of the restraint systems. The rigid wall is composed of load cells measuring the crush forces and moments

acting on the car as shown in Figure 2(a). A typical example for the load cell matrix and its position with respect to the car front are depicted in Figure 2(b).



Figure 1. FWRB frontal impact test [NHTSA, 2018]



(a) (b)

Figure 2. (a) Load cell wall, (b) Locations of load cells relative to the car [NHTSA, 2018]

In these tests, a 50th percentile male Hybrid III dummy and a 5th percentile female Hybrid III dummy are placed in the driver seat and the front passenger seat, respectively. The dummies are belted and equipped with tri-axial accelerometers, potentiometers and load cells. The accelerometers are placed on the head, chest, pelvis and feet of the dummies. Several accelerometers are also attached to the vehicle structure such as the rear sills, rear seats and engine. The responses of the dummies and the vehicle structure are recorded on an on-board data acquisition system.

3. EXTRACTION OF FRONTAL STIFFNESS FROM US NCAP FWRB IMPACT TESTS

In the US NCAP FWRB test, the total barrier force (i.e. crush force or wall force) is obtained by adding the individual forces measured by the load cells on the rigid barrier. However, the individual load cell forces are first filtered according to the Society of Automotive Engineers (SAE) Recommended Practice J211-1 [SAE, 2007]. The linear accelerations of the occupant compartment of the car are recorded by accelerometers which are typically attached symmetrically to the left-and-right rear sills, or left-and-right rear seats, or left-and-right rear floorpan. The occupant compartment linear accelerations are expressed in the x and z

directions of the global coordinate system shown in Figure 1. However, vehicle acceleration data need to be filtered before use. For comparison of vehicle crash performance, vehicle accelerometer data are filtered according to SAE J211-1 [SAE, 2007]. The linear displacement of the undeformed occupant compartment in the global x-direction is used to estimate the deformation of the car. Therefore, the occupant compartment linear acceleration in the global x-direction needs to be double integrated to find the displacement according to SAE J211-1. The filtered linear accelerations on the right and left side of the occupant compartment are averaged to obtain a single average occupant-compartment acceleration in the global x-direction which is then double integrated using trapezoidal rule to find the x-displacement and deformation of the car. Since the deformation of the car is based on the double-integration of accelerometer data, the term "dynamic deformation (or crush)" can be used to indicate the deformation of the car which changes during impact [Swanson et al., 2003]. The time increment for the load cell and accelerometer data is typically 0.1 ms.

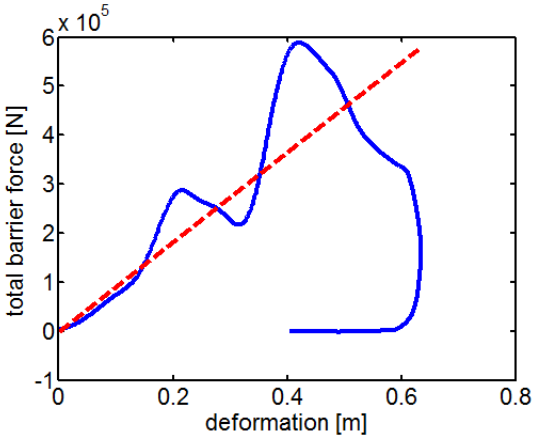


Figure 3. Typical force-vs-deformation behaviour of vehicle structure in US NCAP FWRB test

After having processed the sensor data as described above, the total barrier force is plotted against the displacement of the occupant compartment to obtain the overall force versus deformation characteristics of the structural elements of the car in frontal impact. The blue curve in Figure 3 shows an exemplar of force versus deformation characteristics derived from US NCAP FWRB crash test data. It can be seen that the deformation of the car structure is predominantly plastic.

In order to define an overall frontal stiffness of the car, it is common practice to approximate the force versus deformation behaviour in the loading phase by a straight-line as shown by the red dashed line in Figure 3. The slope of this straight-line is defined as the frontal loading stiffness of the car or simply the frontal stiffness of the car [Mooi and Huibers, 2000; Huston, 2013; Huang, 2002; Himmetoglu, 2016; Wiacek et al., 2015].

The stiffness of the car as defined above can be used in conjunction with lumped-mass modelling of a vehicle for several purposes such as obtaining analytical solutions to vehicle crash mechanics problems [Huston, 2013; Huang, 2002; Mooi and Huibers, 2000; Himmetoglu, 2016], testing the feasibility of proposed design concepts [Pilkey et al., 2009; Elmarakbi and Zu, 2006], performing accident reconstruction [Huang, 2002; Brach and Brach, 2005] and evaluating key responses and parameters regarding the overall crash performance of cars [Mooi and Huibers, 2000; Swanson et al., 2003; Patel et al., 2007; Wiacek et al., 2015; Himmetoglu, 2016].

In this study, in order to simulate US NCAP FWRB frontal impacts, a generic lumped-mass model of a car as shown in Figure 4 is used in which the energy-absorbing structures of the car that deform during the impact is modelled as a spring like element simulating the force versus deformation characteristics of the structures similar to the one given in Figure 3. The block with mass m in the lumped-mass model of the car in Figure 4 is constrained to move only in the x-direction which is the predominant motion in US NCAP FWRB crash tests.

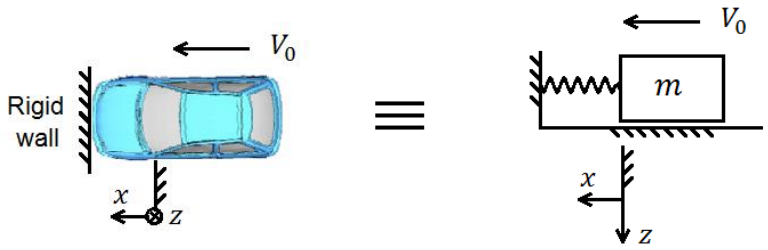


Figure 4. Lumped-mass model of a car to simulate US NCAP FWRB frontal impacts

4. METHODS TO DETERMINE FRONTAL LOADING STIFFNESS OF A CAR

There are several methods to determine frontal loading stiffness based on US NCAP FWRB tests but no single agreed-upon method exists. Based on the previous studies [Swanson et al., 2003; Patel et al., 2007; Wiacek et al., 2015], three different methods are studied to determine the frontal loading stiffnesses of cars to be used together with the lumped-mass model in Figure 4.

The first method is based on fitting a straight-line to the force-versus-deformation curve (see Figure 3) for the interval between zero and maximum deformation by using linear regression with zero intercept. Hence, the stiffness value obtained using this method will be called "regression based frontal loading stiffness (k_{Lr})" in this paper.

The second method is based on equating the area under the force-versus-deformation curve in the loading phase (see Figure 3) to spring energy as shown in Equation (1) in order to obtain the "barrier-force-work based frontal loading stiffness (k_{Lbf})". In Equation (1), the terms x_{max}

, F and x represent the maximum deformation of the car, the total barrier force and the deformation of the car, respectively. x_{max} is estimated from accelerometer data.

$$\frac{1}{2}k_{Lbf}x_{max}^2 = \int_0^{x_{max}} F dx \quad (1)$$

The third method is based on equating the initial kinetic energy of the car to spring energy for the loading phase as shown in Equation (2) in order to obtain the "initial-kinetic-energy based frontal loading stiffness (k_{Lke})". In Equation (2), the terms x_{max} , m and V_0 represent the maximum deformation of the car, the mass of the car and the impact velocity of the car, respectively. x_{max} is again estimated from accelerometer data.

$$\frac{1}{2}k_{Lke}x_{max}^2 = \frac{1}{2}mV_0^2 \quad (2)$$

5. MODELLING THE UNLOADING PHASE OF IMPACT

The methods described in Section 4 are aimed at finding a single loading stiffness value to characterise the overall behaviour of a car in FWRB crash test. In this section, the aim is to determine a single unloading stiffness value to characterise the unloading behaviour of the car. Modelling the unloading phase of the impact using the lumped-mass model in Figure 4 is not studied in detail in the literature [Huston, 2013; Huang, 2002]. In the model of Huang (2002), the unloading phase in the force-versus-deformation curve is approximated by a single straight-line whose slope is defined as the unloading stiffness as shown in Figure 5(a). However, the modelling of unloading phase by Huang (2002) has not been found detailed enough to simulate closely the response of the car in the unloading phase of FWRB impacts. Therefore, in this study, the unloading phase is modelled differently and a method to derive the unloading stiffness is proposed as shown in Figure 5(b).

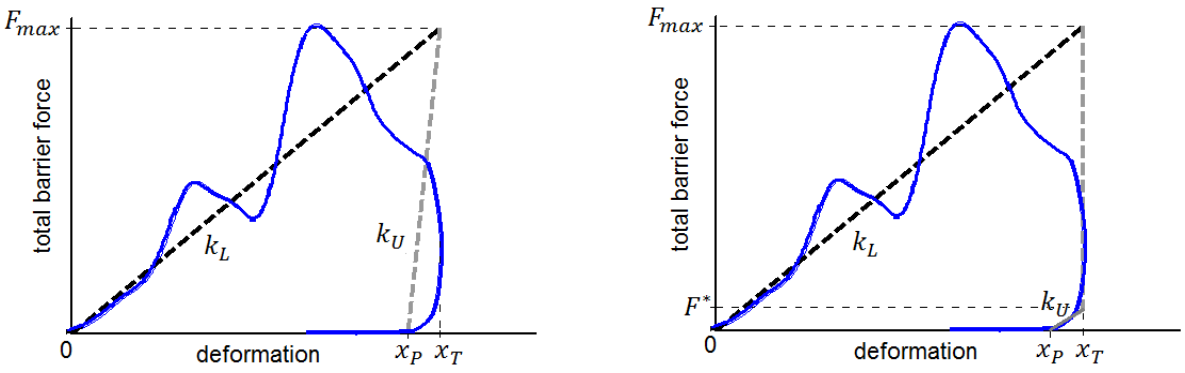


Figure 5. (a) Huang's model [Huang, 2002], (b) Proposed model for the unloading phase

In Figure 5, the unloading phase is represented by thick gray dashed straight-lines. In the proposed model (Figure 5(b)), the unloading stiffness is the slope of the straight line joining the coordinates (x_T, F^*) and $(x_P, 0)$. In Figure 5, k_L and k_U are the loading and unloading stiffnesses respectively; x_P and x_T are the permanent deformation and total (maximum) deformation respectively. In the proposed model, F^* is defined as the "separation force".

6. THE GOVERNING EQUATIONS DESCRIBING THE DYNAMICS OF FWRB IMPACT

In this study, the generic lumped-mass car model in Figure 4 is used in conjunction with the proposed model (or approximation) shown in Figure 5(b) for the force-versus-deformation behaviour of the car structure. In order to describe the dynamics of FWRB impacts in which frictional tyre forces are neglected, the following notation will be used:

x : deformation or displacement of the car

x_T : total (maximum) deformation ; x_P : permanent deformation

x_e : elastic rebound displacement ($x_e = x_T - x_P$) ; V_0 : impact velocity

k_L : loading stiffness ; k_U : unloading stiffness ; e : coefficient of restitution

F_{max} : maximum barrier (or crush) force ; F^*: separation force

c : force drop ratio: F_{max}/F^* ; m : mass of the car

W_T : total crush energy absorbed by the car structure

W_R : elastic energy returned by the car structure ; V': rebound velocity of the car

The governing equations for the lumped-mass car model to describe FWRB impacts are:

$$F_{max} = k_L x_T \quad , \quad F^* = k_U x_e \quad , \quad F_{max} = cF^* \tag{3}$$

$$W_T = mV_0^2/2 = k_L x_T^2/2 = F_{max} x_T/2 \tag{4}$$

$$W_R = m\left(V'\right)^2/2 = F^* x_e/2 = k_U x_e^2/2 \tag{5}$$

$$W_R/W_T = \left(\frac{V'}{V_0}\right)^2 = k_U x_e^2/(k_L x_T^2) = F^* x_e/(F_{max} x_T) = e^2 \tag{6}$$

Using Equation (1), one can obtain

$$k_L/k_U = c\, x_e/x_T \tag{7}$$

Equations (6) and (7) yield

$$e = \sqrt{x_e/(c\, x_T)} = (1/c)\sqrt{k_L/k_U} \tag{8}$$

In order to produce the linear approximation of force-versus-deformation curve of a car in the proposed model shown in Figure 5(b), the separation force F^* needs to be determined. In the crash test report of each car in US NCAP FWRB impact tests [NHTSA, 2018], the rebound velocity V' is reported and the elastic rebound displacement x_e can be estimated from crash test data once the force-versus-deformation curve is constructed as described in Section 3. Hence, F^* can be determined to satisfy the rebound velocity and the elastic rebound displacement in the unloading phase. Using Equation (5), F^* is calculated as

$$F^* = m(V')^2/x_e \tag{9}$$

7. FORCE VERSUS DEFORMATION BEHAVIOUR AT 40 KM/H AND 56 KM/H

Three cars are selected from NHTSA crash test database [NHTSA, 2018] which underwent FWRB frontal impact test at impact speeds of 40 km/h and 56 km/h. In this database, there are no FWRB tests at other impact speeds. These three cars, denoted by CarX, CarY and CarZ, are manufactured between years 2000 and 2010.

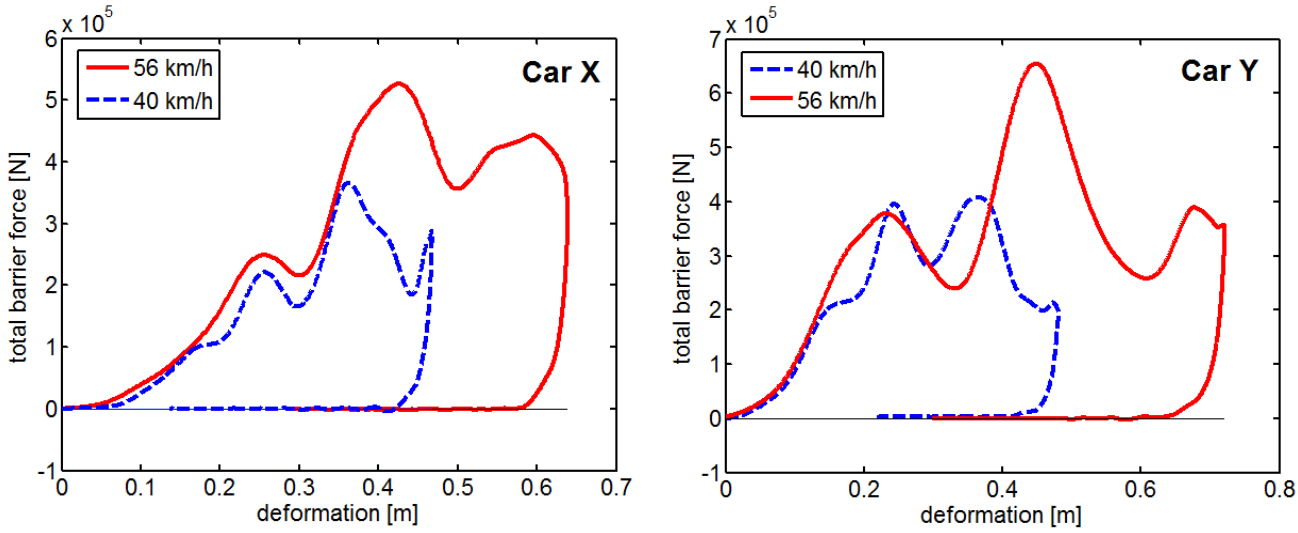


Figure 6. Force versus deformation behaviour of CarX and CarY at 40 km/h and 56 km/h

The force-versus-deformation behaviours of these three cars are given in Figures 6 and 7. The longitudinal member top heights of CarX, CarY and CarZ are 529 mm, 516 mm and 371 mm, respectively. Longitudinal members are at the front of vehicles; they exist in pairs and they are the main structures that absorb crush energy during impact.

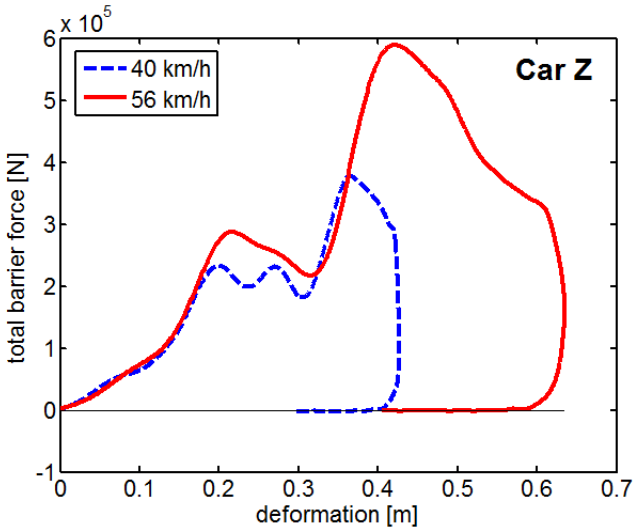


Figure 7. Force versus deformation behaviour of CarZ at 40 km/h and 56 km/h

The proposed linear approximation of the force-versus-deformation curves at a given impact speed must be extended for other impact speeds. A careful analysis of car structure behaviour in Figures 6 and 7 leads to the following model and formulation shown in Figure 8 and Equations (10-12). In Figure 8, F_{max1} and F_{max2} are the maximum crush forces developed at impact speeds 1 and 2, respectively; F_1^* and F_2^* are the separation forces at impact speeds 1 and 2, respectively; x_{T1} and x_{T2} are the maximum deformations at impact speeds 1 and 2, respectively; x_{P1} and x_{P2} are the permanent deformations at impact speeds 1 and 2, respectively.

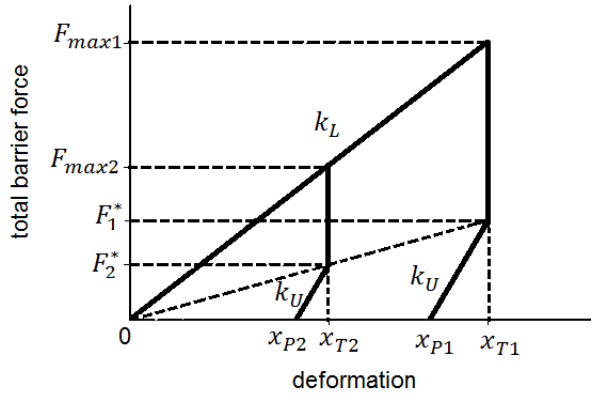


Figure 8. Proposed linear approximation for force-vs-deformation curves at different impact speeds

For both impact speeds, the loading stiffness k_L, the unloading stiffness k_U and the force drop ratio c are defined to be the same. Thus, k_L, k_U and c are the characteristics of the car structure. The geometry of the linear approximation of the force-versus-deformation curves in Figure 8 are described by the following equations:

$$F_1^*/F_2^* = x_{T1}/x_{T2} = F_{max1}/F_{max2} = cF_1^*/(cF_2^*) \quad (10)$$

$$k_U = F_1^*/(x_{T1} - x_{P1}) = F_1^*/x_{e1} = F_2^*/(x_{T2} - x_{P2}) = F_2^*/x_{e2} \quad (11)$$

$$x_{e1}/x_{e2} = x_{T1}/x_{T2} \quad (12)$$

8. VALIDATION OF THE PROPOSED MODEL

FWRB crash test data for CarZ is used to validate the proposed model shown in Figure 8 which is used in conjunction with the lumped-mass car model in Figure 4. First, the loading and unloading stiffnesses (i.e. k_L and k_U), and the force drop ratio c are determined for each car by applying linear approximation to the force-versus-deformation curve at the impact speed of 56 km/h as shown in Figure 5(b). Then, for each car k_L, k_U and c are used as the fixed parameters of the lumped-mass car model whose responses at different impact speeds are estimated by varying only the impact speed in the model.

Key responses regarding the overall crash performance at 56 km/h impact speed are compared in Table 1 in which three different types of frontal loading stiffnesses, given in Section 4, are evaluated. In Table 1, the following notation is used:

V_0 : impact velocity of the car , m : mass of the car

k_L : loading stiffness , k_U : unloading stiffness , c : force drop ratio

x_T : maximum deformation of the car , x_P : permanent deformation of the car

x_e : elastic rebound displacement of the car , F_{max} : maximum crush-force

F_{mean} : mean crush-force , OC : occupant compartment

a_{max} : largest x-acceleration of OC , a_{mean} : mean x-acceleration of OC

t_{zv} : time to zero velocity , V' : rebound velocity of the car , e : coefficient of restitution

Model-r : Model with regression based loading stiffness

Model-bf : Model with barrier-force-work based loading stiffness

Model-ke : Model with initial-kinetic-energy based loading stiffness

In Table 1, there are two numbers for the x_P value obtain from crash test data; the first one is obtained from the crash test report and it is the permanent deformation of the car measured at the centreline of the car after the crash test; the second one is an estimated permanent deformation which is the value of deformation when barrier force becomes zero during rebound. In the "Crash Test" column of Table 1, the values of V_0, m, x_P (the first value), $V'$and e are available in the crash test report while the others are estimated by processing the crash test data.

The mean crush-force and mean acceleration which are given by Equation (13), pertain to the loading phase which is the predominant phase of the impact. In Equation (13), F is the crush force or total barrier force at any instant. t_{zv} is the time at which the velocity of the car becomes zero and at this time the maximum deformation of the car occurs and the loading phase ends. t_{zv} is therefore the duration of the loading or deformation phase of the impact.

$$F_{mean} = (\int_0^{x_T} F dx)/x_T \quad , \quad a_{mean} = F_{mean}/m \tag{13}$$

Table 1. Crash test data versus model responses for CarZ (impact speed: 56 km/h)

	Crash Test	Model-r	Model-bf	Model-ke
V_0	56.3 km/h	56.3 km/h	56.3 km/h	56.3 km/h
m	1349 kg	1349 kg	1349 kg	1349 kg
k_L	--	647556 N/m	912435 N/m	823861 N/m
k_U	--	689512 N/m	689512 N/m	689512 N/m
c	--	10.79	15.2	13.72
x_T	0.635 m	0.717 m	0.604 m	0.635 m
x_P	0.51 m - 0.58 m	0.654 m	0.551 m	0.580 m
x_e	5.53 cm	6.24 cm	5.26 cm	5.53 cm
F_{max}	589121 N	464036 N	550825 N	523407 N
F_{mean}	289839 N	232018 N	275413 N	261704 N
a_{max}	-43.18 g	-35.04 g	-41.59 g	-39.52 g
a_{mean}	-21.89 g	-17.52 g	-20.80 g	-19.76 g
t_{zv}	72 ms	71.72 ms	60.42 ms	63.59 ms
V'	-4.5 km/h	-5.076 km/h	-4.276 km/h	-4.5 km/h
e	0.08	0.09	0.076	0.08

Figures 9 and 10 show the comparison of force-versus-deformation behaviour between the crash test and the models. Looking at the results in Table 1, it can be seen that Model-r shows the worst agreement with the crash test data. Model-ke reproduces the deformations, rebound velocity and e as expected but the crush forces and accelerations involve some disparities. Model-bf shows the best agreement with the crash test data in terms of crush forces and accelerations; moreover the deformations (x_T, x_P and x_e) are more realistic because in FWRB impacts, there is typically a forward pitch of the car (see Figure 1) and since the x-displacement of the car is derived from accelerometers attached to the rear of the car, the maximum deformation of the car is calculated from the crash test data with an excess. Therefore, to further validate Model-bf, the FWRB crash test data at 40 km/h are compared with the responses of Model-bf at this impact speed as shown in Table 2.

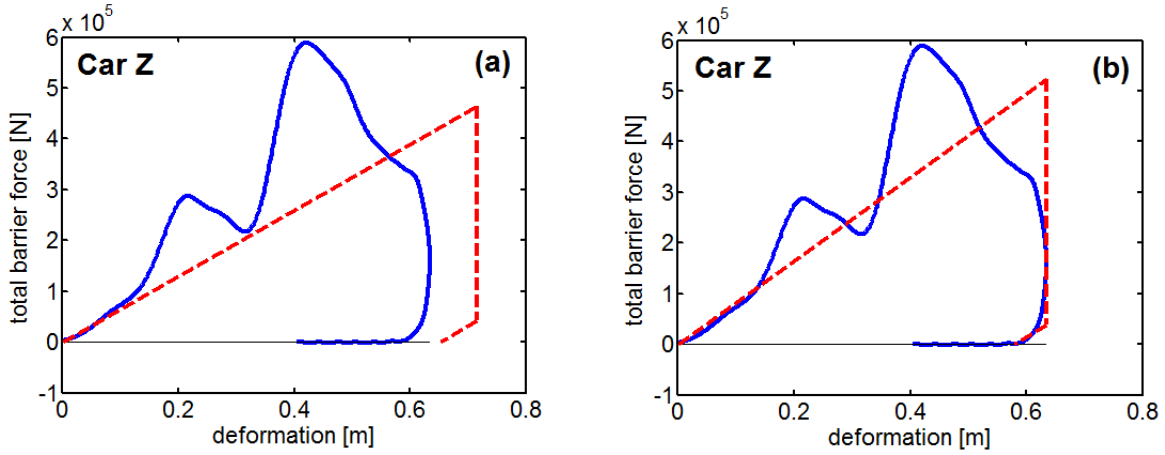


Figure 9. Force-vs-deformation behaviour at 56 km/h, (a) Model-r response, (b) Model-ke response

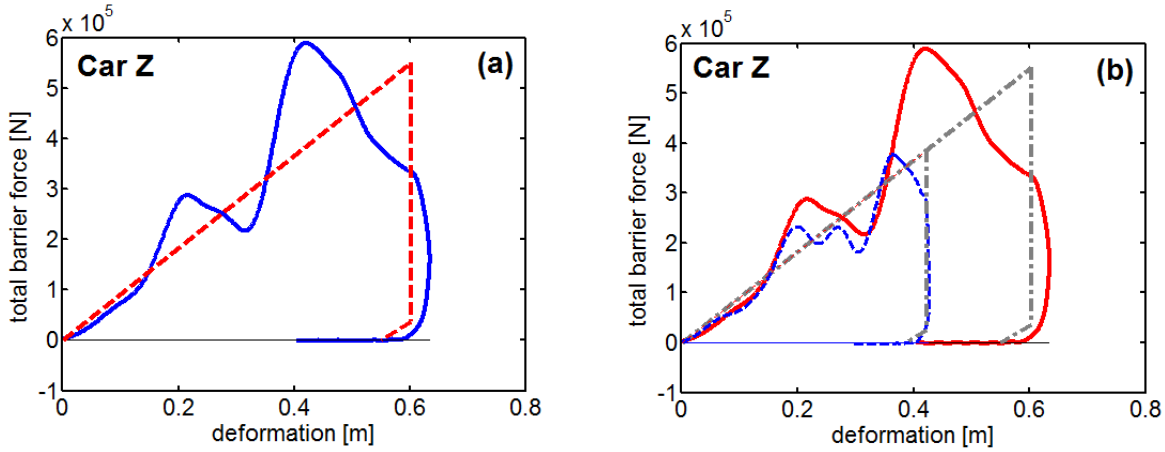


Figure 10. Force-vs-deformation behaviour for Model-bf, (a) 56 km/h, (b) 40 km/h and 56 km/h

Table 2. Crash test data versus model responses for CarZ (impact speed: 40 km/h)

	Crash Test	Model-bf
V_0	39.7 km/h	39.7 km/h
m	1331 kg	1331 kg
k_L	--	912435 N/m
k_U	--	689512 N/m
c	--	15.2
x_T	0.427 m	0.423 m
x_P	0.391 m	0.386 m
x_e	3.57 cm	3.68 cm
F_{max}	377348 N	385709 N
F_{mean}	180385 N	192854 N
a_{max}	-36.65 g	-29.47 g
a_{mean}	-13.78 g	-14.74 g
t_{zv}	67.60 ms	60.06 ms
V'	-3 km/h	-3.012 km/h
e	0.075	0.076

In the "Crash Test" column of Table 2, the values of V_0, m, $V'$and e are available in the crash test report while the others are estimated by processing the crash test data. Table 2 and Figure 10(b) indicate that Model-bf responses are in very good agreement with crash test data although there is some disparity in a_{max} value. Matching a_{max} values are not always possible since there may still occur some sharp peaks in acceleration after the filtering process. Hence, matching a_{mean} values is more reliable in terms of comparing crash severity.

9. SIMULATION OF HEAD-ON FRONTAL COLLISION BETWEEN CarX AND CarY

The modelling and validation procedures described in Section 8 have been applied to CarX and CarY and Model-bf produced the best agreement with the crash test data for both CarX and CarY. In this section, the head-on frontal collision between CarX and CarY is simulated to predict the crash performances of these two cars since experimental data for this accident does not exist. For this purpose, a lumped-mass head-on frontal collision model is used as shown in Figure 11. In this model, the tractional and/or braking forces are neglected during impact. It can be seen that this model applies to central in-line collision which means the energy absorbing structures of the vehicles line up. For this reason, CarX and CarY are selected in this analysis since they have very similar longitudinal member top heights.

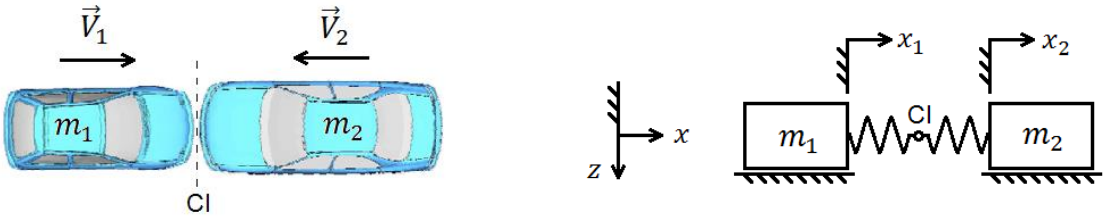


Figure 11. A lumped-mass head-on frontal collision model (CI: contact interface)

The following notation is used in this head-on collision model:

$\vec{V}_1 = V_1\vec{i}$, $\vec{V}_2 = V_2\vec{i}$: velocities of cars 1 and 2 respectively, at the start of the impact

$\vec{V}_1^{'} = V_1^{'}\vec{i}$, $\vec{V}_2^{'} = V_2^{'}\vec{i}$: velocities of cars 1 and 2 respectively, at the end of the impact

$\vec{V}_c = V_c\vec{i}$: common velocity of cars at the end of the loading phase

x_1 , x_2 : displacements of car 1 and car 2, respectively

m_1 , m_2 : masses of car 1 and car 2, respectively

k_{L1} , k_{L2} : loading stiffnesses of the structures of cars 1 and 2 respectively

k_{U1} , k_{U2} : unloading stiffnesses of the structures of cars 1 and 2 respectively

c_1 , c_2 : force drop ratios of cars 1 and 2 respectively

x_{T1} , x_{T2} : maximum deformations of cars 1 and 2 respectively

x_{P1} , x_{P2} : permanent deformations of cars 1 and 2 respectively

x_{e1} , x_{e2} : elastic rebound displacements of cars 1 and 2 respectively

F_{max} : the magnitude of the crush force acting on both vehicles at maximum deformation

W_T : the total crush energy absorbed by the structures of the both cars

W_{T1} , W_{T2} : total crush energies absorbed by cars 1 and 2 respectively

W_R : the crush energy returned as kinetic energy in the unloading phase

W_L : the energy lost in the collision

e : the coefficient of restitution of the collision

The governing work-energy and momentum equations for the lumped-mass head-on collision model are given below (the derivations of these equations can be found in the paper by Himmetoglu (2016).

$$m_1V_1^2/2 + m_2V_2^2/2 = (m_1 + m_2)V_c^2/2 + k_{L1}x_{T1}^2/2 + k_{L2}x_{T2}^2/2 \quad (14)$$

$$m_1V_1 + m_2V_2 = (m_1 + m_2)V_c \quad (15)$$

$$F_{max} = k_{L1}x_{T1} = k_{L2}x_{T2} \quad (16)$$

$$W_T = k_{L1}x_{T1}^2/2 + k_{L2}x_{T2}^2/2 = F_{max}x_{T1}/2 + F_{max}x_{T2}/2 \quad (17)$$

$$W_{T1} = F_{max}x_{T1}/2 \quad , \quad W_{T2} = F_{max}x_{T2}/2 \quad (18)$$

$$W_R = k_{U1}(x_{T1} - x_{P1})^2/2 + k_{U2}(x_{T2} - x_{P2})^2/2 \quad (19)$$

$$W_L = m_1V_1^2/2 + m_2V_2^2/2 - m_1\left(V_1^{'}\right)^2/2 - m_2\left(V_2^{'}\right)^2/2 \quad (20)$$

$$e = (V_2' - V_1')/(V_1 - V_2) \quad (21)$$

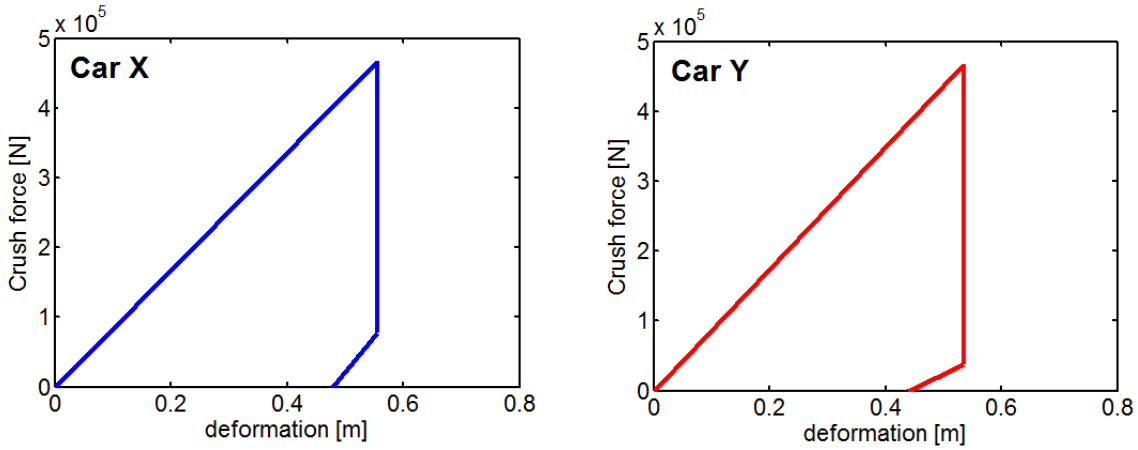


Figure 12. Head-on collision simulation, force-versus deformation behaviour

Application of Equations (14-21) produces the key responses of CarX and CarY in a head-on collision simulation. A case study and results are given in Table 3 and Figure 12.

Table 3. Head-on collision simulation results for CarX and CarY

	CarX	CarY
m (mass of the car)	1280 kg	1630 kg
k_L (loading stiffness)	841626 N/m	871054 N/m
k_U (unloading stiffness)	1011941 N/m.	380741 N/m
c (force drop ratio)	5.98	12.7
V (impact velocity)	48 km/h	-48 km/h
V_c (common velocity)	-5.77 km/h	-5.77 km/h
x_T (maximum deformation)	0.555 m	0.536 m
x_P (permanent deformation)	0.478 m	0.440 m
x_e (elastic rebound displacement)	7.717 cm	9.670 cm
a_{max} (largest acceleration of OC)	-37.204 g	29.215 g
a_{mean} (mean acceleration of OC)	-18.602 g	14.608 g
V' (rebound velocity)	-13.15 km/h	0.02 km/h
ΔV (change of velocity during impact)	-61.15 km/h	48.02 km/h
e (coefficient of restitution)	0.137	

10. FORCE VS DEFORMATION BEHAVIOUR AT HIGHER IMPACT SPEEDS

The regulatory and consumer crash tests are performed at a specific impact speed at or below 56 km/h and the data of these tests are the only ones available for most researchers in the academia. Force versus deformation behaviour of cars in FWRB tests at higher impact speeds would be a useful information for researchers. For this reason, the finite element (FE) model of CarX which was constructed by the National Crash Analysis Center of The George Washington University [NHTSA, 2018] through detailed reverse engineering is subjected to FWRB frontal impacts at impact speeds varying from 20 km/h to 88 km/h. The FE model of CarX was validated against real crash test data from FWRB frontal impacts at 40 km/h and 56 km/h, and offset deformable barrier frontal impact at 64 km/h with 40% overlap [NHTSA, 2018]. In order to test the robustness of the FE model of CarX, other types of impacts were also performed (without validation against real crash test data) including centreline pole impact, full and offset frontal impacts with another FE model of a car [NHTSA, 2018].

In this paper, the FE simulations of CarX are performed using LS-DYNA (2018) finite element program and LS-Prepost (2018) keyword manager program. The generated keyword files are

solved by the LS-DYNA solver in ANSYS Mechanical APDL (2018) using distributed computing for INTEL MPI on a local workstation. Figure 13 shows the FE model of CarX just after the FWRB impact at various impact speeds. The occupant compartment of the car deforms significantly for impact speeds higher than 72 km/h. Figure 14 and 15 show the corresponding crush force versus deformation (i.e. change in car length) characteristics of CarX structure at all impact speeds obtained by using the FE model.

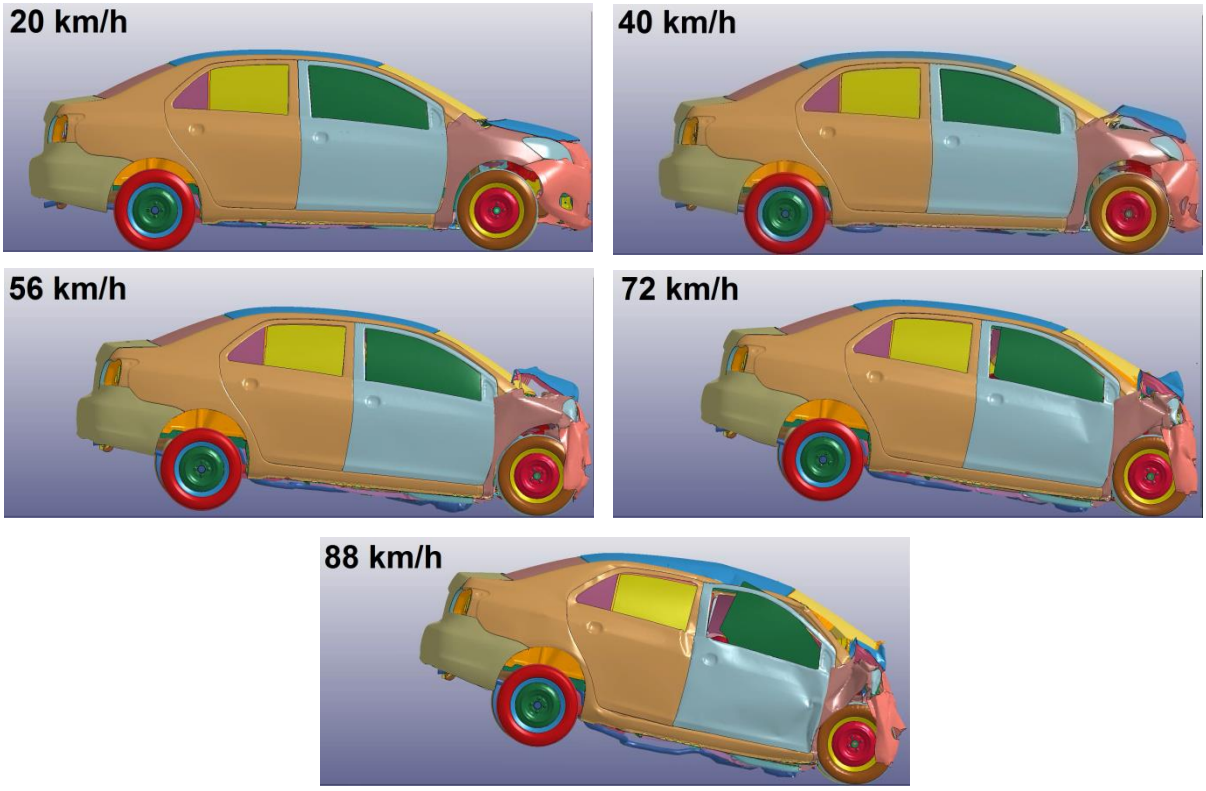


Figure 13. FE model of CarX just after FWRB impact at different impact speeds

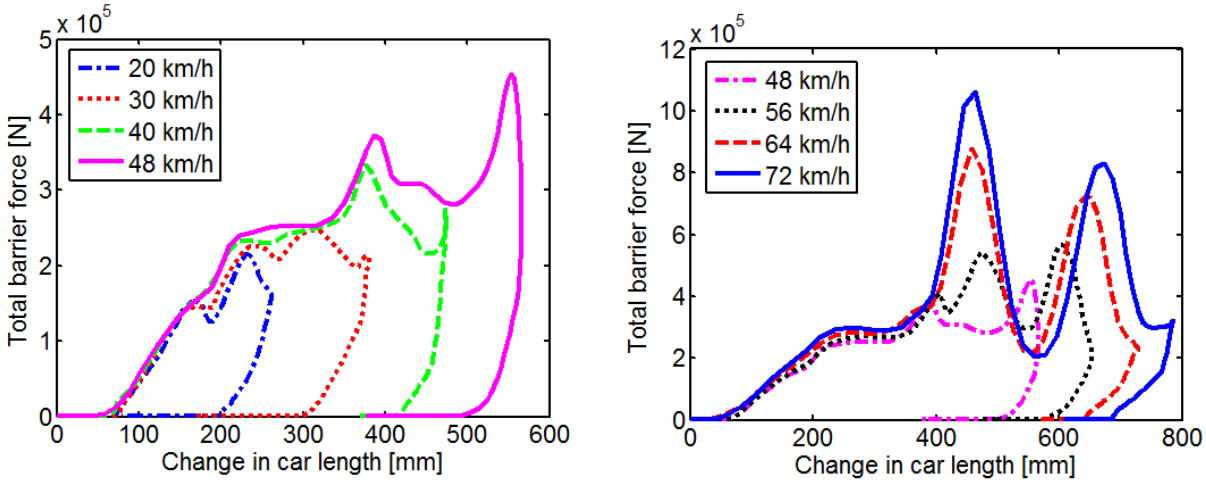


Figure 14. Crush force vs deformation behaviour of CarX FE model in FWRB impacts

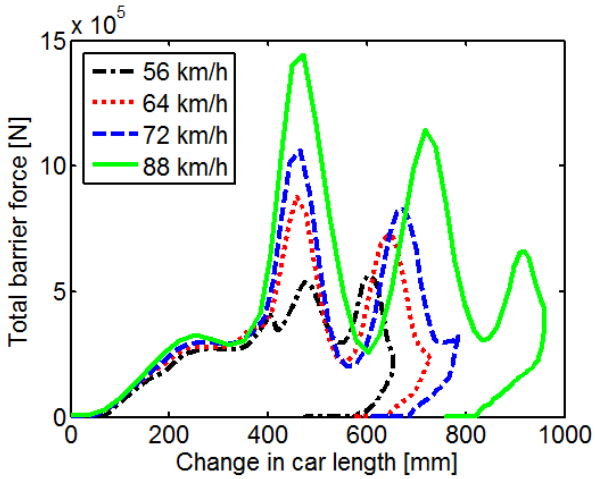


Figure 15. Crush force vs deformation behaviour of CarX FE model in FWRB impacts

It can be seen that crush force versus deformation curve at a higher impact speed encompasses the corresponding curve at a lower impact speed. Figures 14 and 15 indicate that the proposed linear approximation for crush force versus deformation curves as given in Figure 8, applies to impact speeds upto 56 km/h. For impact speeds higher than 56 km/h, the deformation of the occupant compartment becomes significant and the resistance of the structural elements of the car becomes much more sensitive to deformation rate i.e. impact speed. The occupant compartment structures which should stay intact to protect the occupants, are designed to be much stiffer than the energy absorbing front longitudinal members; therefore at impact speeds higher than 56 km/h, significantly higher crush forces are associated with the deformation of the occupant compartment. It is evident that for impact speeds higher than 56 km/h, the modelling of force versus deformation behaviour of the car structure should be treated differently.

11. DISCUSSIONS AND CONCLUSIONS

The formulation presented in this paper is part of an ongoing project aimed at creating a useful and accurate tool which provides the hand computation and analysis of frontal FWRB impacts and head-on collisions.

Linear approximation of force-versus-deformation behaviour of energy-absorbing structures in frontal impact, provides a single loading stiffness, a single unloading stiffness and a force drop ratio to characterise the loading and unloading phases of the impact accurately. The use of a single value for each stiffness helps to classify cars easily especially for statistical analyses; moreover it provides analytical solutions to crash mechanics problems. Three different approaches are evaluated to determine the loading stiffness and a method to obtain the unloading stiffness is proposed. The use of barrier-force-work based loading stiffness and the

proposed unloading stiffness for the lumped-mass car model has been shown to produce model responses which are in very good agreement with the crash test data in FWRB impacts. The proposed linear approximation of the force-versus-deformation curves derived from 56 km/h FWRB impact tests, is extended for other impact speeds. It should be noted that the proposed modelling approach is valid for impact speeds around and below 56 km/h in FWRB frontal impacts since higher severity crash tests are not performed in regulatory and consumer FWRB frontal crash tests. As shown in this study, the limited number of FE models which can be downloaded from the website of NHTSA, can help to understand and model the force versus deformation behaviour of car structures at higher impact speeds. A regulatory or consumer FWRB crash test at an impact speed of 85 km/h would provide very useful data to researchers.

The models developed in this study can be used in collisions with road furniture. The model in this study is valid for 100% overlap impacts therefore the formulations in this paper can be used to study the full-width collision of a car with a concrete road barrier. In order to study frontal collisions of cars with posts or poles using the simple approach given in this study, the stifnesses would have to be modified and post/pole impacts should be along the centreline of the cars. In order to validate the model for central post/pole impacts, experimental data would be required.

Considering the high cost of crash tests, the presented lumped-mass modelling approach is an efficient and analytical tool which can be used in the preliminary design of vehicle safety systems including load compatibility analysis between cars and accident reconstruction. The key responses obtained through this modelling approach can help to predict the crash performance of cars without needing to perform costly crash tests at impact speeds different than the ones used in regulatory and consumer crash tests.

ACKNOWLEDGEMENTS

The author thanks Korhan Babacan Yılmaz of Hacettepe University Mechanical Engineering Department for running the FE simulations.

REFERENCES

1. **National Highway Traffic Safety Administration (NHTSA), (2018),** www.nhtsa.gov

2. **Himmetoglu, S., (2016)**, "An Analysis of Load Incompatibility in Central in-line Collisions of Vehicles Using Lumped-mass Modelling", Proc. of 17th UMTIK Conference, Bursa, Turkey.

3. **Society of Automotive Engineers (SAE), (2007)**, SAE J211-1 (1995): Instrumentation for Impact Test, Part 1, Electronic Instrumentation.

4. **Wiacek, C., Nagabhushana, V., Rockwell, T., Summers, S., and Zhao, L., (2015)**, "Evaluation of Frontal Crash Stiffness Measures from the U.S. New Car Assessment Program", Proc. of 24th ESV Conference, Gothenburg, Sweden, Paper No 15-0257.

5. **Huston, R.L., (2013)**, "Vehicle Occupant Movement and Impact with the Interior in Frontal Collisions - The 'Second Collision' ", International Journal of Crashworthiness, Vol.18, No.2, pp 152-163.

6. **Huang, M., (2002)**, Vehicle Crash Mechanics, CRC Press, Taylor & Francis Group.

7. **Mooi, H.G., and Huibers, J.H.A.M., (2000)**, "Simple and Effective Lumped Mass Models for Determining Kinetics and Dynamics of Car-to-car Crashes", International Journal of Crashworthiness, Vol.5, No.1, pp 7-24.

8. **Swanson, J., Rockwell, T., Beuse, N., Summers, L., Summers, S., and Park, B., (2003)**, "Evaluation of Stiffness Measures from the U.S. New Car Assessment Program", Proc. of 18th ESV Conference, Nagoya, Japan, Paper No 03-0527.

9. **Patel, S., Smith, D., Prasad, A., and Mohan, P., (2007)**, "NHTSA's Recent Vehicle Crash Test Program on Compatibility in Front-to-Front Impacts", Proc. of 20th ESV Conference, Lyon, France, Paper No 07-0231.

10. **Brach, R.M., and Brach, R.M., (2005)**, Vehicle Accident Analysis and Reconstruction Methods, SAE International, Warrendale, PA, USA.

11. **Pilkey, W.D., Balandin, D.V., Bolotnik, N.N., Crandall, J.R., and Purtsezov, S.V., (2009)**, Injury Biomechanics and Control: Optimal Protection from Impact, John Wiley & Sons, Inc., Hoboken, New Jersey, USA.

12. **Elmarakbi, A.M., and Zu, J.W., (2006)**, "Crash Analysis and Modelling of Two Vehicles in Frontal Collisions using Two Types of Smart Front-end Structures: An Analytical Approach using IHBM", International Journal of Crashworthiness, Vol.11, No.5, pp 467-483.

INVESTIGATING THE EFFECTS OF MATERIALS, GEOMETRIC PROPERTIES AND MODIFICATIONS ON THE CRASHWORTHINESS OF BUMPER AND CHASSIS SYSTEM

Batuhan GÜRER, batuhangrer@gmail.com Middle East Technical University, 06800, Ankara, Turkey

Volkan ESAT, evolkan@metu.edu.tr Middle East Technical University – Northern Cyprus Campus, Center for Sustainability (CfS), Kalkanlı, Güzelyurt, KKTC, Mersin 10, Turkey

ABSTRACT

Accidents are one of the main reasons of death for people across the globe, among which automobile accidents are a major portion resulting in fatalities and various injuries. Crashworthiness aims to affect the design of the structure of the vehicle so that it absorbs as much energy as it can which is sustained from an impact by plastically deforming in a controllable behaviour. The current trend in automobile design and manufacturing is to increase the number of lightweight and recycled components that forms the vehicle. However, using unconventional materials might affect the strength and energy absorption capabilities of the automobile chassis and body that may induce a change in the crashworthiness of the vehicle. This study aims to bring insight into the effects of various conventional as well as lightweight and recycled bumper-chassis systems on vehicle crashworthiness subjected to full-frontal impacts through computational modelling. Investigations are carried out for improving crashworthiness through the use of different materials, various profile thicknesses andmodifications on the system geometry. Various finite element models embodying several bumper-chassis systems such as with crush zone, with hexagonal cross-section, with runner, and with range hood are generated and simulated to evaluate the design choices and modifications. Crush force efficiency and specific total strain energy absorbed are used as decisive parameters in assessing the systems. It is observed that some of the geometrical modifications have improved crash performance of the bumper and chassis system. The best alternative as a material is suggested to be “Recycled 7175 aluminium” with its light weight and considerably high impact energy absorption performance.

Keywords: bumper, chassis, finite element analysis, crush force efficiency, specific energy absorption.

1. INTRODUCTION

Every year around 1.25 million people lose their lives in road traffic accidents [WHO, 2016]. Careless driving, ignoring traffic rules, drinking, and speeding are some of the main factors that cause road traffic accidents. Engineers and scientists continuously seek and improve active and passive safety systems to avoid road vehicle crashes as well as to reduce fatalities in case of a collision.

It is estimated that size of automobile production reaches to about 76 million cars annually. Along with the well-known fact that the world has limited petroleum reserves, sustainability and recyclability phenomena gain significant importance. One of the ways to mitigate the adverse environmental effects of vehicles powered by internal combustion engines is to reduce the mass of cars. 250 million barrels of crude oil can be saved annually by reducing cars' weight by 25% [Davoodi et al., 2010]. Today, many automobile manufacturers select lighter materials to be utilised in their cars. Ford Motor Company's Lincoln Mark VIII is designed and manufactured incorporating lighter structural materials by saving 175 kg when compared to its conventional steel models [Cole and Sherman, 1995]. In a similar research, glass mat thermoplastic (GMT) was used as bumper beam material [Hosseinzadeh et al., 2005]. Crash analysis was carried out by using finite element (FE) analysis software which revealed that impact behaviour GMT type bumper showed better performance compared to the conventional ones.

As composite material choices for bumper beam of an automobile, both glass fibre and carbon fibre can be used. Crashworthiness of those materials are investigated and compared with conventional steel bumper [Cheon et al., 1995]. The behaviour of hybrid kenaf and glass reinforced epoxy composites were also compared against GMT [Davoodi et al., 2010]. It was concluded that mechanical properties of such composites can be improved by adding both natural and glass fibres.

Researchers investigated the ribs effect on bumper system which was produced by using GMT and compared results with other bumper models [Hosseinzadeh et al., 2005]. Simulations were conducted by using ANSYS 5.7 software. The bumper was assembled with two semi-cubic plastic propylene holders which acted as shock absorbers. Similarly, a model was created which had four different parts in the form of two longitudinal crash boxes, one rigid wall and one deformable transverse beam [Belingardi et al., 2013]. The beam was made from pultruded E-Glass fibre-epoxy matrix. Mechanical properties of materials were obtained from the literature. The authors claimed that more realistic results can be obtained by modelling whole vehicle's body in the analysis of frontal impact scenarios.

Researchers employed finite element method in investigating the crash performance of circular cross-sectional tubes of 150 mm diameter and 180 mm height [Acar et al., 2011]. Various tubes with and without axisymmetric indentations were developed. In a crash test scenario they used, a rigid wall of 1500 kg and 9 m/s initial velocity, led to a 45 kJ initial impact energy. Wall thickness, number of indentations, radius of indentations, and taper angle were the initial parameters that were utilised by the researchers. Impact performance of the tubes were evaluated through computing the crush force efficiency, and specific energy absorption parameters. In another study, two different crash scenarios were conducted (low and high speed crashes) in both real crash test environment and computer medium [Qi et al., 2006]. Results of both tests were similar, where the computer model simulated the test highly realistically.

Another possibility for light but strong structural materials is the nano composites. Researchers classified nano composites with respect to the separation of nano-clay platelets as clustered, intercalated and exfoliated [Velmurugan and Balaganesan, 2013]. Quasi-static punch test, impact test, and quasi-static test involving estimation of stiffness and energy absorption were then conducted. Layer number and layer orientation affect the energy absorption capacity. They concluded that nano-clay addition to the model protected fibres and improved energy absorption capacity as they acted as a second filler system.

This study aims to investigate the effects of different modifications made on the bumper and chassis system geometry as well as material choices on the structural crashworthiness of the vehicle through various finite element models.

2. METHODOLOGY

In this research, finite element analyses are carried out to investigate the effects of material properties, profile thickness, and modifications of the bumper - chassis rail system geometry Marc Mentat 2013™ finite element method (FEM) modelling software is used in order to analyse the crash performance of bumper beam and chassis system. The simulations are carried out in a way that frontal car bumper and chassis system hits the rigid wall with significant velocity, through which crash performance of different geometrical modifications and types of materials for the bumper and chassis beam system are investigated.

2.1 Finite Element Modelling

Finite element meshed vehicle body is directly taken from and as a courtesy of The George Washington University's National Crash Analysis Center [NCAC, 2015]. Make and model of the meshed car is Toyota Yaris 2010 sedan type. Model was created realistically in such a way

that all parts of vehicle were created and meshed individually. There are 974,383 elements on the model as given in Figure 1. In the original model, five different element classes are used, which are penta6, hex8, tria3, quad4, and line2. Selection of those different element classes requires assigning separate material and geometrical properties. Dimensions of the vehicle are also the same with the real one.

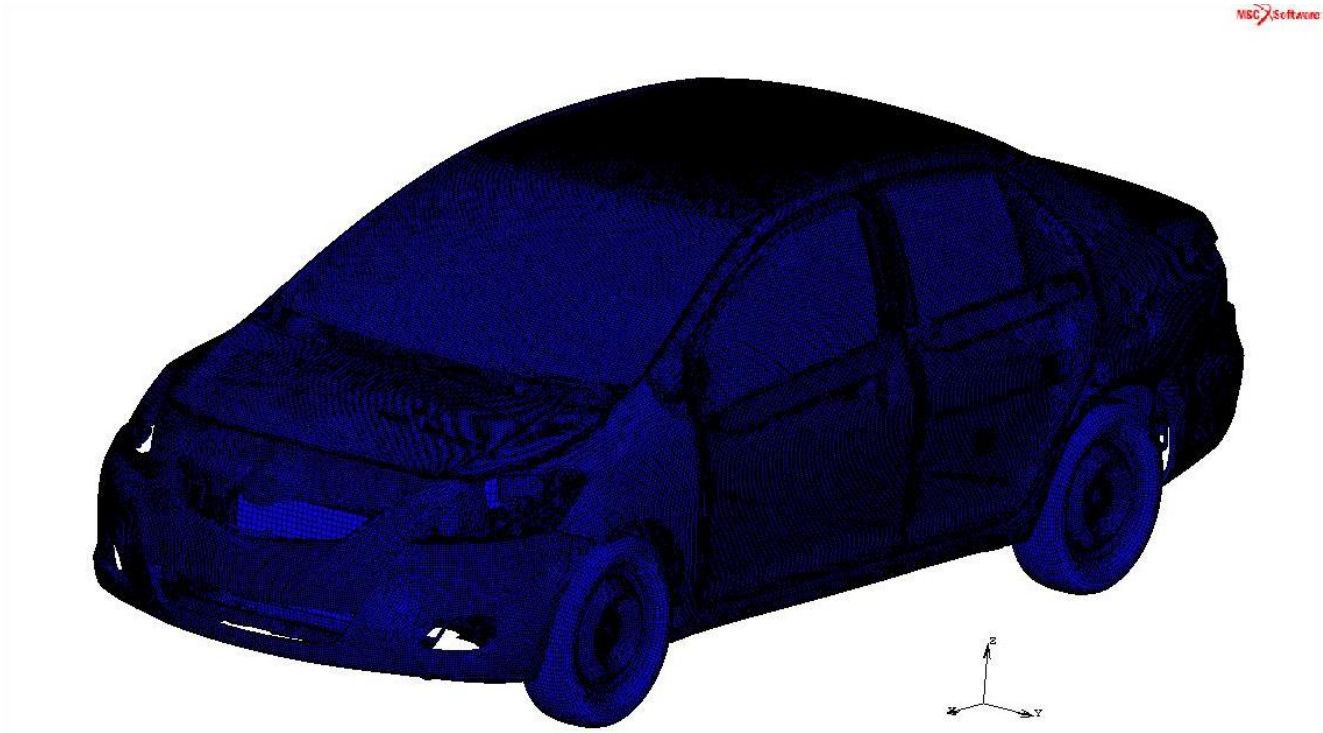


Figure 1. Toyota Yaris 2010 meshed finite element model (The George Washington University's National Crash Analysis Center (NCAC), 2015)

Another reason to select Toyota Yaris 2010 is that it is a typical compact family car with monocoque chassis type. In vehicles with monocoque chassis, loads on the vehicle are supported by the external skin of the vehicle. Moreover, it is cheaper and stronger with respect to other conventional techniques. In this research, the main focus point is to assess the crash performance of the isolated front bumper and frontal chassis system. In order to achieve this, the FE model of the vehicle, first, is reduced to its frontal aspects by deleting the rest of it. Then, nonessential meshed parts of the reduced vehicle are further deleted so that the frontal bumper and the chassis rails are meticulously isolated. Finally, a simplified FE model is created that mimics the isolated realistic model. This simplified front bumper beam and frontal chassis system model has highly similar dimensions, mass, and topological properties as the real Toyota Yaris bumper beam as provided in Figure 2.

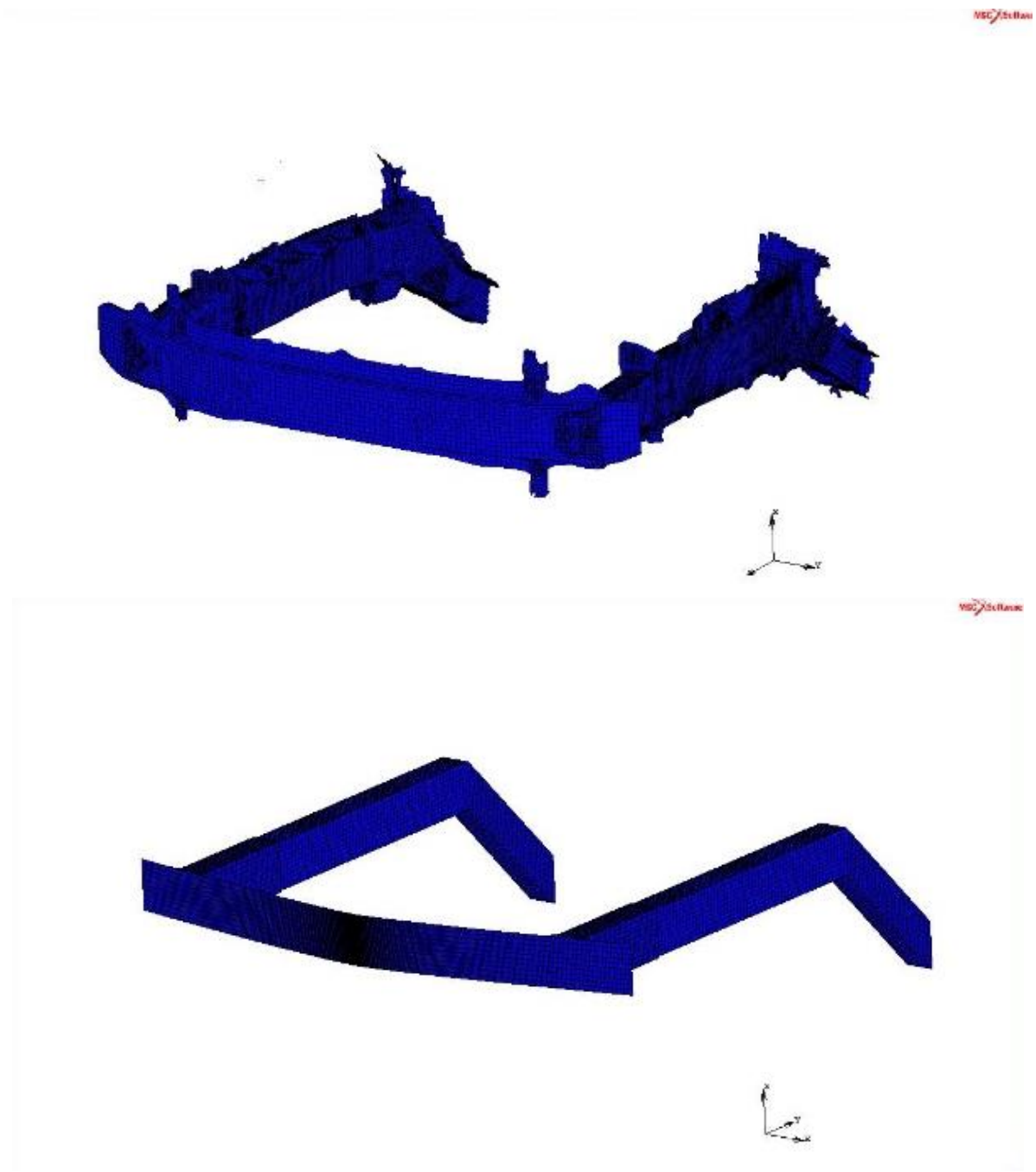


Figure 2. Realistic Toyota Yaris bumper/chassis model (above) and the developed simplified FE model (below)

The simplified model is meshed by using quad (4) type shell elements with varying thicknesses. The minimum number of elements to be used in the model is decided in accordance with sensitivity analysis. As a result, simplified model possesses 23840 elements.

Both quasi-static and dynamic transient types of analysis are tested for the simulations. In quasi-static analysis, bumper and chassis system is fixed at a point but the wall surface is mobile. Motion of the surface is calculated to mimic an impact at a certain velocity. 0.1 s is

decided as crash duration whereas constant velocity of the surface during the crash is taken as 2500 mm/s. The system setup can be seen in Figure 3.

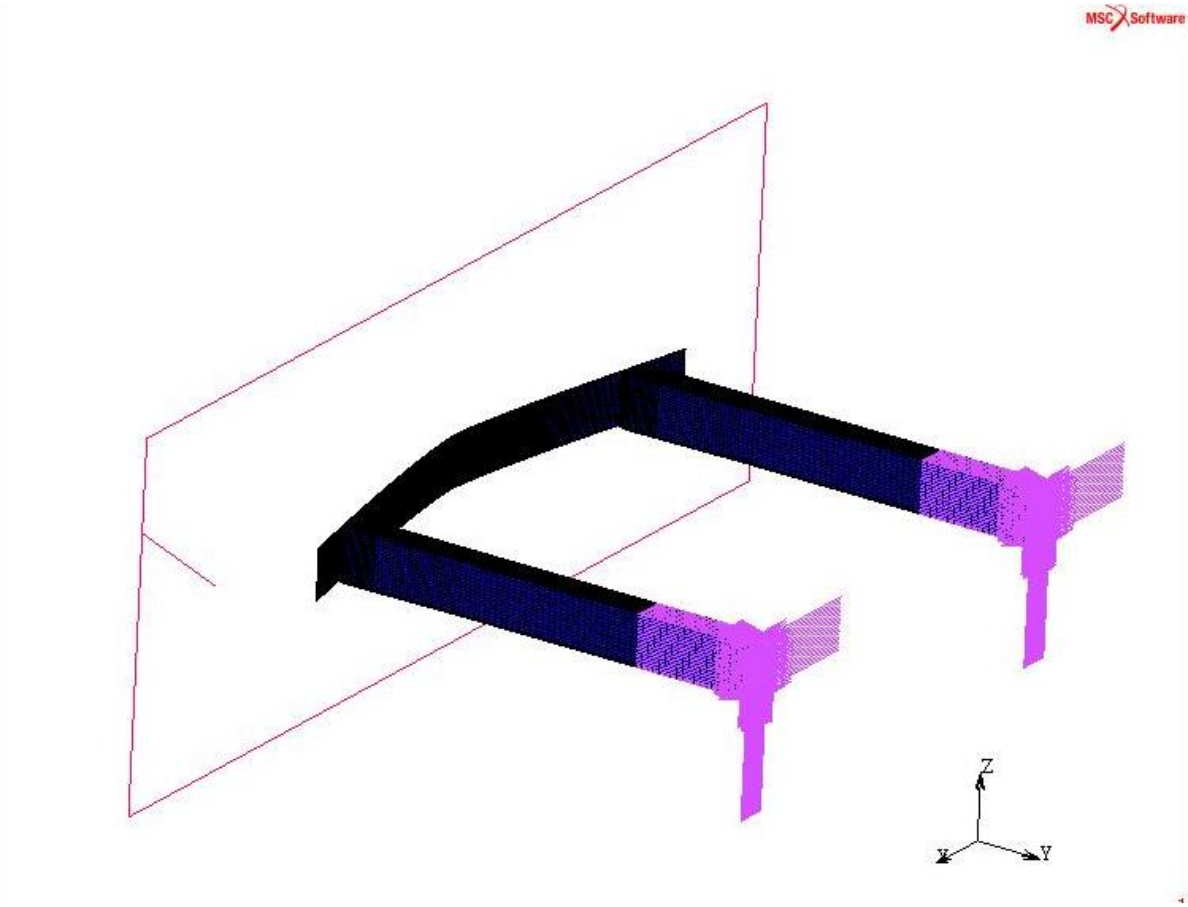


Figure 3. Quasi-static analysis: isometric view of the FE model

Dynamic analysis potentially gives more realistic results with respect to the quasi-static one. In this type of analysis, bumper and chassis system moves freely and rigid wall is stationary. This way, inertia and buckling effects under dynamic load are also taken into consideration. Another difference that comes with the dynamic analysis is the density of the material to be included in the calculations. Instead of constant velocity of the wall, initial velocity applied to the bumper and chassis system is used as 16667 mm/s (60 km/hr). Mass of the car is also incorporated by using solid elements which are located at the end of each rail in the form of 700 kg lumped masses. The total load case time is also selected as 0.1 s. As the chassis rails are in the shape of slender rectangular profiles, they are compressed during impact which might cause buckling. For the non-linear and large scale problem at hand, Lancoz method is chosen to simulate buckling behaviour more realistically. Single and multi-step Houbolt, generalized alpha, Newmark-beta, and modal superposition are the selected options for the dynamic implicit operator.

2.2 Material Properties

Conventional materials like steel and aluminium are used in the structure of vehicles in automobile industry. Although they have relatively high energy absorption capacity, they significantly add to the mass of the whole system. As a result, more fuel and energy are needed to move vehicle. In this research; composite, recycled, and low-weight materials are compared with the conventional ones in order to assess their crashworthiness performances.

Elastic material properties and densities of the selected materials are tabulated in Table 1 below.

Table 1. Elastic material properties and densities of the selected materials

Material	Modulus of Elasticity, E (GPa)	Poisson's Ratio, v	Density (kg/m^3)
Mild Steel	210	0.30	8000
Dual Phase Steel (DP-500)	210	0.30	7850
AA-5182 Aluminium Alloy	70	0.33	2700
Recycled AA-7175 Chips	68.5	0.33	2700
Aluminium with Carbon Nanotube Reinforcement	60	0.33	2654
Titanium Matrix Composite with Carbon Nanotube Reinforcement	105	0.31	4430

Plastic material properties in the form of flow curves can be seen in Figure 4.

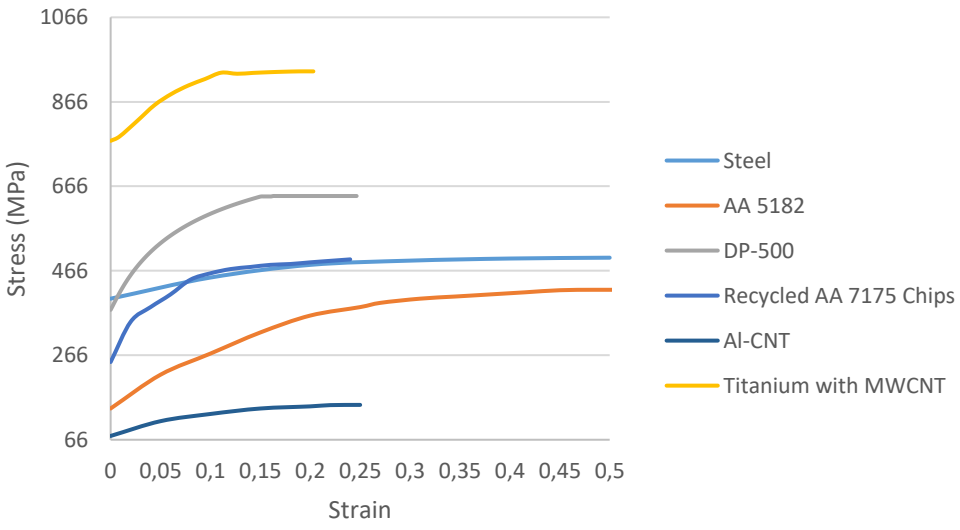


Figure 4. Plastic material properties of the selected materials

2.3 Effect of Profile Thickness

All elements on the model are created as shell type, which are originally 2-D elements. However, thickness is introduced as an FEA parameter into the equations. This research seeks to find a proper thickness for the given bumper and chassis system geometry that has high energy absorption capacity. Two different parameters are taken into consideration in order to assess the crash performance of the thicknesses. Those parameters are crush force efficiency and specific total strain energy absorbed.

Crush force efficiency (CFE) is the ratio of the average force to the peak force value as can be seen in Equation 1.

$$\eta = \frac{F_{average}}{F_{max}} \qquad [1]$$

Specific energy absorbed (SEA) is the ratio of highest value of energy absorbed over total mass of the bumper beam and chassis system (Equation 2).

$$SEA = \frac{E_{max}}{m} \qquad [2]$$

Researchers analysed different shapes of chassis rails to figure out which one shows better crush performance [Acar et al., 2011]. Authors utilised optimization analysis using the parameters CFE and SEA. Same assessment approach is adopted in this research in terms of employing CFE and SEA to evaluate various profile thicknesses of rectangular profile rails.

2.4 Modifications on the Chassis Rail Geometry

Some modifications are carried out on the bumper and chassis system to search for an improved design. These modifications can be listed as removing some parts from the bumper beam, removing some parts from the rails, creating a crash zone, changing the cross sectional shape of rails, creating a runner zone, and creating a range hood crash zone. Impact responses of these modifications are investigated in order to figure out the one that shows better crashworthiness performance. The aforementioned modifications are shown in Figure 5.

This research mainly focuses on the bumper and chassis beam system in full-frontal impact without any offset. If energy absorption capacity of the bumper beam increases, less energy will be transmitted to the other parts of the vehicle and occupants; hence, better protection.

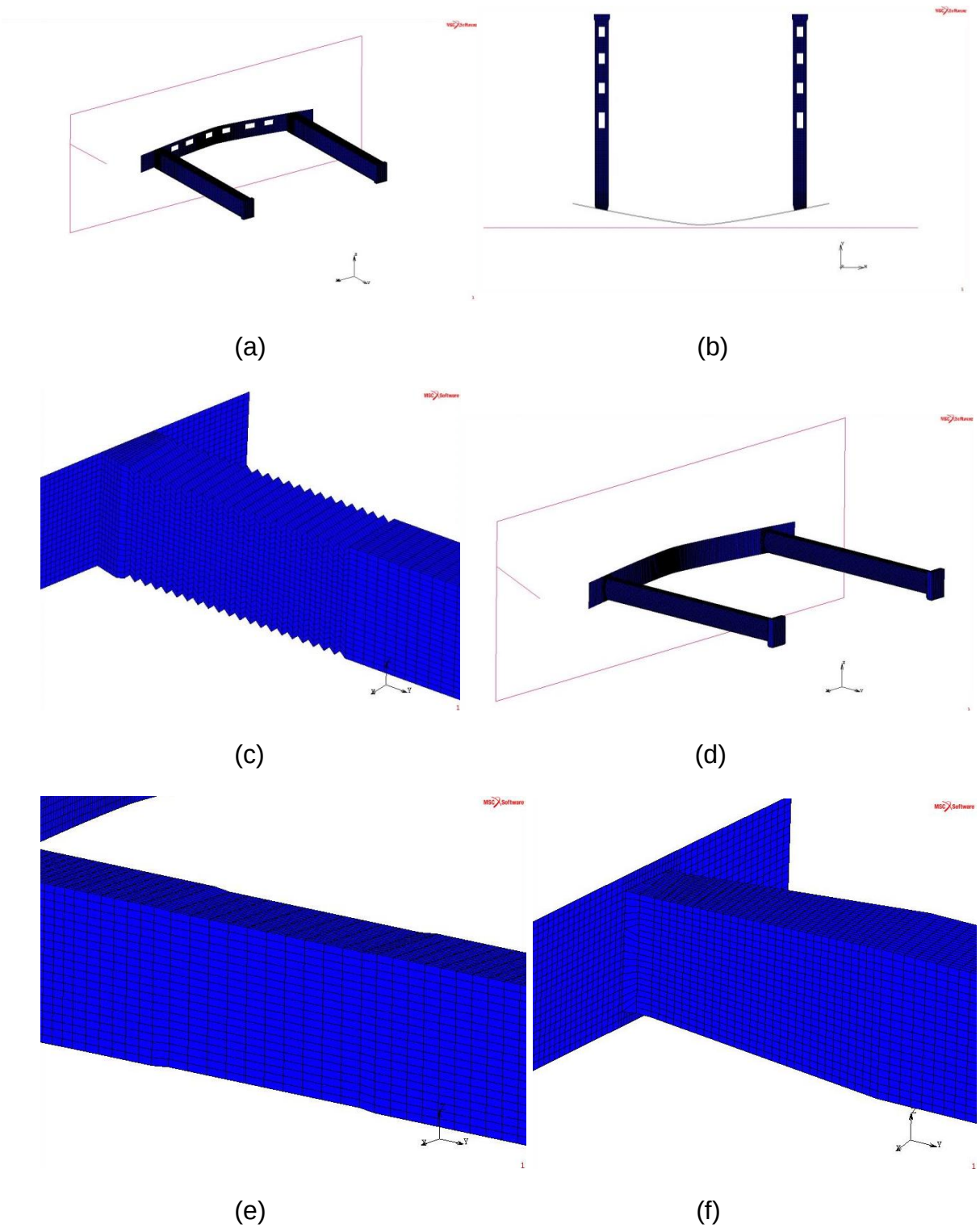


Figure 5. Imposed modifications are carried out on the bumper and chassis system; a. modified bumper beam, b. removed parts from rails, c. with crush zone, d. with hexagonal cross-section, e. with runner, f. with range hood

3. RESULTS & DISCUSSION

In this section, results gathered from the simulations are discussed. Comparison of alternatives played a key role in determining the ideal parameters and modifications which collectively are good at impact energy absorption and being lightweight.

3.1 Quasi-Static Analysis vs Dynamic Transient Analysis

Simulations show that impact characteristics of both quasi-static and dynamic transient analysis are significantly different from each other. After contact starts, impact energy for quasi-static analysis is linearly increasing as seen in Figure 6. In dynamic transient analysis, vehicle bounces back from the rigid wall after the initial crash takes place. Plateau on dynamic transient analysis represents that the crash is over. It can be concluded that quasi-static analysis is not realistic as realistic as the dynamic analysis.

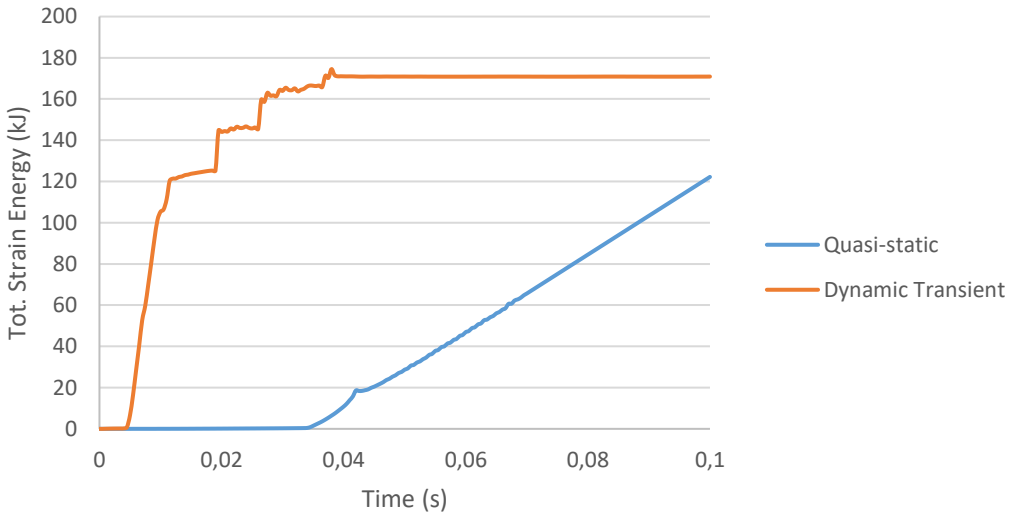


Figure 6. Total strain energy vs time graph for both quasi-static and dynamic transient analysis

3.2 Material Analysis

Six different materials are analysed and their responses to the impact are investigated. Only the material of the model is varied, whereas the other parameters such as initial velocity, thickness of elements, and geometry of system remain the same. As the base material, mild steel is used, alongside which one recycled, two composite and two contemporary materials are investigated. Tables 2 and 3 show that “Recycled AA-7175 Chips” aluminium possesses the best combination of CFE and SEA. Among composite material alternatives, “Titanium with MWCNT” is a good choice with a very high average crush force and a high peak force. CNT

reinforced aluminium yields high CFE and SEA values; however, particularly the peak force it can support is considerably low.

Table 2. Crush force efficiency (CFE) for different materials

Material	Average Force (kN)	Peak Force (kN)	Crush Force Efficiency
Mild Steel	564.67	3145.73	0.18
DP-500	841.92	1565.35	0.54
AA-5182	361.61	1362.24	0.27
7175 recycled	746.55	1342.36	0.56
Al-CNT	513.11	602.32	0.85
Titanium with MWCNT	1221.39	3430.44	0.36

Table 3. Specific energy absorption for different material types

Material	Mass (kg)	Max. Strain Energy (kJ)	Specific Energy Absorption (kJ/kg)
Mild Steel	32.1	170.88	5.32
DP-500	31.5	218.81	6.95
AA-5182	10.63	218.24	20.53
7175 recycled	10.63	204.45	19.23
Al-CNT	10.65	172.19	16.17
Titanium with MWCNT	17.78	201.60	11.34

3.3 Results for the Effect of Profile Thickness

Lowering mass can be achieved by lowering the thicknesses of rectangular chassis rail profiles and bumper beam. Mass of the system significantly decreases when wall thickness of the profile becomes thinner. In Table 4, mass of the system ranges between 37.1 kg to 21.8 kg.

Table 4. Mass values for each thickness

Thickness (mm)	Total Volume (m^3)	Density (kg/m^3)	Mass (kg)
7	0.0046	8000	37.07
6	0.0040	8000	32.10
5	0.0034	8000	27.03
4	0.0027	8000	21.84

Crush force is created on the whole system during impact. Higher crush force is preferable for an impact energy absorbing system. Most of the crash energy is absorbed starting from the bumper beam towards the chassis rails. As absorbed crash energy is the total area under the force vs displacement graph, Figure 7 demonstrates crush force vs displacement and gives an idea about energy absorption characteristics of the specified thickness values.

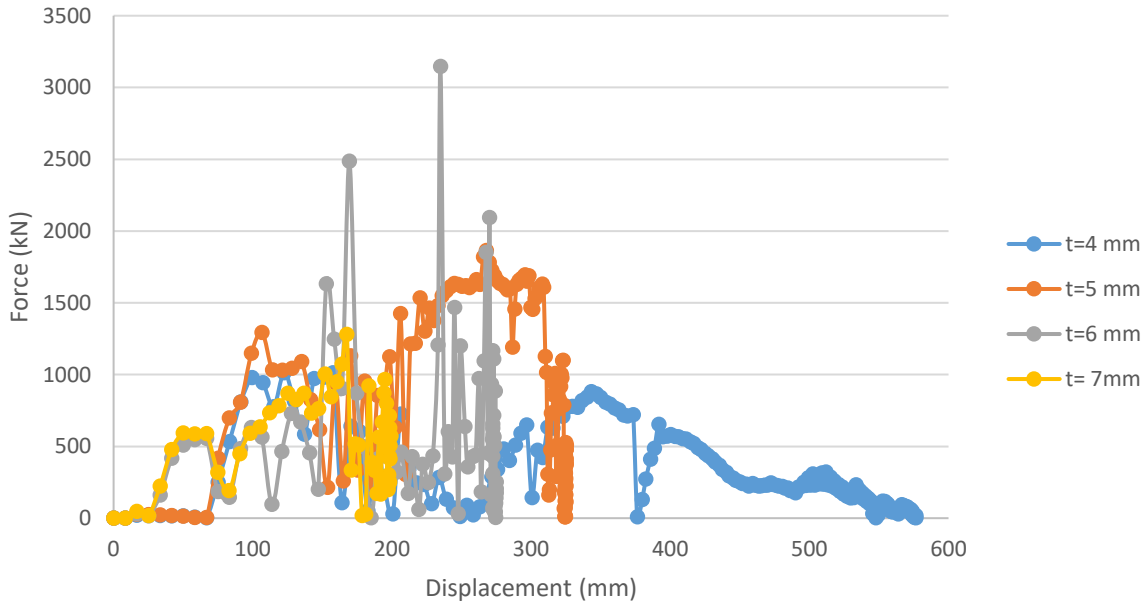


Figure 7. Crush force vs displacement for different thickness values

Crush performance of the system directly depends on parameters of both contact time and mass of the system. Although analysis time of system is the same for all models, contact time shows variation. Smaller thickness means a lighter model. Lighter model's contact time and displacement is higher than the heavier one. End point of rails is used as a reference for displacement measurement. Displacement is measured as 577 mm in the model of 4 mm profile thickness, whereas displacement of 7 mm profile thickness is 200 mm. Reason of fluctuations in force is believed to be the buckling behaviour. Crush force is increasing when

system resist. Buckling starts when this resistance is overcome, soon after which force suddenly drops. As can be seen in Figure 8, higher profile thicknesses shows better energy absorption performance when compared to thinner ones. Lowering mass of the vehicle has significant positive effects; however, vehicle's crashworthiness may be adversely affected, which may lead to injuries and casualties.

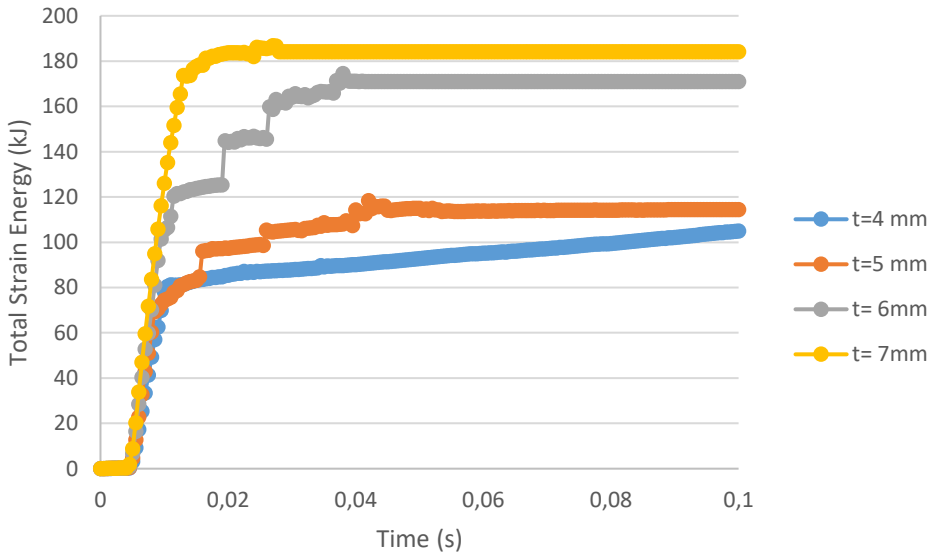


Figure 8. Total strain energy vs crash time for different thickness values

For an ideal case, crush force efficiency should be equal to 1. Therefore, the model with higher efficiency resists more and transmits less impact energy to the occupants. As observed from Table 5, the most resistive bumper and chassis system profile thickness is 5 mm, followed by 7 mm. Another important parameter to justify results is specific energy absorption (SEA). SEA gives a better idea about models crashworthiness performance. Although mass of the model changes with respect to thickness, maximum strain energy absorbed also changes independently. Therefore, as seen in Table 6, model that has the highest energy absorption per unit mass is 6 mm profile thickness.

Table 5. Crush force efficiency (CFE) for different thickness values

Thickness (mm)	Average Force (kN)	Peak Force (kN)	Crush Force Efficiency
4	297.14	1012.56	0.29
5	831.50	1863.87	0.45
6	564.67	3145.73	0.18
7	524.66	1278.80	0.41

Table 6. Specific energy absorption (SEA) for different thickness values

Thickness (mm)	Mass (kg)	Max. Strain Energy (kJ)	Specific Energy Absorption (kJ/kg)
4	21.84	104.92	4.80
5	27.03	114.40	4.23
6	32.10	170.88	5.32
7	37.07	184.03	4.96

3.4 Results for the Modifications on the Chassis Rail Geometry

Energy absorption characteristics and crush force efficiencies of geometrically modified models are compared with the base model with 6 mm wall thickness in Tables 7 and 8. In both weight reduction (WR) models geometrical modifications are the same. Some materials are taken from the bumper beam or the rails to reduce the mass of vehicle. Interpretation of Tables 7 and 8 reveals that the highest crashworthiness may be achieved through “crash zone” modification, followed by “range hood” and “runner” modifications. Crash zone modification gives the highest crush force efficiency of 0.67 among others along with the second highest specific energy absorption of 6.60.

Table 7. Crush force efficiency (CFE) for different geometrical shapes

Model	Average Force (kN)	Peak Force (kN)	Crush Force Efficiency
Base Model	546.67	3145.73	0.17
WR (Bumper)	629.51	2076.01	0.30
WR (Rails)	445.39	1718.43	0.26
Hexagonal	857.39	1446.13	0.59
Crash zone	629.61	941.35	0.67
Range Hood	629.16	1177.53	0.53
Runner	962.79	1728.77	0.56

Table 8. Specific energy absorption (SEA) for different geometrical shapes

Model	Mass (kg)	Max. Strain Energy (kJ)	Specific Energy Absorption (kJ/kg)
Base Model	32.10	170.88	5.32
WR (Bumper)	31.64	147.87	4.67
WR (Rails)	30.86	139.63	4.52
Hexagonal	33.50	201.39	6.01
Crash zone	31.85	210.09	6.60
Range Hood	31.78	210.93	6.64
Runner	32.00	211.03	6.59

4. CONCLUSIONS

This study presents a computational collective effort on assessing various materials and modifications such as with crush zone, with hexagonal cross-section, with runner, and with range hood for front bumper beam and frontal chassis system of an automobile in order to improve its crashworthiness. The assessment of the materials, profile thickness and geometric modifications all in one study is believed to significantly contribute to the design and selection of bumper – chassis system. One of the strengths of this research is the dynamic analysis of the FE models, which represents a more realistic simulation of the impact situations with the capability of showing buckling and collapsing behaviour of the chassis rail columns.

As a conclusion of the analyses, it is observed that some of the geometrical modifications have improved crash performance of the bumper and chassis system. In other words, mass is reduced and more energy is absorbed. Among all geometrical modifications, the best choice turns out to be the “crash zone” one. In terms of wall thickness, the model that has the highest energy absorption per unit mass appears to be the one with 6 mm profile thickness.

Material selection is vital to complete a satisfactory design. Different materials are investigated and compared with conventional ones. Results show that recycled and composite materials are safe enough to use in road vehicles’ chassis. Among all material alternatives, the best alternative is suggested as “Recycled 7175 aluminium” due to its lightweight and considerably high impact energy absorption performance.

Although joining and manufacturing effects play significant roles on the structural system performance, their effects on crashworthiness are not taken into consideration within the context of this research. According to literature, welding can be used where rails and bumper

beam are joined. It should be noted that many real life applications also use detachable bolted joints.

REFERENCES

1. **Acar, E., Guler, M.A., Gerçeker, B., Cerit, M.E. and Bayram, B., (2011),** Multi-objective crashworthiness optimization of tapered thin-walled tubes with axisymmetric indentations. Thin-Walled Structures, Vol. 49, No.1, pp 94–105.

2. **World Health Organization (WHO) (2016)**, Number of road traffic deaths, available at: http://www.who.int/gho/road_safety/mortality/traffic_deaths_number/en/ [Accessed June 18, 2016].

3. **Belingardi, G., Beyene, A.T. and Koricho, E.G., (2013),** Geometrical optimization of bumper beam profile made of pultruded composite by numerical simulation. Composite Structures, Vol. 102, pp 217–225.

4. **Cheon, S.S., Choi, J.H. and Lee, D.G., (1995),** Development of the composite bumper beam for passenger cars. Composite Structures, Vol. 32, No.1-4, pp 491–499.

5. **Cole, G.S. and Sherman, A.M., (1995),** Lightweight materials for automotive applications. Materials Characterization, Vol. 35, No.1, pp 3–9.

6. **Davoodi, M.M., Sapuan, S.M., Ahmad, D., Aidy Ali, Khalina, A. and Mehdi Jonoobi, (2010),** Mechanical properties of hybrid kenaf/glass reinforced epoxy composite for passenger car bumper beam. Materials and Design, Vol.31, No.10, pp 4927–4932.

7. **Hosseinzadeh, R., Shokrieh, M.M. and Lessard, L.B., (2005),** Parametric study of automotive composite bumper beams subjected to low-velocity impacts. Composite Structures, Vol.68, No.4, pp 419–427.

8. **Qi, W., Jin, X.L. and Zhang, X.Y., (2006),** Improvement of energy-absorbing structures of a commercial vehicle for crashworthiness using finite element method. International Journal of Advanced Manufacturing Technology, Vol.30, No.11-12, pp 1001–1009.

9. **The George Washington University, National Crash Analysis Center (NCAC), (2015),** Finite element model archive, available at: http://www.ncac.gwu.edu/vml/models.html [Accessed October 15, 2015].

10. **Velmurugan, R. and Balaganesan, G., (2013),** Energy absorption characteristics of glass/epoxy nano composite laminates by impact loading. International Journal of Crashworthiness, Vol.18 (June), pp 82–92.

EVALUATION OF SOIL CONDITIONS AND POST EMBEDMENT DEPTH ON GUARDRAIL SAFETY PERFORMANCE

Ali Osman ATAHAN, *atahana@itu.edu.tr,* İstanbul Technical University, İstanbul, Turkey

Murat ÖRNEK, *murat.ornek@iste.edu.tr,* İskenderun Technical University, Hatay, Turkey

Murat BÜYÜK, *muratbuyuk@sabanciuniv.edu,* Sabancı University, İstanbul, Turkey

Ercan EPSİLELİ, *eepsileli@kgm.gov.tr,* Turkish DOT Branch, Kayseri, Turkey

ABSTRACT

Guardrails are passive road restraint systems used at roadsides and medians to improve road safety. Crashworthiness of guardrail systems is evaluated through full-scale crash testing. Design parameters, such as post type, soil characteristics, guardrail properties, post-soil interaction and post embedment depth play an important role in the test outcome. In this paper, effect of guardrail post embedment depth and soil characteristics on dynamic impact behavior of a guardrail design is evaluated. Field tests as well as finite element simulation results were used to compare impact performance. Three different soil properties and seven different post embedment depths are assessed as test parameters. A 1000 kg pendulum device was used to apply the dynamic load on guardrail posts. Deceleration as well as post movement during impact were recorded to make comparisons. Optimum post embedment depth charts were constructed based on soil properties.

Keywords: Guardrail; post; soil properties; embedment depth; impact; safety.

1. INTRODUCTION

Guardrails are passive road restraint systems (RRS) used at roadsides and medians to improve road safety. There are two types of guardrails, i.e., embedded in soil and anchored on concrete deck. Guardrails frequently use vertical posts, longitudinal rails and spacers between post and rail. Guardrail posts are usually manufactured using C

or sigma sections. On the other hand rail could have W or box cross-section. Spacers could be manufactured in various geometries, such as cylinder, rectangular etc. Bolts with different properties and cross-sectional areas are used to connect these structural elements.

Roadside can be defined as the area between the outside shoulder edge of a road and the right-of-way limits [AASHTO, 2014]. Utilization of engineering treatments in this area to improve traffic safety is referred as roadside safety design and guardrails are one of the most widely used passive safety devices at roadsides.

Most guardrail designs in the world are made out of steel or concrete. Concrete barrier designs usually do not contain a foundation and they are simply placed on the road surface. Steel guardrail designs are mostly installed in soil since number of bridges in a standard highway project is limited. For steel guardrails with soil driven posts post-soil interaction, properties of soil and amount of post embedment depth (PED) become essential parameters affecting the impact performance [Atahan and Cansız, 2005; Reid, 2004; Wu and Thomson, 2007]. In the lack of post-soil interaction or inadequate post embedment depth steel guardrail may not function as intended and design cannot provide adequate safety nor security for the impacting vehicles. Unfortunately, PED in steel guardrail systems are currently determined based on strong soil properties [Atahan et.al, 2008]. The crash performance of these designs may not be appropriate for locations where soil conditions are weaker than tested conditions.

Crashworthiness of guardrail systems is evaluated through full-scale crash testing. Design parameters, such as post type, soil characteristics, guardrail properties, post-soil interaction and post embedment depth play an important role in the test outcome. Due to the differences in these parameters for a particular guardrail design crash test results vary significantly. In this study, a series of full-scale field impact tests were performed on soil embedded steel posts to determine optimum post embedment depth (PED) for three different soil conditions (soft, medium hard and hard soil). A C120 shape was selected as post since it is the most widely used post section in European guardrail designs [Pezzucchi, 2013]. A C120 section represents a C-shaped steel member with 120 mm web and 60 mm flange length. A pendulum device is designed to apply dynamic impact loads on C120 posts embedded in different soil conditions. Seven different PED’s (650 mm; 700 mm; 750 mm; 800 mm; 850 mm and 900 mm) were used for each soil condition. A total of 21 impact tests proved that increased soil

stiffness resulted reduction in PED for C120 posts. Optimum PED values are determined based on maximum acceleration, absorbed energy, energy absorption capacity and maximum post force according to the soil properties.

2. FIELD TESTS

2. 1. Site Characterization

Three different soil pits were prepared for the field testing of C120 posts. The dimensions for these pits were 1.000mm wide x 60.000mm long x 1500mm deep as shown in **Figure 1**. A total of 21 posts with 1.000mm spacing were installed in these three soil pits. The dimensions of soil pits were selected based on the largest PED used in the study, potential post removal during tests, prevention of any interaction between posts and economic considerations.

The soils used in the pits represent standard base granular material used by Turkish Road Authorities [TRA, 2016]. To determine the geotechnical properties of the granular material to be used at these pits a series of laboratory tests, such as grain size analysis, moisture content, field density, unit weight, shear box, standard and modified proctor tests were performed. Results of these experiments are represented in **Table 1**. After the laboratory tests selected granular materials were used to construct the pits. Sand Cone and California Bearing Ratio tests were used to verify the density of granular material for soft, medium hard and hard soil conditions. Results of these field tests are depicted in **Table 2**. As shown, acceptable soil stiffness levels were reached before the initiation of post installation procedure.

Table 1. Geotechnical Properties of the Soil from Laboratory Tests

Parameter	Property
Soil classification	SP (USCS); A3 (AASHTO); Sand (triangular classification)
Water content	4 %
Dry density	max: 2.10 gr/cm^3 ; min: 1.60 gr/cm^3
Particle density	2.53 gr/cm^3
Internal friction angle	soft: 36°; medium hard: 44°; hard: 48°
Max. dry density and optimum water content (standard proctor test)	ρ_{kmax} =2.10 gr/cm^3 ; ω_{opt}=8%
Max. dry density and optimum water content (modified proctor test)	ρ_{kmax} =2.20 gr/cm^3 ; ω_{opt}=7%

Table 2. Geotechnical Properties of the Soil from Field Tests

Name	Test Result
Sand Cone Test	soft: 1.70 gr/cm^3 medium hard: 1.85 gr/cm^3 hard: 2.00 gr/cm^3
CBR Test	soft: 36 % medium hard: 64 % hard: 95 %



Figure 1. Preparation of Weak, Medium Hard and Hard Soil Pits for Post Installation

2.2. Details of Test Setup Design and Field Impact Test Details

A total of twenty one 4 mm thick S355JR quality C120x60x25 posts were used in the field tests. A single C120 post is used in the impact tests. As shown in Table 3, PED was ranged from 650 mm to 900 mm for all three soil conditions. In this table from the test codes, the letter gives the soil types and the numbers indicate the PED values. Posts were driven into the soil using a post installation machine. To deliver the impact

forces to the posts, a 1.000kg pendulum device was designed. Steel and concrete manufactured and designed 4.0m in total height pendulum was raised 1.5m using an electric motor and impacted C120 posts about 550 mm above ground level. This distance represents bumper height of an average small car. In this test setup, pendulum applied 14.7kJ of kinetic energy to C120 posts. A picture of the designed pendulum used in this study is shown in **Figure 2**. An accelerometer was installed on the pendulum to measure the acceleration-time history during impact. The energy at the top of the pendulum is equal to the value of mgh before it starts to move, and in this case the pendulum has no kinetic energy. When the pendulum moves to the lowest position, all the energy will turn into kinetic energy, so the energy that it has is equal to $0.5mV^2$ and in this case the potential energy is completely transformed into kinetic energy. According to the law of conservation of energy; when $mgh=0.5mV^2$ equation is used, the initial velocity of the pendulum before crash can be calculated as $V=(2gh)^{0.5}$. This history is used to calculate velocity-time and eventually displacement-time histories. The force is calculated based on mass times measured acceleration. Eventually force-displacement history is obtained from all 21 impact cases. The area under these curves represented the work done, in other words, the energy absorbed by the post-soil interaction.



Figure 2. Design of Pendulum Test Device Used in Dynamic Impact Tests

Table 3. Details of Guardrail Posts Tested

Post Designation	PED (mm)	Soil Characterization	Test Code
C120x60x4	600	H (Hard)	H-600
	650		H-650
	700		H-700
	750		H-750
	800		H-800
	850		H-850
	900		H-900
	600	M (Medium Hard)	M-600
	650		M-650
	700		M-700
	750		M-750
	800		M-800
	850		M-850
	900		M-900
	600	S (Soft)	S-600
	650		S-650
	700		S-700
	750		S-750
	800		S-800
	850		S-850
	900		S-900

3. TEST RESULTS AND DISCUSSION

3.1. Visual Inspections and Analytical Calculations

A total of 21 impact tests were performed using the pendulum device and visual inspections were recorded after each test. As shown in **Figure 3** when insufficient PED is used posts exhibited upward movement and some cases almost completely removed from soil. This type of behavior is observed in S-600, S-650, S-700, S750 cases, M-600, M-650, M-700 cases and H-600, H-650 cases. On the other hand when sufficient PED is used posts remained in the soil with minimal upward motion and in some cases post buckling is observed (see **Figure 4**). A qualitative evaluation of all 21 tests is presented in **Table 4**. Maximum measured accelerations and energy absorbed calculated using the area under the force-deformation curve for all 21 impact tests are presented in **Table 5**. Based on test results, it is determined that utilization of insufficient PED poses performance risks for guardrail systems.



Figure 3. Sequential Pictures Taken from H-600 Pendulum Test



Figure 4. Sequential Pictures Taken from H-900 Pendulum Test

Table 4. Qualitative Evaluation of Pendulum Test Results

PED (mm)	Soil Stiffness		
	Hard (H)	**Medium Hard (M)**	**Soft (S)**
600	The post has moved upward in the ground but has not completely removed from the soil. The soil body is collapsed.	Same as H-600	The post has moved upward in the ground and completely removed from the soil. The soil body is collapsed.
650	The post movement in soil is less than D-600 but the soil body is collapsed. The pendulum slowed down after impact.	Same as M-600	Same as L-600
700	The post upward movement is not observed and minimal soil movement is occurred. Post-soil interaction and energy absorption are acceptable.	Somewhat improvement compared to M-650 case. The soil body is collapsed. Pendulum slowed down after impact.	Same as H-600
750	Due to sufficient PED, slight post buckling is observed. Post-soil	Same as H-700	Same as M-700

	interaction and energy absorption is acceptable.		
800	Post buckling becomes more visible. Post-soil interaction and energy absorption is acceptable.	Same as H-750	Same as H-700
850	Same as H-800	Same as H-800	Same as H-800
900	Same as H-800	Same as H-800	Same as H-800

Table 5. Maximum Energy Absorption and Acceleration Calculations for Pendulum Tests

PED (mm)	Soil Stiffness					
	Hard (H)		Medium Hard (M)		Soft (S)	
	Max. Energy Absorbed (kJ)	Max. Accel. (g)	Max. Energy Absorbed (kJ)	Max. Accel. (g)	Max. Energy Absorbed (kJ)	Max. Accel. (g)
600	0.72	- 2.88	0.66	- 2.06	0.49	- 1.08
650	2.93	- 4.05	2.11	- 2.90	1.77	- 2.45
700	3.27	- 4.52	2.35	- 3.25	2.14	- 2.96
750	4.58	- 6.33	3.29	- 4.55	2.89	- 3.99
800	5.75	- 11.95	4.14	-10.72	3.31	- 7.93
850	6.86	- 18.48	4.94	-16.83	4.01	- 13.54
900	7.92	- 25.85	6.13	-24.47	5.19	- 18.87

4. EVALUATION OF FIELD TEST RESULTS ACCORDING TO THE SOIL PROPERTIES

In this study, the embedment depths of the C120 posts (PED) were changed as 600 mm, 650 mm, 700 mm, 750 mm, 800 mm, 850 mm and 900 mm. The visible post length (VPL) above the soil was kept constant as 700mm. **Figure 5** shows cross-sections of soil pits and post embedment depths. The C120 posts were embedded in soft, medium hard and hard soil conditions in which the soil properties are given above. The relations of PED/VPL ratios and i) maximum acceleration; ii) absorbed energy; iii) energy absorption capacity and iv) maximum post force according to the soil properties are given in **Figures 6-12**.

Figure 6 presents the variation of the maximum acceleration (gmax) values depending on the different PED/VPL ratios. The maximum amount of acceleration is defined as g (gravitational acceleration). The graph shows that the gmax increases with the PED/VPL ratios. Significant increases in gmax values are obtained if the PED/VPL ratio is greater than 1.071, while no significant increase in gmax values is observed when the PED/VPL ratio is 1.071 or less in both soft and medium hard and hard soils.

The gmax values were found to be 11.95 g on hard soil, 10.72 g on medium hard soil and 7.93 g on soft soil if the PED was 800 mm.

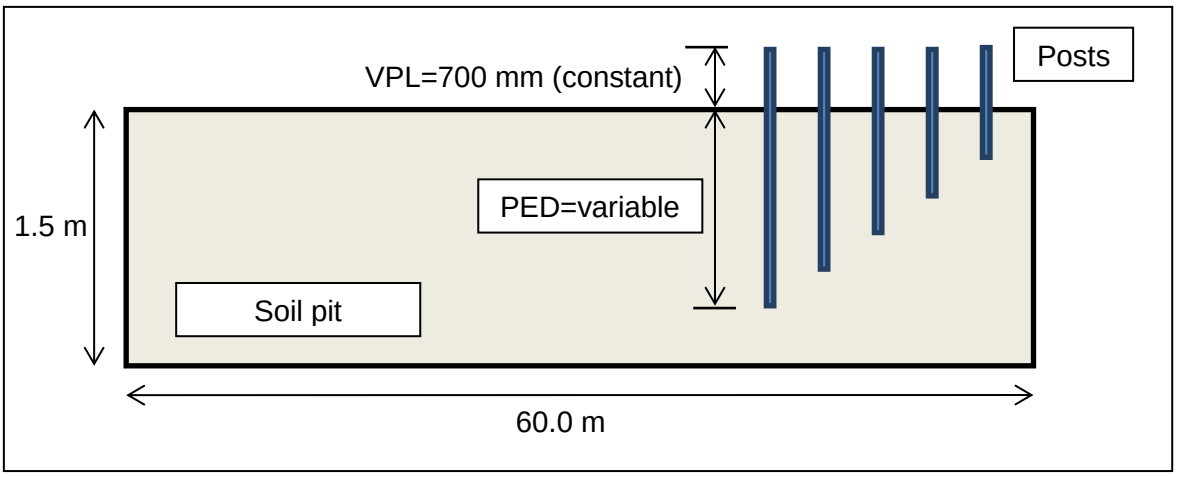


Figure 5. Cross-sections of Soil Pits and Post Embedment Depths

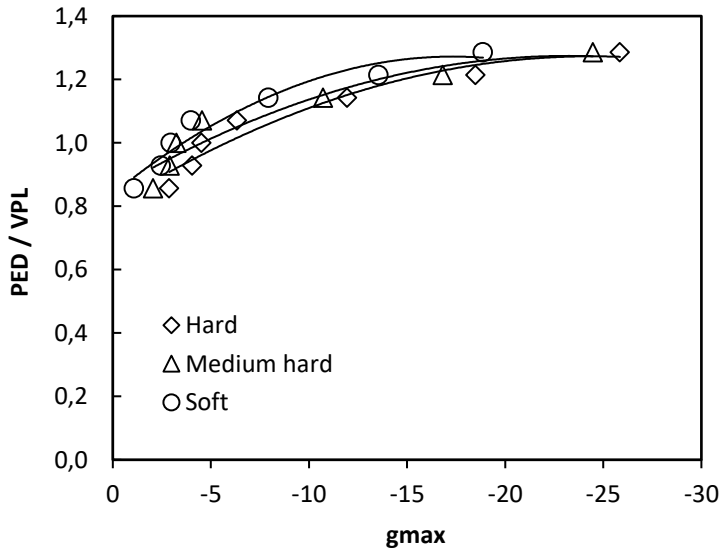


Figure 6. Relations of gmax-PED/VPL Ratios according to the Soil Conditions

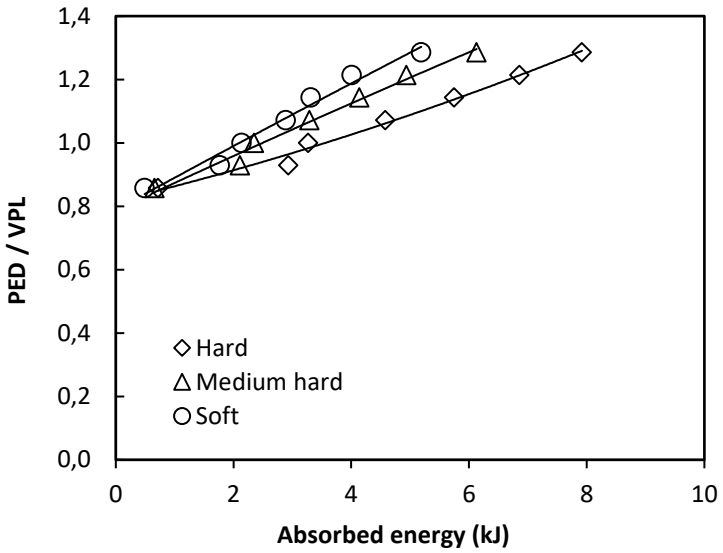


Figure 7. Relations of Absorbed Energy -PED/VPL Ratios according to the Soil Conditions

The relation between absorbed energy and the PED/VPL ratio for different soil types is given in **Figure 7**. As seen there is a linear relationship between the PED/VPL ratio and the magnitude of the absorbed energy increases when the PED/VPL ratio increases for all the types of soil. In the soft soil condition, if the PED exceeds 600 mm to 900 mm, the energy absorbed increases from 0.49 kJ to 5.19 kJ. Similarly, in the case of a medium hard soil environment, when the depth of PED increases from 600 mm to 900 mm, the energy absorbed increases from 0.66 kJ to 6.13 kJ. For hard soil, if the depth of PED increases from 600 mm to 900 mm, the energy absorbed increases from 0.72 kJ to 7.92 kJ. Along with the increase in the soil stiffness, the absorbed energy level increases for the same embedment depth.

The relationship between energy absorption capacity and PED/VPL ratio is shown in **Figure 8**. Similar to the absorbed energy relations, the energy absorption capacity increases according to the PED/VPL ratio and soil stiffness. The energy absorption capacity increases from 4.44% to 47.01% when the PED increases from 600 mm to 900 mm in a soft soil environment. Similarly, in the case of medium hard soil, when the PED increases from 600 mm to 900 mm, the energy absorption capacity increases from 5.98% to 55.53%. In the hard soil conditions, this value is increases from 6.52% to 71.74%.

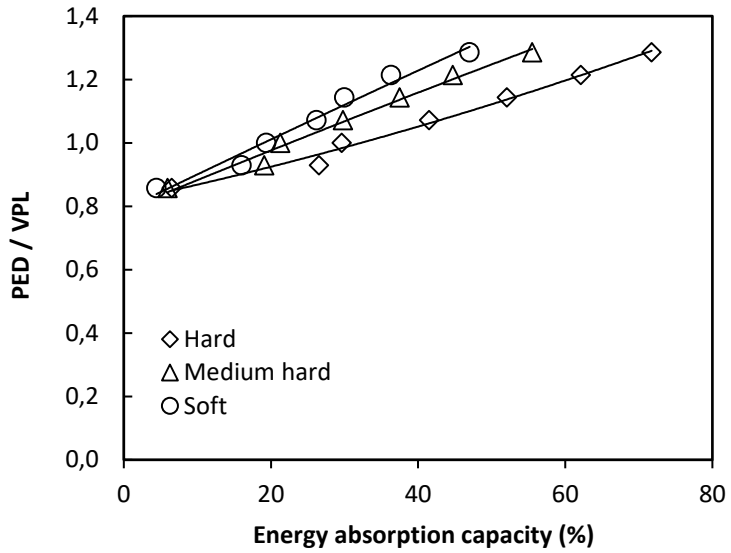


Figure 8. Relations of Energy Absorption Capacity -PED/VPL Ratios according to the Soil Conditions

Figure 9 presents the relationship between the maximum force (in kN) applied to the post and the PED/VPL ratio. The maximum amount of force applied to the post is almost similar for a certain PED (750 mm) for all the three soil types and there is a significant increase after this PED. For a same PED (for example, 900 mm) a total of 138.79 kN force is applied to the post in the soft soil, while these values are 179.98 kN and 190.13 kN, in the medium hard and hard soil conditions, respectively.

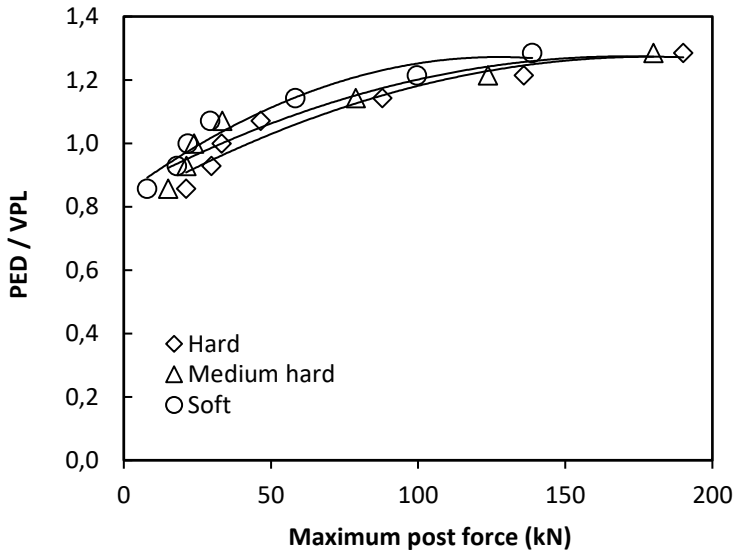


Figure 9. Relations of Maximum Post Force-PED/VPL Ratios according to the Soil Conditions

The internal friction angle of the soil (ϕ) - maximum acceleration (g_{max}) relation of the C120 posts that embedded soft, medium hard and hard soils is presented in **Figure 10**. In the figure, the soft, medium hard and hard soils are represented by internal friction angles of 36°, 44° and 48°, respectively. The maximum acceleration values are defined as g (gravitational acceleration) and given for the PEDs of 600 mm, 650 mm, 700 mm, 750 mm, 800 mm, 850 mm and 900 mm. For each PED value, the maximum acceleration value increases depending on the internal friction angles. There is a significant increase in gmax, especially for the PED values greater than 750mm. As an example; if the PED is 850 mm, the gmax obtained are 13.54 g, 16.83 g and 18.48 g for the internal friction angles of 36° (soft soil), 44° (medium hard soil) and 48° (hard soil), respectively. At the same soil stiffness, the gmax increases as the PED increases. For the cases where the PED is 600 mm, 750 mm and 900 mm, the gmax values are 2.06 g, 4.55 g and 6.13 g, respectively.

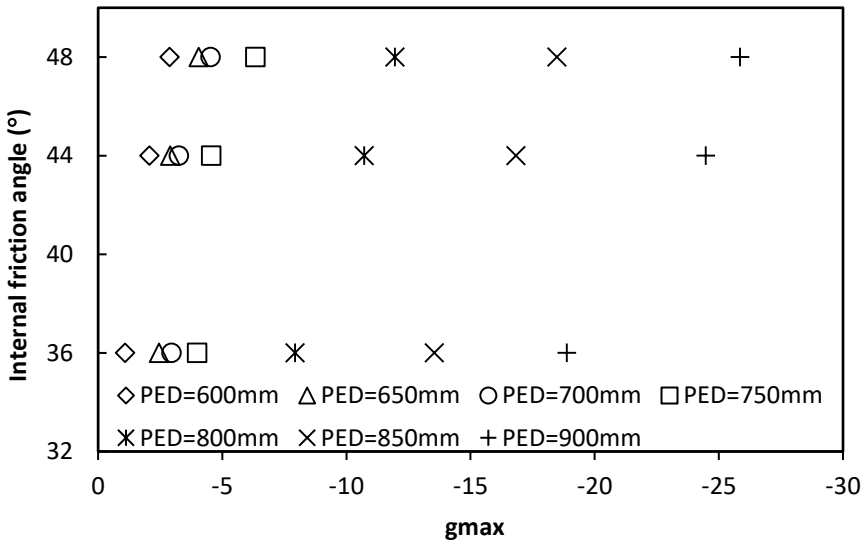


Figure 10. Relations of g_{max}-ϕ according to the PEDs

The California Bearing Ratio (CBR) value of the soil-maximum acceleration relationship for C120 posts is presented in **Figure 11**. The soft soil condition is represented by 36% CBR, medium hard soil condition is 64% CBR and hard soil condition is 95% CBR. And also the PED values are changed as 600 mm, 650 mm, 700 mm, 750 mm, 800 mm, 850mm and 900mm. The gmax for each PED is increased depending on the soil CBR value. In particular, when the PED exceeds 750 mm the

gmax increases considerably. As an example; gmax is calculated as 18.87 g for 36% CBR, 24.47 g for 64% CBR and 25.85 g for 95% CBR. At the same CBR value, the gmax increases as the PED increases. For the cases where the PED is 600 mm, 750 mm and 900 mm, the gmax are 2.88 g, 6.33 g and 25.85 g, respectively. **Figure 12** gives the unit volume weight (γ) - maximum acceleration (gmax) relation for seven different PED values and three different soil conditions. In the figure, the unit weights of the soft, medium hard and hard soil are 1.70 gr/cm^3, 1.85 gr/cm^3 and 2.00 gr/cm^3. The gmax value for each PED increases with the increase in soil weight. The gmax increase significantly especially the PED exceeds 750mm. For the PED of 850mm, the gmax is calculated as 18.48 g for the soil unit weight of 2.00 gr/cm^3. These g_{max} are 16.83 g and 13.54 g for the soil unit weights of 1.85 gr/cm^3 and 1.70 gr/cm^3, respectively. For the different PED-gmax matches are 600 mm -2.06 g, 750 mm -4.55 g and 900 mm -6.13 g.

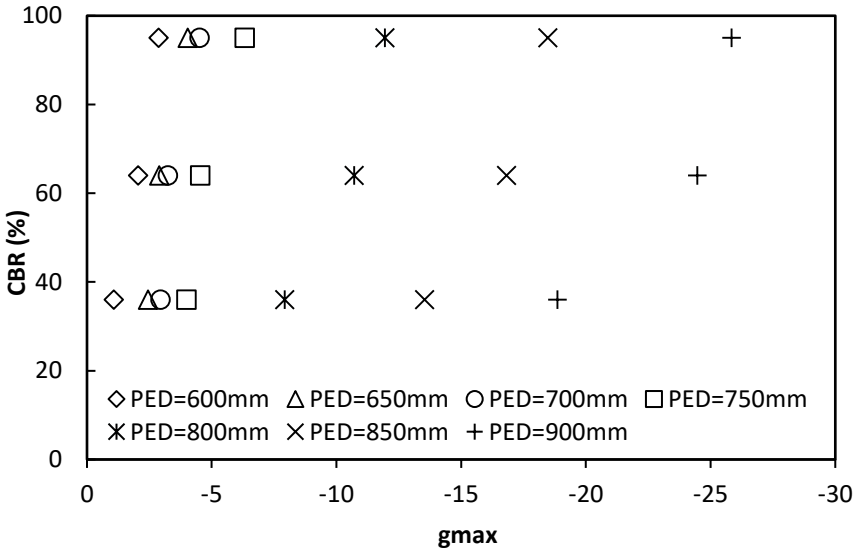


Figure 11. Relations of gmax-CBR according to the PEDs

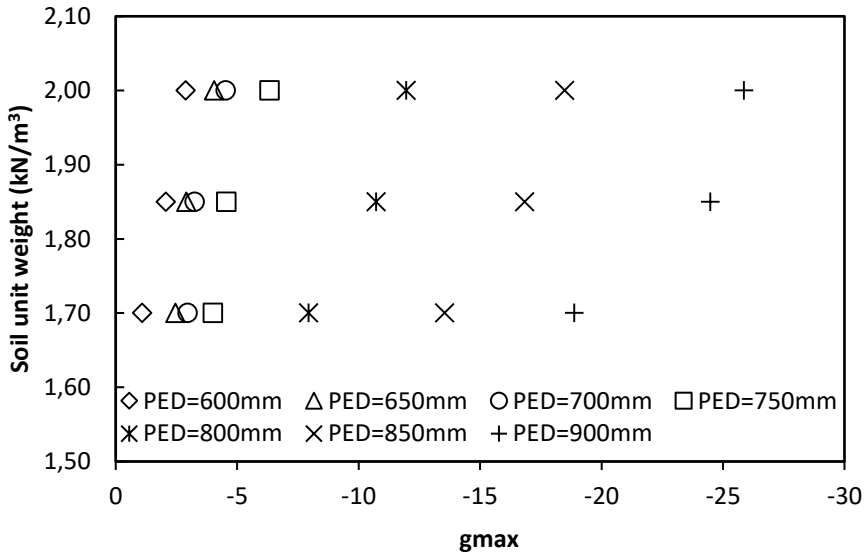


Figure 12. Relations of gmax-Unit Weight according to the PEDs

5. CONCLUSIONS

In this paper, effect of guardrail post embedment depth and soil characteristics on dynamic impact behavior of a guardrail design is evaluated. Three different soil properties and seven different post embedment depths are assessed as test parameters. Based on the research findings the following specific conclusions are reached:

- Dynamic pendulum tests proved that increased soil stiffness resulted reduction in PED for C120 posts due to improved post-soil interaction.
- It is determined that posts tend to move upwards, get out of soil quickly thus could not provide enough resistance when PED is insufficient.
- Optimum PED values are determined as 700 mm, 750 mm and 800 mm for hard, medium hard and soft soil conditions, respectively. Energy absorbed by the post-soil interaction and post behavior is used to reach this conclusion.
- Considering larger PED in similar guardrail systems in use today, designs with optimum PED will help save considerable amount of installation time, labor and material.
- It is expected that 750 mm and 800 mm PED will also be acceptable for C120 posts embedded in medium hard and soft soil conditions, respectively.

ACKNOWLEDGEMENTS

The work presented in this paper was carried out with funding from TUBITAK (Scientific and Technological Research Council of Turkey), grant number 213M516. Their support is gratefully acknowledged.

REFERENCES

AASHTO (2014), "Roadside Design Guide", American Association for State Highway and Transportation Officials, 4th Edition, Washington, D.C.

Atahan A.O. and Cansız Ö.F. (2005), "Improvements to G4(RW) Strong-Post Round-Wood W-Beam Guardrail System", ASCE Journal of Transportation Engineering, Vol. 131, No.1, pp 63-73.

Atahan A.O., Bonin G., Cicinnati L., and Yaşarer H.I. (2008), "Development of a Crashworthy End Terminal TWINY for Thrie-Beam Guardrail. ASCE Journal of Transportation Engineering, Vol. 133, No. 4, pp 467-476.

Pezzucchi, M. (2013), "Soil and EN 1317: Origin, Development and Proposal", AFB20(2) Roadside Safety Meeting European Workshop, Transportation Research Board, Milano.

Reid J.D. (2004), "LS-DYNA Simulation Influence on Roadside Hardware", Transportation Research Board Annual Meeting, Paper No. 04-2619, Washington D.C.

TRA (2016), "Handbook of Properties of Road Construction Materials", General Directorate of Turkish Roads, Turkish Road Association, Ankara.

Wu W. and Thomson R. (2007), "A Study of the Interaction between a Guardrail Post and Soil during Quasi-Static and Dynamic Loading", International Journal of Impact Engineering, Vol. 34, pp 883-898.

HAZARD PERCEPTION TEST SUITABILITY FOR OLDER DRIVERS

B Serpil ACAR, *B.S.Acar@Lboro.ac.uk* Loughborough University, Leics LE11 3TU, UK

Grace SMALLEY, *G.Smalley@Lboro.ac.uk* Loughborough University, Leics LE11 3TU, UK

ABSTRACT

Research has shown that an increase in life expectancy and quality of life in the Western world has similarly given rise to increases in the number of older licenced drivers using their automobile as their primary mode of transport. Older drivers typically drive far less than younger drivers however, 'fatalities per mile driven' data indicates that older drivers have the greater risk of being involved in a fatal crash.

In this study, the experiments were conducted with 50 drivers representing a range of different age groups. A sample of the UK driving licence examination is 'Hazard Perception' video clips were used to measure the drivers' reaction time for the apparent risks. An Eye tracking device was also used to trace and record eye fixations. Reaction time and gaze related data were collected while drivers were asked to identify hazards in the video clips. Case studies were used to simulate driving in various environments such as town, urban, rural and motorway driving.

Analysis of the reaction time data sets reveals that the older drivers' hazard perception do not follow a regular pattern and is in general inconsistent. Further comparisons, by including the eye-tracking data, reveal the reasons behind the inconsistencies. The research suggests that the reaction time data collected by using hazard perception tests alone are not suitable to measure the hazard perception of older drivers.

Keywords: hazard, perception, age, elderly, eye-tracking, safety.

1. INTRODUCTION

It has been estimated that by the year 2030, 25% of the population of the 35 nations within the Organization for Economic Cooperation and Development (OECD) will be over 65 [OECD Scientific Expert Group, 2001]. Research has shown that an increase in life expectancy and quality of life in the Western world has similarly given rise to increases in the number of older

licenced drivers using their automobile as their primary mode of transport [Ferreira et al., 2012; Bromberg *et al*., 2012]. Data from 2009 National Household Travel survey conducted by the US Department of Transportation (Figure 1) reveals that the average annual miles per licenced driver over 65 years of age increases every year [NHTS, 2009]. The pattern in the demography and travel trends suggest that an increase in the number of older licenced drivers and their average milage could be expected in the future.

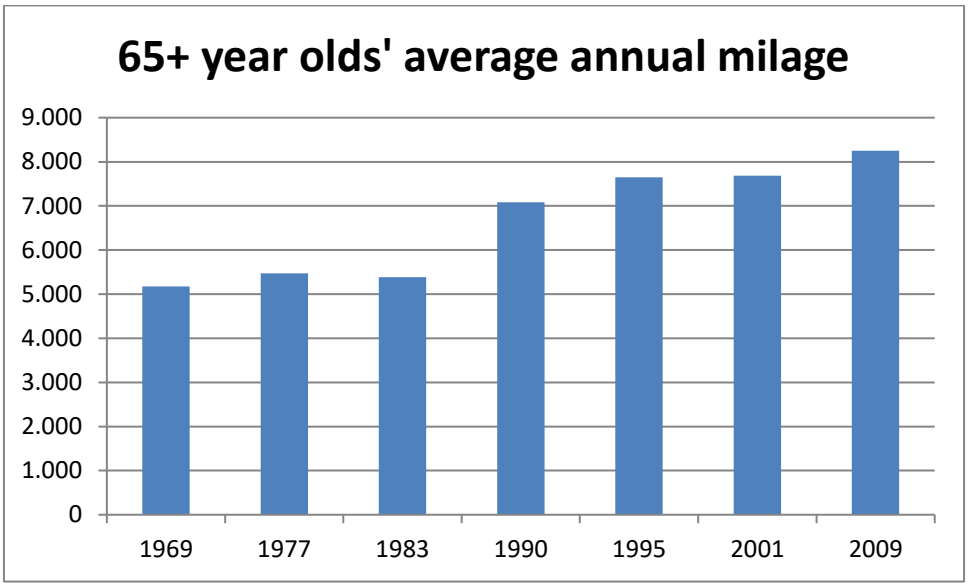


Figure 1. Annual average miles driven by 65+ year olds in the US (Data from NHTS)

Despite the increase in average annual milage of the older drivers they typically drive far less than 20-64 year-olds. Figure 2 illustrates the USA data that older drivers drive fewer miles than their younger counterparts. On the other hand, in Figure 3 'fatalities per mile driven' data indicates that drivers over 65 have the greater risk of being involved in a fatal crash [IIHS].

Interest in the safety of older drivers has grown due to evidence that these drivers are at particular risk of being involved in motor vehicle crashes in challenging driving environments [Schall *et al*., 2012; Mayhew *et al*., 2006; Chandraratna and Stamatiadis, 2003]. Researchers focussed on various aspects of the problems of ageing drivers. For example, [Mayhew *et al* 2006] studied the car crash patterns and report that older drivers are more likely to be involved in intersection crashes and side impact crashes. In-depth analysis of the UK accident data, by [Welsh *et al*, 2006], reveals that the older car occupants are significantly more prone to serious chest injuries than their younger counterparts. [Acar *et al,* 2012] took anthropometric

measurements of older male and female drivers and reports that the anthropometry and posture of the current ATDs (crash test dummies) do not represent ageing drivers hence determines the characteristics of the new representative 'ageing ATDs'. Impairments in various driving related functions such as vision, cognition and motor capabilities are more prevalent with ageing [Abou-Raya and ElMeguid, 2009]. [Carr and Ott, 2010] reports that there is a relation between cognitive decline, greater crash risk and unsafe driver performance.

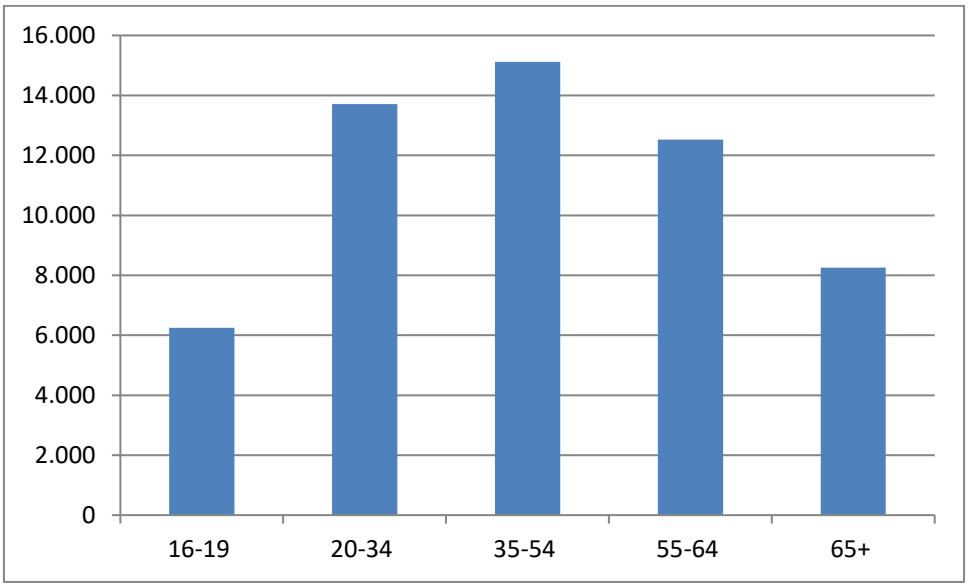


Figure 2. Annual miles driven vs driver age in the US (Data taken from NHTS)

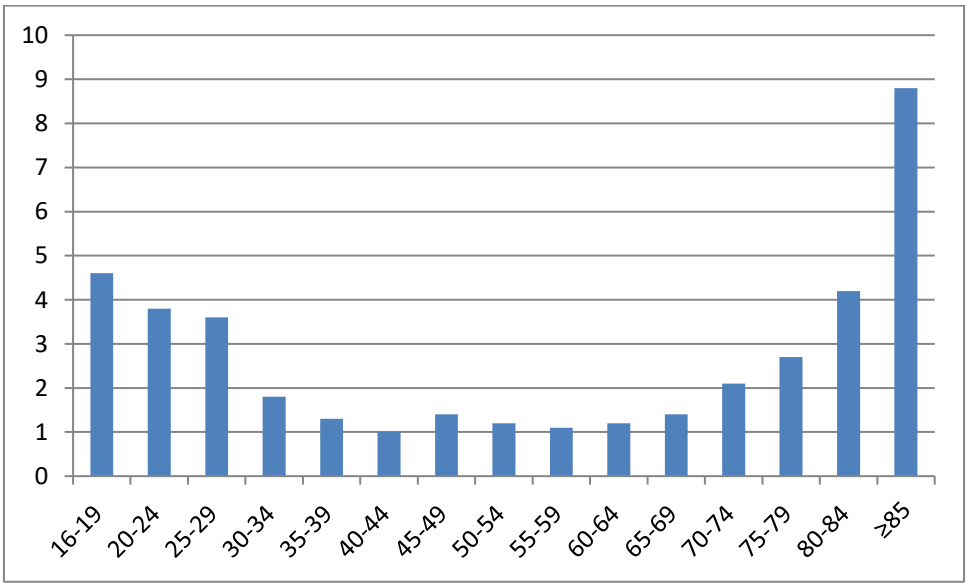


Figure 3. Fatality percentage rate in road traffic accidents per 100 million vehicle miles vs driver age in the US (Data taken from IIHS)

Hazard perception is defined by [McKenna and Horswill, 1999] as “the ability to anticipate dangerous traffic situations”. Hazard perception has been found to correlate with crash involvement therefore can be used to identify drivers at a higher risk of being involved in an accident. Measuring hazard perception is typically achieved through presenting potentially dangerous traffic situations on video or film and calculating participant’s response latencies, however, a number of studies conducted investigating the effects of age on hazard perception skills, seem to have provided results which led to mixed conclusions. The DVLA website states that the candidates watch fourteen one minute long hazard perception test video clips which filmed from the perspective of a passenger car driver. The candidates have to indicate, usually by clicking a mouse button, when they observe a developing hazard. The sooner the candidate reacts to a developing hazard, the more points are scored. Points are from five down to one, with no score if the candidate reacts too late.

Underwood *et a*l 2005 found that novice drivers detect fewer hazards and are slower at detecting hazards than experienced drivers. They found relatively minor differences between younger and older drivers and there was no evidence to suggest that the older drivers were misdirecting their attention while viewing the films. On the other hand, [Horswill *et al*., 2008] found that hazard perception ability declines with increasing age, even in a sample of older adults who considered themselves relatively healthy. Their tests produced evidence that useful field of view (UFV) is important for hazard perception. [Bromberg *et al*, 2012] found that the narrower UFV associated with aging was the likely cause of elderly drivers ‘finding hazard perception of pedestrians in the visual periphery, more difficult than middle aged drivers’.

The aim of this study is to understand whether the hazard perception tests can be conclusive in terms of observing ‘developing hazards’ and whether these tests can be used to examine older drivers’ ability to perceive hazards.

2.METHOD

The experiments were conducted with 50 drivers representing a range of different age groups. Reaction time and gaze related data were collected while drivers were asked to identify hazards in the video clips. A questionnaire was also used to collect personal information. The details of the video selection, data collection, piloting and sampling were as follows:

Hazard Perception Videos and Piloting

Driver and Vehicle Licencing Agency (DVLA) in the UK, has devised two sections to the theory test the drivers are required to pass before being allowed to take their practical driving test. These two sections are the multiple-choice test and the hazard perception test. The hazard

perception test consists of a number of video clips of potentially hazardous situations that the learner drivers must watch and identify the hazards by pressing a button [DVLA website 2015]. These videos have been officially in use for over ten years therefore it was found appropriate to test hazard perception during the experiments. A CD ROM containing 100 hazard perception video clips was purchased with videos being grouped into town, urban, rural, dual carriageway and motorway scenarios. These clips were then assessed as to their suitability for the experiments with regards length, number of hazards and hazard type. The clips were originally over one minute long, therefore some clips were excluded due to the hazard not being visible within the first 50 seconds. This was due to the need to keep the test period to a minimum to try to avoid participant fatigue. Fifteen clips were initially selected for use. The clips presented scenarios in town, urban, rural roads, dual carriageway and motorway setting. They included stopping, pulling out or merging vehicles, animals with owners, child and adult pedestrians. These clips were then cut down to the appropriate length using Movie Maker software. Two further clips were also chosen to be used as a practice for the participants, to familiarise them with the system and the arrow key they needed to press to indicate a hazard as well as allowing time for any questions to be asked.

Four pilot participants were recruited to take part in the study and help assess suitability of the test material. The pilot participants were informed that they were part of a pilot study, were given a short description of the research and what was to be asked of them during the test. A hazard was described as being “any structure, road user or situation that could cause a driver to change speed, course or direction.” The participants were asked to identify hazards by pressing the down arrow key on the keyboard as soon as they became apparent. The participants were then taken through the practice clips and were allowed to ask any questions they had. Once they were comfortable with the task set for them, they proceeded to watch the fifteen hazard perception clips after which they answered the participant questionnaire. Pilot participants were then asked to comment on every aspect of the experiment, with each one stating that there were too many video clips in the main hazard perception test as they lost interest in the latter stages of the test. No further comments were made about the ease of use or content of the test, therefore the length of the main hazard perception test was the only element requiring attention. It was decided to remove three of the video clips to cut down the length of the test by around two minutes. A fifth pilot participant was recruited, taken through the modified process and on completion of the test, did not have any negative comments about the length, content or ease of use of the test. The clips included in the study are listed in Table1.

Table 1: Hazard clips chosen for the study

Number	Clip Type	Hazard type	Length (seconds)
1	Town	Taxi in road	40
2	Urban	Cyclist	50
3	Urban	Car pulling out	50
4	Town	Child running across road	40
5	Dual carriageway	Car merging	50
6	Rural	Runner on road	50
7	Rural	Couple walking a dog	50
8	Dual carriageway	Pedestrian crossing road	40
9	Urban	Children throwing a ball across the road	45
10	Rural	A horse on road	40
11	Motorway	Car pulling into drivers lane	45
12	Urban	Woman with car door open putting child in car	50

Recruitment of the Participants

Ten participants were recruited for each of the five age groups representing novice, experienced, mature, ageing and old drivers: 18-25, 26-55, 56-65, 66-75, 76-85 age groups respectively. Age groups also represented the experience level, rather than the age of the driving licence. An ethical approval to comply with Loughborough University requirements was confirmed. Participants were booked in for a 30-minute session at their convenience and were offered a high street voucher for their time.

Eye Tracking

An SMI RED system attached to a computer screen was used to track the eye movements of participants. Each clip was loaded into SMI Experiment Centre™ and saved. A nine-point calibration was chosen to gain good accuracy without making this stage too long for participants. The participants viewed the hazard perception video clips and when they identified the potentially hazardous situations they pressed the down arrow key. The gaze data presented as heat maps showed the location on the video clip that each participant was focusing upon.

3.RESULTS

The average reaction times to identify the hazards were examined and heat maps for each hazard clip were studied for every age group. When the analysis is based on the reaction times only, the results revealed that there is no regular pattern mainly because, in general, the results

for the old (76-85) and/or ageing (66-75) drivers seem to be inconsistent. Reaction time results varied considerably indicating that the older drivers had similar reaction times in some cases and much slower reaction times in others. The following cases are highlighted as they reveal the situations where the reaction times alone may not be enough to judge the hazard perception of ageing and old drivers.

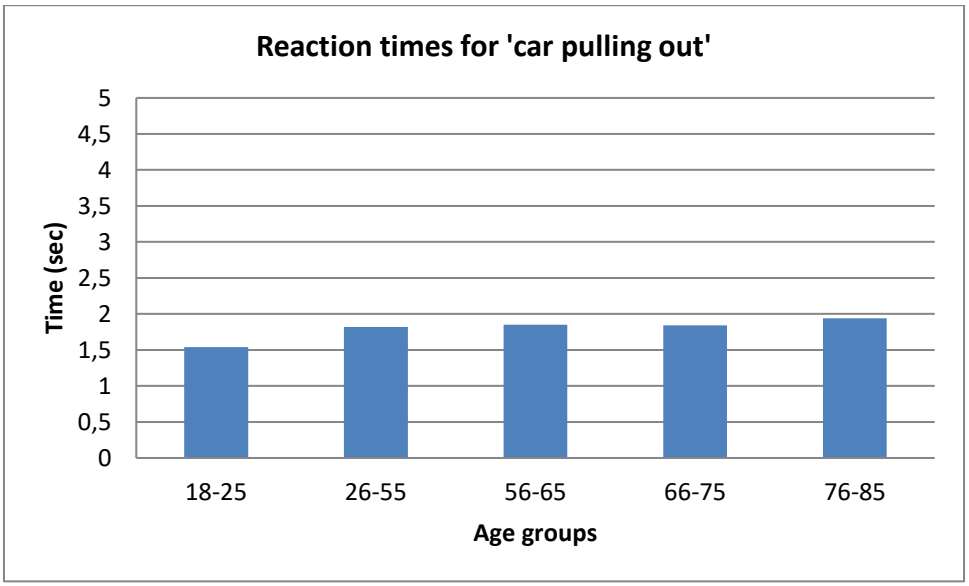


Figure 4. Average reaction time of the age groups for car pulling out hazard

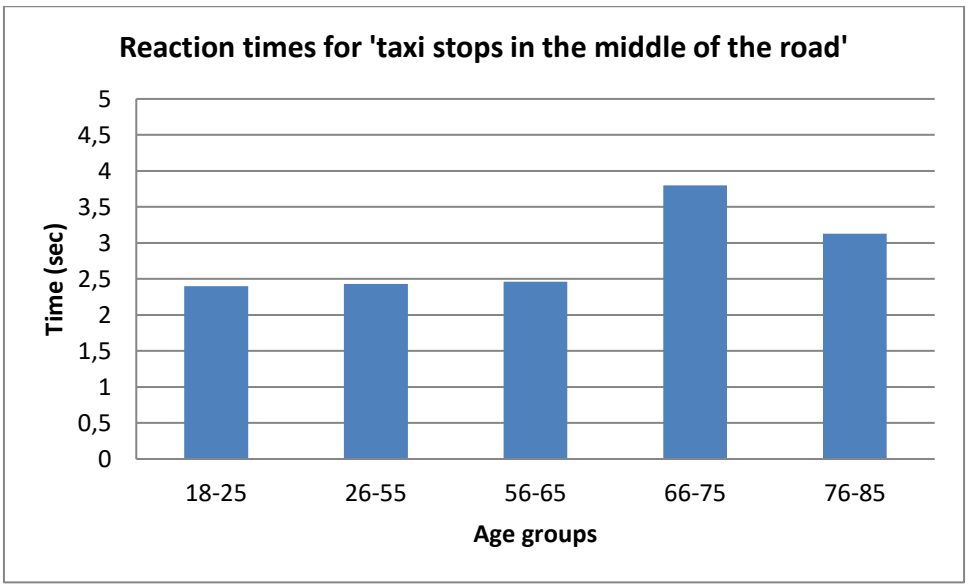


Figure 5. Average reaction time of the age groups for taxi stops in the middle of the road hazard.

For most of the cases there is no significant difference between the groups. An example of 'no significant difference' between the groups can be seen in Figure 4 where the video represented the hazard of a car pulling out in an urban road. Figure 5 illustrates a significant difference in reaction times in an urban area, with the hazard being a taxi stopping in the middle of the road.

Reaction times are easily measurable and indeed used in calculating the points in driving tests as evidence of drivers' perception of developing hazards. Additional data recorded by the Eye tracker, which may provide further insight into the cases, are presented in the heat map Diagrams where the hazards are indicated with a white x sign. Figures 6 and 7 show the heat map for the corresponding case in Figure 4 and 5 respectively.

Figure 6 and Figure 7 reveal that the younger drivers were usually more focused on the hazard in urban environment whereas the ageing and old drivers might see the hazard but their gaze would wander far more. This 'wandering' gaze did not necessarily affect the scores of the ageing and old drivers in every video, therefore revealing no pattern within the results.

Similar characteristics can be observed in rural environment driving examples. Figures 8 and 9 show that the older groups still show more distraction than the younger groups in both cases, however there is no significant difference between the age groups in the 'walkers with a dog on a country road' hazard (Figure 10) and there are significant differences in the a 'horse on a country road' hazard (Figure 11).

More revealing information is presented in the 'child running across road' hazard in a town environment. Statistical analysis suggests no significant difference between age groups and almost every age group acts almost immediately as seen in Figure 12 and potentially score a high mark for 'identifying the developing hazard'. The heat maps in Figure 13 reveal that members of every age group search for potential hazards and due to the town environment almost every member's gaze is unfocused. However, the heat maps also show that only the youngest two groups actually identified the developing hazard.

Further revealing examples have been given in the motorway and dual carriageway scenarios which provided evidence that the older drivers focussed elsewhere rather than on the car on their right on the motorway (Figure 14) and the pedestrian crossing a dual carriageway (Figure 15). In the former, the older drivers would have scored almost as well as the youngest group, however, in the latter the oldest drivers took more time than all other groups as shown in Figures 16 and 17.

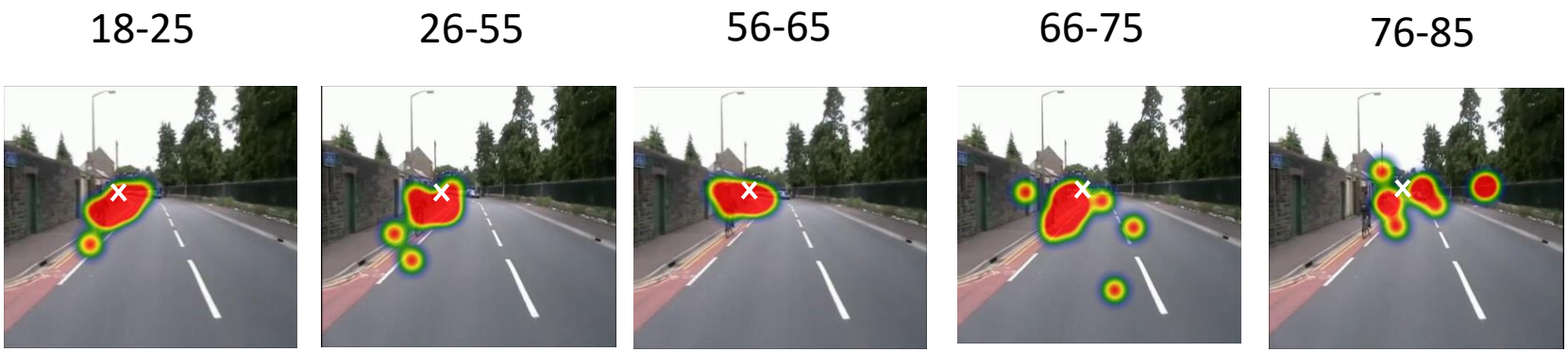


Figure 6 Heat map diagrams for the age groups for car pulling out hazard



Figure 7 Heat map diagrams for the age groups for taxi stops in the middle of the road hazard.

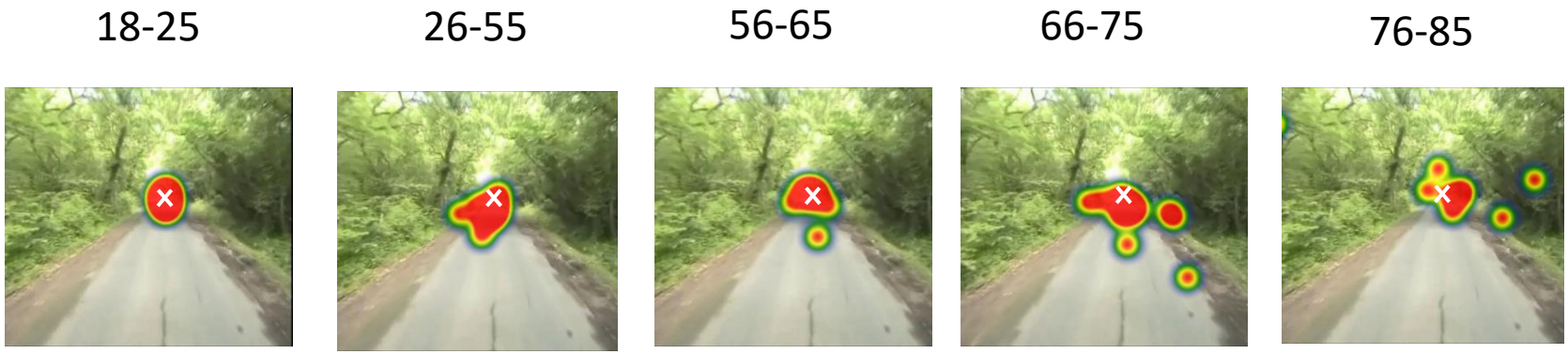


Figure 8 Heat map diagrams for the age groups for walkers with a dog on a country road hazard



Figure 9 Heat map diagrams for the age groups for a horse on a country road hazard

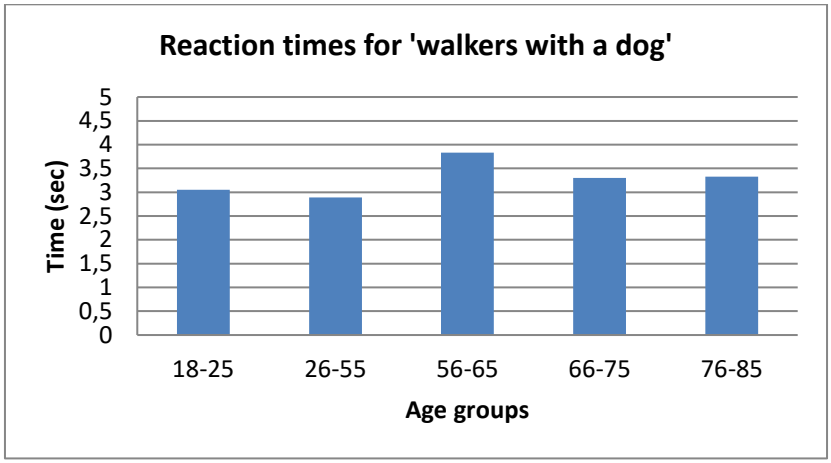


Figure 10. Average reaction time of the age groups for ‘walkers with a dog on a country road’ hazard

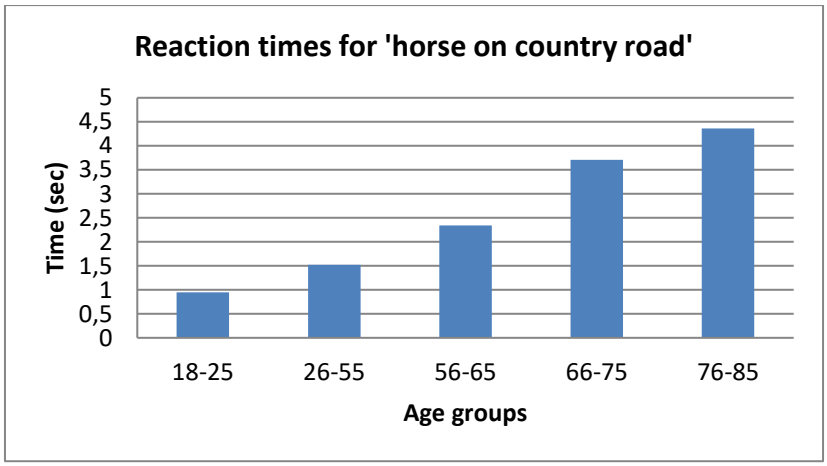


Figure 11. Average reaction time of the age groups for ‘horse on a country road’ hazard

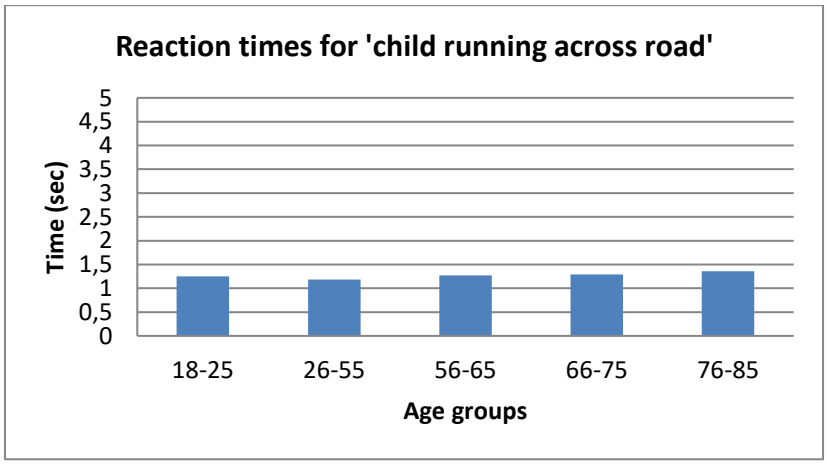


Figure 12. Average reaction time of the age groups for child running across road hazard



Figure 13 Heat map diagrams for the age groups for child running across road in town hazard



Figure 14 Heat map diagrams for the age groups for car on the right moving into driver's lane hazard



Figure 15 Heat map diagrams for the age groups for pedestrian crossing dual carriageway hazard

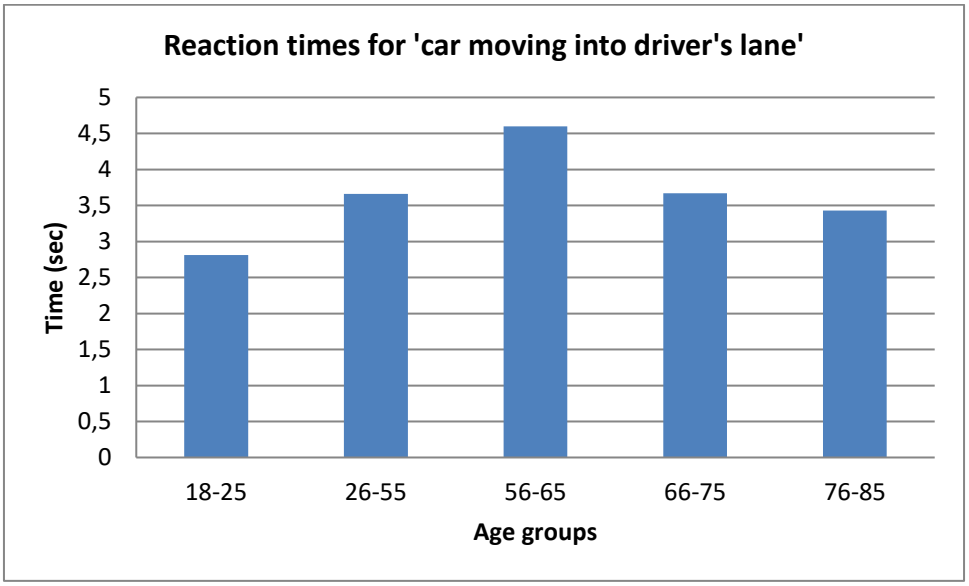


Figure 16. Average reaction time of the age groups for car moving into driver's lane hazard

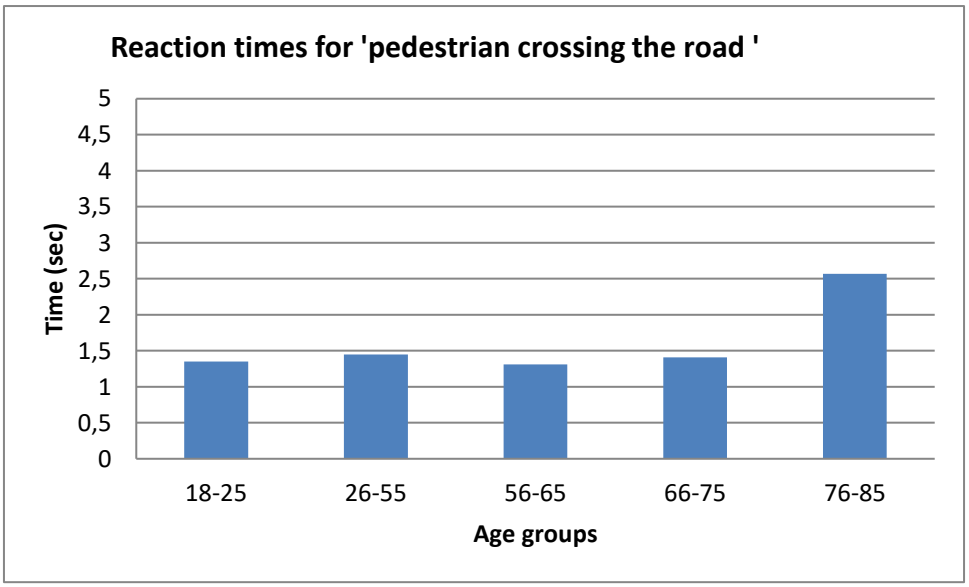


Figure 17. Average reaction time of the age groups for pedestrian crossing dual carriageway hazard

4.DISCUSSION

Reaction times data are easily collectible and used to prove drivers' perception of developing hazards. However, studying the reaction times together with the heat maps reveals that measuring the reaction times alone may be misleading. As demonstrated in the result section, the following observations point out the potential shortfall of the video based hazard perception tests for older drivers:

1. Identifying the hazard almost as quickly as the younger drivers does not mean that older drivers focus on the hazard as well as the younger groups. Examples in countryside and urban environment also demonstrate that being slower than younger drivers does not always mean that they are focusing less than them either.
2. When many more hazards should be expected (e.g. driving in town) all age group subjects can 'identify' the hazard and score high points whereas only the youngest groups identify the developing hazard of a child crossing the road.
3. During motorway and dual carriageway driving where a broader view and instantaneous action are required regardless of the points the oldest drivers score, they fail to identify the hazard of car moving into their lane and pedestrian crossing the dual carriageway
4. Older drivers can score very high in some video clips despite them expecting hazards from elsewhere rather than identifying actual developing hazard.

Therefore, these inconsistencies in older drivers' performance may be due to expecting a hazard from another source in some of the video clips. In general, this may be applied to anyone, i.e. identifying a developing hazard but not the intended one in the film. Identifying a hazard and taking an action - even if it does not exist – may appear to be 'safe', however, the driver's inappropriate actions may create further hazards for other drivers.

In the experiments of this study the younger group almost always focused on actual hazards. This may be because of their abilities or the way they were trained for driving licence tests and how fresh it is in their memories. The purpose of this study is not to compare the driving abilities or safety of young and old but rather to understand whether hazard perception tests can be relied in measuring the older drivers' hazard perception. In this case study we have demonstrated that the current system can be misleading. This may also shed a light on disagreements of earlier studies which compare hazard perception capabilities of age groups.

Limitations

Every person in the youngest group due to the nature of the generation they represent, were more familiar with the video clips as well as the hazard perception tests. Driving requires far

more concentration than watching a video clip on a computer screen. The results could have been different, for example, if the hazard perception tests were performed in real life. Hence the use of the hazard perception clips may not be representative of reaction times of the driver. On the other hand, the hazard perception clips did not give participants peripheral or rear vision, therefore reducing the field of view and allowing them to concentrate only on what was ahead of them. Focus in one direction only could have biased the results as they may have noticed hazards more quickly than they would normally do. In addition some of the older patients' lack of eye-focus may have affected their vision, perception and data collection.

5.CONCLUSIONS

Experiments were conducted in a laboratory environment to understand whether the hazard perception tests can be conclusive in terms of observing 'developing hazards' and whether these tests can be used to examine older drivers' ability to perceive hazards. The case studies show that sometimes older drivers are aware of the developing hazards as quickly as the younger drivers and sometimes they are very slow to identify a developing hazard. Their performance in reaction times is not correlated with the type of road they drive on. However, when the eye-tracking data is observed in parallel, it has been revealed that some of the reactions of older drivers are the result of expecting a hazard from elsewhere. Hence, collecting the reaction time data alone is not always sufficient to measure the ability of hazard perception of older drivers.

Furthermore this study also shows that the youngest group is very successful in recognising the hazards in all cases, however this alone does not make them better drivers as evidenced by the high accident rates of this age group.

ACKNOWLEDGEMENTS

The authors thank all volunteers who participated in the experiments of this study.

REFERENCES

1. Abou-Raya, S. & ElMeguid, L.A. 2009, "Road traffic accidents and the elderly", *Geriatrics & gerontology international,* vol. 9, no. 3, pp. 290-297.

2. Acar B. S., Feng J., Esat V. 2012 "Investigation into Suitability of Current ATDs to Represent Ageing Drivers" *International Journal of Crashworthiness* **18**(1):1-10, 2013

3. Bromberg, S., Oron-Gilad, T., Ronen, A., Borowsky, A. & Parmet, Y. 2012, "The perception of pedestrians from the perspective of elderly experienced and experienced drivers", *Accident Analysis & Prevention,* vol. 44, no. 1, pp. 48-55.

4. Carr, D.B. & Ott, B.R. 2010, "The older adult driver with cognitive impairment", *JAMA: the journal of the American Medical Association,* vol. 303, no. 16, pp. 1632-1641.

5. Chandraratna, S. & Stamatiadis, N. 2003, "Problem driving maneuvers of elderly drivers", *Transportation Research Record: Journal of the Transportation Research Board,* vol. 1843, no. -1, pp. 89-95.

6. DVLA *, Driving tests, motorcycles and learning to drive* [Homepage of DVLA], [Online]. Available: https://www.gov.uk/browse/driving/learning-to-drive [2013, 05/10].

7. Ferreira, I.S., Simões, M.R. & Marôco, J. 2012, "The Addenbrooke's Cognitive Examination Revised as a potential screening test for elderly drivers", *Accident Analysis & Prevention,* .

8. Field, A. 2009, *Discovering Statistics Using SPSS,* 3rd edn, Sage, London.

9. Horswill, M.S. & McKenna, F.P. 2004, "Drivers' hazard perception ability: Situation awareness on the road", *A cognitive approach to situation awareness: Theory and application,* , pp. 155-175.

10. Horswill, M. S., Marrington, S. A., McCullough, C. M., Wood, J., Pachana, N. A., McWilliam, J., & Raikos, M. K. (2008). The hazard perception ability of older drivers. *The Journals of Gerontology Series B: Psychological Sciences and Social Sciences*, *63*(4), P212-P218.

11. Horswill, M.S., Pachana, N.A., Wood, J., Marrington, S.A., McWilliam, J. & McCullough, C.M. 2009, "A comparison of the hazard perception ability of matched groups of healthy drivers aged 35 to 55, 65 to 74, and 75 to 84 years", *Journal of the International Neuropsychological Society,* vol. 15, no. 5, pp. 799.

12. Mayhew, D.R., Simpson, H.M. & Ferguson, S.A. 2006, "Collisions involving senior drivers: high-risk conditions and locations", *Traffic injury prevention,* vol. 7, no. 2, pp. 117-124.

13. McKenna and Horswill (1999) "Hazard perception and its relevance for driver licensing, IATSS Research Vol 23, No 1, 36-41.

14. Nachar, N. 2008, "The Mann-Whitney U: A test for assessing whether two independent samples come from the same distribution", *Tutorials in Quantitative Methods for Psychology,* vol. 4, no. 1, pp. 13-20.

15. NHTS 2009 "Summary of Travel Trends", National Household Travel Survey, US Department of Transportation, Federal Highway Administration.

16. OECD, Ageing and transport: Mobility needs and safety issues. OECD Scientific Expert Group, Paris, 2001. #

17. Schall, M.C., Rusch, M.L., Lee, J.D., Dawson, J.D., Thomas, G., Aksan, N. & Rizzo, M. 2012, "Augmented Reality Cues and Elderly Driver Hazard Perception", *Human Factors: The Journal of the Human Factors and Ergonomics Society,* .

18. Underwood, G., Phelps, N., Wright, C., Van Loon, E. & Galpin, A. 2005, "Eye fixation scanpaths of younger and older drivers in a hazard perception task", *Ophthalmic and Physiological Optics,* vol. 25, no. 4, pp. 346-356.

19. Welsh R , Morris A, Hassan A and Charlton J, 2006 'Crash characteristics and injury outcomes for older passenger car occupants', Transportation Research Part F, **9** (5) 322-334.

TRAFFIC SAFETY AT MEDIAN DITCHES: STEEL VS CONCRETE BARRIER PERFORMANCE COMPARISON USING COMPUTER SIMULATION

Ayhan Öner YÜCEL, *ayucel@metu.edu.tr,* Research Assistant, Middle East Technical University, Dept. of Civil Engineering, Ankara, Turkey

Ali Osman ATAHAN, *atahana@itu.edu.tr,* Professor and Division Head, Istanbul Technical University, Dept. of Civil Engineering, Istanbul, Turkey

Turan ARSLAN, *tarslan@uludag.edu.tr,* Associate Professor, Uludağ University, Dept. of Civil Engineering, Bursa, Turkey

Umur Korkut SEVİM, *ukorkut.sevim@iste.edu.tr*, Professor, Iskenderun Technical University, Dept. of Civil Engineering, Hatay, Turkey

ABSTRACT

In Turkey, concrete V-shaped ditches are formed at the median section of divided highways to provide drainage. Recent accidents showed that these ditches actaully present safety risks for vehicles entering medians. Vehicles either cross over the ditch, roll over or are trapped inside the ditch depending upon the mass, size, speed and angle of the vehicle entered. To overcome this safety risk and reduce the severity of these accidents longitudinal barriers are installed along these ditches.

Currently in Turkey steel barriers are extensively used to improve traffic safety at median ditches. In this paper, crash performance of a steel and a concrete barrier used at medians with ditches are compared. A standard steel EDSP-1.33 barrier and a newly developed concrete C470 barrier models have been constructed and impact simulations were performed when they are installed at ditch slope break point. A nonlinear finite element program LS-DYNA is used for the analysis. A 13,000 kg bus model is used to impact both barriers in accordance with European standard requirements. Simulation results show that when steel EDSP-1.33 barrier is used the bus has the potential for excessive penetration into the ditch with significant barrier deformation. Moreover, the barrier damage is extensive resulting increased maintenance costs. On the other hand, concrete C470 barrier successfully contains and redirects 13,000 kg bus impact with minimal barrier deformation and safety risk. Even though concrete barrier slides toward inside the ditch bus does not enter the ditch area and exits the barrier in a stable manner. Therefore, to increase traffic safety at ditches located at median

section of divided highways in Turkey utilization of newly developed concrete barrier C470 is recommended.

Keywords: Ditch; Traffic Safety; Simulation; Concrete Barrier; Steel Barrier; LS-DYNA; Divided Highway.

1. INTRODUCTION

In recent years, General Directorate of Highways (KGM) of Turkey initiated a major highway rehabilitation program involving the upgrading of existing single platform roads to become divided two or more lane roads separated by a median. A V-shaped ditch with a triangular cross section is designed and constructed along the roads as shown in Figure 1. These concrete median ditches are intended to provide rain water drainage. Although drainage is essential to any roadway project, this particular design represented potential safety hazard to drivers losing control and encroaching the median in an uncontrolled manner.

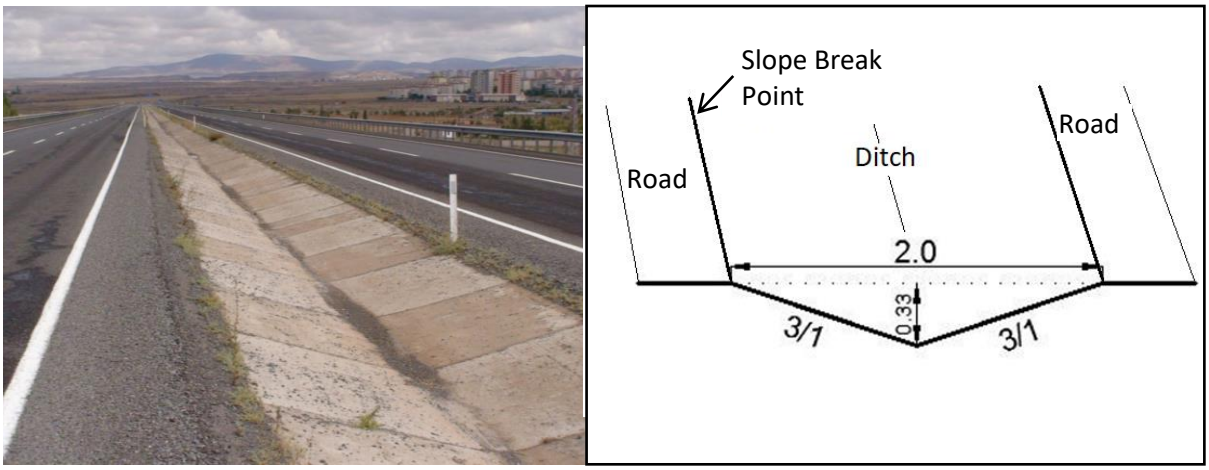


Figure 1. V-shaped ditch constructed at median of divided highways in Turkey

In addition, when a vehicle leaves a divided highway and crosses the median, risk of a high speed head on collision with a vehicle in the opposing traffic becomes imminent [Chitturi et al. 2011]. To prevent or reduce vehicles' crossing over the median usually road restraint systems (RRS) are utilized [AASHTO, 2004]. However, it should be noted that although the existence of median restraint systems can greatly reduce the median cross over accidents it increases the frequency of less severe median barrier crashes [Noyce et al. 2005; Qin et al. 2010; Chitturi et al. 2011].

Previous research suggests that the type of road restraint system and its placement location play essential role in acceptable performance of these designs during an impact [Ray et al. 2009, Atahan et al. 2008]. Therefore, it becomes critical to contain and redirect vehicles from entering the ditches in such cases. As a result, using barriers on both sides of the median becomes critical.

A longitudinal barrier that can be eligible for being used in highways should meet the criteria defined by European standard of EN 1317 for crash tests [CEN, 2010]. In this standard, crash tests are performed with standard vehicle sizes, under controlled speed and impact angles. Usually, barriers are installed on flat surfaces. Some exceptional tests are performed at sloped surfaces. Therefore, the behavior of vehicles on graded surfaces, such as ditches are not well-known. Furthermore and most importantly, in majority of guardrail applications in Turkey, due to restrictions of road space, the guardrails are installed inside or very close to the ditch slope break point [Yucel, 2012]. Hence the wheels of vehicles that contact the guardrail will possibly be trapped in the ditch causing instability problems leading to severe and fatal accidents as shown Figure 2. The damage on the bus is caused partially from contact with the V-shaped ditch. This is particularly valid for high center of gravity vehicles, such as busses.



Figure 2. A bus accident at a V-shaped ditch protected with steel longitudinal barrier

This paper is aimed to evaluate the impact performance and effectiveness of steel and concrete longitudinal barrier designs used long median section. A three dimensional finite element simulation program LS-DYNA was used to determine adequacy of those two types of barriers when installed at slope break point of median ditch. Following sections explain the details of the study.

2. DESCRIPTION OF BARRIERS STUDIED

2.1 Concrete Barrier

A new single sided concrete barrier is developed for the purpose of improving traffic safety at medians. As shown in Figure 3, concrete barrier is 3000 mm long, 470 mm wide and 816 mm tall. Concrete barrier designs are based on designers past experiences and performances of similar barriers. Concrete blocks are connected to each other with three different mechanisims. Figure 4 illustrates central, lower and back connectors. These connections are used to eliminate any possible separation and failure during vehicle impact as well as provide a continuous and easthetically pleasing wall. Compression strength of the concrete used in the barrier is 30 MPa (C30). Impact stregth of concrete is improved with reinforcement bars used inside the blocks. Each block weighs approximately 2 tons and two openings are formed under each block to alleviate hadling and placement.

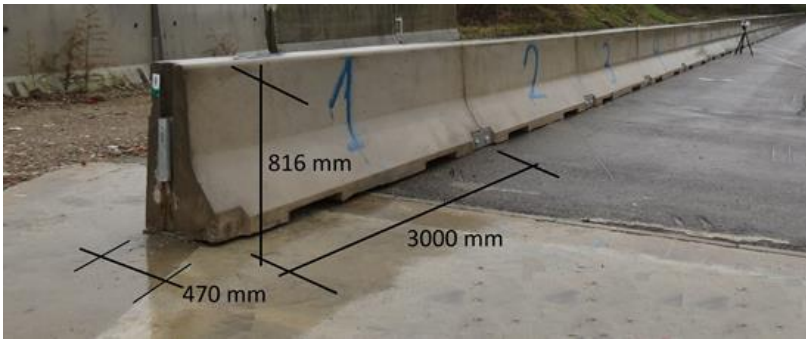


Figure 3. Dimensions of single sided concrete barrier



Figure 4. Concrete barrier connections (a) Lower, (b) Rear and (c) Between blocks

2.2 Steel Barrier

Majority of the guardrail systems used at ditches in Turkey are an old German design, named EDSP-1.33 [RAL, 1990]. As shown in Figure 5, these steel barriers use 5 different components, including, 4.2 mm thick, 1900 mm long sigma shaped post, 3 mm thick W-beam, 5 mm thick, 480 mm long spacer between the rail and post, 5 mm thick connector between post and spacer and 4 mm thick rear beam connecting posts. All these members are produced from S235 quality mild steel. Post spacing and post embedment depth in this design are 1,330 mm and

1,200 mm, respectively. As shown in Figure 5, the top heigth of the design is 750 mm. In most cases, as shown in Figures 2 and 5, posts are installed inside or very close to the ditch slope break point due to 500 mm length of spacer and short distance between the ditch and the roadway. Lack of adequate distance behind the barrier and presence of a steep slope creates a safety risk for vehicles impacting the barrier and entering the slope.



Figure 5. Dimensions and installed view of steel barrier EDSP-1.33

3. FINITE ELEMENT SIMULATION STUDY

In this study, the crash performance of two different guardrails installed along the ditches are investigated using finite element analysis. Finite element models of EDSP-1.33 steel barrier, currently in use, and a newly developed concrete barrier were constructed using LS-DYNA program [LSTC, 2012]. A bus model is used to impact the barriers in accordance with the European crash testing standard EN 1317 part 2. Bus is selected due to its higher center of gravity location, presence of large number of buses on divided highways in Turkey and better evaluate the containment and redirection capacity of both barriers during a large vehicle impact. Details of the both barriers and vehicle model are explained below.

3.1 Description of Finite Element Models

In order to investigate and analyze the crash performance of guardrails placed along a ditch, long enough the finite element models of steel and concrete barriers were created. A versatile, 3D, large deformation finite element code, LS-DYNA is utilized to perform the analysis. This is done in a manner consistent with the actual material behavior and geometry used for guardrails to accurately represent the guardrails used in practice.

A finite element model of the EDSP-1.33 was developed to assess the crash test performance of the design. The model as shown in Figure 6, consisted of 104,321 nodes, 65,956 shell and 17,407 solid elements. Shell elements represented the steel members of the model while solid

elements represented the ditch concrete. The shell elements of the W-beam and post that are expected to get in direct contact with vehicle and thus experience severe deformations are modeled with full integration formulation to accurately represent the complex interactions and behavior. All steel elements were modeled with default element formulation for computational efficiency.

Since barrier is expected to sustain large plastic deformations and possible crushing during vehicle impact a piecewise linear plastic material definition is used to model steel members [Vesenjak, 2005; Atahan and Bonin, 2006]. Failure is included in the model to capture any potential rail ruptures. A rigid material modeling is used to represent concrete surface of the ditch.

In an actual EDSP-1.33 installation, connections between the members, such as W-beam to spacer and post are established using bolts and nuts. To accurately represent the behavior of these connections during simulation CONSTRAINED_SPOTWELD option in LS-DYNA was used [LSTC, 2017]. By definition, this option keeps members connected until a certain force criteria is met. Then the connection fails and members allow moving freely. To accurately represent the crash behavior of EDSP-1.33 design this behavior is essential since connections in EDSP-1.33 barrier are designed to separate when forces reach a certain level. Therefore, a detailed connection model is constructed using LS-DYNA. The behavior of connection was examined under different loading conditions. A reasonable failure criterion obtained from the component simulation was used in the connection model [Atahan and Bonin, 2006].

To model the concrete barrier, as shown in Figure 7, geometry and connection details of the barrier was developed and inputted in LS-DYNA. The model consisted of 82,645 nodes, 15,254 shell and 57,203 solid elements. Shell elements represented the steel members, such as plate connectors and reinforcement of the model while solid elements represented the concrete and ditch. As usual, shell elements that are expected to undergo large deformations and stress concentrations are modeled with full integration formulation to accurately represent the complex interactions and behavior. All steel elements were modeled with default element formulation and a piecewise linear plastic material definition. On the other hand, concrete is modeled with a rigid material approximation since no failure is expected in concrete during crash event.

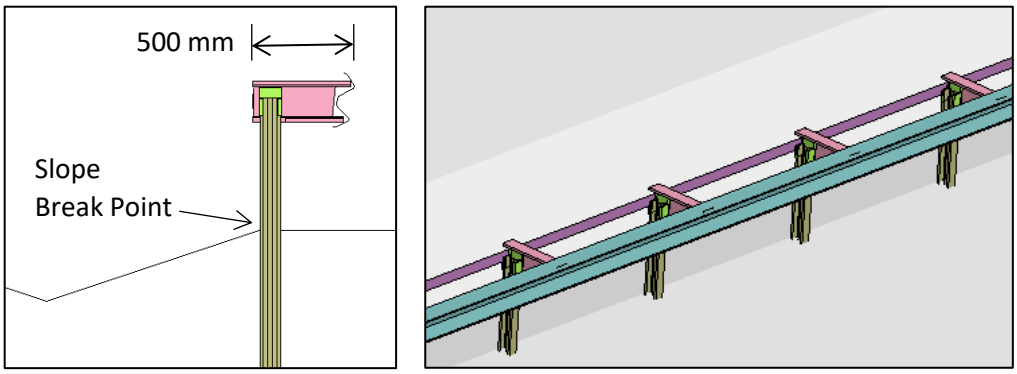


Figure 6. Finite element model of steel EDSP-1.33 barrier installed at slope break point of ditch

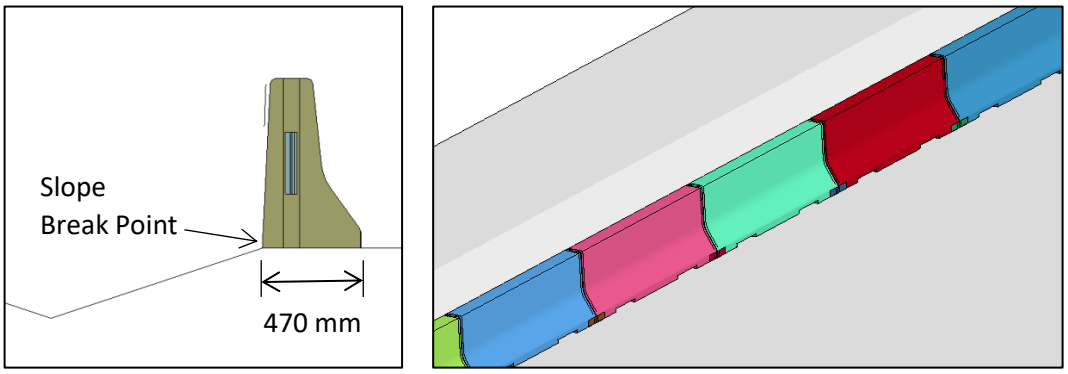


Figure 7. Finite element model of concrete barrier installed at slope break point of ditch

13,00 kg bus model used in the simulation is shown in Figure 8. This model was taken from a vehicle model libabry at the National Crash Analysis Center [NCAC, 2008]. The accuracy of the bus model is validated with actual tests.

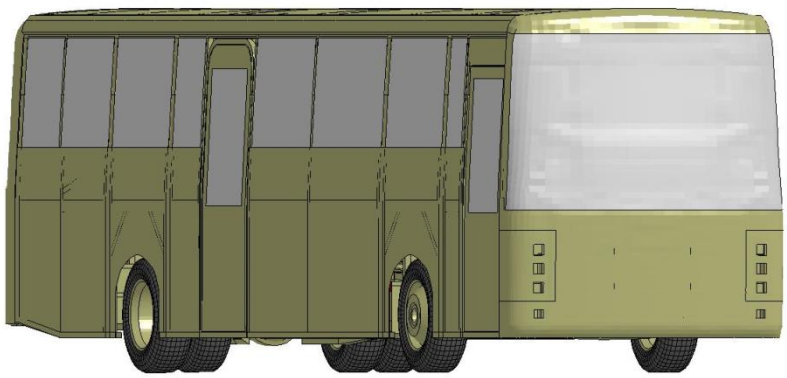


Figure 8. Finite element model of 13,000 kg bus [NCAC, 2008].

Finally, a V-shaped ditch was modelled with the road platform together. Both road section and ditch are modeled with rigid material since they are not expected to sustain any damages during simulations. However, a soil model was constructed to accurately represent post-soil

interaction during impact event. A ditch cross section with steel and concrete barrier installations is shown in Figure 9.

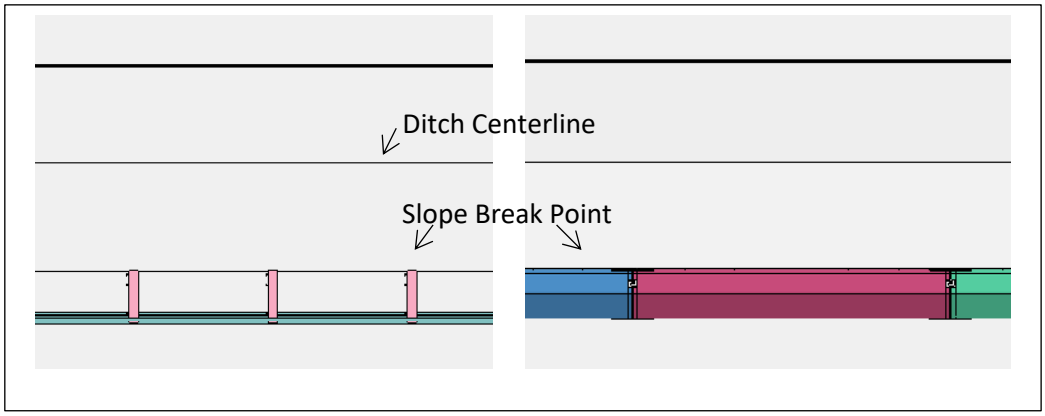


Figure 9. Finite element model of V-shaped ditch with both barriers models and roadway (Overhead View)

3.2 EDSP-1.33 Steel Barrier Simulation Study

After the final preparations on the bus model, 13,000 kg bus was positioned in front of the barrier and impacted the barrier at 70 kph and 20 degrees angle. This impact conditions are determined based on the recommendations set forth in EN 1317 Part 2 [CEN, 2010]. The kinetic energy of the bus just before impact was approximately 287 kJ.

Simulation was run about 1.0 sec until the bus entered into the ditch completely and became parallel with the barrier. As shown in Figures 10 and 11, when vehicle hit the barrier W-rail and posts at the impact area began to deform. At 0.13 seconds after the initial impact spacer blocks started to separate from posts preventing W-rail to move downwards with the posts. As the bus advanced forward, more posts were bent and at 0.3 seconds into the simulation redirection of bus became clear. The velocity of the vehicle at this point was approximately 62 kph. At 0.65 seconds after the initial contact with the barrier, front section of the bus entered into the ditch and almost reached to the opposite side of the roadway. At this point the damage to the EDSP-1.33 was extensive and bus continued its forward movement. As shown in Figures 10 and 11, bus became parallel with the barrier and ditch at around 0.95 seconds and more tahn half of the bus was already inside the ditch. Finally around 1.0 second into the simulation bus began to exit the barrier in a stanble manner. Based on the simulation predictions, it was determined that EDSP-1.33 barrier is able to contain and redirect impacting bus however, the damage to the barrier was extensive and the penetration into the ditch was significant. Picture of the deformed shape of the barrier is shown in Figures 12 and 13. Velocity of the bus at exit of barrier was 49 kph representing 30% reduction in vehicle speed.

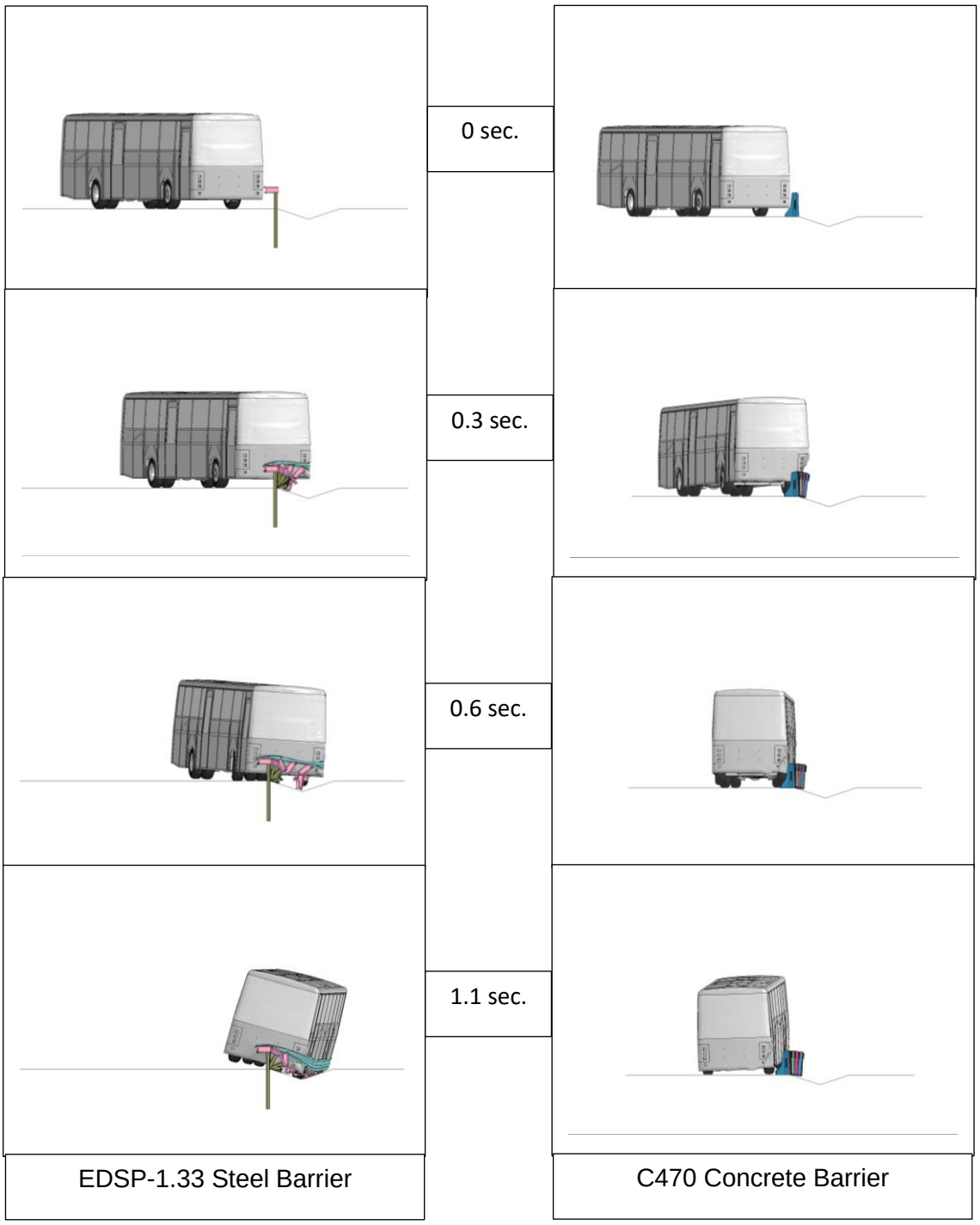


Figure 10. Sequential frontal pictures comparison of steel EDSP-1.33 and concrete C470 barrier after bus impact simulation

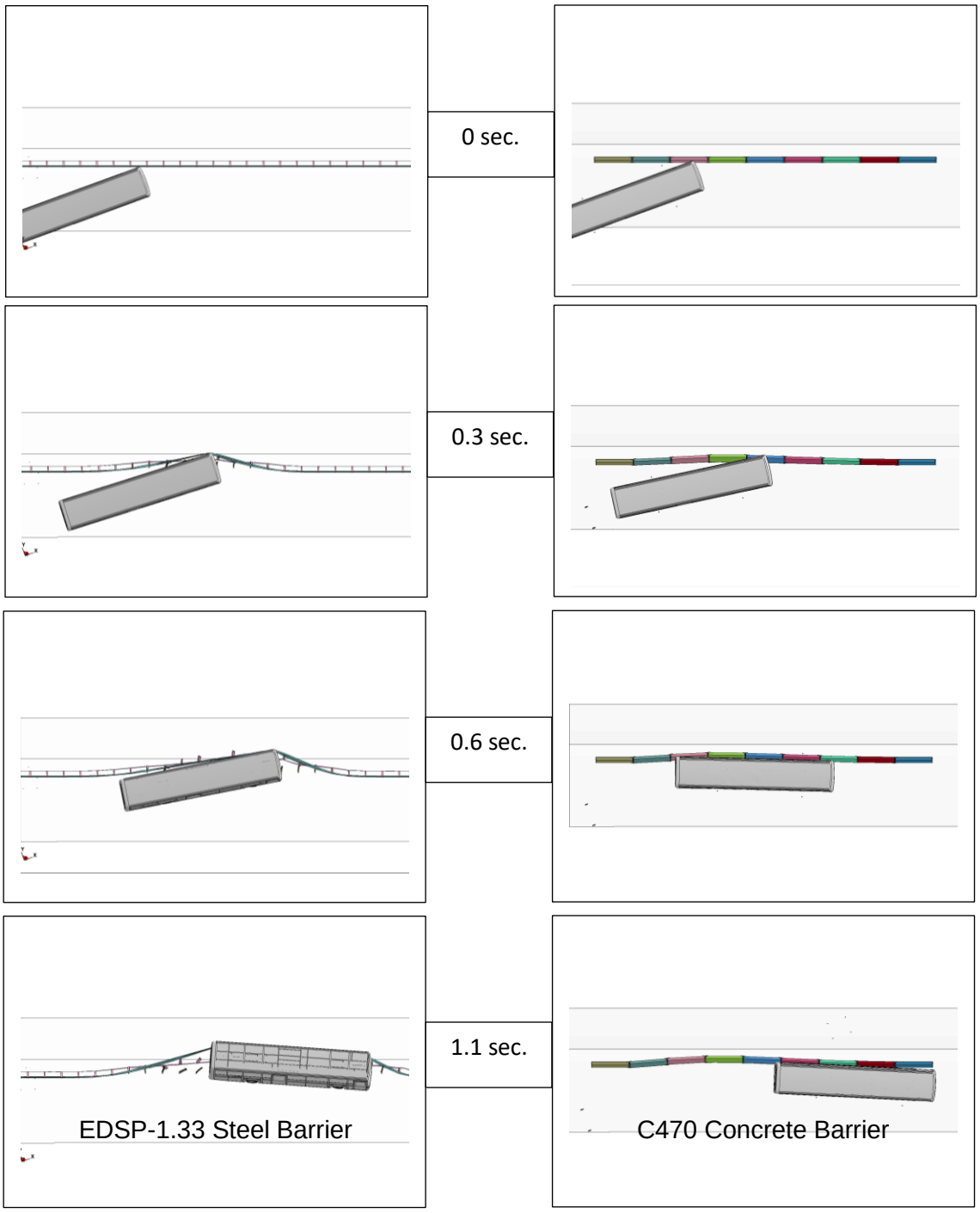


Figure 11. Sequential overhead pictures comparison of steel EDSP-1.33 and concrete C470 barrier after bus impact simulation

3.3 Concrete Barrier Simulation Study

To run the impact simulation, as shown in Figures 10 and 11, 13,000 kg bus model was positioned in front of the concrete barriers. Similar to previous simulation, the bus impacted the barrier at 20 degrees and 70 kph velocity. The bus contacted the connection section of the barrier, which represents the weakest section of the design. Soon after the initial contact barrier

began to deform laterally and the impacting side front tire of the bus began to climb on the barrier. At 0.15 seconds into the simulation a total of three concrete blocks deformed laterally and as they slide backwards they entered into the ditch area. As shown in Figures 10 and 11, the bus began to change direction at 0.3 seconds and at 0.58 seconds it became parallel with the concrete barrier and ditch. At this point, rear left tires impacted the already deformed barrier sections and pushed them further into the ditch. At 0.7 seconods into the simulation, one concrete block almost completely entered teh ditch, however due to strong connections between blocks concrete barriers remained upright and did not show any excessive deformation. Finally at around 0.8 seconds into the simulation, the bus began to exit the concrete barrier. The velocity of the bus at the exit was approximately 58 kph and neither the bus nor the barrier show any penetration to the ditch area. As shown in Figures 12 and 13, damage to concrete barrier was not significant, deformation was concentrated at a fairly small length, and the performance of the barrier was much improved compared to that observed from the steel EDSP-1.33 barrier. Based on the simulation results it could be concluded that a well connected and installed concrete barrier could be a potential alternative to steel barriers used at median ditches.

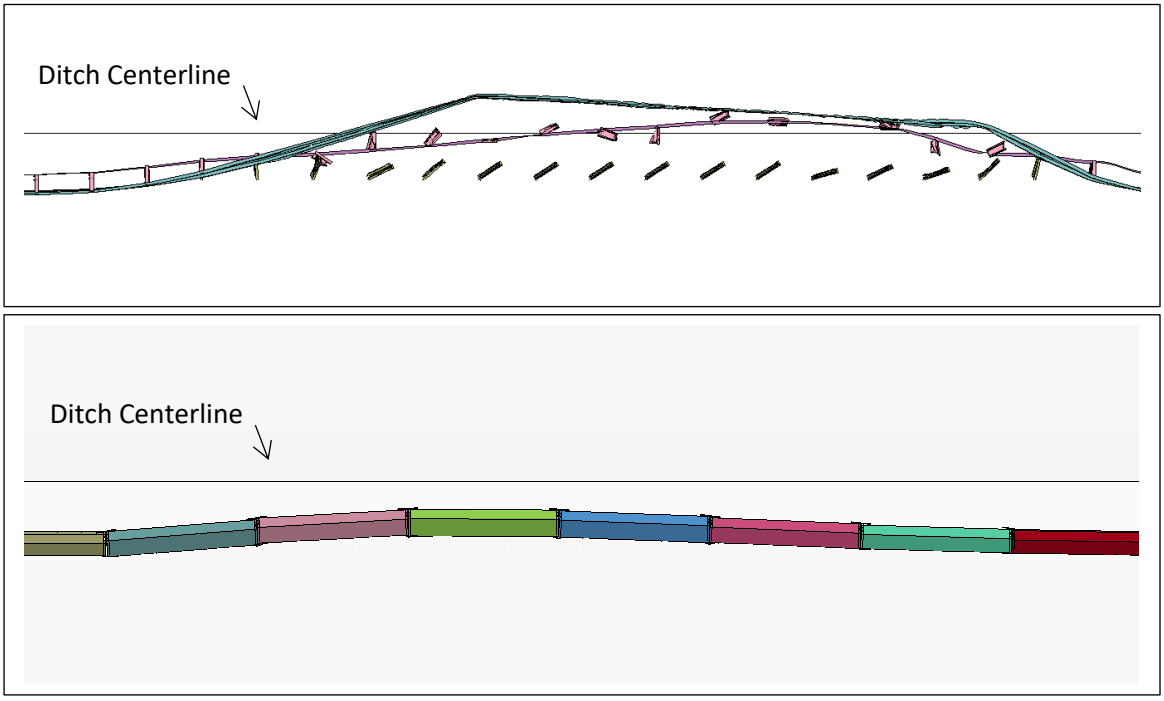


Figure 12. Damage comparison for steel EDSP-1.33 and concrete C470 barrier after bus impact simulation (Overhead View)

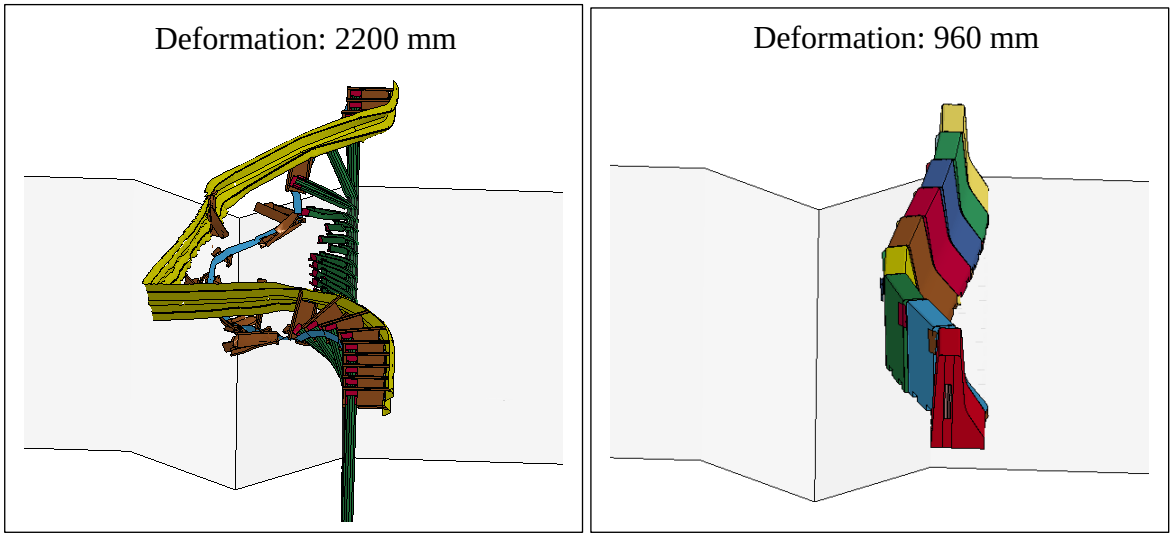


Figure 13. Damage comparison for steel EDSP-1.33 and concrete C470 barrier after bus impact simulation (Frontal View)

4. SUMMARY AND CONCLUSIONS

This paper is aimed to compare impact performance of two different guardrail systems when they are used at slope break point of ditches located at the median of divided highways. Crash test behavior of both steel EDSP-1.33 barrier and concrete C470 barrier were predicted using nonlinear impact simulations. A highly reliable finite element program LS-DYNA is used for the analysis. Models for both barriers, ditch and a bus are prepared and crash simulation is performed in accordance with European standard requirements.

Simulation results show that when steel EDSP-1.33 barrier is used the bus has the potential for excessive penetration into the ditch with 2200 mm barrier deformation. Moreover, the barrier damage is extensive resulting increased maintenance costs. On the other hand, concrete C470 barrier successfully contains and redirects 13,000 kg bus impact with minimal barrier deformation and safety risk. Even though concrete barrier slides toward inside the ditch approximately 960 mm, bus does not enter the ditch area and exits the barrier in a stable manner.

To increase traffic safety, minimize maintenance costs and improve stability of vehicles with high center of gravity at ditches located at median section of divided highways in Turkey utilization of concrete barriers particularly at curve section of roads is strongly recommended.

ACKNOWLEDGEMENTS

Financial support for this study is provided by Tübitak project number 110M235. This support is gratefully acknowledged.

REFERENCES

1. **AASHTO (2004)**, A Policy on Geometric Design of Highways and Streets, Washington, D.C.
2. **Atahan A.O. and Bonin G. (2006),** Numerical analysis of an H4a heavy containment level transition. Int. J. Heavy Vehicle Systems, Inderscience Enterprises, 13(4), 351-365.
3. **Atahan, A. O., Bonin, G., Cicinnati, L., & Yasarer, H. (2008),** Development of European end treatment TWINY using simulation and crash testing. Journal of Transportation Engineering, ASCE,134(11), 467–476. doi:10.1061/(ASCE)0733-947X(2008)134:11(467).
4. **CEN (2010),** EN1317-2, Road restraint systems - Part 2: Performance classes, impact test acceptance criteria and test methods for safety barriers, European Committee for Standardization, Brussels.
5. **Chitturi, M V, A W Ooms, et al. (2011),** Injury outcomes and costs for cross-median and median barrier crashes. Journal of Safety Research 42(2): 87-92, http://dx.doi.org/10.1016/j.jsr.2011.01.006.
6. **KGM (2012),** Highway Design Manual, Turkish Department of Transportation, Ankara.
7. **LSTC (2012),** LS-DYNA user's manual, Livermore Software Technology Corporation, Livermore, CA.
8. **NCAC (2008),** National Crash Analysis Center, George Washington University, http://www.ncac.gwu.edu/vml/models.html.
9. **Noyce, D. A., & McKendry, R. J. (2005),** Analysis of Median Crossover Crashes in Wisconsin. University of Wisconsin Traffic Operations and Safety Laboratory, WI.
10. **Qin, X., Wang, F., Bill, A. R., Chitturi, M. V., & Noyce, D. A. (2010),** Evaluation of High Tension Cable Barriers in Wisconsin, Report No. FEP-04-09, University of Wisconsin-Madison, WI.
11. **RAL (1990),** International standard for evaluation of steel for road safety systems. Germany.
12. **M. H. Ray, C. Silvestri, C. Conron (2009),** "Experience With Cable Median Barriers in United States: Design Standards, Policies and Performance," Journal of Transportation, Vol. 153 No. 10, American Society of Civil Engineering, , Washington, D.C.
13. **Vesenjak M., Borovinsek M. and Ren Z. (2005),** Computational and experimental crash analysis of the road safety. Engineering Failure Analysis, 12, 963-973.

14. Yucel, A.Ö. (2012), Evaluation of effects of median ditches on the vehicle stability using dynamic analysis" Masters Thesis, Mustafa Kemal University, Hatay.

ANALYSIS OF A COACH SIDE FLAP UNDER CYCLIC LOADS

Burkay Yılmaz DEMİR, *burkay.demir@dynamuhendislik.com*, 06800, Ankara, Turkey

Zeki Mert BARUT, *mert.barut@man.eu*, MAN Türkiye A.Ş., 06750, Ankara, Turkey

Umut AKTAŞ, *umut.aktas.a@man.eu,* MAN Türkiye A.Ş., 06750, Ankara, Turkey

ABSTRACT

The main objective of this study is to determine whether the coach side flap material and supports are strong enough for a certain amount of life cycle, also to optimize the weight by eliminating unnecessary supports and cost by choosing an optimum material. This study is aimed to model coach side flaps kinematically to obtain the forces acting on the flap cover and carrying out non-proportional fatigue analysis based on opening and closing cases. The flap is modeled and also the Rigid Body Simulation is performed in CATIA. The piston forces modelled as preloaded linear springs with a small amount of damping which is determined based on real opening timing of the flaps. The fatigue analysis is performed in ANSYS Workbench according to the reaction forces obtained from the simulation results from CATIA. Since there is no correlation between the boundary and load conditions in opening and closing cases, non-proportional fatigue method is used. The results were compared with two different available aluminum materials. Also some case studies with elimination of some support structures are performed.

Keywords: Coaches, side flaps, fatigue, AlMg3 H12, AlMg3 H22

1. INTRODUCTION

Coaches are the types of road vehicles used for transporting passengers. Unlike buses, which are generally designed for shorter journeys, coaches have large compartments under the passenger cabin used for storing passenger luggage or utilities. Access to these compartments is provided by the side flaps, which are consisting of a door and a linkage mechanism located on the both sides of the coach exterior and opening to the inner luggage compartments of the vehicle. The dimensions of the side flaps may vary up to 2,3 m in width and 1,2 m in height, depending on the opening area of the compartment. Side flaps are

generally embodied in two main different forms: Bar linkage side flaps and hinge linked side flaps.

Hinge linked side flaps are used in the access to utility compartments. The openings of these compartments are relatively small and these compartments generally contain devices like repair and emergency kits which are not very frequently used and when in need, these compartments have no or very few limitations in opening clearence. Hinge linked mechanisms require a wide opening clearence. On the other hand, they are relatively a reliable and a low cost solution for providing a connection between the flap and the bodyframe.

Bar linkage side flaps are generally used in the luggage compartments where the requirement of an area to be controlled is relatively high and a limited opening clearence is required. Luggage loading and unloading procedures are handled in the station platforms, where the distance between two parked vehicles are limited, thus the hinge mechanisms are of no use in such areas of use. On the contrary to their advantages in the opening clearence, bar linkage mechanisms are more sensitive to the failures in the assembly process and a little harder to adjust correctly.

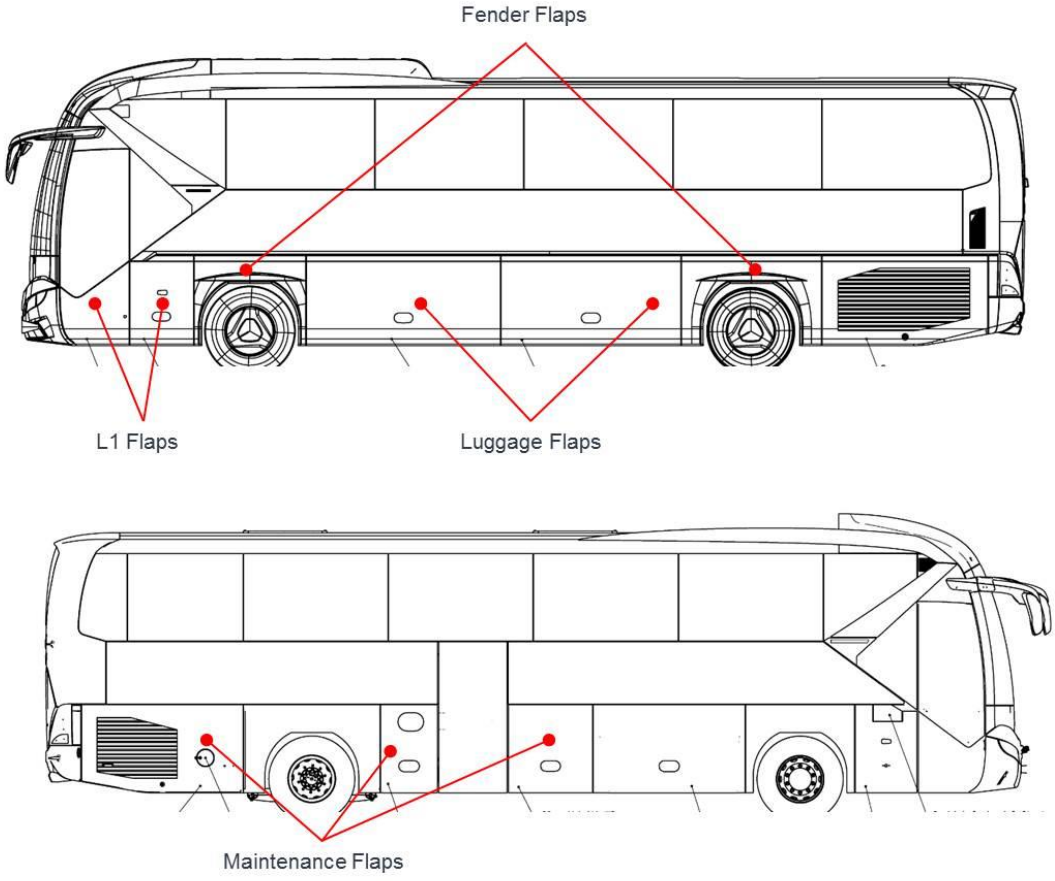


Figure 1. Types of flaps used in coaches

The requirements for both types of flaps are similar: the flaps must be durable and the mechanism must withstand and remain operable for the entire service life of the vehicle; opening and closing forces must not exceed the maximum amounts that can be applied by a woman or a man; the parts used in the mechanism shall not produce any noise during operation; flaps must be watertight when the flaps are closed and the maximum extent of the flaps must not exceed the limits defined by MAN when swivelled out.

In a recent study, the designs of the flaps and its mechanisms have faced with comprehensive changes. In the previous design, the material used in the flaps was AlMg3 H22, which is more economical and easier to supply. In the new design; a new material, AlMg3 H12, which is relatively expensive and difficult to supply, is considered to replace the H22. In this study, flaps made of both materials was analysed by examining its fatigue behaviour under cyclic loads.

2. METHODOLOGY

The cyclic loads will be applied to the 3D model of the two flaps, one is made of H12 and the other one is made of H22 Aluminum, and the results will be compared. The mechanical properties (refer to URL1) of the two materials are shown in Table 1.

Table 1 Mechanical properties of the two alternative flap material

Properties	AlMg3 H12	AlMg3 H22
Elasticity Modulus	71 GPa	
Density	2700 kg/m^3	
Yield Stress	190 MPa	150 MPa
Fatigue strength	140 MPa	110 MPa

2.1. Load Conditions

Forces acting on the flaps are measured using a spring scale and the opening force is defined approximately as 200 N, but taken as 300 N for safety, acted directly to the opening handle, and closing force is determined as 250 N total and doubled in simulation for safety, applied with 2 hands to the both sides of the flap surface as shown in the Figure 2.The springs connected to the main arms of the mechanism are simulating the gas pistons.

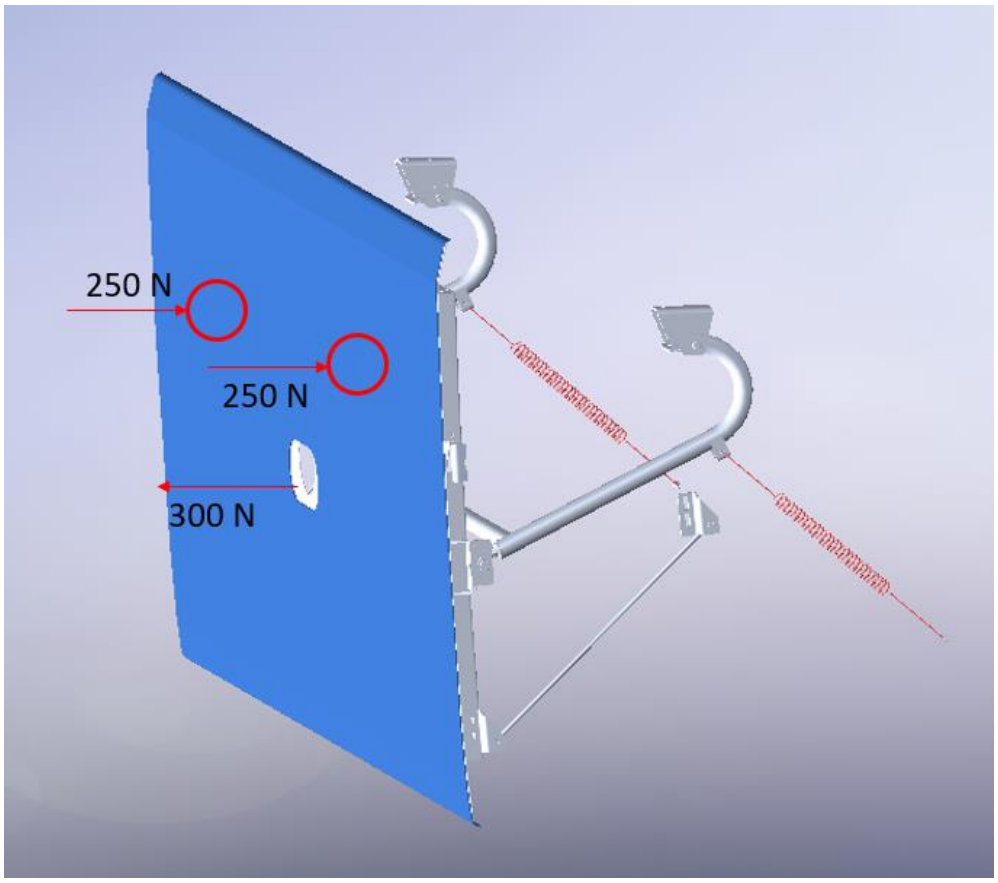


Figure 2. The magnitude of the forces applied

All the other forces acting on the mechanism components of the flaps are calculated using a rigid body simulation in CATIA. The spring constant k and spring free length L_f are calculated according to the total open length L_1, Stroke H_1, Minimum Force F_1, Maximum Force F_4, of the gas springs as shown below.

Table 2. Variables used in the spring force calculation

Variable	Symbol	Value
Max. distance between the axes	L_f	885 mm
Stroke	H_1	398 mm
Minimum force	F_1	500 N
Maximum force	F_4	820 N

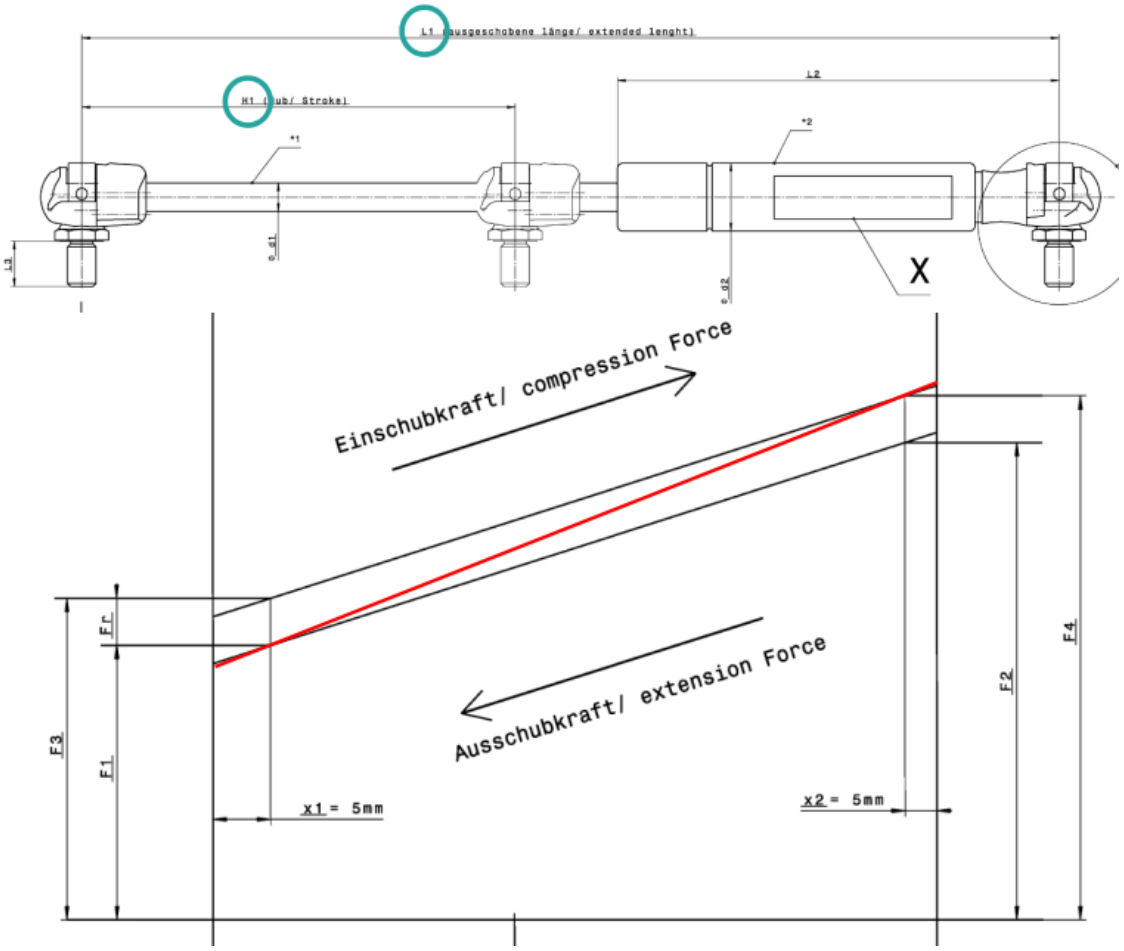


Figure 3. Spring element (above) and the dimensions of the other elements of the linkage mechanism (below)

From the dimensions of the components and the forces acting on these components listed above, the free length (L_f) and the spring coefficient (k) are calculated as follows:

$$L_f = \frac{F_1 \times H_1}{F_4 - F_1} + L_1 = 1.507\ mm \tag{1}$$

$$k = \frac{F_4}{L_f - (L_1 + H_{1)}} = 0,8\ \frac{N}{mm} \tag{2}$$

2.2. Rigid Body Simulation Results

The flaps are connected to the bodyframe with two main arms and two support arms via joints as shown in the Figure 4. The simulation is performed for 4 seconds for each scenarios to a total of 8 seconds, with the aforementioned load conditions. One cycle starts with the opening of the flap where the flap is initially closed and ends at the end of the closing

procedure where the flap returns to its closed position at the beginning.The reaction forces in y and z directions, in the main arm and support arm revolute joint locations are graphically read, recorded and plotted in a spreadsheet.

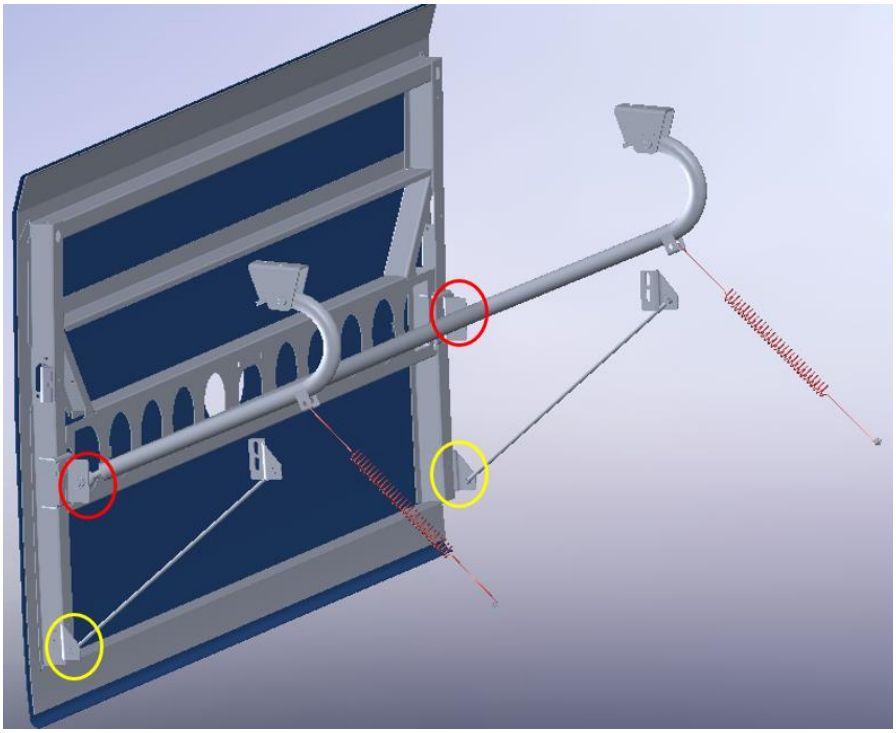


Figure 4. Joints of the main arms (red) and support arms (yellow)

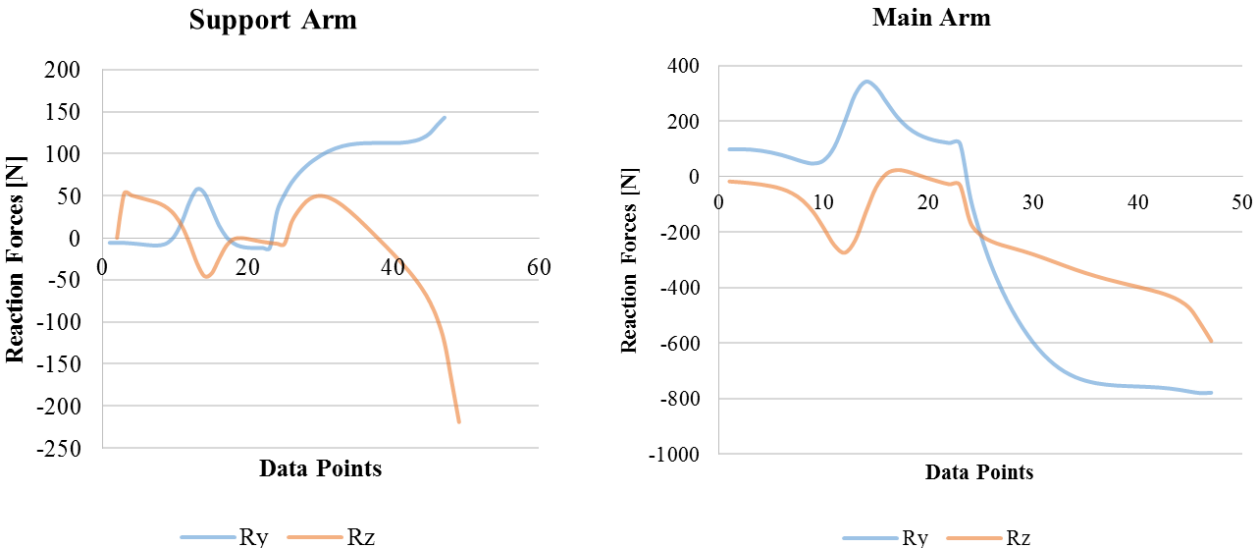


Figure 5. Average reaction forces in the support arm and the main arm joints

According to the graphs plotted, the minimum and maximum forces acting on the support arm and the main arm connection hinges are extracted from the graphs to be used in the fatigue simulation are given in the Table 3.

Table 3. Minimum and maximum reaction forces acting on the support and main arm joints

	Symbol	Value
Support arm	$R_{y\ max}$	143 N
Support arm	$R_{y\ min}$	-12 N
Support arm	$R_{z\ max}$	53 N
Support arm	$R_{z\ min}$	-219 N
Main arm	$R_{y\ max}$	343 N
Main arm	$R_{y\ min}$	-780 N
Main arm	$R_{z\ max}$	24 N
Main arm	$R_{z\ min}$	-591 N

2.3. Fatigue analysis

Setup: Ansys Workbench Static Structural Module is used for fatigue analysis. Two separate Static Structural module are connected, opening and closing cases.

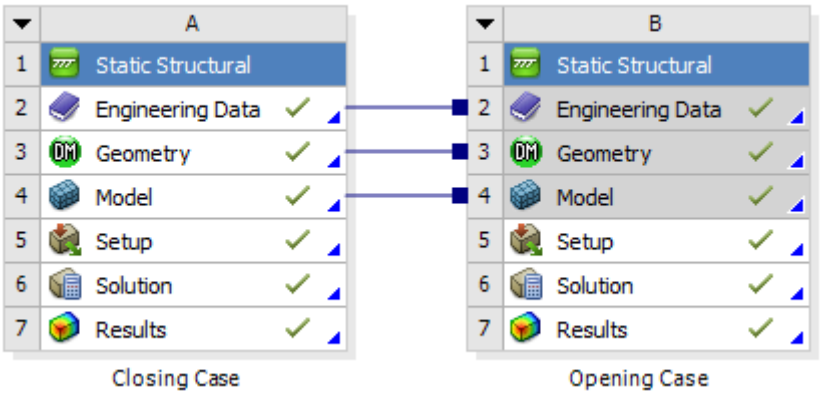


Figure 6. ANSYS Workbench Analysis Setup

The joints and linkages are removed from the model, and the cover of the flap with the supports are modelled with reaction forces, and boundary conditions instead of the external forces.

Closing Case : From the square shaped faces, all dof are constrained as boundary condition, and the loads obtained from rigid body simulation is applied to the joint location. Gravity is also applied in the model. Also, the material is defined as Aluminum H12. The material Aliminum H22 and H12 only differ with their Endurance and Yield Limits. In Summary, the deformation and stress results should be the same.

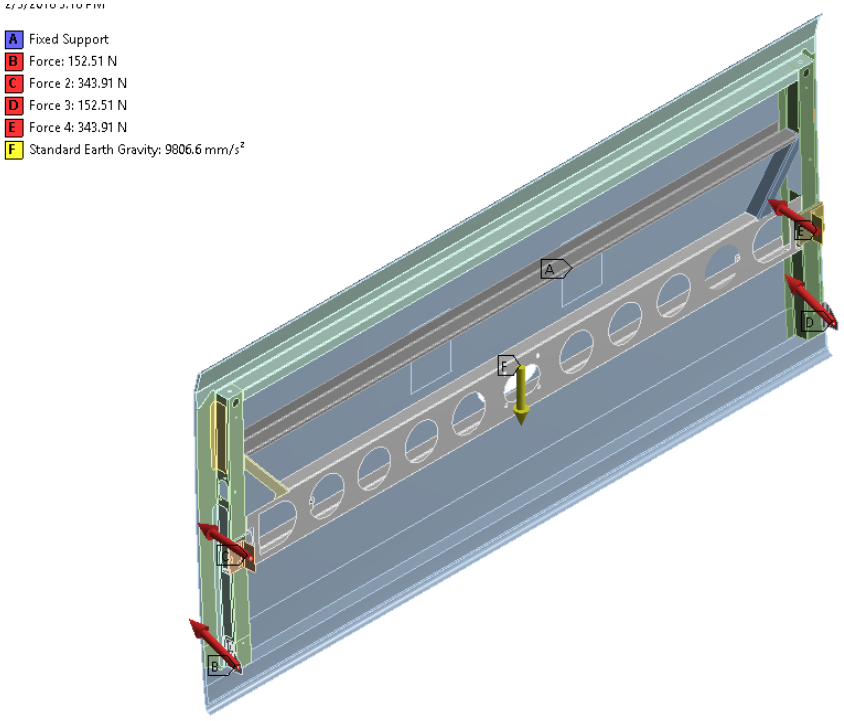


Figure 7. Closing case structural analysis setup

Opening Case : From the locking mechanism center, all dof are constrained as boundary condition, and the loads obtained from rigid body simulation is applied to the joint location. Gravity is also applied in the model.

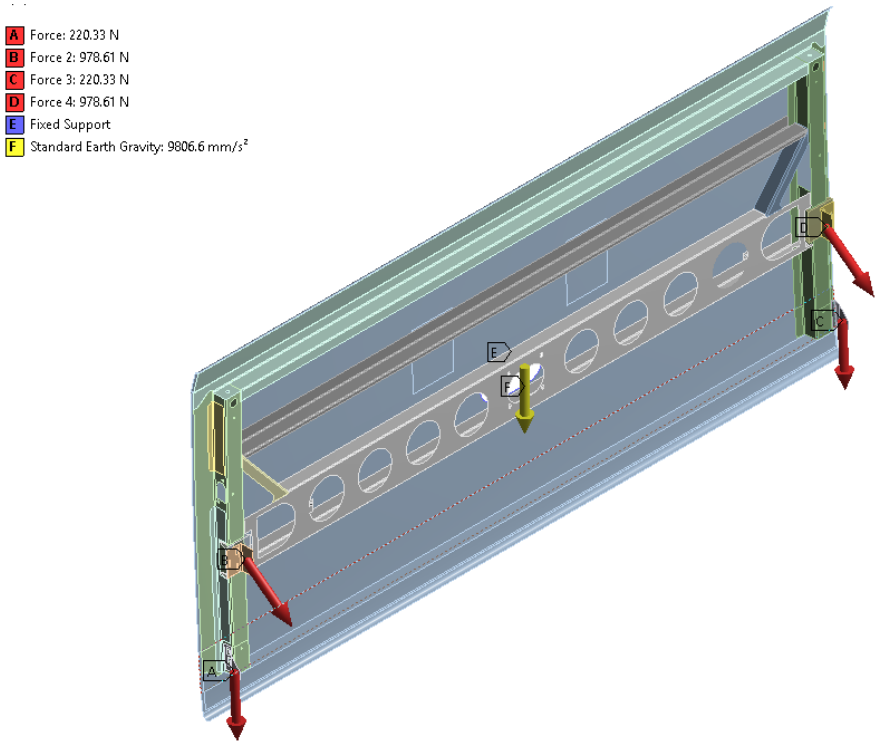


Figure 8. Opening case structural analysis setup

Non-Proportional Fatigue Simulation : Solution Combination is used to add the results obtained in two scenarios. In the solution combination branch a fatigue tool is added with Non-Proportional Type.

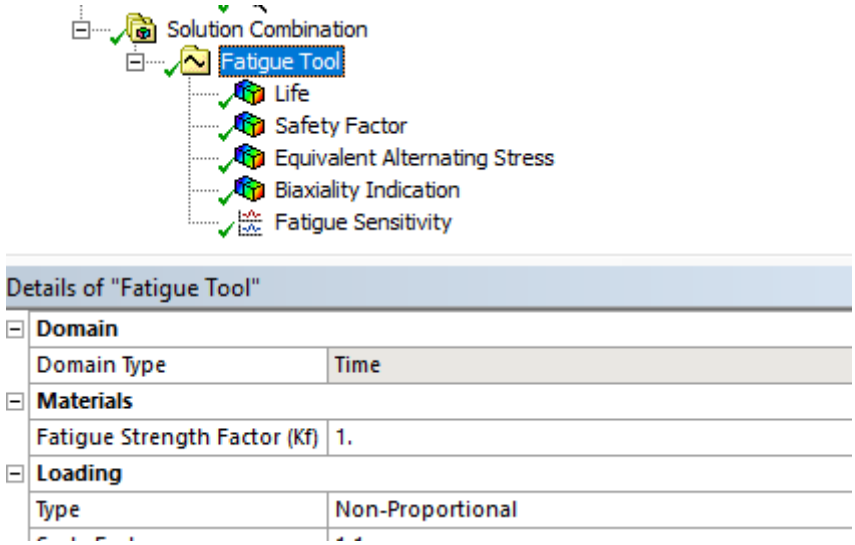


Figure 9. Non-Proportional Fatigue Setup in Ansys Workbench

Solution combination is basically adding the two result sets of the above simulations. Non-proportional fatigue tool on the other hand, basically multiplies first result with ½ and second result with -½ and add them together. So one such simulation can be performed by adding the two results with ½ and – ½ coefficients and solving as fully reversed as an alternative.

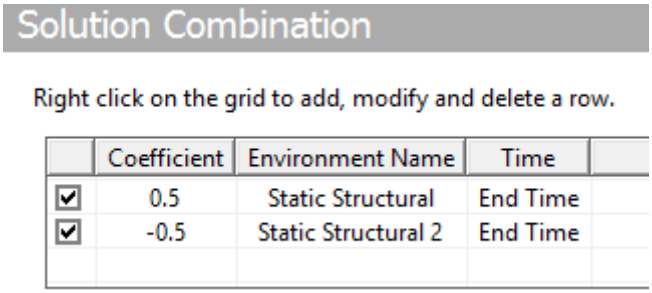


Figure 10. Alternative solution combination for fully reversed solution

Deformations and stress distribution : The side flap is loaded with the maximum and minimum forces acting to the side flap via joints are exerted to the flap and the deformation and the stress distribution on the flap is analysed. The results indicate that the outer surface of the flap shows a 2 mm of displacement during the closing process and 5 mm in the opening process. Considering the stress distribution, the deformations stays in the elastic deformation and no permanent changes in the flap is occurred.

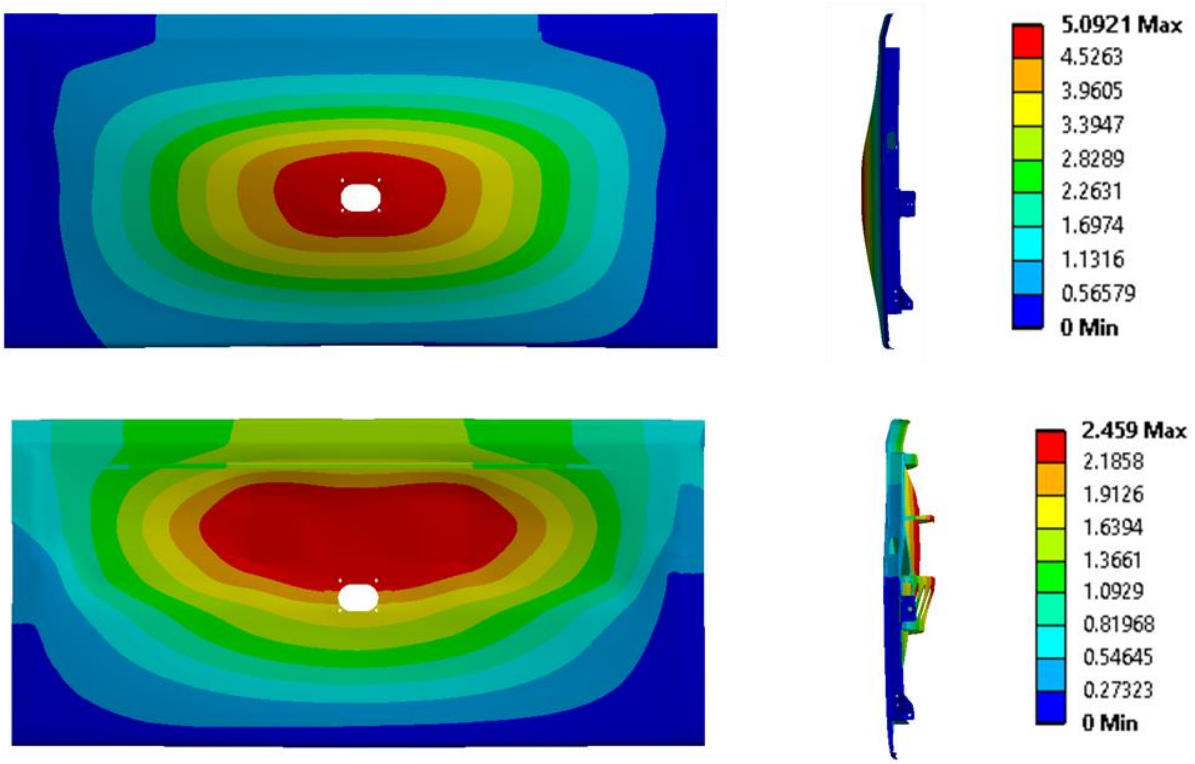


Figure 11. Deformations in the outer sheet of the side flap during opening (above) and closing (below)

When the stress distribution is examined, it can be seen that the maximum stresses in the closing and opening processes (75 and 130 MPa respectively) are below the yield stress of the material (150 MPa). Even though the stresses in the opening processes are relatively close to the yield limit, the exaggeration of the forces acted by the user on the side flap should be considered.

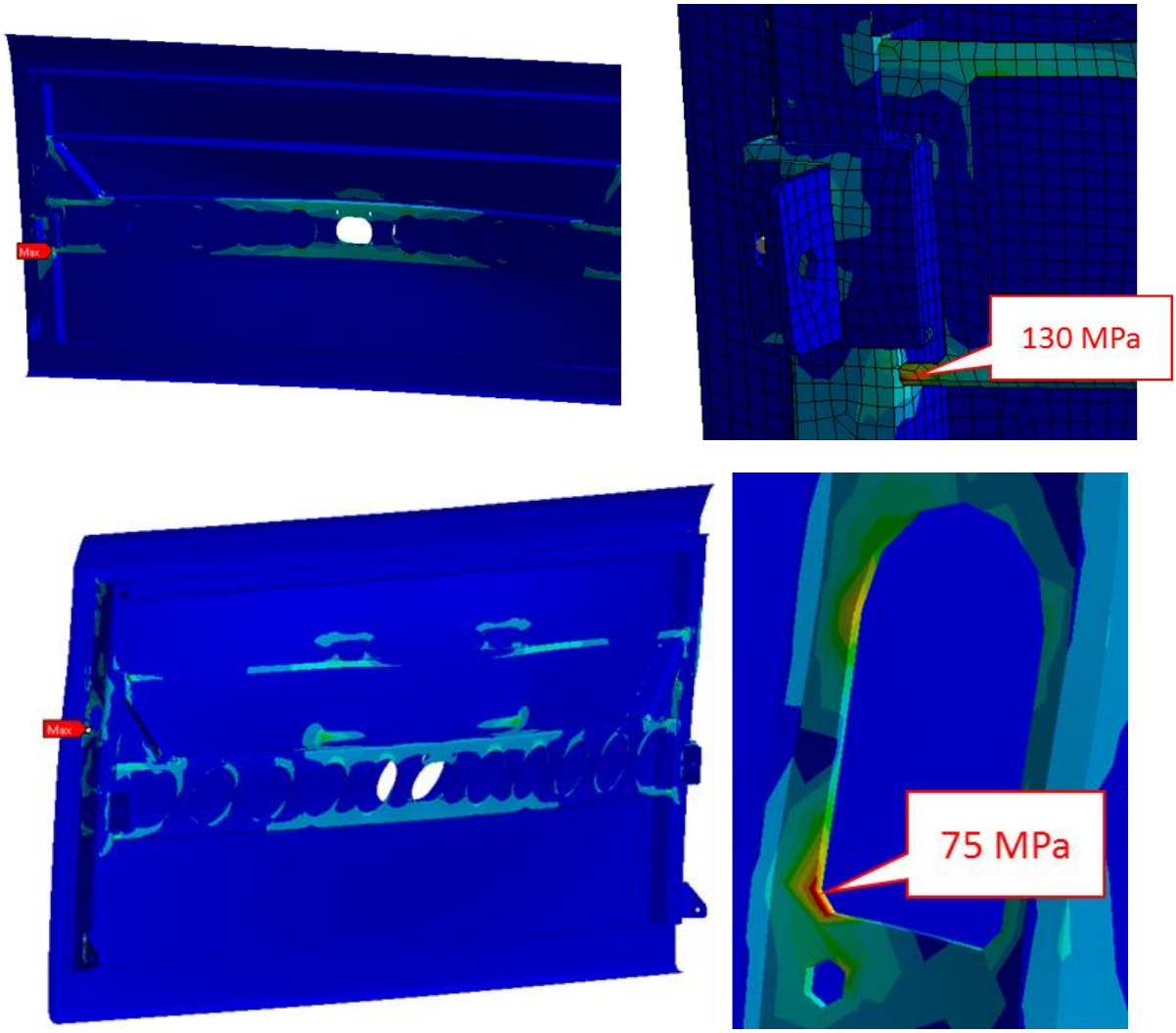


Figure 12. Maximum stresses occured on the side flap during opening (above) and closing (below)

S-n curves : The S-n curves of the both flaps made of different types of Aluminum are plotted and shown in the figure below. The curves are indicating that both of the flaps have infinite fatigue lifes. The flaps made of H22 can withstand to $9x10^6$ cycles and H12 can $5x10^8$ cycles.

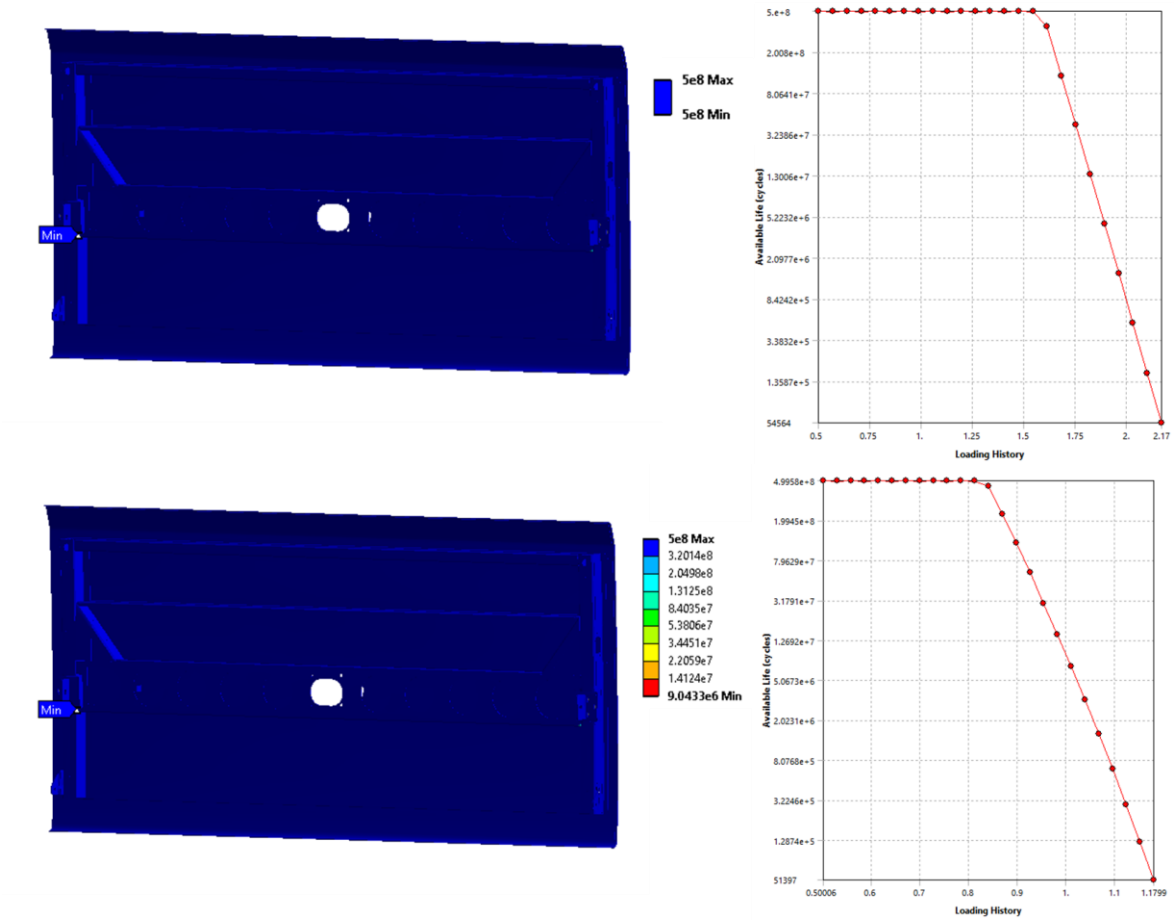


Figure 13. Fatigue behavior of the flap made of AlMg3 H12 (above) and AlMg3 H22 (below)

3. CONCLUSION

According to the fatigue analysis, both of the two flaps made of AlMg3 H12 and AlMg3 H22 can withstand 60.000 cycles which is required as a standart. The new design is proven that it has an infinite fatigue life and does not need any material change in order to increase its durability. Despite the fact that H12 is more durable and has a longer fatigue life, it has a higher price tag and a lower availability in the market which makes it unfeasible to be an alternative to the currently used H22.

The study also proves the durability of the flaps made of both materials and indicates that any probable failure in the flaps is caused by either by a user or an assembly error.

4. REFERENCES

1. URL1: Mechanical Properties of Aluminum Alloys, https://www.makeitfrom.com/material-properties/5754-AlMg3-3.3535-A95754-Aluminum

TOPOLOGY OPTIMISATION OF AN AUTOMOBILE BRAKE SYSTEM COMPONENT UNDER DYNAMIC LOADING CONDITIONS

Betül Sultan YILDIZ, *betulsultan.yildiz@gmail.com* Bursa, Turkey

ABSTRACT

The topology of the structure has an important effect in achieving the design goals. The purpose of topology optimization is to find the best use of material in a specific design area. Topology optimization provides an initial design concept for designers in R&D departments of the automobile companies. In this research, the optimal design of a vehicle brake pedal was determined using a topology optimization approach. The solid model of a brake pedal was design using Catia software. Altair Optistruct was used for topology optimization. After topology optimization, material was removed from some region of the initial design. In this research, optimal layout of vehicle brake pedal under dynamic loading conditions is determined using topology optimisation approach. The result shows that the weight of a new designed brake pedal was reduced as compared to the initial design.

Keywords: Structural design, Gravitational search, Hybrid Optimization

1. INTRODUCTION

The shape, size, topology, topography and topometry optimization of the vehicle structures have been attractive research subjects in literature [1-13]. The initial design of vehicle component has significant effect on product performance and manufacturing cost. if topology is not optimal, structure of the initial design may lead to non-optimum designs. Topology optimization of automotive components has received increasing attention from industry due to its success in achieving optimum product design.

In recent years and various topology optimization methods have been developed, such as the homogenization method [2], solid isotropic material with penalization (SIMP) method [3-4], evolutionary structural optimization (ESO) method [5], and level set method (LSM) [6-8].

The car braking system works by transferring the force exerted on the brake pedal to the brakes in the wheels via hydraulic fluid. The main task of the brake pedal is to transfer the command given by the driver to the brake system to reduce or stop the speed of a vehicle.
The pressure required for the brakes to reduce or stop the vehicle speed is much higher than the pressure applied by the driver [9].
Vehicle elements such as brake components generally face with dynamic loading during working conditions. One of the earliest works on structural optimisation under dynamic loads is presented in the paper by Fox and Kapoor [10]. Another paper that includes finding optimal topology under dynamic loads presented in 1999 [11]. It is seen that there are only few works related to topology optimisation under dynamic loading conditions. Most of the work is related to static loading conditions.
In this research, optimal layout of vehicle brake pedal component under dynamic loading conditions is determined using topology optimisation approach. In the present study, layout optimisation of the brake pedal is performed using topology optimisation based on a density formulation.

2. TOPOLOGY OPTIMIZATION OF VEHICLE BRAKE PEDAL

Automobile brake pedal is face with dynamic loading during working conditions. In this paper, the optimal topology design of a brake pedal is made using Hyperworks OptiStruct. The following optimization stages are carried out to obtain the optimal topology of the brake pedal.

The initial design of the pedal is given in Figure 1.

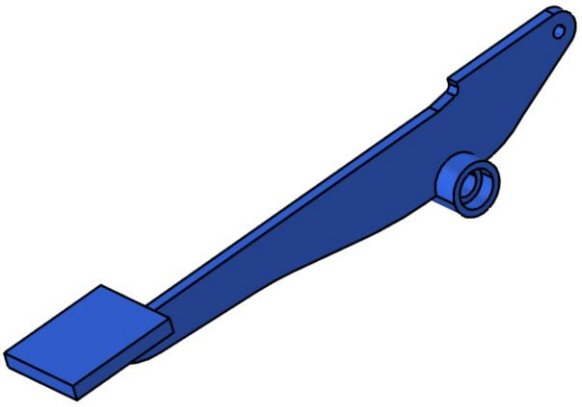


Figure 1. Initial Design of the Brake Pedal

The finite element model and boundary conditions are shown in Figure 2. and Figure 3. The finite element model contains 18167 elements and 28729 nodes. Youngs's modulus (E),

Poission's ratio (ν) and density (ρ) for the material of the pedal are 2.1 x 10^5 N/mm^2, 0.3 and 7.82 x 10^{-6} kg/m^3, respectively.



Figure 2. FE Model of the Brake Pedal

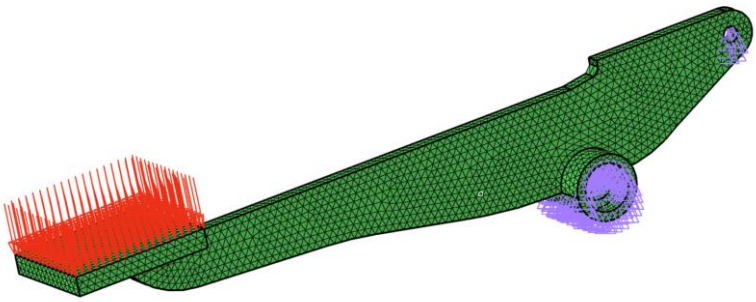


Figure 3. Boundary Conditions

Topology optimization is used to find the best possible solution of problem by considering the objective and constraints such as compliance minimization and volume reduction. In this study, topology optimisation of the brake pedal is carried out in OptiStruct software. In topology optimization, objective function was chosen to maximize the natural with a 30 % material usage constraint. The density of each element is selected as the design variable. The material distribution after topology optimization loop is obtained as shown in Figure 4. The blue region in the brake pedal indicates the unnecessary material to be removed from the design. The optimized design is extracted from the initial design obtained through analysis. The optimized design is prepared in the 3-D software.

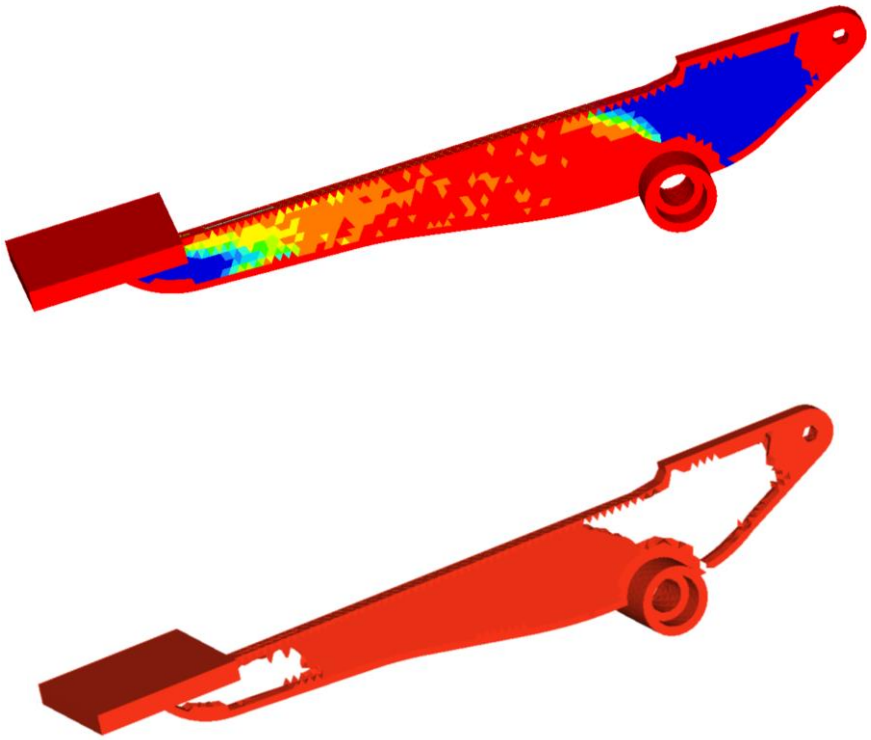


Figure 4. Topology Optimization Results of Brake Pedal

According to results of topology optimization, the bracket structure is redesigned as being based on material distribution (Figure 5).

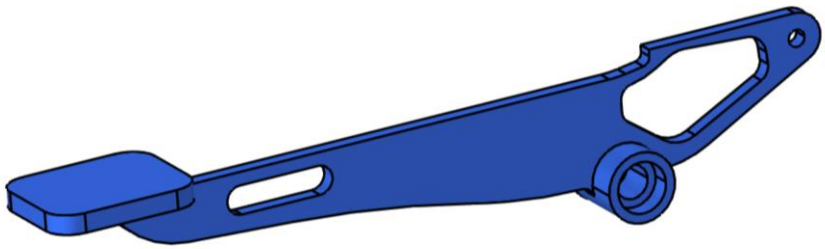


Figure 5. The Brake Pedal After Material Removed

Above figures shows that blue region can be removed from the design space while keep the red region in the design space as it is. Mass of the optimised design is obsereved to be 463 gram. The total reduction in mass is observed by 16.5 %. Since, Mass of the model is decreased from 555 gr to 463 gr.

The natural frequency of the initial design is 105.8 Hertz. After redesigning of the brake pedal as topology optimization results, it is calculated as 106.9 Hertz.

3. CONCLUSIONS

Topology optimization is an important structural optimization approach in optimizing vehicle components. Since 30 years, it is an important research subject for researcher and engineers. In this research, topology design approach of the brake pedal design under dynamic load condition is carry out. After topology optimization, but natural frequency of the brake pedal is increase and weight of the pedal is reduced. The results show that topology optimization method is an important technique to optimize vehicle components.

Shape optimization of the brake pedal considering topology optimization results must be made to reach final design as a future work. Additionally, the experimental tests on road and laboratory conditions must be carried out to evaluate the final layout of the brake pedal and to measure the performance of the proposed approach.

REFERENCES

1. **Michell, A. G. M., (1904),** “The Limits Economy in Frame Structures”, Philo. Mag. Sect. Vol.6, No.8, pp 589-597.
2. **Bendsoe, M.P. and Kikuchi, N.,(1988),** “Generating Optimal Topologies İn Structural Design Using A Homogenization Method”, Comput. Meth. Appl. Mech. Engng, Vol.71, pp 197-224.
3. **Zhou, M. and Rozvany, G., (1991),** “The COC Algorithm, Part II: Topological, Geometrical and Generalized Shape Optimization”, Comput. Meth. Appl. Mech. Eng., Vol.89, No.1–3, pp 309–36.
4. **Bendsoe, M.P. and Sigmund, O., (1999),** “Material Interpolation Schemes in Topology Optimization”, Arch. Appl. Mech., Vol. 69, pp 635–54.
5. **Xie, Y.M. and Steven, G.P., (1993),** “A Simple Evolutionary Procedure for Structural Optimization”, Comput. Struct., Vol.49, No.5, pp 885–896.
6. **Sethian, J.A. and Wiegmann, A., (2000),** “Structural Boundary Design Via Level Set and Immersed Interface Methods”, J. Comput. Phys., Vol.163, No.2, pp 489–528.
7. **Wang, M.Y., Wang, X. and Guo, D., (2000), “**A Level Set Method for Structural Topology Optimization”, Comput. Meth. Appl. Mech. Eng., Vol.192, No.1, pp 227–246.

8. **Allaire, G., Jouve, F. and Toader, A.M., (2004),** "Structural Optimization Using Sensitivity Analysis and A Level-Set Method", J. Comput. Phys., Vol. 194, No.1, pp 363–393.
9. **Kurkure, B. and Sadaphale, D.B., (2015),** "Optimization of Brake Pedal", International Journal of Mechanical and Industrial Technology, Vol.3, No.1), pp 175-183.
10. **Fox, R. L. and Kapoor, M.P., (1970),** "Structural Optimisation in The Dynamic Regime: A Computational Approach", AIAA J., Vol.8, pp 1789-1804.
11. **Min, S., Kikuchi, N., Park, Y.C., Kim, S. and Chang, S., (1999),** "Optimal Topology Design of Structures Under Dynamics Loads", Structural Optimisation, Vol.17, pp 208-218.
12. **Yildiz, B.S., (2017), "**Natural Frequency Optimization of Vehicle Components Using The Interior Search Algorithm", Materials Testing, Vol.59, No.5, pp 456-458.
13. **Yildiz, B.S., (2017),** "A Comparative İnvestigation of Eight Recent Population-Based Optimisation Algorithms for Mechanical and Structural Design Problems", International Journal of Vehicle Design, Vol.73, No.1-3, pp 208-218.

INVESTIGATING THE EFFECTS OF PROCESS PARAMETERS ON RESIDUAL STRESS EVOLUTION IN PLASMA TRANSFER ARC (PTA) CLADDING OF TI-6AL-4V

Hadi MOZTARZADEH, *H.Moztarzadeh@warwick.ac.uk, WMG, University of Warwick, Coventry,* UK, CV4 7AL

Sampan SETH, *S.Seth@gmail.com, Advanced Remanufacturing and Technology Centre (ARTC), Singapore, 637143*

Hoda AMEL, *Hoda.Amel@the-mtc.org, National Centre for Additive Manufacturing, Manufacturing Technology Centre (MTC), Coventry, UK, CV7 9JU*

Gregory J. GIBBONS, *G.J.Gibbons@warwick.ac.uk, WMG, University of Warwick, Coventry, UK, CV4 7AL*

ABSTRACT

The evolution of residual stresses during Plasma Transferred Arc (PTA) cladding of Ti-6Al-4V was investigated. The PTA cladding was used as an Additive Manufacturing (AM) process to build parts in a layer-by-layer fashion. The process parameters were therefore defined based on the PTA cladding and AM process. A series of results from two residual stress measurement techniques provided a baseline to understand the effect of this metal-based AM technology on residual stress evolution and hence geometrical accuracy of the PTA AM components.

Keywords: Plasma Transferred Arc (PTA), Additive Manufacturing (AM), Titanium Alloy, Residual Stress, Neutron Diffraction, Synchrotron X-ray Diffraction, Contour Method

1. INTRODUCTION

As a Directed Energy Deposition technique, Plasma Transferred Arc (PTA) cladding can use wire or powder as the material supply and laser or electron beam or plasma arc as the heat source. Wire has generally a higher purity of the starting feedstock than powder and is less susceptible to contamination during the process due to its reduced surface area. Further advantages of wire feedstock include high deposition efficiency, high deposition rate, good availability and simplified handling and storage (Baufeld et al. 2011).

The wire-based PTA has been coupled with a 3-axis CNC bed to manufacture parts in a layer-by-layer fashion; by moving the arc and wire across a substrate using a range of possible deposition strategies. Therefore, similar to typical welding, this AM process is subject to high thermal gradients which affects the microstructural formation and residual stresses evolution within the final component. A range of metallic materials are used in this technique, such as Titanium alloys, Inconel and high chromium steel (Moztarzadeh et al. 2017).

Residual stress is an important factor which can cause both distortion and reduced lifetime of the manufactured components. Understanding the effects of the manufacturing process on the performance of the final part is critical when a highly reliable functional product is required (Brown et al. 2011). In this study the influence of two key process parameters of the wire-feed PTA process on resulting residual stresses in parts made out of Ti-6Al-4V is investigated. Two methods were used to determine residual stresses: neutron diffraction (non-destructive) and the contour method (destructive).

2. METHODOLOGY

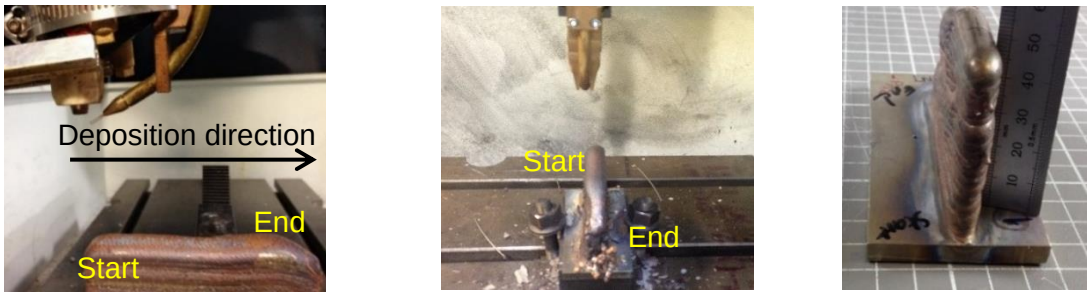
Process parameters for a PTA welding are described in the literature (Wilden et al. 2006), and also summarized in Table 1 for the PTA set-up used in this study (Moztarzadeh et al. 2017).

Table 1 – Process parameters for PTA as an AM process

Parameter	**Value Range**	**Unit**
Plasma Gas Flow Rate (PGFR)	0.5	l/min
Wire Feed Rate (WFR)	1	m/min
Traverse Speed/Weld Speed	50	mm/min
Energy Density	~270	MJ/m^2
Deposition Strategy	Linear or Zig-Zag	-
Dwell Time	60 or 180	s

Two samples were built to study the effect of deposition strategy and dwell time. As shown in Table 1, sample 1 was built by using the linear deposition strategy and had a dwell time of 60 s. Zig-zag deposition strategy was used to manufacture sample 2, which had a dwell-time of 180 s. The rest of process parameters were the same for both samples. The fixture of the substrate and the direction of deposition are shown in Figure 1. A one-way deposition path

was chosen due to the position of the wire-feeder and the torch on the PTA (Parimi et al. 2014; Martina et al. 2016). The deposition was continued until the height reached 50 mm for each sample. This has resulted in ~27 layers for sample 1 and 24 layers for sample 2. Each sample had a width of ~12 mm.



(a) One-way deposition; torch and wire Feeder

(b) Deposition direction and clamping of the substrate

(c) Sample No. 1

Figure 1 – Building / deposition strategy and sample No. 1

Neutron diffraction provides information on the average lattice spacing (d) within the gauge volume (Moztarzadeh et al. 2017; Akman et al. 2009). Residual strains were measured for PTA clad samples using the non-destructive neutron diffraction technique at the SALSA beamline at the Institut Laue-Langevin (ILL), Grenoble, France. Two scan-lines were defined to study the stress state within the parts. Assuming a plane stress condition for the measurements the results provide the residual stress state in two principal directions, as shown in Figure 2.

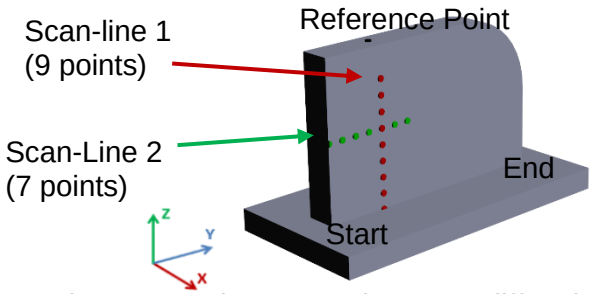


Figure 2 – Schematic of the part and neutron diffraction measurement points

The contour method is based on solid mechanics concept; where the part is cut through a section of interest to produce deformed contours which could be used to determine residual strain/stress (Baufeld et al. 2011). This is a destructive method and measures residual stresses in one principal direction, perpendicular to the cut-section (Schajer 2010). By implementing the same plane stress condition, the stress state was determined on corresponding planar section

to the scan-line 1 for neutron diffraction, to provide a complementary set of data for residual stress state within the parts.

3. RESULTS

Longitudinal component of residual stress (σ_Y) was determined along scan-line 1, by neutron diffraction and contour method, for samples 1 and 2, and the results are shown in Figures 3 and 4, respectively. The results are calculated based on a plane stress condition (out-of-plane stress assumed to be zero).

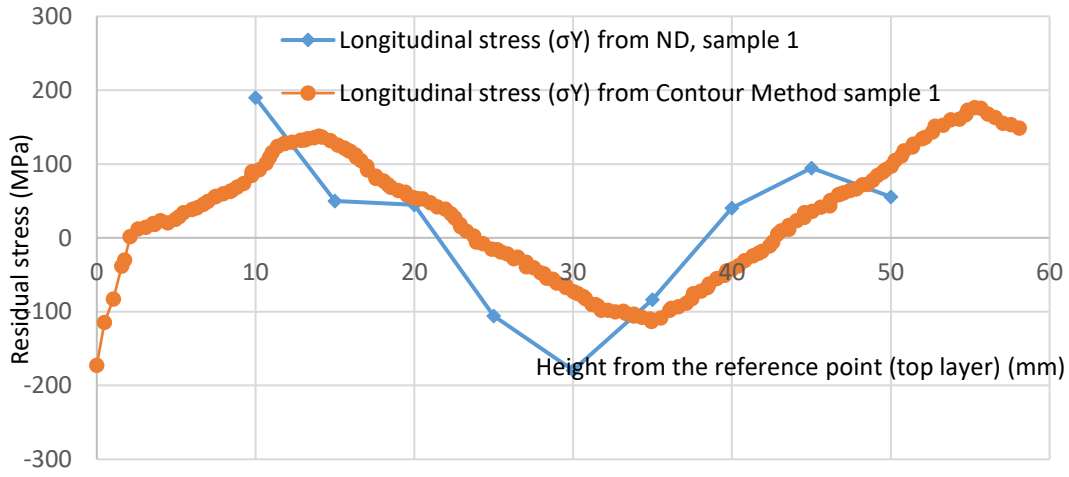


Figure 3 – Residual stresses along scan-line 1 (vertical) in sample 1, based on plane stress condition, by neutron diffraction and contour method

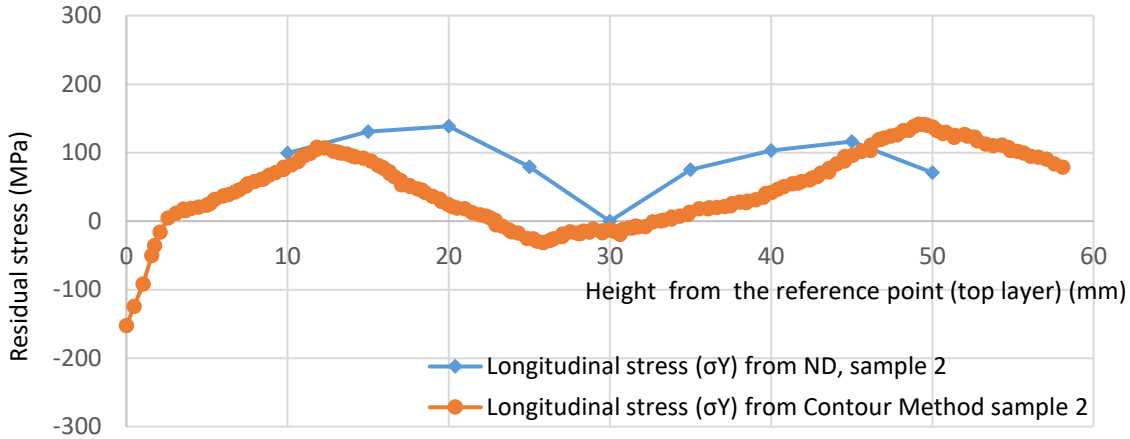


Figure 4– Residual stresses along scan-line 1 (vertical) in sample 2, based on plane stress condition, by neutron diffraction and contour method

According to the residual stress results along scan-line 1, an agreement between the data from both neutron diffraction and contour method can be observed, noting the fact that the scan-line 1 for neutron diffraction started from 10 mm below the top layer of the sample, while contour method could provide a more comprehensive results along the whole section, associated to the scan-line.

Also, the longitudinal residual stresses (σ_Y), along scan-line 2 (horizontal) was calculated and plotted for both samples 1 and 2, in Figure 5.

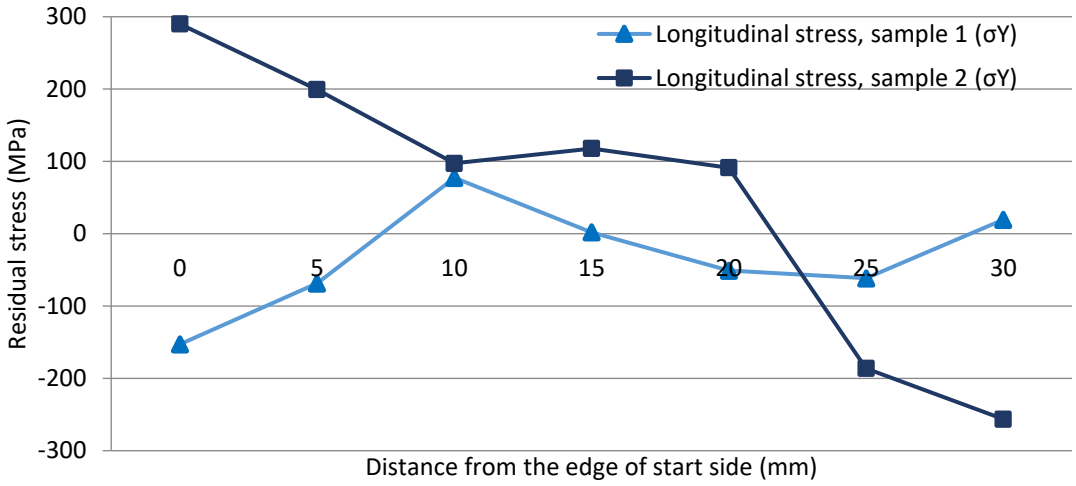


Figure 5 – longitudinal component of residual stresses (σ_Y), along scan-line 2 (horizontal) in samples 1 and 2, based on plane stress condition, by neutron diffraction

Comparing the results from both samples along scan-line 1, it seems the level and variation of residual stresses in sample 1 is higher than sample 2, which suggests the effectiveness of longer dwell-time (180 s) and zig-zag deposition strategy in alleviating residual stresses. This is valid for the vertical scan-lines where the scan-points were chosen from different heights/layers of the samples. Within an individual layer, however, the level and variation of residual stresses seems to be lower in sample 1 than in sample 2.

4. CONCLUSION

The wire-based PTA coupled with a 3-axis CNC was used as an AM technique. This fabrication method offers exciting potential for net shape manufacturing of metal-based components. To investigate the evolution of residual stresses associated with the process parameters, two samples with two different dwell times and two different deposition strategies were built, out of Ti-6Al-4V on the substrates of the same material. A correlation between the results from

neutron diffraction and contour method along the vertical scan-line 1 confirms that the majority of the residual stress could be interpreted as longitudinal (bending) stress.

It was shown that increasing the dwell time could reduce the peak levels of residual stresses within the part, along the height of the samples. On the horizontal scan-line however, residual stresses seems to be higher for the sample with higher dwell-time and linear strategy. This could be due to the linear deposition strategy for this sample as it provided an undeviating effect of the heat source within an individual layer.

REFERENCES

1. **Akman, E. et al., 2009.** Laser welding of Ti6Al4V titanium alloys. Journal of Materials Processing Technology, 209(8), pp.3705–3713.
2. **Baufeld, B., Brandl, E. & Van Der Biest, O., 2011.** Wire based additive layer manufacturing: Comparison of microstructure and mechanical properties of Ti-6Al-4V components fabricated by laser-beam deposition and shaped metal deposition. Journal of Materials Processing Technology, 211(6), pp.1146–1158.
3. **Brown, D.W. et al., 2011.** Critical comparison of two independent measurements of residual stress in an electron-beam welded uranium cylinder: Neutron diffraction and the contour method. Acta Materialia, 59(3), pp.864–873.
4. **Martina, F. et al., 2016.** Residual stress of as-deposited and rolled wire+arc additive manufacturing Ti–6Al–4V components. Materials Science and Technology, 836
5. **Moztarzadeh, H. et al., 2017.** Evolution of Residual Stresses in Linear Deposition Wire-Based Cladding of Ti-6Al-4V. Materials Science Forum, 905, pp.101–106.
6. **Parimi, L.L. et al., 2014.** Microstructural and texture development in direct laser fabricated IN718. Materials Characterization, 89, pp.102–111.
7. **Schajer, G.S., 2010.** Relaxation Methods for Measuring Residual Stresses: Techniques and Opportunities. Experimental Mechanics, 50(8), pp.1117–1127.
8. **Wilden, J., Bergmann, J.P. & Frank, H., 2006.** Plasma Transferred Arc Welding—Modeling and Experimental Optimization. Journal of Thermal Spray Technology, 15(4), pp.779–784.

A TECHNOLOGICAL AND BUSINESS PERSPECTIVE OF ADDITIVE MANUFACTURING FOR DEFENSE INDUSTRY

Dr. Kıvılcım ERSOY, *kivilcim.ersoy@fnss.com.tr* FNSS Savunma Sistemleri A.Ş., Ankara, Turkey

Barış KOÇ, *baris.koc@fnss.com.tr* FNSS Savunma Sistemleri A.Ş., Ankara, Turkey

Dr. Evren YASA, *eyasa@ogu.edu.tr* Eskişehir Osmangazi Universitesi, Eskişehir, Turkey

ABSTRACT

In the recent years the enhancements in destructive technologies necessitate higher requirements for survivability; both for mine, ballistic and IED protection. At the same time, payloads increase and mobility requirements are becoming more and more challenging. These trends make lightweight design indispensable. Besides, another trend is the increasing the number of variants for different missions, which results in smaller amounts of serial production. The need of prototypes often utilized in land vehicle industry as technology demonstrators necessitate the use of fast and flexible manufacturing techniques. All these trends and needs make additive manufacturing (AM) technologies a favorable production process if combined with the appropriately optimized design for AM. On the other hand, cost efficiency is becoming more and more important. Additional constraint for ground vehicles in AM is the large component sizes. This study presents the view of FNSS Savunma Sistemleri A.Ş. on additive manufacturing technologies taking all these constraints and boundary conditions into account to determine the deployment and roadmapping strategy.

Keywords: Additive Manufacturing, Land Vehicles, Roadmapping Techniques

1. INTRODUCTION

Although Additive Manufacturing (AM) was there for more than 3 decades, it has started to have an impressive effect on many industries over the last five years or so. Many industrial applications for Additive Manufacturing have been developed for industries such as aerospace, automotive and medical exploring the advantages of AM. The list of potential applications for AM is extensive due to provided advantages compared to conventional manufacturing

techniques. The main advantages include geometrical complexity at almost no added cost making it possible to produce lattice structures for especially lightweight applications. The weight reduction is of utmost importance for some industries such as aerospace and transportation. The possibility to make very complex structures is very short lead times without any need to make special tools or molds attracts the attention of many applications. This is very advantageous not only for functional prototypes but also to validate design issues.

Additive manufacturing refers to a group of processes by which digital 3D design data is directly used to build up a component in a layerwise manner by depositing material in contrast to subtractive machining (see Figure 1 for the process flow).

Additive manufacturing refers to a group of technologies rather than a single process. There are many different types of technologies which utilize different binding and fusion mechanisms. ASTM-approved classification for AM processes is shown in Figure 2.

For metallic materials, in order to obtain highly complex geometries, powder bed fusion processes are preferred. Powder bed fusion is a process whereby the thermal energy selectively fuses metallic powder particles in a layerwise manner. The thermal energy may be obtained by a laser source or an electron gun.

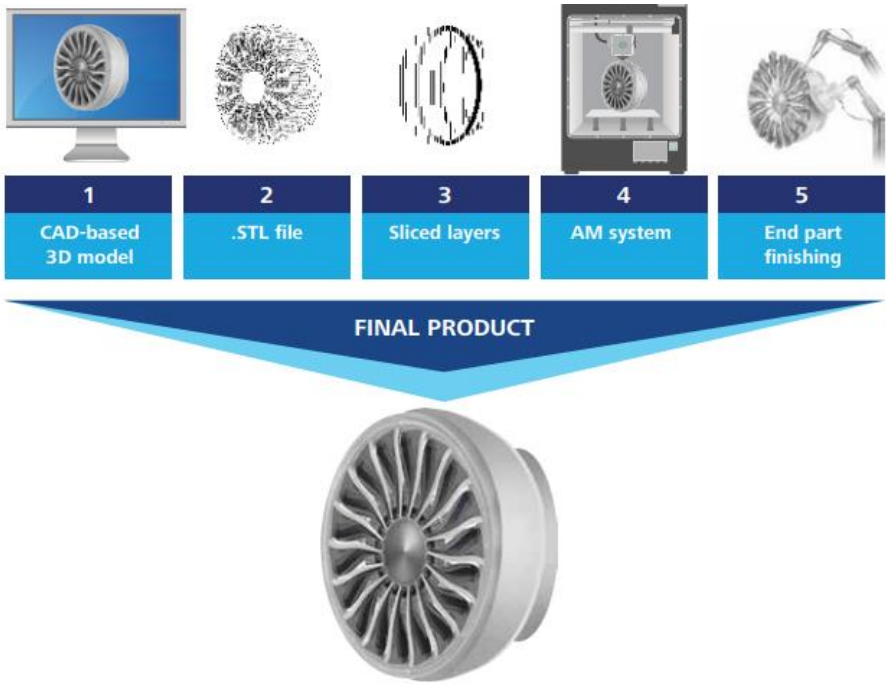


Figure 1. AM process flow [1]

The thermal energy provided by these sources melts the powder followed by a sudden consolidation. Powder-bed fusion processes include electron beam melting, selective laser sintering, selective laser melting, direct metal laser sintering/melting, laser cusing and laser

sintering. Although many different names are used such as selective laser sintering, selective laser melting, direct metal laser sintering/melting, laser cusing and laser sintering, they refer to the same process provided that the process involves melting of metallic powder materials without any infiltration processes. The laser systems commercially available today employ fiber lasers with a laser power from 50 W to 4 X 1000 W for various applications. Moreover, it can be seen that the build volume is limited to only 800x400x500 mm^3 (Concept Laser X Line 2000R). For aircraft and automotive applications, this is rather insufficient. Depending on the application, the layer thickness and the focus diameter also change. For very intricate features, a smaller layer thickness and focus diameter is utilized. However, to increase production rate, a larger focus diameter as well as a thicker layer thickness is preferred [2].

On the other hand, Arcam is the sole producer of EBM machines on the market. Alternative machines, claimed to be open-source, are on the way but not yet commercialized. Freemelt, a Swedish startup founded in January 2017 by former personnel of Arcam, intends to design small electron beam based system to meet the specific needs of universities and research institutes. The schematic demonstration of EBM and SLM processes is shown in Figure 3.

As compared to SLM, due to higher energy density and higher scanning speeds, EBM has higher build rates. Moreover, the process being executed under vacuum atmosphere leads to a cleaner material and better material properties. Elevated pre-heating temperatures lowers the cooling rates in EBM resulting in less problems related to cracking, deformation and warping. On the other hand, the dimensional accuracy and surface quality are inferior in the EBM process. Intricate details are more difficult to be manufactured by EBM. The comparison of SLM and EBM is presented in Table 1 [3].

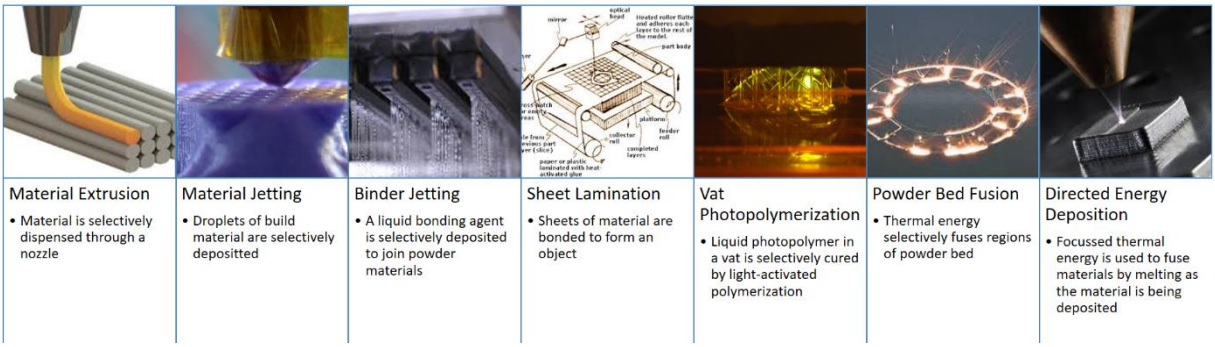


Figure 2. The ASTM-approved AM process classification

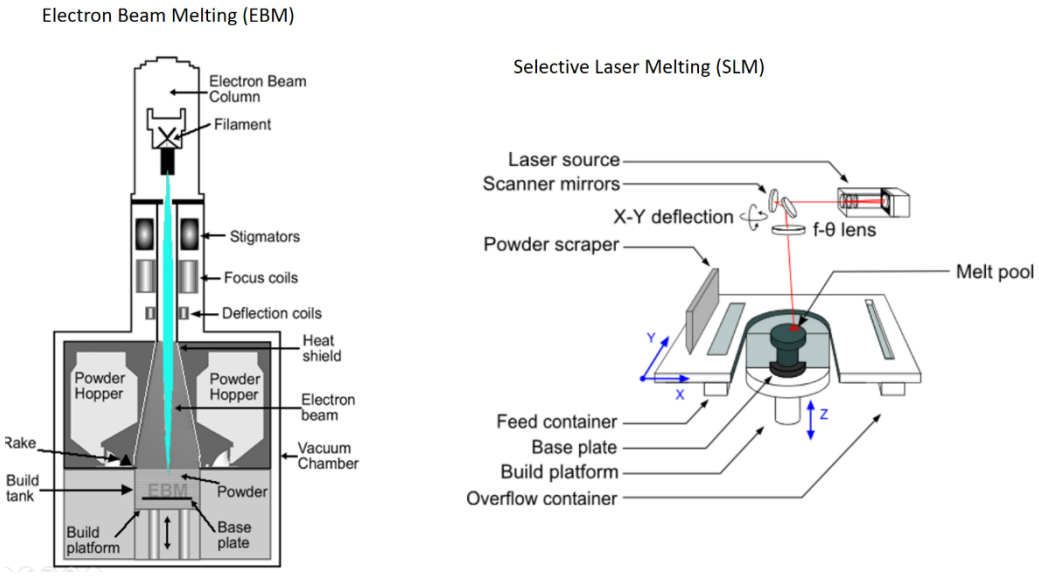


Figure 3. Schematic demonstration of EBM-left [3] and SLM-right [5]

On the other hand, for large part manufacturing, direct energy deposition techniques are more attractive. Directed Energy Deposition (DED) processes covers a range of terminology including Laser engineered net shaping (LENS®), directed light fabrication, direct metal deposition, 3D laser cladding, laser cladding, Electron beam additive manufacturing, shaped metal deposition, etc. The processes may depend on the energy of electron beam, laser beam or even arc plasma. Some of these processes are in use for repair applications in many industrial sectors for more than 2 decades.

Table 1. Comparison of SLM and EBM processes [3]

	SLM	**EBM**
Power source	One or more fiber lasers of 200 to 1000 W	High power Electron beam of 3000 W
Build chamber environment	Argon or Nitrogen	Vacuum / He bleed
Method of powder preheating	Platform heating	Preheat scanning
Powder preheating temperature (^{0} C) [34,35]	100-200	700-900
Maximum available build volume (mm)	500 x 350 x 300	350 x 380(ØxH)
Maximum build rate (cm^3/hr)	20-35	80
Layer thickness (µm)	20-100	50-200
Melt pool size (mm)	0.1-0.5	0.2-1.2
Surface finish [7] (Ra)	4-11	25-35
Geometric tolerance (mm) [12]	± 0.05-0.1	± 0.2
Minimum feature size(µm) [39]	40-200	100

Unlike powder bed fusion techniques, Directed Energy Deposition (DED) systems are generally able to build large build volumes (>1000 mm^3) and able to process at relatively high deposition rates. In these processes, the feedstock is directly delivered to the melt pool making it possible to have functionally graded materials (FGMs). Another advantage of these processes is to be able to deposit onto existing components which makes them very suitable for repair applications [7]. Moreover, processes employing laser beam and arc plasma have efficient energy and strong energy coupling to feedstock [8]. Some DED processes are shown in Figure 4 ranging from coaxial powder fed laser to coaxial wire fed laser to plasma arc systems.

Laser cladding (LC), also known as laser deposition or laser engineered net shaping (LENS®), uses a high energy laser beam to melt a metal powder/wire onto a metal substrate resulting in formation of a high-quality layer or coating with excellent bonding to the substrate [10]. Laser cladding is suitable for making metallic large parts as opposed to powder bed AM techniques where the component size is very much limited. However, aircraft, automotive and marine applications and some other industries generally need bigger parts. The real benefit of AM for such big parts lies in the significant reduction of lead and manufacturing times. For example, the lead time for casting and forging of special geometries can go up to several months which can only start after the design is frozen. Due to the delays in the design stage, the deadlines are always difficult to match with such long lead times. Therefore, using AM techniques, the time from design to testing can be shortened significantly.

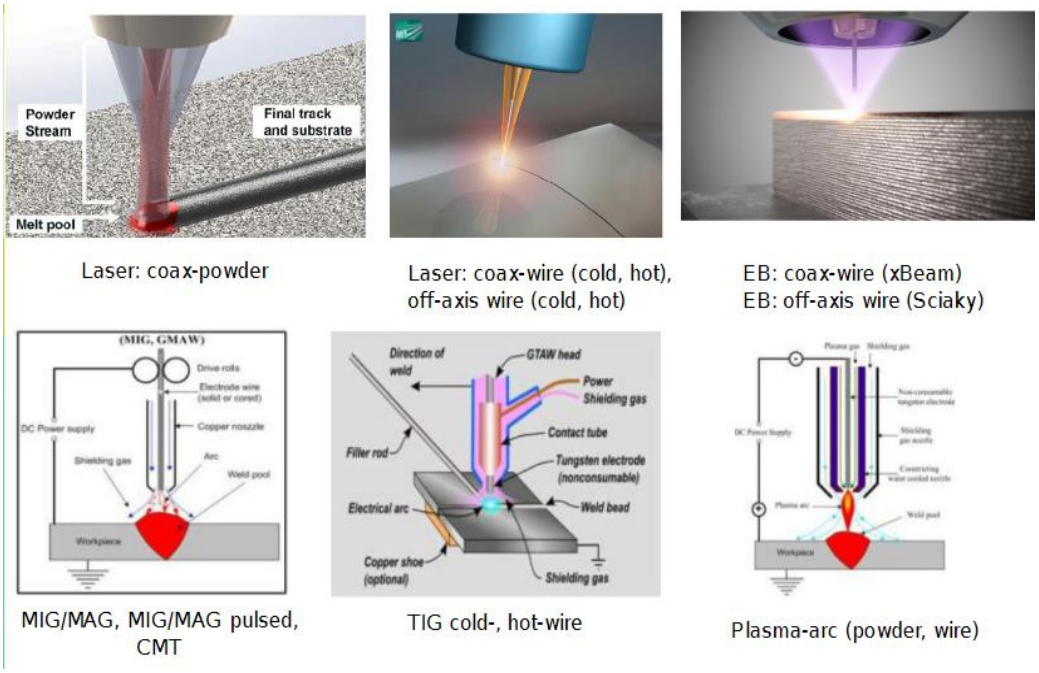


Figure 4. DED Methods [9]

Moreover, large parts having intricate geometries such as bosses/deep pockets need to be machined for long hours to get the final geometry. Instead, AM techniques can be combined with subtractive machining to shorten the manufacturing cycle times. In case of a design change, AM can easily be applied without any need for a new tool/mold or exhaustive tool path generation and machining operations. In LC, metal powder is entered into the focused beam of a high-power laser under controlled atmospheric conditions. The focused laser beam melts the surface of the target material and generates a small molten pool of base material. Strong metallurgical bond with no porosity, high cooling rates leading to fine microstructures, low dilution between the substrate and the track, high adoption to near-net-shape manufacturing, material flexibility, large build envelope, etc. are main advantages [10, 11]. Moreover, the process offers a good control of the HAZ thanks to its local and defined energy input leading to using heat sensitive materials and monitoring of the solidification rate. In contrast to CM, LC allows graded functional parts with a metallurgical bond, which is a significant plus [12]. As shown in Figure 5 LC also has the advantage of reducing process chain steps for high value parts with complex geometries, i.e. the blisks or thin walled structures [11]. Using LC also for part/tool repair can increase the product life cycles in a cost-efficient way, especially for cost-intensive parts.

Electron Beam Additive Manufacturing is also a direct energy deposition method which uses an electron beam as the energy source and wire as feedstock. It is also called as “Electron Beam Free Form Fabrication” (EBF3) by NASA. Invented at NASA Langley Research Centre, this technology is highly considered by numerous aerospace organizations such as Airbus, Lockheed Martin, Boeing and NASA. This is due to its high potential and for its ability to achieve high deposition rates, process large parts, achieve near-net shape depositions but most of all complex geometries [16]. This technology has been extensively tested on many parts for practical applications and a miniature version has been installed and run aboard a NASA reduced gravity aircraft [14]. Aluminum losses in this process for titanium alloys which is mainly attributed to the vacuum environment.

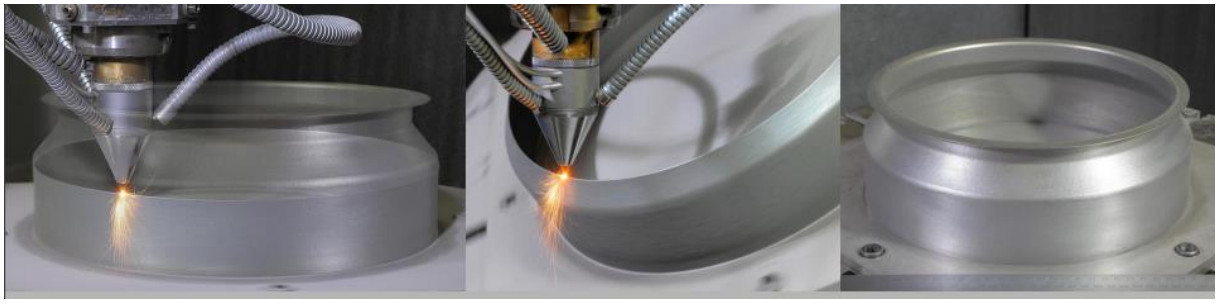


Figure 5. Laser cladding of thin walled casing-type structures [11]

Some other areas also need enhancement and related to the quality assurance which is a common problem for almost all AM technologies [14,15]. The need to monitor beam degradation and melt pool size are the most significant issues related to the quality assurance. Unfortunately, as is the case with other immature AM technologies, there is still a lack of good understanding of the interactions between the process parameters which are many: “there is no unifying equation or other understanding that reveals mastery of the process” [16].

As evident, there are many processes suitable for metallic materials. The selection of the most suitable process for a specific application needs experienced staff and good knowledge of available processes as well as the of the requirements of the specific application. Like many other defense companies, FNSS is also exploring additive manufacturing technologies to benefit from weight reduction, ability to create complex geometries at almost no added cost, reduced lead time from design to testing as well as cost reduction. This paper presents the perspective of FNSS for adopting AM technologies following a systematic approach. The next section will focus on this approach and outline specific examples.

2. ROADMAPPING FOR ADDITIVE MANUFACTURING AT FNSS

Additive manufacturing technologies may be a good solution if the company looking for adoption of AM technologies needs;

- to manufacture complex geometries with added functionalities,
- to manufacture components that require extensive machining,
- to reduce part weight or to reduce the assembly efforts,
- to reduce time to market either from design to testing/design validation or from design to serial production.

Otherwise, additive manufacturing would definitely be a more expensive option compared to conventional processes for today. If the company satisfies one of the conditions above, it makes sense to investigate which AM technology would be the best option for the specific application. FNSS satisfies more than one condition above. Some structural parts with deep pockets, such as turret system components and electronic components packaging need extensive machining whereas the weight reduction is a significant design criterion for amphibious vehicles as well. The time needed to validate the design or for testing is significantly reduced by AM technologies since they do not special tools or dies with lead times of several months. Various land vehicle parts may not be geometrically very complex but it is in need of severe assembly efforts. Being able to manufacture mono-parts by AM is thus a significant advantage to be explored for the case of FNSS.

Figure 5 summarizes the strategic considerations and benefits of AM adoption across value chain elements [1]. As shown, at each value chain stage, companies need to make changes to gain benefits depending on the extent of AM adoption. While most of the AM opportunities and the likely benefits from AM are more obvious and more pronounced in the earlier stages of the value chain, the technology's impact should not be dismissed for later stages. The first stage of the value chain is need identification/procurement where most of the companies wobble the most. If the above stated conditions are satisfied, then the company shall first understand in which stages of the value chain AM will present the highest value opportunities. For companies in defense industry, this mostly corresponds to R&D manufacturing [1]. However, to gain the highest benefit, correct identification of the needs and choice of right applications are of critical importance because different applications may call for different processes.

FNSS has decided to follow a systematic approach before any investment is carried out. The following steps have been taken and the output will be discussed in more detail in the next section.

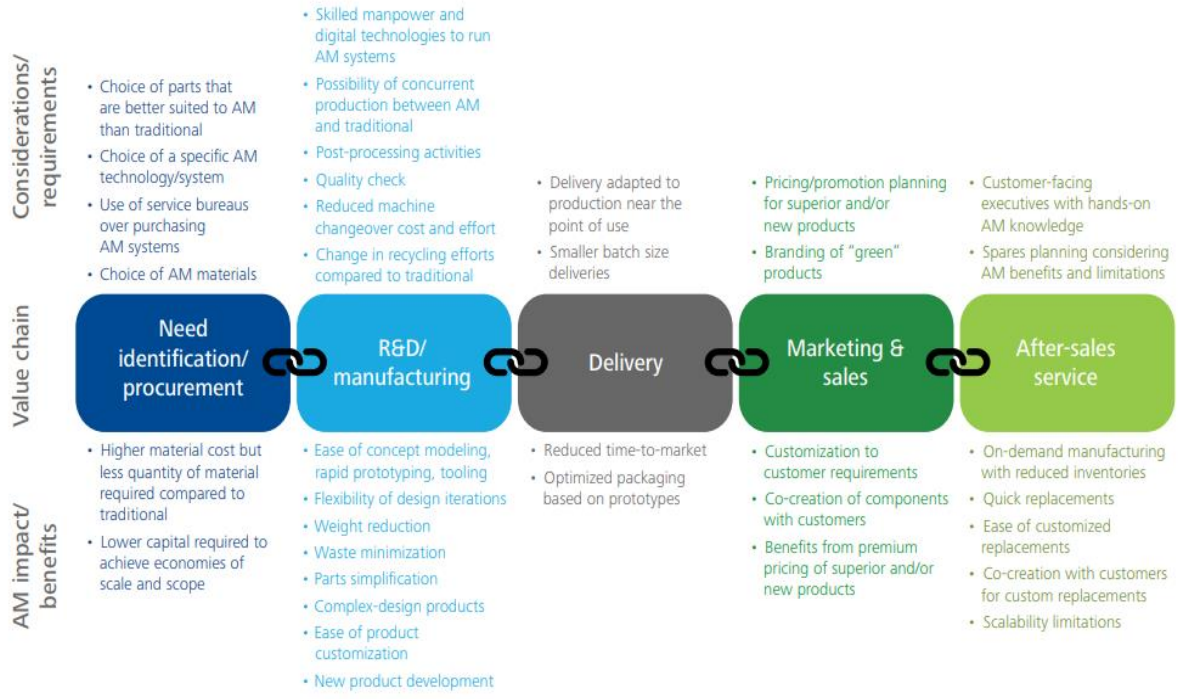


Figure 5. Strategic considerations and benefits for AM adoption across value chain elements [1]

1. ***Detailed literature review:*** After the product portfolio is investigated, it was decided to conduct a detailed literature review for the most interesting material groups including metallic materials, reinforced polymer composites and engineering polymers. A detailed literature review is especially necessary to understand what each process

promises and to learn about new processes and machines available on the market. AM has a significantly growing market and thus it is possible to miss newly developed processes and machines if this step is skipped. A detailed literature review report including three material groups was written and kept up-to-date with the recent developments in the AM world.

2. ***Selection of application part groups and processes for feasibility studies:*** With the knowledge coming from detailed literature review, the selection of application part groups for feasibility studies was carried out as the next step. For reinforced polymer composites and metallic materials, different part groups were targeted. Examples of these material groups (composite by FDM and metallic material by WAAM) are shown in Figure 6. For example, for composite materials, a tubing and duct assembly was selected. This part was before manufactured by welding of two separate tubes. As the metallic part feasibility, cost effectiveness plays an important role as the land vehicle industry becomes more competitive with increasing number of new comers. Also, the large component size is of crucial importance. Therefore, direct energy deposition methods seem to be more preferential for FNSS' purposes.

   The selection of processes is quite a complicated task since there exist many processes suitable for metallic and composite materials.

a)  b) 

Figure 6. Sample parts from FNSS portfolio for AM roadmapping a) Composite tubing part manufactured by FDM b) WAAM component – unfinished condition

A summary of various processes and their specifications for metallic materials is shown in Table 2 whereas a summary of possible processes and their specifications for polymers/composites is given in Table 3. All evaluations are based on the studies found in open literature and experience.

In Table 2, many processes from powder bed fusion, direct energy deposition, sheet lamination, material extrusion and binder jetting AM groups are included. For high geometrical accuracy and surface quality for applications where no final machining is required, powder bed fusion processes are a good option. However, the production speeds are not at demanded rates for PBF processes compared to DED processes, which are more suitable for large part manufacturing at high production speeds. Moreover, arc based DED technologies present a low cost solution compared to DED and PBF processes utilizing a laser or electron as the energy source. At this stage, the part screening should be considered. Two groups of parts are observed: a) geometrically complex and small parts having intricate details, which could not be produced by conventional processes; b) large parts in need of extensive machining with simple geometries.

The priorities of FNSS for the first group of metallic parts can be summarized as high accuracy, high surface quality, high geometrical complexity, low operational /investment cost with good mechanical properties. On the other hand, for the second group of parts, maximum build volume to allow large part manufacturing, high build rates, low operational/investment cost with good mechanical properties are more critical. For the feasibility study, since large parts are of most importance, a part from the second group is selected while the cost efficient process seem to dominate.

Regarding composite materials, carbon fiber reinforced polymers were of interest. Since FDM is the only method to be able to deposit continuous fibers. Even, there is only one brand allowing this type of production, namely Markforged printers. As shown in Table 3, same specifications are used for comparing different processes such as build speed, accuracy, surface quality, maximum part size, investment and production cost and mechanical properties. Taking the FNSS priorities, for large part manufacturing from composites, Big Area Additive Manufacturing is the leading process whereas for smaller parts, FDM may be a better option due to its wider availability and low investment costs. For the feasibility study, carbon fiber reinforced nylon material is selected whereas the process is preferred as the FDM.

Table 2. Comparison of various AM processes only for metals

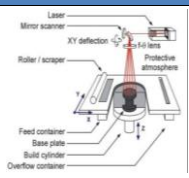
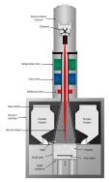
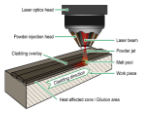
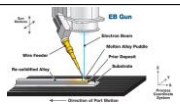
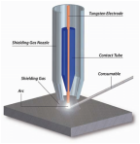
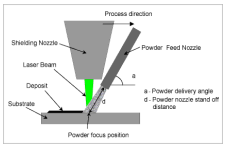
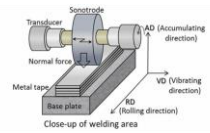
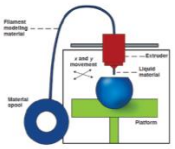
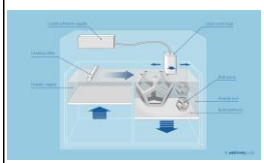
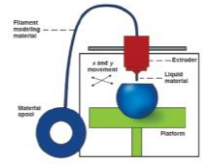
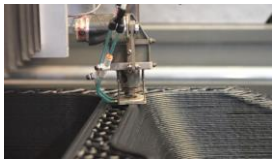
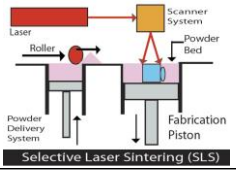
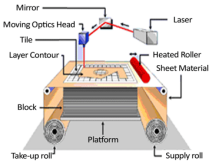
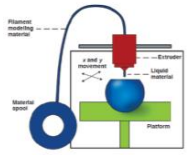
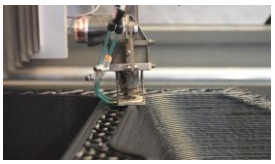
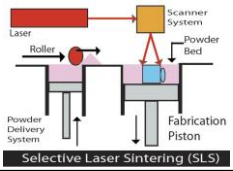
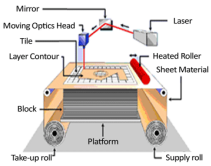
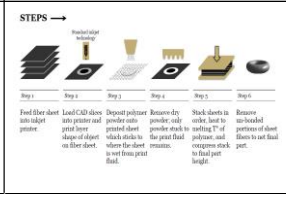
#	Process Category	Available Materials	Process	Schematic Demo	State of the starting material	Typical Applications	Build speed	Accuracy	Surface quality	Max part size	Investment Cost	Production Cost	Mechanical Properties
1	PBF	Titanium Alloys, CoCr, pure titanium, stainless steels, maraging / tool steels, Al alloys, nickel superalloys	Selective Laser Melting		Powder	Functional Prototype/ Part Manufacturing	+	+++	+++	+	$$$	$$$	++
2	PBF	Titanium alloys, pure titanium, CoCr, Inconel 718, Titanium Aluminides	Electron Beam Melting		Powder	Functional Prototype/ Part Manufacturing	++	++	++	+	$$$	$$$	+++
3	DED	Titanium Alloys, CoCr, pure titanium, stainless steels, maraging / tool steels, Al alloys, nickel superalloys	Laser Cladding (Laser Engineered Net Shaping - LENS, Laser Deposition, etc.)		Powder / Wire	Repair	++	+	+	++	$$	$$	++
4	DED	Titanium, nickel, steel, aluminium, refractory metals, zirconium, copper	Electron Beam AM		Wire	Near-Net Shape Part Manufacturing / Repair	+++	++	+	+++	$$$$	$$$	+++
5	DED	Titanium, nickel, mild steel, high strength steels, aluminium alloys and copper alloys	Wire Arc AM		Wire	Near-Net Shape Part Manufacturing / Repair	+++	+	+	+++	$	$	++
6	DED	Titanium alloys, nickel superalloys, steels	Shaped Metal Deposition		Powder	Near-Net Shape Part Manufacturing / Repair	+++	+	+	+++	$$	$$	++
7	Sheet Lamination	Aluminium, copper, steel, titanium, nickel, gold, silver, refractory metal	Ultrasonic Additive Manufacturing (Ultrasonic Freeform Consolidation)		Metal Foils	Near-Net Shape Part Manufacturing	++	+	+	+++	$$$ (sold in hybrid form)	$$$ (sold in hybrid form)	++
8	Material Extrusion	Stainless Steels, Aluminium, Titanium, nickel superalloys, Carbides, high performance steels, tungsten alloy, Copper, Bronze, low expansion Invar / Kovar	Fused Deposition Modeling		Filament	Functional Prototype/ Part Manufacturing	++	+	+	+	$$	$	+
9	Binder Jetting	420 Stainless Steel / Bronze Matrix, 316 Stainless Steel / Bronze Matrix, 316L Stainless Steel, 17-4PH Stainless Steel, IN Alloy 625, IN Alloy 718, Iron / Bronze Matrix, WC, Iron-Chrome-Aluminum	Binder Jetting		Powder + Binder Material	Prototyping / non-structural parts	++	++	++	+++	$$	$$	+

Table 3. Comparison of various AM processes only for polymers/ polymer composites

#	Process Category	Material	Available Materials	Process	Schematic Demo	State of the starting material	Typical Applications	Build speed	Accuracy	Surface quality	Max part size	Investment Cost	Production Cost	Mechanical Properties
1	Material Extrusion	Polymers	ABS, PPS, PEKK, PEI, ASA,PC, PPSF, PA and ULTEM	Fused Deposition Modeling		Filament	Functional Prototype/ Part Manufacturing	++	+	+	+	$	$	+
2	Material Extrusion	Polymers	ABS, PPS, PEKK and ULTEM	Big Area AM (BAAM)		Filament	Functional Prototype/ Part Manufacturing	+++	+	+	+++	$$$	$$	+
3	Powder Bed Fusion	Polymers	Polyamide, PEEK, Polystrene	Selective Laser Sintering		Powder	Functional Prototype/ Part Manufacturing	+	++	++	+	$$$	$$	++
4	Sheet Lamination	Polymers	PEEK, PEI,PPS, PP, PE, PC, PET, PES, Nylon, PEKK	Selective Lamination Composite Object Manufacturing		Sheet	Functional Prototype / Part Manufacturing	++	++	++	++	$$$	$$$	
5	Material Extrusion	Composites	Carbon fiber, Kevlar fiber, or glass fiber reinforced thermoplastics	Fused Deposition Modeling		Filament	Functional Prototype/ Part Manufacturing	++	+	+	+	$	$	+
6	Material Extrusion	Composites	Carbon fiber or glass fiber reinforced thermoplastics	Big Area AM (BAAM)		Filament	Functional Prototype/ Part Manufacturing	+++	+	+	+++	$$$	$$	+
7	Powder Bed Fusion	Composites	Alumide (polyamide Al-filled), Carbonmide (Polyamide carbon reinforced)	Selective Laser Sintering		Powder	Functional Prototype/ Part Manufacturing	+	++	++	+	$$$	$$	++
8	Sheet Lamination	Composites	Carbon fiber,fiberglass, aramid fiber and metal fibers reinforced thermoplastics	Selective Lamination Composite Object Manufacturing		Sheet	Functional Prototype / Part Manufacturing	++	++	++	++	$$$	$$$	++
9	Sheet Lamination	Composites	Thermoplastics reinforced with anything from carbon fiber, fiberglass, polyester, polyvinyl alcohol and PLA to silk and cotton	CBAM (Composite based AM)		Sheet	Functional Prototype / Part Manufacturing	+++	+	+	+	$$	$$	+++

3. ***Feasibility studies for the most interesting processes for the selected applications:***

   Regarding the composites, the feasibility study was conducted to be able to answer the question whether the fiber reinforced polymers could be used replacing aluminium alloys. In order to give an answer, the mechanical properties of the chopped carbon fiber reinforced nylon were investigated. The main outcome of this feasibility study, of which the results are being published somewhere else, is that the anisotropy encountered in mechanical properties is a significant barrier for utilizing this material + process combination in structural parts because there is a lack of good bonding between successive layers. This is highly undesirable and may lead to catastrophic failures in structural parts. After the mechanical tests were performed, some simple component testing was conducted and the main outcome of the study was also validated. Tubes were built with one side closed by FDM process from Onyx material which is chopped carbon fiber reinforced nylon developed by Markforged. The tubes were then tested under pressure to see the limit they could bear. Although in-planar strength was in harmony with announced properties by the vendor, due to bad bonding between successive layers, an unexpected failure of the closed side was encountered. Moreover, it was seen that trials with another FDM 3D printer, Roboze, did not result in water/air proof caps due to infill strategies utilized.

4. ***Feasibility studies involving targeted application parts:***

   Regarding the metallic materials, the feasibility study was carried out in order to understand the geometrical limits of the selected process. For each component the importance of the process variables can be different and needs to be evaluated separately. Therefore, the feasibility was directly conducted on a selected part.

3. DISCUSSION AND CONCLUSIONS

This work represents an overview of the additive manufacturing processes and a method to downselect the additive methods with the help of a roadmap for defense and land vehicle sector. As each method have its advantages and drawbacks, the methods to be focused on must be selected according to the component specific prioritization. Unlike conventional machining processes, the variations in additive manufacturing processes are significant. In addition to component specific requirements, financial criteria may play a role as well. Investment capital, payback duration, operational costs are some examples for financial critera. The roadmapping study being carried out FNSS showed that a targeted feasibility study

with a good knowledge of specific requirements needed to validate the suitability of the process in focus is a necessary step in order not to give wrong long-term decisions.

REFERENCES

1. **Coykendall, J., Cotteleer, M., Holdowsky, J., Mahto, M.,** https://www2.deloitte.com/content/dam/insights/us/articles/additive-manufacturing-3d-opportunity-in-aerospace/DUP_706-3D-Opportunity-Aerospace-Defense_MASTER2.pdf
2. **Schrage, J. (2014),** "Additive Manufacturing with Selective Laser Melting (SLM) and Laser Metal Deposition (LMD)", presented at Forum Produktion Nordwest 2014, 18th June 2014, Papenburg.
3. https://freemelt.com/
4. **Rashed, M. G., Ashraf, M., Mines, R., Hazell, P. (2016),** "Metallic microlattice materials: A current state of the art on manufacturing, mechanical properties and applications", Materials & Design. 95. 518–533.
5. **Craeghs, T., Clijsters, S., Yasa, E., Kruth, J.-P. (2011),** "Online Quality Control of Selective Laser Melting", Proc. of Solid Freeform Symposium, Austin, TX, USA.
6. **Bhavar, V., Kattire, P. Patil, V., Khot, S., Gujar, K., Singh, R. (2014),** "A Review on Powder Bed Fusion Technology of Metal Additive Manufacturing", 4th International conference and exhibition on Additive Manufacturing Technologies-AM-2014, September 1 &2 ,2014, Banglore, India.
7. **Yellup, J.M. (1995),** "Laser cladding using the powder blowing technique", Surface and Coatings Technology 71, pp. 121-128.
8. ASTM F3187 – 16 Standard Guide for Directed Energy Deposition of Metals
9. **Tuominen, J. (2017),** "Directed energy deposition - Review of materials, properties and applications", presented at 3D Boosti ja Invest - seminar, Tampere, Finland, Tampere University of Technology available at https://www.researchgate.net/publication/316698894_Directed_energy_deposition_-_Review_of_materials_properties_and_applications
10. **Jayakumar, K., Senthil kumar, T., Shanmugarajan, B. (2015),** "Review study of laser cladding processes on ferrous substrate", International Journal of Advanced Multidisciplinary Research 2(6), pp. 72–87.
11. **Hauser, C. (2014)**, "Case Study: Laser Powder Metal Deposition Manufacturing of Complex real Parts, reducing the environmental impact of air transport using additive

manufacturing", Dissemination Workshop of MERLIN FP7 PROJECT, available at http://www.lortek.es/files/merlin/05-C_Hauser-TWI-Case-Study.pdf

12. **Kaierle, S.,Barroi, A., Noelke, C., Hermsdorf, J., Overmeyer, L., Haferkamp, H. (2012),** "Review on Laser Deposition Welding: From Micro to Macro", Physics Procedia 39, pp. 336 – 345.
13. **Kelbassa, I., Gasser, A.,Meiners, W.,Hinke, C.,Backes, G. (2015),** "Laser Additive Manufacturing to Digital Photonic Production", Euromold Duesseldorf, Germany, September 25 available
14. **Seufzer, B. (2013),** "Automating Electron Beam Free Form Fabrication with MATLAB", Technical Articles and Newsletter available at https://www.mathworks.com/company/newsletters/articles/automating-electron-beam-free-form-fabrication-with-matlab.html
15. **Seufzer, W.J. (2014), "**Additive Manufacturing Modeling and Simulation (Literature Review No. NASA/TM-2014-218245)", available at https://ntrs.nasa.gov/archive/nasa/casi.ntrs.nasa.gov/20140005339.pdf
16. **Busachi, A., Erkoyuncu, J., Colegrove, P., Martina, F., Watts, C., Drake, R. (2017),** "A review of Additive Manufacturing technology and Cost Estimation techniques for the defence sector", CIRP Journal of Manufacturing Science and Technology, article in press, https://doi.org/10.1016/j.cirpj.2017.07.001.

EFFECTS OF LIQUEFIER DESIGN ON THERMAL PROFILE IN FUSED FILAMENT FABRICATION BASED ADDITIVE MANUFACTURING PROCESS

Chirayu H. SHAH, *cs1285@rutgers.edu* Rutgers University, 08854, New Jersey, U.S.A.
Harshal N. SHAH, *hs765@rutgers.edu* Rutgers University, 08854, New Jersey, U.S.A.
Kaushalendra PATEL, *kvp44@rutgers.edu* Rutgers University, 08854, New Jersey, U.S.A.
Tuğrul ÖZEL, ozel@*rutgers.edu* Rutgers University, 08854, New Jersey, U.S.A.

ABSTRACT

Material extrusion processes such as fused filament fabrication (FFF) are among the most widely used additive manufacturing (AM) technologies. The fused filament fabrication process consists of simultaneously feeding and melting a filament of polymer material through a computer controlled liquefier. The material then flows through the nozzle under pressure, which must fully solidify while remaining in extruded shape. Deposited layers are fused together as the melted material quickly solidifies to form layers of a solid 3-D object. The key elements are material feed mechanism, liquefier, print nozzle, build surface and environment. The general applications are production of prototypes during product development phase, short series production runs where tooling cost is high, and parts with high geometrical complexity which cannot be produced by means of conventional manufacturing. The liquefier, core of a material extrusion system, is a metal block with a channel designed for the filament to flow through. Often, time evolution of temperature as recorded by thermography and adhesion behavior of filament are investigated by considering main process parameters, such as filament dimensions and material, sequence of deposition and environment temperature. In this paper, thermal behavior of material extrusion liquefier with varying heat sink designs and cooling fan speeds is analyzed.

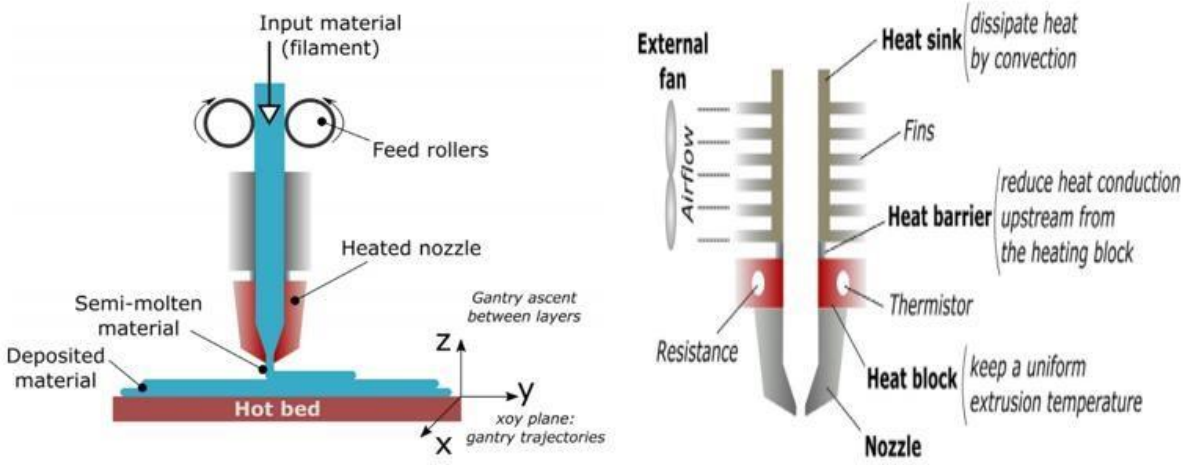
Keywords: Fused filament fabrication, liquefier, temperature, heat sink

1. INTRODUCTION

Additive manufacturing is one of the most important drivers of innovation in manufacturing industries. Melt extrusion based additive manufacturing processes such as fused filament fabrication is widely used. FFF consists of pushing a filament of thermoplastic (e.g.

Acrylonitrile-Butadiene Styrene (ABS), polylactic acid (PLA), polystyrene (PS), polyamides (nylon)) through a liquefier and depositing the semi-molten extruded thin filament onto the support surface.

The key elements of melt extrusion are material feed mechanism, liquefier, print nozzle, build surface and environment. The working of FFF process and the components of the liquefier are shown in Fig. 1.



(a) Overall system view (b) Cross sectional view

Figure 1: A typical fused filament fabrication system (Turner et al. 2014)

In this system, the liquefier is a metal block with a hole machined for the filament to flow through. Filament refers to the total length of extrudate used to manufacture the part. Filament segment is the length of filament that is deposited by the machine nozzle in one horizontal plan before reversing the deposition direction. A gantry moves the print nozzle in the horizontal x–y plane as the material is deposited on a build surface that can be moved in the vertical z direction. Build surface is a surface on which the melted extrudate is deposited layer upon layer.

Turner et al. (2013) proposed that the system should be designed to maintain the uniform temperature throughout the liquefier. As the temperature in the liquefier increases, the viscosity of the melt decreases, allowing it to flow through the print nozzle more readily with a smaller pressure drop. Higher melt temperature also leads to better adhesion between successive beads or roads of printed material, and therefore greater mechanical strength in the finished part. However, higher temperature can also lead to polymer degradation, breaking down polymer chains, weakening the finished part and leaving residue on the inside of the melt channel. Furthermore, Jerez-Meza et al. (2017), described that the temperature at top of the liquefier should be kept low. They also analyzed the performance of liquefier on

thermal behavior. They focused on convective heat dissipation developed along the liquefier body. The influence of fan speed was also taken into consideration by varying the fan speed.

Jerez-Meza et al. (2017) has also developed a Finite Element Model (FEM) to analyze the thermal performance of the liquefier. The air velocity induced by the refrigeration fan was one of the variables. The other variable of analysis was the fin design and the outcome of this variable is the temperature at the top of the liquefier body, T_t. The Finite Element Analysis (FEA) was done using COMSOL Multiphysics 4.4. The parts of the liquefier were defined in a SolidWorks Computer Aided Design (CAD) model.

In their study, governing equations for the air domain were the continuity equation and Navier-Stokes equation for a Newtonian fluid. For the solid parts of liquefier, only energy equation was solved. To solve these equations, initial and boundary conditions were defined such as the velocity of the fan, the temperature of nozzle, energy generation rate of the heater, air heat transfer coefficient, temperature at the top of the liquefier, and the deposition rate. Moreover, experiments were also carried out to register the temperature at adjacent points along the heat sink temperature profile in a steady state, with the goal of comparing them with the proposed computational fluid dynamics design implemented through the FEA, and calibrating the actual air flow velocity generated by the fan.

A resistor and a thermistor were embedded inside their corresponding hole inside the heating block. Then, four thermocouples were attached to the external wall of the heat sink at four different levels, including the top of the liquefier body and the lower point coinciding with the heat barrier. The standard ARDUINO-Marlin system was used to regulate the fan velocity, the heat generated by the resistor, and monitoring the heat block temperature through the embedded thermistor. All of the four thermocouples were also controlled by the ARDUINO-Marlin system.

As shown in Fig. 2, the resulting temperature profiles were compared with discrete temperature values registered through an experimental setup to confirm the adequacy of the model generated by governing equations and boundary conditions. Hence, the described model defined in COSMOL was adequate to predict the temperature profile of the liquefier.

For instance, when PLA material is extruded, the temperature at the top of the liquefier was measured as 72 °C. Thus, extrusion of PLA material should be performed while the fan is running. Fan speed was not measured directly. To measure the fan speed, repeater host were defined and calibrated for air velocities. When the fan speed was increased, the temperature at the top was decreased but the fan power was also increased. So, if the temperature at the top is defined, optimal fan speed is taken for the energy saving.

Turner et al. (2013) mentioned in their paper that the build surface upon which the melt is printed is a critical element of the system design. The melt must adhere to this surface, but not so well that the part cannot be removed when the print process is complete.

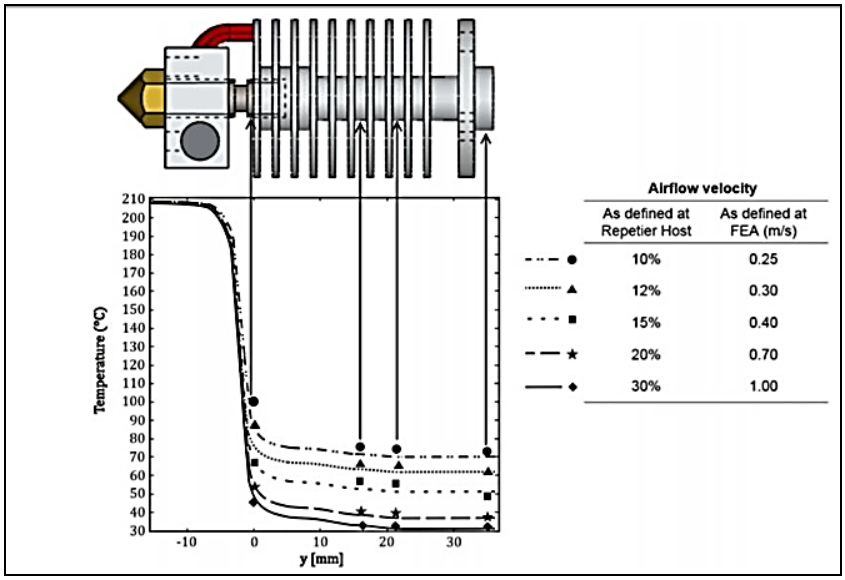


Figure 2: Temperature profile of the liquefier measured from experiment and predicted with the FEA. (Jerez-Meza et al. 2016)

Thermal gradients are necessarily present in parts, as they are built in material extrusion based additive manufacturing machines. Sufficiently large thermal gradients can lead to warping and distortion of the final structure. Domingo-Espin et al. (2014) had also mentioned the effect of high thermal gradient. They proposed that a weak interlayer bonding between extruded filament is responsible for the decrease in strength because distortion occurs with high temperature gradient toward the bottom layers. They also discussed that if the diameter of the extruded filament is smaller, the temperature gradient between its inner and outer part is smaller; consequently, the bonding quality between filaments in the same layer would be better.

Process models that describe the dynamics of the melt and extrusion process and the bonding process between successive layers of material are also critical in developing advanced control strategies for FFF based AM systems. Understanding the relationships between process parameters and final part properties will be critical in enabling design of parts for manufacturing, in developing methods of qualifying parts for industrial use and in facilitating more intelligent material development strategies. Domingo-Espin et al. (2014) focuses on understanding the influence of three process parameters (nozzle diameter, number of contours, and raster-to-raster air gap) on mechanical behavior of the final parts.

The process parameters are defined as follows: (i) tip size which is the size of the tip determines the diameter of the extruded filament and defines the slice height, (ii) number of contours which is the number of trajectories to build around all outer and inner part curves, and (iii) raster-to-raster air gap which is defined as the trajectory of the nozzle inside contour filling interior of the nonvisible section of the part.

Domingo-Espin et al. (2014) also introduced three test parameters (temperature, amplitude, and frequency) to find whether the influence of process parameters is more significant than test parameters. Taguchi experimental design methodology was used. Also, an analysis of variance had been performed to detect the most significant parameters that influence the dynamic properties of the final parts. From their experiments, they concluded that process parameters can control the elastic behavior (modulus and stiffness) of the manufactured parts built by the FFF. In their case, test parameters did not affect the outcome significantly. On the other hand, testing parameters show a great influence on the viscous behavior (loss modulus and damping capacity) of the final manufactured part. Overall, the number of contours was the most influential parameter since it affected all of the properties analyzed (elastic and viscous). Pollard et al. (2017) reported that there are significant variations in filament temperature on extrusion during step changes in feed rate and priming. A sudden decrease in feed rate could cause structural weaknesses due to the lower extruded temperature. They found that the ABS filament had higher temperature variations during all feed rate variations than PLA.

Costa et al. (2017) presents an analytical solution to the transient heat conduction developing during filament deposition in FFF to compare it with experimental data and look how well they complement each other. Their analytical solution considers local boundary conditions depending on part geometry, operating conditions, and deposition strategy. Boundary conditions include contact between filament segment and support, between two filament segments, as well as heat transfer with the environment. They proposed an analytical solution for the transient heat transfer during filament deposition and cooling. Entire physical contacts between filament segments are considered to check whether the heat transfer is through conduction or convection. Their model attempted to predict the time evolution of filament temperature as well as the bond quality between all adjacent filament segments of a FFF built. For this, the deposition of a filament segment at any cross section along its length was taken as a series of successive lengths for modelling such that each given length is associated to a given deposition time (t_d). It was found that the deposition time (t_d) should be less than or equal to the ratio of cross section area of the filament (A) and the deposition velocity (v) to maintain good balance between computational time and required

accuracy. Different build strategies as shown in Fig. 3 are also taken into consideration to determine the type of contact taking place.

They developed a MATLAB code in which the user defines the geometry of the part, build strategy and the deposition sequence (number of layers, number of filament segments and type of contact of the filament segments). They also utilized extrusion conditions and thermal properties. They implemented an adhesion criterion that was used to check whether successive filament segments would adhere properly to each other before solidification. They assessed their predictions experimentally where ABS polymer was used as FFF material.

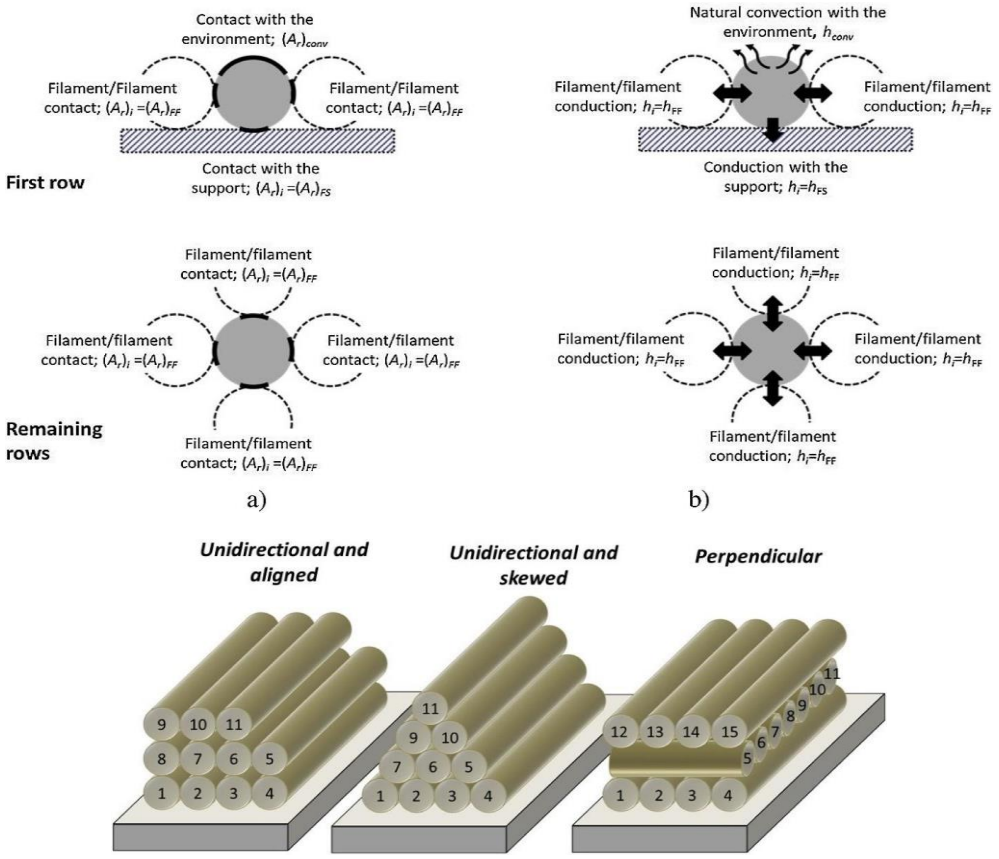


Figure 3: Possible contact areas (a) and heat transfer modes (b) for a filament segment (in grey). (Costa et al. 2017)

Furthermore, they validated their analytical solution experimentally validated for filament surface temperature using data recorded by thermography for different conditions such as determining the heat transfer convention coefficient, h_{con}, coefficient of heat transfer by conduction between filament and support, h_{fs}, coefficient of heat transfer by conduction between two filaments, h_{ff}, and the evolution of temperature with time for two filament segments deposited on top of each other for different time intervals (0s, 3s, 5s, 6.7s and 17.6s) between successive deposition of filament, all taken at different temperatures.

They conducted peel-like tests by pulling apart the ends of the filament under a certain load and measured the relative adhesion strength in order to correlate the adhesion strength with experimental built. The surviving contact length, B_p, was taken as a measure of adhesion strength. Their study showed good agreements between predicted and experimental data for the filament surface temperature. Also, adhesion predictions were in harmony with the results of real peel-like tests which was the main objective of their work.

2. MATERIALS AND METHODS

In this paper, we consider that the temperature profile of liquefier is essential for the quality of parts manufactured by fused filament fabrication method. Therefore, analyzing the temperature profile of liquefier has been the main focus in this work. Heat sink is critical part to obtain desired temperature profile of the liquefier; therefore we also compared three different geometrical designs for the heat sink. The fan speed is also considered as a factor, as it affects the temperature profile of the liquefier.

The liquefier of the FFF printer consists of several sections; heater (ceramic heater with outer shell made out of copper), print nozzle, heat block, heat break and heat sink. The material used for a specific section, their thermal conductivity, density and specific heat are as shown in Table 1.

Table 1: Material properties of liquefier sections

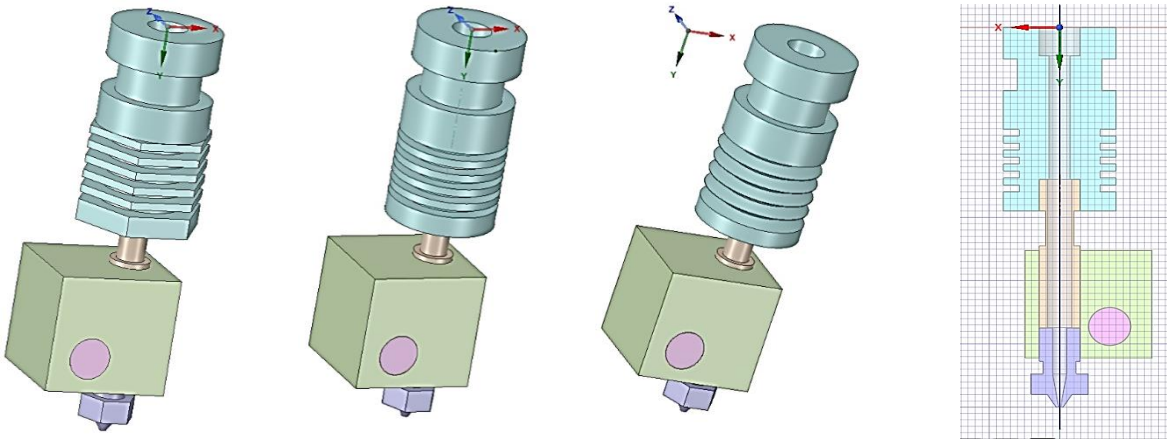
Section	Material	Density (kg/m^3)	Thermal Conductivity (W/m/^{0}C)	Specific Heat (J/kg/^{0}C)
Heat Sink	Aluminum	2689	237.5	951
Nozzle	Bronze	8890	64	420
Heater	Copper	8933	400	385
Heat Block	Stainless Steel	8055	13.8	480
Heat Break	Titanium	4500	21	522

3. 3-D MODELLING OF HEAT SINK GEOMETRIES

In order to conduct thermal analysis, we considered 3-D model of the liquefier assembly. The dimensions and the materials considered are taken from an actual liquefier in Lulzbot 3-D fused filament fabrication system. 3-D model was designed using Creo Parametric 2.0 which generated 3-D model in creo(.prt) file. Three different fin designs were realized in the 3-D model which includes (i) hexagonal, (ii) parallel, and (iii) pointed fins. These geometries are shown in Figure 4.

Finite Element Model of Heat Sink Geometries

For the FEA, ANSYS 18.2 software was used. As the conditions are transient with time, the transient thermal analysis system in ANSYS software was adopted. The 3-D liquefier CAD models were converted to the parasolid file format. ANSYS project was defined using the materials from the engineering data source. A manual contact surface between heat brake and heat sink was defined because it was the only part which did not show proper connection with the one and the other.



(a) (b) (c) (d)

Figure 4: (a) Hexagon fins, (b) Parallel fins, (c) Pointed fins, (d) Cross-sectional view of (b).

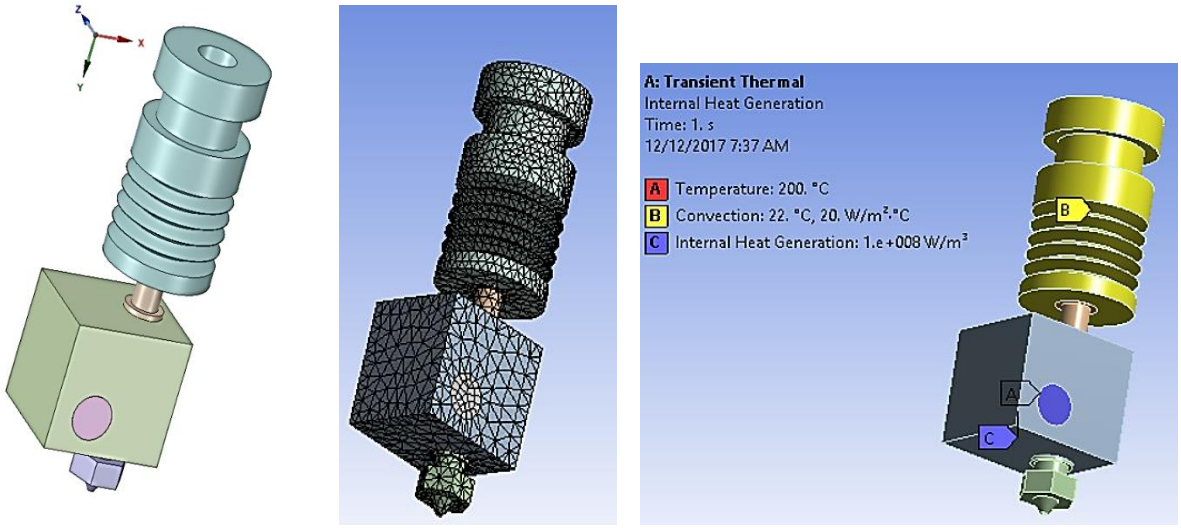


Figure 5: (a) CAD model, (b) Meshed model, (c) Thermal Boundary conditions.

After adding reference points for heat probes at different locations ANSYS project was updated. In the model, mesh was generated and material was assigned for each section of the liquefier, as defined in Table 1. A nodal limit of 34,000 nodes was selected. Adaptive

meshing method with a mean element size of 0.0012 mm was adopted which provided the desired meshing for the liquefier. Due to the limited computing power of the computer, the calculation was limited up to 10 minutes (600 seconds) of transient thermal analysis.

Boundary conditions were defined as 200 °C on the surface of the heater. Heat probes were added into the models at various locations of liquefier to get the temperature profile with time. 10^8 W/m^3 (30 W per volume) heat generation was added for the heater body. Convection heat transfer was given to the heat sink body. Film coefficients of air for convection were taken as 20 W/m^2/°C, 30 W/m^2/°C and 40 W/m^2/°C for steady, flowing air with velocity of 10 m/s, and flowing air with velocity of 15 m/s respectively. Heat sinks with different type of fins were taken into consideration. The simulations have taken a total 18 hours using a computer with Intel® i7-7700 quad core processor and 8GB RAM.

4. RESULTS AND DISCUSSION

Thermal analysis simulations with three different fin designs and three different fan speed conditions were conducted. Since the octagonal shaped fins have the most surface area, this design showed the highest heat convection at all three fan speed conditions. With the fan velocity increasing, the heat transfer is more and the temperature at the top of the sink reduces effectively.

From the simulation results, it was observed that once the fused filament fabrication process has been started and reached up to working temperature after about 200 s, the change in the temperature over time is insignificant and temperature stays constant up to 600 s. This can be seen from the temperature at the top of the heat sink over time which is shown in Figs 6 and 7. This is due to the fact that entire heat is generated by the heater is taken away by the fused filament and by air convection as this heat transfer comes to equilibrium.

4.1 Finite element analysis of liquefier with hexagonal fins

The temperature profiles calculated from the simulation was similar to the expectations. High temperatures near the heat block and low temperatures at the far end of the heat sink were predicted. The heat barrier has a low thermal conductivity so it has a large temperature gradient. Heat block temperature was predicted as 200 °C, and heat break showed a large temperature gradient over its length (195 °C to 35 °C). The heat sink showed a very small temperature gradient (42 °C to 48 °C without considering convection and 35 °C to 36 °C with convection). The predicted temperatures at the top of the sink and bottom of the sink for the hexagonal shaped fins were the lowest.

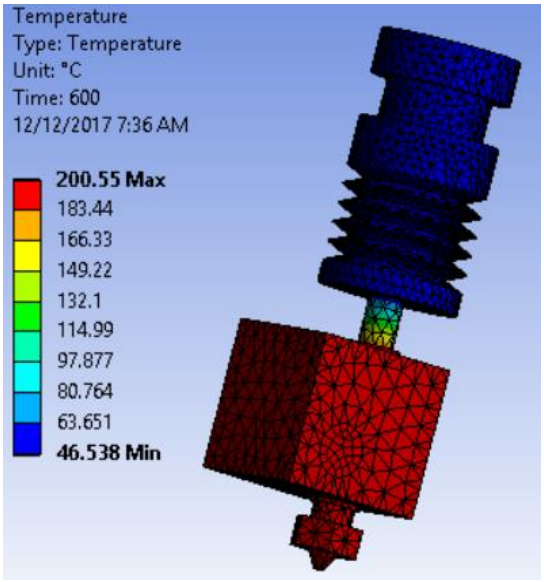


Figure 6: A sample temperature distribution result of FEA.

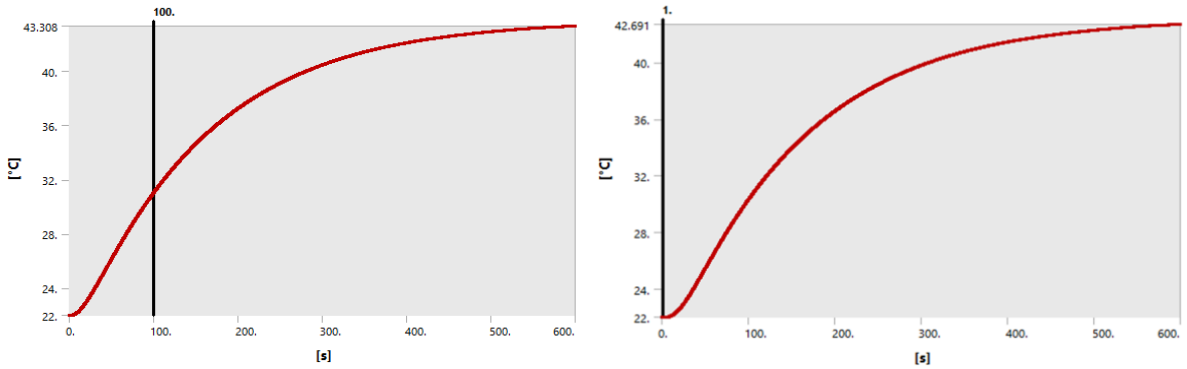
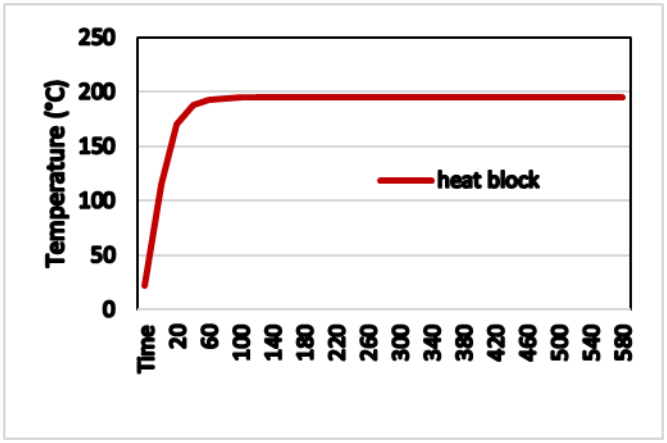
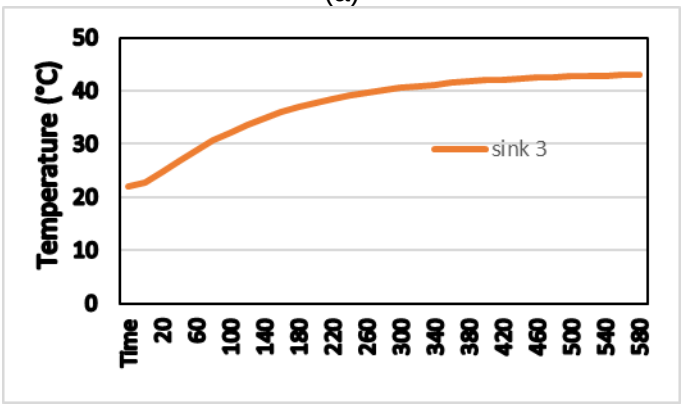


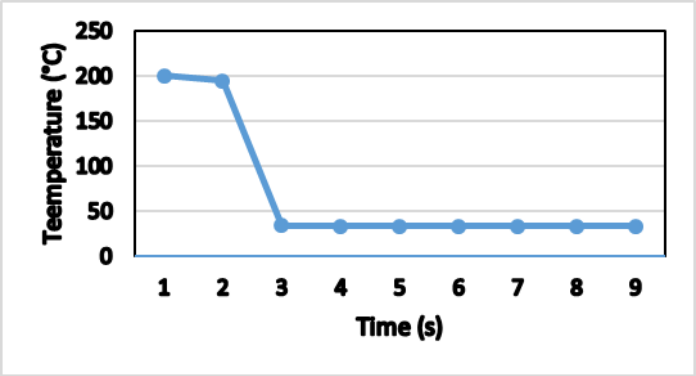
Figure 7: (a) Temperature vs. time plot for the heat sink bottom, (b) temperature vs. time plot for the heat sink top.



(a)



(b)



(c)

Figure 8: (a) Temperature vs. time plot for the heat block, (b) temperature vs. time plot for Fin 3, and (c) temperature profile of the liquefier.

4.2 Effects of heat sink design over temperature profile

With the hexagon fin type heat sink design, the lowest temperature at the top of the sink among all three fin designs (hexagon, parallel, and pointed type) was predicted since there is more air flow contact on the heat sink surfaces achieved with a larger fin surface area. The table below shows us temperature profile for all three fin types. Hexagonal fin type works efficiently and has about 2 °C to 4 °C less temperature compared to parallel and pointed fin types respectively. Thus, to obtain lower temperatures, hexagonal fin type heat sink geometry for the liquefier is found ideal.

Table 2. Temperature probe reading for different fin geometries (in °C).

Fin type	Heater (1)	Heat block (2)	Sink bottom (3)	Fin1 (4)	Fin2 (5)	Fin3 (6)	Fin4 (7)	Fin5 (8)	Sink top (10)
Hexagon	200.5	195.1	43.3	43.1	43.0	42.9	42.9	42.8	42.7
Parallel	200.0	195.1	44.9	44.8	44.7	44.6	44.6	44.5	44.3
Pointed	200.5	195.2	47.2	47.0	46.9	46.8	46.8	46.7	46.5

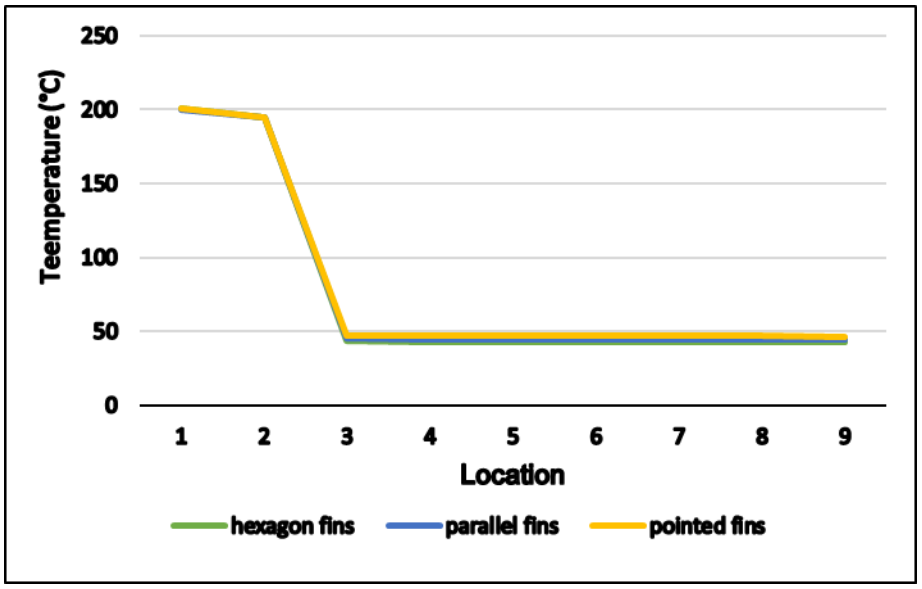


Figure 9: Temperature profile for different fin geometries

4.2 Effects of fan speed over temperature profile

For providing better convection, the area and temperature difference will be same as the ambient temperature which will always be 22 °C. Only thing changing is the film coefficient for the convection achieved by controlling the fan speed. With a higher fan speed, there will be more heat transfer to air so it will reduce the temperature at the top further down which is desirable. This reduction of temperature is observed for all of the fin geometry sections.

Table 3: Temperature probe reading for different fan speed for hexagonal fins (in °C).

Fan speed	Heater (1)	Heat block (2)	Sink bottom (3)	Fin1 (4)	Fin2 (5)	Fin3 (6)	Fin4 (7)	Fin5 (8)	Sink top (10)
0 m/s	200.5	195.1	43.3	43.1	43.0	43.0	42.9	42.8	42.7
10 m/s	200.5	194.9	37.4	37.2	37.1	37.0	36.9	36.8	36.7
15 m/s	200.5	194.8	33.8	33.7	33.5	33.4	33.4	33.3	33.2

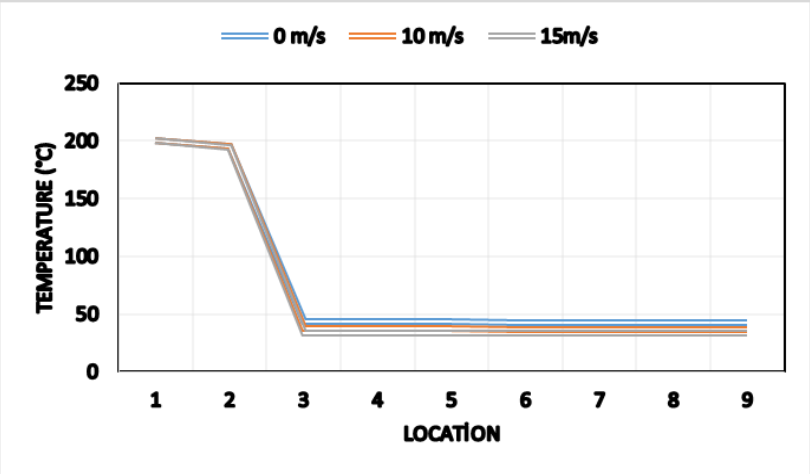


Figure 10: Temperature profile for three different fan speeds.

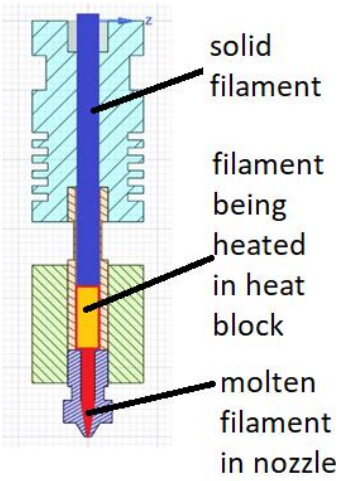


Figure 11: Filament phase change in the cross section.

As the filament material passes through the heat sink, it must be below the glass transition temperature. When it reaches to heat break, the temperature will rise suddenly and it will soften the material. The glass transition temperature is the temperature at which the material starts to soften. After coming into heat block it will melt and due to pressure from upcoming solid filament, it will be pushed out from the nozzle down below. If the temperature at the heat sink is high then it will make filament softer, and it will not be able to push the molten filament out. PLA cannot be extruded without using a fan. Other two materials (ABS and PS) can be extruded with or without using a fan.

5. CONCLUSION

This paper investigated liquefier as a thermal system in a fused filament fabrication based additive manufacturing machine by considering three different heat sink designs and various fan speeds for cooling. The following specific conclusions can be made:

- With the hexagonal heat sink design, the lowest temperature at the top of the sink is achieved.
- Heat sink design with pointed fins is the easiest to be manufactured but provides the highest temperature at the top of the heat sink.
- With a higher fan speed there will be more heat transfer to air, so it will reduce the temperature at the top further down which is desirable.
- While production using PLA material, a higher fan speed is required as it has very low glass transition temperature (50 °C).
- As it can be seen from the temperature profile vs time plot a stable temperature after 200 s for the fixed deposition rate is achieved. With the increased deposition rate more heat will be carried away and with that more heat generation power will be required to maintain the constant temperature profile.

REFERENCES

1. **Bourell, D.L., Rosen, D.W., Leu, M.C. (2014),** "The roadmap for additive manufacturing and its impact, 3D Print". *Additive Manufacturing* 1 (1): 6–9.

2. **Chua C.H., Leong, K.F. (2015)** *3D printing and additive manufacturing: principles and applications*, World Scientific.

3. **Pollard, D., Ward, C., Herrmann, G., Etches, J. (2017),** "Filament temperature dynamics in fused deposition modelling and outlook for control," *Procedia Manufacturing* 11: 536 – 544.

4. **Turner, B.N., Strong, R., Gold, S.A., (2014),** "A review of melt extrusion additive manufacturing processes: I. Process design and modelling", *Rapid Prototyping Journal*, Vol. 20 Issue: 3, pp.192-204.

5. **Domingo - Espin M., Borros S., Agullo N., Garcia – Granada A.A., Reyes G. (2014),** "Influence of Building Parameters on the Dynamic Mechanical Properties of Polycarbonate Fused Deposition Modeling Parts," *3D Printing*, Vol. 1 No. 2, doi:10.1089/3dp.2013.0007

6. **Jerez-Mesa, R., Gomez, G., Travieso-Rodríguez, X.Corbella, R. Busque (2016),** "Finite element analysis of the thermal behavior of RepRap 3D printer liquefier." *Mechatronics* 36, pp.119-126

7. **S.F. Costa, F.M. Duarte b, J.A. Covas (2017)**, "Estimation of filament temperature and adhesion development in fused deposition techniques," *Journal of Materials Processing Technology* Vol. 245 pp. 167–179.

DESIGN AND FABRICATION OF LARGE-SIZE FFF 3D PRINTER

Gokberk SERİN, *gserin@etu.edu.tr* TOBB University of Economics and Technology, 06560,Ankara, Turkey.

Hakki Ozgur UNVER, *hounver@etu.edu.tr* TOBB University of Economics and Technology, 06560,Ankara, Turkey.

Recep Muhammet GORGULUARSLAN, *rgorguluarslan@etu.edu.tr*, TOBB University of Economics and Technology, 06560,Ankara, Turkey.

Sadik Sinan KOSUMCU, *sadik.kosumcu@formcnc.com.tr*, Form Makina A.Ş., 34775, İstanbul, Turkey.

ABSTRACT

Additive manufacturing, also known as “3D printing” keeps diffusing into many industries with a rapid pace. The greatest advantage of 3D printers is that it allows the designers to produce a prototype in a very short time that can be tested and quickly remodeled if necessary. This significantly reduces the required time to advance from the design phase to the final product. Another great advantage is manufacturing components which have very complex and precise forms through this technique. It is also possible to speed the process of manufacturing of complex parts which can be produced in a long time with conventional methods. In this paper, the design and fabrication of a large size FFF 3D delta printer, also the challenges encountered during the fabrication are presented.

Keywords: 3D Delta Printer, Fused Filament Fabrication (FFF), Thermoplastic Polymer Materials

1. INTRODUCTION

Three-dimensional (3D) printing is a new technology which was first invented in 1984 by Chuck Hull. 3D printing technologies have been developed rapidly over the last 30 years and provide practical solutions for many application areas. It allows for manufacturing any part regardless of the complexity with many different materials. 3D printer is a machine that transforms 3D computer data (i.e. an STL.file) into real solid objects that you can hold with your hands by

building the part layer by layer. This technology is capable of producing geometries that cannot be manufactured by conventional manufacturing methods. It also has other advantages such as cost-effective prototype production, which is also known as rapid prototyping, quicker launch to market, and ability to print customized products with very little waste [1-3].

The first application of the 3D printing technologies dates back to 1984, but in the past 20 years, this method has not received much attention apart from the rapid prototyping area. The Reprap (replicating rapid prototyper) project, which was started in 2006, has reached much wider masses. The increase of the compound annual growth rate of the 3D printing technology is shown in Figure 1. The compound annual growth rate (CAGR) from 2016 to 2024 is estimated to be 21.7% and the global market volume of the 3d printer estimated by Variant Market Research is expected to reach $ 3.628 billion [4]. Thanks to the Reprap project, many ordinary users, hobbyists and people in need to produce any parts themselves in their home or office can fabricate a 3D printer. Even about three years after the start of the project, many companies have been able to spread the technology to a wider user mass by taking advantage of the Reprap project to produce relatively low-cost and sell open source 3D printers [1]. According to Berman's study, the waste material in 3-D printing technology is reduced by 40% in comparison to machining/subtractive technologies. Furthermore, 95% - 98% of waste material can be recycled in 3-D Printing. In addition, the subtractive technologies such as machining can remove as much as 96% of the raw material when creating a product. In terms of the cost per part in mass production, the 3D printing technology doesn't have much advantage than injection molding and machining as yet [5].

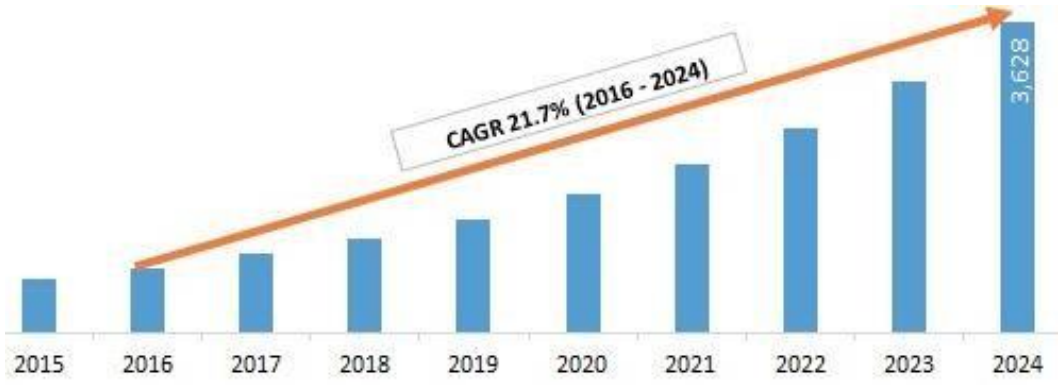


Figure 1. Global Automotive 3D Printing Market Size and Forecast, 2015 - 2024 ($ Million) [4]

3D printers can be built using many different technologies. Nowadays, the most popular method is material extrusion method which is a stacking technology and also known as Fused Filament Fabrication (FFF). Thermoplastic polymer materials (PLA, ABS) which can be formed by heat are used in this method. The heated material (filament) is extruded and the desired parts are produced with the principle stacking layers together in the FFF technology as shown

in Figure 2. The parts which have high strength are achieved with this technology, if the material of filament is plastic. In other respects, in FFF technology, it is quite troublesome to produce stalactite suspended structures in the air. In such situations, support structures are used to carry the bulk of the mass on the stalactite suspended structures [2-6].

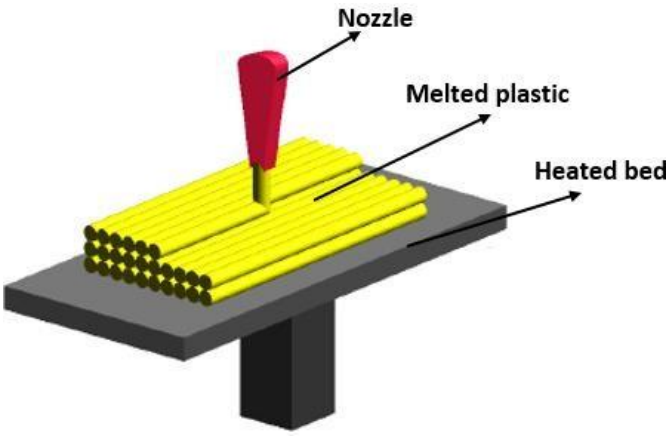


Figure 2. The operation method of the material extrusion process [6]

Acrylonitrile butadiene styrene (ABS) is a light and hard polymer widely used in products produced by molding. Its chemical formula is $(C_8H_8.C_4H_6.C_3H_3N)_n$. Pipes, automotive parts, protective helmets and toys (e.g. Lego) are just a few of its usage areas [4]. Poly (lactic acid) (PLA), one of the biodegradable polymers, is used in the field of medicine, wrapping, packaging and textile very effectively. There are various differences between PLA and ABS as shown in Table 1. The most important difference is that the filament from PLA is abundant, natural and renewable resource, nevertheless, ABS is petroleum based plastic. Thus, PLA is more harmless than ABS for human health. Second difference is that, it is necessary to heat the print bed to higher degrees when using ABS as a filament material since the ABS is more influenced by the temperature difference. Because of the lower printing temperature, when the PLA is properly cooled down, it is possible to print more sharp edges and features compared to ABS [4, 5]. The other difference is that PLA is generally used if the form is more critical than the function, because PLA is less stretchy than ABS. However, ABS has higher flexural strength and better elongation properties [6-9].

Table1. Comparison of PLA and ABS properties

Type of filament	Resource	Mechanical behavior	Print bed temperature	Printing temperature	Common Products
PLA	Organic	Brittle	20-60°C (optional)	180-230°C	Lego, automotive parts, electronic housing etc.
ABS	Petroleum-based	Ductile	80-110°C (mandatory)	210-250°C	Cups, plastic bags, cutlery etc.

1.1 Types of FFF 3D Printers

Delta and cartesian printers are the most popular FFF 3D printers on the market. However, there are important differences between the two. For instance, the delta 3D printer usually has a circular print bed that is immovable, because its natural shape is circle. On the other hand, the cartesian printer has a rectangular print bed. The volume of the 3D printer and its bottom surface area (print bed) need to be increased when printing large parts, thus the moving parts of the cartesian printer heavier than the moving parts of delta printer. This situation influences sensitivity of positioning. At the same time, the fact that each element can move only in one direction for the cartesian printer affects the sensitivity of positioning. In the delta printer, the nozzle head can move in any direction quickly. Therefore, on the contrary to the cartesian printer, the delta printer is preferred to print large and big parts [10-12].

Moreover, the nozzle head of the cartesian printer can move only in X and Y axes. The z axis represents the direction in which the surface area can move. Unlike the cartesian printer, the delta printer moves the nozzle in X, Y, Z axes as shown in Figure 3. Hence, calibration of the delta 3D printers becomes more troublesome [11, 13].

In a study, in vase mode, print speeds of the delta and cartesian 3D printer have been compared. Cartesian printers achieve print speeds of up to 200 mm / sec, while delta printers have a speed of 350 mm / sec. The biggest reason of this situation is that the positioning speed and sensitivity of the nozzle in the delta printer is better than the cartesian printer [13].

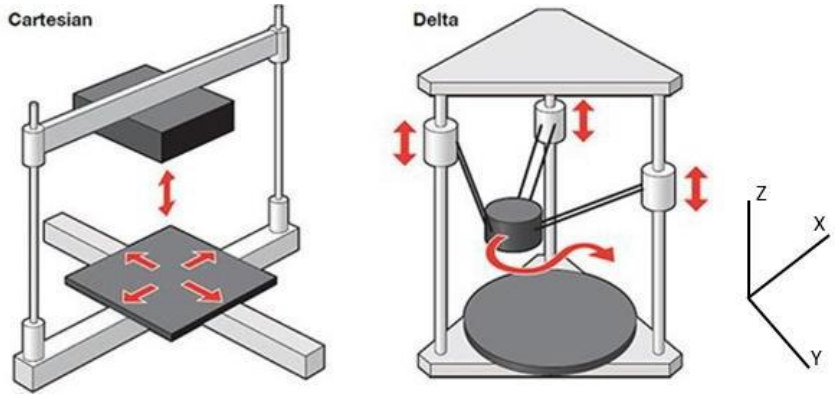


Figure 3. Cartesian and delta printer [11]

Laplume et al. (2016) have studied on differences between MOST Prusa RepRap (Cartesian Printer) and MOST Delta RepRap Printers. Their study shows capital cost of the delta printer (400$) is lower than the cartesian printer (575$) as shown in Table 2. Also, the energy consumption to warm up the printer and for movement of axes is lower in the delta printer [12].

Table 2. Comparison of the delta printer and the cartesian printer [10-13]

Type of Printer	Capital cost ($)	Weight	Print speed	Sensitivity of positioning	The nozzle movement axes	Calibration
Delta Printer	400	Light	High	High	X,Y,Z	Difficult
Cartesian Printer	575	Heavy	Medium	Medium	X,Y	Easy

In this study, a delta type FFF printer is developed due to its above-mentioned advantages over the cartesian type printers. Furthermore, it is aimed to develop a large-scale printer to be able to print large parts with high accuracy, which differs from the existing delta type FFF printers in the literature. For this purpose, the product architecture of a delta type FFF printer is investigated first and details are provided in Section 2. Then, the development process of the large-scale printer is described in Section 3. An accuracy study is carried out and many challenging parts are produced and the results are given in Section 4. The challenges during the development process and the solutions suggested are explained in Section 5 and the conclusions are given in Section 6.

2. PRODUCT ARCHITECTURE

In the production process of a part using a delta type FFF printer, some steps should be followed as shown in Figure 4. First, a computer-aided design (CAD) file of the 3D model is created in “STL” file format. Afterwards, this file is sent to the slicing software which slices the 3D model to the thin layers and creates g-codes for these layers. These g-codes are sent to the controller (Arduino Mega). A Ramps 1.4 board is used together with Arduino which controls to electronic components such as servo motors. A few steps should be taken while printing a product from 3D printer.

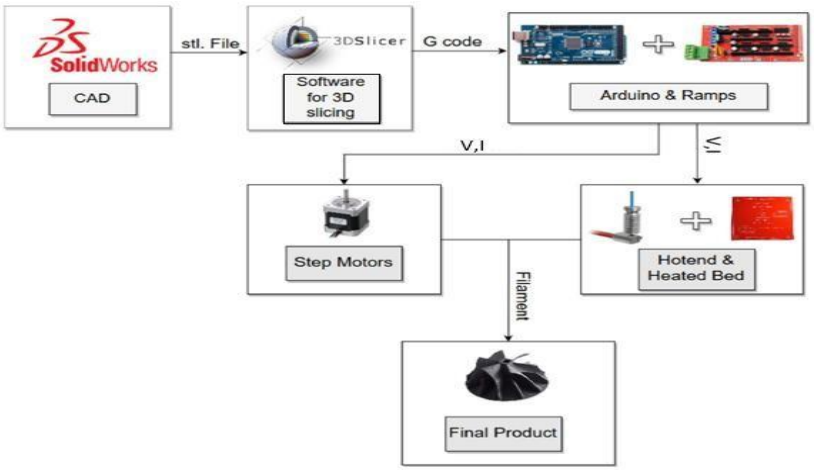


Figure 4. Operational flowchart of a delta type FFF printer

Step I: Designing the part to be printed

The CAD file formats such as part file (.prt), step file (.step) and Catia model file (.model) can be created using 3D modeling program such as Autocad, Solidworks, Catia, Simens NX etc. Then, the CAD file is converted to an STL file, which is the format that is sent to the slicer software tools such as Cura, Simplify 3D or 3D Slicer.

Step II: Generating G-code

G-code is created to determine the printing process of a product using a 3D printer. The generated G-code includes the type of movement of the nozzle head, setting units toinches/millimeters, setting absolute/relative positioning etc.. Also, there are M commands to indicate program end, enable/disable all stepper motors, turn off bed, turn off extruder etc..The definitions of some important G and M commands are listed in Table 3.

Table 3. Common G and M codes for 3D printer

G0	Rapid move
G1	Linear motion at feed rate
G4	Pause the printer for a period of time
G28	Move to origin
G90	Set to absolute positioning
G91	Set to relative positioning
M2	Program end
M17	Enable all stepper motors
M18	Disable all stepper motors
M104	Set extruder temperature

Step III: M**otor control**

The operation of a 3D printer needs motors with low torque and high accuracy, so the best motor to do this function is stepper motor. It is an electromagnetic device that converts digital pulses into mechanical shaft rotation. Advantages of step motors are low cost, high reliability, and high torque at low print speeds. They are also a special type of the synchronous motors which are designed to rotate a specific number of degrees for every electric pulse received by its control unit. In a delta type 3D printer, four stepper motors are needed to do the specific function, three of them are used for moving in X, Y, Z direction of the printer head, the 4th one is needed to move the filament.

Step IV. Printing

The final step is to print the product using ABS or PLA. The dimensions of the 3D printer must be introduced to slicer software tools before printing product. Also, process parameters determining to quality of product, printing time and density of the product should be regulated. Thereafter, the product in desired size can be printed by the delta printer.

3. DEVELOPMENT OF THE DELTA TYPE FFF 3D PRINTER

3.1. Mechanical design of the developed FFF printer

3D printers have several main design requirements such as mechanical design, kinematic analysis, and control system. In order to run the delta type 3D printer and produce the product, mechanical design must be done before creating the kinematic analysis and control system of the system. Therefore, the structural parts that create the basic shape of the printer and carry moving parts must be designed. These are principally aluminum profiles, angle brackets, linear rail system, carriage, carbon fiber rods and effector as shown in Figure 5. The definitions of the numbered components in Figure 5 are given in Table 4.

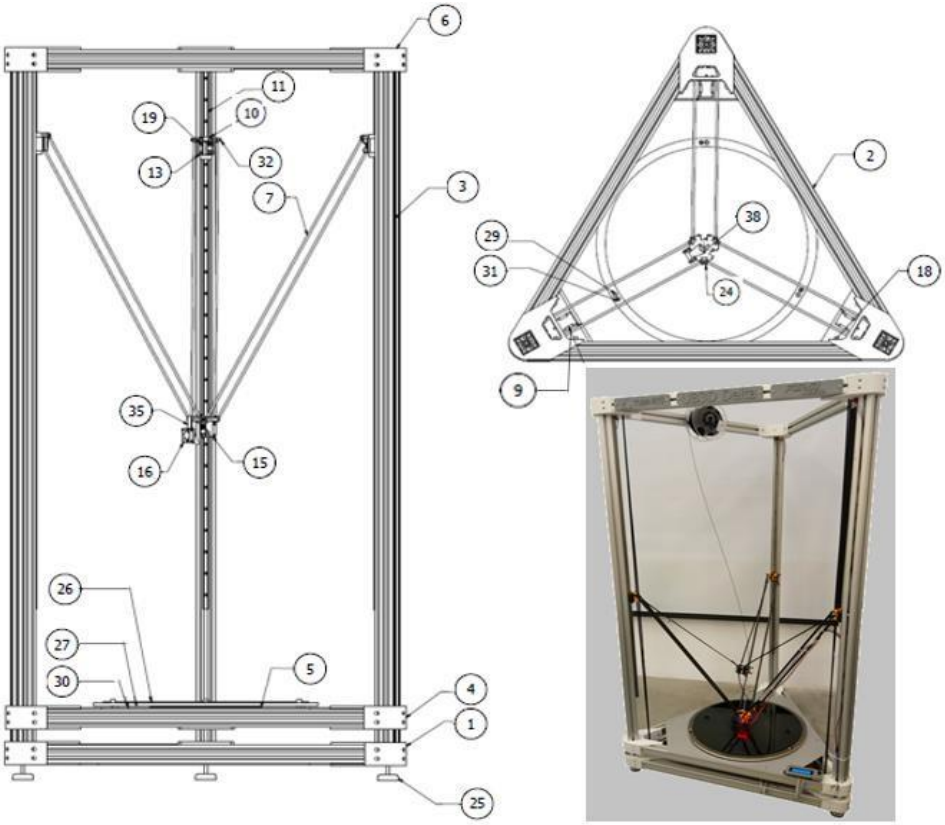


Figure 5. 3D CAD model of delta 3D printer

Aluminum sigma profiles given by number 3 in Figure 5 create the main frame of the printer

and carry the rail system. Therefore, in the development process of the delta type printer, first, the aluminum profiles were designed by considering the main dimensions of the printer. There are three different type of brackets used in this system, which enable the connections of the aluminum profiles, such as top, middle and bottom brackets, shown by numbers 6, 4, and 1 in Figure 5, respectively. These brackets provide enough support and rigidity. They are designed on a commercial CAD software Solidworks by accounting for the geometry of the aluminum profiles. These customized angle bracket designs are manufactured using PLA material in a cartesian type FFF printer. Also, linear rail system consists of stepper motor, timing belt, rods, effector and carriage, shown by numbers 7, 9, 13, and 14 in Figure 5, respectively. The carriage is used to carry rods from carbon fiber and PLA-made effectors. This rail system is moved by three different stepper motor and timing belt. It is connected to the aluminum profiles with hammer nuts. Detailed descriptions of the parts shown in Figure 5 are mentioned in Table 4.

Table 4. Bill of materials of delta printer fabricated

ITEM	QTY	PART NAME	DESCRIPTION
1	3	Bottom Angle Bracket (60 degrees)	3D Printed
2	9	50x50x850mm Sigma Profile	
3	3	50x50x2000mm Sigma Profile	
4	3	Mid Angle Bracket (60 degrees)	3D Printed
5	1	300x300mm Heated bed	
6	3	Top Angle Bracket (60 degrees)	3D Printed
7	6	900mm Carbon Fiber Rod	ID:8mm, OD:10mm. Ball Joints are included
9	3	Step Motor	Nema 17
10	3	HGH15CA	
11	3	[Z] HGR15R	
13	3	Carriage	3D Printed
14	1	Effector	3D Printed
15	1	Hot End Holder	3D Printed
16	2	FAN 40x40x10	
17	18	AS 1420 - 1973 - M5 x 30	ISO metric hexagon socket head cap screws
18	12	AS 1420 - 1973 - M5 x 20	ISO metric hexagon socket head cap screws
19	12	AS 1420 - 1973 - M4 x 12	ISO metric hexagon socket head cap screws
20	1	AS 1420 - 1973 - M3 x 14	ISO metric hexagon socket head cap screws
21	1	Cooling Fin	
22	1	Jhn_nozzle_v4(1.75m)	
24	6	AS 1420 - 1973 - M4 x 16	ISO metric hexagon socket head cap screws
25	3	Support	
26	1	Glass	Ø550mmx6mm
27	1	Aluminium Plate	Ø600mmx10mm

29	3	AS 1420 - 1973 - M8 x 30	ISO metric hexagon socket head cap screws
30	1	Sheet Metal	3mm thickness
31	3	AS 1421 - M12 x 20 Cup Point	ISO metric hexagon socket set screws
32	6	AS 1420 - 1973 - M4 x 25	ISO metric hexagon socket head cap screws
33	6	AS 1112 - M4 Type 5	ISO metric hexagon nuts, including thin nuts, slotted nuts and castle nuts
34	3	AS 1112 - M8 Type 5	ISO metric hexagon nuts, including thin nuts, slotted nuts and castle nuts
35	1	Nozzle Fan Holder	3D Printed
36	3	AS 1112 - M3 Type 5	ISO metric hexagon nuts, including thin nuts, slotted nuts and castle nuts
37	2	AS 1420 - 1973 - M3 x 20	ISO metric hexagon socket head cap screws
38	5	AS 1420 - 1973 - M3 x 16	ISO metric hexagon socket head cap screws
39	39	AS 1420 - 1973 - M4 x 20	ISO metric hexagon socket head cap screws

3.2. Kinematic analysis of the developed FFF Printer

In a cartesian printer, the mechanism moves along the rails independently of each other in the x, y, and z directions. With a delta configuration, it's not that simple. Moving any of the three vertical carriages upward and downward causes the nozzle head to move simultaneously in x, y, and z. Therefore, it isnecessary to calculate how each of three carriages will move in order to move the nozzle head to the right place [14].

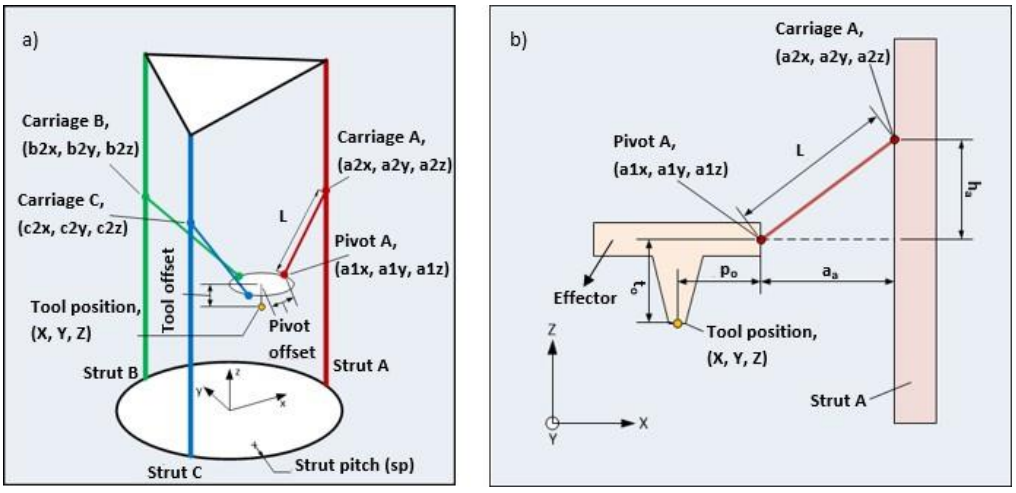


Figure 6. a) Delta printer diagram, b) Positioning of the carriage and effector

The delta robot has three columns as shown in Figure 6. These columns are called as A, B,

and C. Each column has a carriage that can move up and down on the column. Each carriage has two parallel arms which connect to the effector platform. It is crucial that each of the parallel arms (rods) is the same length and the platform of the effector must be parallel to the print bed in order to print correctly. In accordance with this purpose, the distance between the junction of the each carriage with columns and effector platform must be the same. Thus, the nozzle head moves parallel to the print bed when designed in this way [15].

After the rods, carriages and platform of the effector are positioned correctly, the positions of the carriages must be calculated by kinematic analysis so that the nozzle head can move to the desired point on the print bed. It is shown in Equations (1), (2), and (3).

$$\begin{aligned} a_{2z} &= Z + t_0 + \sqrt{L^2 - {a_a}^2} \\ &= Z + t_0 + \sqrt{L^2 - (a_{2x} - a_{1x})^2 - (a_{2y} - a_{1y})^2} \\ &= Z + t_0 + \sqrt{L^2 - \left(s_p - (X + p_0)\right)^2 - (0 - Y^2)} \\ &= Z + t_0 + \sqrt{L^2 - \left((s_p - p_0)^2 - 2\left(s_{p-}p_0\right)X + X^2\right) - Y^2} \end{aligned} \tag{1}$$

$$\begin{aligned} b_{2z} &= Z + t_0 + \sqrt{L^2 - {a_b}^2} \\ &= Z + t_0 + \sqrt{L^2 - (b_{2x} - b_{1x})^2 - (b_{2y} - b_{1y})^2} \\ &= Z + t_0 + \sqrt{L^2 - (s_p cos120° - (X + p_0 cos120°))^2 - (s_p sin120° - (Y - p_0 sin120°))^2} \end{aligned} \tag{2}$$

$$\begin{aligned} c_{2z} &= Z + t_0 + \sqrt{L^2 - {a_c}^2} \\ &= Z + t_0 + \sqrt{L^2 - (c_{2x} - c_{1x})^2 - \left(c_{2y} - c_{1y}\right)^2} \\ &= Z + t_0 + \sqrt{L^2 - (s_p cos240° - (X + p_0 cos240°))^2 - (s_p sin240° - (Y - p_0 sin240°))^2} \end{aligned} \tag{3}$$

Equations (1), (2), and (3) are analyzed in MATLAB^{TM} to obtain final position of the nozzle head. For example, the nozzle head moves from (0, 0, 0) to (150, -150, 300) with 200 mm/s velocity and 2000 mm/s^2 acceleration/deceleration. The Figure 7 shows the final position of the nozzle head.

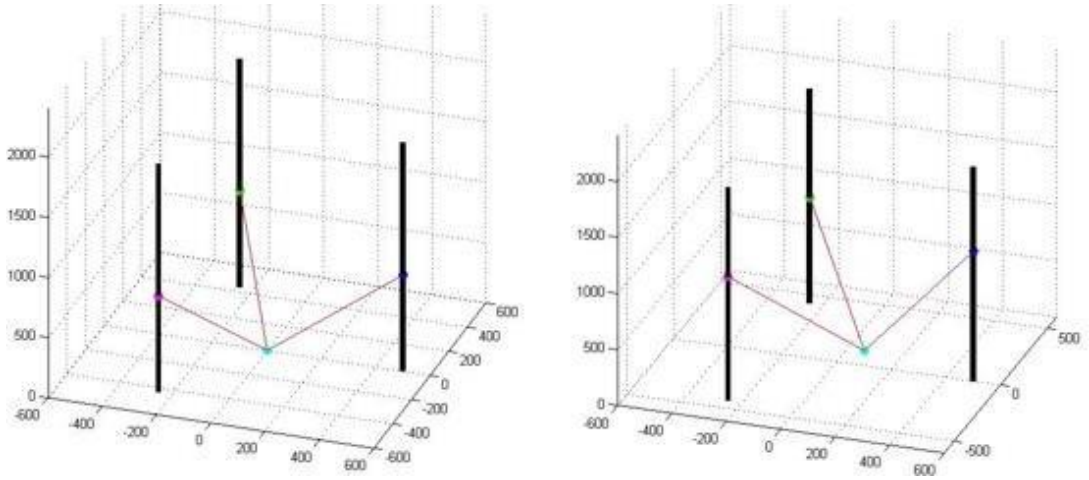


Figure 7. Matlab graphs of the position of the nozzle head at a) (0, 0, 0) and b) (150, -150, 300)

3.3. Control system of the developed FFF Printer

The diagram shown in Figure 8 points the detailed relationships between all electrical components such as Arduino Mega 2560, RAMPS 1.4 (RepRAP Arduino Mega Pololu Shield), A4988 Motor drivers (x4), 12v PSU, NEMA 17 step motors (x4), hot end and heatbed. The ATmega2560 (datasheet) is an Arduino based card. There are 54 digital I / O pins. 14 of them can be used as PWM output. PWM (pulse width modulation) is a way to control analog components using digital signals. Also, there are 16 analog inputs, 4 UART (serial port), 16 MHz crystal oscillator, USB connection, an adapter input, an ICSP output and a reset button.

The system takes the power from main supply and a direct current power supply regulates this power to send it to the controller. After that Arduino sends digital, PWM and analog signals to Ramps board. Ramps board uses these signals and controls the current from the dc power supply. All electronic components use this current to work.

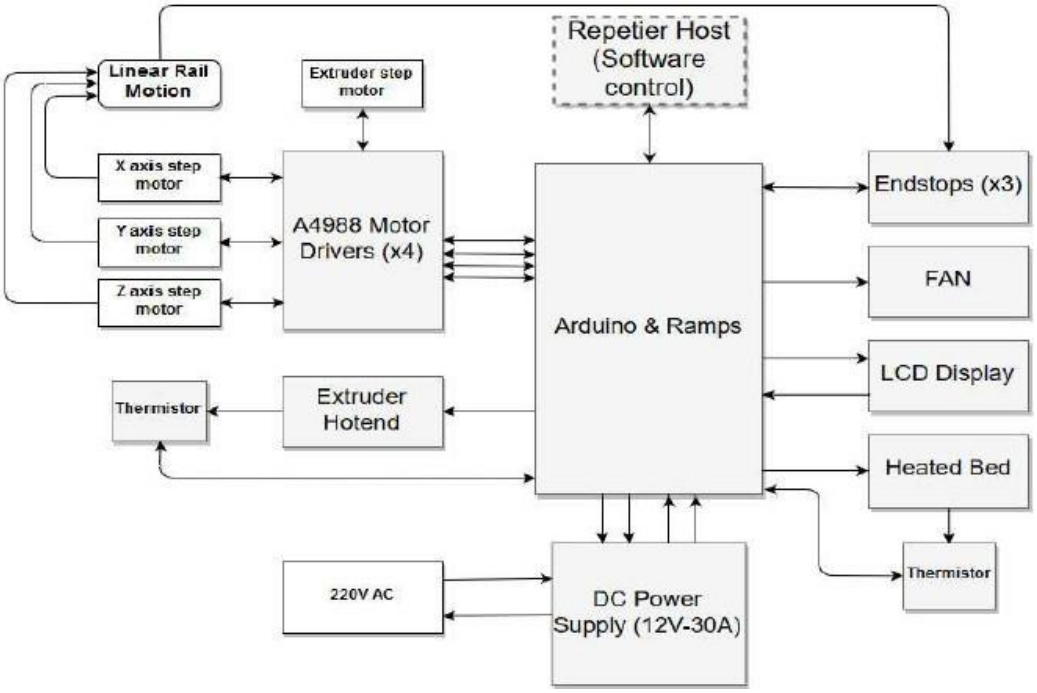


Figure 8. Electronic system diagram

3.4. Specifications of the developed delta type FFF printer

The developed 3D printer has a delta head and large build volume. Therefore, it has unique design compared to other 3D printers in the literature. The final specifications of the developed 3D printer are given in Table 5.

Table 5. Specifications of delta printer manufactured

Technology	Fused Filament Fabrication (FFF)
Control system	Arduino based control system, open source control software
Print head	Single
Maximum speed (mm/s)	200
Printer dimensions (mm)	1050 X 950 X2050
Build volume (mm)	500 diameter X 750 height
Nozzle temperature (°C)	280
Supported materials	ABS, PLA, PLA+
Noise level (dB)	65
Weight (kg)	90
XY resolution (mm)	0.03
Z resolution (mm)	0.06

4. PRINTING RESULTS

Several parts have been printed in different sizes by the developed delta type FFF 3D printer. First, a dimensional deviation analysis has been performed on 20*20*20 mm cubes, which are placed in different positions on the print bed, as shown in Figure 9. It is observed that deviation values are between 1.1%-0.1% in X axis, 2.5%-0.75% in Y axis and 2%-0.4 in Z axis. Table 6 shows the results of the dimensional deviation occurred in X, Y, Z axes.

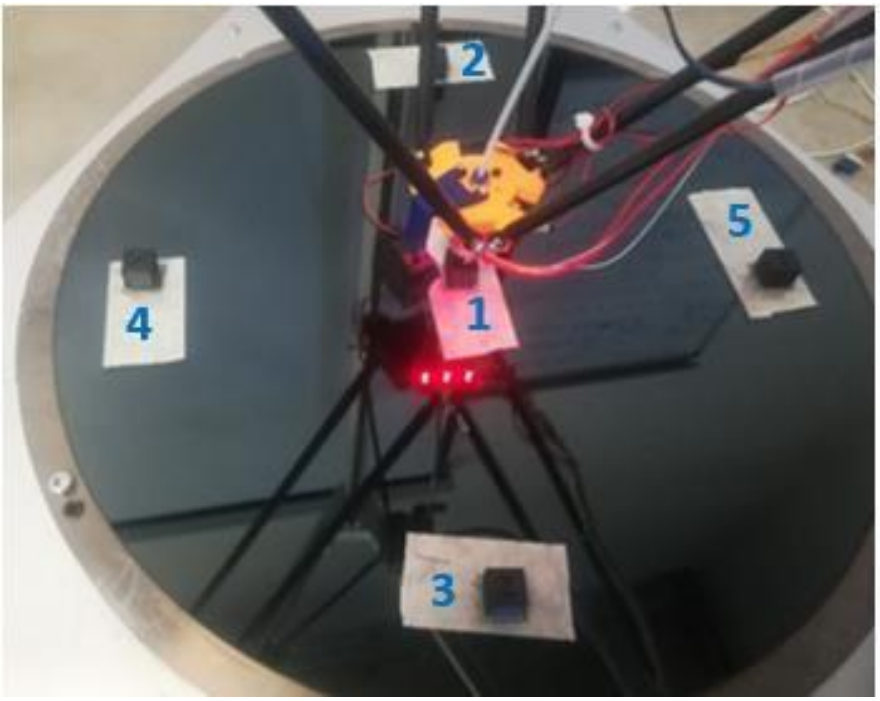


Figure 9. Cubes printed for dimensional deviation analysis

Table 6.Dimensional deviation values in X, Y, Z axes

Zone	Location		Actual Dimensions			Dimensions of Printed Part			Dimensional Deviation		
	X-coordinate (mm)	Y-coordinate (mm)	in X axis (mm)	in Y axis (mm)	in Z axis (mm)	in X axis (mm)	in Y axis (mm)	in Z axis (mm)	in X axis (%)	in Y axis (%)	in Z axis (%)
1	0	0	20	20	20	19,98	19,78	20,18	0,1	1,1	0,9
2	0	-220	20	20	20	19,98	20,15	20,08	0,1	0,75	0,4
3	0	220	20	20	20	19,86	19,62	20,14	0,7	1,9	0,7
4	-220	0	20	20	20	19,78	19,96	20,4	1,1	0,2	2
5	220	0	20	20	20	20,04	19,5	20,25	0,2	2,5	1,25

As can be seen from Table 6, the dimensional deviations of the printer parts compared to the actual dimensions are mostly less than 1.1%. In some cases (such as the Y axis deviation of

Zone 3, Y axis, and Y and Z axes of zone 5 those are less than 2.5%. These results show that the developed 3D printer can accurately print parts at any location of the 3D printer on XY plane.

Once the geometric deviation study has been completed, then various parts have been manufactured by the developed printer. First, small parts have been manufactured by the developed delta printer, then moved on to larger parts which can take up to 35 hours to print. The herringbone gear with an outer diameter of 70 mm and a thickness of 10 mm shown in Figure 10(a) has been printed in 3.5 hours using the nozzle with 0.4 mm radius. The spiral vase with a height of 300 mm in Figure 10(b) has been printed in 4.5 hours using the nozzle with 0.8 mm. It was printed in the vase mode at 200 mm/s print speed. The Eiffel tower with a height of 500 mm in Figure 10(c) has been printed in 26 hours using a nozzle with a radius of 0.8 mm. Although it has very small features, the developed printer was able to print those without any issues. The cylindrical hollow part shown in Figure 10(d) was printed in 36 hours using the nozzle with 0.4 mm radius. This part has a height of 650 mm which is used to test if the developed printer can print high parts in Z direction. This part is also designed using lattice structures with strut members having circular cross sections with a constant dimeter of 5 mm to have a lightweight design. It was shown by printing this part that the developed printer can manufacture large components with high complexity such as lattice structures with interconnected strut members.

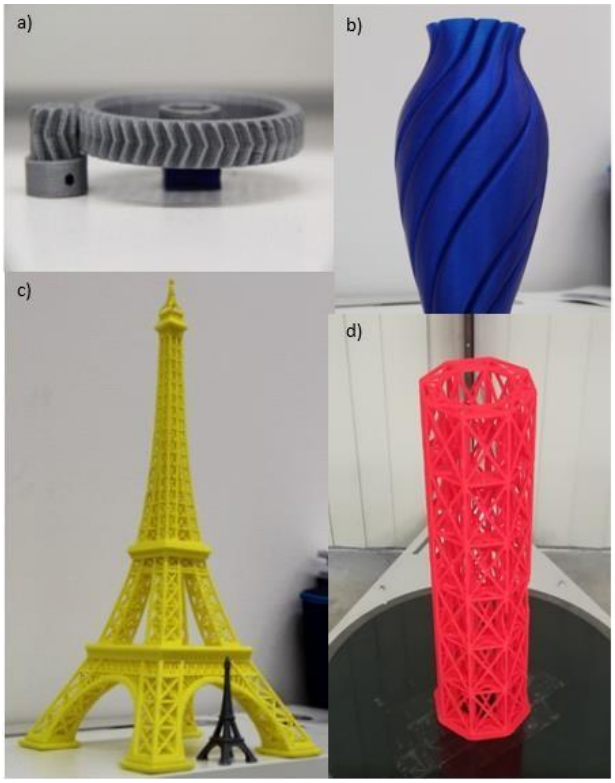


Figure 10. Sample parts printed by the developed delta printer

5. CHALLENGES IN THE DEVELOPMENT OF THE PRINTER

Some challenges have been encountered while developing 3D delta printer. Vibration is the most important problems occurred during the printing. Vibration mostly occurs due to height of the printer. Some head movements can resonate the system and magnify the vibration. As a result of vibration, waviness can be seen at the printed layer. To overcome this problem, the printer has been made rigid as much as possible. Another problem encountered is that the power of the extrusion becomes insufficient. When the Teflon tube is too long, the buckling between extruder system and cold end of the extruded filament has been occurred and in this case, the movement of the filament in the Teflon tube becomes more difficult. To solve this problem, the extrusion motor has been relocated by making a design change. Length of the Teflon tube is shortened by moving the extrusion system closer to the effector. This reduces the additional buckling in the Teflon tube. Therefore, required force for pushing the filament inside of the tube is decreased. Also the position of the potentiometers are adjusted, torque of the stepper motors are increased by 20%. Thus, sufficient power could be provided for the extrusion.

Moreover, initially, a fixed printing surface has been designed but the printing surface was not horizontally placed. Since the printing surface was fixed, no changes could be made to adjust its leveling setting. For this reason, the printing surface caused an inconsistent first layer of the print, which lead to failures in printing in later stages of the process. To address this issue, the printing plate redesigned in a way that its leveling setting can be adjusted by rotating the set screws on it.

The last challenge encountered during this study was stringing issue when the nozzle moves from one part of the print to another. To overcome problem, the retraction speed between two printed areas and excessive hot end temperature must be increased.

6. CONCLUSION

In this study, a large-scale delta type FFF 3D printer is developed and components with various sizes and complexities are modeled and manufactured to show its efficacy. The results showed that the developed printer can manufacture large scale parts with high accuracy. Some issues have been encountered during the development process such as the insufficient power of the extrusion, uneven printing surface, and the stringing issue. These issues are solved by making additional modifications on the design of the printer. As a result, it was possible to print with a dimensional error below 2.5% after the mentioned problems have been solved.. The dimensional tolerance of the 3D printers in the literature is also below 4%, which show that the developed printer can achieve better tolerance values than the existing printers. Unlike the

existing FFF 3D printers in literature, the developed printer, namely, UB3D, have a larger print volume and can manufacture large scale parts with high accuracy.

ACKNOWLEDGEMENTS

The authors would like to express their deepest gratitude to the undergraduate students Batihan SENER, Dogukan TURAN, Mehmet Emin CAGIL and Uluc PINAR due to their efforts for realization of this work. Advanced Manufacturing Laboratory Technician, Kamil ARSLAN, is gratefully acknowledged. This study was supported by Form Makina A.Ş.

REFERENCES

1. **Hao, L.J., (2014),** "3D-Printing: the Future of Manufacturing", https://junhaolimtwc.wordpress.com/2014/03/19/individual-report-draft-2/, date accessed: 15.02.2018.

2. **Roberson, D.A., Espalin, D., Wicker, R.B., (2013),** "13D Printer Selection: A Decision-Making Evaluation and Ranking Model", Virtual and Physical Prototyping, 8(3), 201-212.

3. **Braankeri G.B., Duwel, J.E.P., Flohil, J.J., Tokaya, G.E., (2010),** "Developing a Plastics Recycling Add-on for the RepRap 3D printer".

4. **Variant market research, (2016),** "Automotive 3D Printing Market Overview", https://www.variantmarketresearch.com/press-release/global-automotive-3d-printing-market-is-estimated-to-reach-usd-3628-million-by-2024-says-variant-market-research, date accessed: 22.02.2018.

5. **Berman, B., (2012),** "3D Printing: the New Industrial Revolution", Business Horizons, 55(2), 155-162.

6. **Santos, R., James, J., Chris, T:, Marshall, S., Maalouf, P., (2015),** "Deltronic Solutions", Senior Project, Cal Poly IME Department, America.

7. **Rohringer, S., (2017),** "PLA vs ABS: Filaments for 3D Printing Explained & Compared", https://all3dp.com/pla-abs-3d-printer-filaments-compared/, date accessed: 01.03.2018.

8. **Tymrak, B.M., Kreiger, M., Pearce, J.M., (2014),** "Mechanical Properties of Components Fabricated with Open-Source 3-D Printers under Realistic Environmental Conditions", Materials & Design, 58, 242-246.

9 .**Ferreira, R.T:L., Amatte, I.C., Dutra, T.A:, Burger, D., (2017),** "Experimental Characterization and Micrography of 3D Printed PLA and PLA Reinforced with Short Carbon

Fibers", Composites Part B: Engineering, 124(1), 88-100.

10. **Tractus 3D company report, (2018),** "3D Printing Technology Delta versus Cartesian", https://tractus3d.com/3d-printing-technology/#, date accessed: 05.03.2018.

11. **Alex, M., (2017),** "The 4 Types pf FFF/FDM 3D Printer Explained (Cartesian, Delta, Polar)", https://www.3dnatives.com/en/four-types-fdm-3d-printers140620174/, accessed date: 11.03.2018.

12. **Laplume, A., Anzalone, G.C., Pearce, J.M., (2016),** "Open-Source, Self-Replicating 3-D Printer Factory for Small-Business Manufacturing", The international Journal of Advanced Manufacturing Technology, 85(1-4), 633-642.

13. **Plasticwrap3d, (2017),** "3D Delta vs Cartesian High Speed Print Test", https://plasticwrap3d.wordpress.com/2017/04/12/3d-delta-vs-cartesian-high-speed-print-test/, accessed date: 13.03.2018.

14. **Graves, S., (2018),** "Johann C. Rocholl (Rostock) Style - Delta Robot Kinematics", http://fab.cba.mit.edu/classes/863.15/section.CBA/people/Spielberg/Rostock_Delta_Kinematics_3.pdf, accessed date: 20.03.2018

15 **Scary Maths- Tiny gadgets, (2017),** "How to Convert from x,y,z Coordinates to Delta Robot Position", http://robinsonia.com/wp/?p=161, accessed date: 21.03.2018

ADDITIVE MANUFACTURING OF THE MILITARY ORIENTED MEDICAL DEVICES WITH STEREOLITHOGRAPHY METHOD

Erdem İnanç BUDAK, ebudak@*etu.edu.tr* TOBB University of Economics and Technology, 06560, Ankara, Turkey

Osman EROĞUL, erogul@*etu.edu.tr* TOBB University of Economics and Technology, 06560, Ankara, Turkey

ABSTRACT

The additive manufacturing have been used by researchers in academy, engineers in industry and other users for consumer products over the 30 years. On the contrary of machining, additive manufacturing has some serious advantages which are production complexity, process speed, less swarf during manufacturing and nullary operation to setup manufacturing. In addition to various material which is using in additive manufacturing make possible for production in medical sector with additive manufacturing technologies. In this study an additive manufacturing technique, which is stereolithography, have been used to produce a military oriented medical device. 5 different version have been designed and one useful prototype have been produced with downward stereolithography printing using with photopolymer resin. The developed medical device, which is called military tourniquet system, is a smart system which can communicate with GPS, GSM and Bluetooth for different task. Thanks to the system's robust structure, injured person can be applied the system both are their arm and leg extremities. When the system starts, the required force is applied on the injured extremities, then the injured location information, the tourniquet force and application time information is sent a central to inform injured health conditions and call a medics or first aid teams. The smart tourniquet system is not only use in the military field but also it can use in civilian area to prevent emergency injuries.

Keywords: Additive manufacturing, stereolithography, medical device, smart tourniquet, extremity injury

1. INTRODUCTION

3D printing, which is also called as additive manufacturing (AM), is a production method which manufacture a designed model as layered-by-layered to overcomes the limitations of machining techniques with saving time and low-cost production of 3D printing techniques [Berman, 2012]. Especially, it is possible to make many revisions quickly at the prototyping stages without passing to the serial production stage of the products which will be produced, and to allow the industrial design can be completely changed until producing the final product, cause preferring AM. In the era of Industry 4.0, where technology developed at an incredible rate, AM techniques have increased using frequency over the last few years by reaching wider masses due to lower costs.

The eventual construction time depends on the specific method used, as well as the size and complexity of the model [Rengier et al., 2010]. On the contrary of CNC machining, AM systems can fabricate parts of almost any geometrical complexity in relatively lower time and with reduced cost and without significant requirements in technical expertise [Giannatsis and Dedoussis, 2009].

AM is performed directly from a 3-D CAD file in which a part's model is stored. The usual file format is STL. The STL file is imported into a specific software, where it is pre-processed. The part is oriented for building and a support structure is made for the part's surfaces that are facing down. Afterwards, cross-sections of a given thickness, known as 'slices', are generated from 3-D CAD descriptions of the part and support structures. The slices are saved in a slice file. After pre-processing, the slice file is sent to the machine to be 'printed' slice-by-slice. The fabrication process consists of two basic steps: coating and fusing. The coating step is the process in which material is laid over the working surface forming a very thin layer. The thickness of the layer depends on the chosen technology and is in the range of 0.025 mm to 0.20 mm. The fusing step refers to the process of printing the part slice by the action of a source of energy. The active principle can be a light source, laser beam or electron beam. It acts over the layer of material and produces fusion, which fuses the part slice's footprint to the layer below it. Once fabrication is finished, the part is taken out to be cleaned of material that is not fused and, if necessary, to be given further post-processing. The most common post-processing techniques are solvent bathing, sanding, polishing, homogenization, thermal treatment, etc [Petrovic et al., 2011].

In AM technologies, there are three common techniques with 3D printers. These techniques are given below respectively.

1) FDM – Fused Deposition Modeling: FDM is the most preferred technique in AM. 3D printers, which are using FDM technique, use thermoplastic material to produce a designed

model where the material melts and pastes above the layers that construct the model. FDM printers have a nozzle which melts the thermoplastic material and pour on the layers. The nozzle sensitivity's depends on liquid material density after melting process. For this reason, FDM is preferred for prototyping and hobby purpose production due to lack of resolution in a unit area, whereas FDM is a good solution according to their production speed. Due to the fact that FDM products have lower resolution, the AM manufacture has worse surface quality. Particularly, this AM technique is not preferring for mass-production [Formlabs, 2018a].

Other methods which are the laser-based processes can be distinguished in two sub-categories, depending on the phase change mechanism, namely laser polymerization (SLA – Stereolithography) and laser melting Selective Laser Sintering (SLS) [Bikas et al., 2016].

2) SLA – Stereolithography: SLA technique was presented to the world users as the first AM techniques in 1980. SLA still the most popular AM techniques and it is using in producing manufactures professionally as well as in industry. In SLA technique, a liquid photo polymeric resin is being cured and hardened by a laser power source to construct a 3D body. On the contrary of FDM technique, SLA can be reach high resolution thanks to laser curing technology. However, SLA technique use support to produce the designed model layer-by-layer for robustness. Thus, cured supports just are a garbage and they never use again. On the other hand, this technology products' surface are much better than fusing techniques. Moreover, SLA manufacturers specify SLA resin using with different material. Hereby different structures can be manufacture with one SLA printer. Accordingly, SLA printers can be use in professional prototyping [Formlabs, 2018a]. Because of this property SLA AM can be preferred end prototype before the mass production.

3) Selective Laser Sintering (SLS): SLS technique is generally use in industry which is preferring for especially metal AM as well as plastic material based on polymeric. Similar to SLA in SLS technique, a more powerful laser power supply cure polymeric powder layer-by-layer. After each curing period a specific thickness powder spread out on layer then a stripping knife slips off and presses built platform. Therefore, a printed model can be produced without supports. After printing process, the uncured powder has to be clean, then the SLS manufacture is completed [Formlabs, 2018a]. SLS printed parts have better mechanical properties than FDM and SLA, whereas prototyping with SLS technique can be reached high cost.

According to worldwide AM statistics, AM is using in 32% of motor vehicles, 18% of consumer products, 11% of business machines, 9% of medical application, 9% of academic studies, 8% of aerospace industry, 5% of military purpose, 8% of other areas [Bikas et al., 2016].

Medical applications for 3D printing are expanding rapidly and are expected to revolutionize health care. Medical uses for 3D printing, both actual and potential, can be organized into several broad categories, including: tissue and organ fabrication; creation of customized prosthetics, implants, and anatomical models; and pharmaceutical research regarding drug dosage forms, delivery, and discovery [Tuomi et al., 2014, Ventola, 2014]. Some medical devices serve with their functionality. Tourniquet is a medical device which has a case to cover their equipments. In this study a tourniquet case has designed and manufactured with AM.

The tourniquet is a medical device that has been used for a century and a half ago and that is being used to stop blood flow in amputee operations and to stop bleeding in the limb injuries. When lower extremity injured, 3 liters amount of blood can be lost during 10 minutes. Thus, extremity injured must be stopped urgently [Pienkowski and Barnett, 2010]. Tourniquets have only one purpose which is stopped bleeding, while they don't have any communication substructure. Especially in military, the injured location very important information who has to be known by headquarters, similar to any emergency case the injured location gives vital data about them.

With this motivation, researchers produced smart tourniquet systems which can be applied both their arm and leg extremity, sent; tourniquet application time, tourniquet application location and tourniquet application pressure information, and worked only one button for both military and civil area where they work in TOBB University of Economics and Technology at Biomedical Engineering Department. The developed tourniquet system has been funded by The Scientific and Technological Research Council of Turkey as a science – industry project which has "Military and Emergency Field Smart Tourniquet (Harp ve Acil Yardım Akıllı Turnikesi - HAYAT)" name and "0932.STZ.2015" project no. The project has been completed end of February 2018 and one of the project outputs in military area was named as Military Smart Tourniquet (MST) and other one was named as Emergency Smart Tourniquet System (ESTS). Both tourniquet cases have produced with AM, because of the best solution of today's technologies due to their manufacturing speed and endurance of cases. MST and ESTS are manufactured with downward SLA technic using 50 μm layer thickness.

2. MATERIALS AND METHODS

2.1. Designing of Military Oriented Medical Devices with Three Dimensional Manufacture Technics

MST is an electromechanical system as well as has a main purpose is applying tourniquet which is combined more than one equipment. MST's case has sealing tools to prevent water entrance inside. For these reasons, MST can only be produced with AM the reason why the

MST has a complex structure. The medical device of MST uses all AM advantages and it has been designed after five revisions for a prototype. The tourniquet case's design works were started three different concepts at the first version. These systems are given below in Figure 1.a belt pulled tourniquet system, in Figure 1.b belt wrapped tourniquet system, in Figure 1.c belt locked tourniquet system respectively. The tourniquet of first versions design are realized with SOLIDWORKS software as appropriate in real dimensions.

In the one of the first concept design version, the injured pulls the tourniquet from distal side of their wounded extremity to proximal in order to apply the tourniquet system and pull the belt where it is fixed in the tourniquet case to eliminate belt gap, then push the button on the case to initialize tourniquet system was aimed. When the system works, the device is starting to apply tourniquet on the injured extremity then bleeding is going to stop. This application ease to apply for upper extremity, whereas the injured most probably is hard to apply tourniquet their lower extremity due to lean their distal side of extremity. Thus, the concept was rejected due to application difficulties.

In the other one of the first concept design version, the injured pulls the tourniquet from distal side of their wounded extremity to proximal in order to apply the tourniquet system and push the button on the case to initialize tourniquet system, then the system wrap the tourniquet belt to eliminate belt gap where it is released before by the tourniquet was aimed. However, similar to first design concept, this concept was rejected due to same application difficulties.

In the last one of the first concept design version, the injured can apply the tourniquet on proximal of their extremity. In this concept one side of the tourniquet belt separate form the case. Hereby the tourniquet can don both right and left side of the extremity, then the separate belt binds the case with a special locking system. Afterward the injured presses the button on the case to initialize tourniquet system. Therefore, the system works and wraps on the tourniquet's pulley to eliminate belt gap at first, then applies the tourniquet on extremity. On contrary to previous concepts, this concept was accepted due to ease of application.

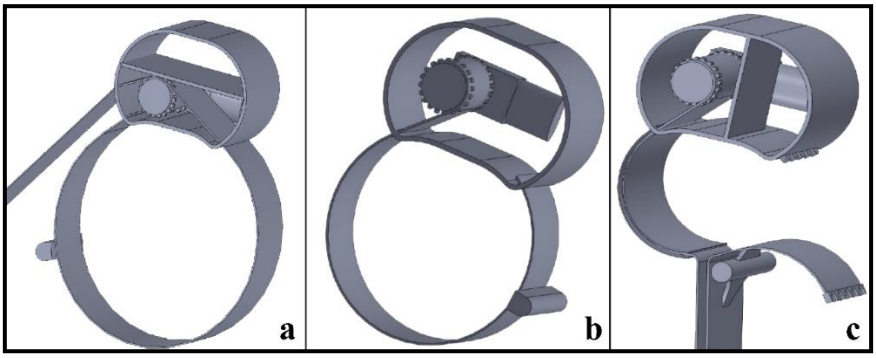


Figure 1. a Belt Pulled Tourniquet System, b Belt Wrapped Tourniquet System, c Belt Locked Tourniquet System.

After decided concept design, the concept design of working mechanism was realized for belt locked tourniquet system. After this phase the SIEMENS NX software has been used for designing the tourniquet system. Due to the fact that, it gives better results for engineering solution, provides ease of design with intersectional views, prepares real time simulations and kinematic analyze and especially provides ease of parametric designing this software was preferred. The second version of the belt locked tourniquet system (Figure 2) was designed with SIEMENS NX software as well as the concept of working mechanism which is a worm gear mechanism.

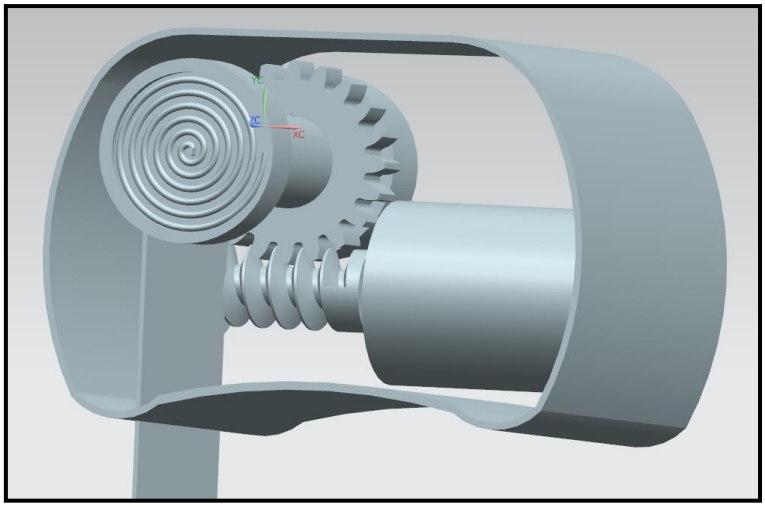


Figure 2. MST Second Revision Design

Studies done on belt locked tourniquet systems main body design to strengthen mechanical base by engineering calculations led to the development of the third version which is shown in Figure 3.a. In the third version a worm gear mechanism is designed, a motor is selected appropriate to the calculations, the pulley which the belt of the tourniquet is wrapped and tourniquet lock mechanism is designed. In the third version where the mechanical base is strengthened, a body design which consists of whole mechanical system is made also this structure's sealing gaskets which prevents liquids to enter the system are designed. The main body where the existing mechanical base will be kept has its dimensions decided.

In Figure 3.b the forth version of tourniquet system is given with transparency view. With revisions, the system's electronical substructure was improved, the system's user buttons were added, the system's electronical control card and case sealing cover was designed respectively. In Figure 3.c the forth version of tourniquet system is given with exterior view.

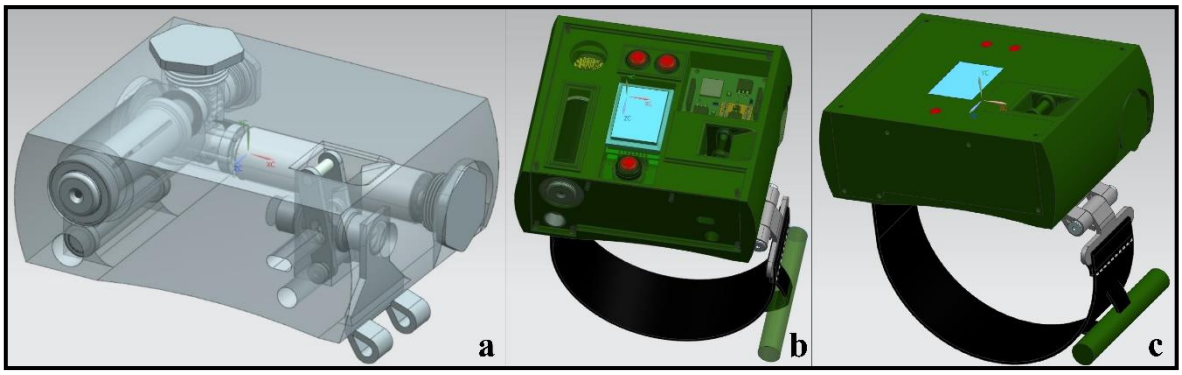


Figure 3. a MST Third Revision Design, b MST Fourth Revision Design Interior View, c MST Fourth Revision Design Exterior View

Belt locked tourniquet system fourth version is the first design to be prototyped. When the first prototype design is evaluated besides satisfying needs of both functionality and mechanic base some doubts are arised about the main function which is applying the tourniquet procedure. Appliance of the tourniquet got difficult due to the distance between the point where the belt is wrapped to the pulley and the point where the belts other end meets and locks to on the main body being approximately 127 mm long which is shown in Figure 4. Generally, perimeter of the lower extremity is bigger than perimeter of the upper extremity. Thus, the system can be used in lower extremity injuries but due to inapplicability caused by the small perimeter in upper extremity injuries causes the tourniquet to not be applied which leads to blood flow could not being stopped. As a result, a revision on design is made. In this direction the fifth version of the main body design, the output of the thesis, is made.

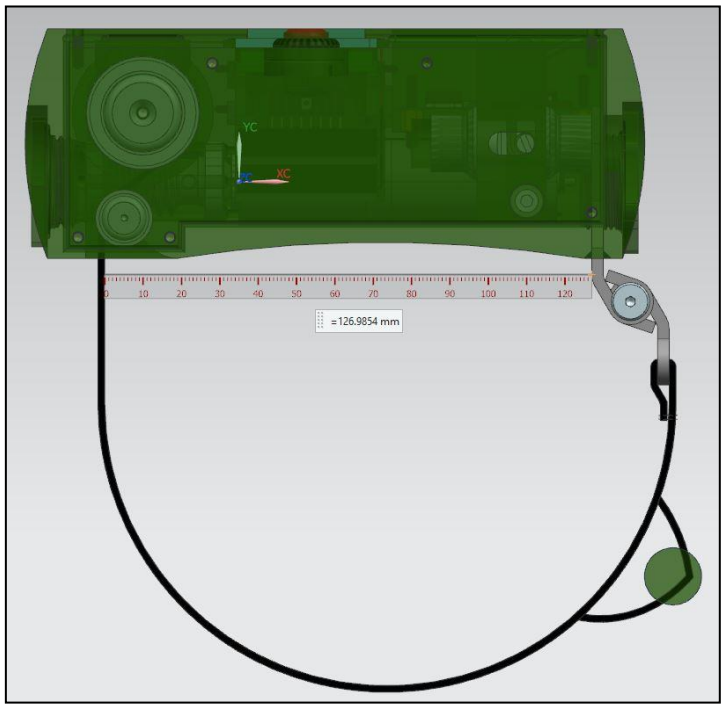


Figure 4. MST Fourth Version Distance Between Belt Pulley Tip and Belt Lock Tip.

Designing of MST main body is finished within fifth revision. Main body holds together; motor, worm gear mechanism, tourniquet pulley which the belt wraps up, bearings, tourniquet lock mechanism, system battery, battery charge socket, electronic control card, force sensor, system user buttons, sealing gaskets and motor worm gear mechanism's sealing covers. While designing the main body a volume which can keep in the whole system in the shape of a rectangular prism is modeled. Afterwards considering the given order of montage main body is extracted for the systems to be montaged. For each different model a cavity that will hold these model in place. With the main body being a single piece part, the robustness of the system is higher. In Figure 5.a a transparent and in Figure 5.b a non-transparent design of the main body is shown. System's control card and buttons which are used for the communication between user and the control card; the button for applying the tourniquet procedure to arm extremity, the button for applying the tourniquet procedure to leg extremity and the button to start and end the system are selected to comply with IP67 standard.

On Figure 6 with last MST's main body design revisions the distance between tourniquet belts gap is reduced by 47,5% which leading to the applicability of the tourniquet system to both arms and legs. As shown in the same figure the windlass structure exists in manual tourniquets. Windlass is used for situations, in which a failure leading to the system mechanism to not work, to tighten the belt with hands manually to apply the tourniquet operation. Hereby MST's 3D mechanical design ends.

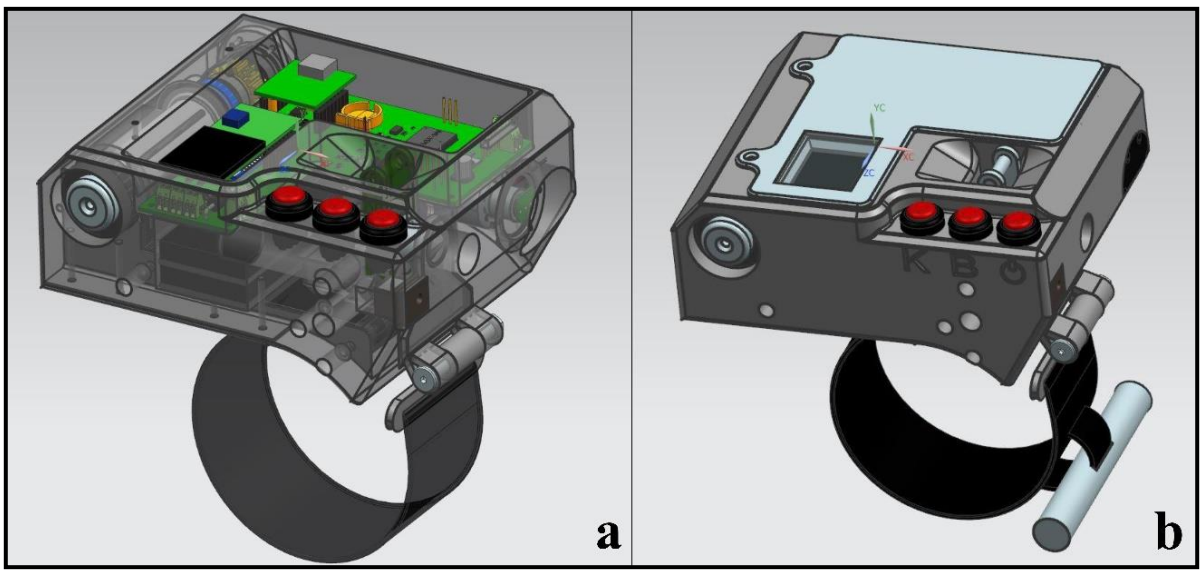


Figure 5. a MST Fifth Revision Transparent Main Body Design, b MST Fifth Revision Non-Transparent Main Body Design.

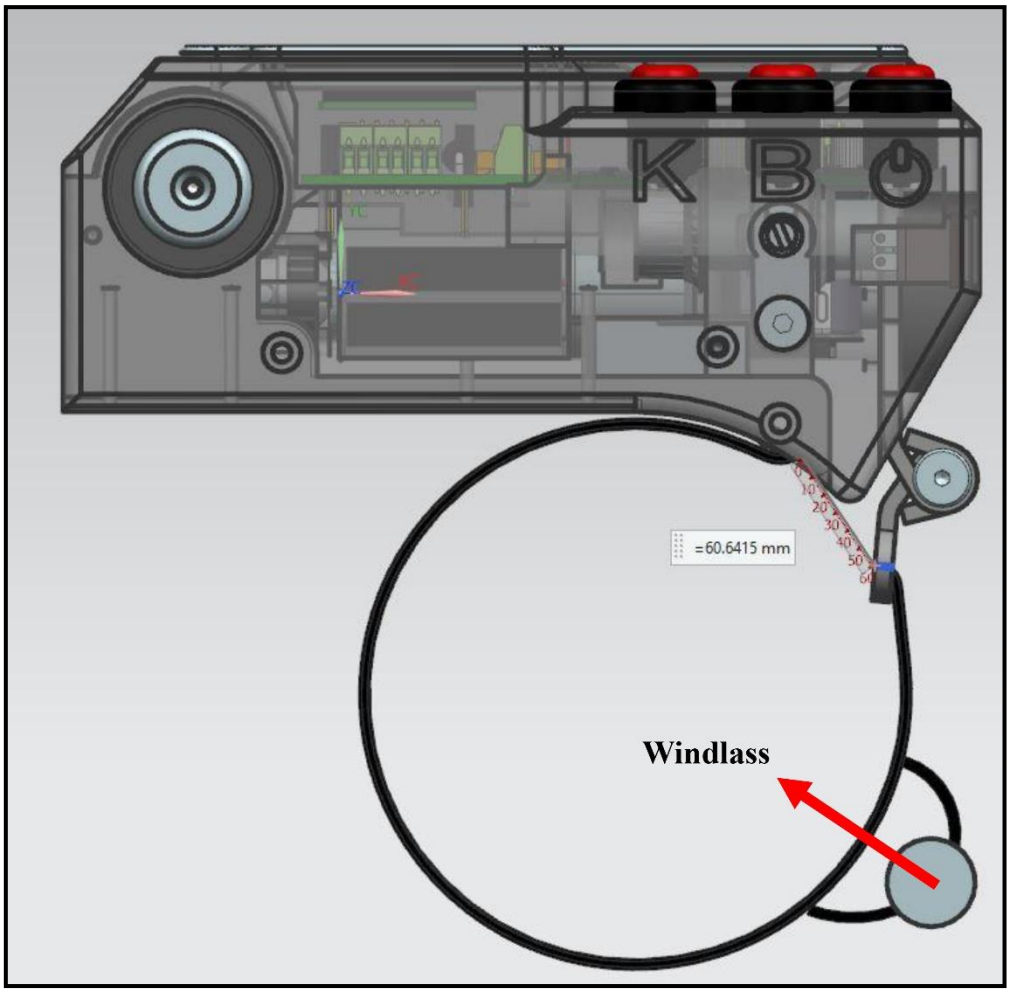


Figure 6. Belt Locked Tourniquet System Fifth Version Distance Between Two Points on Belt.

2.2. Three Dimensional Manufacture Technics for Military Oriented Medical Devices

AM techniques have been evaluated according to their pros and cons. In Table 1 shows summarize each technique. Belong the best average technique, which is SLA, have been preferred for MST parts, except for high mechanically strength parts, such as pulley, worm gear, locking tourniquet mechanism. FORMLABS brand three-dimensional SLA printer is used in manufacturing of MST main body by curing photopolymer resin with laser to harden the material. In manufacture using SLA technic there are two methods to be used which are downward and upward SLA printing. Upward SLA printing is defined as, manufacturing the part by curing the photopolymer resin in a big tank with a laser on a movable build platform inside the tank. This technic is often considered in industry. The forces on model upon manufacture are reduced by the space provided by the big tank. Hence the manufactured model has high details and accuracy. However, for this technic to be applicable, the considerably high dimensions of designed device and installation requirements raises the cost of the manufacture using upward SLA technic [Formlabs, 2018b].

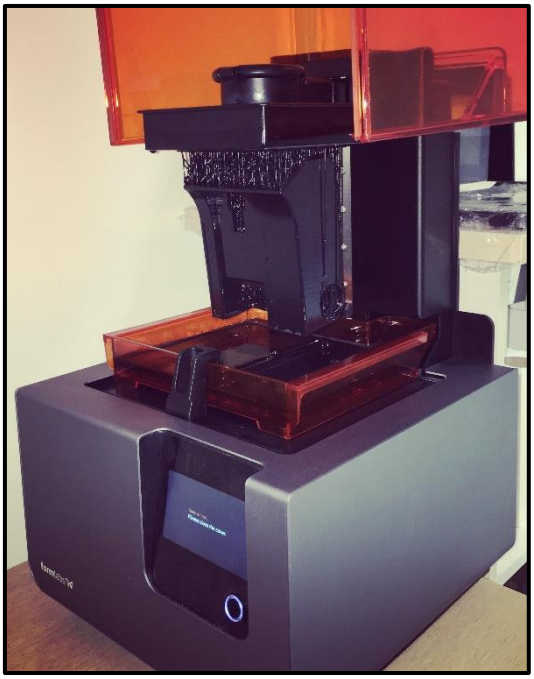
Downward SLA printing is defined as, manufacture process by dipping the build platform into the manufacture tank filled with a certain amount of photopolymer resin and curing the part to be manufactured onto the build platform in reverse of the gravity. When the printing is finished manufactured model hangs to the build platform reverse to the gravity. Later on, the build platform is turned upside down by the user for removal of the manufactured model using a spatula. Because the manufacture is made in reverse of gravity, the gaps in the manufactured material needs to be supported furthermore to avoid the snap of the model upon printing necessary points should be supported to strengthen the printed part [Formlabs, 2018b].

Downward SLA technique has a lesser cost due to its difference form upward SLA technique due to the fewer need of resin which is determined by the number of layers because of the need of a smaller tank in comparison to upward SLA technic.

Table 1. Detailed comparison of three-dimensional manufacture techniques.

Three-Dimensional Manufacture Techniques	FDM	SLA	SLS
Resolution	2	5	4
Accuracy	4	5	5
Surface Quality	2	5	4
Manufacture Speed	4	4	5
Design Complexity	3	4	5
Ease of Use	5	5	4
Average	3.33	4.67	4.50

MST main body and the insulation covers are manufactured using downward SLA printing technic. As can be seen on Picture 1, printing of MST main body is completed by a 3D printer which uses downward SLA technique.

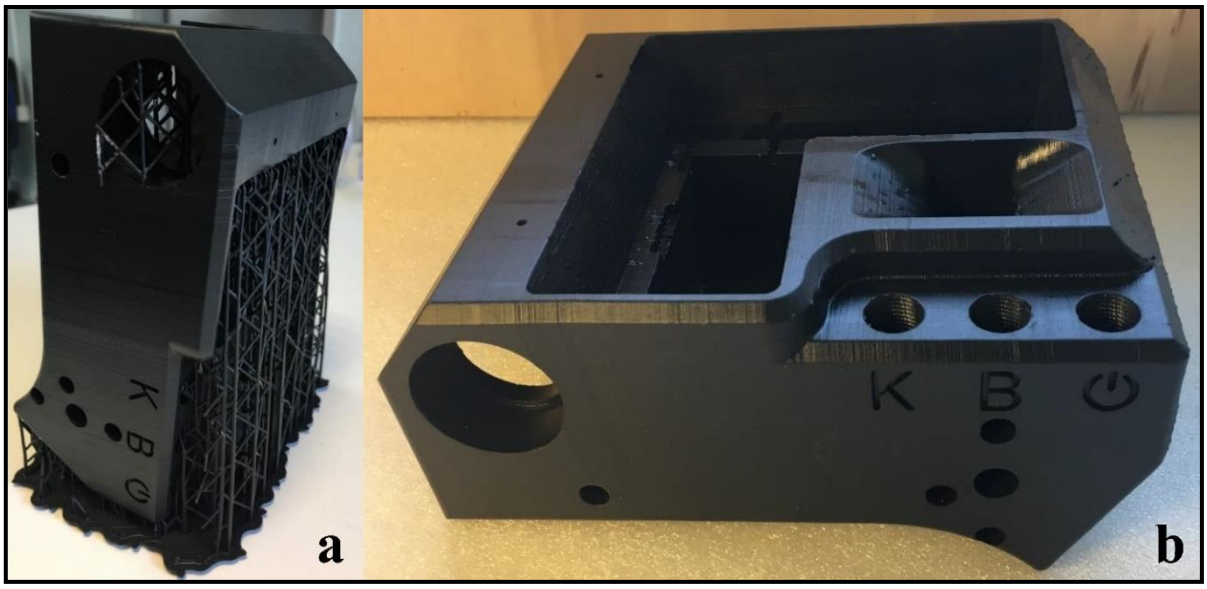


Picture 1. Manufacture of the MST main body using 3D Printer.

Upon the 3D printing, the temperature of the photopolymer resin is raised to 32 °C by the device. The black photopolymer resin which is used for printing is a product developed by FORMLABS company.

2.3. Three Dimensional Manufacture of Military Tourniquet System's

Before printing the MST main body, fifth version of the locked tourniquet system that has its development explained in detail in the third part of the thesis must be saved as in. stl form in SIEMENS NX software. The. stl form which all 3D printers use is a universal and three-dimensional additive manufacture form. This form creates vectors by the relative distances in space of the points specifying a solid body. With the combination of vectors, a data cloud arises. Therefore, the software made by the manufacturer of the 3D printer, layers the before mentioned form of file by the precision of the 3D printer. These programs which are called "Slicer" layers the model which is in. stl form by the quality of the 3D printer's printing. For each separated layer, the coordinates of points that will be exposed to laser beams are created by solvent functions running in the background of the software. All of the 3D printed parts of MST are manufactured with downward SLA technic using 50 µm layer thickness. In Picture 2.a the main part laying on the table which is removed from the build platform is shown.



Picture 2. a MST case with supports, b MST case

As one can see in the figure, the manufactured main body can stand on a plain surface with supports. In Picture 2.b a plain body is shown in which the manufactured MST main body with supports has its supports removed and all insulation covers, system battery, electronic control card and user buttons in which the machined parts are prior are prepared to be assembled.

3. RESULTS

In this study, a military oriented medical device has been designed within 5 different revisions. The first version comprises of 3 different concept designs which are belt pulled tourniquet system, belt wrapped tourniquet system, belt locked tourniquet system respectively. First and second concept were rejected due to application difficulties, then the concept design of belt locked tourniquet system was accepted to work upon. Second and third revision were designed to prove concept design of working and locking mechanism. Forth revision was the first design prototype which is include all working and bearing mechanism, locking mechanism, electronical card, user display and buttons and sealing equipment. Nonetheless, the tourniquet belt interval between from it was fixed point to locked point too long to apply tourniquet both of leg and arm extremities. Due to the interval magnitude, forth version of MST was rejected. And then last version of MST was appropriated to manufacturing after revision to reduce interval of tourniquet belt between two points. The designed MST's case data was converted to .stl data type then processed in SLA printer slicer software. Approximately in 48 hours, the .stl MST data was manufactured in SLA printer with AM technique. A black photopolymer resin was cured layered-by-layered and the MST case have been produced certain 3288 layers which every layer has 50 um thickness. Afterwards, military oriented MST system has been assembled in the Medical Device Design Laboratory where it is in the TOBB University of Economics and Technology Biomedical Engineering Department. The whole tourniquet system weight is 1606 gr and the AM product of MST's case has 75x125x155 mm dimensions. The developed system was electronically tested in computer environment and the system passed all the hardware and software tests [Budak, 2017]. The most important test of tourniquet systems is stopping bleeding. For this reason, we have developed a limb phantom which is nearly the same with human tissue in terms of mechanical characteristic that can be used in flow and pressure tests [Budak et al., 2017]. With the developed leg phantom, the tourniquet system was tested and the blood flow was stopped with MST. In order to test the MST on humans, a medical device ethics committee permission must be obtained. If necessary permissions are obtained, the system will be tested on human and the accuracy of operation of the system will be determined statistically. Moreover, the MST has been tested in both cold and hot condition according to MIL-STD-810G Method 502.5 and the system has been accomplished the test in -33 ^{o}C and 43 ^{o}C stabilize temperature. The smart tourniquet system is not only use in the military field but also it can use in civilian area to prevent emergency injuries.



Picture 3. MST

ACKNOWLEDGMENTS

The developed tourniquet system has been funded by The Scientific and Technological Research Council of Turkey as a science – industry project which has “Military and Emergency Field Smart Tourniquet (Harp ve Acil Yardım Akıllı Turnikesi - HAYAT)” name and “0932.STZ.2015” project no. Besides, we thanks to project industry partner of ASELSAN A.Ş. which is a Turkish Armed Forces Foundation company.

REFERENCES

1. **Berman, B. (2012)**. 3-D printing: The new industrial revolution. Business horizons, 55(2), 155-162.

2. **Rengier, F.**, Mehndiratta, A., Von Tengg-Kobligk, H., Zechmann, C. M., Unterhinninghofen, R., Kauczor, H. U., & Giesel, F. L. **(2010)**. 3D printing based on imaging data: review of medical applications. International journal of computer assisted radiology and surgery, 5(4), 335-341.

3. **Giannatsis, J., & Dedoussis, V. (2009)**. Additive fabrication technologies applied to medicine and health care: a review. The International Journal of Advanced Manufacturing Technology, 40(1-2), 116-127.

4. **Petrovic, V**., Vicente Haro Gonzalez, J., Jordá Ferrando, O., Delgado Gordillo, J., Ramón Blasco Puchades, J., & Portolés Griñan, L. **(2011)**. Additive layered manufacturing: sectors of industrial application shown through case studies. International Journal of Production Research, 49(4), 1061-1079.

5.https://formlabs.com/blog/fdm-vs-sla-vs-sls-how-to-choose-the-right-3d-printing-technology/, retrieved: 22.03.2018

6. **Bikas, H**., Stavropoulos, P., & Chryssolouris, G. **(2016)**. Additive manufacturing methods and modelling approaches: a critical review. The International Journal of Advanced Manufacturing Technology, 83(1-4), 389-405.

7. **Tuomi**, J., Paloheimo, K. S., Vehviläinen, J., Björkstrand, R., Salmi, M., Huotilainen, E., ... & Mäkitie, A. A. **(2014)**. A novel classification and online platform for planning and documentation of medical applications of additive manufacturing. Surgical innovation, 21(6), 553-559.

8. **Ventola, C. L. (2014).** Medical applications for 3D printing: current and projected uses. Pharmacy and Therapeutics, 39(10), 704.

9. **Klenerman, L. (1962).** The tourniquet in surgery, Journal of Bone & Joint Surgery, British Volume 44.4 937-943.

10. **Pienkowski, D. & Barnett L. G. (2010)**. Electromechanical Tourniquet For Battlefield Application, United States Patent, No: US 2010/0234877 A1 Tarih: 16.09.2010

11.https://formlabs.com/blog/ultimate-guide-to-stereolithography-sla-3d-printing/>, retrieved: 22.03.2018

12. **Budak, E. İ. (2017).** Development of Tourniquet System For Military Use (master thesis). TOBB University of Economics and Technology, Ankara, TURKEY.

13. **Budak, E.,** Beytar, F., Özdemir, M., Susam, B. N., Göker, M., Ünlü, A., & Eroğul, O. **(2017).** Lower limb phantom design and production for blood flow and pressure tests, The EuroBiotech Journal, volume 1, issue 4, 278-284, October 2017.

PRACTICE-ORIENTED METAL AM PROCESS SIMULATION AND OPTIMIZATION

Michel PEREME, *michel.pereme@simufact.com* Simufact Engineering GmbH Hamburg, Germany

Patrick MEHMERT, Simufact Engineering GmbH Hamburg, Germany

ABSRACT

Although powder bed fusion metal additive processes such as Selective Laser Melting offer unique advantages in the production of light weight, complex parts, major challenges, such as keeping stress and distortion levels as low as possible remain. This is achieved by performing a number of stages such as 3D-printing, heat treatment and machining. The final result depends on a combination of parameters through the process chain, which leads to time consuming and costly trial-and-error iterations.

Numerical simulation can help shorten the process design stage and improve quality by virtually opimizing the different parameters involved. Distortions, can be predicted at an early stage and minimized by improving the support structures and pre-distorting the part. A concept based on the Simufact Additive software is presented and discussed. Examples are shown and an outlook into future developments is given.

Keywords: Additive Manufacturing, Powder Bed Fusion, Process Chain, Numerical Simulation, Finite Element Method, MARC Solver, Analysis Scale, Optimization

1. INTRODUCTION

Additive Manufacturing is not a new topic, although the number of events, products, companies and articles related to 3D-printing seem to increase exponentially nowadays. Various materials can be used in 3D-printing such as plastics filaments, plastics powders, resins, ceramics and metals.

When talking about metal AM there are mainly two different approaches: Direct Deposition and Powder Bed Fusion (PBF), see Figure 1 and Figure 2.

Direct Deposition is in fact a build-up welding approach either with a wire or powder material feed. The heat source can be an electric arc, an electron beam or a laser. The main advantage of direct deposition fabrication is the possibility to add a high amount of material per time to achieve a near net shape. The disadvantage is that only a rough semi-finished part is produced and relatively high efforts must be spent on manufacturing post-processing like machining to achieve the target geometry.

In Powder Bed Fusion one can differ between using a laser as heat source or an electron beam. The most common systems are laser based, while due to patent reasons there is currently only one supplier of electron beam PBF machines today. In this article powder bed fusion processes are referred with a focus on a laser based systems.

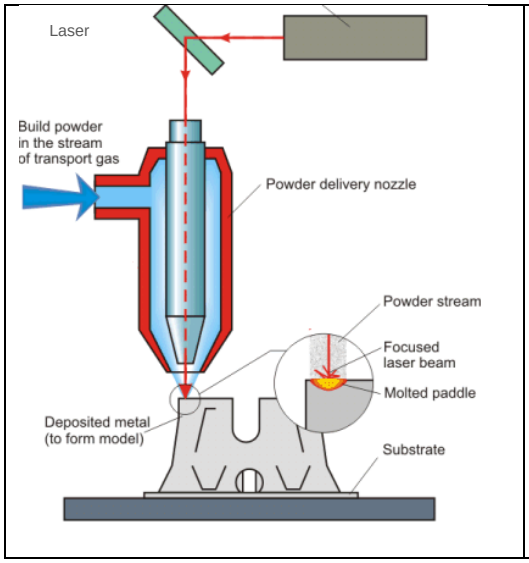


Figure 1. Principle of a laser direct deposition AM machine

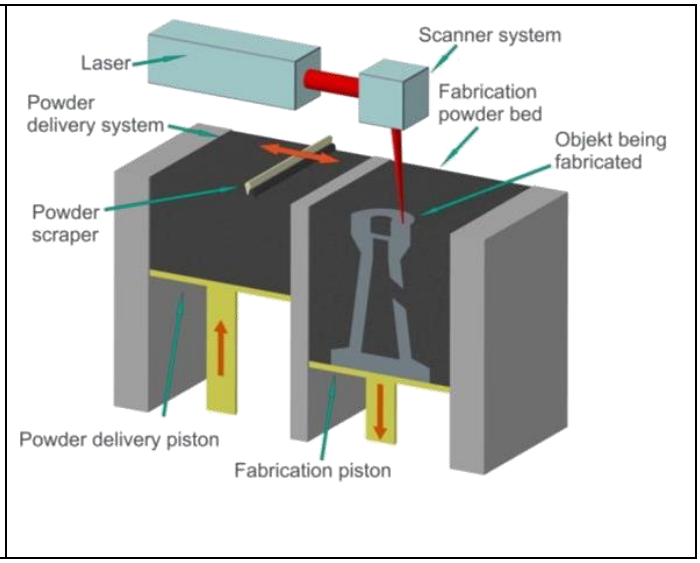


Figure 2. Principle of a laser powder bed fusion AM machine

Powder Bed Fusion systems allow the production of lightweight complex parts even with bionic shapes that could not be produced before by traditional technology. This offers the opportunity to reduce the assembly complexity and even integration of functionalities.

However, metal powder bed fusion manufacturing processes face a lot of challenges. Main issues observed are support failure, distortions, high residual stresses and print process abortion, such as blade crash.

Distortion can lead to parts being out of the required geometrical tolerance, see Figure 3. Furthermore, distortions can even lead to a manufacturing abortion during the build, if the powder scraper collides with the part and is not able to apply another layer of powder. Residual stresses can lead to failure of the part, its support structures or the connection between them, see Figure 4.



Figure 3. Round structure distorted to ellipse



Figure 4. Support structure failure

A number of other challenges like low relative material density, pores, insufficient powder binding, surface quality, strength and durability of the additively manufactured part also exist.

Usually, three to ten or more physical try-outs with different parameters have to be performed before a satisfying process is identified.

In conclusion this implies a strong need for a manufacturing process simulation that helps reduce trial & error iterations, thus reducing needed time & costs and can help identify optimum manufacturing conditions.

2. THE ADDITIVE MANUFACTURING PROCESS CHAIN

When talking about AM the focus is often set solely on the process to build the part by the available manufacturing approaches. In fact, one must be aware that AM as a whole consists of a longer process chain with steps before and after building the part, see Figure 5.

Naturally the desired part must be designed first and being available in a digital format. In this step, often numerical topology optimization is used to get the principal idea of an ideal part.

When the shape of the part is determined, the AM build job has to be prepared. That means the position, especially rotation, of the part within the available build space must be set and additional supporting structures created.

In some cases, after building the part, a stress relief heat treatment is recommended to reduce the residual stresses induced by the thermal effects of the manufacturing.

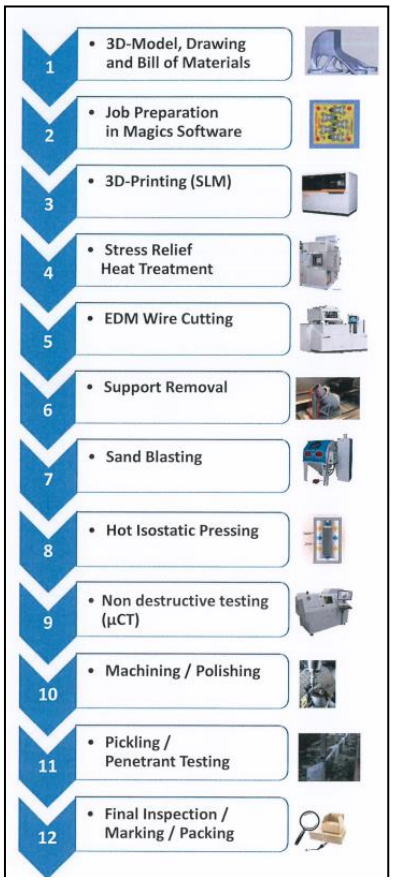


Figure 5. Generic AM process chain for metal PBF [2]

After the manual removal of the support structures the manufacturing of the part is mainly finished. Nevertheless, more subsequent steps can follow. These can be related to the shape and surface (sand blasting, machining, polishing) or for test purposes.

One important step especially used in aerospace applications is Hot Isostatic Pressing (HIP). This is to put the part in a highly pressurized environment (about 100 MPa surrounding atmospheric pressure) while simultaneously applying heat.

3. SIMULATING THE AM PROCESS CHAIN

From the standpoint of simulation, the real-life AM process chain can be mapped to a numerical analysis process chain, see Figure 6.



Figure 6. Possible numerical analysis process chain for Additive Manufacturing

The core analysis steps can be seen in simulating building of the part, relieving stress by heat, cut the part and supports off the plate, remove the supports and possibly perform a HIP treatment. Subsequent analysis steps can be machining, further surface treatment and final stress and fatigue analyses based on the as-built conditions. Prior steps can be to start with a topology optimization and derive a design, either manually or by automatic smoothing operations.

3.1 Analysis scales

Simulating additive manufacturing, especially building or printing the part, can be performed on different physical scales, where none of them can be considered as the naturally given best suitable scale.

3.1.1 Nano scale

In the metal powder bed fusion process, a laser or electron beam moving heat source selectively melts metal powder. The melted metal cools down and solidifies thus leaving a layer of solid material, while layer by layer are produced on each other and a complete three-dimensional part is finally created, see Figure 7.

So, one approach is to look on the powder level with its individual particles. Simulations at this level often use CFD codes to reflect the behavior of the melted phase. At this scale very detailed basic investigations on the heat source – powder interaction, fluid dynamics and

solidified material properties - are possible. Obviously analyzing a real-life AM part is not feasible by this approach.

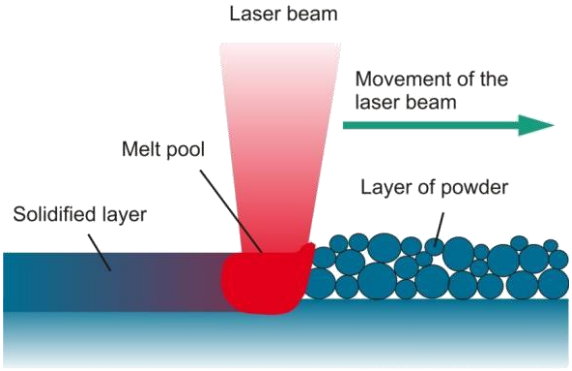
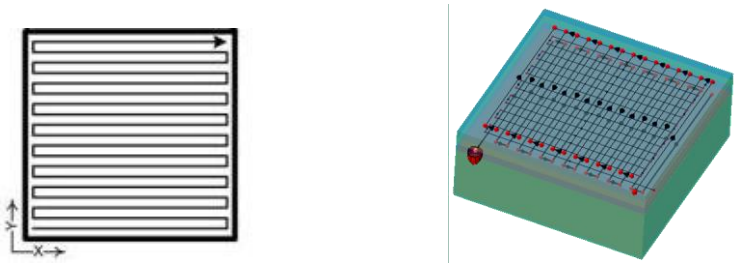


Figure 7: Detail principle of laser powder bed fusion additive manufacturing

3.1.2 Micro scale

Another approach is to see the AM build process as a micro welding process. The numerical simulation of welding processes is being analyzed for many years [3] and can be well performed with commercially available multi-purpose FE codes MSC Marc with quite an amount of modeling effort. Furthermore, there is specialized software available like Simufact Welding which eases the modelling and analysis by providing tailored simulation environments.

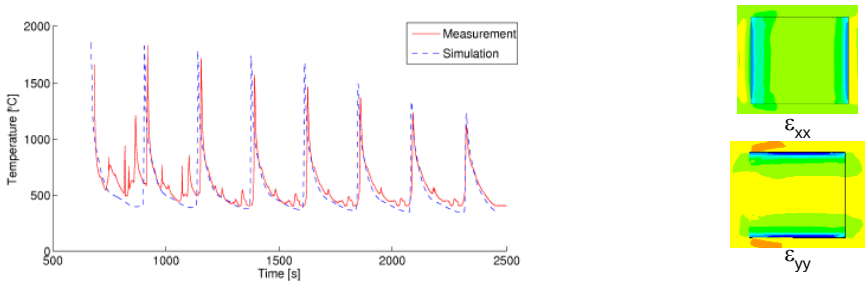
However, this approach is also limited due to the complex non-linear and coupled behavior of welding processes. Nevertheless, a micro welding simulation of the moving heat source, e.g. the laser scan hatching path, can deliver an insight into principal process details. By knowing the temperature history more results can be derived like the metallic microstructure, chemical composition and mechanical as-built properties, e.g. based on empirical data like time-temperature-transformation diagrams. Also, mechanical effects like the strains induced by the AM process can be investigated and used for larger scale simulations.



(a) (b)

Figure 6. (a) Example of a laser scan hatching strategy (bidirectional meander)

(b) According weld path model in an FE simulation (Simufact Welding)



(a) (b)

Figure 7. (a) Simulated and measured temperature history of an AM welding process [8] (b) Strains derived from an AM micro welding simulation

3.1.3 Meso scale

We can further climb up the scale ladder by comprising scan patterns like stripes and chessboards. The thermal or mechanical load is then applied per these patterns, either consecutively in the right order or in one step within one powder layer. To simplify and speed up several powder layers can be summarized in one element layer where the loads through the different powder layers are averaged.

This scale firstly allows the analysis of complete parts at affordable computational costs including the possibility to obtain some thermal information. On the one hand the local thermal history will be more approximate, but on the other hand it is possible to have an insight into the thermal behavior of the complete part and its interactions with its environment like base plate, supports, powder and free build space.

3.1.4 Macro scale

At this scale the AM part is analyzed by applying the average load per sequentially activated element layer, which summarizes multiple powder layers. Theoretically the thickness of the element layers could be decreased down to the real powder layer size, but the additional computational costs are not justified by the achieved increase of accuracy. In fact, it can be shown that starting from very coarse meshes and decreasing the mesh size the results quickly converge and a further decrease of the element size does deliver a mentionable benefit.

3.1.5 Meshing at Meso and Macro Scale

At the mesoscopic and macroscopic scale different layer respecting meshing technologies can be applied:

- Tetrahedral mesh
- Hexahedral mesh

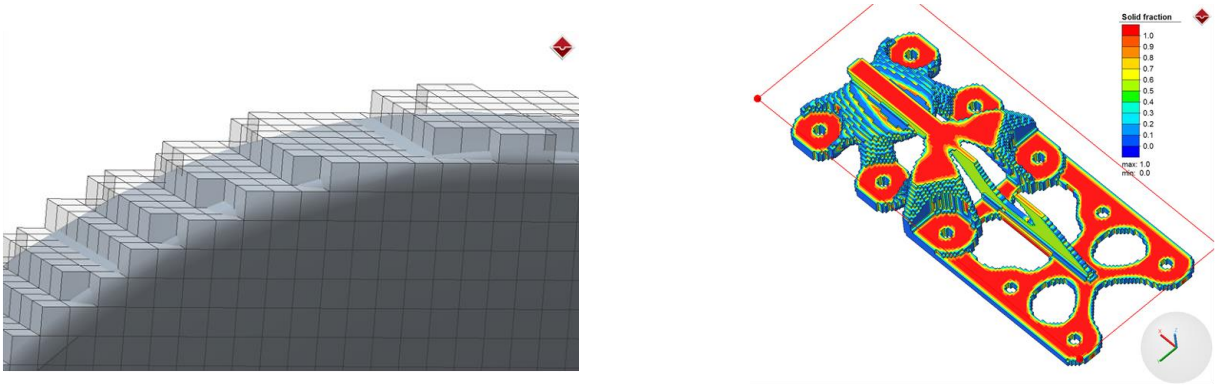
- Voxel mesh

The tetrahedral mesh has the advantage to well approximate the surface contour.

Generally hexahedral elements can deliver a superior solution to tetrahedral elements even with linear interpolation.

Both approaches have the disadvantage that complicated filigree AM parts and support structures might not be meshable.

To overcome these limitations a voxel mesh approach can be used. This is based on hexahedral elements either being perfectly cubical-shaped or at least being totally rectangular. The two big advantages are that trustful element shapes are used and almost any shape independent of its complexity can be meshed. In order to sufficiently represent the outer shape of a part, fine voxels can be used. To increase the analysis speed a multi-level coarsening can be utilized allowing larger voxels in bulky areas.



(a) (b)

Figure 8. (a) Voxel mesh representation (translucent) of a curved geometry (opaque) (b) Solid volume fraction distribution of a voxel meshed geometry (with x-y cutting plane)

Another approach is using a rather coarse mesh, but respecting the fraction of the AM structure that is covered by a voxel to scale down the material properties accordingly. The simplest way is to allocate the geometrically measured solid volume fraction to the element. A more precise way is to map the local fraction of a hexahedral element's octant to the according integration point.

3.2 Additively building the part

In the following paragraphs a finite-element analysis approach to simulate the core AM process chain is presented with a focus on the macro- and meso-scale approaches.

A very fast approach to simulate the AM build process is based on the so-called inherent strains, that are induced into the solidified structure by the manufacturing process [4]. The inherent strains comprise plastic, thermal, creep and transformation provoked strains [5].

Assuming these strains are known, they can be applied as load to a finite element model and the resulting deformation and residual stresses can be calculated. It must be emphasized that all effects of the additive manufacturing process are assumed to be condensed in the inherent strains. That means though the real process is driven by heat energy input and thermal effects any inherent strain analysis is purely mechanical.

Usually the inherent strains are determined by a calibration procedure and are valid for a certain material, the (individual) AM machine and the manufacturing parameters like power, speed and laser hatching strategy used. Any change in one of these independent variables requires a re-calibration of the strains. Due to the welding-like directional nature of AM scan processes the inherent strains are orthotropic with different values in longitudinal, transversal and vertical local direction.

The calibration can be performed with test geometries like the cantilever specimen shown in Figure 9. The according specimen is additively manufactured, partially cut or completely removed from the plate and the resulting deformation (see **Error! Reference source not found.** for explanation) measured. Based on the observed deformation the inherent strains that caused the deformation are calculated analytically or are determined by a numerical optimization. In the numerical optimization the cantilevers from the test are simulated in an FE analysis and the final deformation measured. A start vector for the inherent strains is assumed and incrementally adapted by the optimization script to match the observed deformations. The calibration is successful when the simulated deformations are within the given tolerance compared to the test results, see Figure 10.



(a) (b)

Figure 9. (a) AM printed cantilever specimen (b) Simulated cantilever (built and cut) with deformation

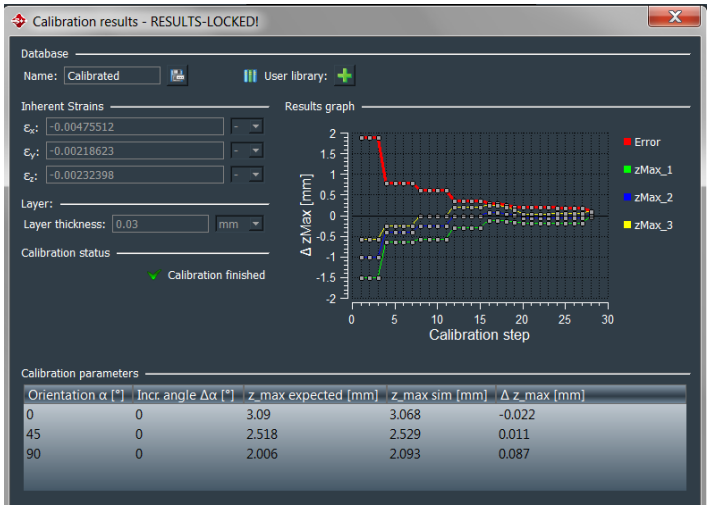


Figure 10. Output of a successful calibration process based on numerical optimization

The determined inherent strains can be applied layer- or segment wise as an average or spatially distributed to reflect the different scanning strategies like stripes or chessboard. In all cases the rotation of the laser scan pattern per powder layer and therefore also of the inherent strains needs to be taken into account. Another simplification is to use element heights that are much larger than the real powder layer height. In this case an average of the inherent strains through the powder layers must be calculated for one element layer.

To reflect the generating nature of the AM, process the element layers are activated sequentially. I.e. the first layer is activated, the inherent strains applied and the mechanical equilibrium determined. Now the next layer is activated, where the bottom nodes are connected to the already distorted first layer and the upper nodes are in their originally defined position. The inherent strains are applied with their updated rotation, the mechanical equilibrium is determined and so forth until the complete part is virtually created.

It must be noted that for this analysis approach only the resulting material properties at room temperature are required as all thermal effects are already included in the calibrated inherent strains.

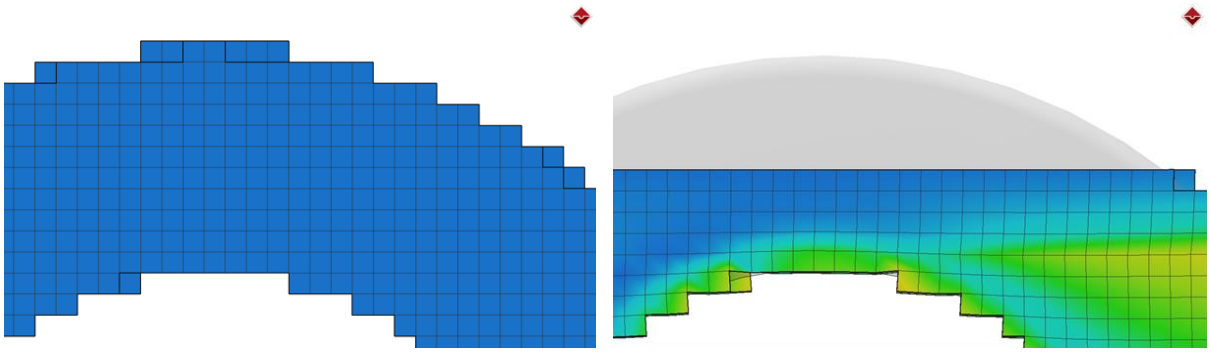


Figure 11. (a) Layer based voxel mesh (b) Sequential activation and loading of layers

3.3 Stress relief heat treatment

In this stage two effects lead to the desired stress relief. First of all, the elevated temperature leads to reduced mechanical properties regarding the elastic modulus, the yield strength and the plastic flow curve. The material gets less stiff and weaker; it does not resist mechanical loads as much it does at low temperatures. That means that residual stresses can be relieved by an internal plastic deformation that was not possible at lower temperatures.

But this effect does not sufficiently explain the observed stress relief. Otherwise only the maximum reached temperature would influence the stress relief. Also, it can be shown by simulation that just increasing and decreasing the temperature does not relief the stresses realistically. In a real-life stress relief heat treatment after heating up a significant holding time is respected. In this holding time, not only the temperature is reached through the whole part but also there is time for stress relaxing creep effects. Creep relaxation generally occurs under constant loading like it is given with the residual stresses. At room temperature this effect is neglectable. At elevated temperatures creep effects intensify exponentially, therefore creep contributes significantly to the achieved stress relief.

Regarding simulation this means temperature and plastic strain dependent mechanical properties must be given as well as the creep properties for the selected creep model.

3.4 Cutting operations

Simulating the cutting operation is straightforward. If the part and the supports are virtually connected to the base plate by constraints these can be released. The release can happen immediate (all constraints at once) or follow an advancing cutting front. Cutting can lead to additional distortion if there are still residual stresses inside the part, see **Error! Reference source not found.**.

If the base plate is part of the meshed model or the cutting should be simulated at an elevated height either the affected elements can be deleted respectively deactivated or the elements are separated by duplicating their shared nodes.

In all cases the changed boundary conditions or geometry will lead to a new state of equilibrium that can be determined numerically. It must be noted that after the part and possibly connected supports are completely cut off the plate there is no defined fixation anymore. To avoid unwanted rigid modes or even a failure of the analysis the part must be fixed by boundary conditions or otherwise stabilized. Nevertheless, this state is kind of arbitrary and any deformation shown is non-unique. To overcome this issue a user-defined positioning (respectively distortion measuring) against the original part can be introduced like this is done in metrology applications.

3.5 Hot isostatic pressing

Hot isostatic pressing or HIP means to expose a part to elevated surrounding static pressure at high temperatures. The high temperatures have the same effect as for the pressureless heat treatment: the mechanical resistance of the part is reduced. Again, remaining residual stresses can relax through the weakened mechanical properties and the according temperature and time-dependent intensified creep effect.

The additionally applied pressure load now can lead to a densification of the additively manufactured part. Typically, this already has relative densities between 95 and more than 99% compared to conventional bulk material. The reduced mechanical resistance together with the pressure load now can lead to a collapse of pores especially close to the surface. That means the material is densified and has improved mechanical properties, that were reduced by the pores before.

Regarding the numerical simulation the same approach as for the heat treatment applies plus the additional pressure load. For the densification various powder models can be used, that describe the densification dependent on the increased hydrostatic pressure.

3.6 Optimizing the AM process chain

When the core AM process chain can be simulated this immediately enables to virtually optimize it. One possibility is to adapt the parameters of each single stage of a given process chain in order to find the desired best end result. As a second possibility the process chain itself can be changed to investigate the possible effects on the part properties. The reluctance to explore new ideas is much less when “only” modeling and calculation time needs to be spent instead of the enormous effort to test different process chain setups in reality.

Optimization can be understood in two different ways: the first and current approach is an engineering judgement driven manual iteration while the second approach is an automatic optimization by the software towards defined targets while given boundary conditions are respected.

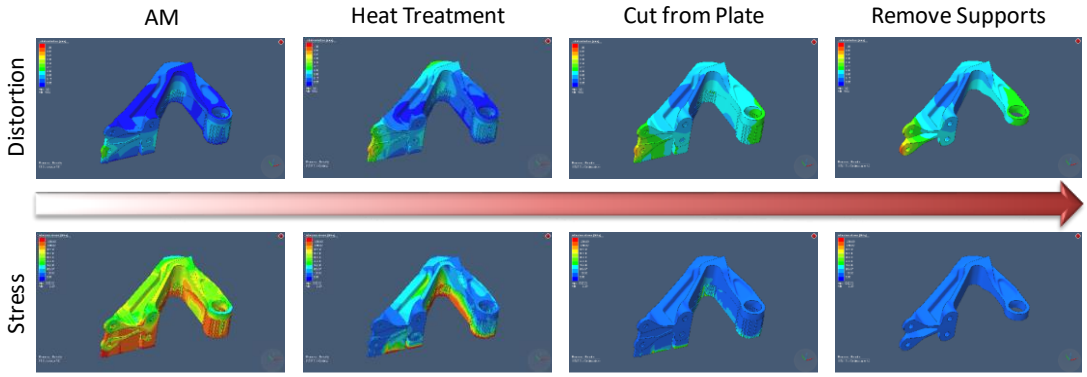


Figure 12. Simulation results of an AM process chain

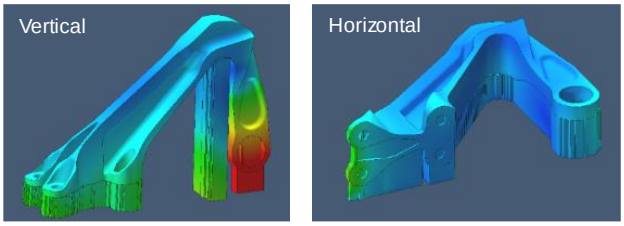


Figure 13. Simulated influence of different build-up orientations on distortion (same scale left & right)

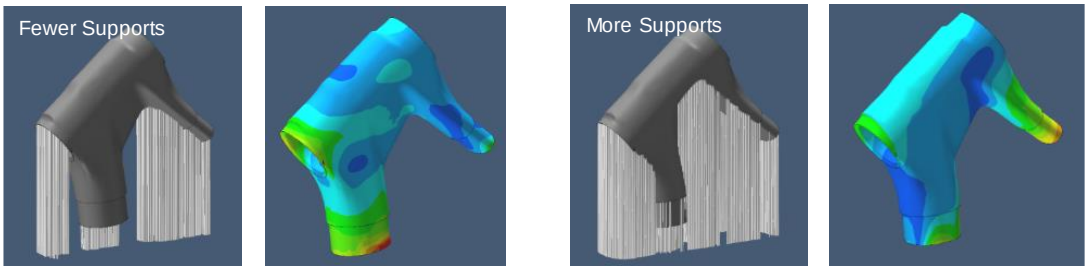


Figure 14. Simulated influence of different support configurations on distortion (same scale left & right)

4. DISTORTION COMPENSATION OF THE SIMULATED PART

As previously said, one of the main challenges in PBF metal additive processes is to minimize distortions in the part. This can be achieved by optimizing the build orientation, the number, geometry and location of support structures. Another approach is to print a pre-distorted part, with the objective to get the right geometry,once this part has distorted.

5. OUTLOOK

5.1 Extending the simulation process chain

The more of the real process chain can be covered by simulation the better it can be virtually optimized.Therefore the simulation process chain currently covered by *Simufact Additive* as shown in Figure is planned to be extended step by step. Looking downstream the next stage targeted is machining, which comprises the mechanical answer to the material removal under the given fixing conditions. Furthermore, the export of results in a Nastran or Marc readable format would enable stress and fatigue analyses based on the as-built conditions. Looking upstream a call of the Nastran topology optimization would enable a requirement driven bionic lightweight design.

5.2 Automatic optimization

In order to speed-up a manual iterative optimization driven by engineering judgement and to achieve results closer to the optimum an automatic optimization by the software is intended. Two examples are the build-up orientation and the support configuration.

For the build-up orientation a range of rotation angles could be specified and automatically simulated. Iteratively the optimal rotation is determined. A speed-up can be achieved by first exploring the whole range of rotations by large steps and coarse, fast calculating meshes. The most promising intervals are then investigated by smaller steps and with finer meshes until a convergence criterion is met.

The holy grail of AM optimization is the determination of the optimal support structure. On the one hand it should reliably prevent the part from distortion and failure. On the other hand, it should be as less as possible to minimize powder, energy and time consumption during the build as well as the removal and surface finishing efforts.

The support optimization task can be seen as a parameter optimization or a topology optimization. Parameters would be the criteria where to put the supports (e.g. surface inclination against base plate) as well as the parameters defining their shape (e.g. distance between walls). In a topology optimization an arbitrary shape can be determined in the given space.

5.3 Link simulation into AM process chain

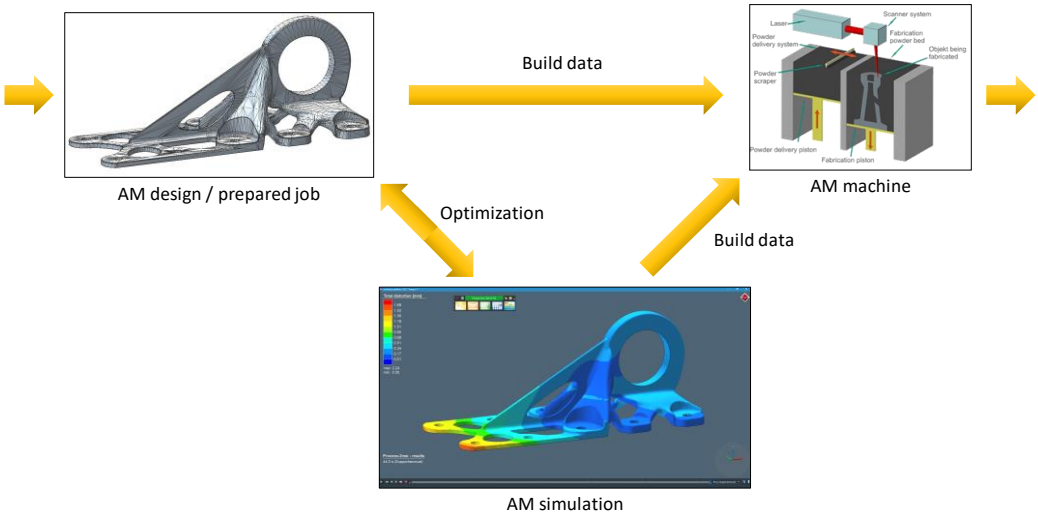


Figure 15. Integration of simulation in AM process chain

Logically simulation should not only serve to virtually explore the AM process chain, but it should become a part of the process chain itself. According to Figure 15 simulation can be a step between the part design respectively prepared job and the build job on the machine. The simulation should be used to optimize the planned build, which can happen as interaction with

the job preparation software or solely in the simulation software. After that the updated build data is sent to the machine either by the job preparation or the simulation software.

REFERENCES

[1] **Grund, M.: „Implementierung von schichtadditiven Fertigungsverfahren“**, 2015, p. 35-37

[2] Bundesverband Deutsche Luftfahrtindustrie (BDLI): process chain issued at kick-off competency network, Bremen, 13.9.2016

[3] **Mehmert, P.**: “Numerische Simulation des Metallschutzgasschweißens von Grobblechen aus un- und niedriglegiertem Feinkornbaustahl”, TU Clausthal, 2000

[4] **Keller,N.; Ploshikhin, V.**: New Method for Fast Predictions of Residual Stress and Distortion of AM Parts, Proceedings of the Solid Freeform Fabrication Symposium, 2014, p. 1229

[5] **MURAKAWA, H.; DENG, D.; MA, N.**: Concept of inherent strain, inherent stress, inherent deformation and inherent force for prediction of welding distortion and residual stress, Transactions of JWRI. 39(2), 2010, P.103-P.105

[6] NTT DATA ENGINEERING SYSTEMS Corporation (NDES)

[7] **Töppel, T., Kordass, R., Beyer, U, Seiderer, J.**: “Numerical simulation of residual stresses and deformations in laser beam melting”, in Numerical Analysis of Weldability, 2015, in press

[8] **Lindgren, L., Lundbäck, A., Fisk, M., Pedersen R., Andersson, J.**: SIMULATION OF ADDITIVE MANUFACTURING USING COUPLED CONSTITUTIVE AND MICROSTRUCTURE MODELS, Additive Manufacturing, Volume 12, Part B, October 2016, Pages 144–158

EFFECTS OF STRUCTURAL HYBRID DESIGN OF CoCr-ALLOY SCAFFOLDS FABRICATED BY SELECTIVE LASER MELTING FOR BIOMEDICAL APPLICATIONS

Emre ÖZEREN, *emreozeren07@gmail.com,* Yildiz Technical University, 34349, Istanbul, Turkey

Mihrigül ALTAN, *meksi@yildiz.edu.tr,* Yildiz Technical University, 34349, Istanbul, Turkey

ABSTRACT

The production of scaffold structures for biomedical applications by using Additive Manufacturing (AM) has become widespread due to possibility of the customized fabrication depending on the demands of the patient. However, design of the scaffold is seriously important in improving the mechanical and biological properties of the product. In this study, Selective Laser Melting (SLM) was used to fabricate CoCr-alloy scaffolds consisting of different hybrid designs with the constant porosity ratio and strut diameter. In designing the scaffolds, a computed tomography of a human femur was processed by medical image processing software and 3D model of the human femur was obtained. The hybrid designs of scaffolds were composed of dodecahedron, grid, grid+dodecahedron structures with partially-dense and fully-dense external sidewalls. After designing, scaffold samples for compression test and cell adhesion test were fabricated from CoCr-alloy powders on the SLM machine. In order to observe the variation in mechanical strength of the scaffolds according to the developed designs, compression test was performed. Cell adhesion test (MTT-cytotoxicity) was applied to investigate the cell adhesion ability of the scaffolds. The results indicated that although hybrid scaffolds had the same porosity ratio and the same strut diameter, they showed apparent variations both in mechanical and biological properties.

It has been seen that scaffold having partial dense sidewall within hybrid structure showed %14,6 of higher mechanical strength in comparison with non-hybrid structure. Cell viability of the scaffolds showed variations due to the developed designs. As a result, it could be claimed that scaffolds with complex designs fabricated by SLM method are promising for future applications due to the satisfactorily increments in mechanical strength and cell viability.

Keywords: Additive manufacturing, selective laser melting, scaffold, porous scaffold, lattice structure, hybrid design, medical image processing

1. INTRODUCTION

Additive manufacturing (AM) methods enable great geometrical freedom for fabricating structures with complex or customized architecture such as porous scaffolds [1-4]. By the help of medical image processing softwares, CAD design softwares and additive manufacturing technology, the porous scaffold structures can be designed and fabricated by mimicking human hard tissue with appropriate mechanical properties and biological properties [5-7].

Selective Laser Melting (SLM), one of the most popular method among the AM applications, is a powder-based additive manufacturing method that enables the manufacturing of 3D parts effectively and efficiently directly from CAD model by exposuring fiber laser energy to powder beds [5,8-10]. Firstly, a CAD model is imported to a CAM system or directly to the SLM system and then the model is sliced in many thin layers. Fusion of the powder bed occurs with the metallic plate and a second layer is fabricated by spreading the powder bed on the merged layer by lowering the metallic plate. The laser beam scans the powder bed again and merges with the previously scanned layer.

Selective laser melting method has been used in biomedical applications. In these applications different metallic biomaterials have been used such as Cp-Ti, Ti6Al4V(Grade 5), Ti6Al4V ELI(Grade 23) , 316L Stainless Steel and CoCr-Alloys [9,11-15]. Fabrication of highly porous scaffolds by SLM is popular due to the customized demands of the patients in tissue engineering [16]. Scaffolds are porous structures that act as a substrate and enable the cells to adhere and grow by means of porous surface. Porous scaffold structures require some characteristics such as; proper porosity that enable the cells to attach to pore network and grow through the pores, necessary mechanical properties that mimic the tissue or non-defected natural bone, biocompatible with living tissue and eliminating or minimizing tissue rejection, an appropriate surface roughness to promote cell attachment and proliferation. The summary of the required characteristics for scaffolds is given in Figure 1 [17].

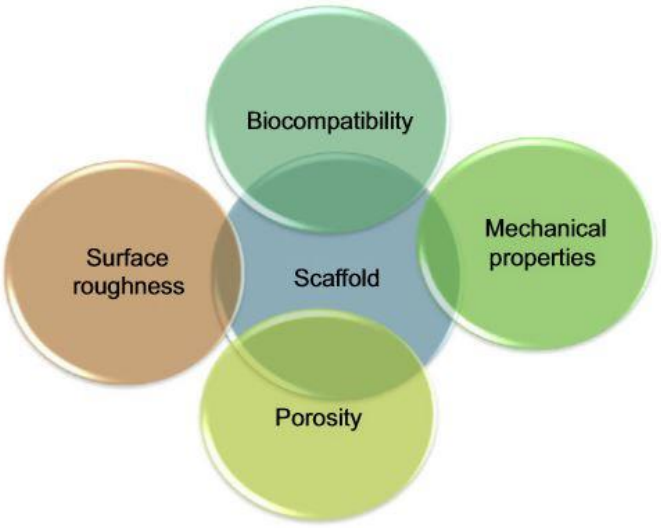


Fig 1. The required characteristics of scaffold structure

There are different scaffold fabrication techniques to perform the cell distribution and guide their growth into 3D space. Each of them has some merits and demerits. Additive manufacturing based scaffold fabrication has merits such as controlling over geometry, porosity and enabling customized structures in an easy way [18]. In this regards, to be able to reduce loss of the bone, increase the osseointegration and matching between implant and surrounding tissue, porous metallic biocompatible scaffolds are designed by mimicking human bone tissue and manufactured by additive manufacturing methods such as SLM, SLS OR EBM. Thus, both mechanical and biological requirements are fulfilled by using these additive manufacturing methods [19].

Generally, there is a relationship between porosity of porous scaffold and their elastic modulus and yield stress. By changing the type of unit cell, different mechanical properties can be obtained because of the coefficient of unit cells [10]. Obtaining different unit cells allows for freedom in the design of porous scaffold that meets appropriate mass transport properties and pore size and in this way the required mechanical properties can be achieved.

An ideal biomedical scaffold should mimic the natural extracellular matrix (ECM) [20]. Therefore, the scaffolds with different unit cell or hybrid types which match and mimic strengths, stiffness, porosity and mechanical behavior, allows for avoiding stress shielding and stimulating bone regeneration. Additive manufacturing methods with its advantages on control over porosity and geometry, can allow good match between implant and natural bone tissue by optimizing mechanical and biological properties.

There are several studies on additively manufactured scaffolds. As emphasized in the studies, the design phase of porous scaffold is one of the most valuable phase. Therefore, many researchers focused on the design of porous scaffolds in their additively manufactured

scaffold studies. As additive manufacturing technology is a promising option to fabricate complex designed structures in near-net form and to control over porosity and pore size/shape, Fousová et al.[10], used selective laser melting (SLM) method to produce gradient porosity model specimens of titanium alloy Ti-6Al-4V. Choy et al. [21], also used selective laser melting method to fabricate the functionally graded lattice structures with Ti-6Al4V. Su et al.[6] designed the porous artificial femur model and several vessel scaffolds with personalized design by using computed tomography (CT) technology and a CAD software. Besides these studies, it was stated that the design phase of porous scaffold can enhance the biodegradability, cell biology, biomolecules design of the biomimetic scaffolds, so this allows scaffold to promote the success of clinical outcomes in musculoskeletal surgeries [20]. One of the main points of these studies is showing the design effects on scaffold fabrication.

In this study, different from previous studies, a novel hybrid designs for CoCr alloy based scaffold fabrication by SLM were developed in order to enhance the biological and mechanical properties of the structures. In this regard, customized/patient specific porous scaffold fabrication was done after processing a computed tomography of a human femur by medical image processing software. The built scaffolds were examined by compression test and cell adhesion test.

2. EXPERIMENTAL STUDY

2.1 Materials

CoCr-alloy based powders were used to fabricate the scaffold samples. The particle size of the spherical CoCr-alloy powder is in range of 10-40 µm (Figure 2). The chemical composition of the CoCr-alloy is shown in Table 1.

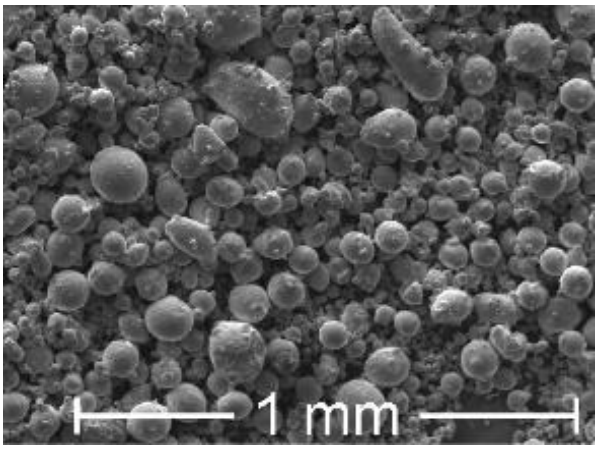


Fig. 2 Microstructure of CoCr-alloy powders

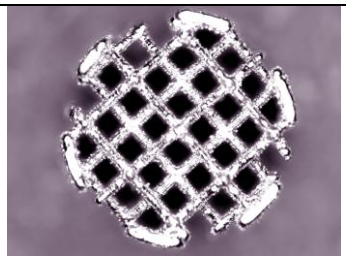
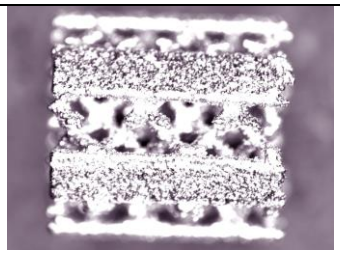
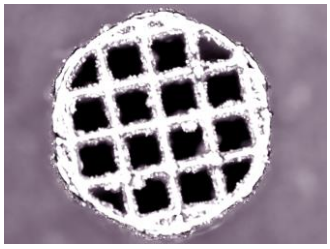
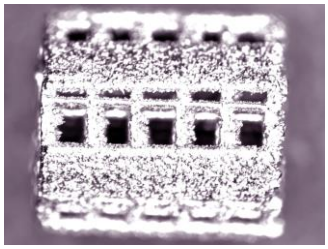
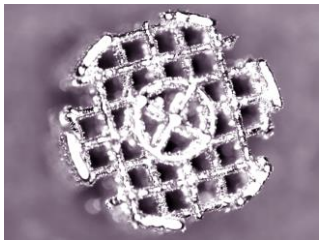
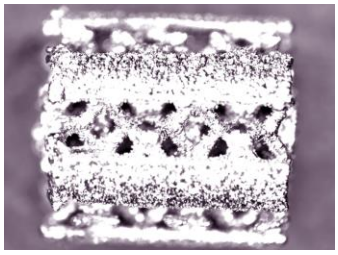
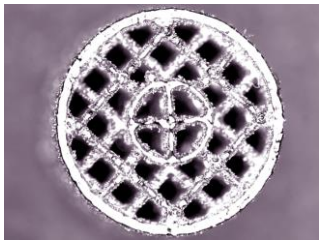
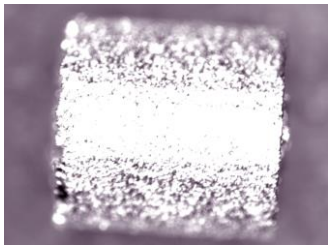
Table 1. Chemical composition of CoCr-Alloy

Component	Mass (%)
Co	60,5
Cr	28
W	9
Si	1,5
Other elements <1 %: Mn, N, Nb, Fe. free from nickel, beryllium and gallium	

2.2 Scaffold Fabrication

Scaffolds were fabricated within novel designs in the light of medical imaging systems (µCT, CT, CBCT) medical image processing and CAD software. In scaffold designing, dodecahedron and grid cell units were selected shown in Figure 3. The generated scaffolds with different designs as follows; Partially Dense surface layer (PDsl)+dodecahedron, (PDsl)+grid,PDsl+dodecahedron+grid and Fully Dense surface layer (FDsl)+ dodecahedron+grid. The coding of the samples and their optical images are given in Table 2. The porosity ratio of the scaffolds was as follows; % 87, % 87 and % 86,5 and %82. The metallic biomedical scaffolds in disc shape for compression test (10 x Φ20 mm) and for cell culture cytotoxicity test (5 x Φ5 mm) were fabricated on Mlab cusing 200R system from Concept Laser GmbH, equipped with a 200 W single mode Ytterbium fiber laser from IPG Photonics. The photograph of the scaffolds are given in Figure 4 and Figure 5. The compression test samples had strut diameters of 400 µm. For cytotoxicity test samples in order to achieve the same porosity rate with the sample of mechanical test. The strut diameter was kept as 200 µm.

Table 2 Coding of the samples and their optical images

Design of the scaffolds	Coding	Top view	Side view
Partially Dense surface layer + dodecahedron	PDsl+DCH		
Partially Dense surface layer + grid	PDsl+G		
Partially Dense surface layer + grid+ dodecahedron	PDsl+G+DCH		
Fully dense surface layer +grid+ dodecahedron	FDsl+G+DCH		

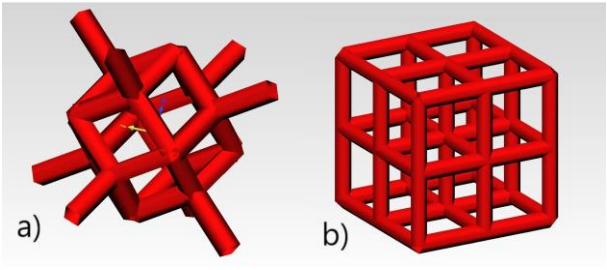


Fig 3. a) Dodecahedron unit structure, b) Grid unit structure

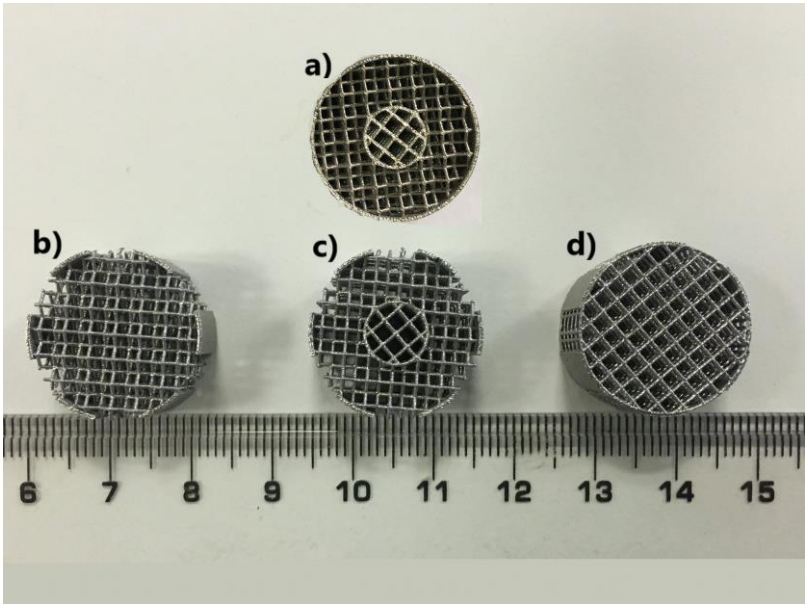


Fig 4. Hybrid designed scaffold specimens for compression tests: (a) FDsl+G+DCH (b) PDsl+ DCH, (c) PDsl+G+DCH, (d) PDsl+G

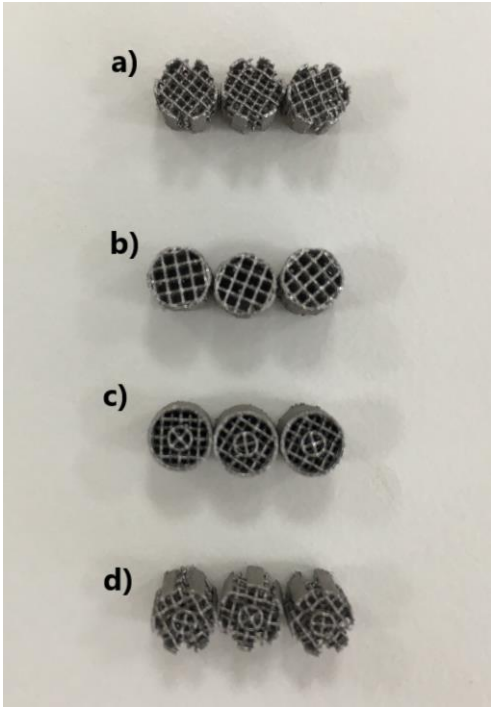


Fig 5. Hybrid designed 5mm x Φ5mm scaffold samples for cell culture cytotoxicity test: (a) PDsl+ DCH, (b) PDsl+G, (c)FDsl+G+DCH, (d) PDsl+G+DCH

The metallic scaffolds were fabricated at 180 W laser power, 1500 mm/s laser speed, 60 μm hatch spacing, and 30μm layer thickness. Three duplicates were fabricated for each type of designs. Heat treatment was not applied to the samples and nitrogen gas was used for inert gas.

Porosity (%) calculation for designed scaffolds was established using the following equation;

$$\text{Porosity (\%)} = [1 - (V_V/V_T)]^* 100 \quad (1)$$

where V_V is volume of designed specimen, V_T is bulk volume of the scaffold specimen .

2.3 Mechanical Test

Compression test was performed at room temperature by universal testing machines (INSTRON 5982) with 100 KN load cell with a test speed of 0.05 mm/min. Positioning of the scaffolds on the load cell was taken into account according to whether supported surface or non-supported surface.

2.4 Cytotoxicity test (MTT)

Cell culture cytotoxicity test (MTT) was applied by seeding L929 fibroblast cells in the ratio of 10^5 cell/ml onto the scaffolds samples. The same ratio of negative control cells were seeded in the wells nearby the scaffolds. Positive control cells were interacted with %1 phenol solution. After 24 h of cultivation, the scaffolds were washed with phosphate buffered saline (PBS), taken out from the well and cultured in the new wells. In order to dissolve the occurring formozan crystals, dimethyl sulfoxide(DMSO) was added. Absorbance was read at 570 nm.

3. RESULTS AND DISCUSSION

3.1 Compressive strength depending on hybrid design

Compressive strength of the highly porous hybrid scaffolds showed different mechanical properties under almost the same porosity rate (~ 87%) and the same strut diameter (400µm). The comparison of the mechanical test results is given in Table 3.

There are three partial surface layered samples as PDsl+ DCH, PDsl+G+DCH and PDsl+G within the same porosity ratio. However, the highest compressive strength was obtained in PDsl+G. The reason for this was due to the effect of anisotropic porous structure of dodecahedron cell unit which have an angle (58°) between the compressive direction and vertical struts of unit cell. This weakened the strength of the structure. On the other hand, the grid structure, refers to a cubic structure, had ability to work under higher compressive forces due to the vertical struts [22]. Fully dense surface layer structures (FDsl+G+DCH) gave the highest elastic modulus and compressive strength because full filled external surface of the samples increased the strength of the scaffold totally. The developed scaffolds within partially dense surfaces mimic the human cortical bone behavior in the sense of both topological and mechanical. For future studies, the partial dense surfaces can be

redesigned under different interspacing between each other. Thus, this may lead to increment in the mechanical strength of the scaffold.

Table 3. Mechanical behavior of fabricated hybrid scaffolds

Specimen	Pore size of designed specimen (µm)	Porosity rate of designed specimen (%)	Max. Compressive Strength (MPa)	Max. Compressive Strain (mm/mm)	Elastic Modulus (GPa)
PDsl+ DCH	1040	%87	49,3±0,2	0,2032	1,45
PDsl+G+DCH	1040-1600 (hybrid)	%86,5	56,5±0,5	0,2050	1,37
PDsl+G	1600	%87	65,7±0,27	0,2097	1,49
FDsl+G+DCH	1040-1600 (hybrid)	%82	100,4±0,6	0,2088	2,19

Under the compressive loading, the scaffolds with dodecahedron cell unit showed the similar deformation behavior while the ones with the grid structure showed different deformation behavior as given in Figure 6. It could be reported that the direction of the vertical structures of grid structure under the same direction of the compressive force had deformed less.

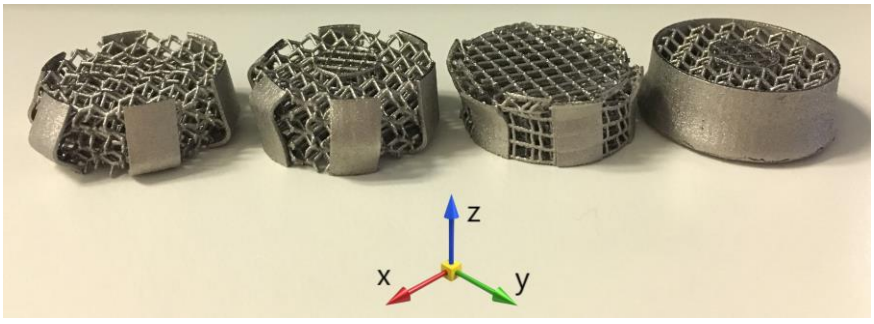


Fig 6. Deformation behavior of fabricated specimens

The scaffold with grid structures showed asymmetric deformation while the other specimens showed symmetric deformation behavior in the compressive direction which can be seen in Fig 6. as z axis. This is a negative situation for grid structure because this behavior forces the scaffold to be slipped from its compressive direction (z axis). In case of the implantation

of scaffold, this may lead to loosening of scaffold fixation plate by reason of the stress on screws.

As a result, the increased porosity contributes to better bone growth but there should be a limit on porosity rate due to the mechanical strengths of scaffolds. Higher porosity rates decrease mechanical strength. In such circumstances, in order to mimic the mechanical strength properties to the natural bone tissue and in order to avoid from the negative effects such as stress shielding, hybrid designs with different unit structure and different dense surface layers may be needed.

3.2 Biological properties depending on hybrid design

The samples with same porosity rate specimens (PDsl+G+DCH, PDsl+G and PDsl+DCH) with different pore size (1040µ, 1600µ and 1040µ -1600µ hybrid) showed that each scaffold had different cell viability. As it can be seen in Table 4, PDsl+G, PDsl+DCH and PDsl+G+DCH which have the same surface layers and porosity rate, showed different cell viability. In literature there are different results obtained by the researcher depending on the pore size and porosity rate. Chen et al. [23] reported that increasing levels of porosity allowed cell proliferation within pores and increased porosity increases the implant surface area, which provided space for cell interaction and tissue formation. Furthermore, mimicking the human porosity rate (%70-%90) in porous scaffold fabrication allowed ideal bone ingrowth and highest cell viability. Pore size also plays an important role for improving biological behaviors of the scaffolds. It was reported that larger pore size demonstrates better bone ingrowth. However, for both porosity and pore size, some contrasting results have been reported [24].

Table 4. MTT assay test results of fabricated hybrid scaffolds

Cell Assay	Specimen	Average Absorbance	% Viability
L929 Fibroblast	PDsl+G	0,616 ± 0,073	53,49
	PDsl+DCH	0,916 ± 0,080	79,51
	PDsl+G+DCH	0,764 ± 0,061	66,35
	FDsl+G+DCH	0,785 ± 0,134	68,12
	Negative Control	1,152 ± 0,036	100
	Positive Control	0,191 ± 0,012	16,57

4. CONCLUSION

SLM has emerged as a promising method that allows the scaffolds to be fabricated in desired pore shape, pore size and porosity rate. Furthermore, hybrid structures can be fabricated as mimicking natural bone tissue after a desired design via SLM.

In this study novel hybrid designs were developed for scaffold fabrication in order to improve their mechanical property and cell viability. Depending on the improved designs on the scaffolds, It has been observed that PDsl+G+DCH showed %14,6 of higher mechanical strength in comparison with PDsl+DCH. FDsl+G+DCH gave % 77,7 of higher mechanical than that of PDsl+G+DCH. On the other hand, the biological test observations showed that PDsl+G had %12,8 lower cell viability in contrast with PDsl+G+DCH. It can be concluded that hybrid structures showed different of mechanical and biological characteristics even they had the same porosity rate and strut diameter. While interconnectivity of different unit structures provided higher mechanical strength, as it can be seen in relationship of PDsl+G+DCH and PDsl+DCH, biological properties gave lower values. As a result, grid structures showed the highest mechanical strength because of its vertical struts in the direction of compressive direction. Furthermore, although the grid structures had bigger pore size (1600µ) and porosity ratio, they showed worse cell attachment than the other scaffolds.

In standardization of a customized scaffold depending on the patient's demand, designing and fabrication of hybrid structured scaffolds within different unit cells can be used for controlling the porosity, pore size and strut diameter in order to achieve the required mechanical properties and desired biological properties. This study is an ongoing work that different various designs are still under investigation of the authors.

ACKNOWLEDGEMENT

The authors would like to thank to The Scientific Research Council of Yildiz Technical University (YTU-BAP) for their support in scope of the research project (Project no: FYL-2018-3222).

REFERENCES

1. **Munir, K.S., Li, Y. and Wen, C., (2017)**, Metallic scaffolds manufactured by selective laser melting for biomedical applications, Metallic Foam Bone, pp 1-23
2. **Zadpoor, A., (2017), "**Mechanics of additively manufactured biomaterials", Journal of the Mechanical Behavior of Biomedical Materials, vol.70, pp 1–6

3. Wang, X., Xu, S., 1 , Zhou, S., Xu, W., Leary, M., Choong, P., Qian, M., Brandt, M and Xie, Y.M., (2016), "Topological design and additive manufacturing of porous metals for bone scaffolds and orthopaedic implants: A review", Biomaterials, vol. 83, pp 127-141

4. Bartolomeua, F F., Sampaioa, M., Carvalhoa, O., Pintob, E., Alvesb, N., Gomesa, J.R., Silvaa, F.S. and Miranda, G., (2017), "Tribological behavior of Ti6Al4V cellular structures produced by Selective Laser Melting", Journal of the Mechanical Behavior of Biomedical Materials, vol. 69, pp 128-1347

5. Wysocki, B., Wojciech Święszkowski, W. and Kurzydłowski, K.J., (2014), "Porous Titanium Scaffold Fabrication For Bone Tissue Engineering By SLM (Selective Laser Melting) Method", Fraunhofer direct digital manufacturing conference, 12-13 March ., Berlin.

6. Su X. , Yang Y., Yu P. ve Sun J., (2012), "Development of porous medical implant scaffolds via laser additive manufacturing", Trans. Nonferrous Met. Soc. China, 22, (2012), pp181-187

7. Bael, S.V., Vandenbroucke, B., Kerckhofs, G., Schrooten J. and Kruth J.P., (2009), " Design and production of bone scaffolds with selective laser melting", 138th TMS Annual Meeting and Exhibition, 15-19 Feb., San Francisco.

8. Xiao, D., Yang, Y., Su, X., Wang, D., and Luo, Z., (2012), "Topology optimization of microstructure and selective laser melting fabrication for metallic biomaterial scaffolds", Trans. Nonferrous Met. Soc. China, 22(2012), pp 2554-2561

9. Čapek, J., Machová, M., Fousová, M. , Kubásek, J., Vojtěch, D. , Fojt, J. , Jablonská, E., Lipov, J. and Ruml, T., (2016), "Highly porous, low elastic modulus 316L stainless steel scaffold prepared by selective laser melting", Materials Science and Engineering, vol. 69, pp 631–639

10. Fousová, M., Vojtěcha D., Kubáseka, J., Jablonskáb, E., Fojt J., (2017), "Promising characteristics of gradient porosity Ti-6Al-4V alloy prepared by SLM process" Journal of the mechanical behavior of biomedical materials, 69 (2017), pp 368–376

11. Li, G., Wang L., Pan W., Yang F., Jiang W., Wu X., Kong X., Dai, K. and Hao, Y. (2016), "In vitro and in vivo study of additive manufactured porous Ti6Al4V scaffolds for repairing bone defects.", Sci Rep., 26;6:34072. doi: 10.1038/srep34072.

12. Peppo, G.M., Palmquist, A., Borchardt, P., Lenneras, M., Hyllner, J.,Snis, A., Snis, J., Thomsen, P. and Karlsson, C., (2011), "Free-Form-Fabricated Commercially Pure Ti and Ti6Al4V Porous Scaffolds Support the Growth of Human Embryonic Stem Cell-Derived Mesodermal Progenitors", The Scientific World Journal, 10.1100/2012/646417.

13. Van Hoorewedera, B., Lietaert, K., Neirinck, B., Lippiatt, N. and Wevers, M., (2017), "CoCr F75 scaffolds produced by additive manufacturing: Influence of chemical etching on powder removal and mechanical performance.", Journal of the mechanical behavior of biomedical materials, vol. 68, pp 216–223.

14. Shah, A.F., Omara, O, Suska, F., Snis, A., Matic, A., Emanuelsson, L., Norlindh, B., Lausmaab, J., Thomsen, P. and Palmquist, A. (2016), "Long-term osseointegration of 3D printed CoCr constructs with an interconnected open-pore architecture prepared by electron beam melting", Acta Biomaterialia, vol. 36, pp 296–309.

15. Yanjin L., Songquan W., Yiliang G., Shuyuan Z. Sai G., Junjie L. and Jinxin L., (2016), "Microstructure, mechanical property and metal release of As-SLM CoCrW alloy under different solution treatment conditions", Journal of the Mechanical Behavior of Biomedical Materials, vol. 55, pp 179-190.

16. Chan, B. P. and Leong, K. W., (2008), "Scaffolding in tissue engineering: general approaches and tissue-specific considerations ", Eur Spine J,vol 17. , pp 467–479.

17. Sabree, I., Gough, J.E. and Derby, B., (2015), "Mechanical properties of porous ceramic scaffolds: Influence of internal dimensions", Ceramics International, Vol. 41, pp 8425–8432.

18. Subia, B., Kundu, J. and Kundu, S.C., (2010), Biomaterial Scaffold Fabrication Techniques for Potential Tissue Engineering Applications, Tissue Engineering and Regenerative Medicine, India

19. Jonitz-Heincke, A., Wieding, J., Schulze, C., Hansmann, D. and Bader, R., (2013), "Comparative Analysis of the Oxygen Supply and Viability of Human Osteoblasts in Three-Dimensional Titanium Scaffolds Produced by Laser-Beam or Electron-Beam Melting", Materials, vol.6, pp 5398-5409.

20. Wu, S., Liu, X., Yeungb K.W.K., Liu, C. and Yang X., (2014), "Biomimetic porous scaffolds for bone tissue engineering", Materials Science and Engineering, vol 80, pp 1 – 36.

21. Choya, S.Y., Suna, C., Leong,a K.F. and Wei, J., (2017), "Compressive properties of functionally graded lattice structures manufactured by selective laser melting", Materials & Design, vol. 131, pp 112–120.

22. Yavari, S.M., Ahmadi, S.M., Wauthle, R., Pouran, B., J.Schrooten, J., Weinans, H. and Zadpoor, A.A., (2015), "Relationship between unit cell type and porosity and the fatigue behavior of selective laser melted meta-biomaterials", Journal of the Mechanical Behavior of Biomedical Materials, vol. 43, pp 91-100.

23. Chen, Y., Frith, J. E., Dehghan-Manshadi, A., Attar, H., Kent, D., Soro, N.D.S., Bermingham, M. J. and Dargusch, M. S., (2017), "Mechanical properties and biocompatibility of porous titanium scaffolds for bone tissue engineering", Journal of the Mechanical Behavior of Biomedical Materials, vol. 75, pp 169–174.

24. Wang, Z., Wang, C., Li, C., Qin, Y., Zhong, L., Chen, B., Li, Z., Liu, H., Chang, F. and Wang, J., (2017), "Analysis of factors influencing bone ingrowth into three-dimensional printed porous metal scaffolds: A review", vol 717, pp 271-285.

DESIGN OF A QUADCOPTER ARM FOR ADDITIVE MANUFACTURING USING OPTIMIZATION AND LATTICE STRUCTURES

Recep Muhammet GÖRGÜLÜARSLAN, *rgorguluarslan@etu.edu.tr* TOBB University of Economics and Technology, 06560, Ankara, Turkey

Şükrü Taha AKSOY, *staksoy@etu.edu.tr* TOBB University of Economics and Technology, 06560, Ankara, Turkey

Tarkan TURNACILAR, *tturnacilar@etu.edu.tr* TOBB University of Economics and Technology, 06560, Ankara, Turkey

Aybars Feyzi KÖKSAL, *akoksal@etu.edu.tr* TOBB University of Economics and Technology, 06560, Ankara, Turkey

ABSTRACT

A quadcopter arm design optimization process using lattice structures is presented. A linear elastic finite element analysis of the lattice-based arm is developed by modeling the strut members using beam elements. The optimal lattice-based design is obtained using size and topology optimization methods. Minimum printable diameter and the inclination angle of the struts are considered for additive manufacturing. The designed structure is successfully fabricated by using an in-house developed 3D printer. The comparison of the FEA results with an existing design in the literature proved that the proposed lattice-based arm design has better weight-to-stiffness performance.

Keywords: Optimization, Lattice Structure, Additive Manufacturing, Quadcopter

1. INTRODUCTION

The quadcopters are the types of drones that have four rotors and propellers for movement. Their main advantage over the other types of drones is that they can achieve vertical flight in a more stable condition [1]. The quadcopters have a great interest nowadays in the areas such as video surveillance, transportation, search and rescue operations, etc. with the advances in electronics, controlling and modeling techniques. Since the components of quadcopters such as the batteries and rotors are relatively heavy to enable lifting easily, a

rigid and light-weight design of the structural frame is required. There exist four arms in the structure of a quadcopter which are connected to the body frame. The design of these arms is critical since they are subjected to high loadings during lifting. Therefore, the studies have focused on the lightweight but strong design of the arm frame of the quadcopters in the literature. The most common arm frame designs have circular and rectangular profiles since those are cost-effective and easy to manufacture [2]. More advanced designs include perforations on the frame to further decrease the weight of the frame [3–5]. These designs focus on the manufacturability of the frame structure by the traditional subtractive manufacturing techniques such as CNC machining. Therefore, the complexity of the designs is aimed to be minimum by using simple two-dimensional perforation shapes such as circular holes since complex geometries hinders the manufacturing of the design.

With the advances in additive manufacturing (AM), which is also known as 3D printing, on the other hand, the fabrication of complex structures, which cannot be fabricated by traditional subtractive manufacturing techniques is possible. In AM, the geometry is built layer by layer so that it is easy to manufacture geometries with high complexity such as lattice structures. Lattice structures are known as the structures composed of a complex network of interconnected strut members at micro- and millimeter scales [6]. These structures have recently gained interest in aerospace, automotive and biomedical engineering because lightweight but still strong structures and materials can be achieved.

In this study, it is expected to have a better weight-to-stiffness performance by using lattice structures in the design of a quadcopter arm compared to the existing designs in the literature which consider only simple geometries as mentioned before. For this purpose, a design optimization process is developed and utilized for the design of a quadcopter arm design using lattice structures. Since the lattice structures can be fabricated by AM, the constraints of the AM process, i.e. the minimum printable diameter and strut angle, are considered during the proposed design process. The designed arm structure results are compared with the existing ones to show the effectiveness of the use of lattice structures in design optimization of quadcopter arm. The designed structure is also additively manufactured to show that it can be fabricated without requiring any further process.

The rest of the paper is organized as follows: In Section 2, the background of the methods used for the lattice-based quadcopter arm design process are presented. In Section 3, the example for the design process is described in detail. In Section 4, the results of the design process are provided and discussed. The conclusions are given in Section 5.

2. MATERIALS AND METHODS

2.1. Lattice structure optimization methods

When the material layout or topology of engineering applications is filled by lattice cells at micro- or millimeter scales, those are called lattice structures or mesostructured materials [7]. The notion of optimal lattice structures started by study of Michell [8], where optimal analytical solutions for the so called Michell structure were developed. With the advent of computer technologies, finite element analysis (FEA) of the lattice structures and optimization algorithms can now be utilized to determine the optimal cross-sectional lengths of the strut members in the design of lattice structures. In the optimization processes, in which the target is to maximize the stiffness of the lattice structure, the strain energy (*SE*) of the lattice structure is minimized as the objective function. Then a general optimization formulation that can be used for the design can be stated by

$$\begin{aligned} &\text{Find} && \mathbf{d} \\ &\text{Minimize} && SE \\ &\text{Subject to} && V - v_f V_T \le 0 \\ & && \mathbf{d}_l \le \mathbf{d} \le \mathbf{d}_u \end{aligned} \tag{1}$$

where $\mathbf{d}$ is a row vector of design variables, which are the cross-sectional lengths of each strut member. In this study, the diameter *D* of each strut is the design variable since a circular cross-section is used to model the struts. The volume of the lattice structure, calculated by, $V = 0.25\pi\, \mathbf{d}^2 \mathbf{L}^T$ is set as a constraint in Eq. (1) and it is aimed to be equal or smaller than the total solid volume of the entire geometry, V_T, multiplied by a volume fraction value, v_f. The lower and upper bounds of the design variables denoted by $\mathbf{d}_l$ and $\mathbf{d}_u$, respectively. Two different optimization methods, so-called size optimization and topology optimization can be used to design lattice structures using Eq. (1).

2.1.1. Size Optimization: The lengths of the strut cross-sections (i.e. diameters in this study) are customized in the optimization process in the range of lower and upper bounds without changing the overall dimensions of the structure topology or layout.

2.1.2. Discrete Topology Optimization: Topology optimization of lattice structures is first proposed by Dorn et al. [9] as the “ground structure optimization method”. In this method, an initial “ground structure”, which is a grid of all potential discrete truss members connecting the nodes in the design space is optimized by eliminating the non-optimal members. For this purpose, the size optimization method can be extended to design also the topology of the structure simply by setting the lower bounds of the design variables $\mathbf{d}_l$ to near zero in Eq. (1) and removing the strut members and connectivity nodes when their cross-sectional lengths

reach this value. Since the ground structure approach is the discrete approximation of the continuous material, this method is also called “discrete topology optimization” [10,11].

2.1.3. Finite Element Model: In both size and topology optimization processes, an FEA is carried out to evaluate the objective function. The formulation of the FEA is given by

$$\mathbf{F} = \mathbf{K}\mathbf{U} \tag{2}$$

where $\mathbf{F}$ denotes the global force vector, $\mathbf{U}$ is the global displacement vector, $\mathbf{K}$ is the global stiffness matrix, which is formed by the element stiffness matrices after applying global coordinate transformations. The element stiffness matrix, $\mathbf{k}$, is determined based on the element type used in the FEM. Since the lattice structures have slender strut members, linear bar, truss [12–14], and beam elements [15,16] are suitable to use in the FEM. The Euler-Bernoulli beam element formulation is used in this study for which the formulation details are skipped for brevity and can be found elsewhere [17].

2.2. Quadcopter structure and the arm length formulation

A basic quadcopter structure and its components are illustrated in Figure 1. The quadcopter arm structure consists of the sections shown by 2, 3, and 4. Since the sections 2 and 4 are the link parts of arm with body and rotors, the arm frame shown by section 3 remains as the design space. Hence, in this study, the design of the quadcopter arm frame shown by section 3 is the focus by using the design optimization methods described in Section 2.1. The length of the arm, denoted by L_A in Figure 1 can be determined by

$$L_A = \frac{\sqrt{2}}{2}\left(D_P - L_B + C\right) \tag{3}$$

where L_B is the length of the body.

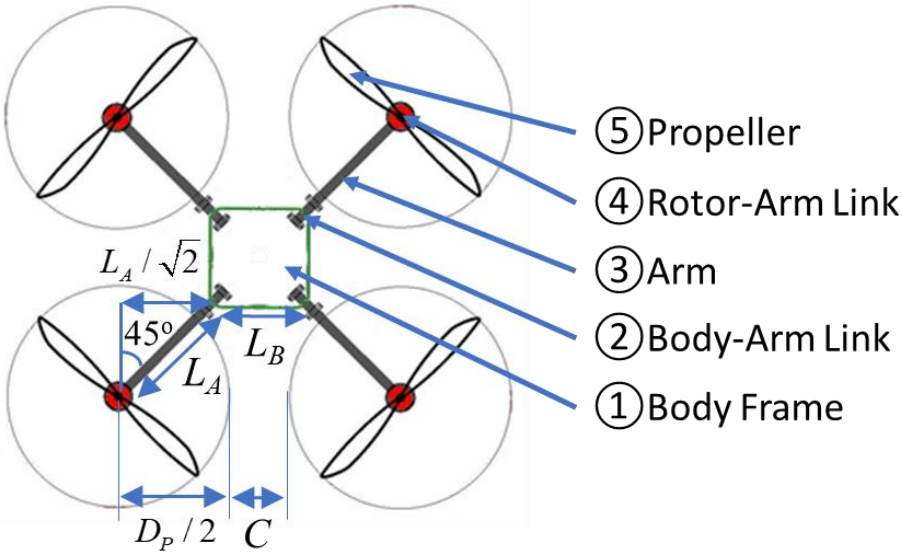


Figure 1. A basic quadcopter structure and its components.

The clearance value, C, can be determined by the designer as a positive value to prevent the collision of two adjacent propellers. The propeller diameter, D_P, is obtained when the appropriate propeller is selected to carry the desired load, P. That means one quadcopter arm is subjected to the take-off load on the rotor side, denoted by F_T, which is the quarter of P. A safety factor, k_{sf}, is included while determining the take-off load to include the uncertainties that can occur due to the factors that can affect the loading. The factor of safety can be taken as $k_{sf} = 2$ as a rule of thumb [5]. Thus, the take-off load can be calculated by

$$F_T = k_{sf}\left(P/4\right) \tag{4}$$

2.3. Quadcopter arm cross-sectional lengths and initial lattice design

A rectangular cross-section with two lengths, L_{C1} and L_{C2}, are considered in this study. The arm geometry is divided into cells in rectangular prism shapes with the lengths of the edges given by $\mathbf{l} = \{l_1, l_2, l_3\}$, which can be populated by different types of lattice cells, as shown in Figure 2. L_{C1} and L_{C2} should be smaller than the arm length, L_A as well as the body length L_B. Furthermore, at each direction, the following inequality relationships between the lattice cell lengths and the quadcopter arm lengths should be satisfied:

$$l_1 \le L_A,\ l_2 \le L_{C1},\ l_3 \le L_{C2} \tag{5}$$

To determine the initial cross-sectional lengths and the lattice structure, various design alternatives are generated by changing the cross-sectional lengths of the arm frame and the lattice cell type used. The linear static FEA of these alternative designs are carried out by fixing all degrees of freedoms of one end of the arm geometry and applying the take-off load, F_T, to the top nodes of the other end as shown in Figure 2.

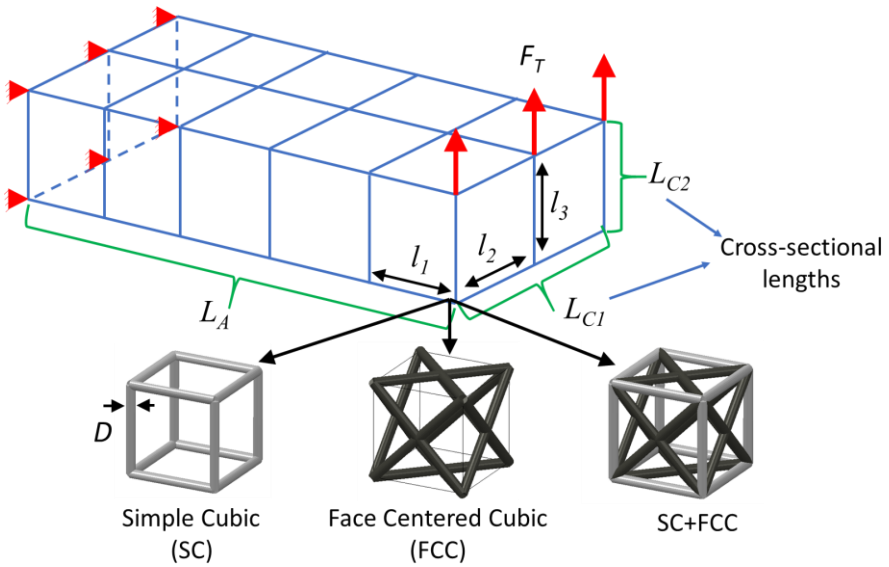


Figure 2. Initial quadcopter arm geometry and lattice cell types. Simple Cubic (SC) cell, Face Centered Cubic (FCC) cell, and combination of SC and FCC (from left to right, respectively).

2.4. Additive manufacturing constraints for lattice structure design

The AM machine that will be used in the fabrication of the designed structure will bring some constraints on the design process. The constraints proposed to consider in this study are described in the following subsections:

2.4.1. Minimum printable diameter: The first and the most critical constraint is the minimum printable diameter of the strut members [18]. Since the optimization process will change the diameter values of each strut member, the lowest diameter value that can be obtained after the optimization should be the minimum printable diameter, denoted by D_{min}. This value can be different for different AM machines. Therefore, D_{min} should be determined before the design process. One way to determine it is to consider the processing parameters as Rosen [7] proposed. Another way is trial-and-error approach, where various diameter values are attempted to be fabricated by the machine and the minimum is determined. In this study, the second approach is utilized.

2.4.2. Manufacturing constraints for lattice cell lengths: The second constraint is for the lattice cell lengths, $\mathbf{l} = \{l_1, l_2, l_3\}$ in Figure 2. In general, when we consider a unit cell that will be filled with a lattice cell, the volume of the lattice cell with strut members, each having D_{min} value, calculated by $V_{\min} = \frac{\pi D_{\min}^{\ 2}}{4} \sum_{k=1}^{m} L_k$, should be smaller than the solid volume of the unit cell, $V_s = l_1 l_2 l_3$, multiplied by a factor, k_l, i.e.

$$V_{\min} = \frac{\pi D_{\min}^{\ 2}}{4} \sum_{i=1}^{m} L_i \le k_l l_1 l_2 l_3 \tag{6}$$

where L_i is the i^{th} strut member's length in the lattice cell, which can easily be calculated by using the lattice cell length values, and m is the total number of the struts. The factor k_l depends on the lattice cell type and used because the struts on the surface of the lattice cell will have excessive parts which should not be included into the volume calculation [19]. For instance, $k_l = 4$ for the SC lattice cell shown in Figure 2, since only the quarter of each strut will remain in the cell. For the SC+FCC, the crossed struts on the surface have the half of the strut in the cell. Therefore, it is approximated as $k_l = 2$ for SC+FCC cell. In addition, the lattice cell lengths determined for the design should satisfy Eq. (6) for maximum diameter, D_{max}, (or upper bound denoted by $\mathbf{d}_u$ in Eq. (1)). For this purpose, once the cell length values are determined by considering Eq. (6), D_{max} is determined by

$$D_{\max}^{\ 2} \le \frac{4 k_l l_1 l_2 l_3}{\pi \sum_{k=1}^{m} L_k} \tag{7}$$

It should be noted that if the lattice cell length values are selected as the minimum allowable values according to Eq. (6), there will be no range between the lower and upper bounds (i.e. D_{min} and D_{max} will be the same) as Eq. (7) will produce the same D_{min} value for D_{max}. This value will not allow any design space for the optimization algorithm to change the diameter values. To eliminate this issue, it is recommended to select relatively larger values of lattice cell lengths that satisfy Eq. (6) to be able to have a larger D_{max} value in Eq. (7) which will allow for changing the diameter values in the optimization in a certain range.

2.4.3. Strut Angle: The angle of the strut from the printing plane is a critical parameter to minimize the support structure required during the fabrication process. The use of support structure may harm the surface quality and increase the printing time dramatically. Therefore, it is better to minimize the support structure usage. For this purpose, the minimum angle, θ_{min} will be determined by experimentation for the AM machine that is used for manufacturing.

3. DESIGN EXAMPLE

In this section, a quadcopter arm example is designed and the design process is described in the following sub-sections.

3.1. Determination of the quadcopter arm length

For the quadcopter arm design example, the load to be carried by the quadcopter is chosen as P=3.6 kg. A safety of k_{sd} = 2 is considered, which makes the take-off load that one arm will carry to be F_T = 1.8 kg according to Eq. (4). To carry this load, the motor type and the propeller type are determined from the available products in the market as TMOTOR U7-KV420 and TMOTOR P16*5.4 inc, respectively [20]. The diameter of this propeller is D_P = 406.4 mm. The body length L_B=180 mm and the clearance value of C = 28 mm is chosen in this design example. Then the length of the arm is calculated using Eq. (3) as L_A = 180 mm.

3.2. Additive manufacturing process and constraints

An in-house developed delta type material extrusion 3D Printer (UB3D Printer) is decided to be used in the fabrication of the quadcopter arm since it is available at the TOBB University of Economics and Technology. The cost-effective but durable ABS and PLA plus materials, which are suitable for the fabrication of the quadcopter arm, can also be fabricated by this printer. The ABS material properties (i.e. elastic modulus of 2600, Possion's Ratio of 0.3, and Tensile strength of 63 MPa) are used in the FEA and optimization processes.

Once the AM machine and the material are chosen, the manufacturing constraints (i.e. the minimum printable diameter and the strut angle) should be determined. It was observed from printed parts that a minimum diameter of D_{min} = 2mm can safely be fabricated using this 3D

printer. Smaller diameter values can also be fabricated, but with the increase of the length of the struts those diameter values may fail to be fabricated. Therefore, to be on the safe side, a conservative value of 2mm is selected in this study.

Furthermore, the minimum inclination angle should be selected. In the experiments, it was observed that depending on the lattice cell size and strut diameter value, this value might show difference. In some lattice cell sizes (especially for small sizes) and larger strut diameter values even horizontal struts can be fabricated by the printer since the supports by the other struts from the first and last point of a horizontal strut will be sufficient to manufacture it. Hence, a detailed experimentation process is necessary to gain more insights about the relationship between the maximum inclination angle and the affecting parameters such as the cell size and strut diameter. In this study, this process is left as a future work and assumed that a conservative value θ_{min} = 45° because usually strut members with larger angle values are manufactured without any issues. In other words, if the strut angle is less than this value, it is not guaranteed to be fabricated by the 3D printer.

3.3. Arm cross-sectional lengths and lattice cell lengths

Two different values for L_{C1} and L_{C2} are considered in this study along with 5 different the lattice cell lengths for l_2 and l_3. In addition, two types of lattice cell types, namely SC and SC+FCC illustrated in Figure 2 are considered in this study. The corresponding eight design alternatives generated are illustrated in Figure 3. The lattice cell length l_1 in the direction of L_A is kept the same for all design alternatives. The maximum diameter is set to be D_{max} = 6 mm. For the eight design alternatives in Figure 3, Eqs. (5), (6), and (7) are checked and made sure that those equations are satisfied. Furthermore, the length values for these design alternatives are chosen such that the minimum strut angle θ_{min} = 45° constraint is mostly satisfied. Only the horizontal struts do not meet the angle constraint. Nevertheless, these designs are suitable to minimize the use of support structure.

4. RESULTS AND DISCUSSIONS

4.1. Alternative lattice designs results

The design alternatives given in Figure 3 are generated by using an equivalent diameter value of D_{min} = 2mm. Then, the linear static FEA under the boundary conditions given in Figure 2 are carried out. The maximum deflection, δ_{max}, and the maximum stress, σ_{max}, values were obtained. Since each design will have a different volume, V, due to the change of the cross-sectional lengths and the lattice lengths, these results were normalized by dividing by

the volume of the corresponding design to make a fair comparison. The normalized deflection, $\bar{\delta}_{max} = \delta_{max} / V$, and maximum stress, $\bar{\sigma}_{max} = \sigma_{max} / V$ results are listed in Table 1.

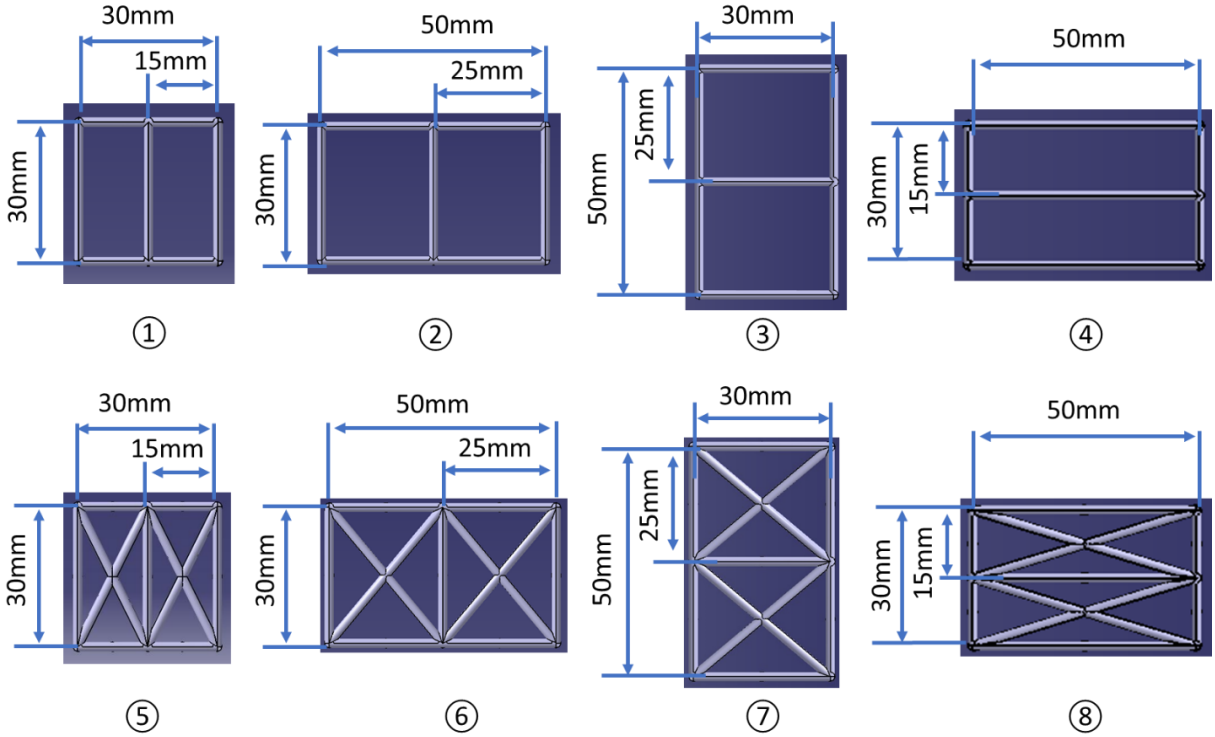


Figure 3. Eight alternative lattice-based arm designs

Table 1. FEA results for each of the ten design alternatives

Design #	①	②	③	④	⑤	⑥	⑦	⑧
$\bar{\delta}_{max}$ (x10^4) mm^{-2}	70.4	63.4	53.9	48.41	**0.92**	0.98	0.77	2.01
$\bar{\sigma}_{max}$ (x10^3) /mm^5	16.9	15.0	11.5	9.82	**0.55**	0.74	0.92	1.54

As seen in Table 1, the designs using SC+FCC lattice cells (i.e. designs 5 to 8) have smaller deflection and stress results compared to the designs using SC lattice cells (i.e. designs 1 to 4). These results are consistent with the literature where again SC+FCC cells determined to produce better performance [18]. Among all alternative designs, it is seen that the one numbered by 5 produce the smallest values as shown in Table 1 by bolded numbers. Hence, design number 5, which has l_2 x l_1 = 15x30mm SC+FCC lattice cells with the cross-sectional lengths L_1 x L_2 = 30x30mm, is chosen as the initial design for the optimization procedure.

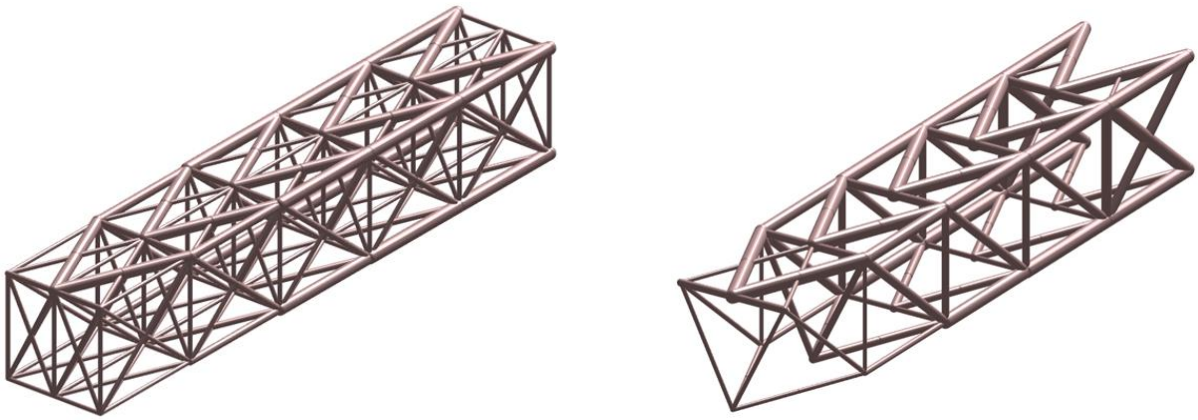
4.2. Optimization Results

Once the initial design is determined, the size and discrete topology optimization processes are implemented. The optimization algorithm used is the “fmincon” command of the MATLAB Optimization Toolbox, which is based on the gradient-based optimization algorithms. The

beam element FEA formulation developed in MATLAB is integrated with this optimization algorithm and the optimization formulations given by Eq. (1) are utilized in the code. The initial design variables are set to D_{min} = 2 mm and a volume fraction of v_f = 0.25 is aimed for the volume constraint. The optimized designs in Figure 4 are obtained and the optimization results are listed in Table 2 along with FEA results using constant diameter values.

As seen in Table 2, the designs obtained by both optimization processes have much less strain energy and maximum displacement values compared to the initial design with 2mm diameter and design with constant 3mm diameter. The design with 3 mm diameter results are included because it has a very close volume with the optimized designs. Although they have similar volumes, it is clear that the optimization processes produce a design with better performance according to the results in Table 2.

Furthermore, the design obtained by the topology optimization gave slightly better results compared to the one obtained by the size optimization. The design by the topology optimization is also advantageous because it has a smaller number of struts than the design by the size optimization because the strut members that have near zero diameter values are removed from the topology. This way, the manufacturing process will be faster for design with the topology optimization. Furthermore, most of the struts that lays on the printing plane, which is the plane of L_1 and L_2 lengths, are removed from the topology in the design by topology optimization. Thus, the need for support structures is also reduced by this design.



(a) (b)

Figure 4. Lattice-based arm designs (a) by size optimization, (b) by topology optimization.

Table 2. Optimization results

Design	Design with D_{min} = 2 mm	Design with D = 3 mm	Design by Size Optimization	Design by Topology Optimization
Volume (x10^3) (mm^3)	18.067	40.65	40.5	40.5

Strain Energy	27.95	12.27	4.94	4.21
Max. Disp. (mm)	3.17	1.39	0.56	0.48

4.3. Refined design and fabrication by AM process

Although the design with topology optimization looks preferable due to its above-mentioned advantages, the front side of this design has very few strut members and nodes which will cause problems when the rotor-arm link is added to the design. Since the topology optimization process does not consider this link, it can remove the strut members which will needed for structural rigidity. To address this issue, a refined design is required by including some strut members in this region again to the design. This refinement can be achieved by leveraging from the design result of the size optimization. Specifically, the strut members on this rotor side of the arm that have a strut angle largen than $\theta_{min} = 45^{o}$ are included to the design by topology optimization using their diameter values obtained from the size optimization. In addition, the strut members in the design by topology optimization, which were not removed from the design but have diameter values smaller than D_{min} = 2mm, are modified and their diameter values were changed with the values obtained by the size optimization to have a final printable design.

The CAD model of the refined design obtained by the proposed methodology is generated and then converted to the STL model using the commercial CAD software CATIA. The rotor-arm link and the propeller-arm link are also included into the design to have the entire arm geometry. Thus, a refined design is obtained for the arm frame of the quadcopter. The STL models are created for both design by size optimization and refined design, since those are the ones that were designed considering the AM constraints. Then, these models are fabricated using the selected delta type 3D printer. The CAD models and the printed designs are illustrated in Figure 5.

4.4. Verification and validation of the designed quadcopter arm results

For the verification of the FEA results obtained by the beam element formulation used in MATLAB, the lattice structure FEA is also carried out in the commercial software CATIA. In CATIA, the lattice structure FEM is generated using solid tetrahedral elements instead of the beam elements. Specifically, the maximum displacement obtained from these two FEAs are compared for the same lattice structure and a relative error of 8% was obtained. This can be considered as an acceptable result because the solid tetrahedral elements in CATIA will produce more accurate results compared with the beam element formulation [18].

For the validation of the FEA results, the fabricated part of the refined design is experimentally put under 1 kg weight and the body-arm link is fixed as shown in Figure 6(a).

Since the load that the quadcopter will carry is chosen as 3.6 kg in the beginning of the design process, each arm is expected to carry 0.9 kg load in real world. 1 kg weight used in this experimentation should be fine because a safety factor of 2 was considered in the design which means the design of the arm can carry loads up to 1.8 kg. In the experimentation, it is validated that the refined design successfully carried the load.

Furthermore, a comparison of the refined design results with a design from the literature is done to see the effectiveness of the proposed lattice-based design methodology. Similar hollow-based structures are used in the literature to design lightweight quadcopter arms, but these are designed to manufacture by subtractive manufacturing techniques. Kuantama et al. [4] has such a design in his study. If the lattice structure is used in the design it is expected that it should be advantageous over such designs in the literature. For this purpose, the refined design of the quadcopter arm is assembled with the body of the quadcopter arm as shown in Figure 6(b) and a static linear FEA of the assembly is carried out in CATIA software. A similar FEA result exist in Kuantama et al. [4] for the assembly of the quadcopter frame and therefore, the results were compared as given in Table 3.

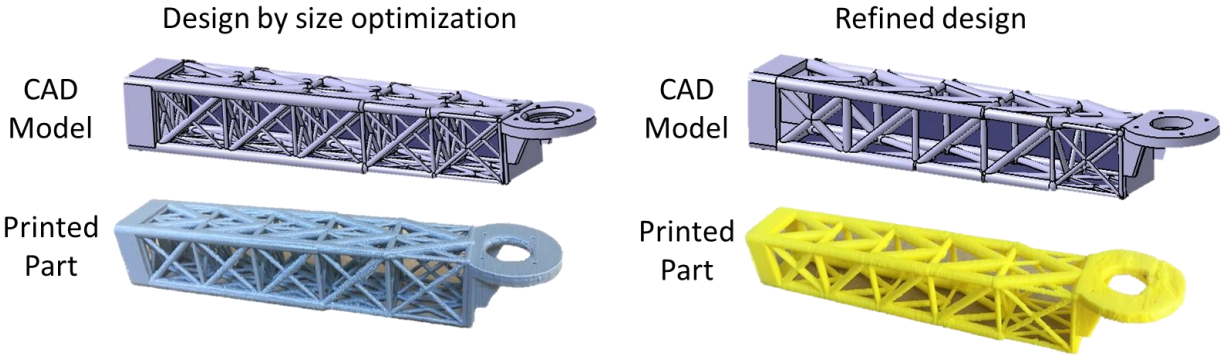


Figure 5. CAD models and the fabricated designs



(a) (b)

Figure 6. (a) Experimentation of the refined design (b) Assembly of the quadcopter frame

Table 3. Comparison of the FEA results of the refined design by literature

	Total Weight of the Quadcopter Frame	Lifting capacity (without the safety factor)	Maximum Displacement
Refined Design	346 gr	7.2 kg	1.1 mm
Kuantama et al. [4]	560 gr	5.3 kg	3.3. mm

The comparison of the results show that the refined design obtained in this study is 38% lighter than the design in Kuantama et al [4]. Furthermore, although the lifting capacity of the refined design is 36% greater, the maximum displacement obtained by the refined design is 67% less than the design used in Kuantama et al. [4]. These results prove that a more rigid and lighter design is obtained by using the proposed design methodology and lattice structures for AM.

5. CONCLUSIONS

A design process light weight quadcopter arm that can carry the desired loading without failure using lattice structures is presented in this study. Since the lattice structures have complex geometry those can be fabricated by AM. Therefore, the AM constraints such as the minimum printable diameter and the inclination angle that can be printed without support structure are effectively considered in this design process. The lattice cell lengths and the minimum and maximum dimeter values in the optimization process are determined based on these AM constraints. A refined design is created using the results of both size optimization and discrete topology optimization to achieve a printable design. The results showed that a lighter and stronger quadcopter arm design can be achieved using lattice structures and optimization process. It was also validated that the designed structure can carry the desired load when fabricated by AM, and therefore can be used for real world applications.

ACKNOWLEDGEMENTS

The authors greatly appreciate the help of Assoc. Prof. Dr. Hakkı Özgür ÜNVER and his PhD student Gökberk SERİN for the fabrication of the designed quadcopter arm structures using

the in-house developed UB3D delta type printer at the TOBB University of Economics and Technology.

REFERENCES

1. **Gapanov, I., and Razinkova, A., (2012),** "Quadcopter Design and Implementation as a Multidisciplinary Engineering Course," IEEE International Conference on Teaching Assessment, and Learning for Engineering, Hong Kong, pp. 16-19.

2. **Anudeep, M., Diwakar, G., and Katukam, R., (2014),** "Design of a Quadcopter and Fabrication," International Journal of Innovations in Engineering and Technology, Vol.4, No.1, pp 59-65.

3. **Gadiya, P., Patheria, A., Chib, K., and Gore, A., (2017)**, "Design, Analysis and Fabrication of QuadCopter for Emergency Medical Services Using GPS," International Journal of Research in Mechanical Engineering and Technology, Vol.7, No.2, pp. 65-68.

4. **Kuantama, E., Craciun, D., and Tarca, R., (2016),** "Quadcopter Body Frame Model and Analysis," Annals of the University of Oradea, Fascicle of Management and Technological Engineering, Vol.25, No.15, pp. 71-74.

5. **Selvaganapathy, S., and Ilangumaran, A, (2017),** "Design of Quadcopter for Aerial View and Organ Transportation using Drone Technology," Asian Journal of Applied Science and Technology, Vol.1, No.3, pp. 311-315.

6. **Fleck, N. A., Deshpande, V. S., and Ashby, M. F., (2010),** "Micro-Architectured Materials: Past, Present and Future," Proceedings of the Royal Society A: Mathematical, Physical and Engineering Sciences, Vol.466, No.2121, pp. 2495-2516.

7. **Rosen, D. W., (2007),** "Computer-Aided Design for Additive Manufacturing of Cellular Structures," Computer-Aided Design and Applications, Vol.4, No.5, pp585-594.

8. **Michell, A. G. M., (1904),** "The Limits of Economy of Material in Frame Structures," The London, Edinburgh, and Dublin Philosophical Magazine and Journal of Science, No.8, Vol.47, pp. 589-597.

9. **Dorn, W., Gomory, R., and Greenberg, H., (1964),** "Automatic Design of Optimal Structures," Journal de Mecanique, Vol. 3, No.6, pp. 25-52.

10. **Richardson, J.N., Adriaenssens, S., Bouillard, P., and Coelho, R.F., (2012),** "Multiobjective Topology Optimization of Truss Structures with Kinematic Stability Repair," Structural and Multidisciplinary Optimization, Vol.46, No.4, pp. 513-532.

11. **Rozvany, G.I.N., Bendsoe, M., and Kirsch, U., (1995),** "Layout Optimization of Structures," Applied Mechanics Reviews, Vol.48, No.2, pp. 41-119.

12. **Gilbert, M., and Tyas, A., (2003),** "Layout Optimization of Large-scale Pin-jointed Frames", Engineering Computations, Vol.20, No.8, pp. 1044-1064.

13. **Wallach, J.C., and Gibson, L.J., (2001),** "Mechanical Behavior of a Three Dimensional Truss Material," International Journal of Solids and Structures, Vol. 38, pp 7181-7196.

14. **Deshpande, V.S., Fleck, N.A., and Ashby, M.F., (2001),** "Effective Properties of the Octet-Truss Lattice Material," Journal of the Mechanics and Physics of Solids, Vol.49, No.8, pp. 1747-1769.

15. **Chiras, S., (2002),** "The Structural Performance of near-Optimized Truss Core Panels," International Journal of Solids and Structures, Vol.39, pp. 4093-4115.

16. **Johnston, S.R., Reed, M., Wang, H.V., and Rosen, D.W., (2006),** "Analysis of Mesostructure Unit Cells Comrised of Octet-Truss Structures," 17th Solid Freeform Symposium, SFF 2006, pp. 421-432.

17. **Kattan, P.I., (2008),** "MATLAB Guide to Finite Elements: An Interactive Approach," Springer-Verlag, New York.

18. **Gorguluarslan, R.M., Gandhi, U.N., Song, Y., and Choi, S-K., (2017),** "An Improved Lattice Structure Design Optimization Framework Considering Additive Manufacturing Constraints," Rapid Prototyping Journal, Vol.23, No. 2, pp. 305-319.

19. **Gorguluarslan, R.M., Gandhi, U.N., Mandapati, R., and Choi, S-K., (2016),** "Design and Fabrication of Periodic Lattice-based Cellular Structures," Computer-Aided Design and Applications, Vol.13, No.1, pp. 50-62.

20. **T-MOTOR**, "Propulsion Systems", [Online], http://store-en.tmotor.com/. Access date: 04/18/2018.

HIGH VIBRATION ABSORPTIVE BODY PRODUCTION FOR TURNING CUTTING TOOLS WITH ADDITIVE MANUFACTURING TECHNOLOGY

Uğur MALAYOĞLU, *ugur.malayoglu@deu.edu.tr* Dokuz Eylul University, 35390, Izmir, Turkey

Tuğrul SOYUSİNMEZ, *tsoyusinmez@totomak.com.tr* Totomak, 35620, Izmir, Turkey

Gökçe AKKUŞ, *gakkus@totomak.com.tr* Totomak, 35620, Izmir, Turkey

Oğuzcan GÜZELİPEK, *oguzelipek@totomak.com.tr* Totomak, 35620, Izmir, Turkey

ABSTRACT

The dynamic behavior of a machine tools body directly influences key metal cutting performance like cutting speed, cutting depth or minimize movements on the high-speed movements. That will affect directly results of the parts surface quality, cutting time and also tool life.

In this study, usage of the alternative material with complex geometry for tool body with additive manufacturing methods had been experimentally checked for effects on the surface quality, machining parameters, dimensional changes and tool life. Alternative body material usage effect which can absorb high vibration on the system and experimentally test results had compared on different materials like grey and ductile iron casting and SAE 1117 steel.

Keywords: Vibration, Cutting Tools, Additive Manufacturing

INTRODUCTION

Different kinds of sensors and signal processing techniques have been developed for the direct or indirect detection of tool wear, breakage and vibration analysis in machining process. Vibration measurement is one of the indirect methods of tool condition monitoring [1]. Metal cutting processes can entail three different types of mechanical vibrations that arise due to the lack of dynamic stiffness of one or several elements of the system composed by the machine tool, the tool holder, the cutting tool and the workpiece. These three types of vibrations are known as free vibrations, forced vibrations and self-excited vibrations [1, 4]. Several machining variables, such as cutting speed, depth of cut, feed rate, workpiece

material, and cutting tool geometry have significant effects on the machining process and vibrations.

In a machining process, three different types of mechanical vibrations are present due to a lack of dynamic stiffness and rigidity of the machine tool system comprising tool, tool holder, work piece and machine tool itself. These are the free, forced and self-excited vibrations. Free or transient vibrations are induced by shock, such as impulses transferred to the structure of machine tool or from the initial engagement of cutting tools. Forced vibrations, resulting from periodic forces within the system such as unbalance defects in machine tool components (like gears, spindles and bearings), and vibration transmitted through the foundations from other machinery in the shop.

Material Information's and Design of Experiment

In this trail the work-piece is a round bar (50mm diameter and 200mm long) of SAE 117 steel. The chemical composition of the steel had present on Table 1. The cutting tool and tool holder figures are presented on Figure 1 and Figure 2. On the other hand, during the machining trails have been conducted in under cutting fluid which density %6. Tool work-piece combination have significant role on cutting forces and vibration signals. The cutting conditions are presented in Table 2.

Table 1. Chemical Composition of SAE 1117

SAE No.	C	Mn	P	S
1117	0.14 to 0.20	1.00 to 1.30	0.040 max	0.08 to 0.13

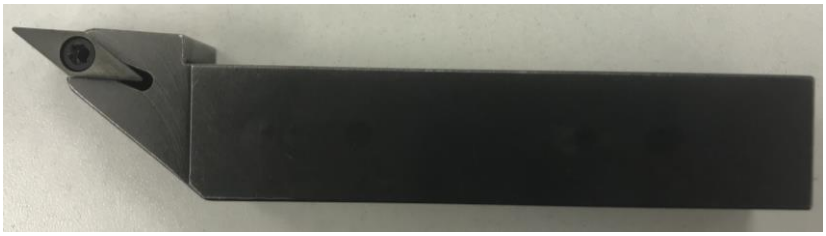


Figure 1. Actual Photograph of Tool Holder



Figure 2. Actual Photograph of Cutting Tool Insert

The experimental machining process parameters had used as Table 2.

Table 2. Machining Process Parameters

Trail	Cutting Speed (m/min)	Feed (mm/rev)	Depth of Cut (mm)
1	150	0,3	1
2	175	0,5	1,5
3	200	0,7	2

Experimental Details

Experimental test had completed within CNC machine, FFT analyser, digital tool dynamometer, and accelerometer and tool dynamometer sensor. Digital tool dynamometer sensor and accelerometer is mounted on tool holder as close to cutting tool insert. Figure 3 shows the design of the experimental set-up test machine and Table 3 indicates CNC machine details.

Table 3.CNC Machine Specifications

Specification		**Bed Length -500U in**
Capacity	Maximum Swing	610 mm / 24.02 in
	Maximum Machining Diameter	350 mm /13.780 in
	Maximum Bar Work Capacity	77 mm / 3.0 in
	Maximum Machining Length	483 mm / 19.020 in
Main Spindle	Chuck Size	10 in
	Maximum Speed	4000 rpm
	Motor Output (30 minute rating)	26 kw / 35.0 hp
Turret (Upper)	Number of Tools	12
Feed Axes	Travel (X Axis)	190 mm / 7.48 in
	Travel (Z Axis)	515 mm / 20.28 in
	Travel (W Axis)	525 mm / 20.67 in

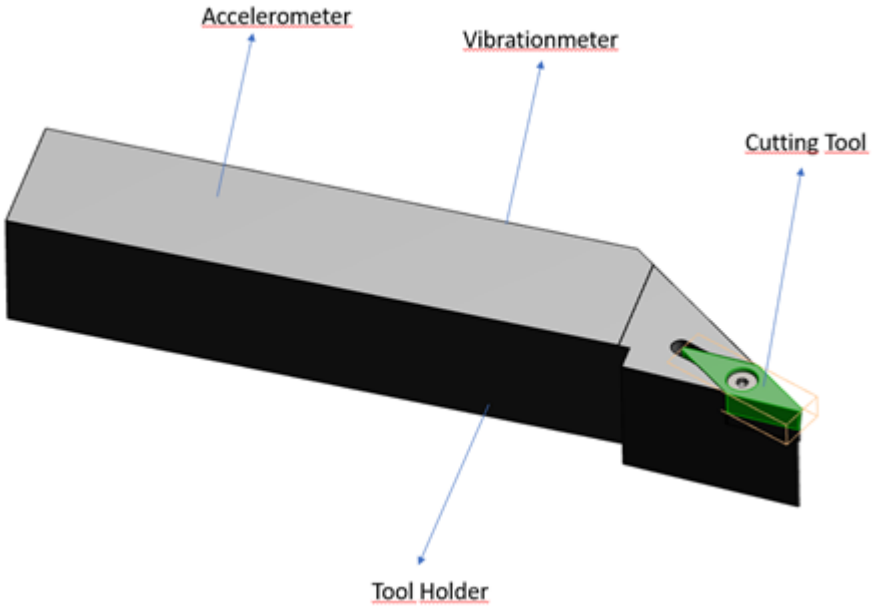


Figure 3. Experimental set up

During the machining phase 3 different cutting force effect on the tool and the body. With additive manufacturing we had designed the damping capacity of a material is an evaluation of the energy dissipated in the material during mechanical vibration. High damping materials, which possess the ability to dissipate mechanical vibration energy, are valuable in the application fields of noise control and for stabilizing structures to suppress mechanical vibrations and attenuate wave propagation. Practical applications need low density materials that simultaneously exhibit a high damping capacity and good mechanical properties. However, in metals these properties are often incompatible, due to the dependence of the microscopic mechanisms involved in strengthening and damping [5,8]. Therefore, it would be of interest to develop new materials that simultaneously exhibit good mechanical properties and high damping. This is possible only when the microscopic mechanisms responsible for dissipation of the vibration energy are independent of that of the hardening and strengthening. Such a compromise can be achieved by the development of two-phase composites, in which each phase plays a specific role: damping or providing mechanical strength. Metal matrix composites (MMCs) are good candidates because firstly, MMC processing allows the possibility of tailoring the resultant damping properties by selecting high damping reinforcements, secondly, MMC processing modifies the microstructure of metals and alloys, thus introducing energy dissipation sources and thirdly, typically hard and high strength reinforcements will improve the mechanical properties of the composites [9,12].

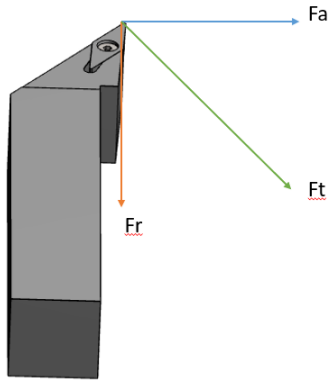


Figure 4. Tool and Tool Holder Force Diagram

RESULTS AND DISCUSSIONS

During the machining trails 3 different test had applied with current and MMC tool holder for each combination of cutting speed, feed rate and depth of cut the output results of cutting forces and Vibration signals in tangential (Va), Feed (Vr) and Radial (Vt) direction are presented in Table 4 and Table 5.

Table 4. Test Results Observation Table for Current Tool Holder

			Force (kg)			Vibration (Hz)		
Speed (m/rev)	Feed (mm/rev)	DOC (mm)	Fa	Fr	Ft	Va	Vr	Vt
150	0,3	1	104	45	52	458	888	595
175	0,5	1,5	101	41	49	533	955	651
200	0,7	2	98	39	47	632	985	685

Table 5. Test Results Observation Table for Additive MMC Tool Holder

			Force (kg)			Vibration (Hz)		
Speed (m/rev)	Feed (mm/rev)	DOC (mm)	Fa	Fr	Ft	Va	Vr	Vt
150	0,3	1	93	42	48	383	823	553
175	0,5	1,5	91	39	47	461	870	584
200	0,7	2	85	36	43	567	907	614

On the other hand, frequency during the cutting trails with MMC Tool Holder had present on Figure 5 during rough cutting time and Figure 6 during with finish cutting time.

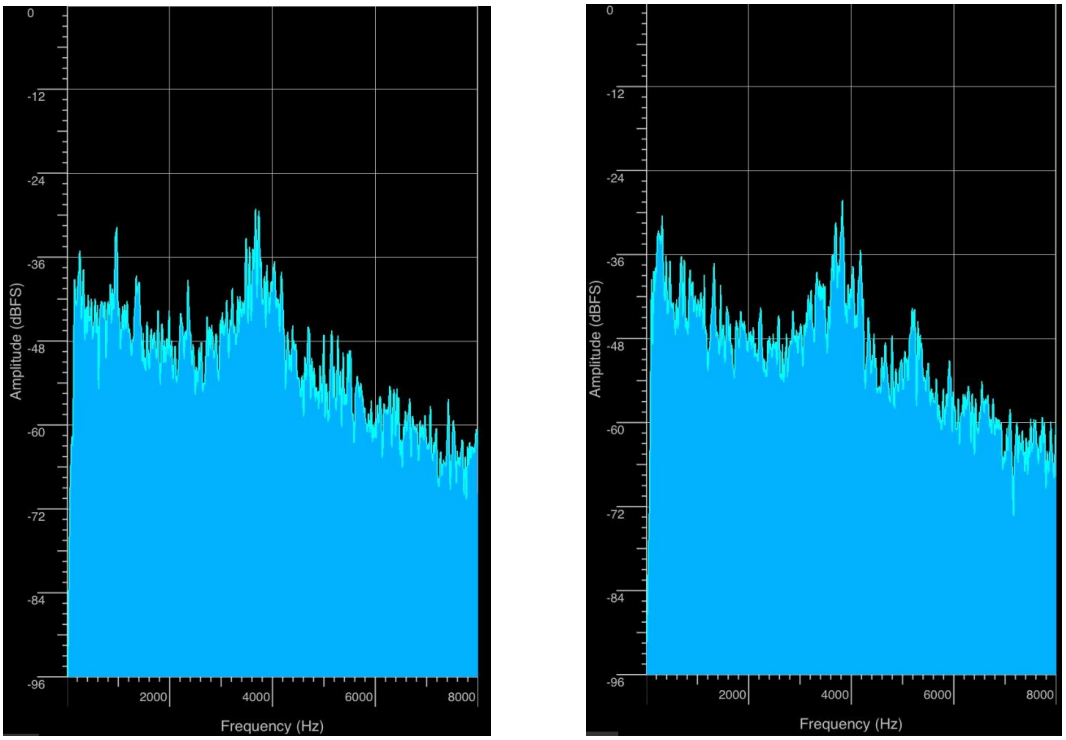


Figure 5. Rough Cutting Tool Vibration Analysis

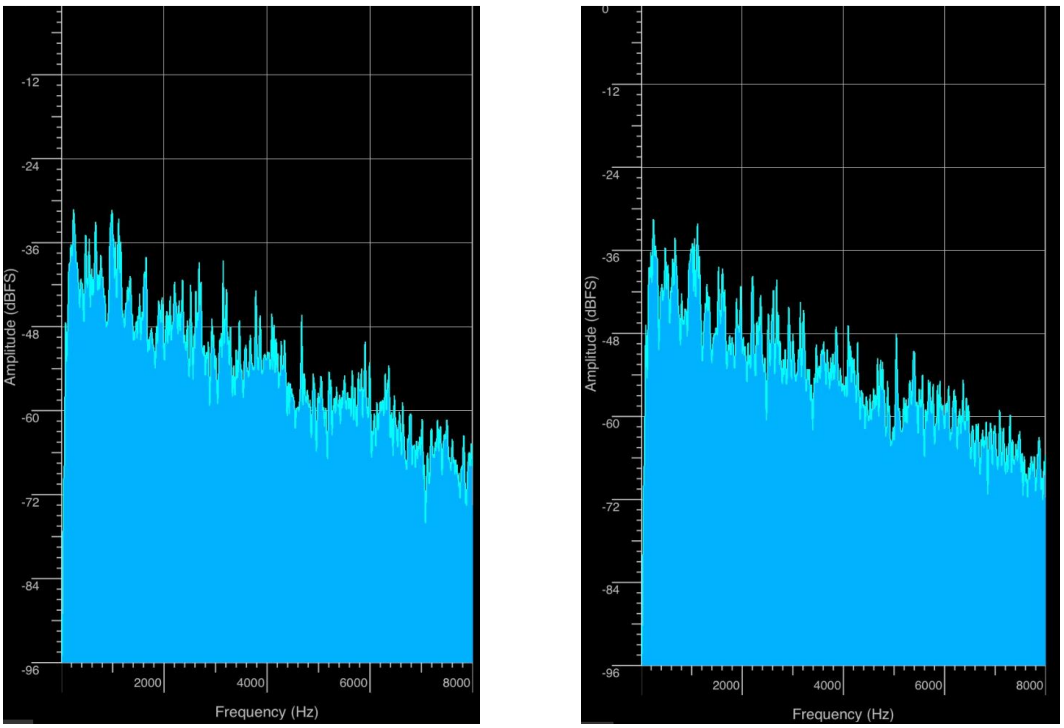


Figure 6. Finish Cutting Tool Vibration Analysis

CONCLUSION

This study is carried out to investigate the cutting forces and vibration signal at different cutting tool holder condition using the standard and MMC material. The results show that the tangential force is largest followed by the feed force and radial force. The vibration signal and the cutting forces well to investigate the tool state as well as the different occurrences during turning. The following are the main points out during this investigation.

• The vibration signal measured along the three directions tangential, feed, and radial direction respectively shows the same chronological order as like the cutting forces.

• During this investigation it is observed that MMC tool holder absorb vibration and force better than current material tool holders.

• MMC tool holder is present better results and absorption for all different cutting conditions.

REFERENCES

1. **Teti R., Jemielniak K., Donnell G. O, Dornfeld D. (2010),** “Advanced monitoring of machining operations”, CIRP Annals – Manufacturing Technology, Vol. 59, 2010, p. 717-739.

2. **S. A. Tobias (1961),** Machine Tools Vibrations (Vibraciones en Ma ´quinas-Herramientas). URMO,Spain.

3. **Dimla E. Dimla Snr (2006),** “Sensor signals for tool-wear monitoring in metal cutting operations – a review of methods”, International Journal of Machine Tools & Manufacture, Vol. 40, p. 1073-1098.

4. **G. Litak, R. Rusinek (2011),** “Vibrations in stainless steel turning: multifractal and wavelet approaches”, Journal of Vibroengineering, Vol. 13, Issue 1, 2011, p. 102-108

5. **Choi, G. H., Wang, Z. X., Dornfeld, D. A., Tsujino, K (1990),** “Development of an intelligent on-line tool wear monitoring system for turning operation”, Proc. USA-Japan Symposium on Flexible Automation, A pacific Rim Conference ISCIE, Kyoto, Japan, 683-690.

6**. Byrne, G., Dornfeld, D., Inasaaki, I., Koning, W., Teti, R.(1995),** “Tool condition monitoring system (TCMS)- the state of research and industrial application”, annals of CIRP, (49), 541-567.

7. **Oraby, S. E., Hayhurst, D. E. (1991),** “Development of models for tool wear force relationship in metal cutting”, International Journal of Mechanical Tool Manufacturing, (33), 125-138.

8. **Jemieelniak, K., Bombin'ski, S., Arissimuno, P.X. (2008),** Tool condition monitoring in micromilling based on hierarchical integration of signal measure, Manufacturing Technology, (57), 21-124.

9. **Burke, L. I., (1989),** "Automated identification of tool wear states in machining processes: an application of self of self- orgnising neural networks", Ph.D. thesis, Department of Industrial Engineering and Operation Research, UC at Berkeley.

10. **Bhuiyan, M. S. H., Choudhary, I.A., Yuoff, N., (2012**), "A new approach to investigate tool condition using dummy tool holder and sensor set-up", International Journal of Advanced Manufacturing & Technology, (61), 465-479.

11. **Li, X., (2002), "**A brief Review: Acoustic emission method for tool wear monitoring during turning", Interanational Journal of Machine Tool & Manufacturer, (42), 157-165.

12. **Abouelatta, O., Madi, J., (2001),** "Surface roughness prediction based on cutting parameter and tool vibrations in turning operation", Journal of Material Process & Technology, (118), 269-277s

DESIGN AND DEVELOPMENT OF AN ADDITIVE MANUFACTURING SYSTEM FOR METAL PRINTING

S. Shahid MUSTAFA, *smustafa14@ku.edu.tr Manufacturing and Automation Research Center, Koc University,* 34450*, Istanbul, Turkey*

Ismail LAZOGLU, *ilazoglu@ku.edu.tr Manufacturing and Automation Research Center, Koc University,* 34450*, Istanbul, Turkey*

ABSTRACT

Direct metal laser sintering (DMLS) is an additive manufacturing (AM) technology, based on powder bed fusion (PBF) process. By layer-wise selective melting of metal powder, it can fabricate functional parts of any geometrical complexity. However, the challenge of exploring the metal powder processing from the research point of view is impeded by the predominance of commercial systems. Which are costly and offer very limited access to underlying operations and hence appear to be a black box to its users. In this article, the development of an open control-architecture DMLS machine, designed specifically for research in this area is presented.

Keywords: Metal AM, PBF, SLM, DMLS.

1. INTRODUCTION

AM allows the manufacturing of Freeform structures with intricate geometries and optimize their design in terms of cost, functionality and weight. Among the processes for metal AM are powder bed fusion (PBF), powder feed and wire feed systems [Attaran 2017]. The latter two systems share the principle with feed filament fusion (FFF) class of 3D printers, where the printer head moves and deposits the molten material (metal in this case) on to the previously built layer. However, on the contrary PBF metal printer s make use of either laser or electron beam as energy source to melt the powde. The energy beam moves along parallel tracks and melts the powder, which upon cooling fuses with the adjoining material and transforms into bulk metal [Nadammal et al. 2017]. The laser powder bed fusion (L-PBF) as shown in Figure 1 uses optical deflecting units such as galvanometer scan heads to control the movement of laser beam in XY plane [Kruth et al. 2005].

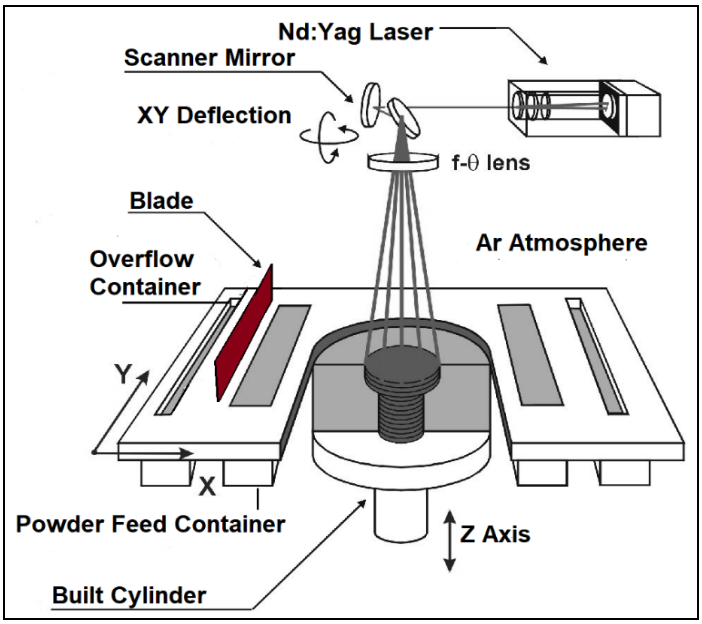


Figure 1: Elements of basic L-PBF process for metal 3D printing as reported in literature [Craeghs, Clijsters, Yasa, and Kruth 2011]

For electron beam melting (EBM) electromagnetic deflectors replace the scanners [Murr et al. 2012]. In this article only laser based process for metal 3D printing, which is alternately termed direct metal laser sintering (DMLS) or selective laser melting (SLM) [Pinkerton 2015] is considered. This is a digitally driven additive manufacturing technology making it an emerging and viable option for many hard to manufacture, low batch and customized metal parts. For the same reason DMLS has been attracting biomedical orthopaedic implant fabrication, aerospace, tool making and other high technology manufacturing fields [Attaran 2017]. DMLS shows unlimited potential for manufacturing highly complicated, precise and high performance metal parts of virtually any complexity, one can design in CAD tools [Darwish and Aslam 2014][Berumen et al. 2010].

Metal powder generally exhibits very complex thermodynamic behavior during the SLM process [Berumen et al. 2010]. Which tends to cause deformation, porosity and other repeatability related issues in the manufactured part, thus making the quality in product difficult to achieve [Peralta et al. 2016]. This places a technical barrier to the widespread proliferation of DMLS in many industries, such as small and medium enterprises. To address this accessibility barrier, an open architecture L-PBF based metal 3D printer is developed. This system is expected to enable the researchers, exploration of new materials and the better understanding of the underlying physics of the thermo-mechanical behavior of metal powders. The melt-pool level closed loop control of the metal powder processing and thermal deformation is the primary motivation here. By doing so the aforementioned quality

barriers can be removed, which might result the cost to go down [Craeghs, Clijsters, Yasa, and Kruth 2011].

Besides, the area of the intended research ranges from AM software development to topological optimization algorithms, so that quality can meet desired standards with minimum cost, which the DMLS is capable of. The capabilities of this technology can be fully explored such as customization of parts and fabrication of intricate geometries, which are difficult to produce using conventional manufacturing methods such as milling, turning or casting. In addition, possibility of functionally integrated device fabrication for aerospace and biomedical industry [Frazier 2014], which otherwise require extensive post-manufacture assembly work is among the primary motivations.

2. CONTROL SYSTEM ARCHITECTURE

An open-architecture galvanometer scanner control system along with powder layer spread mechanism is developed in this research. The modules of the control system are shown in Figure 2. Here, a host computer runs a master control application. The details of which are not covered in this article. This software generates commands for scan head controller and feed powder servo control sub modules based upon G-code instructions. The host computer communicates with its slave controllers via Universal Serial Bus (USB). The details of the system are briefly explained in the following sections.

Laser Exposure System

Selective laser melting is a layer-wise process in which a laser beam is required to scan the 2D layer of metal powder according to the given scan track (vector) with sufficient power, resolution (spot size), speed and positional accuracy [Grünberger and Domröse 2014]. The generalized concept is depicted in Figure 1, where a moving blade spreads the metal powder of appropriate particle size on top of a previously melted surface and scanner exposes the powder in a layer according to a predefined scan pattern and process is repeated. The laser exposure system consists of multiple components, such as guiding optics, galvanometer scan head, focusing lens, laser source, optic fiber and collimator etc. For metal powder processing, owing to the absorptivity characteristics, Nd:YAG (neodymium-doped yttrium aluminum garnets) as a preferred laser [Everton et al. 2016] [Clijsters et al. 2014].

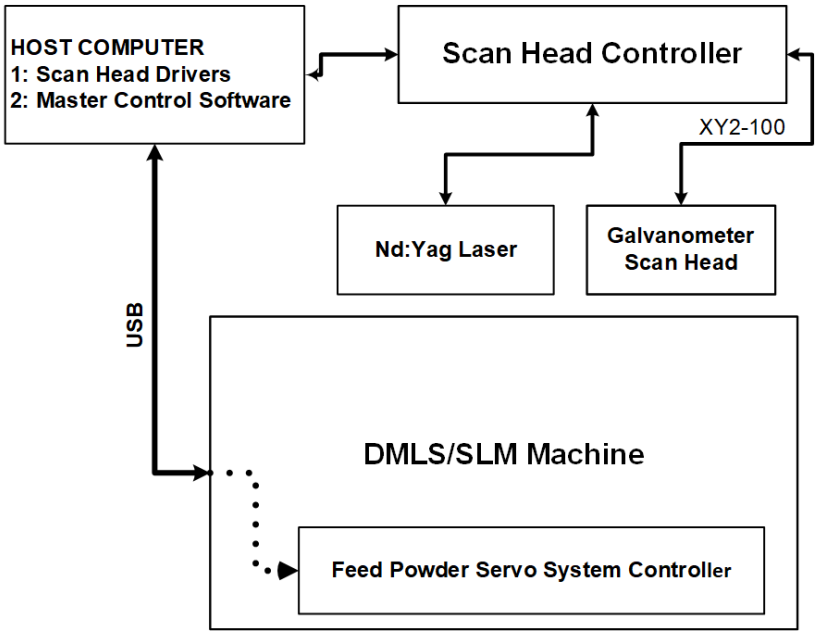


Figure 2: A simplified depiction of control architecture implemented in proposed research.

Special scanning lenses are required for applications in laser scanning where a planar imaging field is a must, as the common spherical lens can only image along a circular plane. While this nonlinear displacement can be accounted for with the proper software algorithms, the ideal solution in DMLS is to produce a linear displacement (i.e. constant scan rate). F-theta lenses are designed for this purpose with a barrel distortion that yields a displacement which is linear with θ (i.e. $f \times \theta$). This simple response removes the need for complicated electronic correction and allows for a fast, relatively inexpensive, and compact scanning system. A f-theta lens of $f = 160mm$ is selected in this design. A pulsed laser (1.064 um) beam exiting the cavity terminates into a collimator, which expands its diameter to 9 mm and then deflects onto lens using galvanometer scan head produces a diffraction limited spot size of approximately 80 um. The introduction of an additional beam expander allows to vary the spot size at the working plane within a certain limit if needed. The other option is to employ 3 axis scan head, which can be used in the future upgrade of the current system.

Powder Layer Feed Mechanism

The handling and layering of powder is automatized with a control system, which is built around three mechanisms, namely powder sweeper, build plate cylinder and powder cylinder.



Figure 3: A view of the powder layer of both powder cylinder and built plate while in process.

The sweeper mechanism of the DMLS machine consists of a blade, an active and a passive axis. The lateral movement in addition to the longitude movement is added to increases the performance of the metal powder sweeping. The longitudinal movement of the blade is provided by an active toothed belt axis. The lateral movement of the blade is provided by a stepper motor and a linear guide with ball screw system. The build cylinder and powder units consist of two sets of piston and cylinder bores which are moved by independent servo motors and ball screw system. The layer thickness in the accuracy of 10 um is achieved with acceptable smoothness such as depicted in Figure 3. The unexposed powder in the build unit remains as the support of the solidified final product and can be removed easily after the built. The extra powder, which is left on the powder bed, is guided by the sweeper blade into the powder bin and can be used for next fabrication. This cycle is repeated until all the layers of the 3D part are processed. The whole system is sealed and the built operation is performed in an inert atmosphere to avoid the oxidation of the metal. Argon gas (Ar) is used for this purpose and a pressure gauge monitors the chamber pressure during built.

3. PROCESS CONTROL SYSTEM

For the purpose of keeping system modularity, the control system is separated into two sub modules which take care of laser plus galvanometerr scan head and powder layer making system as shown in Figure 2. To spread a smooth but thin layer of metal powder, the piston inside of the powder chamber is raised using a stepper motor and an accurate ball-screw system. At the same time the built plate is lowered by the layer thickness and subsequently

blade, which is assembled in the sweeping unit of the machine, sweeps across and spreads the powder onto build plate evenly. The laser beam, which is controlled and moved by the galvanometer mirrors, scans the powder as instructed by G-code. To control three stepper motors of the powder layer feed system a dedicated controller is employed. It is a fundamental requirement to sync the deflection unit with one or multiple laser sources and direct the laser power when mirrors achieve desired scan speed. The controller is needed to provide low level interface with the laser, which is achieved by a specialized Interface hardware along with the implementation of XY2-100 protocol. Both these systems are derived by a Windows-based master control software which is written in C++.

Both the powder layer feed servo control software and galvanometer scanner application are deployed on dedicated computers and communicate with each other through USB port as described in Figure 2. The master control software reads and parses the G-code, separates commands and loads the memory space of galvanometer controller. This main application requests for the layer preparation from the powder feed controller and waits for its response. A layer of CoCr metal powder is shown in Figure 3. The powder feed cylinder top and surface of the built plate is visible here after making a smooth layer of $100\ um$ thickness.

Once a successful spread of the layer is achieved, the master application directs execution of the exposure process from the galvanometer scan head controller. When the laser exposure is completed according to the given laser power and scan speed, as instructed in G-code, the master control application reads the data and instructions of the next layer and repeats the process.

There is no open-source G-code generator/ slicer available for PBF based layer additive manufacturing of metal powder. Therefore, in order to implement the additive manufacturing process with this newly developed DMLS machine, a custom slicer program is developed in MATLAB. This application takes an STL file of CAD models and slices it into layers of user-defined thickness. The laser vectors are generated with correctly assigned scan parameters. The output of this slicer is a text file containing G-code instructions, understandable to DMLS machine. The scan patterns or laser exposure paths are generated using the ray tracing algorithm. In Figure 4 shows a CAD model (femoral component of knee implant), sliced with the MATLAB based slicer. Figure 5 depicts layer exposure vectors of the same model. The layer thickness of 200 um and hatch spacing of 200 um is selected in this case.

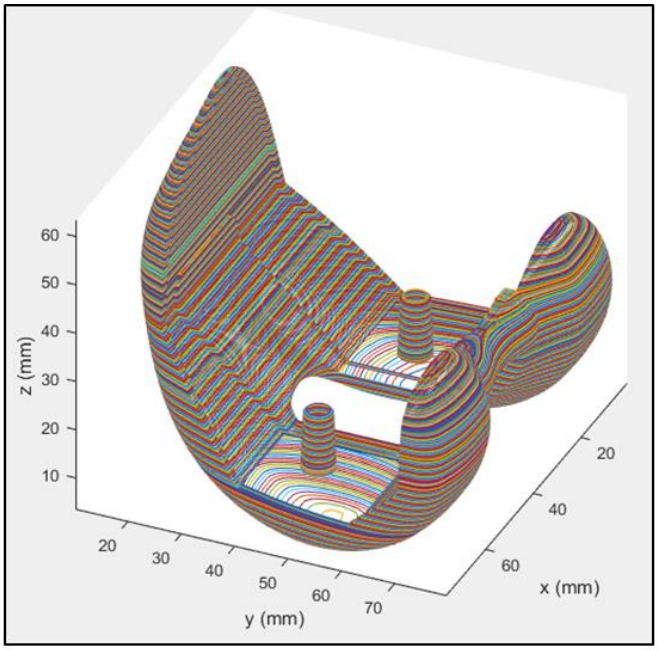


Figure 4: Sliced model of femur component of a knee implant (layer thickness 200um).

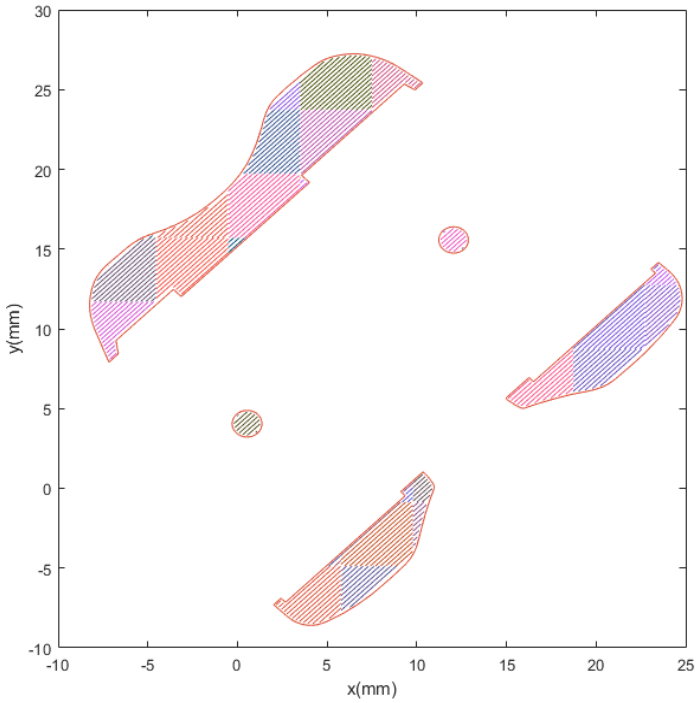


Figure 5 : Laser scan pattern in the layer No. 200 (height 10mm) of femoral component of knee implant with hatch spacing (200um).

4. RESULTS AND DISCUSSION

Several experiments have been performed to fine tune the control software of the machine. It included the calibration of important system components, such as servo mechanism, laser

beam size and scanner settings. The proposed design of the machine is successfully integrated with control software and slicer application. The modularity in the design process has been the cornerstone of this research, so that future improvements and modifications can be easily incorporated in the system.

For the preliminary experiments with this newly built system, Chrome Cobalt (CoCr size $20 - 53\,um$ metal powder) is used to fabricate a series of metal parts. The laser scan speed of 10 mm/Sec and 30-Watt laser power (In the range) is used to melt the powder. A metal cube produced during this exercise is shown in Figure 6. Here, a $15 \times 15 \times 15\,mm$ solid part is manufactured to assess the robustness and repeatability of the layering and scanning process. The surface appearance of the cube thus built after milling is shown in Figure 7. This looks shiny and solid, but macro porosity and delamination is evidently visible.

After conducting a number of experiments, it is concluded that: thermal stress causes the part deformation during built, resulting in in-situ failure. The recoating blade strikes metal part and gets damaged. This demands further Investigations on support structures and better anchoring with the built plate. It is further deduced that investigations on laser process parameters are required to achieve desired quality in built using this system (i.e. laser power, hatch-spacing and scan speed etc.). However, the experiments established satisfactory performance of all the subsystems and control software of the developed DMLS machine in this research.



Figure 6: A view of CoCr metal cube in the machine just after built.



Figure 7: Surface of the metal cube after post processing (milling).

REFERENCES

1. **Attaran, Mohsen**. (**2017**), “The Rise of 3-D Printing: The Advantages of Additive Manufacturing over Traditional Manufacturing.” , Business Horizons, Vol 60, No.5, pp 677–88.

2. **Nadammal, Naresh … others**. (**2017**), “Effect of Hatch Length on the Development of Microstructure, Texture and Residual Stresses in Selective Laser Melted Superalloy Inconel 718.” , Materials & Design, Vol 134, pp 139–50.

3. **Kruth, J- P, P Mercelis, J Van Vaerenbergh, L Froyen, and M Rombouts**. (**2005**), “Binding Mechanisms in Selective Laser Sintering and Selective Laser Melting.” , Rapid Prototyping Journal, Vol 11, No.1, pp 26–36.

4. **Craeghs, Tom, Stijn Clijsters, Evren Yasa, and Jean-Pierre Kruth**. (**2011**), “Online Quality Control of Selective Laser Melting.” , Solid Freeform Fabrication Proceedings,pp 212–26.

5. **Murr, Lawrence E … Ryan B Wicker**. (**2012**), “Metal Fabrication by Additive Manufacturing Using Laser and Electron Beam Melting Technologies.” , Journal of Materials Science & Technology, Vol 28, No.1, pp 1–14.

6. **Pinkerton, Andrew J**. (**2015**), “Lasers in Additive Manufacturing.” , Optics & Laser Technology, Vol 78, pp 25–32.

7. **Darwish, Saied MH, and Muhammad Usman Aslam**. (**2014**), “Auxetic Cellular Structures for Custom Made Orthopedic Implants Using Additive Manufacturing.” , International Journal of Engineering and Advanced Technology, Vol 4, No.2, pp 10–15.

8. **Berumen, S, F Bechmann, S Lindner, JP Kruth, and T Craeghs**. (**2010**), “Quality Control of Laser- and Powder Bed-Based Additive Manufacturing (AM) Technologies.” , Physics Procedia, Vol 5, pp 617–22.

9. **Peralta, AD, M Enright, M Megahed, J Gong, M Roybal, and J Craig**. (**2016**), “Towards Rapid Qualification of Powder-Bed Laser Additively Manufactured Parts.” , Integrating Materials and Manufacturing Innovation, Vol 5, No.1, pp 8.

10. **Frazier, William E**. (**2014**), “Metal Additive Manufacturing: A Review.” , Journal of Materials Engineering and Performance, Vol 23, No.6, pp 1917–28.

11. **Grünberger, Thomas, and Robert Domröse**. (**2014**), “Optical In-Process Monitoring of Direct Metal Laser Sintering (DMLS).” , Laser Technik Journal,pp 40–42.

12. **Everton, Sarah K, Matthias Hirsch, Petros Stravroulakis, Richard K Leach, and Adam T Clare**. (**2016**), “Review of In-Situ Process Monitoring and in-Situ Metrology for

Metal Additive Manufacturing.” , Materials and Design, Vol 95, pp 431–45.

13. **Clijsters, S, T Craeghs, S Buls, K Kempen, and JP Kruth**. (**2014**), “In Situ Quality Control of the Selective Laser Melting Process Using a High-Speed, Real-Time Melt Pool Monitoring System.” , International Journal of Advanced Manufacturing Technology, Vol 75, No.5–8, pp 1089–1101.

USING MULTI-AXIS ADDITIVE MANUFACTURING IN SUPPORT-LESS PART FABRICATION

Mohammed A. ISA, *misa13@ku.edu.tr,* Koc University, Manufacturing and Automation Research Center, Mechanical Engineering Department, Rumeli Feneri Yolu, Sariyer, Istanbul 34450, Turkey

Ismail LAZOGLU, *ilazoglu@ku.edu.tr,* Koc University, Manufacturing and Automation Research Center, Mechanical Engineering Department, Rumeli Feneri Yolu, Sariyer, Istanbul 34450, Turkey

ABSTRACT

Additive manufacturing can be enhanced through augmentation of additional axes of motion. This paper shows that such improvement allows support-less additive manufacturing of parts that will otherwise require support structures. By utilizing multi-axis additive manufacturing, model can be divided and sliced to avoid using support. The possibility of laying an unsupported roofing layer using our created path is also studied. In addition, through manual mixing of the 3D printer's motion, it is demonstrated that other kinds of geometric samples can also be manufactured. Beyond the shown samples, considering applicational purposes, the relevance of a general multi-axis path planner is acknowledged.

Keywords: Additive manufacturing, Support-less, Multi-axis, 5-axis

1. INTRODUCTION

Multi-axis manufacturing which is popular in machining literature, generally refers to fabrication done with more degree(s) of freedom(s) in addition to the native spatial three axis in machining centers. In machining, the flexibility of multi-axis machines can produce more complex free-form parts and improves overall machining efficiency of parts. This has led to wide research in four(five)-axis machining [Layegh K., Yigit and Lazoglu, 2015] and several commercial multi-axis machining centers. On the contrary, most additive manufacturing (AM) is carried out using 3-axis of movement. This is the case for major AM methods, such as fused deposition modeling (FDM) and selective laser sintering(SLS). Even though AM is known for its ability to fabricate complex geometries, many AM methods are constrained by

the need for a support beneath each layer [Upcraft and Fletcher, 2003]. Consequently, in most AM, overhangs are supported by an additional support structure which negatively affects production time, labor and part quality [Nee, Fuh and Miyazawa, 2001].

Analogous to how the extension of axes of motion in machining can enhanced the machining process, AM can also benefit from multi-axis promotion to mitigate some of its inherent limitations. Despite being in its primitive stage, multi-axis additive manufacturing(MAAM) is shown to eliminate the need for support structures and improve part strength and surface quality [Doubrovski, Verlinden and Geraedts, 2011; Wulle et al., 2017]. Due to the anisotropic property of parts manufactured by AM [Ahn et al., 2002; Bellini and Güçeri, 2003], with the weakest direction being along the build direction [Kshitiz Upadhyay, Ravi Dwivedi, 2017], the possibility of varying the build direction within a part can go long way in strength improvement of the part. With the flexibility offered by variable build direction in MAAM, the part strength can be tailored to substantially improve the load bearing capacity of the part [Yerazunis, Barnwell and Nikovski, 2016].

For a complete MAAM system, it is required to construct the 3D printer, evaluate its kinematics, program the numerical controller to listen and interpret commands, and finally design the path planner. Each of the mentioned requirements can be set out as an individual scope of research. The 3D printer used in this work is designed to perform fused deposition AM process, depicted in Figure 1. As shown in Figure 2, the gantry that carry the deposition print-head is constructed from RepRap Delta design concept [Graves et al., 2012] with the addition of tilting and rotation of the build platform. Details of the design, kinematics and controller are out of scope of this paper. The paper will concentrate on how the MAAM 3D printer can be used in manufacturing specific parts that cannot be produced on normal planar 3D printers without support structures.

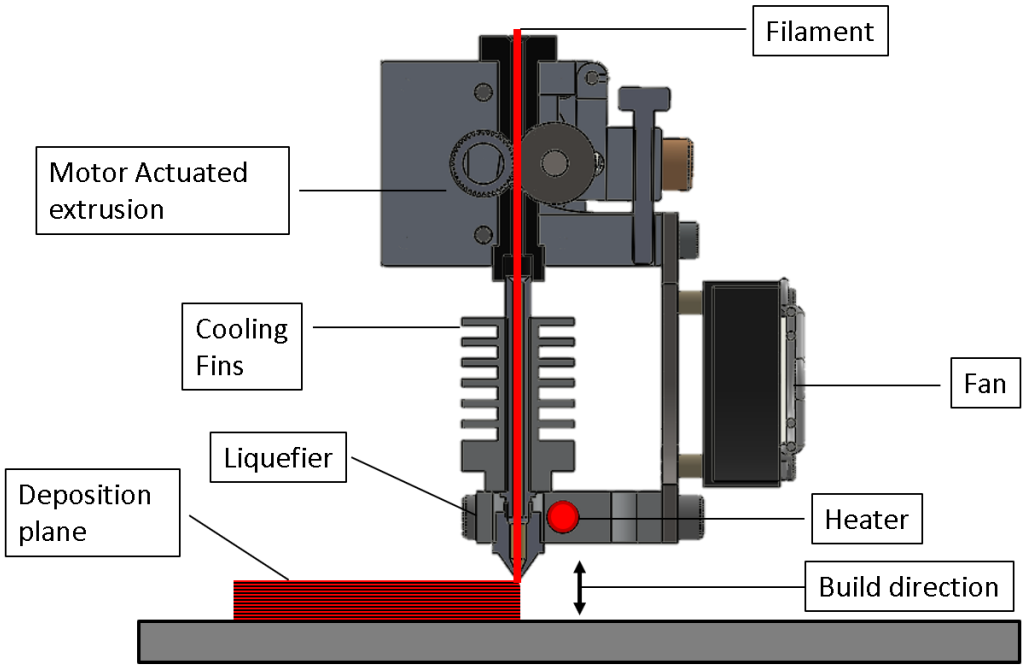


Figure 1:Fused deposition modeling print-head showing the build direction and plane

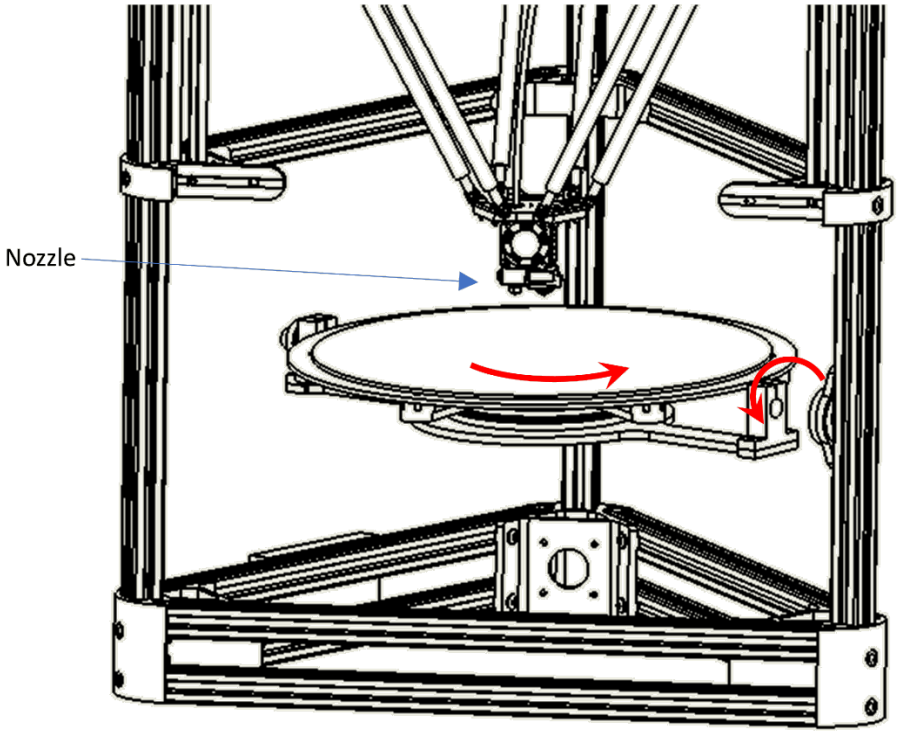


Figure 2: Multi-axis additive manufacturing device with 2 degrees build platform movements

During planar AM, the boundaries of successive layers do not have to be precisely vertically aligned. Depending on the layer spacing and the wall thickness, it is possible for the boundaries to slant away from the vertical to some extent. This slant angle popularly termed overhang angle is critical for a successful AM process. For both FDM and SLS, a typical overhang angle not exceeding 45^0 is usually permissible [Ahn et al., 2002; Gaynor et al., 2014; Wulle et al., 2017]. Support structures are usually generated before or during slicing of parts. Regions on the part that protrude by an angle greater than the critical overhang angle must therefore be supported.

2. PLANAR SLICING OF BY PART DECOMPOSITION:

The usual fused deposition AM can only eject molten filament in a uniaxial direction, leading to parallel deposition planes. The 3D printing paths are therefore in a stack of parallel layers that are generated by planar slicers [Mohd Ariffin et al., 2018]. In this section, the ability of MAAM to produce a part using more than one build direction is demonstrated using a part that is divided into two and sliced with the usual slicer. A diagonally split cuboid is sliced horizontally at the lower portion while the top part is sliced diagonally. While the first part is 3D printed with zero tilt, the second is manufactured on the first part at a tilt angle of 26.57^0 when the diagonal surface becomes perpendicular to the build direction as shown in Figure 3.

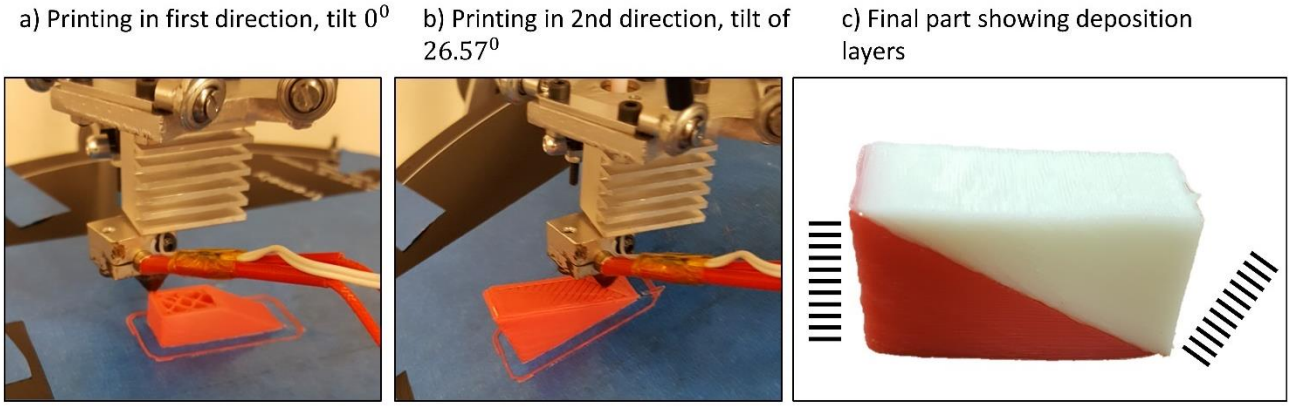


Figure 3: Demonstration of multi-axis AM using two build directions

Using the same rationale mentioned above, it is possible to fabricate parts that will usually require support such as the part shown in Figure 4a without any support. The part to be fabricated needs to be dissected into smaller parts, where each of the trimming planes serves as a build direction. With respect to each of the build directions, there should not be any overhang exceeding the critical overhang angle in each of the divided parts.

To avoid using the supports shown in Figure 4, the part is divided into 5 regions. Each of the region is to be fabricated in a suitable build direction—which must start from the build platform direction. The subdivided parts must be transformed in such a way that the initial plane coincides with the horizontal plane of the slicer. Popular open-source slicers such as Cura, Skeinforge and Slic3r can generate support structures together with the complete planar path for a tessellated model in STL format. Using such slicers, the 3D printing path of each division can be found. If the division is done right, there should be no necessity of support when slicing each subdivision. Finally, using the path, each region should be 3D printed at the determined build directions. The process of MAAM using slicers is summarized in Figure 5.

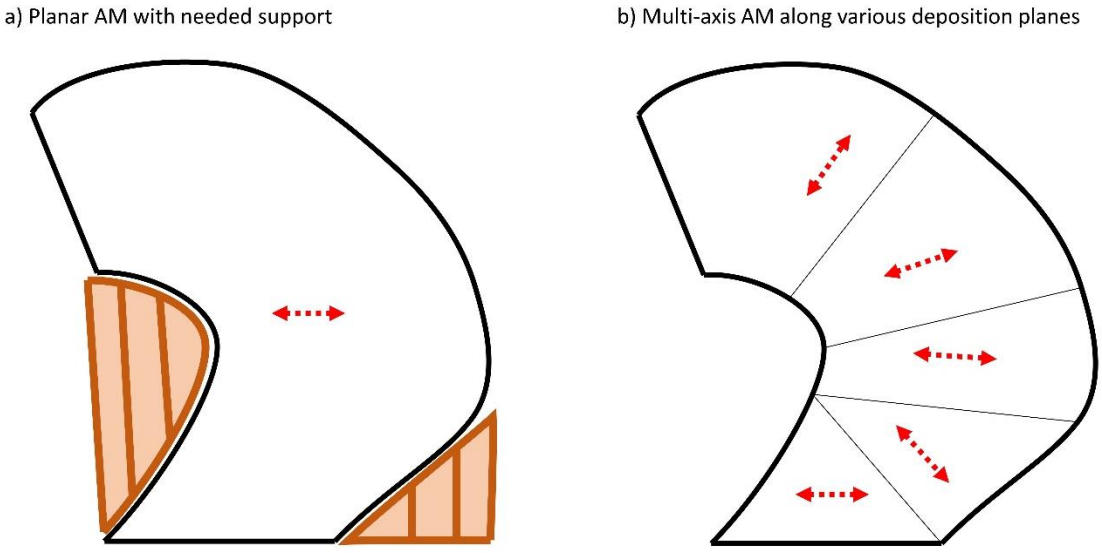


Figure 4: Illustration of how MAAM can be used with planar slicers to 3D-print without supports

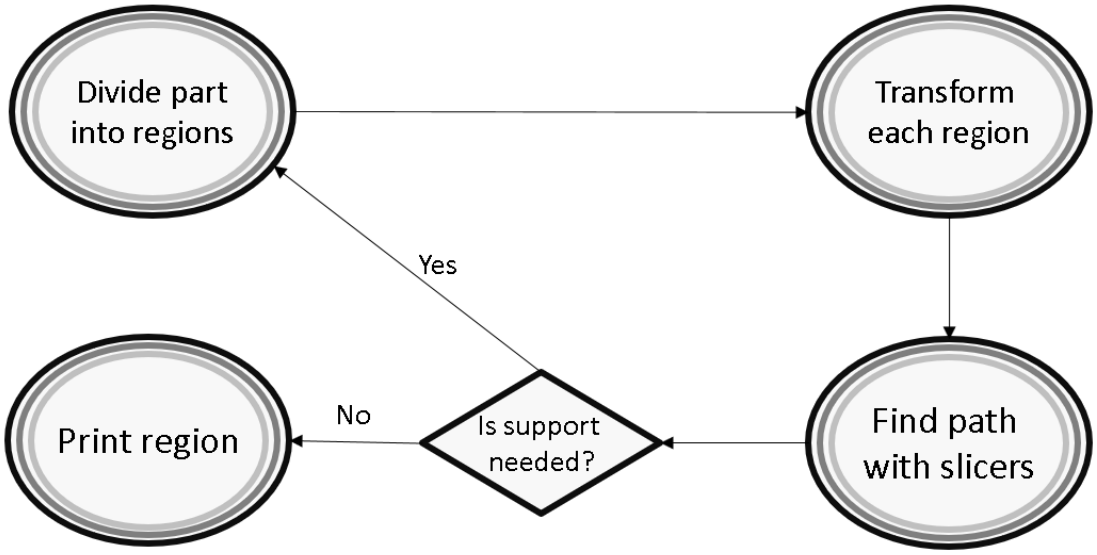


Figure 5: MAAM process using slicers on divided parts

3. APPLICATION IN ROOFING WITHOUT SUPPORT

In this section, a method of adding a roof over an open 3D printed part will be discussed. Laying such roof is not possible on planar AM because the overhang angle of a typical roof is around 90^0. However, when the open part is tilted by some angle, it becomes possible to incrementally fabricate the roof component at an overhang angle that is less than the critical overhang angle.

It should be noted that in some cases, even for planar AM, it is possible to 3D print at an angle greater than the critical angle. When the gap between two vertical pillars is only a few centimeters, a bridging process where small horizontal overhangs are created without support is possible [Vincent Khau, Eleanor lourey, 2015]. It is therefore possible to carry out a roofing process in planar AM if the opening is small. However, for a part with significant size, obtaining good outcome without support requires a multi-axis method.

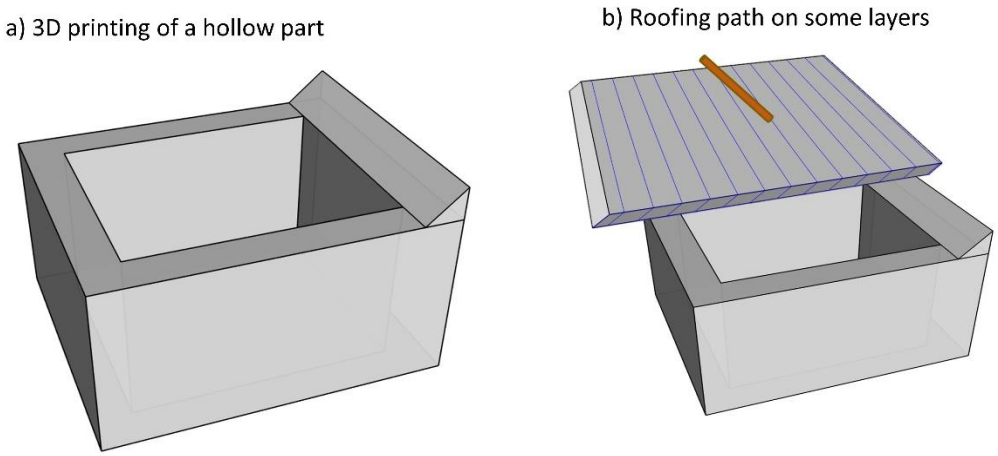


Figure 6: a) An open cuboid to be covered b) and the path of the roofing operation for some layers with build direction shown

The roofing strategy requires the lid to be separated from the part as illustrated in Figure 6. A prescribed tilt angle of the print platform should be chosen such that the already manufactured portion will not collide with print-head during manufacturing. The roofing process starts by using one side of the hole as start layer. Adding a small wedge at one side of the hole is found to improve the first layer deposition. The whole process is summarized in Figure 7.

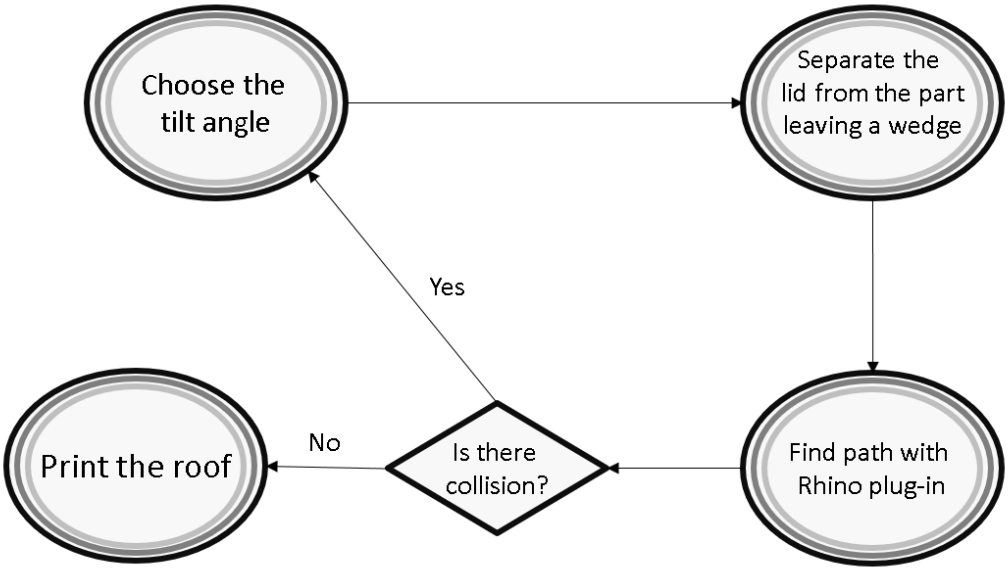


Figure 7:The roofing procedure

With the aid of Rhinoceros® CAD software, geometric data of the roof is used in a programmed plugin script to plan the path of the AM. Using this path along with the given tilt angle, g-code is generated in the plugin script. The path starts from a layer that is on the wedge surface as shown in Figure 8. Subsequent layers are then added until the roof structure is complete. It is found that decreasing the speed of deposition, especially around the edges, helps in ensuring better binding with hollow part.

If the roofing specimen is fabricated using a planar slicer, the interior of the part will require support structure like the one shown in Figure 9. The proposed roofing method makes it possible to manufacture the part without the additional structures.

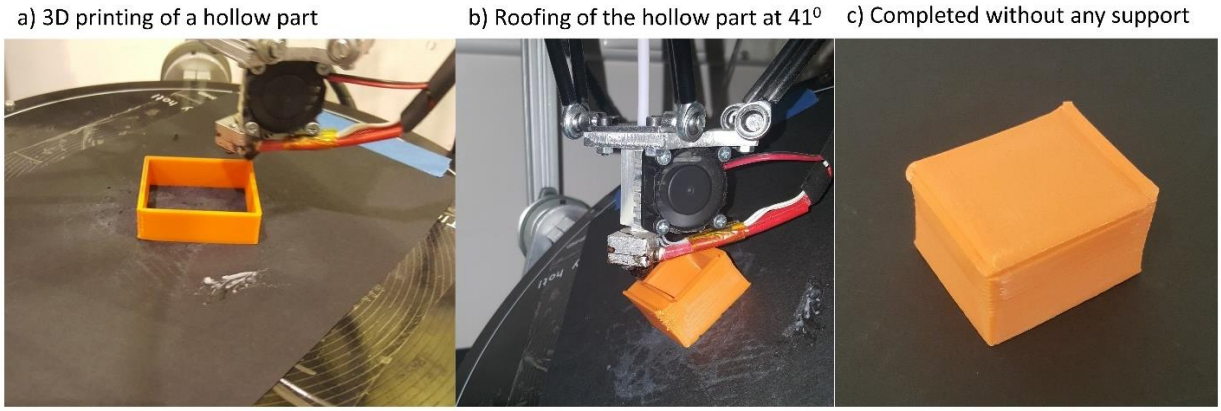


Figure 8:3D printing of a hollow cuboid and the roofing operation

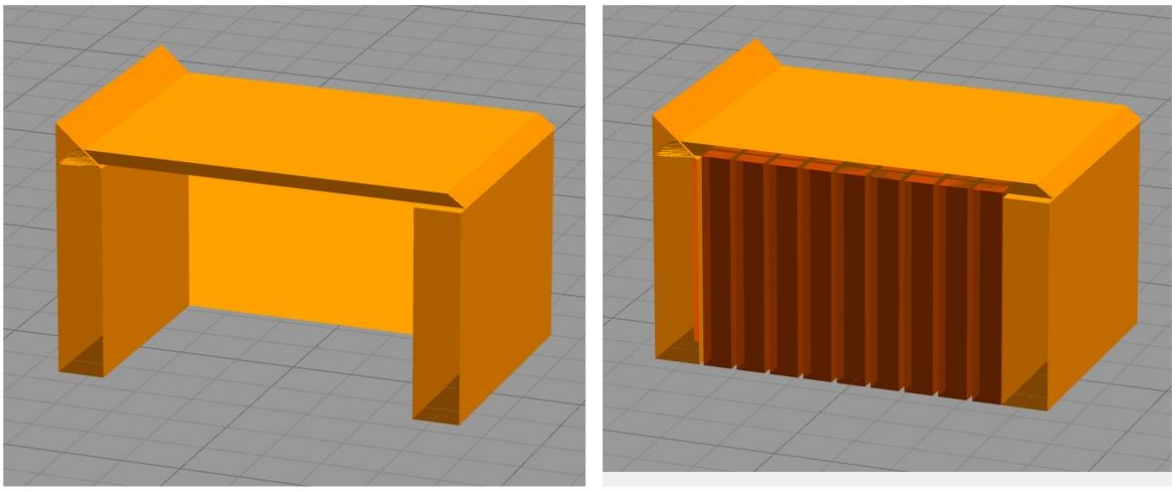


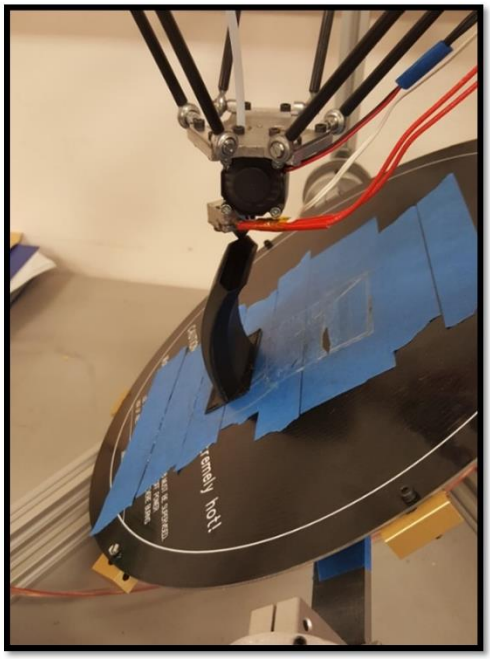
Figure 9:Cross-section of the roofing sample and the needed support

4. USE OF MISCELLANEOUS PATHS AND THE NEED FOR A GENERAL PATH PLANNER

There are other ways of multi-axis 3D printing of parts that require support in planar AM. Just like the previous methods, these strategies depend on the nature of the part. For some parts that are obtainable by revolution or sweeping of a cross-section, the cross-sections can be manufactured incrementally at different platform orientation. The platform orientation must be changed slowly between consecutive layers so that each cross-section is supported. The way the print platform moves determines how the cross-section is swept or revolved. Figure 10-a shows a sample revolved part constructed without any support structure.

It is also possible to make use of non-linear layer paths in multi-axis part construction without support. A sample of application of non-linear path is shown in Figure 10-b. A combination of linear and circular passes in each layer is used in the MAAM. When making the path, caution must be given to the gap between the nozzle and the deposited part especially during the circular pass. The nozzle must not jam into the part and the gap should not be greater than a few micrometers. It should be observed that since the layers are non-planar, an initial base part needed to be constructed.

a) Manufacturing of a revolved section



b) Part with straight and circular layer path

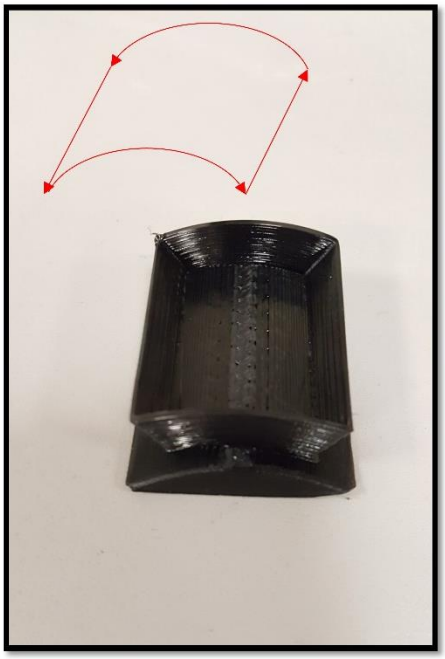


Figure 10: Manufacturing of a) revolved part and b) linear-circular paths without supports

5. CONCLUSION

For the two parts discussed in the previous section, each of the solid part is constructed as a byproduct of a sequentially arranged set of 4-axis motion to produce a 3D part by mere intuition. In fact, there are many different solid parts that can be manufactured with the 5-axis AM machine, but producing their path manually can be difficult. In engineering application, designs are made in solid models and there is usually no information on the manufacturing motion path. As a result, precedence needs to be given to finding a 5-axis path from a given solid model. The multi-axis path can be generated from a collection of 3D curves, as shown in Figure 11. Despite the significant progress in multi-axis path planning in machining, path planning needs to be studied for additive manufacturing since the two types of manufacturing methods are characterized by different constraints. Nevertheless, multi-axis machining literature can still provide some guidance on MAAM path planning.

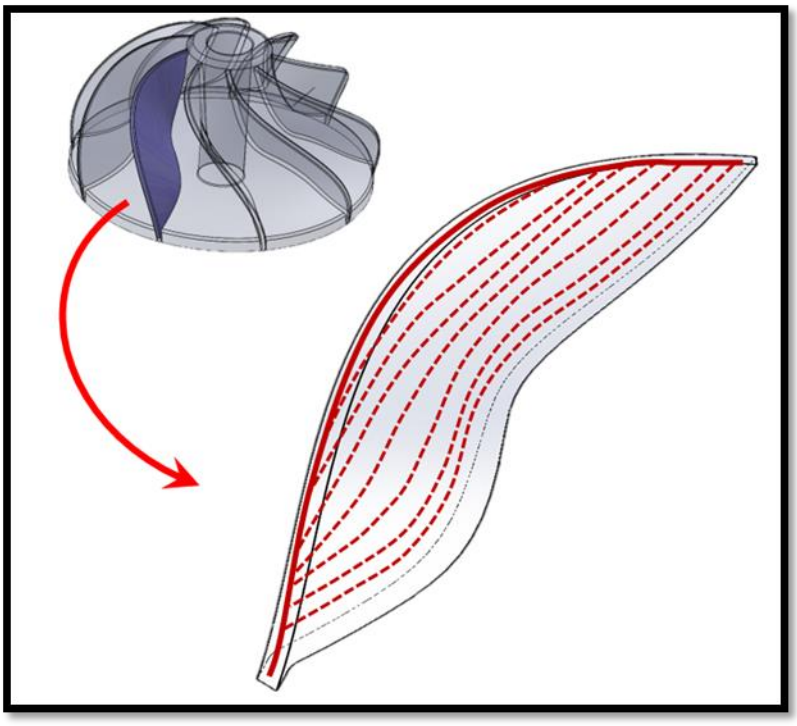


Figure 11: The problem of multi-axis path planning

REFERENCES

1. **Ahn, S. et al. (2002)** 'Anisotropic material properties of fused deposition modeling ABS', Rapid Prototyping Journal, 8(4), pp. 248–257. doi: 10.1108/13552540210441166.

2. **Bellini, A. and Güçeri, S. (2003)** 'Mechanical characterization of parts fabricated using fused deposition modeling', Rapid Prototyping Journal, 9(4), pp. 252–264. doi: 10.1108/13552540310489631.

3. **Doubrovski, Z., Verlinden, J. C. and Geraedts, J. M. P. (2011)** 'Optimal design for additive manufacturing: Opportunities and challenges', Proceedings of the ASME Design Engineering Technical Conference, 9, pp. 1–12. doi: 10.1115/DETC2011-48131.

4. **Gaynor, A. T. et al. (2014)** 'Topology Optimization for Additive Manufacturing: Considering Maximum Overhang Constraint', 15th AIAA/ISSMO Multidisciplinary Analysis and Optimization Conference, (June), pp. 1–8. doi: 10.2514/6.2014-2036.

5. **Graves, S. et al. (2012)** 'Johann C . Rocholl (Rostock) Style Delta Robot Kinematics'.

6. **Kshitiz Upadhyay, Ravi Dwivedi, A. K. S. (2017)** 'Determination and Comparison of the Anisotropic Strengths of Fused Deposition Modeling P400 ABS', in Advances in 3D Printing & Additive Manufacturing Technologies, pp. 95–100. doi: 10.1007/978-981-10-0812-2.

7. **Layegh K., S. E., Yigit, I. E. and Lazoglu, I. (2015)** 'Analysis of tool orientation for 5-axis ball-end milling of flexible parts', CIRP Annals - Manufacturing Technology. CIRP, 64(1), pp. 97–100. doi: 10.1016/j.cirp.2015.04.067.

8. **Mohd Ariffin, M. K. A. et al.** (2018) 'Slicer Method Comparison Using Open-source 3D Printer', IOP Conference Series: Earth and Environmental Science, 114(1). doi: 10.1088/1755-1315/114/1/012018.

9. **Nee, A. Y. C., Fuh, J. Y. H. and Miyazawa, T.** (2001) 'On the improvement of the stereolithography (SL) process', Journal of Materials Processing Technology, 113(1–3), pp. 262–268. doi: 10.1016/S0924-0136(01)00634-3.

10. **Upcraft, S. and Fletcher, R. (2003)** 'The rapid prototyping technologies', Assembly Automation, 23(4), pp. 318–330. doi: 10.1108/01445150310698634.

11. **Vincent Khau, Eleanor lourey, S. N. (2015)** '3D Printing Tips and Tech'. Available at: http://www.cytofluidix.com/3d-printing-tips-and-tech-get-to-know-those-acronyms/.

12. **Wulle, F. et al. (2017)** 'Workpiece and Machine Design in Additive Manufacturing for Multi-Axis Fused Deposition Modeling', Procedia CIRP. Elsevier B.V., 60, pp. 229–234. doi: 10.1016/j.procir.2017.01.046.

13. **Yerazunis, W. S., Barnwell, J. C. I. and Nikovski, D. N. (2016)** 'Strengthening ABS, Nylon, and Polyester 3D Printed Parts by Stress Tensor Aligned Deposition Paths and Five-Axis Printing', Solid Freeform Fabrication Symposium, pp. 1259–1271. doi: 10.1021/acsnano.6b02108.

ROBOTIC ADDITIVE MANUFACTURING OF TOOLING FOR COMPOSITE STRUCTURES

I. E. YİĞİT, *iyigit13@ku.edu.tr* Koc University, 34450, Istanbul, Turkey

Shaheryar A. KHAN, *skhan17@ku.edu.tr* Koc University, 34450, Istanbul, Turkey

Ismail LAZOĞLU, ilazoglu@ku.edu.tr Koc University, 34450, Istanbul, Turkey

ABSTRACT

The use of composite materials in the aerospace and automotive industries have been increasing rapidly. The molds, also known as tools, used for laying the composites are generally made from metals which are manufactured by subtractive manufacturing. This is not only an expensive option but also results in long lead times. Additive manufacturing (AM) is an alternative method for manufacturing the tooling. With robotic additive manufacturing (RAM), tools for large parts can be manufactured relatively quickly. After the tooling has been manufactured, non-autoclave processing methods such as the vacuum molding (VM) is used to obtain the final desired part geometry.

Keywords: Robotic, Additive manufacturing, Composites, Carbon fiber

1. INTRODUCTION

With benefits like high specific stiffness, high specific strength, high fatigue strength and high corrosion resistance, composites have become the go-to material in the transportation industry [Sandjay; K. Mazumdar, 2001]. The aerospace industry was among the first industries to realize these high-performance benefits of composites, especially those of the carbon fiber for unmanned aerial vehicles, rockets, and satellites. Today composites make up fifty percent of the total aircraft weight in the new Boeing 787 Dreamliner, while this was only twelve percent for its predecessor [Hale, J., 2006]. With such advancements, the Dreamliner will be able to fly more economically while reducing the impact on the environment.

Since composites are relatively expensive compared to their counterparts, the automotive industry still has time to realize the full potential that composites have to offer. The main drive for composites in the automotive industry comes from weight reduction. The heavier the vehicle is, it will have higher fuel consumption and lower range. With regulations for fuel

efficiency getting stricter and range demand for electric cars increasing every day, it is in the industry's best interest to reduce weight. For that, they are investigating affordable carbon fiber applications.

The raw carbon fiber takes the desired final shape with the lay-up on a mold (also known as tooling). The tooling used for laying the composites such as the carbon fiber reinforced plastics (CFRP) are generally made from various metals such as aluminum, steel or invar. While metal tooling takes months to manufacture and prepare for lay-up, additive manufacturing (AM) tools are printed and be ready in hours. AM tools also cost a fraction of the metals and can be tested and iterated for optimized designs. Thus, design cycles are accelerated. For a small tool given in Table 1 over 90% of cost and time reduction is obtained whereas 75% reduction is obtained for large tooling in Table 2 [Stratasys, 2017].

Table 1. Time and cost comparison of a small tool (~1.8 meters long) [Stratasys, 2017]

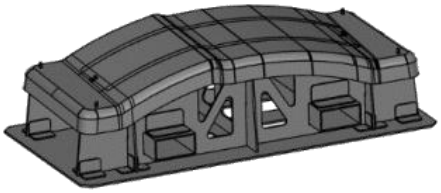
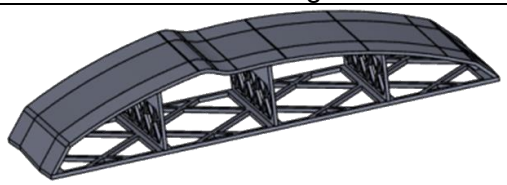
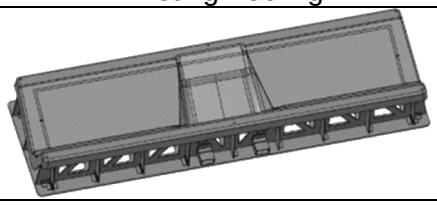
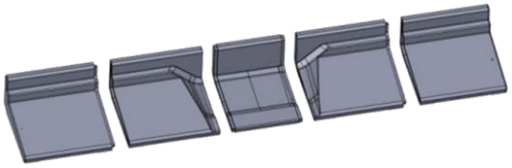
	Existing Tooling	AM tooling
		
Cost	$40-60K	$2500
Build Time	10-14 weeks	40 Hours
Weight	More than 69 kilograms	Less than 6.8 kilograms

Table 2. Time and cost comparison of a large tool (~4.5 meters long) [Stratasys, 2017]

	Existing Tooling	AM tooling
		
Cost	$80-120K	$25K
Build Time	15-20 weeks	2 weeks

Contrary to traditional subtractive manufacturing, in AM the computer-aided design (CAD) data on the computer is manufactured by adding material in layers where each layer is a cross-section of the part derived from the original CAD data [Gibson, I., Rosen, D.W. and Stucker, B., 2010]. Although AM's most obvious advantage is direct part production without the need for tooling, its use for rapid manufacturing of tooling to keep pace with faster composite part design cycles, cheaper costs, and the demand for faster overall manufacturing times is one of the growing trends in the aerospace and automotive industries [Black, S., 2015]. Other than tooling, AM can also support the production of

composite parts along the whole process chain ranging from tooling to post-processing. Türk et. al. have demonstrated the use of AM in additional fields reported as integrated positioning and fixation elements, lay-up and handling aids, structural curing aids and post-processing aids [Türk, D.A. et al., 2017].

Accordingly, it is possible to create complex, optimized tooling directly from CAD models instead of milling them from solid materials as is frequently done today. However, since AM is a relatively new field and AM for tooling is even more recent, design concepts are still driven by producing components with traditional subtractive manufacturing processes [Gao, W. et al., 2015]. This leads to additive manufactured tools that are conservatively designed, which means they are composed fully of solid material. However, AM permits control over how the part will be manufactured such as the part's interior fill strategy. By selecting the optimal infill for a given part, manufacturing time, as well as material consumption, can be minimized while obtaining the requirements for CFRP tooling [Lušić, M., Schneider, K. and Hornfeck, R., 2016].

With AM tooling repairing of the defects on the tool is made available. A 3D scan can capture part surfaces, either with a contact device like a coordinate measuring machine (CMM) or noncontact laser scanning, and the scanned data are converted into a solid CAD model. From there, the data can be fed to an AM machine to quickly manufacture the missing part of the tooling for a replacement part [Black, S., 2015]. The defected part of the tool is cut away with an angle grinder and replaced with the newly manufactured replacement. It is then spot welded with a hot air welder and sanded down until it is flushed with the rest of the tool. The sanded surfaces are then coated with epoxy and sanded again. With this process given in Figure 1, the tooling can be used for several more cycles.

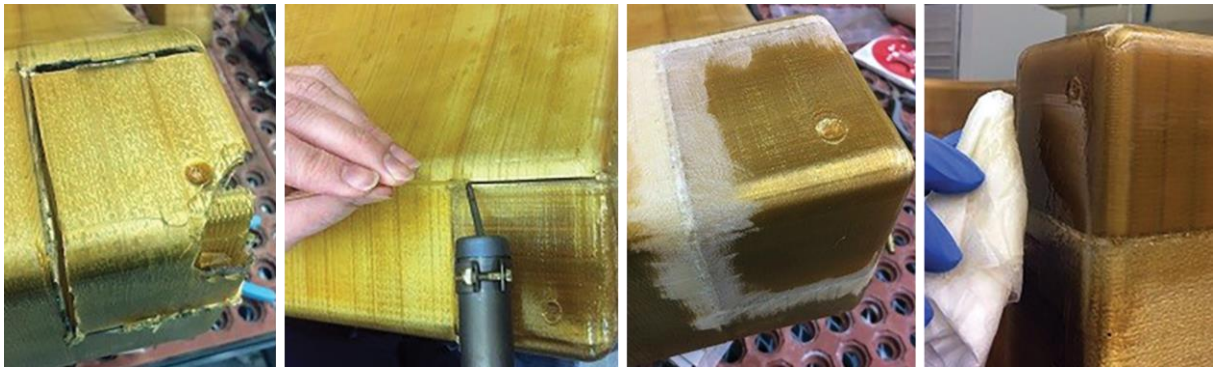


Figure 1. AM Tool repairing process [Stratasys, 2017]

One of the challenges in traditional AM of tooling is the size limitation due to limited machine build space. It was previously solved by manufacturing the tools in segments, which increases the complexity and the man-hours required to finish the job. This challenge can be

resolved with a robotic additive manufacturing (RAM) which has high reach distances and exceptionally large build spaces compared to conventional cartesian machines.

Another challenge is the temperature. The tools must withstand the heat cycles which are required for the curing of the epoxy. Also, Coefficient of thermal expansion (CTE) should be low to achieve accurate final geometry. It is desired that the CTE of the tool is equal to that of carbon fiber. This can be compensated with design decisions to a certain extent. For example, preferring male tooling instead of female tooling is a better option. Nevertheless, development of new materials which have low CTE and withstand high temperatures will be greatly beneficial for extending the applications of this field.

Once the composite fabrics are laid-up on the AM tooling, it is enclosed in a vacuum bag tailored to the desired shape and the assembly is placed in an autoclave, a pressure vessel designed to contain a gas at pressures generally up to 1.5MPa and heat up to temperatures to that required to cure the epoxy. The vacuum bag is first evacuated by using a vacuum, thereby removing trapped air and organic vapors from the composite, after which is placed into the chamber which is pressurized to provide additional consolidation during the curing process. The process produces structures of low porosity, less than 1%, and high mechanical integrity. Large autoclaves have been installed in the aircraft industry capable of housing complete wing or tail sections. For low-cost applications, such as the one in this paper, non-autoclave processing methods are sufficient. Non-autoclave processing methods such as the vacuum molding (VM), resin transfer molding (RTM), vacuum assisted RTM (VARTM), and resin film infusion (RFI) can be used to affordably obtain the final desired part geometry [Soutis, C., 2005].

2. RAM OF THE TOOLING

The advantage of an AM tool versus a traditionally manufactured tool is that an AM tool can have a complex, highly functional design without sacrificing cost or time. The large build space of the RAM setup allows large tool designs to be fabricated as a single piece, removing the need for assembly. AM also brings the opportunity for optimization. Analysis indicates that sparse-build tools are preferable to solid-build tools as the former not only saves tooling cost but also tends to cause less thermal expansion mismatch between the tool and composite part manufactured [Li, H. et al., 2015]. The tooling can also be shell type rather having infill. This will further decrease the costs and speed up the manufacturing process. Figure 2 shows the CAD geometry of the Interior panel of an aircraft with composite lay-up. This geometry is sliced in a vertical build orientation with a slicing software. With a selection of 15% infill, the toolpath in Figure 3 is obtained.

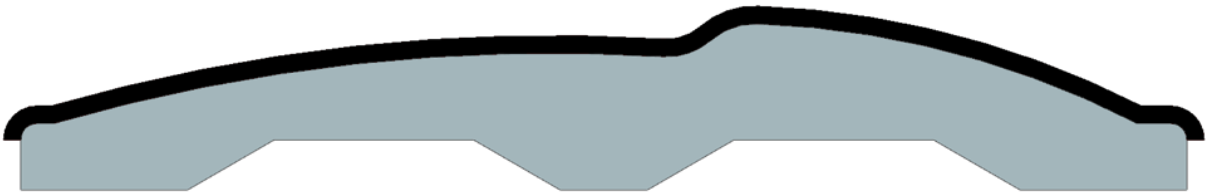


Figure 2. Cad geometry of the Interior panel of an aircraft with composite lay-up

The toolpath in Figure 3 shows outer perimeter of the layer in blue and the rectilinear infill pattern in green and the extruder in grey at the bottom left corner. The layer is repeated until the desired extrusion height is achieved. This toolpath is given to the 6 degrees of freedom manipulator. After the reverse kinematics have been solved, the robot arm can start fabricating the layers one by one. In the RAM setup, fused filament fabrication which is more commonly referred as fused deposition modeling (FDM) method is implemented. The raw material is stored on spools in filament form and deposited at the desired locations with the help of a hot end, for melting the material, and feeding mechanism, which feeds the filament into the hot end. With the pressure of the feeder, the melted material at the hot end will come out of the extruder and laid on top of the previous layers.

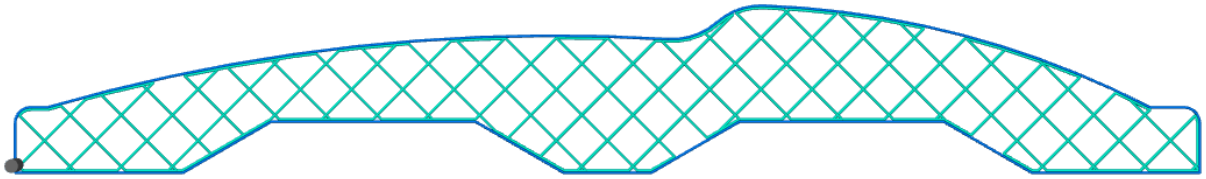


Figure 3. Toolpath for the AM tooling with 15% infill

Figure 5 shows the simulation and the actual setup of the RAM. The manipulator is given in blue where the feeding mechanism is in grey is attached. The filament comes in the white Teflon tubing. The hot end is shown in brown and has the yellow extruder at the tip where the material is deposited from. The tooling can be seen to be manufactured in upright vertical position.

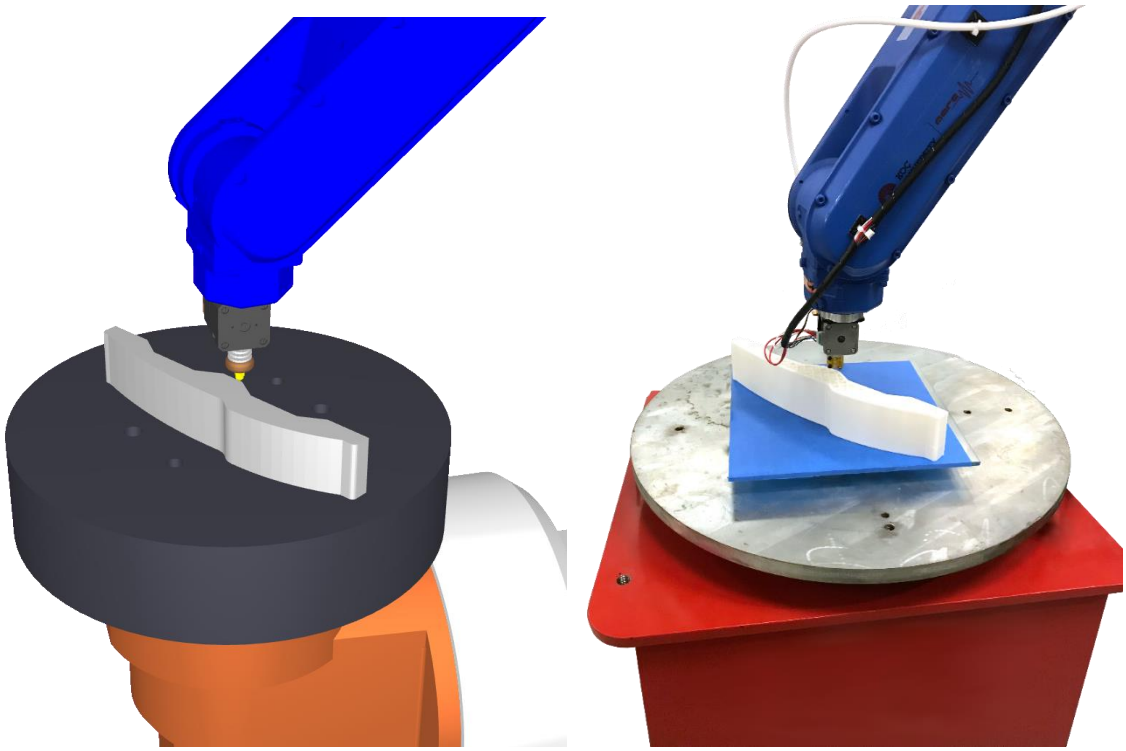


Figure 4. Robotic additive manufacturing setup

Due to layer-wise manufacturing nature of AM, the tool surface is a comes out rough. This is minimized by selection of vertical manufacturing orientation. For further improvement, the surface of the tools can be treated with an epoxy coating and sanded to reduces the roughness and provides a better part surface finish.

4. RESULTS AND DISCUSSION

The tooling which is manufactured using white polylactic acid (PLA) filament is shown in Figure 5. The tool is a smaller model of aircraft interior panel with the dimensions of 350x50x64 [mm] and was manufactured under an hour. This tooling is manually laid-up with carbon fiber and placed in a vacuum bag and the resin is cured at 50 °C for 10 hours since PLA used in this study has distortion temperature of 52 °C [Esun3d, 2007]. Where higher curing temperatures are needed, the ULTEM 1010 can be used for fabrication of composite structures which can withstand temperatures exceeding 177 °C and pressures of 690 kPa [Stratasys, 2015].



Figure 5. AM tooling for the Interior panel of an aircraft

4 layers of 245gr/m2 3k twill were laid-up using L285 epoxy with H285 hardener [PRF Composites, 2013]. A release agent was applied to the surface of the tool and the vacuum bag before the lay-up. Figure 6 shows the carbon fiber Laid-up on top of the manufactured tooling curing inside the vacuum bag under vacuum.



Figure 6. Laid-up part curing inside the vacuum bag

After the part is taken out of the vacuum bag, it is separated from the tooling with gentle plying. Extra material on the sides is cut with a hacksaw and sanded. One last layer of epoxy is applied and cured to get the final surface as shown in Figure 7.



Figure 7. Manufactured carbon fiber part of the Interior panel of an aircraft

Currently, the tooling is made with RAM, but the lay-up process is still manual and laborious. This step can be automated with robotic automated fiber placement (AFP). The concept is to compress the entire part design/tool production/robotic programming and part lay-up time. Future work would be to use high-performance materials such as the ULTEM 1010 for the

RAM of the tooling and lay-up the fibers with an AFP setup and cure the final assembly in an autoclave to achieve the best possible results.

5. CONCLUSION

With the development of AM, toolmaking is no longer limited to conventional subtractive manufacturing methods. To demonstrate, AM tooling of an aircraft interior panel was fabricated and laid-up with layers of carbon fiber impregnated with resin. The assembly was vacuumed and left for curing. After the resin has cured, the cured CRFP part was taken out of the vacuum bag and separated from the tooling. A final layer of epoxy was applied to get a good surface finish and the final desired part was obtained. With AM, iteration in design can be done relatively quickly and the results can be optimized. Design cycles can be accelerated, and companies can reduce costs especially for low volume productions. Up to %90 percent cost and time savings can be achieved. These benefits will increase the adoption of CFRP in the aerospace and automotive industries.

REFERENCES

1. **Sandjay; K. Mazumdar**, (**2001**), COMPOSITES MANUFACTURING: Materials, Product, and Process Engineering.

2. **Hale, J.**, (**2006**), "Boeing 787 from the Ground Up", AERO Mag., pp 17–23.

3. **Stratasys**, (**2017**), “FDM for Composite Tooling Design Guide,” 2017. [Online]. Available: http://www.stratasys.com/campaign/resource-guide/composite-tooling.

4. **Gibson, I., Rosen, D.W. and Stucker, B.**, (**2010**), Additive manufacturing technologies.

5. **Black, S.**, (**2015**), “A growing trend: 3D printing of aerospace tooling,” 2015. [Online]. Available: https://www.compositesworld.com/articles/a-growing-trend-3d-printing-of-aerospace-tooling.

6. **Türk, D.A. et al.**, (**2017**), "Composites Part Production with Additive Manufacturing Technologies", Procedia CIRP, Vol. 66, No. section 4, pp 306–311.

7. **Gao, W. et al.**, (**2015**), "The status, challenges, and future of additive manufacturing in engineering", Comput. Des., Vol. 69, pp 65–89.

8. **Lušić, M., Schneider, K., and Hornfeck, R.**, (**2016**), "A Case Study on the Capability of Rapid Tooling Thermoplastic Laminating Moulds for Manufacturing of CFRP Components in Autoclaves", Procedia CIRP, Vol. 50, pp 390–395.

9. **Soutis, C.**, (**2005**), "Carbon fiber reinforced plastics in aircraft construction", Mater. Sci. Eng. A Vol. 412, No. 1–2, pp 171–176.

10. **Li, H. et al.**, (**2015**), "Modeling and characterization of fused deposition modeling tooling for vacuum assisted resin transfer molding process", Addit. Manuf., Vol. 7, pp 64–72.

11. **Esun3d**, (**2007**), “eSUN 3D New Optimized PLA+ Filament,” 2007. [Online]. Available: http://www.esun3d.net/products/142.html.

12. **Stratasys**, (**2015**), “ULTEM 1010 Resin FOR FORTUS 3D PRODUCTION SYSTEMS ULTEM 1010 Resin,” 2015. [Online]. Available: http://usglobalimages.stratasys.com/Main/Files/Material_Spec_Sheets/MSS_FDM_ULTEM1010.pdf.

13. **PRF Composites**, (**2013**), “Product Data Epoxy Resin Systems RS-L285,” 2013. [Online]. Available: http://www.prfcomposites.com/store/image/data/PDF/RS-L285.pdf.

EFFECTS OF THE ROTATIONAL SPEED ON THE DYNAMICS OF MICRO CUTTING TOOLS

Bekir BEDIZ, *bbediz@sabanciuniv.edu* Sabanci University, 34956, Istanbul, Turkey

ABSTRACT

This paper investigates the rotational dynamics of the micro cutting tools using a spectral modeling approach. To accurately model the dynamics of micro cutting tools, a three-dimensional (3D) solution approach is needed since the fluted section of the cutting tool presents 3D coupled motions especially at high rotational speeds and for high aspect ratio tools. In this technique, the integral boundary value problem derived using Hamilton's principle is solved using a spectral method where Tchebychev polynomials are used as basis functions. The calculated natural frequencies are compared to those found using a finite element solution approach.

Keywords: Rotational dynamics, micro cutting tool, spectral-Tchebychev

1. INTRODUCTION

In the past few decades, there has been an increasing demand for micro-scale three-dimensional features and parts from various fields such as medical devices, aerospace applications, energy storage and conversion devices, etc. [Ehmann, 2005], [Salomon, 2005]. Concordantly, new manufacturing technologies (*e.g.* photo-lithography, focused ion beam machining, femtosecond laser micromachining, selective laser sintering, and electro-chemical machining) has been investigated and developed. Mechanical micromachining is one of the promising manufacturing technique since it enables fast and cheap fabrication of highly complex fully 3D micro-scale features/parts on a variety of materials.

Although the mechanical micromachining has come a long way in the last few years and does not have the limitations compared to other micro manufacturing techniques, its full potential cannot be realized without a thorough understanding the micromachining process. One of the most significant challenges in understanding the micromachining process is the unwanted vibrations, which arise from the dynamic response of the machining-system structure, as reflected at the cutting points, due to the excitation from (micro) machining

forces, since these vibrations limits the achievable quality and productivity [Tlusty, 2000], [Schmitz, 2009]. Therefore, the dynamics of the machining-system structure (composed of micro cutting tool, collet/tool holder, miniature ultra-high-speed -UHS- spindles and the machine) need to be well-understood.

Micro cutting tools are the most flexible part of the micro machine tool (μMT) assembly; thus their dynamics dominate the dynamic response reflected at the tool tip. Furthermore, due to the high rotational speeds (the spindle speeds can reach up to 400,000 rpm), the dynamics of the system vary significantly. Therefore, accurately obtaining the rotational dynamics of the cutting tools is crucial in enhancing the quality and productivity of the micromachining process. In the recent years, a large body of literature has been devoted to understanding the dynamics of the cutting tools. Since a wide selection of cutting tools can be used in a machining tool, obtaining the dynamics of cutting tools through experimentation is not feasible. Therefore, analytical/numerical approaches are the prevailing methods for modeling cutting tool dynamics. However, modeling the dynamics of micro cutting tools poses several significant difficulties due to the size effects and characteristics of the micromachining processes [Filiz, 2011]. First of all, micro cutting tools have sectioned geometries (shank, taper, and fluted parts, *etc.*) including stubby sections and generally there is an order of magnitude difference in diameters of these sections. Furthermore, due to the fluted part, the motion of the cutting tool becomes coupled (*i.e.* it presents coupled torsional-axial, of non-symmetric bending motions). Secondly, the micro-cutting tools experience high rotational speeds leading to gyroscopic effects that alters the dynamic behavior substantially. Particularly, as a result of the coriolis forces, that are proportional to the rotational speed, a non-proportional damping, which couples the axial and transverse motions, occur; thereby necessitating a state-space approach for calculating the dynamics [Genta, 2005]. Lastly, the tool attachment errors (*i.e.* the attachment errors between the tool and the spindle), the effects of the centrifugal forces are amplified; thus these errors need to be included in the modeling approach [Bediz, 2015].

The most common method in determining the dynamics of cutting tools is beam-based modeling techniques such as Euler-Bernoulli [Schmitz, 2001] and Timoshenko [Schmitz, 2005] beam models. However, these techniques become insufficient while modeling the fluted part of the tool and predicting the coupled motions. Thus, to accurately capture the coupled dynamics of rotating cutting tools, three-dimensional techniques need to be utilized. One common approach is to use finite element (FE) method [Rantatalo, 2007]. Although, this method enables accurate prediction of the coupled dynamics, the modeling procedure is arduous and computationally inefficient, especially in determining the dynamic response of the structure to arbitrary forcing excitations [Bediz, 2015]. Alternatively, many researcher

used series-based approaches such as Rayleigh-Ritz [Dawson, 1968] or Galerkin's methods [Rao, 1965]. However, these methods necessitate identifying a new set of basis/trial functions that are fast converging for each different boundary condition.

Recently, the author developed a new series based approach that uses Tchebychev polynomials, that have exponential convergence behavior, as its basis functions [Bediz, 2015], [Filiz, 2014]. The integral boundary value problem is obtained through Hamilton's principle. To impose the essential boundary conditions, projection matrices approach [Yagci, 2009] is used; thereby eliminating the need to use different basis/trial functions for each different structure and boundary condition.

This paper presents, the application of the developed analytical based 3D-ST modeling approach to predict the 3D dynamics of rotating micro-tool dynamics considering the attachment (setup) errors. To simultaneously attain numerical efficiency and modeling accuracy, a unified modeling approach is followed where the circular sections of the micro-tools are modeled using 1D-ST approach and the fluted section is modeled using 3D-ST approach. To couple the dynamics of each individual part, a component mode synthesis approach is used. The calculated natural frequencies and mode shapes are validated (for a micro-endmill and micro-drill geometries) by comparing the results to a FE solution.

2. MODEL DEVELOPMENT

The geometry of a (traditional) micro-endmill including the attachment errors (eccentricity, tool tilt and tool plane angle) is depicted in Figure 1. The micro-endmill geometry includes a meso-scale shank section, a micro-scale fluted region, and a taper section that connects the meso-scale shank to the micro-scale fluted region. Shank diameter (d_s), tool diameter (d_t), taper angle (γ), free shank length (L_s), taper length (L_t), tool length (L_t), twist angle (η) are the parameters used to define geometry.

Due to the errors during the attachment of the cutting tool to the holder/collet, spindle and tool axis differs. To define the orientation of the tool with respect to the spindle axis, attachment/setup errors are defined. These attachment errors can be defined as an axial error (spindle axis offset, e) and two tilt angles (α and ϕ) in two perpendicular planes (xz and xy planes). As a result of these errors, the tool will have a quasi-static error that the tool follows a circular path having the radius r_{ts} (see Fig. 1b).

To increase the numerical efficiency and attain modeling accuracy simultaneously, a unified modeling approach is used. Thus, the shank and taper sections are modeled using one-dimensional (1D) modeling approaches since they have simple geometries (that leads to

uncoupled motions). However, the fluted section necessitates a 3D modeling approach due to the complex curved cross-section and pretwist along the length of the tool. Therefore, the complete dynamics of the cutting tool is obtained through a component mode synthesis approach to couple each individual section (the details will be given in the following sections).

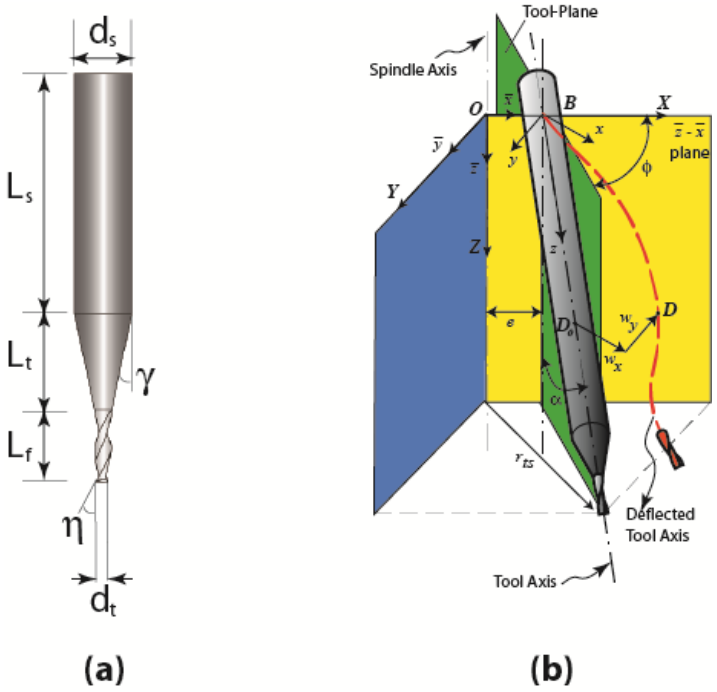


Figure 1. Schematic of **(a)** a micro-endmill geometry **(b)** including attachment errors.

To derive the integral boundary value problem (IVBP) that governs the dynamics of each section of the cutting tool, extended Hamilton's principle is used.

$$\int_{t_1}^{t_2} (\delta E_k - \delta E_s + \delta W_{knc}) dt = 0, \qquad \delta q_i(x,y,z,t) = 0 \quad at \quad t = t_1, t_2 \tag{1}$$

Here, E_k, E_s, and W_{nc} are the kinetic and strain energies, and the work done by non-conservative forces, respectively; t_1 and t_2 indicates two instants of time where the variation is zero; x, y, and z are the spatial variables and q_i is the generalized coordinate corresponding to the ith term of the deflection vector ***q* = {u; v; w}**; and δ is the variational operator.

To simplify the problem domain in deriving the IBVP, three coordinate frames are used (see Fig. 1b): **(i)** a fixed coordinate frame, *XYZ*, where the *Z* axis is aligned with the spindle axis is defined at point *O*; **(ii)** a rotating coordinate frame, $\bar{x}\bar{y}\bar{z}$, defined at the same point as the fixed coordinate frame but rotates around the *Z* or $\bar{z}$ axis with the spindle speed, Ω; and **(iii)** a

rotating coordinate frame, xyz, where the z axis is aligned with the tool axis. To express the relationship between the rotating tool frame and the rotating spindle frame, two consecutive counter-clockwise rotations are defined using the tool tilt (α) and tool plane angles (γ).

Derivation of the 1D Model: For the shank and taper sections of the tools, Timoshenko beam modeling approach is used. Since, the fluted region will be modeled using 3D techniques, for the Timoshenko beam model the strain and kinetic energies of the structures need to be written including bending, axial and torsional motions. Thus, the strain energy can be expressed as

$$E_s = \frac{1}{2}\int_0^L \left\{ EI\left(\frac{\partial \psi_x}{\partial z}\right)^2 + EI\left(\frac{\partial \psi_y}{\partial z}\right)^2 + EA\left(\frac{\partial w_x}{\partial z}\right)^2 + GJ\left(\frac{\partial \psi_z}{\partial z}\right)^2 + kAG\left[\left(\frac{\partial w_x}{\partial z} - \psi_y\right)^2 + \left(\frac{\partial w_y}{\partial z} - \psi_x\right)^2\right]\right\} dz \tag{2}$$

where *L* is the length of the beam, *E* is the Young's modulus, *I* is the second area moment (since the shank and taper sections are symmetric, $I_{xx} = I_{yy} = I$), *A* is the area of the beam along the *z* axis, *G* is the shear modulus, *J* is the polar moment of inertia, and *k* is the shear constant, and q is the deflection vector that includes three displacements and three rotations as $\boldsymbol{q} = \{\boldsymbol{w_x}; \boldsymbol{w_y}; \boldsymbol{w_z}; \boldsymbol{\psi_x}; \boldsymbol{\psi_y}; \boldsymbol{\psi_z}\}$.

The kinetic energy term for 1D structures are basically the combination of translational and rotational kinetic energies as

$$E_k = \frac{1}{2}\int_0^L m(v_D . v_D)\, dz + \frac{1}{2}\int_0^L \rho(I{\omega_1}^2 + I{\omega_2}^2 + I{\omega_3}^2)\, dz \tag{3}$$

where, *m* is the mass per unit length, ρ is the density of the beam, $\boldsymbol{v_D}$ is the velocity vector of any point on the shank and taper sections, and $\boldsymbol{w_1}$, $\boldsymbol{w_2}$, $\boldsymbol{w_3}$ are the components of the rotational velocity vector, that is applied to the center of the tool cross-section on the $t_1t_2t_3$ frame subjected to rotary vibrations (see Figure 2).

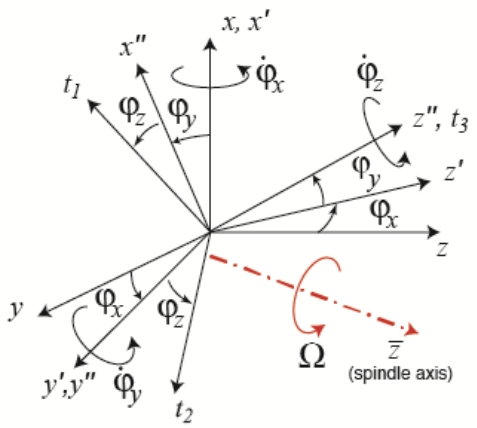


Figure 2. Moving frame and rotating tool frame related through bending (φ_x and φ_y) and torsion (φ_z) angles.

The velocity vector with respect to point *O* can be written using the unit vectors corresponding each coordinate frame as,

$$\boldsymbol{r_{OD}} = e\boldsymbol{i_{\bar{x}}} + w_{x_D}\boldsymbol{i_x} + w_{x_D}\boldsymbol{i_y} + \left(w_{x_D} + z_D\right)\boldsymbol{i_z} \tag{4}$$

Thus, the velocity of any point on the beam can be found using

$$\boldsymbol{v_D} = \dot{\boldsymbol{r}}_{\boldsymbol{OD}} + \boldsymbol{\Omega} \times \boldsymbol{r_{OD}} \tag{5}$$

Here, $\boldsymbol{\Omega}$ is the rotational velocity vector. To obtain the rotational part of the kinetic energy, the components of the rotational velocity can be written as,

$$\boldsymbol{\omega_r} = \dot{\varphi}_x\boldsymbol{i_x} + \dot{\varphi}_y\boldsymbol{i_y} + \dot{\varphi}_z\boldsymbol{i_z} + \Omega\boldsymbol{i_{\bar{z}}} = \omega_1\boldsymbol{i_{t_1}} + \omega_2\boldsymbol{i_{t_2}} + \omega_3\boldsymbol{i_{t_3}} \tag{6}$$

Performing three consecutive coordinate transformations (using Figure 2), the components of the rotational velocity terms can be derived. Including the work done by non-conservative forces and applying integration by parts once, the IBVP can be obtained as,

$$\begin{aligned}\int_{t_1}^{t_2}\Bigg\{\int \Big[&\rho\ddot{\boldsymbol{q}}^T\boldsymbol{N_M}^{\boldsymbol{1D}}\delta\boldsymbol{q} + 2\rho\Omega\dot{\boldsymbol{q}}^T\boldsymbol{N_{C_{cor}}}^{\boldsymbol{1D}}\delta\boldsymbol{q} + \boldsymbol{q}^T\boldsymbol{N_K}^{\boldsymbol{1D}}\delta\boldsymbol{q} - \rho\Omega^2\boldsymbol{q}^T\boldsymbol{N_{K_{spin}}}^{\boldsymbol{1D}}\delta\boldsymbol{q} \\ &- \rho\Omega^2\boldsymbol{q}_{ip}^T\boldsymbol{N_{F_c}}^{\boldsymbol{1D}}\delta\boldsymbol{q} - \left(\boldsymbol{n_{F_c}}^{\boldsymbol{1D}}\right)^T\delta\boldsymbol{q} - \boldsymbol{f}_{\boldsymbol{q}}^T\delta\boldsymbol{q}\Big]\,dz\Bigg\}\,dt = 0\end{aligned} \tag{7}$$

where $\mathbf{N_i^{1D}}$ are the operator system matrices given in the Appendix section.

Derivation of the 3D Model: The strain (potential) energy of the system can be obtained using the 3D elasticity equations as

$$E_s = \frac{1}{2}\int \boldsymbol{\varepsilon}^T\boldsymbol{\sigma}\,dxdydz \tag{8}$$

Here, $\boldsymbol{\varepsilon}$ represents strain and $\boldsymbol{\sigma}$ represents stresses. The effect stress-stiffening (i.e. a nonlinear term) for rotating cutting tools is negligible since the rotation behavior is similar to spinning and the errors between the spindle axis and tool axis are quite small [Bediz, 2015]. Therefore, using the constitutive matrix (**C**) and the differential operator matrix (**B**), the strain energy equation can be expressed as.

$$E_s = \frac{1}{2}\int \boldsymbol{q}^T\boldsymbol{B}^T\boldsymbol{C}\,\boldsymbol{B}\,\boldsymbol{q}\,dxdydz \tag{9}$$

where **q** = {**u**; **v**; **w**}. The kinetic energy and the work done by non-conservative forces can be written as,

$$E_k = \frac{1}{2}\int \rho\dot{\boldsymbol{q}}^T\dot{\boldsymbol{q}}\,dV \tag{10}$$

$$W_{nc} = \int \boldsymbol{f}_q^T \boldsymbol{q}\, dV + \boldsymbol{f}_b^T \boldsymbol{q}_b \tag{11}$$

Noe that, the velocity vector for the rotating cutting tool including the attachment errors can be written as

$$\boldsymbol{r_{OD}} = e\boldsymbol{i}_{\bar{x}} + (x_D + u_D)\boldsymbol{i_x} + (y_D + v_D)\boldsymbol{i_y} + (z_D + w_D)\boldsymbol{i_z} \tag{12}$$

Here, $\mathbf{x_D}$, $\mathbf{y_D}$, and $\mathbf{z_D}$ represents the initial geometric locations of any point within the fluted region. Following the Hamilton's principle, the IBVP for the 3D part can be obtained as

$$\int_{t_1}^{t_2} \left\{ \int \left[\rho \ddot{\boldsymbol{q}}^T \delta\boldsymbol{q} + 2\rho\Omega \dot{\boldsymbol{q}}^T \boldsymbol{N}_{\boldsymbol{C_{cor}}}{}^{\boldsymbol{3D}} \delta\boldsymbol{q} + \boldsymbol{q}^T \boldsymbol{B}^{\boldsymbol{T}} \boldsymbol{C}\boldsymbol{B}\delta\boldsymbol{q} - \rho\Omega^2 \boldsymbol{q}^T \boldsymbol{N}_{\boldsymbol{K_{spin}}}{}^{\boldsymbol{3D}} \delta\boldsymbol{q} \right.\right. \\ \left.\left. - \rho\Omega^2 \boldsymbol{q}_{ip}^T \boldsymbol{N}_{\boldsymbol{F_c}}{}^{\boldsymbol{3D}} \delta\boldsymbol{q} - \left(\boldsymbol{n}_{\boldsymbol{F_c}}{}^{\boldsymbol{3D}}\right)^T \delta\boldsymbol{q} - \boldsymbol{f}_{\boldsymbol{q}}^T \delta\boldsymbol{q} \right] dz \right\} dt = 0 \tag{13}$$

where $\mathbf{N_i^{3D}}$ are the operator system matrices given in the Appendix section.

Solution of the 1D Problem Using Spectral-Tchebychev Method: To solve the IBVP for 1D parts (given in Eq. 7), the generalized coordinates are discretized using Tchebychev polynomials and Gauss-Lobatto sampling method. For the details of the derivation, the reader is referred to [Yagci, 2009]. Here, a short summary is provided.

To evaluate the terms in IVBP, the derivative and inner product operations need to be defined in the sampled domain as

$$\boldsymbol{q_i}^n = \boldsymbol{Q_n}\boldsymbol{q} \tag{14}$$

where $\mathbf{Q_n}$ is the nth derivative matrix. And the inner product matrix can be derived as,

$$\int_a^b r(x)\, f(x)\, g(x)\, dx = \boldsymbol{f}^T \boldsymbol{V}^{\boldsymbol{r}} \boldsymbol{g} \tag{15}$$

Here, $\mathbf{V^r}$ is the weighted inner product matrix. Thus, after discretizing and applying the derivative and inner-product operations, the IBVP can be transformed into

$$\boldsymbol{M}\ddot{\boldsymbol{q}} + \boldsymbol{C_{cor}}\dot{\boldsymbol{q}} + \left(\boldsymbol{K} - \boldsymbol{K_{spin}}\right)\boldsymbol{q} = \boldsymbol{f} \tag{16}$$

where $\mathbf{M}$, $\mathbf{C_{cor}}$, $\mathbf{K}$, and $\mathbf{K_{spin}}$ are the mass, coriolis, stiffness and spin-softening matrices, respectively; and $\mathbf{f}$ is the forcing vector.

Solution of the 3D Problem Using Spectral-Tchebychev Method: The IVBP that governs the dynamics of the fluted region is defined over a complex domain; thus performing the integral and derivative operations are highly difficult. To address this issue, the complex geometry is mapped on to a straight beam with rectangular cross-section using two coordinate transformations: **(i)** a rotating coordinate frame is defined that rotates with the

defined helix angle and **(ii)** a cross-section mapping algorithm is defined to map the complex cross-section to a simple rectangular one. Thus, a Jacobian matrix can be derived to relate the physical coordinates to the mapped coordinates:

$$\frac{\partial}{\partial \epsilon_i} = \sum_{k=1}^{3}\sum_{l=1}^{3} J_{kl}^{q_c q} J_{li}^{\epsilon q_c} \frac{\partial}{\partial q_j} \tag{17}$$

$$\frac{\partial}{\partial q_j} = \sum_{k=1}^{3} \Im_{ij}^{-1} \frac{\partial}{\partial \epsilon_i} \tag{18}$$

where, $J_{kl}^{q_c q}$ and $J_{li}^{\epsilon q_c}$ are the elements of the Jacobian matrices [Filiz, 2014].

After simplifying the geometry, the problem can be discretized using the Tchebychev polynomials and Gauss-Lobatto sampling approach similar to 1D case. However, here, triple expansion of Tchebychev polynomials need to be used since the deflection terms are three-dimensional:

$$q_\iota(\xi,\eta,\zeta,t) \cong \sum_{l=1}^{N_\xi}\sum_{m=1}^{N_\eta}\sum_{n=1}^{N_\zeta} a_{qi}(t) T_{l-1}(\xi) T_{l-1}(\eta) T_{l-1}(\zeta) \tag{19}$$

Here, a's are the coefficients of the expansion. Then, following the procedure described in [Bediz, 2015], the system matrices can be obtained in a similar format as given by Eq. 15 for the 3D part of the tool.

Coupling the Individual Sections for the Complete Tool Dynamics: The formulation of the IBVP for the sectioned endmill using both the 1D and 3D-ST models, results in different deflection vectors, inner product matrices, and derivative matrices. To obtain the complete tool's system matrices, compatibility conditions are written at the connection boundaries where the degrees of the freedom of the connected sections are related. For the 1D parts it is done basically equations the six degrees of freedom at the connection boundary. However, for the 1D-3D connection (connecting taper and fluted parts), compatibility equations for the three displacement degrees of freedom (**u**; **v**; **w**) for the 3D model and the six degrees of freedom $\{\boldsymbol{w_x}; \boldsymbol{w_y}; \boldsymbol{w_z}; \boldsymbol{\psi_x}; \boldsymbol{\psi_y}; \boldsymbol{\psi_z}\}$ for the 1D model are formulated. Assuming small angles, this compatibility condition can be expressed mathematically as

$$\begin{Bmatrix} \boldsymbol{u} \\ \boldsymbol{v} \\ \boldsymbol{w} \end{Bmatrix} = \begin{Bmatrix} \boldsymbol{w_x} - \boldsymbol{y\phi_z} \\ \boldsymbol{w_y} + \boldsymbol{x\phi_z} \\ \boldsymbol{w_z} + \boldsymbol{x\phi_y} + \boldsymbol{y\phi_x} \end{Bmatrix} \tag{20}$$

To incorporate these compatibility boundary conditions or any other boundary condition to the global system matrices, projection matrices approach is used [Yagci, 2009].

3. MODEL VALIDATION

In this section, the application of the presented is demonstrated on a two-fluted micro-endmill (geometric properties are given in Table 1, and the fluted region is shown in Fig. 3). The actual geometry of the cutting tool is obtained through the CAD model, and the cross-section information along the length of the tool is extracted to be used in the 3D modeling part. The natural frequencies and the corresponding mode shapes are calculated using the presented technique and compared to the results obtained from a FE solver.

Table 1. Geometric properties of the modeled micro-endmill.

Shank diameter (mm)	Shank length (mm)	Taper angle (deg.)	Tip diameter (μm)	Fluted length (mm)	Helix angle (deg.)
3.175	30.83	12.3	811	2.7	46.8

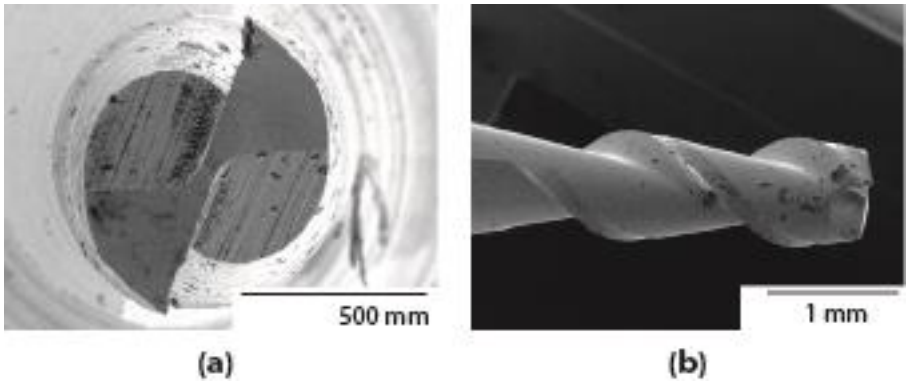


Figure 3. (a) Front and **(b)** side view of the fluted region of the two-fluted endmill.

First, to investigate the effect of the rotational speed, the natural frequencies and mode shape are obtained for spindle speeds ranging from 0 to 10 kHz. Furthermore, to investigate the effects of the rotational terms, the coriolis and spin softening terms are added sequentially (see Fig. 4a). To compare the results with the stationary tool, the natural frequencies are also plotted by dotted black lines. The results obtained using ANSYS are given by circle markers. Thus, it was calculated that the percent differences in natural frequencies are in perfect agreement (the maximum difference is less than 1% for all the investigated modes and rotational speeds). However, the another critical point here is the computational time; the presented solution approach can achieve the same level of precision as a FE solver, yet at a fraction of the computational time.

The addition of the coriolis forces results in a skew-symmetric damping matrix that leads the bending pair natural frequencies to split into forward and backward modes [Rao, 2011]. And, a result of the centrifugal forces (leads to the spin-softening matrix), the structure softens; thus the natural frequencies decrease.

As observed in Fig. 4a, a frequency crossing phenomena is observed around 8-9 kHz between the third and fourth modes and sixth and seventh modes. To clearly illustrate this, the mode shapes of the rotating micro-endmill is plotted for 5 kHz and 10 kHz rotational speeds (see Fig. 4b). Comparing the obtained mode shapes with the ones calculated using ANSYS, modal assurance analysis is performed and the minimum MAC number for the first nine natural frequencies is calculated as 0.9895. Therefore, it can be concluded that both the natural frequencies and the mode shapes can be accurately predicted using the presented solution technique.

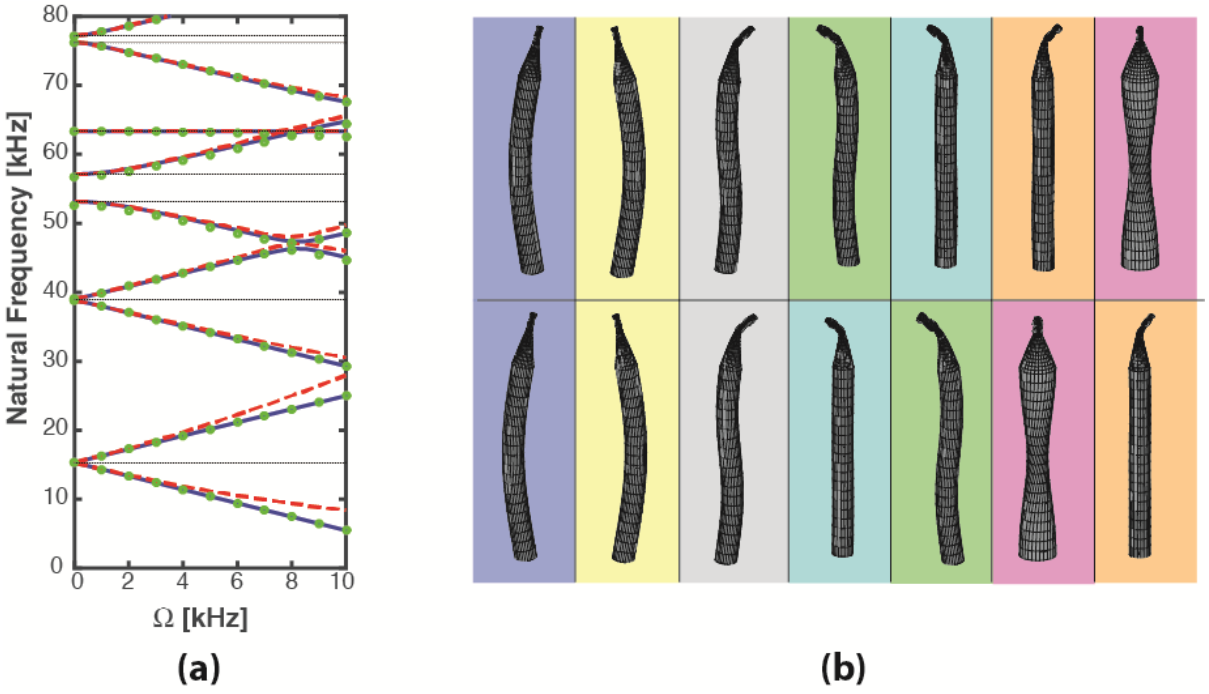


Figure 4. (a) The variation of natural frequencies as a function of rotational speed. Dotted (black) lines show the results for non-rotating cases. The dashed dotted (red) lines show the results with only the coriolis effect. The solid (blue) lines include both the coriolis and spin-softening effect. The green markers represent the results calculated using 3D-FEM analysis. **(b)**The first seven mode shapes (mode numbers are increasing from left to right) of the (unconstrained) micro endmill at Ω = 5 kHz (top row) and Ω = 10kHz (bottom row).

To compare the rotational dynamics of the micro-endmill, the frequency response functions (FRFs) are calculated and given in Fig. 5. In this analysis, the (rotating) tool dynamics is also

calculated using only 1D-ST approach (including the rotary inertia variation in the fluted region [Filiz, 2011]). Several important inferences can made through the investigation of the FRF plots. First of all, since the 1D approach cannot predict the coupled motions. Second, the difference in natural frequencies can go up to 3% (maybe even more for tools having a longer fluted region as micro-endmills). Third, the errors in the magnitudes of the resonance peaks may reach up to 25%.

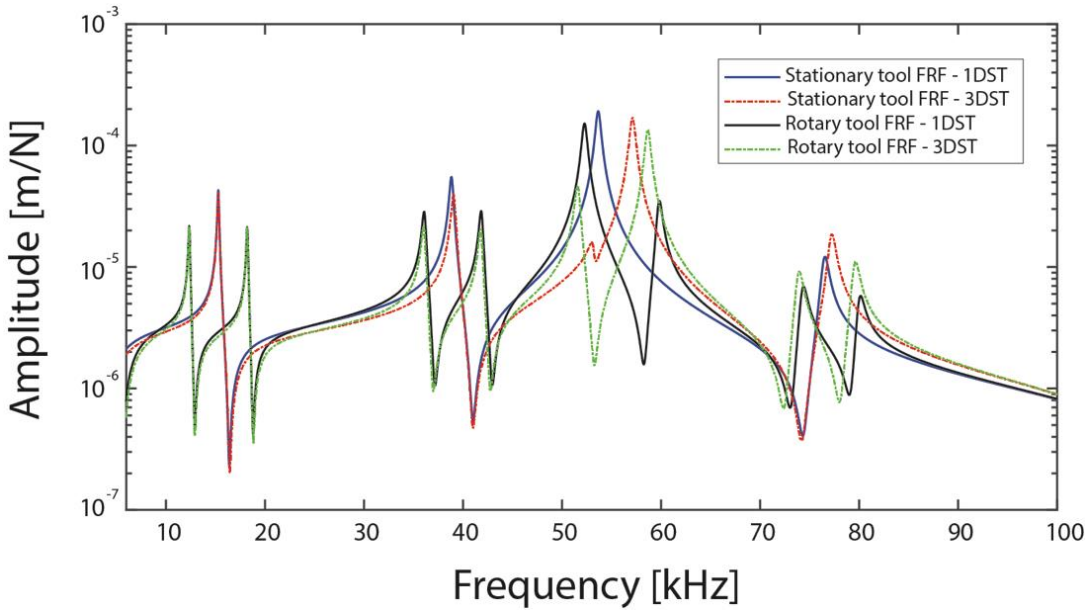


Figure 5. The frequency response plots (FRFs) of stationary and rotating micro-endmill (To calculate the rotating FRF, the rotational speed is taken as 3 kHz).

Finally, to understand the effect of the attachment errors, a parametric study is performed and both quasi-static and dynamic tool tip runout (radial throw) is found by varying the eccentricity and the tool tilt angle for increasing rotational speed. For instance, Fig. 6a shows the contour plot of the static and dynamic tool tip runout for a rotational speed of 120 krpm. Note that, the rotational effects can increase the runout values around 25% for the selected tool geometry and the spindle speed. To see the effect of the speed, the percent increase in tool runout is calculated as a function of spindle speed (in this analysis tool tilt angle is kept at 0.002º and the tool plane angle is kept at 90º). It is clearly seen from Fig. 6b that the dynamic tool tip runout can be more than twice the amount of the static tool tip runout.

4. SUMMARY AND CONCLUSIONS

This paper presented a unified spectral Tchebychev modeling approach to accurately and efficiently model the dynamics of rotating micro cutting tools including the attachment errors. The predicted natural frequencies and mode shapes are compared to those obtained from a

FE approach. The results showed excellent agreement; the difference in natural frequencies are less than 1% for the first ten modes and the corresponding minimum MAC value is 0.9895. To illustrate the effect of spindle speed on the dynamics of the cutting tools, FRF plots are determined; and the results showed that both the natural frequencies and the amplitudes of the peaks are significantly affected by the spindle. Furthermore, the effect of the tool attachment errors are investigated and it is clearly observed that the tool tip runout can increase significantly as a result of the high rotational speeds used in micromachining.

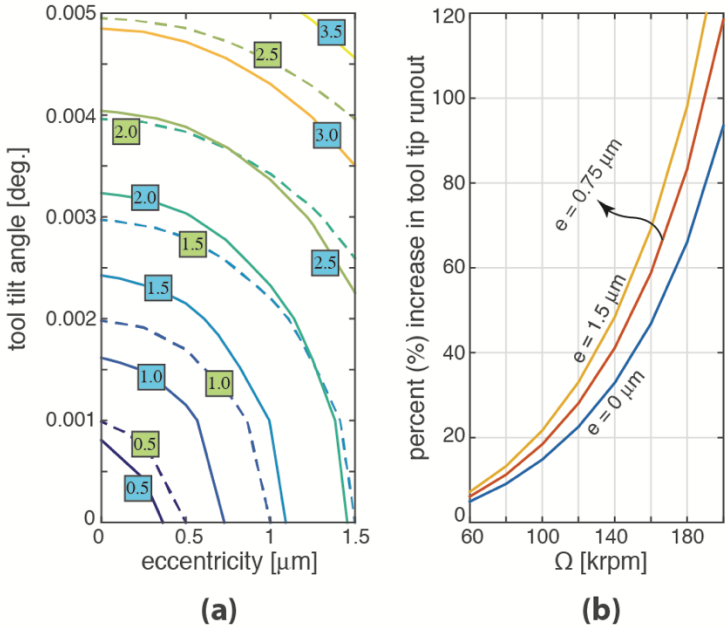


Figure 6. (a) Contour plot showing the effect of tool attachment errors on static and dynamic runout (represented by the contour lines labeled in micrometers) for a spindle speed of 120,000 rpm (2 kHz). The solid contour lines represent the dynamic runout values whereas the dashed lines represent the static runout values; **(b)** Percent increase in tool tip runout for increasing rotational speed.

ACKNOWLEDGEMENTS

This work was supported by the Scientific and Technological Research Council of Turkey (TÜBİTAK) under Grant No. 116C085 (PI: Bekir Bediz).

REFERENCES

1. **Ehmann**, “International assessment of research and development in micromanufacturing,” 2005.
2. **Salomon**, “Nexus market analysis report for MEMS and micro-systems,” 2005.
3. **Tlusty**, *Manufacturing Processes and Equipment*. Prentice Hall, Upper Saddle River, NJ, 2000.
4. **Schmitz**, *Machining Dynamics: Frequency Response to Improved Productivity*. Springer, New York, NY, 2009.
5. **Filiz, 2011**, “A three-dimensional model for the dynamics of micro-endmills including bending, torsional and axial vibrations,” *Precis. Eng.*, Vol. 35, No. 1, pp. 24–37.
6. **Genta**, *Dynamics of rotating systems*. New York, NY: Springer Science+Business Media, 2005.
7. **Bediz, 2015**, “Three dimensional dynamics of rotating structures under mixed boundary conditions,” *J. Sound Vib.*, Vol. 358, pp. 176–191.
8. **Schmitz, 2001**, “Tool point frequency response prediction for high-speed machining by RCSA,” *J. Manuf. Sci. Eng.*, Vol. 123, No. 4, p. 700.
9. **Schmitz, 2005**, “Three-component receptance coupling substructure analysis for tool point dynamics prediction,” *J. Manuf. Sci. Eng.*, Vol. 127, No. 4, pp. 781–790.
10. **Rantatalo, 2007**, “Milling machine spindle analysis using FEM and non-contact spindle excitation and response measurement,” *Int. J. Mach. Tools Manuf.*, Vol. 47, No. 7–8, pp. 1034–1045.
11. **Dawson, 1968**, “Coupled bending-bending vibrations of pre-twisted cantilever blading treated by the rayleigh ritz energy method,” *J. Mech. Eng. Sci.*, Vol. 10, No. 5, pp. 381–388.
12. **Rao, 1965**, “The fundamental flexural vibration of a cantilever beam of rectangular cross section with uniform taper(Natural frequency of fundamental flexural vibration of rectangular cantilever beam with uniform taper determined, using Galerkin method),” *Aeronaut. Q.*, Vol. 16, pp. 139–144.
13. **Filiz, 2014**, “Three dimensioanl dynamics of pretwisted beams - A spectral-Tchebychev solution,” *J. Sound Vib.*, Vol. 333, pp. 2823–2839.
14. **Yagci, 2009,** “A spectral-Tchebychev technique for solving linear and nonlinear beam equations,” *J. Sound Vib.*, Vol. 321, No. 1–2, pp. 375–404.

15. **Rao**, *History of rotating machinery dynamics*. Springer, 2011.

APPENDIX

APPENDIX A. Operator System Matrices for 1D Models

The operator system matrices defined in the IBVPs for 1D model can be expressed as:

$$\boldsymbol{N_M^{1D}} = diag(A\mathbf{I}, A\mathbf{I}, A\mathbf{I}, I\mathbf{I}, I\mathbf{I}, I\mathbf{I}) \tag{21}$$

$$\boldsymbol{N_{C_{cor}}^{1D}} = \begin{bmatrix} \mathbf{0} & -Acos(\alpha)\boldsymbol{I} & \mathbf{0} & \mathbf{0} & \mathbf{0} & \mathbf{0} \\ Acos(\alpha)\boldsymbol{I} & \mathbf{0} & Asin(\alpha)\boldsymbol{I} & \mathbf{0} & \mathbf{0} & \mathbf{0} \\ \mathbf{0} & -Asin(\alpha)\boldsymbol{I} & \mathbf{0} & \mathbf{0} & \mathbf{0} & \mathbf{0} \\ \mathbf{0} & \mathbf{0} & \mathbf{0} & \mathbf{0} & \mathbf{0} & \mathbf{0} \\ \mathbf{0} & \mathbf{0} & \mathbf{0} & \mathbf{0} & \mathbf{0} & Isin(\alpha)\boldsymbol{I} \\ \mathbf{0} & \mathbf{0} & \mathbf{0} & \mathbf{0} & -Isin(\alpha)\boldsymbol{I} & \mathbf{0} \end{bmatrix} \tag{22}$$

$$\boldsymbol{N_K^{1D}} = \begin{bmatrix} k_sGA\boldsymbol{Q_1}^T\boldsymbol{Q_1} & \mathbf{0} & \mathbf{0} & \mathbf{0} & -k_sGA\boldsymbol{Q_1} & \mathbf{0} \\ \mathbf{0} & k_sGA\boldsymbol{Q_1}^T\boldsymbol{Q_1} & \mathbf{0} & k_sGA\boldsymbol{Q_1} & \mathbf{0} & \mathbf{0} \\ \mathbf{0} & \mathbf{0} & EA\boldsymbol{Q_1}^T\boldsymbol{Q_1} & \mathbf{0} & \mathbf{0} & \mathbf{0} \\ \mathbf{0} & k_sGA\boldsymbol{Q_1} & \mathbf{0} & k_sGA\boldsymbol{I} + \boldsymbol{I}\boldsymbol{Q_1}^T\boldsymbol{Q_1} & \mathbf{0} & \mathbf{0} \\ -k_sGA\boldsymbol{Q_1} & \mathbf{0} & \mathbf{0} & \mathbf{0} & k_sGA\boldsymbol{I} + \boldsymbol{EI}\boldsymbol{Q_1}^T\boldsymbol{Q_1} & \mathbf{0} \\ \mathbf{0} & \mathbf{0} & \mathbf{0} & \mathbf{0} & \mathbf{0} & GJ\boldsymbol{Q_1}^T\boldsymbol{Q_1} \end{bmatrix} \tag{23}$$

$$\boldsymbol{N_{K_{spin}}^{1D}} = \begin{bmatrix} Acos^2(\alpha)\boldsymbol{I} & \mathbf{0} & 0.5\sin(2\alpha)\boldsymbol{I} & \mathbf{0} & \mathbf{0} & \mathbf{0} \\ \mathbf{0} & A\boldsymbol{I} & \mathbf{0} & \mathbf{0} & \mathbf{0} & \mathbf{0} \\ 0.5\sin(2\alpha)\boldsymbol{I} & \mathbf{0} & Asin^2(\alpha)\boldsymbol{I} & \mathbf{0} & \mathbf{0} & \mathbf{0} \\ \mathbf{0} & \mathbf{0} & \mathbf{0} & -Icos^2(\alpha)\boldsymbol{I} & \mathbf{0} & \mathbf{0} \\ \mathbf{0} & \mathbf{0} & \mathbf{0} & \mathbf{0} & I[\sin(\alpha) - \cos^2(\alpha)]\boldsymbol{I} & \mathbf{0} \\ \mathbf{0} & \mathbf{0} & \mathbf{0} & \mathbf{0} & \mathbf{0} & Jsin(\alpha)\boldsymbol{I} \end{bmatrix} \tag{24}$$

$$\boldsymbol{N_{F_c}^{1D}} = \begin{bmatrix} \mathbf{0} & \mathbf{0} & \mathbf{0} & \mathbf{0} & \mathbf{0} & \mathbf{0} \\ \mathbf{0} & \mathbf{0} & \mathbf{0} & \mathbf{0} & \mathbf{0} & \mathbf{0} \\ \mathbf{0} & \mathbf{0} & Asin^2(\alpha)\boldsymbol{I} & \mathbf{0} & \mathbf{0} & \mathbf{0} \\ \mathbf{0} & \mathbf{0} & \mathbf{0} & \mathbf{0} & \mathbf{0} & \mathbf{0} \\ \mathbf{0} & \mathbf{0} & \mathbf{0} & \mathbf{0} & \mathbf{0} & \mathbf{0} \\ \mathbf{0} & \mathbf{0} & \mathbf{0} & \mathbf{0} & \mathbf{0} & \mathbf{0} \end{bmatrix} \tag{25}$$

$$\boldsymbol{n_{F_c}^{1D}} = \begin{Bmatrix} \rho A\Omega^2 ecos(\alpha)\cos(\phi)\mathbb{i} \\ -\rho A\Omega^2 e\sin(\phi)\mathbb{i} \\ \rho A\Omega^2 esin(\alpha)\cos(\phi)\mathbb{i} \\ \mathbb{0} \\ 0.5\rho Isin(2\alpha)\mathbb{i} \\ \mathbb{0} \end{Bmatrix} \tag{26}$$

Here, $\mathbf{0}$ and $\boldsymbol{I}$ are (N_z *x* N_z) zero and identity matrices; $\mathbb{0}$ and $\mathbb{i}$ are (N_z *x* 1) zero and identity vectors.

APPENDIX B. Operator System Matrices for 3D Models

Similarly, the operator system matrices defined in the IBVPs for 3D model can be expressed as:

$$\boldsymbol{N}_{\boldsymbol{C}_{cor}}^{\boldsymbol{3D}} = \begin{bmatrix} \mathbf{0} & -\cos(\alpha)\boldsymbol{I} & \mathbf{0} \\ \cos(\alpha)\boldsymbol{I} & \mathbf{0} & \sin(\alpha)\,\boldsymbol{I} \\ \mathbf{0} & -\sin(\alpha)\,\boldsymbol{I} & \mathbf{0} \end{bmatrix} \tag{27}$$

$$\boldsymbol{N}_{\boldsymbol{K}_{spin}}^{\boldsymbol{3D}} = \begin{bmatrix} \cos^2(\alpha)\boldsymbol{I} & \mathbf{0} & 0.5\sin(2\alpha)\,\boldsymbol{I} \\ \mathbf{0} & \boldsymbol{I} & \mathbf{0} \\ 0.5\sin(2\alpha)\,\boldsymbol{I} & \mathbf{0} & \boldsymbol{I} \end{bmatrix} \tag{28}$$

$$\boldsymbol{N}_{\boldsymbol{F}_c}^{\boldsymbol{3D}} = \begin{bmatrix} \cos^2(\alpha)\boldsymbol{I} & \mathbf{0} & 0.5\sin(2\alpha)\,\boldsymbol{I} \\ \mathbf{0} & \boldsymbol{I} & \mathbf{0} \\ 0.5\sin(2\alpha)\,\boldsymbol{I} & \mathbf{0} & \boldsymbol{I} \end{bmatrix} \tag{29}$$

$$\boldsymbol{n}_{\boldsymbol{F}_c}^{\boldsymbol{3D}} = \begin{Bmatrix} \rho\Omega^2 e_x \cos(\alpha)\,\mathbb{i} \\ -\rho\Omega^2 e_x \sin(\phi)\,\mathbb{i} \\ \rho\Omega^2 e_x \sin(\alpha)\cos(\phi)\,\mathbb{i} \end{Bmatrix} \tag{30}$$

Here, $\mathbf{0}$ and $\boldsymbol{I}$ are ($N_xN_yN_z$ *x* $N_xN_yN_z$) zero and identity matrices; $\mathbb{O}$ and $\mathbb{i}$ are ($N_xN_yN_z$ *x 1*) zero and identity vectors.

EFFICIENCY OPTIMIZATION METHOD OF STABILITY PARAMETERS FOR THIN-WALLED WORKPIECE MILLING PROCESS

Chung-Yu TAI, *Harkat_Tai@itri.org.tw* Industrial Technology Research Institute, 40852, Taichung, Taiwan, R.O.C

Ta-Jen PENG, *darjenpen@itri.org.tw* Industrial Technology Research Institute, 40852, Taichung, Taiwan, R.O.C

Tzuo-Liang LUO, *TzuoLiangLo@itri.org.tw* Industrial Technology Research Institute, 54041, Nantou, Taiwan, R.O.C

ABSTRACT

Thin-walled structures are common in aerospace machines, like turbo blades and blisks, but these kinds of structures are difficult and time-consuming to be machined. The dynamics of the workpiece may be changed continuously during machining. In this study, the prediction technology of processing simulation is presented to solve the manufacturing problems of flexible structures. Each FRF is used to integrate a 3-D stability lobe diagram which can also be called as a whole process diagram of each operation. The optimized material moving rates computed from the chosen parameters on stability lobe diagrams can increase the maximum processing efficiency.

Keywords: Thin wall, Stability lobe diagram, Material removal rate

1. INTRODUCTION

Process virtualization is the key in improving efficiency in the manufacturing sector, as it reduces the need of prototyping and reduce the cost for machining process development. To achieve high precision and maintain stability during machining processes, the dynamic properties of the work piece at each stage of the process should be investigated. Such an approach is especially useful, yet difficult, in aerospace-related manufacturing, which involves machining, thin articles such as compressor blades.

Chatter is a common phenomenon for these case machining. It comes from the self-excited vibration of the cutting tool and the workpiece. The workpiece chatter is less often investigated because the workpiece dynamic effects are not concerned. There were some

researches focused on this topic. [Lee et al., 1991] focused on workpiece chatter and its relationship among the axial limits of the cutting depths, the natural frequencies of the workpiece, and the spindle speeds. [Budak et al., 2012] focused on the effects of the processing method for the chatter stability in milling.

The finite element model was used to establish the workpiece and the cutter location file for determining the removed elements at each tool location along the cutting cycle. [Tai et al., 2016] and [Tai et al., 2017] presented a scanning method which used laser Doppler velocimetry to measure the dynamics of the thin wall structure. By using the accurate experimental data, the contact stiffness of the clamped thin wall at the vice could be identified with the tool of model updating. The sensitivity method was used to update the dynamic model for predicting the stable machining parameters to improve the accuracy of the prevention of chatter. In IPT [Kalocsay et al., 2014], the clamping damper was used to reduce the workpiece vibration. The vibration reduction mechanism was designed in the clamping device which is used to fix the flexible blade structure for expanding the cutting stability area. Otherwise, [Matsubara et al., 2017] designed a supporting device on the side of the workpiece to reduce the vibration. The pivot mechanism provided a rotation motion to the surface support and damping to the vibration modes. The dynamometer and displacement sensors were also used to monitor the vibration of the machining process in their design.

In this study, the following diagram of the technology is shown in Figure 1. The continuous-changed dynamics can be predicted by using the numerical simulation model. The models which have some errors with real dynamics can be updated by the sensitivity method. The updated models are used to predict the workpiece dynamics which include the dynamics changed during machining. Finally, the stable cutting parameters chosen by the optimization calculation may also be validated by the measurement during machining.

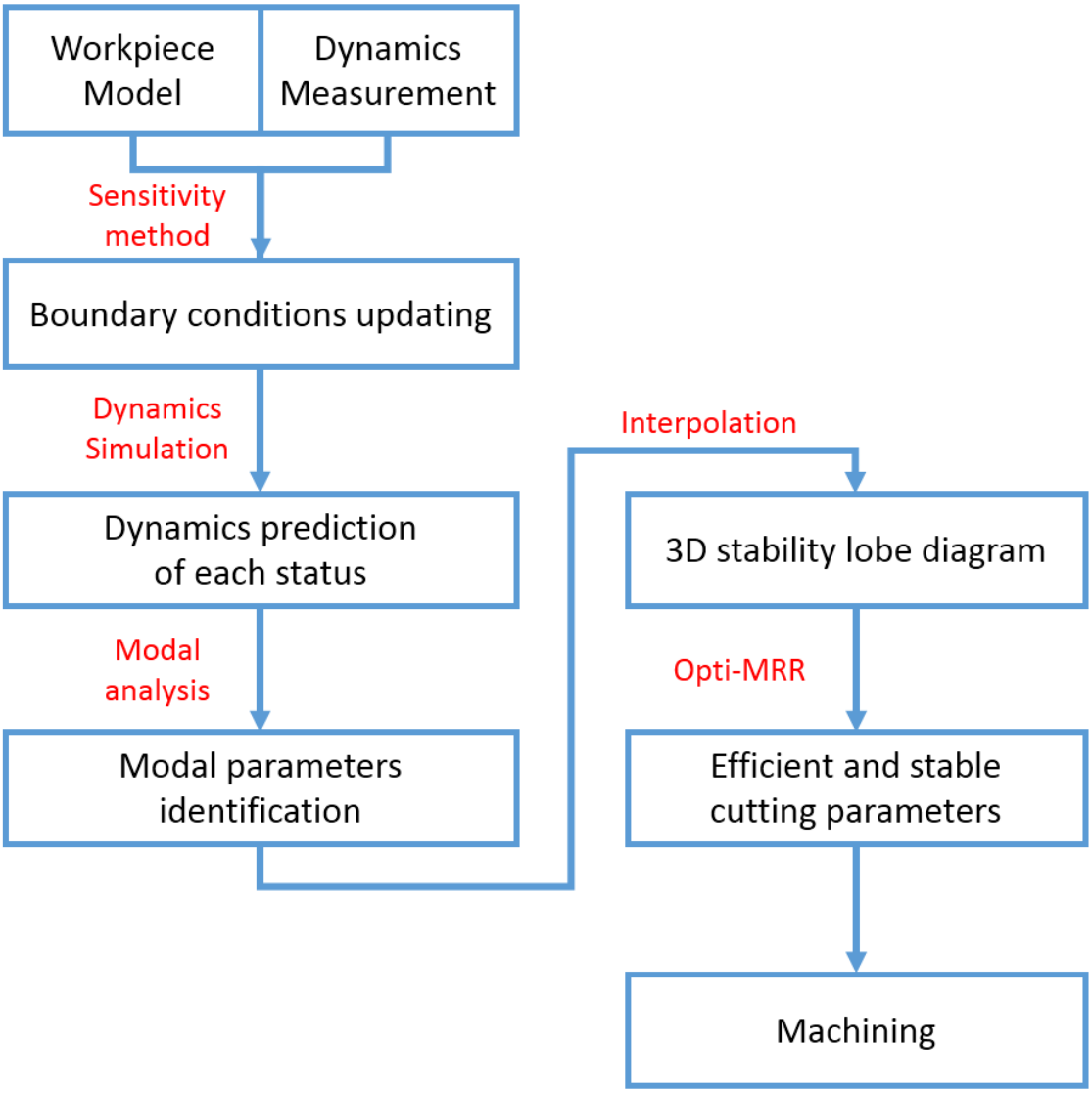


Figure 1. Following diagram in this study

2. PREDICTION

The efficient cutting stability during the thin-walled process can be predicted by the workpiece dynamics which include natural frequencies, dynamic stiffness, and damping effects. Another step is to calculate stability lobe diagram for each cut of the structure. Finally, the material removal rate is used to optimize the cutting efficiency. According these computing steps, the cutting conditions which are spindle speeds, cutting depths and feed rates on the 3-D stability lobe can be predicted as an optimization line. It can provide the effective processing recommendations for users or engineers to plan the thin-wall workpiece process.

Governing equations for machining chattering can be derived from the vibration equations and regenerative chatter equations. The frequency response functions of the cutting tool and the workpiece are used for computing the stability lobe diagram. The stability lobe diagram can be used for the prediction of the machining conditions which are the cutting depth and the rotating speed of the spindle.

Dynamics

The workpiece dynamics which include natural frequencies, dynamic stiffness, and damping effects are the most important parameters for the stability prediction. These can display the real phenomenon of the workpiece during machining. These parameters are always calculated as the frequency response function (FRF) obviously. The orthogonal cutting force F can be described as [Yue, 2006]:

$$F = k_s bh = k_s b[x(t-T) - x(t)] \quad (1)$$

where k_s is the cutting stiffness, *b* is the chip depth, *h* is the thickness, and *x* which should be considered of the time *t* and the time interval *T* between the previous and current cuts is the displacement of the cutter normal to the cut. In order to describe the simulation model as the real part, the vibration system which are built with mass *M*, stiffness *K*, damping *C* and cutting forces *F* is used and shown as the function below:

$$[M]\{\ddot{x}\} + [C]\{\dot{x}\} + [K]\{x\} = \{F\} \quad (2)$$

The frequency response function *G* also can be established as

$$G = \frac{x}{F} = \frac{1-\omega^2}{k[(1-\omega^2)^2 + (2\xi\omega)^2]} + i\frac{-2\xi\omega}{k[(1-\omega^2)^2 + (2\xi\omega)^2]} \quad (3)$$

where ξ is the ratio of the damping coefficient to the critical damping coefficient and ω is the ratio of the chatter frequency to the natural frequency. The FRFs of the system are the sum of tool point FRFs and the workpiece FRFs [Budak et al., 2010].

$$[G(\omega)] = G_{tool}(\omega) + G_{workpiece}(\omega) \quad (4)$$

Generally, the dynamics of the tool tip would not be changed during machining. For the workpiece dynamics, material mass and dynamic stiffness are continuously different with cutting which might be along to the depth of workpiece. The thinner the workpiece, the greater the dynamic change. In order to predict dynamics change of the workpiece at whole process, the simulation model need to be changed along with the difference. It is said that $G(\omega)$ of the equation (4) will be updated by $G_{workpiece}(\omega)$ in machining. There is the dynamics stiffness trend of the simulation workpiece shown in Figure 2. It can be seen that the dynamic stiffness will increase when the cutting position get close to the clamping edge. The most flexible stiffness will be at the free end of the workpiece. The probability of chatter of the thin wall free end will be higher than other positions.

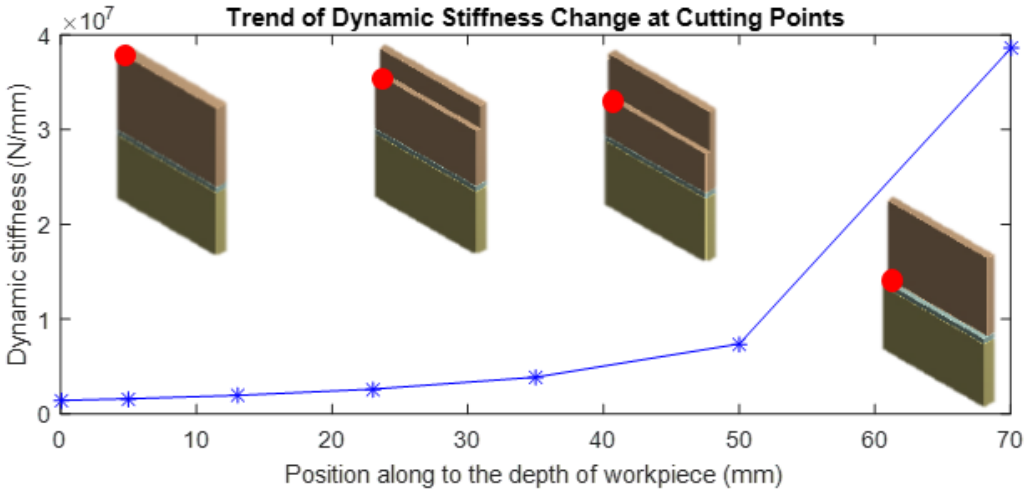


Figure 2. Trend of dynamic stiffness change

Stability Lobe Diagram

By solving equations (1) and (2), the chip width should be positive that the cutting process will be stable. Therefore, the axial depth of cut limit occurs at the true minimum value of real FRF G_R of the system when $\omega = \sqrt{1+2\xi}$:

$$b = \frac{-1}{2k_s G_R} = \frac{2k\xi(1+\xi)}{k_s} \tag{5}$$

The equation of regenerative chatter which are the relationships among the chatter frequency *f*, the tooth frequency f_t, and the lobe number *n* are obtained by [7]:

$$\frac{f}{f_t} = \frac{\omega}{\omega_t} = n + \frac{1}{2} + \frac{1}{\pi}\tan^{-1}\frac{-2\xi\omega}{1-r^2} \tag{6}$$

where ω_t is the ratio between the tooth frequency and natural frequency. From equations (5) and (6), a stability lobe diagram can be created by the chip width *b* and spindle speed *N*. The frequency response function is important for the prediction of the SLD following to the reference [Altintas et al., 1995].

3. OPTIMIZATION

The machining efficiency is more and more required. Especially for high accuracy products, it is difficult to improve whereas the surface accuracy should be based on. The stability lobe diagram has been used for increasing the machining benefit, but it could not be enough for the whole states. In order to predict the entire process of thin walls, stability lobe diagram can be expend to 3 dimensions which should include the dynamics along to the cut position of the workpiece. Material removal rates (MMR) might be calculated at each stable area of the diagram and optimized for the maximum efficiency of the machining conditions.

3-D SLD

According to the dynamics of the workpiece, natural frequencies, dynamic stiffness, and damping are identified to calculate the stability lobe diagram. It can be used to show the stable and unstable area which are also about chatter or not. The calculation method can be referred to [Budak et al., 2012]. It is said that each dynamics of the cut status of workpiece can be calculated easily. Each stability lobe diagram might also be predicted.

For the purpose of the whole process prediction, stability lobe diagrams of each cutting step need to establish the 3-D stability lobe diagram, shown as Figure 3. The three axis include spindle speed, cutting depth and position where the workpiece was cut. The position is used to predict the changed stable conditions of different cuts along to the workpiece. Specifically, when the workpiece was machined by 2 cut, the dynamics of the new structure would be different between the first status. Naturally, the stability could be changed according to the dynamics. Then, the stability of the whole statuses of the workpiece can be established as a 3D diagram that is easy for process planning.

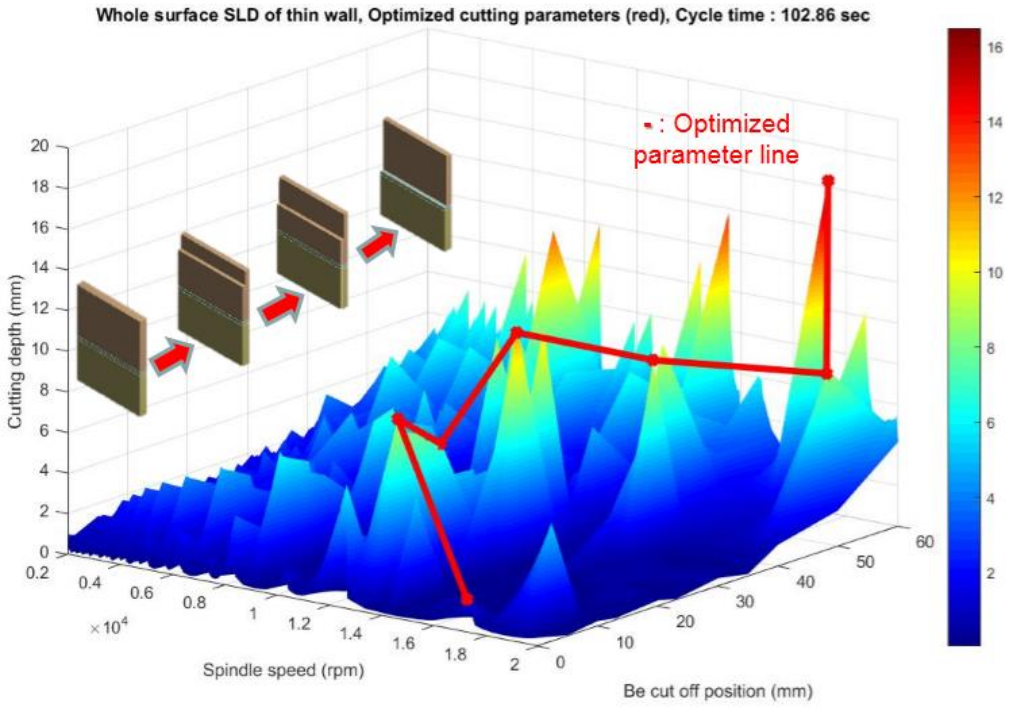


Figure 3. 3D stability lobe diagram

Opti-MRR

The removal rates of the materials are used to describe how fast the workpiece machining. The calculation method can also be referred to [Budak et al., 2005]. The optimized material removal rate function can be established as:

$$\max MRR(x, y, z) = \mathrm{D(x, y, z)} \times \mathrm{W} \times \mathrm{F(x, y, z)} \qquad (7)$$

where D is the depth of cut, W is the width of cut and F is the feed rate. The variables in the equation are according to the 3 axis parameters of 3D stability lobe diagram. Constraints of this optimization are that MRR should be lower than stability surface of the diagram. The width of cut should be lower than diameter of cutting tool which should be a chosen constant. Finally, the feed rate should accord to spindle speed.

Solutions should be followed and calculated from the stability lobe diagram shown as a red point in Figure 4. With the calculation of these, the maximum moving rates of each cut can be programed in the process by users. After that, the cycle time of the process can be decreased with the optimized cutting parameters.

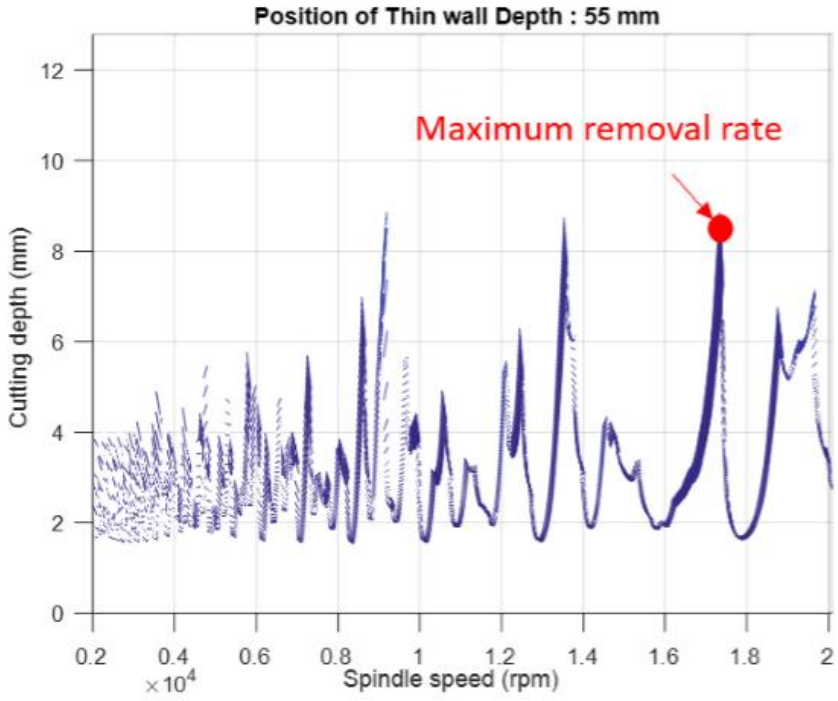


Figure 4. Stability area on depth 55mm

4. CASE STUDY

According to the simulation, the thin-walled workpiece was needed to validate the process planning. The thin-walled cutting system could also be established as shown in Figure 5. The sizes of the thin wall structure were set as a 100mm*120mm*10mm plate which was clamped 50mm by the device. The sizes of the free part of the structure became 100mm*70mm*10mm. Otherwise, the most of the cutting conditions were predicted by the 3D stability lobe diagram which was shown as in Figure 3, but one of them which is called cutting width should be planned before the simulation. In this case, the cutting widths of each operate were defined as 4.5mm.

As shown in Table 1, the process planning which used the simulated parameters were predicted by the process optimization. Each cutting depth should be followed the results by the stability lobe and opti-MMR computation. It could be seen that the cutting depths could be changed to upgrade the efficiency without traditional process planning which must be the same cutting depths for each operation. The closer the cutting position is to the clamping end, the deeper the cutting depth because of the high-clamping rigidities. The results could also be validated the simulations which used the stability lobe to calculate the opti-MMRs for the process parameters. The process efficiency was increased 43.27% which were compared between traditional machining method by using the same parameters in whole process and the newest prediction in this study. Finally, it could be seen that the processed surface of the thin wall shown as in Figure 5 was clear without chatter lines.

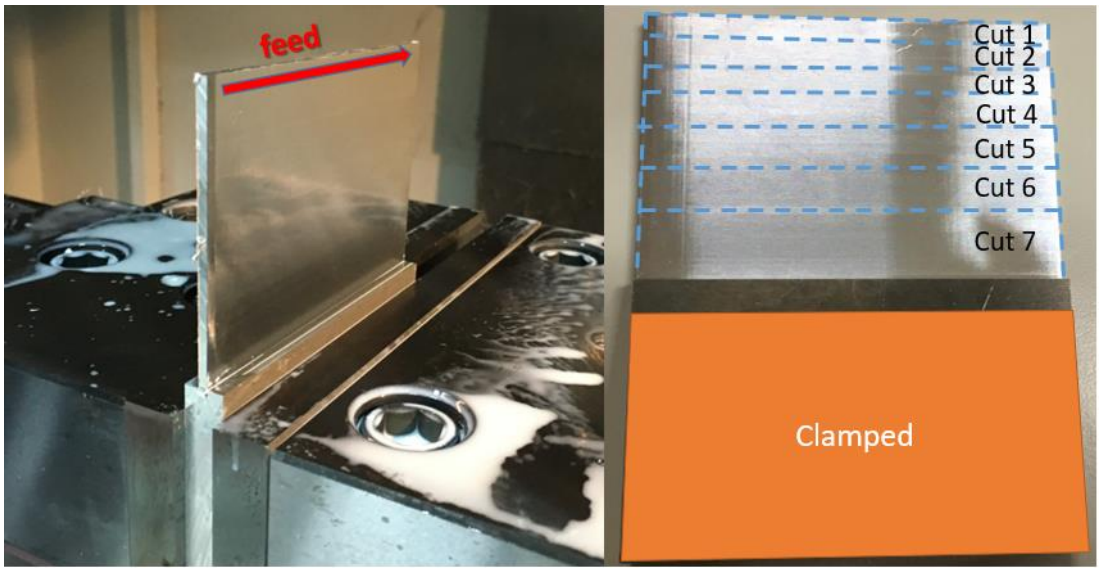


Figure 5. Thin wall case and cutting depth predictions

Table 1. Simulated process parameters

Cut	Depths (mm)	Spindle speed (rpm)	Total (mm)
1	1.8	17,250	1.8
2	8.2	12,700	10.0
3	6.4	12,350	16.4
4	12.2	14,100	28.6
5	13.0	16,130	41.6
6	12.0	19,200	53.6
7	16.4	17,500	70.0

5. CONCLUSIONS

Owing to predicting an efficient 3D stability lobe diagrams of the whole process of the thin-walled workpiece, the dynamics should be simulated at the first step. The next step is to calculate stability lobe diagram of each cut and establish the 3D stability lobe diagram which the third axis is the cut off positions. Otherwise, the opti-MRRs of each diagrams should be identified. Each maximum moving rate point on the stability lobe can be connected to a bend line which can be called the optimized parameter line for the thin-walled machining process. With the 3D stability lobe diagram and optimized parameters, engineers can use the intelligent calculation to predict and plan the thin-walled process which is considered the dynamic effect and high efficiency of the fixture structure in manufacturing.

ACKNOWLEDGEMENT

This project was supported by Industry Technology Research Institute and the Ministry of Science and Technology project MOST103-2218-E-005-003.

REFERENCES

1. **An-Chen Lee, Chia-Shang Liu, (1991),** "Analysis of Chatter Vibration in the End Milling Process", International Journal of Machine Tools and Manufacture, vol. 31, no. 4, pp. 471-479.

2. **Erhan Budak, L.Taner Tunç, Salih Alan, H. Nevzat Özgüven, (2012),** "Prediction of Workpiece Dynamics and its Effects on Chatter Stability in Milling", CIRP Annals - Manufacturing Technology, vol. 61, no. 1, pp. 339-342.

3. **Chung-Yu Tai, Yi-Hsuan Chen, Chi-Cheng Lin, Ci-Rong Huang, Ta-Jen Peng, Derek Luo, (2016),** "Prediction of Thin Wall Dynamics for Chatter Stability by Using Laser Doppler Velocimetry", The 17th International Conference on Machine Design and Production, vol. 17, no. 70, pp. 1-12.

4. **Chung-Yu Tai, Yi-Hsuan Chen, Chi-Cheng Lin, Ci-Rong Huang, Ta-Jen Peng, (2017),** "Contact Stiffness Identification Between Thin-walled Workpiece and Vice by Model Updating", IMAC XXXV Society for Experimental Mechanics, vol. 35, pp. 115.

5. **Roman Kalocsay, Thomas Bergs and Fritz Klocke, (2014),** "Impact of Clamping Technology on Horizontal and Vertical Process Chain Performance", New Production Technologies in Aerospace Industry, Lecture Notes in Production Engineering, Springer International Publishing Switzerland.

6. **Atsushi Matsubara, Yukihiro Taniyama, Jun Wang, Daisuke Kono, (2017),** "Design of a support system with a pivot mechanism for suppressing vibrations in thin-wall milling", CIRP Annals - Manufacturing Technology, vol. 66, pp. 381-384.

7. **J. Yue, (2006),** "Creating a Stability Lobe Diagram", in Proceedings of the 2006 IJME-INTERTECH Conference, Newark.

8. **Salih Alan, Erhan Budak, and H. Nevzat Özgüven, (2010),** "Analytical Prediction of Part Dynamics for Machining Stability Analysis", Journal ref: International Journal of Automation Technology, vol. 4, no. 3, pp. 259-267.

9. **Y. Altintas, E. Budak, (1995),** "Analytical Prediction of Stability Lobes in Milling", Annals of the CIRP, vol. 44, pp. 357-362

10. **E. Budak, A. Tekeli, (2005)**, "Maximizing Chatter Free Material Removal Rate in Milling through Optimal Selection of Axial and Radial Depth of Cut Pairs", CIRP Annals - Manufacturing Technology, vol. 54, pp. 353-356

INVESTIGATION OF EFFECT OF MINIMUM QUANTITY LUBRICATION TECHNIQUE ON SURFACE ROUGHNESS DURING MILLING OF TITANIUM ALLOY (TI-6AL-4V)

Khaled Ali OSMAN, *kalidaliosman@yahoo.com* Atilim University, 06836, Ankara, Turkey

Volkan YILMAZ, *volkan@gazi.edu.tr* Gazi University, 06500, Ankara, Turkey

Hakkı Özgür ÜNVER, *hounver@etu.edu.tr* TOBB University of Economics and Technology 06520, Ankara, Turkey

Ulvi ŞEKER, *useker@gazi.edu.tr* Gazi University, 06500, Ankara, Turkey

S. Engin KILIÇ, *engine.kilic@atilim.edu.tr* Atilim University, 06830, Ankara, Turkey

ABSTRACT

This study deals with experimental investigation of the effect of minimum quantity lubrication (MQL) on the surface roughness (Ra) of slot milled titanium alloy parts in comparison to those obtained under dry and flood lubrication conditions. The results revealed that with all cooling/lubrication conditions, surface roughness (Ra) is sensitive to changes in the feed per tooth, the axial depth of cut and the cutting fluid flow rate; but not sensitive to changes in the cutting speed. In addition, the Ra values with MQL were found to be lower in most of the conditions than those under flood lubrication. Dry cutting gave the highest surface roughness values for all conditions.

Keywords: Minimum Quantity Lubrication (MQL), Slot Milling, Surface Roughness, Response Surface Methodology (RSM).

1. INTRODUCTION

It is becoming more challenging for making the machining processes eco-friendly and acceptable for sustainable manufacturing due to the enforcement of stricter regulations on the wastes generated as byproducts of machining processes and their impact to protect the environment and the decreasing resources on Earth

[Fratila,2009][Sharma,2009]. The challenge is even harder when it is needed to machine difficult-to-cut materials where great amount of cutting fluids needs to be wasted to ease the process. In addition to their highly adverse effect on the environment, use of cutting fluids in conventional machining processes represents up to 20 % of the total machining cost [Sreejith,2000][zhang,2012]. There is therefore a stringent financial incentive as well as keeping up with sustainability restrictions for reducing the cutting fluid consumption.

Several works in the literature report the comparative test results for various type of cooling/ lubrication strategies for machining difficult-to-cut materials, such as dry machining (without cutting fluid) and minimum quantity lubrication (MQL) versus flood cooling. The minimum quantity lubrication (MQL) technique، also known as near dry machining (NDM) or micro-lubrication .is reported to have given much better performance than the flood cooling and dry cutting for a wide range of cases [Dudzinski,2004],[MaClure,2001], [Rahman,2002], [Lawal,2013].

This study proposes to implement MQL in the investigation and formulation of the predictive models of a machining performance; İ.e. surface roughness (Ra). The study presents the results of a detailed investigation using 2D and 3D graphical plots and ANOVA for variance analysis to determine the effect of three control factors in the slot milling of titanium alloys under dry, flood and MQL conditions.

2. EXPERIMENTAL METHOD

2.1 Machine tool, Workpiece Material and Cutting Tool

All of the slot milling experiments were carried out on a 3-axis CNC milling machine with a maximum spindle speed of 8000 rpm. In all experiments, the titanium alloy Ti-6Al-4V (grade 5) was used as the workpiece material with a block dimension of 50x50x100 mm. In these experiments, six slots were made along the workpiece block on each surface under different cooling conditions and table1 and table 2 illustrated levels of parameters and experimental parameters used respectively while the design of experiments for all conditions are shown in table 3.

Measurements of surface roughness were performed with a **Mahr Perthometer M1** as shown in Fig 1 and Fig 2 regarding the nozzle position during the process.

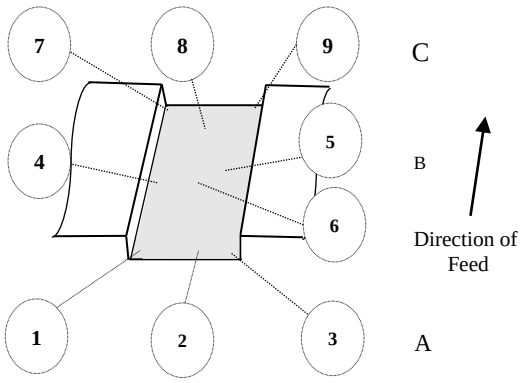


Figure 1. Locations of Measurements

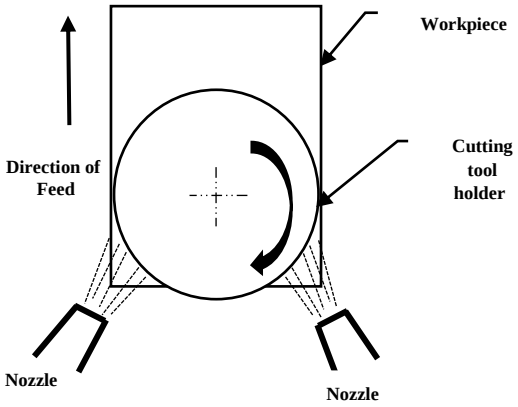


Figure 2. Schematic Diagram of Nozzle Setup

Table 1. Parameters and Levels.

Factor	Levels Values				
Vc (m/min)	56.835	60	65	70	73.165
F (mm/tooth)	0.010505	0.02	0.035	0.05	0.059495
ap (mm)	0.6835	1	1.5	2	2.3165
Q (ml/h)	18.8855	23	29.5	36	40.1145
Coding	-1.633	-1	0	1	1.633

Table 2. Experimental Parameters Used

Machining Type	Slot Milling
Work piece Materials	Ti-6Al-4V
Cutting Tool	Coated Cementite Carbide (coated Al Cr x Ni)
Machining Parameters	Feed rate (0.02,0.03,0.04, 0.05) mm/tooth
	Cutting speed (50,60,70) m/min
	Radial depth of cut (10 mm)
	Axial depth of cut (1,2,3 mm)
Cooling Techniques	Flood, Dry and MQL
MQL Technique	Cutting fluid type (Fetty acid ester)
	Flow rate of cutting fluid (18, 29.5,36,40 ml/h)
	Compressed air pressure (3 bar)

Table 3. Design Experiments for Dry, Flood and MQL conditions

Condition	Condition	Run Order	Cutting speed, Vc (m/min)	Feed /tooth, *f* (mm/tooth)	Depth of cutting, ap (mm)	Flow Rate of Cutting Fluid for MQL, (ml/h)	surface roughness (µm)	surface roughness (µm)	surface roughness (µm)
							Dry	Flood	MQL
MQL	Dry & Flood	1	60	0.02	1	36	0.425	0.372	0.259
		2	70	0.05	2	36	0.601	0.589	0.593
		3	60	0.05	1	23	0.662	0.512	0.407
		4	70	0.02	2	36	0.489	0.401	0.285
		5	70	0.05	1	36	0.664	0.535	0.417
		6	65	0.035	1.5	29.5	0.544	0.522	0.375
		7	65	0.035	1.5	29.5	0.53	0.521	0.374
		8	65	0.035	1.5	29.5	0.547	0.532	0.379
		9	60	0.02	2	23	0.427	0.329	0.398
		10	70	0.02	1	23	0.521	0.336	0.412
		11	65	0.035	1.5	29.5	0.542	0.539	0.435
		12	60	0.05	2	36	0.61	0.554	0.535
		13	65	0.01051	1.5	29.5	0.511	0.333	0.351
		14	65	0.035	1.5	29.5	0.552	0.528	0.38
		15	65	0.035	2.3165	29.5	0.825	0.727	0.536
		16	56.835	0.035	1.5	29.5	0.467	0.419	0.474
		17	65	0.035	1.5	29.5	0.549	0.530	0.376
		18	65	0.0595	1.5	29.5	0.764	0.641	0.5031
		19	73.165	0.035	1.5	29.5	0.57	0.456	0.404
		20	65	0.035	0.6835	29.5	0.572	0.488	0.376
		21	70	0.05	2	23	--------	--------	0.622
		22	60	0.05	1	36	--------	--------	0.392
		23	70	0.05	1	23	--------	--------	0.594
		24	60	0.02	2	36	--------	--------	0.227
		25	70	0.02	1	36	--------	--------	0.217
		26	60	0.05	2	23	--------	--------	0.693
		27	70	0.02	2	23	--------	--------	0.293
		28	65	0.035	1.5	18.8855	--------	--------	0.522
		29	65	0.035	1.5	40.1145	--------	--------	0.378
		30	60	0.02	1	23	--------	--------	0.354

3. RESULTS AND DISCUSSION

3.1 Analysis of Variance

The statistical analysis of the data is carried out in the form of variance analysis using Minitab 17. It includes F value and p-value. If the p-value is less than or equal to 0.05, the process parameters and their interactions are significant (α-level of 0.05). The proposed quadratic model is analyzed using the variance techniques (ANOVA) so that it is ensured that the model is usable

The regression models have been formulated for the surface roughness (Ra) in

terms of the cutting speed (Vc), feed per tooth (f) and depth of cut (ap). Tables 4 provides the statistical information (ANOVA results) regarding the most important factor affecting surface roughness (Ra) under different cooling conditions. With condition when the MQL is used, the effect of cutting fluid flow rate (Q) on the surface roughness (Ra) is noticeable. The value of R^2 for the current surface roughness (Ra) model is 97.31% for flood conditions, while for dry and MQL conditions, these are 88.75% and 83.21 %, respectively. Hence, the model can be characterized as effective. The analysis of P-value reveals that the feed per tooth (f) and depth of cut (ap) are statistically significant for the surface roughness (Ra) under flood and dry conditions, but the cutting fluid flow rate (Q) and the feed per tooth (f) are statistically significant under the MQL condition.

- Ra (Dry) = -5.64 + 0.1861 Vc +1.34 f – 0.33 ap + 0.001374 Vc^2 +45.6 f^2+ 0.1326ap^2 Eq.(1)
- Ra (Flood) =-7.15 + 0.2360 Vc+ 10.9 f – 0.559 ap - 0.001877 Vc^2 - 126 f^2 + 0.0673 ap^2 +0.037 Vc * f +0.006 Vc * ap+ 1.23 f * ap Eq.(2)
- Ra (MQL)= 2.19 + 0.0316 Vc – 26.9 f - 0.185 ap - 0.0191 Q + 0.000264 Vc^2+ 9.5 f^2 + 0.0519 ap^2 + 0.000254 Q^2 - 0.323 Vc * f - 0.00325 Vc * ap - 0.00246 Vc*Q + 4.28 f * ap + 0.159 f *Q+ 0.00527 ap *Q Eq.(3)

Table 4. Analysis of Variance (ANOVA) Considering the Surface Roughness Values.

Surface Roughness, (µm)	Flood			DRY			MQL		
Source	F-Value	P-Value	Contribution	F-Value	P-Value	Contribution	F-Value	P-Value	Contribution
Model	10.94	0.001	92.40%	6.76	0.002	79.77%	6.23	0.001	83.21%
linear	26.58	0.000	67.37%	10.05	0.001	50.84%	20.05	0.000	74.65%
Vc (m/min)	1.02	0.338	0.86%	5.89	0.032	9.93%	0.04	0.849	0.04%
f (mm/tooth)	67.62	0.000	57.13%	19.53	0.001	32.92%	55.26	0.000	51.45%
ap (mm)	11.09	0.009	9.37%	4.74	0.050	80.0%	9.56	0.008	8.90%
Q (ml/h)	------	------	------	-----	-----	-----	55.33	0.002	14.27%
S	0.0417			0.056			0.059		
R-squared	92.04%			79.77%			86.97%		
Adj *R*-squared	83.93%			76.25%			73.00%		

3.2 Effects of Machining Parameters on Surface Roughness (Ra)

In present study, the surface roughness (Ra) was utilized as a measure of the quality of the slot surface produced by an end-milling process under different cooling conditions. Applying the developed RSM models, we created the surface plots and contour plots of each model of dry, flood and MQL.

Figures 3, 4 and 5 show the 3D surface plots of the average surface roughness

against the machining parameters. It can be observed that the values of surface roughness (Ra) with flood and MQL conditions are less than those in the dry condition. At higher feed rates, this leads to an increase in the surface roughness (Ra) values as shown in figure 6.

This could be due to an increase in the value of the coefficient of friction at the tool-workpiece interface [Rahim, 2011]. The highest surface roughness values during various cooling/lubrication conditions are recorded at dry conditions due to the fact that intense heat is generated under such circumstances [Sreejith, 2000]. At the eems to be equal to ay result in better . A high lubrication rface, consequently ure shows that the orizontal. It can be ess (Ra) is smaller

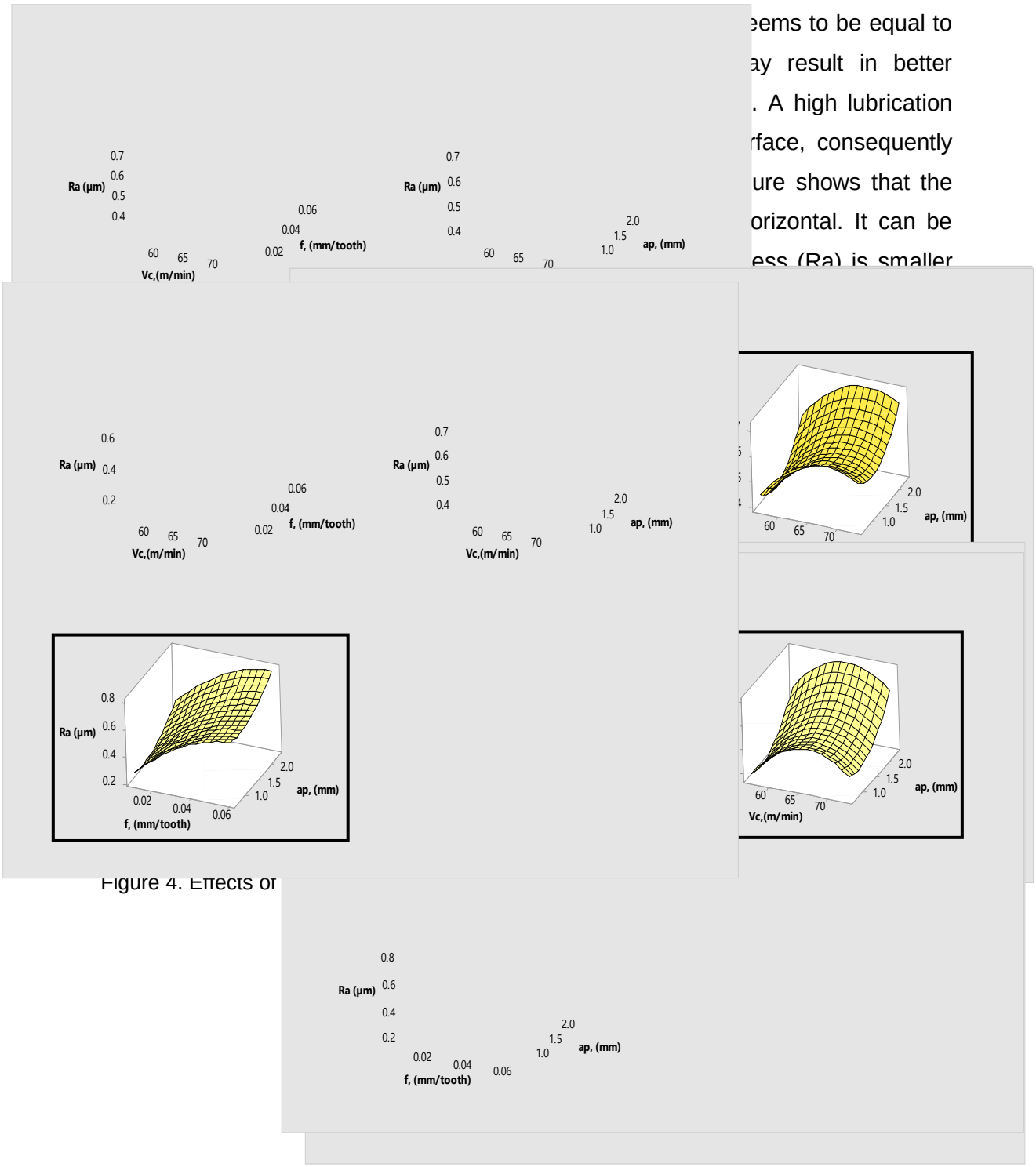


Figure 4. Effects of

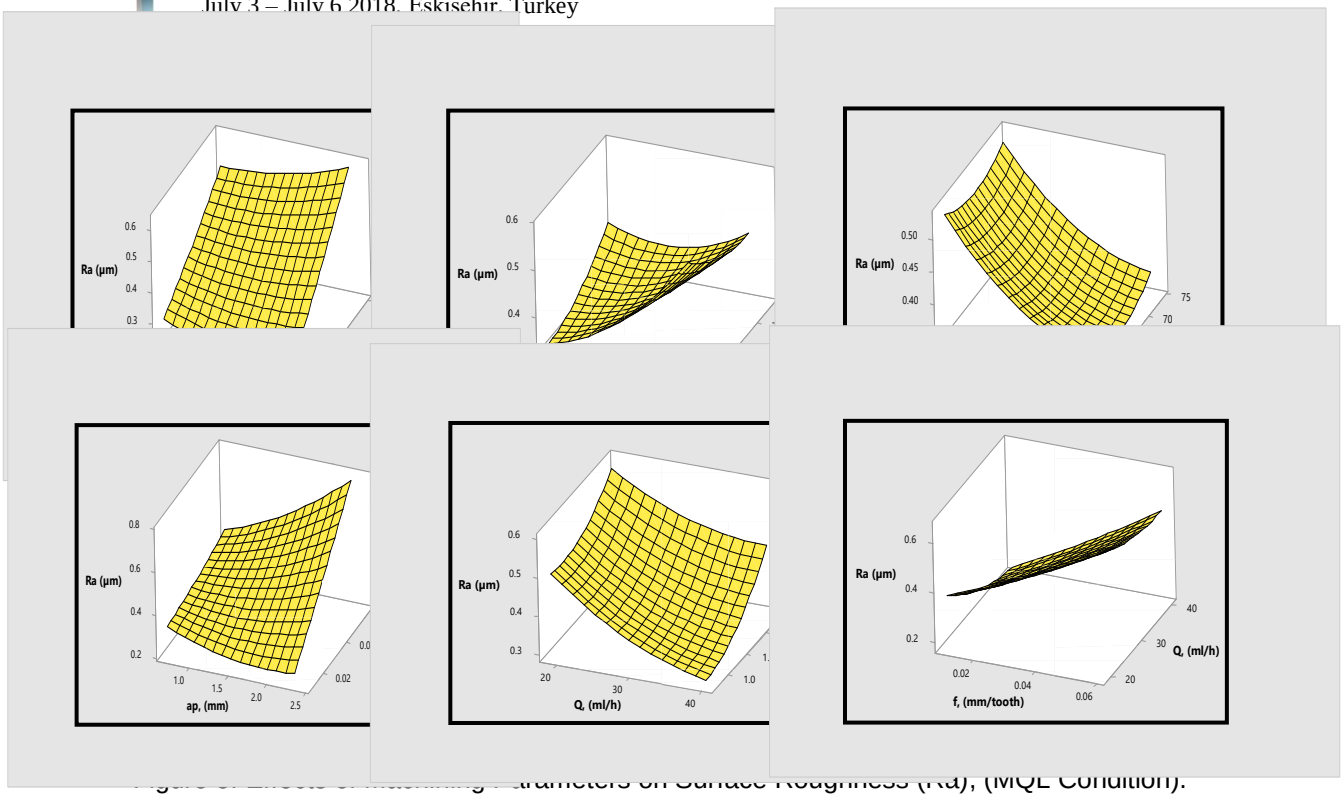


Figure 5. Effects of Machining Parameters on Surface Roughness (Ra), (MQL Condition).

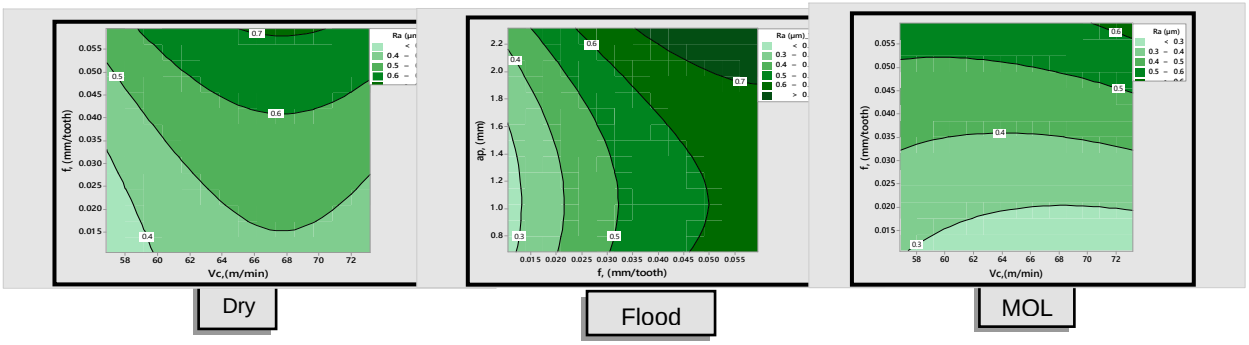


Figure 6. Surface Roughness (Ra) with Respect to All Conditions.

3.3 Comparison of the Effect of Machining Parameters on Surface Roughness (Ra)

The influence of the various cooling/lubrication conditions on surface roughness (Ra) were also studied as a response in the end-milling of titanium alloy. Quite a few researchers report that the results obtained in various cutting tests under different cutting conditions using MQL are in general somehow in between those of dry cutting and flood cutting [Kamata,2007][Zhigiang,2014]. As shown in figure 7, a comparison between the values of all responses under different conditions reveals that MQL is more effective than dry cutting and a better alternative to the flood condition. Compared to dry cutting, the MQL technique can reduce the surface roughness (Ra) reliably due to better lubrication and cooling effect.

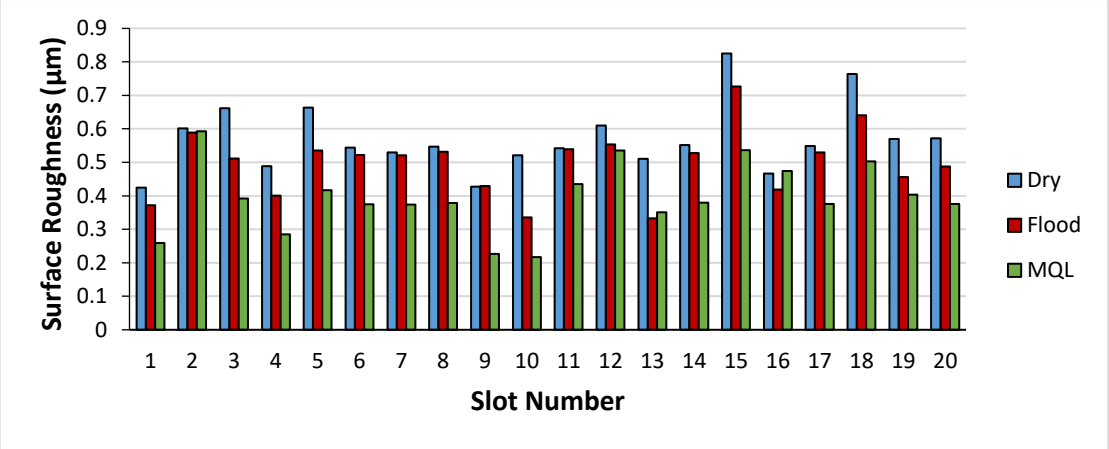


Figure 7. Surface Roughness Results at Different Cooling/Lubrication Conditions.

3.4 Comparison of Surface Roughness under Different Flow Rates

Figure 8 represents the surface roughness (Ra) results attained for dry, MQL with both flow rate 23 &36 ml/h and flood conditions. It can be seen that the influence of flow rate (Q) on surface roughness (Ra) at machining conditions Vc=60 m/min and *f*= 0.02mm/tooth, is reduced from 0.427 to 0.398 µm with flow rate (Q) 23ml/h and then reduced to 0.227mm with increasing flow rate (Q) to 36 ml/h. The value of surface roughness (Ra) was changed slowly at an increased flow rate (Q) under same machining conditions. However, at the machining conditions Vc =70 m/min and *f*= 0.05mm/tooth, the value of surface roughness (Ra) slight change by all conditions as following 0.601, 0.622, 0.593 and 0.589 µm for dry,23ml/h,36 ml/h and flood respectively. This led to display a weak effect of the MQL performance under a rise in both cutting speed and a feed per tooth.

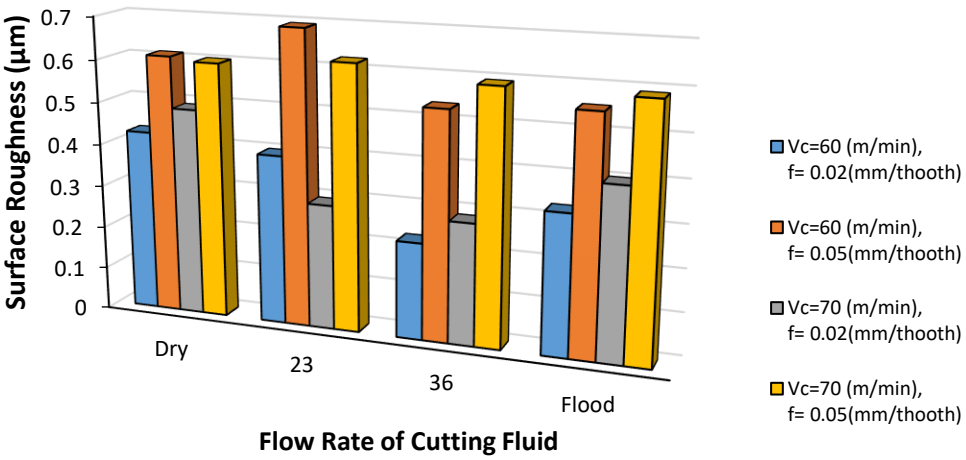


Figure 8. Comparison of Surface Roughness under different Flow Rates

4. CONCLUSION

In this study, the effect of cooling/lubrication conditions on the process of titanium alloy milling is investigated and discussed. Three cooling/lubrication conditions have been implemented to studies changing the surface roughness (Ra) during slot milling process. Based on this study, a number of conclusions can be made as follows:

1) The full quadratic models most appropriately define the effect of the surface roughness (Ra) in terms of the cutting speed (Vc), feed per tooth (f), depth of cut (ap) and flow rate (Q). Furthermore, the formulated mathematical relations exhibit a high degree of determination coefficient ($R^2 \longrightarrow 1.0$), making them as usable.
2) The ANOVA results show that the feed per tooth (f) and flow rate (Q) are the most significant control factors for all responses; and lastly, the depth of cut (ap).
3) The values of all the responses when milling under with the MQL technique were found close to the flood condition, at times even better. Therefore, the application of the MQL technique can be considered as future work to improve the machining of titanium (Ti-6Al-4V) alloys. Accordingly, the MQL technique is an effective alternative approach for conventional cooling conditions.
4) Increasing the amount of the lubricating oil in MQL does not necessarily improve the machining performance. A better performance was found at flow rate (Q) of 36 ml/h, under machining condition *f*=0.02 mm/tooth and Vc = 60 m/min .

REFERENCES.

1. **Fratila, D. (2009)**. Evaluation of near-dry machining effects on gear milling process efficiency. Journal of Cleaner Production, 17(9), 839–845.
2. **V. S. Sharma, M. Dogra, and N. M. Suri.(2009).** Cooling techniques for improved productivity in turning," Int. J. Mach. Tools Manuf., vol. 49, no. 6, pp. 435–453.
3. **Sreejith, P. S., & Ngoi, B. K. A. (2000)**. Dry machining: machining of the future. Journal Materials Processing Technology, 101(1), 287–291.
4. **S. Zhang, J. F. Li, and Y. W. Wang. (2012).**Tool life and cutting forces in end milling Inconel 718 under dry and minimum quantity cooling lubrication cutting conditions," vol. 32.
5. **D. Dudzinski, A. Devillez, A. Moufki, D. Larrouquere, V. Zerrouki, and J. Vigneau.(2004)**. A review of developments towards dry and high speed machining of Inconel 718 alloy," Int. J. Mach. Tools Manuf., vol. 44, no. 4, pp. 439–456.

6. **T. F. MaClure, R. Adams, M. D. Gugger, and M. G. Gressel.(2001).** Comparison of flood vs. microlubrication on machining performance," Internet http//www. unist. com/techsolve. html.
7. **M. Rahman, A. S. Kumar, and M. U. Salam. (2002).** Experimental evaluation on the effect of minimal quantities of lubricant in milling," Int. J. Mach. Tools Manuf., vol. 42, no. 5, pp. 539–547.
8. **S. A. Lawal, I. A. Choudhury, and Y. Nukman(2013).** A critical assessment of lubrication techniques in machining processes: a case for minimum quantity lubrication using vegetable oil-based lubricant," J. Clean. Prod., vol. 41, pp. 210–221.
9. **Rahim, E. A., & Sasahara, H. (2011).** Investigation of tool wear and surface integrity on MQL machining of Ti-6AL-4V using biodegradable oil. Proceedings of the Institution of Mechanical Engineers, Part B: Journal of Engineering Manufacture, 225(9), 1505-1511.
10. **Dhar, N. R., Islam, M. W., Islam, S., & Mithu, M. A. H. (2006)**. The influence of minimum quantity of lubrication (MQL) on cutting temperature, chip and dimensional accuracy in turning AISI-1040 steel. Journal of Materials Processing Technology, 171(1), 93–99. article..
11. **Kamata, Y., & Obikawa, T. (2007)**. High speed MQL finish-turning of Inconel 718 with different coated tools. Journal of Materials Processing Technology, 193, 281–286.
12. **Zhiqiang, L. (2014)**. Green Machining of Ti-6Al-4V Under Minimum Quantity Lubrication (MQL) Condition. Materials Forming, Machining and Tribology, 113–129.

GRINDING OPERATION OF A WORKPIECE WITH AN UNKNOWN SHAPE CONSIDERING TOOL DEFLECTION COMPENSATION

Abdulhamit DONDER, *adonder@metu.edu.tr* Middle East Technical University, 06800, Ankara, Turkey

Masoud LATIFINAVID, *mlatifinavid@thk.edu.tr* University of Turkish Aeronautical Association, 06790, Ankara, Turkey

E. ilhan KONUKSEVEN, *konuk@metu.edu.tr* Middle East Technical University, 06800, Ankara, Turkey

ABSTRACT

In robotic-machining, the effort on the pre-processes, such as path planning, is felt deeply as the customized products are in demand. In this study, the elimination of these preprocesses was aimed and a novel method, which considers the tool deflection compensation, for grinding operation of a workpiece with an unknown shape was proposed. The algorithm was tested on a robotic-grinding setup and experimental result were discussed.

Keywords: Grinding, Unknown shape, Tool deflection compensation

1. INTRODUCTION

Grinding operation has an advantage of precise form shaping in machining processes. However, if the surface profile is not known before the machining process, it is hard to obtain an accurate surface profile using this operation. In the proposed study, a novel method to compensate the form shaping errors in grinding operations due to the lack of a priori knowledge of the surface profile is presented. Grinding operation on a workpiece with an unknown surface profile is performed. Compliance force control is implemented by means of admittance control in two degrees of freedom using a piezo actuator and a hexapod parallel manipulator. The desired force interaction between the tool and the workpiece is achieved by imposing an offset from the preset depth of cut. Additionally, tool deflection due to the grinding forces of the robotic grinding setup is taken into consideration. The deflections are computed from the grinding forces in real time and the compensation is performed by the hexapod robot in six degrees of

freedom. Based on the literature review, this is the first study in which grinding on a workpiece with an unknown surface profile was performed while tool deflection due to the grinding forces was compensated.

Grinding with constant normal force and constant tangential velocity is a well-known approach for increasing the operation accuracy and getting constant depth of cut and surface quality along work-piece. However, the mentioned approach is effective when using universal grinding machines that are stiffer than CNC type machines and the deflection of the tool and setup is negligible. In the case of robotic grinding, the stiffness of the robot and setup is approximately 30 times lower than CNC type grinding machines (this was concluded by comparing [1] and [2]). Consequently, there are considerable tool deflections, which causes the ground surface to become inclined as shown in Fig. 1

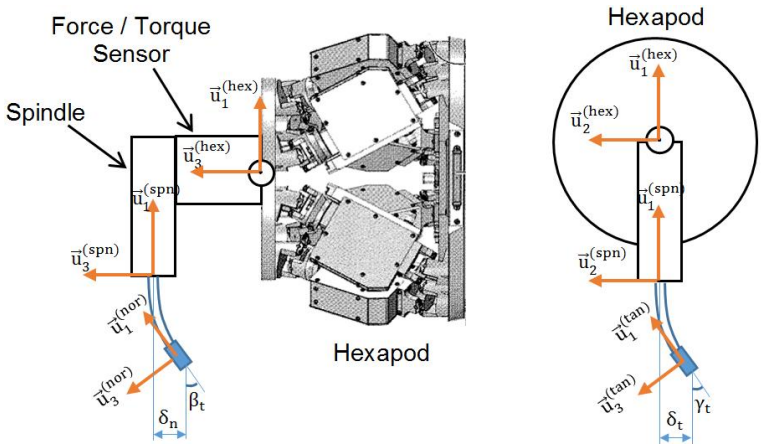


Fig. 1 - Illustration of the deformation of a grinding tool

2. LITERATURE REVIEW

With the advances in control techniques, the researchers embarked on machining of a work-piece with an unknown shape. In order to obtain constant depth of cut from a homogeneous-flat surface material, the grinding parameters such as feedrate, spindle speed, should be invariant throughout the surface profile. These requirements can be achieved via hybrid force/velocity control [3].

In [4], the implementation of grinding of a work-piece with an unknown shape was performed. As the control algorithm, hybrid force/velocity control structure was utilized. The authors dealt with the problems related to configuration dependent dynamics of the manipulator. Jatta et al. [5] investigated the effects of elastic transmission of the robots during contour tracking of a work-piece with an unknown shape. The large force oscillations due to the elasticities in joints are compensated by an additional normal velocity feedback loop. Pedrocchi et al. [6] studied the decoupling of normal force and tangential velocity control loops. The controller was

expressed as multi input – multi output, time varying, PID controller. In [7], joint friction effects to normal force and tangential velocity variations in hybrid force / velocity controller were investigated.

Additionally, [8] and [9] are the examples of contour tracking.

There are several researches in literature related to the compensation of tool deflection effect on work-piece. In this section a review of different strategies of these studies are expressed. Most of the mentioned studies are related to the end milling operation.

Kline et al. [10] proposed a method for prediction of tool and work-piece deflection amount in end milling operation based on cantilever beam theory. They used a force model and cantilever beam theory for obtaining deflection amount. Similarly, Ryu et al. [11] investigated side wall machining operation and tried to predict the errors caused by tool deflection. But, they did not express a solution for compensation of these errors. The effect of work-piece curvature on tool deflection and resulting surface errors are investigated in [12].

A method based on path correction is proposed by Law et al. [13]. Their aim was to decrease tool deflection and its effect on work-piece using optimum tool path.

Approaches for path correction in the end milling operation were presented in [14]–[17] by adding an offset to the tool path. They used cantilever beam theory in order to calculate the amount of tool deflection. Rao et al. [18] proposed an iterative approach instead of single offset for compensation of offset error caused by tool deflection. However, they did not investigate tool angle compensation.

A method for compensation of tool angle and tool displacement during end milling operation is proposed by Yang et al. [19] where a sensor is used for detecting tool deflection amount. The strong side of their research is that they considered both tool angle and tool tip displacement by compensation of errors.

3. EXPERIMENTAL SETUP

In addition to 6-DoF parallel manipulator, the experimental setup has an additional 1-DoF which is actuated by a piezo actuator. The actuator is fixed to the properly constrained table, presents a single degree of freedom. While performing grinding, the machining errors can be reduced by admittance control based negative compensation by the actuation of the piezo actuator. The force/torque sensor is able to measure the data of the forces on 3 Cartesian basis axes and of the torques about the same axes.

The parts used in experimental setup shown in Fig. 2 are:

1. *Hexapod (6 DoF): It has 6 DoF and is used to move the spindle which carries the tool.*
2. *ATI Gamma IP60 Force / Torque Sensor*
3. *Spindle*
4. *Workpiece (St37)*
5. *Piezo Actuator*
6. *Table (which has 1 DoF in x direction as shown in Fig. 3 during machining)*

In order to control and drive hexapod, force/torque sensor, piezo actuator and spindle; MATLAB SIMULINK software running on the workstation was utilized. These four devices are connected to the workstation using the protocols summarized in Fig. 3.

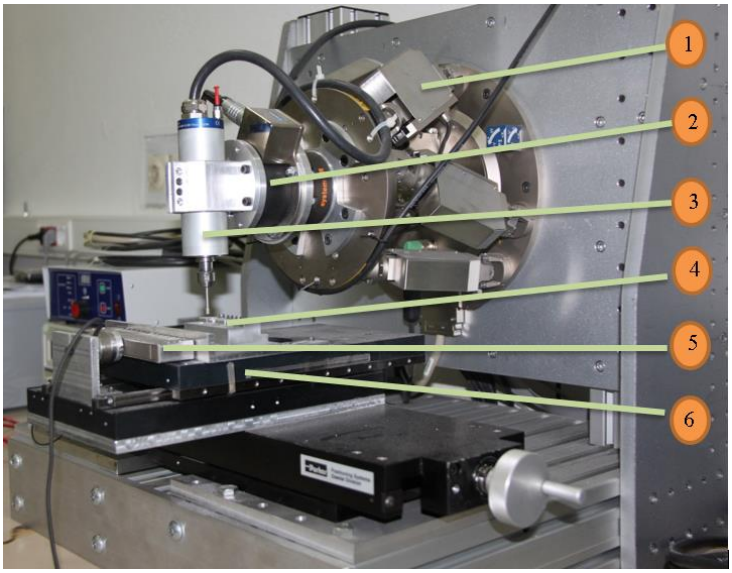


Fig. 2 The overall appearance of the setup.

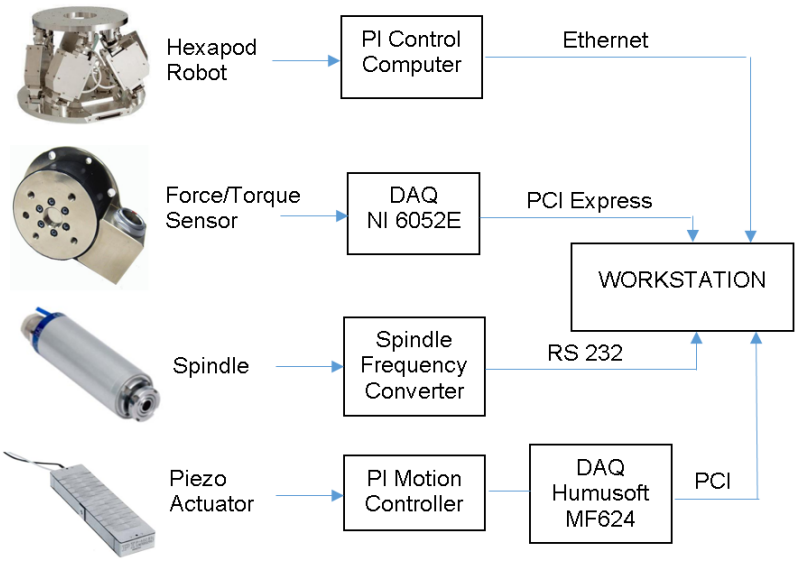


Fig. 3 Devices and Connection Protocols

4. MODELLING AND COMPENSATION OF THE TOOL DEFLECTION

In this section the tool deflection in normal and tangential directions are calculated using cantilever beam theorem. Considering feedbacks from force sensor, the normal and tangential grinding forces were used for calculating the tool deflection.

In normal direction:

$$\delta_n = \frac{F_n L^3}{3EI} \tag{1}$$

$$\beta_t = \frac{F_n L^2}{2EI} \tag{2}$$

In tangential direction:

$$\delta_t = \frac{F_t L^3}{3EI} \tag{3}$$

$$\gamma_t = \frac{F_t L^2}{2EI} \tag{4}$$

Where

E: Modulus of Elasticity

I: Moment of Inertia

L: Tool length

F_n: Normal grinding force

F_t: Tangential grinding force

δ_n: Displacement in normal direction

δ_t: Displacement in tangential direction

β_t: Tool deflection in normal direction

γ_t: Tool deflection in tangential direction

A kinematic solution was proposed for tool deflection compensation. Five reference frames were assigned on the grinding setup where the first frame was on the base (f_{base}), the second frame was on the top plate of the hexapod (f_{hex}), the third frame was on the tool holder of the spindle (f_{spn}) and the fourth and fifth frames ($f_{tan}\ and\ f_{nor}$) were on the tool tip point (Fig. 1).

The reference frames from the base frame to the tool tip are shown in Eq. 5.

$$f_{base} \rightarrow f_{hex} \rightarrow f_{spn} \rightarrow f_{tan} \rightarrow f_{nor} \tag{5}$$

Considering the end axis of the assigned reference frames that are shown in Fig. 1, the rotation matrix from f_{hex} to f_{nor} can be calculated as Eq. 6.

$$\hat{R}^{(hex,nor)} = \hat{R}^{(hex,spn)}\hat{R}^{(spn,tan)}\hat{R}^{(tan,nor)} \tag{6}$$

The orientation ($\hat{R}^{(hex,spn)}$) and translation (t_{spn}^{hex}) of the spindle tool holder with respect to the hexapod reference frame is because of assembly errors. The mentioned orientation and translation are calculated by a coordinate measurement machine (CMM).

$$\hat{R}^{(hex,spn)} = \hat{R}_{CMM} \tag{7}$$

$$t_{spn}^{hex} = \begin{bmatrix} r_x \\ r_y \\ r_z \end{bmatrix} \tag{8}$$

Tool deflection was modeled as two successive rotations in the tangential and normal directions. γ_t is the rotation of the tool around the z-axis (u_3) of f_{spn} due to deflection in the tangential direction. So the rotation matrix from R_{spn} to R_{tan} can be written as Eq. 9.

$$\hat{R}^{(spn,tan)} = \begin{bmatrix} \cos\gamma_t & -\sin\gamma_t & 0 \\ \sin\gamma_t & \cos\gamma_t & 0 \\ 0 & 0 & 1 \end{bmatrix} \tag{9}$$

β_t is rotation about the y-axis (u_2) of f_{spn} due to deflection in the normal direction. So the rotation matrix from R_{tan} to R_{nor} can be written as Eq. 10.

$$\hat{R}^{(tan,nor)} = \begin{bmatrix} \cos\beta_t & 0 & \sin\beta_t \\ 0 & 1 & 0 \\ -\sin\beta_t & 0 & \cos\beta_t \end{bmatrix} \tag{10}$$

Expressing Eq. 10 in the spindle reference frame, the rotation from f_{hex} to f_{nor} can be written as follows:

$$\hat{R}^{(hex,nor)} = \hat{R}_{CMM}\,\hat{R}^{(tan,nor)}\,\hat{R}^{(spn,tan)} \tag{11}$$

The translation matrix and transformation homogenous matrix from f_{hex} to f_{nor} can be written as follows:

$$t_{nor}^{hex} = \begin{bmatrix} r_x - L\cos\gamma_t\cos\beta_t \\ r_y + \delta t \\ r_z + \delta n \end{bmatrix} \tag{12}$$

$$H_{nor}^{hex} = \begin{bmatrix} \hat{R}^{(hex,nor)} & t_{nor}^{hex} \\ 0 \quad 0 \quad 0 & 1 \end{bmatrix} \tag{13}$$

Here, the normal grinding force is negative. Therefore, δn is always a negative value. Considering the feeding direction, δt can be a positive or negative value. The controllable parameters in this grinding setup are rotation and translation of the hexapod. Considering the

rotation and translation of the hexapod moving plate with respect to the base reference frame, the forward kinematics of the grinding setup can be obtained.

$$H_{FK} = H_{hex}^{base}\ H_{nor}^{hex} \tag{14}$$

Where

$$H_{hex}^{base} = \begin{bmatrix} \hat{C}_{hexapod} & t_{hexapod} \\ 0 \quad 0 \quad 0 & 1 \end{bmatrix} \tag{15}$$

In this study the goal is to compensate the tool deflection and keep it in vertical direction. So, the desired forward kinematics of the robot ($H_{FK-desired}$) was defined in this way. The desired hexapod motion and orientation that compensate the tool deflection and keeps it vertical was defined as $H_{hex-desired}^{base}$.

$$H_{hex-desired}^{base}\ H_{nor}^{hex} = H_{FK-desired} \tag{16}$$

Finally, multiplying the desired forward kinematics of the grinding setup by the inverse of H_{nor}^{hex}, the new position and orientation of the hexapod were calculated where this new hexapod kinematic values compensate the geometrical errors caused by the tool deflection.

$$H_{hex-desired}^{base} = H_{FK-desired}\ H_{nor}^{hex^{-1}} \tag{17}$$

5. EXPERIMENTAL PROCEDURE

In order to obtain constant depth of cut from variable surface, the key strategy that should be implemented is imposing appropriate normal force and tangential velocity. That is, classical explicit hybrid force/velocity control can be implemented [3]. In order to obtain the actual local normal force from measured X and Y force components the algorithm which is explained in [21] was utilized.

MATLAB SIMULINK was utilized for controlling the devices of the grinding setup. The “Plant” block without its control part is shown in Fig. 5. Note that hexapod orientation compensation is considered as a separate independent loop shown in Fig. 6.

In Fig. 5, “Controller Output” is the amount of change in the piezo position. It is added to the current position of the piezo actuator.

In order to calculate the velocity of the hexapod robot, the data which is given to the piezo actuator goes through a discrete derivative block in order to determine the velocity of the piezo actuator. After that the velocity of the hexapod robot is calculated from the set feedrate value by considering the current velocity of the piezo actuator.

Single pass grinding operation was performed. The used sample form is shown in Fig. 4

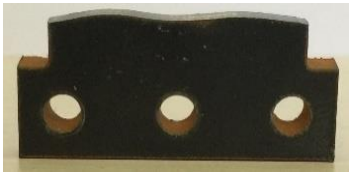


Fig. 4 - Sample

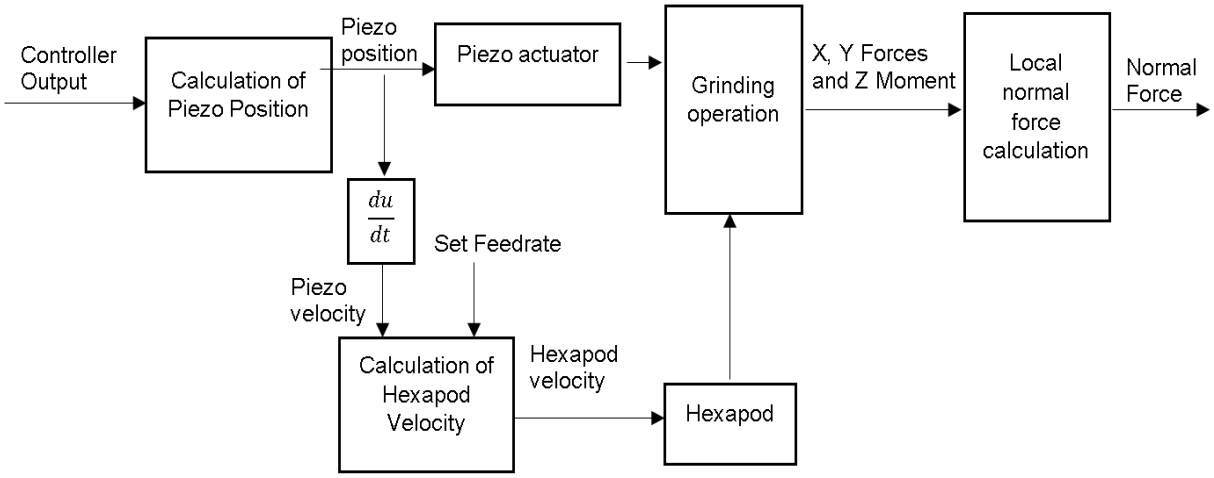


Fig. 5 - Plant Model for Experiment

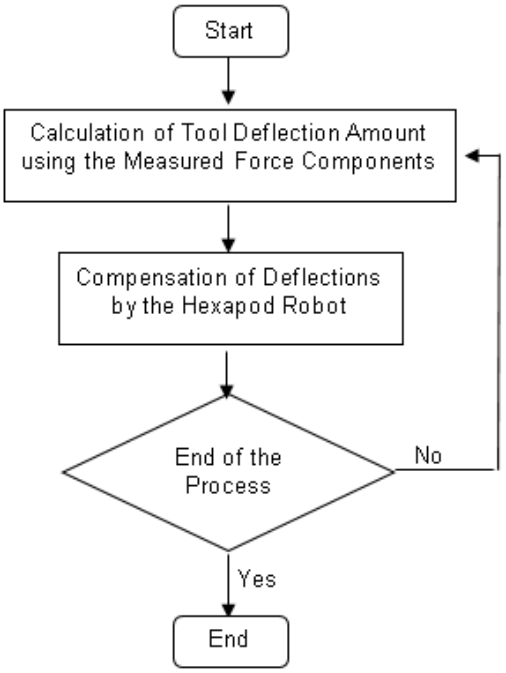


Fig. 6 – Hexapod controller algorithm

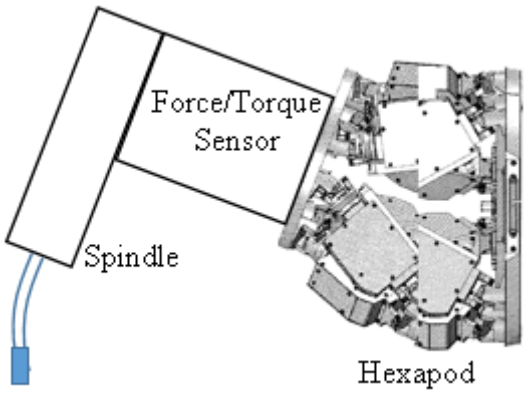


Fig. 7 – Illustration of the hexapod during Tool Deflect. Comp.

The PID parameters were determined by genetic algorithm as:

- Kp: 84.06
- Kd: 14.1
- Ki: -0.01766

The experimental parameters are:

- Set feedrate: 0.1 mm/sec
- Spindle speed: 25000 rpm
- Material: 4mm ST37
- Diameter of the used CBN tool: 4mm
- Down-cut grinding operation
- Length of the tool: 23.5 mm

6. RESULTS OF THE EXPERIMENT

The variation of the local normal force when it is set to 7.5 N is shown in Fig. 8.

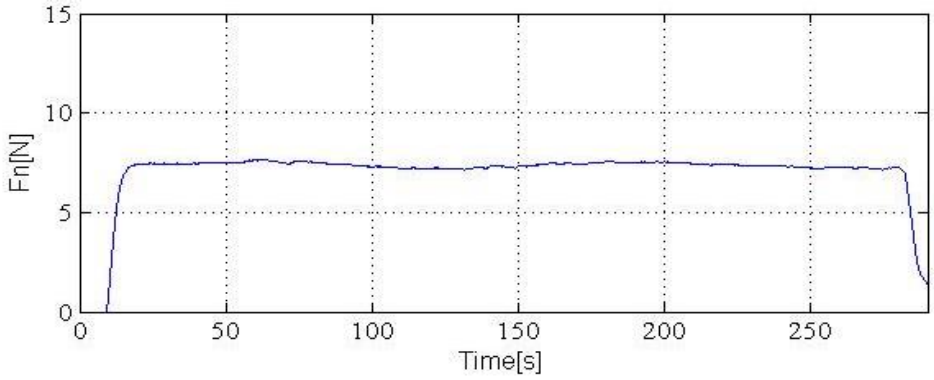


Fig. 8 - Local Normal Force (PID Fn=7.5N)

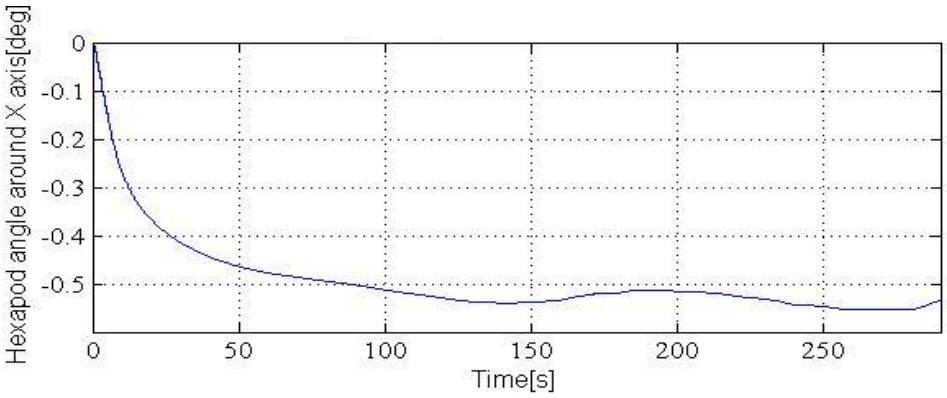


Fig. 9 - Hexapod angle variation around X direction (PID Fn=7.5N)

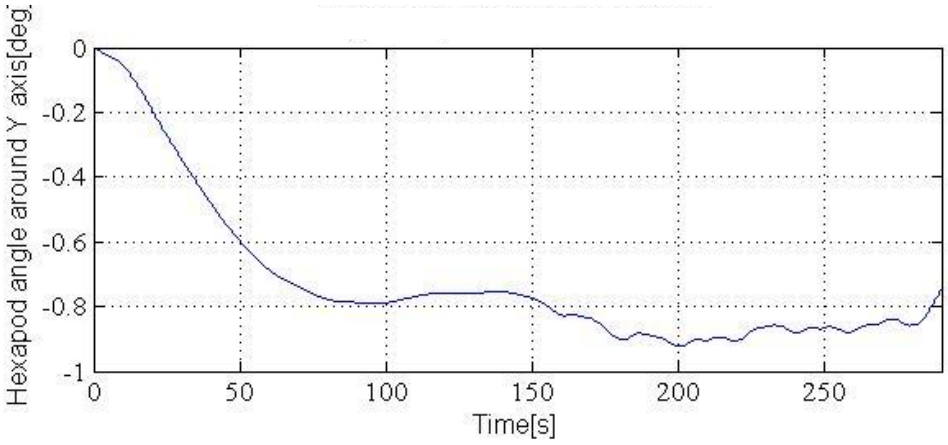


Fig. 10 - Hexapod angle variation around Y direction (PID Fn=7.5N)

The change in the surface form is shown in Fig. 11.

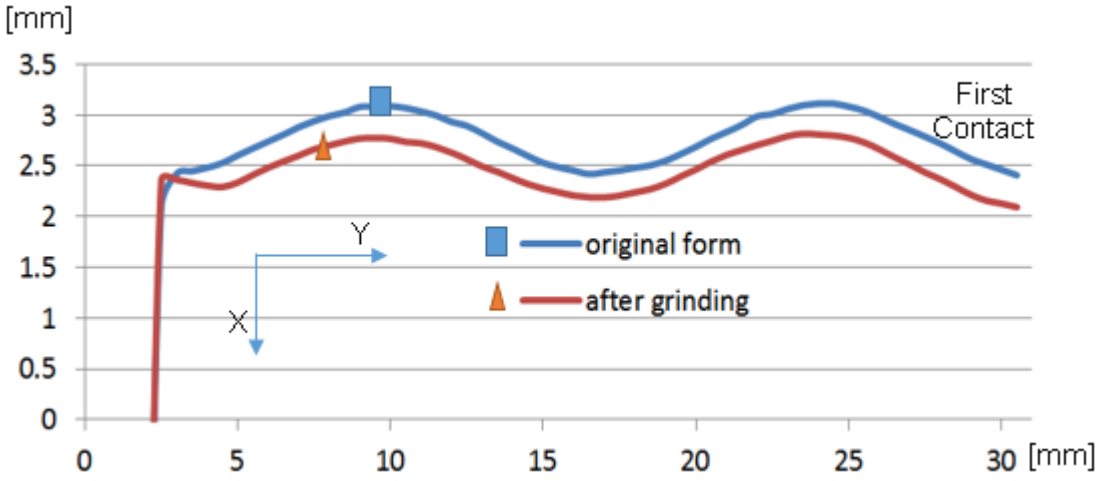


Fig. 11 - Surface forms before and after grinding operation. The measurement is taken from the mid-section of the workpiece (PID Fn=7.5N)

In order to compare two surface forms, shown in Fig. 11, they were superimposed and root mean square error was calculated as $42\ \mu m$.

Additionally, several scans were performed in vertical direction in order to understand the success of angle compensation controller. After that, lines were fit to the scans. The angle of the line, which has the maximum amount of angle with respect to the vertical axis, is $0.17°$

The reaction of hexapod against the force variations can be seen in Fig. 9 and Fig. 10. The $4°$ angle (the angle after water jet cutting) with respect to the vertical axis was reduced to maximum of 0.17° while it can be decreased to 0.5° without angle compensation.

7. CONCLUSION

In this study, hybrid force/velocity control method was implemented to the robotic grinding setup with tool angle compensation. While the local normal force is tried to be kept constant by the movements of the piezo actuator, the compensation of the local tangential velocity and tool compensation are performed by the hexapod robot. Based on literature review, this is the first study in which these two control algorithms were used simultaneously in real time. The results show that significant amount of path planning and calibration effort can be saved by the proposed approach.

REFERENCES

[1] S. Son, T. Kim, S. E. Sarma, and A. Slocum, “A hybrid 5-axis CNC milling machine,” *Precis. Eng.*, vol. 33, no. 4, pp. 430–446, 2009.

[2] V. I. Guzeev and A. K. Nurkenov, “Researching the CNC-Machine Stiffness Impact on the Grinding Cycle Design,” *Procedia Eng.*, vol. 150, pp. 815–820, 2016.

[3] M. H. Raibert and J. J. Craig, “Hybrid Position / Force Control of Manipulators,” *J. Dyn. Syst. Meas. Control*, vol. 102, no. June 1981, 1981.

[4] F. Jatta, G. Legnani, A. Visioli, and G. Ziliani, “On the use of velocity feedback in hybrid force/velocity control of industrial manipulators,” *Control Eng. Pract.*, vol. 14, no. 9, pp. 1045–1055, 2006.

[5] F. Jatta, G. Legnani, and A. Visioli, “Hybrid force / velocity control of industrial manipulators with elastic transmissions,” in *Proceedings of the 2003 IEEE/RSJ Int. Conference on Intelligent Robots and Systems*, 2003, no. October, pp. 3276–3281.

[6] N. Pedrocchi, A. Visioli, G. Ziliani, and G. Legnani, “On the elasticity in the dynamic decoupling of hybrid force/velocity control in the contour tracking task,” in *2008 IEEE/RSJ Intern. Conf. on Intell. Robots and Sys., IROS*, 2008, pp. 955–960.

[7] F. Jatta, G. Legnani, and A. Visioli, “Friction Compensation in Hybrid Force / Velocity Control of Industrial Manipulators,” *IEEE Trans. Ind. Electron.*, vol. 53, no. 2, pp. 604–613, 2006.

[8] G. Ziliani, A. Visioli, and G. Legnani, “A mechatronic approach for robotic deburring,” *Mechatronics*, vol. 17, no. 8, pp. 431–441, 2007.

[9] T. Thomessen and T. K. Lien, “Robot Control System for Safe and Rapid Programming of Grinding Applications,” *Ind. Robot An Int. J.*, vol. 27, no. 6, pp. 437–444, 2000.

[10] W. A. Kline, R. E. Devor, and I. A. Shareef, “The Prediction of Surface Accuracy in End Milling,” in *Trans, of ASME*, 1982, vol. 104, no. 3, pp. 272–278.

[11] S. H. Ryu, H. S. Lee, and C. N. Chu, “The form error prediction in side wall machining considering tool deflection,” *Int. J. Mach. Tools Manuf.*, vol. 43, pp. 1405–1411, 2003.

[12] V. S. Rao and P. V. M. Rao, “Effect of workpiece curvature on cutting forces and surface error in peripheral milling,” in *Proceedings of the Institution of Mechanical Engineers*, 2006, vol. 220, no. 9, pp. 1399–1407.

[13] K. M. Y. Law, A. Geddam, and V. A. Ostafiev, “A process-design approach to error compensation in the end milling of pockets,” *J. Mater. Process. Technol.*, vol. 89–90, pp. 238–244, 1999.

[14] S.-H. Suh, J.-H. Cho, and J.-Y. Hascoet, “Incorporation of Tool Deflection in Tool Path Computation: Simulation and Analysis,” *J. Manuf. Syst.*, vol. 15, no. 3, pp. 190–199, 1996.

[15] B. Denkena, H. C. Möhring, and J. C. Will, “Tool deflection compensation with an adaptronic milling spindle,” in *Conference on Smart Machining Systems*, 2007.

[16] M. Soori, B. Arezoo, and M. Habibi, “Virtual machining considering dimensional, geometrical and tool deflection errors in three-axis CNC milling machines,” *J. Manuf. Syst.*, vol. 33, no. 4, pp. 498–507, 2014.

[17] M. Habibi, B. Arezoo, and M. Vahebi Nojedeh, “Tool deflection and geometrical error compensation by tool path modification,” *Int. J. Mach. Tools Manuf.*, vol. 51, no. 6, pp. 439–449, 2011.

[18] V. S. Rao and P. V. M. Rao, “Tool deflection compensation in peripheral milling of curved geometries,” *Int. J. Mach. Tools Manuf.*, vol. 46, no. 15, pp. 2036–2043, 2006.

[19] M. Y. Yang and J. G. Choi, “A tool deflection compensation system for end milling accuracy improvement,” *J. Manuf. Sci. Eng.*, vol. 120, no. 2, pp. 222–229, 1998.

[20] K. Açıkgöz, “Prediction Of The Cutting Forces for Robotic Grinding Processes with Abrasive Mounted Bits,” Middle East Technical University, 2015.

[21] A. Donder and E. I. Konukseven, “Contour Tracking by Hybrid Force/Velocity Controlled Grinding: Comparison of Controllers ADRC -PID,” in *International Conference on Modeling, Simulation and Control*, 2017.

DESIGN FOR MANUFACTURABILITY: DETERMINATION OF MINIMUM MANUFACTURABLE WALL AND FLOOR THICKNESS OF MACHINED PARTS BY UTILIZING FINITE ELEMENT ANALYSIS

Candaş URUNGA, *candas.urunga@parttime.atilim.edu.tr* Atilim University, 06830, Ankara, Turkey

ABSTRACT

During manufacturing of a machined part, cutting forces may create excessive stresses and strains in the part. Design engineers should take into account not only the loads that their designs shall encounter during their life cycle but the forces exerted during manufacturing processes. Finite element analysis can be used also for analysis of these manufacturing effects. This study uses finite element analysis. The results of these analyses are used to find generic formulas for determination of manufacturable thicknesses of walls and floors of any design. The findings may be very useful for designing manufacturable parts and reduce scraps and costs.

Keywords: Manufacturability, Wall thickness, Floor thickness

1. INTRODUCTION

In this study, formulas shall be generated for guiding the design engineers to give sound design decisions for determination of the thickness values of walls and floors of machined parts that withstand the cutting forces during manufacturing.

2. FINITE ELEMENT MODEL (FEM)

Wall Thickness FEM

Wall shape in the 2D model is chosen as a rectangle with depth of the wall is lower than length as this is the most generic situation for the machined parts manufactured. Constant wall length of 300mm is taken. Force is applied pointed outwards to the middle point of the upper side, as this location is structurally weakest location of the wall.

Mesh: 2D

Element Type: CQUAD

Element Size: 1mm

Force: 10N

Constraints: Left side, right side and bottom side are constrained with fixed constraints.

Material: Aluminum 2014 alloy is selected.

Finite element model for wall thickness determination can be seen in Figure 1.

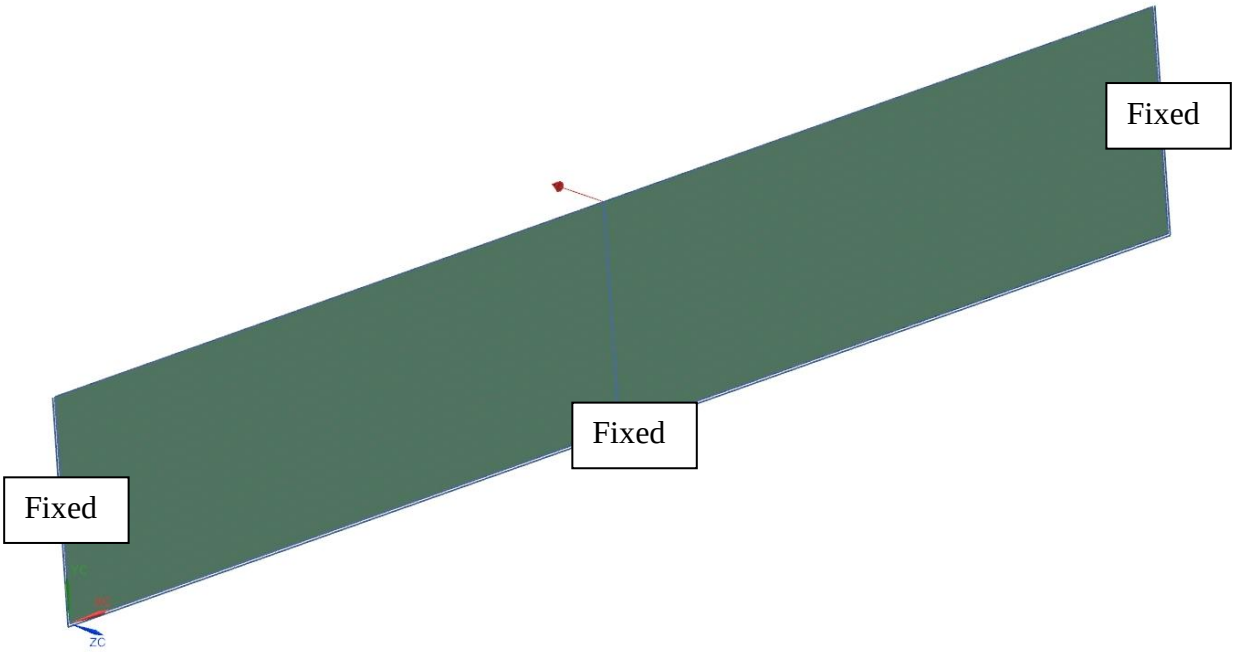


Figure 1. FEM for Wall Thickness Determination

Analysis Method

First analysis is made by applying an arbitrary force value of 10N to 50mm depth of the wall and 2mm wall thickness as this thickness is minimum manufacturable thickness by experience for the 50mm depth of the wall in the aluminum parts. Resulted displacement magnitude is 0,0786. Values of wall thicknesses iteratively tried to be obtained for same displacement magnitude and for different depths of the wall (75mm, 100mm, 125mm and 150). Results are listed in finite element analysis results section. Post view for wall displacement can be seen in Figure 2.

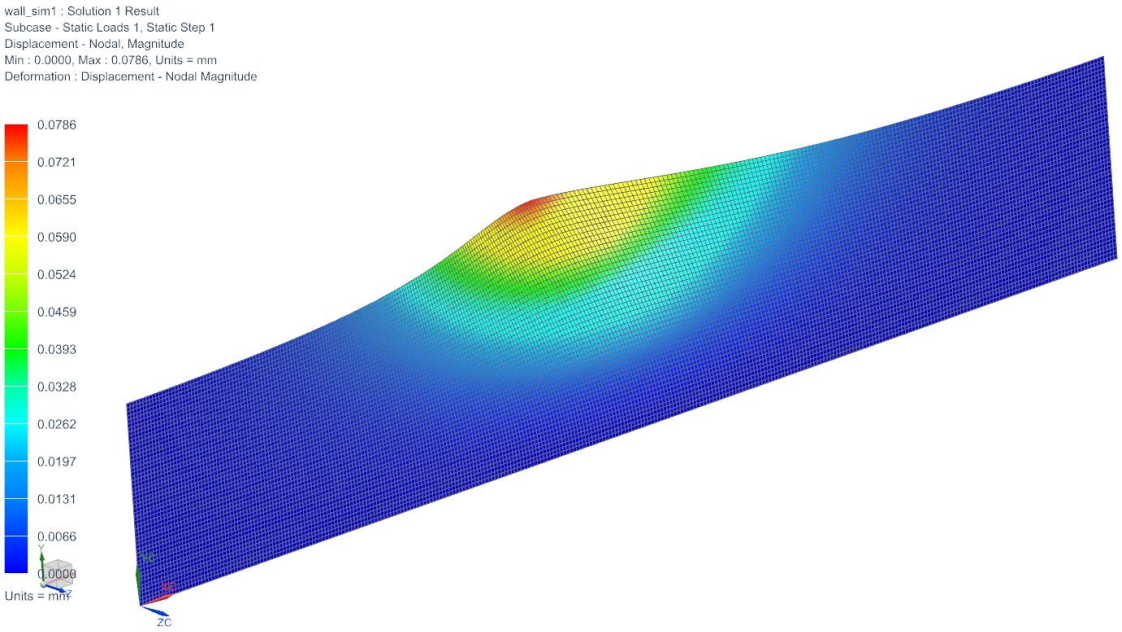


Figure 2. Post View for Wall Displacement

Floor Thickness FEM

Pocket shape in the 2D model is chosen as rectangular (square) as this is the most generic pocket shape that is manufactured in the industry. Triangular or circular pocket shapes are less common. The term pocket diameter is used for the diameter of the circle that fits the pocket and can be used as pocket width in the formula that shall be obtained. Force is applied to the middle point (intersection of the two diagonals) of the floor, as this location is the weakest location of the floor.

Mesh: 2D

Element Type: CQUAD

Element Size: 1mm

Force: 10N

Constraints: Left, right, top and bottom side are constrained with fixed constraints.

Material: Aluminum 2014 alloy is selected.

Finite element model for floor thickness determination can be seen in Figure 3.

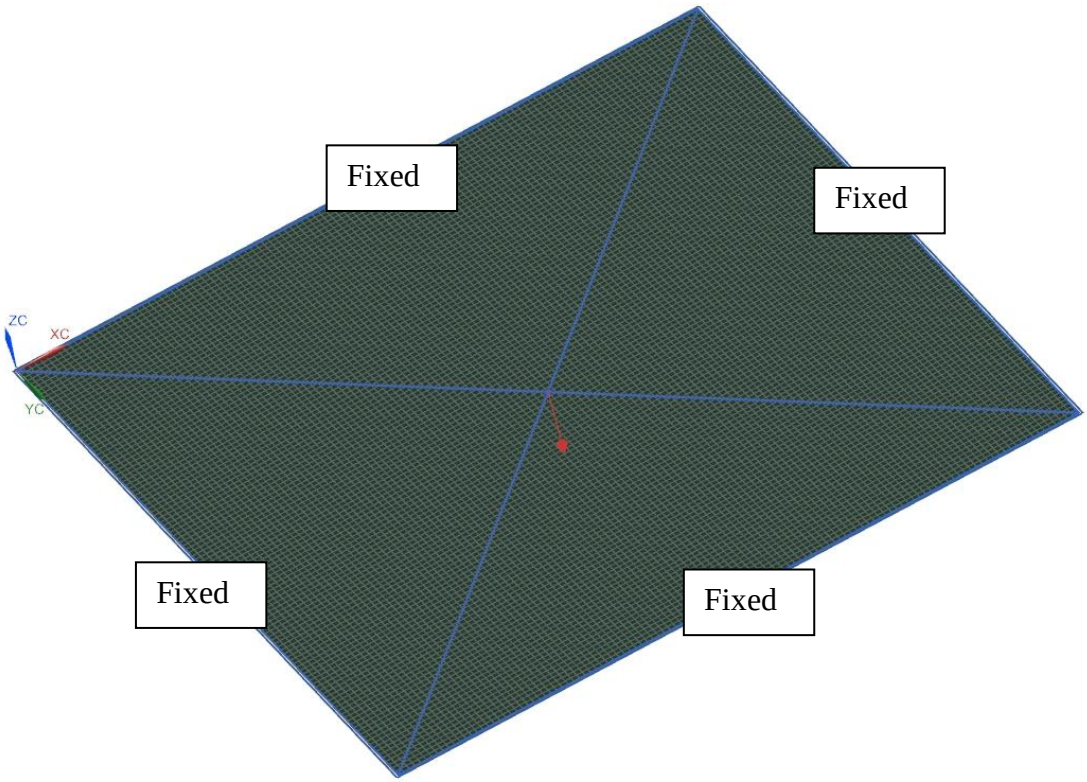


Figure 3. FEM for Floor Thickness Determination

Analysis Method

First analysis is made by applying an arbitrary force value of 10N to 120mm pocket length and 120 mm pocket width and a 2mm floor thickness as this thickness is minimum thickness by experience for the 120mm X 120mm pockets in aluminum parts. Resulted displacement magnitude is 0,015mm. Values of floor thicknesses iteratively tried to be obtained for same displacement magnitude and for different pocket widths (80mm, 160mm, 200mm and 240mm). Results are listed in finite element analysis results section. Post view for floor displacement can be seen in Figure 4.

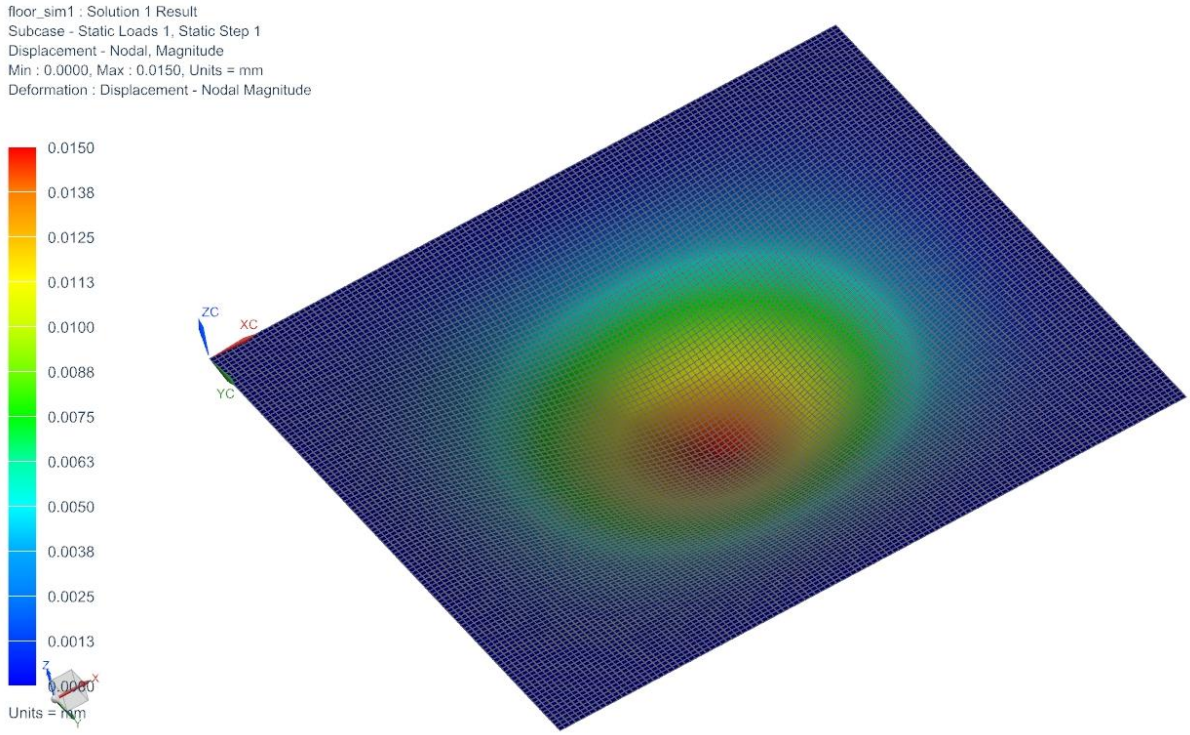


Figure 4. Post View for Floor Displacement

3. FINITE ELEMENT ANALYSIS RESULTS

Wall Thickness Results

For the same displacement, wall thickness results for various depth of the wall values can be seen in Table 1.

Table1. Wall Thickness Results for Various Depth of the Wall Values

DEPTH OF THE WALL(mm)	50	75	100	125	150
WALL THICKNESS(mm)	2	2,595	3,03	3,297	3,44

Related chart can be seen in Figure 5.

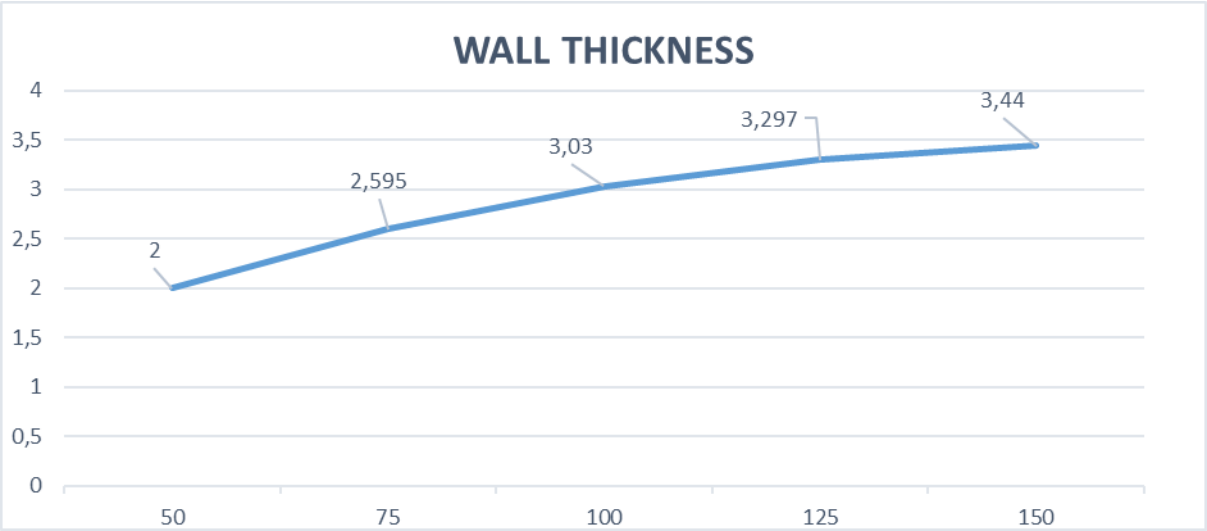


Figure 5. Wall Thickness vs. Depth of the Wall

From these results

$y = 0{,}0144x + 1{,}28$ (Equation 1)

linear formula can be generated where y is the Wall Thickness and x is the Depth of the Wall.

Floor Thickness Results

For the same displacement, floor thickness results for various pocket width values can be seen in Table 2.

Table2. Floor Thickness Results for Various Pocket Width Values

POCKET WIDTH(mm)	80	120	160	200	240
FLOOR THICKNESS(mm)	1,53	2	2,42	2,81	3,17

Related chart can be seen in Figure 6.

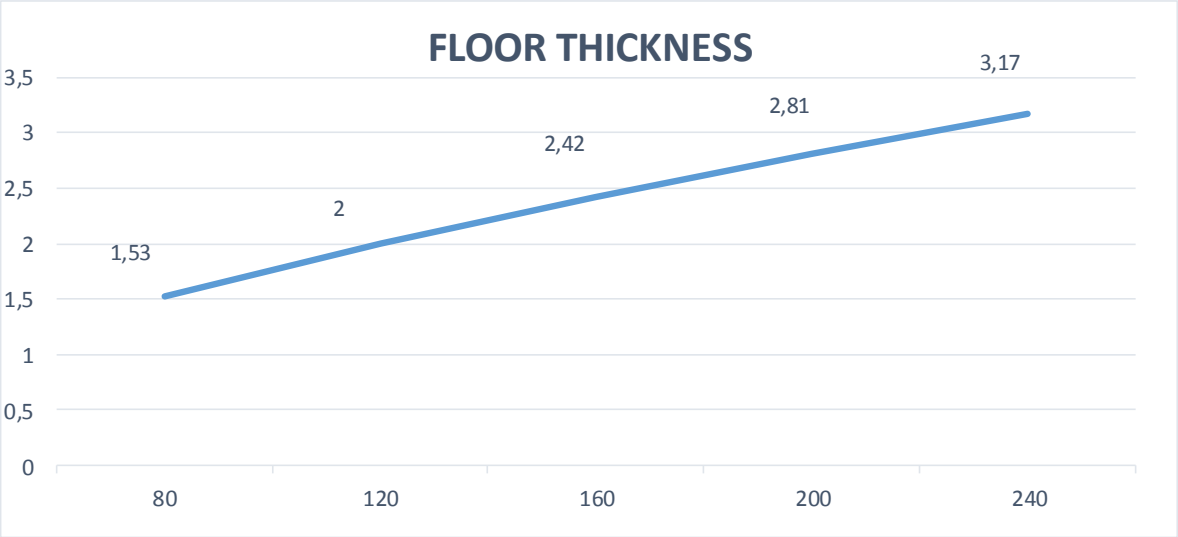


Figure 6. Floor Thickness vs. Pocket Width

From these results

y=0,01025x+0,71 (Equation 2)

linear formula can be generated where y is the Floor Thickness and x is the Pocket Width.

4. CONCLUSION

These basic analyses proves that FEA results can be used to generate basic formulas for design engineers. These results are in harmony with manufacturing experience and can guide the design. The results obtained here are not the final design values. They are important if the thicknesses in the finalized design analyzed for critical load cases are lower than these thicknesses. Then the design engineer should acknowledge that there can be possible problems in the manufacturing process and consult to manufacturing engineering. Manufacturing engineering can find special solutions to manufacture these machined part designs or issue a design change request.

REFERENCES

1. **TĂNASE, I., GHIONEA, A. and GHIONEA, I., (2010),** "Measurement and Analysis of Cutting Forces and Deformation at Milling Thin Parts", Proceedings in Manufacturing Systems, Vol. 5, No. 4, pp 243-248.

INVESTIGATING THE EFFECT OF MILLING PARAMETERS ON RESIDUAL STRESSES OF *Ti-6AL-4V*

Ramazan H. NAMLU, *ramazan.namlu@atilim.edu.tr* Atilim University, 06830, Ankara, Turkey

O. Deniz YILMAZ, okan.yilmaz@*atilim.edu.tr* Atilim University, 06830, Ankara, Turkey

Caner ŞİMŞİR, *caner.simsir@atilim.edu.tr* Atilim University, 06830, Ankara, Turkey

ABSTRACT

Titanium alloy *Ti-6Al-4V* is broadly used in aerospace industry, biomechanical applications and additive manufacturing because of its low density, excellent corrosion resistance, and high strength. Residual stress has a major effect on reliability and product life of the components on these areas. Machining of the titanium alloys results in change of the subsurface layer. This paper presents number of trials, changing the milling parameters on *Ti-6Al-4V* and their effect on the residual stresses. Experiments were done in different stages of cutting speed and feed rate. Residual stress measurement was done by X-Ray diffraction method. There is lack of study investigating the effect of milling parameters on residual stresses of *Ti-6Al-4V*. The result shows that the subsurface residual stresses can be adjustable by selection of milling parameters.

Keywords: Ti-6Al-4V; Milling; Residual Stress; X-Ray diffraction

2. INTRODUCTION

Because of its excellent corrosion resistance, high mechanical strength and low density profile *Ti-4Al-4V* is always a suitable material in aerospace industry, biomechanical applications and additive manufacturing. Blade integrated disk for engines of aircraft's is a good example. However, its desired properties like low thermal conductivity, low elastic modulus and serrated chip formation bring about low machinability [1]. This titanium based alloy can work under variable loads and this will lead to create stresses on surface and for airplane parts create distortion because of residual stress is compelling [2].

Its known that milling cause in residual stresses in the surface and sub-surface of the manufactured parts. Residual stresses may possible be compressive on the surface and appear to be tensile underneath the surface or vice versa. Compressive residual stresses may be improving the performance and life of the manufactured parts because of reducing the magnitude of tensile stresses on the surface where cracks initiate and disseminate in the meantime tensile residual stresses increase the service stresses and this may lead to premature and unpredictable failure of the parts [3]. The residual stresses due to milling may have destructive effects and magnitude of milling residual stresses highly depend on cutting parameters [4]. Thus, cutting parameters seem to have undeniable effects on residual stresses and they must be optimizing for controlling the surface residual stresses of manufactured parts.

There are number of previous studies on residual stress due to milling of *Ti-6Al4-V*, one study based on peripheral milling they found out that residual stresses can adjustable by optimizing the cutting parameters [5]. Another research is about complex ball end milling, its reported that subsurface residual stresses depended on process kinematics such as cutting edge radius and also the work piece geometry [6]. A comprehensive experimental study was done by Sun and Guo for end milling of *Ti-6Al-4V*, they reported that compressive residual stresses increase with cutting speed until a certain speed and compressive residual stresses also decrease with feed in general, residual shear stress magnitudes was much smaller than the magnitudes of residual normal stress also reported but their most interesting finding was residual stresses showed that nonlinear coupling at some manners [7]. Also, there are different kind of materials studied on this area such as medium carbon steel and its reported that with the increasing of the machined surface inclination angle the residual stress turned out more tensile [8]. Another material which studied on residual stresses due to milling is Inconel 718 which has similar mechanical properties like *Ti-6Al-4V*, this study based on milling with the conventional flood application and MQL used application comparison, they found out that flood conditions shows better results for residual stresses [9].

There is lack of studies on milling cutting parameters effects on the residual stresses of *Ti-6Al-4V* Grade 5. Attention must be paid on about the cutting parameters because its directly related to the physical conditions of the components. In this paper experimental investigation effects of cutting speed and feed rate on residual stress in milling of *Ti-6Al-4V* was done and at last residual stress results were evaluated and compared for the changing the parameters.

3. METHOD

The work material is *Ti-6Al-4V* alloy, detail chemical composition listed in Table 1. A series of end milling tests were performed on CNC milling center. Prepared samples were 20*20*5 mm^3 size and it is shown with the cutting conditions in Fig. 1a. The 50 mm diameter cutting tool is a

5-Flute solid carbide mill with carbide coating. Milling operations were carried out with water-soluble cutting fluid. Four levels of cutting speed and feed were selected. The detail milling conditions are listed in Table 2.

Table 1. Chemical Composition of *Ti-6Al-4V*

Component	**Wt.%**
Al	6
Fe	Max 0.25
O	Max 0.2
Ti	90
V	4

Table 2. Milling Conditions

Experiment No.	Cutting Speed V [m/min]	Feed f [mm/tooth]	Depth of Cut a_e [mm]	Depth of Cut r_e [mm]
1	50	0.06	2	10
2	60	0.06	2	10
3	70	0.06	2	10
4	80	0.06	2	10
5	50	0.04	2	10
6	50	0.05	2	10
7	50	0.06	2	10
8	50	0.07	2	10

Although some studies reported that direct measurement methods are applicable for the determination of residual stresses on large grained materials, X-Ray diffraction method still the most common method for measurement of residual stresses of *Ti-6Al-4V* [10]. Residual stress measurements were done by X-Ray Diffraction (XRD) with Doelle-Hauk method. The residual stress measurement parameters are listed in Table 3.

Table 3. Residual Stress Measurement Parameters

Measurement Method	**Doelle-Hauk**
Radiation	Cu Kα
Spot Size [mm]	3

Voltage [kV]	45
Amperage [mA]	45
φ (˚)	0,45,90
2θ (˚)	141.7

In XRD method with assuming a linear elastic distortion of the crystal lattice, strain in the crystal lattice is measured and stress producing the strain is calculated. Chancing of lattice spacing d results in a change in the diffraction peak position. The stress is normal to the surface σ_{33} will cause curvature in *d* vs $\sin^2 \varphi$ plots that can be seen in several experimental studies. However, shear stresses σ_{13} and σ_{23} produce different curves for negative and positive φ tilts. Doelle and Hauk have extended study classical stress analysis theory to include triaxial stress state to increase measurement efficiency. Doelle-Hauk method uses the average strain for negative and positive φ spacing vs $\sin^2 \varphi$ at θ equal to 0°, 45° and 90° to calculate σ_{11}, σ_{22}, σ_{12} and σ_{33}. The stress σ_{13} and σ_{23} are calculated from strain difference for positive and negative φ spacing vs $\sin^2 \varphi$ [11].

4. RESULTS AND DISCUSSION

Plane stresses were measured on the surfaces of the work material. There were only residual normal stress σ_{11} and σ_{22}, and shear stress σ_{12} found. The other stresses were very close to zero with uncertainties. Results are given at Table 4 and uncertainties (+/-) based on UNI EN 15305 non-destructive testing - test method for residual stress analysis by x-ray diffraction are given at Table 5.

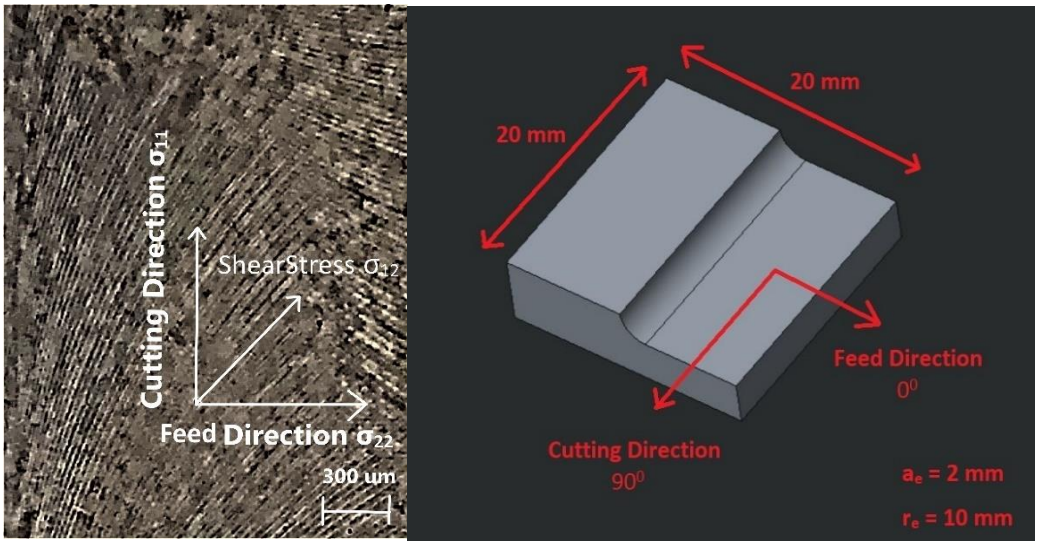
Table 4. Experimental results of the residual stress measurement

Number of experiments	σ_{11} [MPa]	σ_{12} [MPa]	σ_{22} [MPa]
1	-459.4	-59.6	-299.8
2	-439.6	-0.3	-263.2
3	-443.3	-52.0	-314.4
4	-437.2	-49.4	-437.2
5	-377.5	-22.4	-277.4
6	-441.3	-13.6	-351.2
7	-465.1	-12.9	-355.1
8	-541.7	-46.6	-418.7

Table 5. Uncertainties based on UNI EN 15305

Number of experiments	σ_{11} [MPa]	σ_{12} [MPa]	σ_{22} [MPa]
1	23,50	20,4	23,5
2	24,5	21,3	24,5
3	21,7	18,9	21,7
4	19,4	16,8	19,4
5	21,3	18,5	21,3
6	24,5	21,3	24,5
7	19,3	46,8	19,3
8	20,7	18	20,7

The effect of cutting speed on surface residual stresses is shown in Fig. 2 and Fig 3. In feed direction compressive residual normal stress σ_{11} generally decrease with the cutting speed between range of around 30 MPa and it is maximum at 50 m/min with -459.4 MPa. In cutting direction residual normal stress σ_{22} generally increase and magnitude of it is greater than decreasing of σ_{11} and its up to 130 MPa at higher speeds. The shear residual stress σ_{12} is varying between 0 to -60 MPa with different stage of cutting speed and compare those residual normal stresses magnitude of shear residual stress is much smaller.



(a) (b)

Fig. 1. Schematic of samples with dimensions (a) and Residual stress directions (b)

The results show that there is residual stress variation between different stage of the cutting speeds. The main reason for this is mechanical and thermal deformation. Due to the

mechanical deformation at cutting operation it produces compressive residual stresses and magnitude of residual stresses at different cutting stages are more prominent at higher cutting speeds. According σ_{11} and σ_{12} the most significant magnitude difference is observed in σ_{22}, and based on this difference, we can say that as the cutting speed increases, the compressive residual stresses also increase.

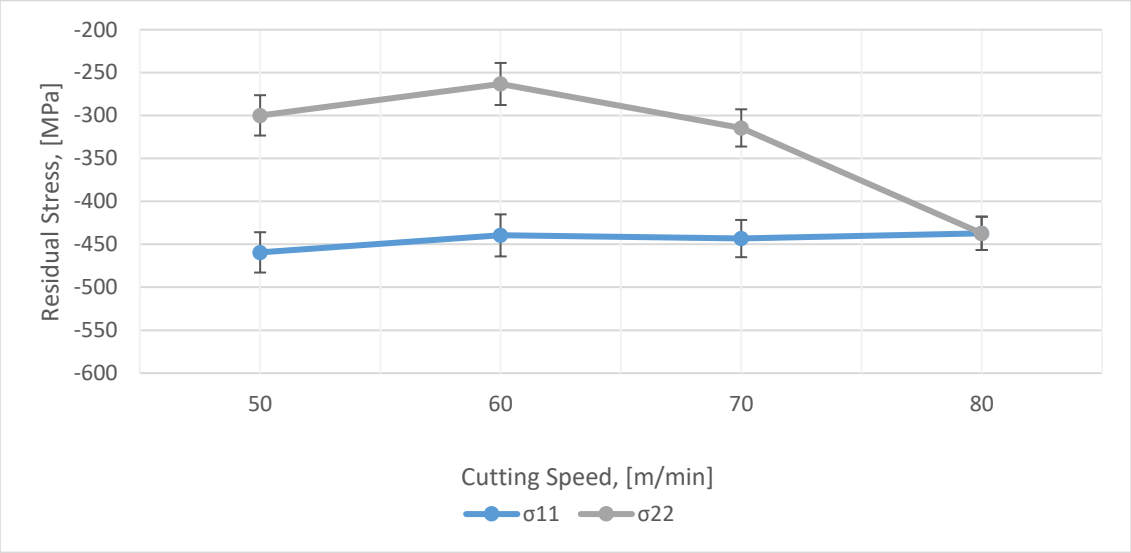


Fig 2. The influence of cutting speed parameter on the surface normal residual stress (f: 0.06 [mm/tooth], a_e: 3 [mm]: r_e: 10 [mm])

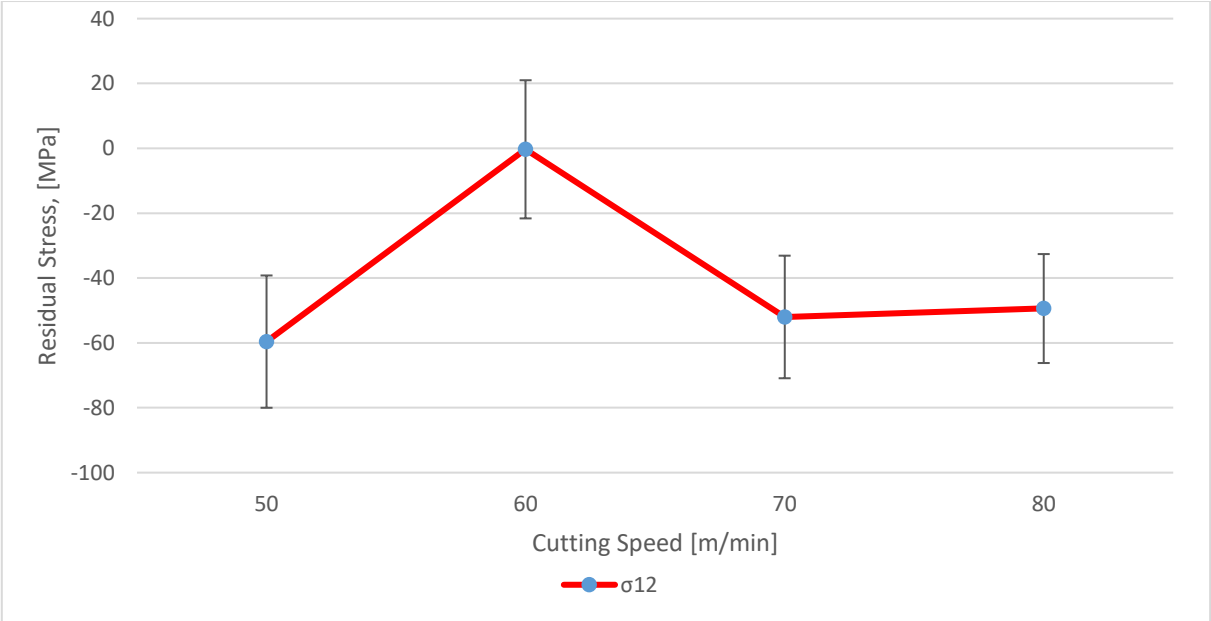


Fig 3. The influence of cutting speed parameter on the shear residual stress (f: 0.06 [mm/tooth], a_e: 3 [mm]: r_e: 10 [mm])

As shown in Fig. 4. compressive residual normal stress generally increases with the feed. Residual normal stresses σ_{11} and σ_{22} have a parallel increase in every stage of the feed and

this increasing is up to 150 MPa. σ_{12} is also join this increasing trend but with smaller magnitude.

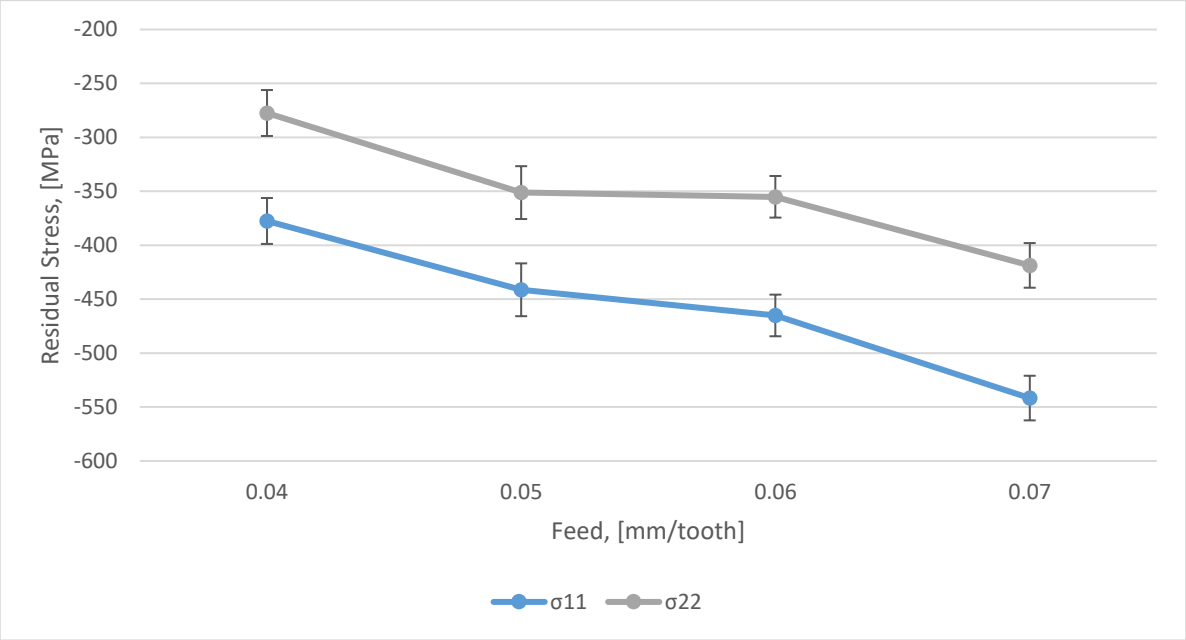


Fig 4. The influence of feed parameter on the surface residual stress (V: 60 [m/min], a_e: 3 mm: r_e: 10 [mm])

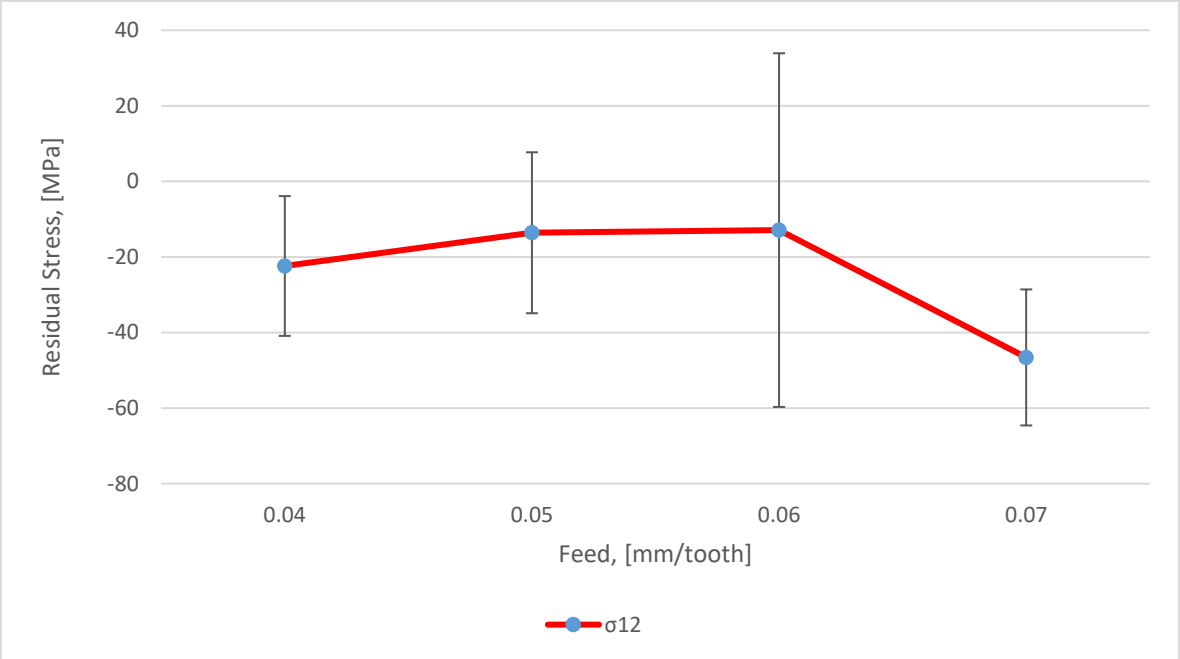


Fig 5. The influence of feed parameter on the shear residual stress (V: 60 [m/min], a_e: 3 [mm]: r_e: 10 [mm])

The unexpected variations of the residual stress between different stage of cutting speed and feed rate depend on the non-uniform surface deformation as shown in Fig 1b. Surface deformations are dissimilar at different locations. Measured residual stress values are average residual stresses of the measured area therefore with every non-uniformity of the surface change the value of the measured residual stress. Besides the spot of the XRD covers certain locations at different angles and it creates uncertainties of calculation the average residual stresses. Furthermore, numerous error sources like human factor at milling operation, repeatability of the measurement were cause to unexpected variations.

5. CONCLUSIONS

In the research paper here, the end milling of *Ti-6Al-4V* with different cutting speeds and feed rates was investigated influence on surface residual stresses. The main conclusions may be summarized as follows:

- The normal residual stresses σ_{11} and σ_{22} were affected by the cutting speed parameter more than the shear residual stress σ_{12}.
- Cutting speed has no significant effect on the feed direction residual normal stress σ_{11} and the shear residual stress σ_{12} but increases the cutting direction residual normal stress σ_{22} up to 66%.
- Feed rate increases residual normal stresses σ_{11} and σ_{22} up to 43% and 50% respectively. Besides, the shear residual stress σ_{12} increase but magnitude of this increasing has no significant effect.

6. ACKNOWLEDGEMENTS

The authors would like to thank Atılım University Metal Forming Center of Excellence for preparing the samples and measurement of the residual stresses.

REFERENCES

1. **McQuillan, A.D. and McQuillan, M.K., (1956),** “Titanium, no. 4 in Metallurgy of the rarer metals”, Butterworths, London.

2. **Dege, J. H., (2012),** “High performance machining of large titanium structural parts, in: New manufacturing technologies in aerospace industry”, Hannover

3. **El-Axir M.H. (2002),** “A method of modelling residual stress distribution in turning for different materials”, International Journal of Machine Tools & Manufacture, 42:1055-1063.

4. **El-Khabeery, M.M. and Fattough, M., (1989),** “Residual stress distribution caused by milling” International Journal of Machine Tools & Manufacture, 29, Pp (391-401)

5. **Krajewska-Śpiewak, J. and Gawlik, J. and Piekoszewski, W. and Stachura, K., (2018)** “Identification of residual stresses in a surface layer of Ti6AL4V and Inconel 718 after process of peripheral milling”, Tehnicki Vjesnik, 25(1):88-91

6. **Nespor D. and Denkena B. and Grove T. and Böß V., (2015),** “Differences and similarities between the induced residual stresses after ball end milling and orthogonal cutting of Ti–6Al–4V”, Journal of Materials Processing Technology Volume 226, Pp (15-24)

7. **J.Sun,Y.B. and Guo A., (2009),** “Comprehensive experimental study on surface integrity by end milling Ti-6Al-4V”, Journal of Materials Processing Technology, 209, Pp (4036-4042)

8. **Masmiati N. and Sarhan A.D., (2015),** “Optimizing cutting parameters in inclined end milling for minimum surface residual stress Taguchi approach”, Measurement, 60, Pp (267-275)

9. **Paula Oliveira G. and Fonseca M. C. and Araujo A. C., (2017),** “Analysis of residual stress and cutting force in end milling of Inconel 718 using conventional flood cooling and minimum quantity lubrication”, Internatıonal Journal of Advanced Manufacturing Technologies, 92, Pp (3265-3272)

10. **Grove T. and Köhler J. and Denkena B., (2014),** “Residual Stresses in Milled β-Annealed Ti4Al4V”, 2nd CIRP Conference on Surface Integrity (CSI), Procedia CIRP, 13, Pp (320-326)

11. **Dölle, H. and Hauk, V., (1979),** Härterei-Techn. Mitt. , 34, 272.

DAMAGE IDENTIFICATION IN A CANTILEVER BEAM USING MODAL STRAIN ENERGY

Allan C. DOMINGUES, *allancdomingues@gmail.com* Campus UnB Gama, University of Brasília, 72445-010, Distrito Federal, Brazil.

Tharcísio C. SANTOS, *tharcisio.castro@gmail.com* Campus UnB Gama, University of Brasília, 72445-010, Distrito Federal, Brazil.

Carla T. M. ANFLOR, *anflorgoulart@gmail.com* Campus UnB Gama, University of Brasília, 72445-010, Distrito Federal, Brazil.

Sergio H. S. CARNEIRO, *shscarneiro@gmail.com* Campus UnB Gama, University of Brasília, 72445-010, Distrito Federal, Brazil.

ABSTRACT

This paper aims to analyze the modal strain energy method for damage identification. It is a non-destructive method that compares the deformation energy of a structure with and without damage through its modal characteristics. For this, a beam model was elaborated using the finite element method with and without damage and its deformation energy was numerically analyzed using MATLAB.

Keywords: Modal Strain Energy Method, Damage Identification, Finite Element Method

1. INTRODUCTION

A good method for identifying damage should be able to detect, locate and estimate the severity of damage. There are several methods and algorithms to identify the presence of structural damage. Generally, this identification is composed of three phases: the detection of the existence of the damage; the determination of the place where this damage is in the structure; and finally its quantification (Hu*, et. al.* 2001).

The modal strain energy is a non-destructive method for damage identification that uses modal parameters to detect, locate and quantify damage. The modal analysis is a method for obtaining the dynamic characteristics of a structure such as natural frequencies and natural modes of vibration. These quantities are related to the stiffness and mass of a structure. It's

also important to highlight that when a structure has a presence of damage the stiffness changes. For this reason, methods based on modal analysis have been used to identify damage, once the presence of any defect over the structure disturbs significantly the modal characteristics. (Pereyra, et al., 1999).

Another method that has been widely used in engineering to study the identification of damage in structures is the Modal strain energy method (Pereyra, *et. al.*1999, Otieno, *et. al.*, 2000, Trendafilo, *et. al.*, 2008, Yu, *et. al.* 2007). This method consists of analyzing the strain energy variation when a structure has damage based on the variation of modal characteristics of the structure. In this work the efforts will be devoted on implementing the method.

2. THEORETICAL FORMULATION

The strain energy can be described as a function of the stiffness matrix of the element and the vibration mode vector of this element.

$$U_{ik} = \frac{1}{2}[\Phi_{ik}]^T[K_i][\Phi_{ik}] \tag{1}$$

Where Φ_{ik} represents the k-mode vector of element i and K_i is the stiffness matrix of element i. When applied to a beam the strain energy can be simplified for an analysis in one dimension, as introduced by equation (2).

$$U_{ik} = \frac{1}{2}\int_{x_i}^{x_i+\Delta x_i} EI_i\left(\frac{d^2\Phi_k(x)}{dx^2}\right)^2 dx \tag{2}$$

The limits of the integration will be the coordinates of each element of the subdivision of the beam. Moreover, the modes can be calculated based on the model of Euler Bernoulli equation (3).

$$\Phi_k(x) = \left(\cosh\frac{\beta_k Lx}{L} - \cos\frac{\beta_k Lx}{L}\right) - \sigma_k\left(\sinh\frac{\beta_k Lx}{L} - \sin\frac{\beta_k Lx}{L}\right) \tag{3}$$

Where β_k and σ_k are given for the bending mode k of the beam according to the Euler-Bernoulli model for different contour types to which it will be subordinate (Robert, *et. al*.1980). For a better location of the damage region, the damage index method is applied. This method applies a ratio between the deformation energy of the beam with damage and no damage equation (4).

$$B_{ik} = \frac{(\bar{U}_{ik} + \bar{U}_k)U_k}{(U_{ik} + U_k)\bar{U}_k} \tag{4}$$

Where U_k and U_{ik} are the undamaged deformation energy of the beam and the element i of the beam respectively for the k mode. $\overline{U}_k$ and $\overline{U}_{ik}$ are the deformation energy with damage of the beam and the element i of the beam respectively for the k mode. According to Stubbs (1995) the normalization of B_{ik} is proposed as,

$$Z_{ik} = \frac{B_{ik} - \mu_{B_k}}{\sigma_{B_k}} \tag{5}$$

The energy of each element will be given by the sum of the energies that each mode generates.

$$Z_i = \frac{\sum_{k=1}^{m} Z_{ik}}{m} \tag{6}$$

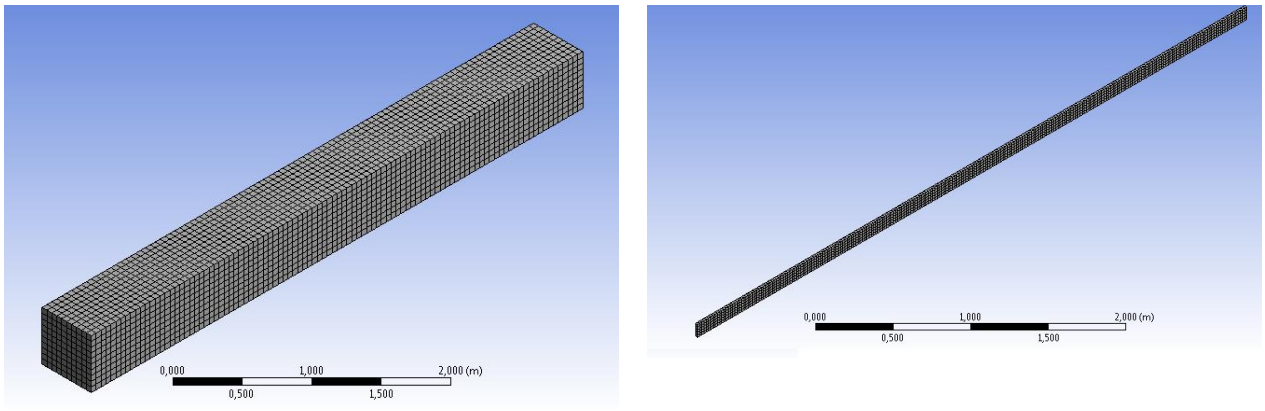
where Z_i is the normalized energy of element i and m is the number of modes being used to calculate the strain energy.

3. METHODOLOGY

In order to implement and verify the damage identification method using strain energy, a 3D model of beams clamped-free was elaborated using the finite element method (FEM). The material used in the models was Steel with Young's Module of 200GPa, Poisson coefficient of 0.3 and density of 7850kg/m^3. Five Beam models with different length, height and width were investigate and the geometric parameters are presented in Table 1. All modal analysis were performed using the ANSYS software.

Table 1. Beam models with different dimensions.

Beam Model	**1**	**2**	**3**	**4**	**5**
Cross section height (h) [m]	0.5	0.1	1.5	0.3	0.4
Cross section thickness[m]	0.5	0.02	1.5	0.3	0.4
Length (L) [m]	5	5	15	5	5
Ratio L/h	10	50	10	16.67	12.5



(a) (b)

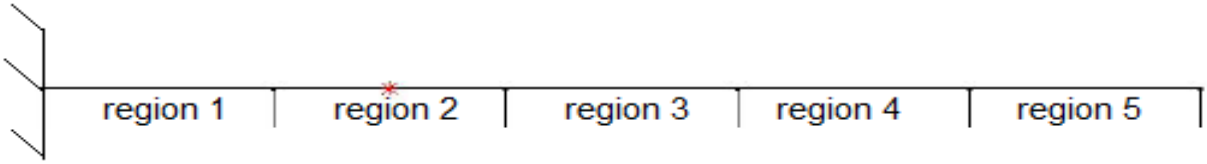
Figure 1. Beam model (a) 1, 3, 4, 5 and (b) 2

The first step was to obtain the modal characteristics of each model without damage and compare with the values of the Euler-Bernoulli modes. The next step consists in analyzing these characteristics with circular damage on the surface with the dimensions and location, considering clamped side as reference, presented in Table 2.

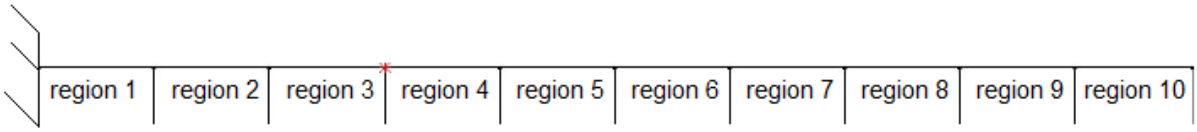
Table 2. Dimensions of damage on each beam model

Beam Model	**1**	**2**	**3**	**4**	**5**
Cross-sectional area (A_s) [m^2]	0.25	0.002	2.25	0.09	0.16
Damage area (A_d) [m^2]	$1.96e^{-3}$	$1.57e^{-5}$	$1.77e^{-2}$	$7.07e^{-4}$	$1.26e^{-3}$
A_d/A_s	$7{,}85e^{-3}$	$7{,}85e^{-3}$	$7.85e^{-3}$	$7.85e^{-3}$	$7.85e^{-3}$
Damage radius [m]	0.025	0.0022	0.075	0.015	0.02
Damage location [m]	1.5	1.5	4.5	1.5	1.5

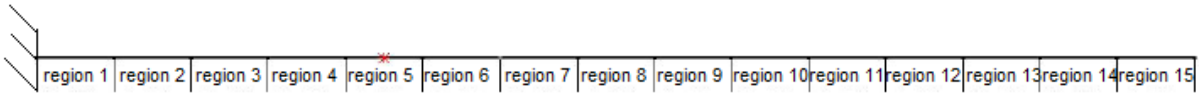
Only bending natural frequencies and mode shapes were considered. Once the bending natural frequencies and modal shapes were calculated via FEM, a routine was written in order to analyze the results and apply the strain energy to identify the location of the damage. Figure 2 introduces the sub regions employed for the beam models investigated and points out in which element the damage was artificially imposed. The analysis consisted in dividing the models into several regions that were numbered from the clamped. The beams were divided into 5, 10 and 15 regions in order to determine the accuracy of the method. When divided into 5 regions the damage will be in region 2, when divided into 10 regions the damage will be between region 3 and 4 and when divided into 15 regions the damage will be in region 5.



(a)

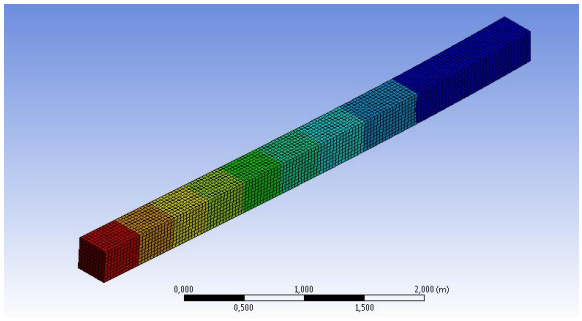


(b)

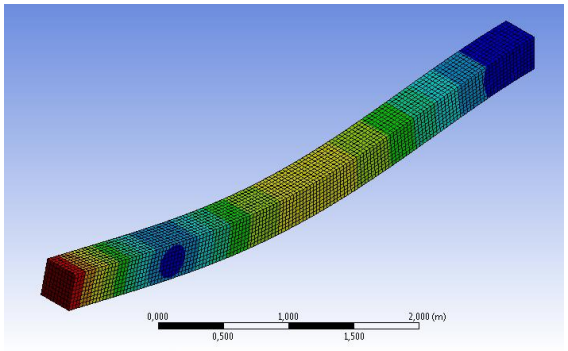


(c)

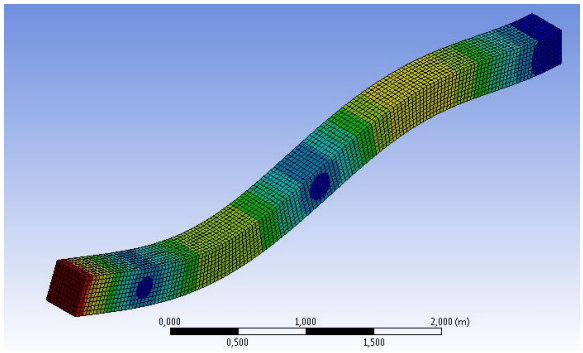
Figure 2. Position of damage considering the sub regions: (a) 5 regions (b) 10 regions (c) 15 regions



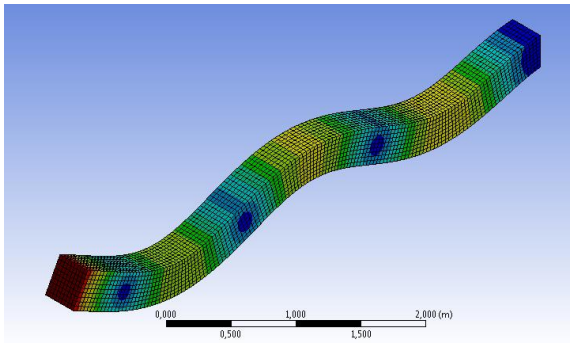
(a)



(b)



(c)



(d)

Figure 3. Bending modes shape of cantilever beam models using FEM: (a) 1th mode shape (b) 2th mode shape (c) 3th mode shape (d) 4th mode shape

4. RESULTS AND DISCUSSION

For the present analysis, only the first four bending modes were considered. These modes values are close to those obtained by Euler-Bernoulli theory, allowing applying equation (3) to the beam modes.

Table 3. Natural frequencies for beam model 1

Bending frequencies	**1th**	**2th**	**3th**	**4th**
Analytical [Hz]	16.308	102.198	286.157	560.753
Numerical No Damage [Hz]	16.991	101.640	266.790	483.020
Dif. Analytical x Numeric %	+4.2	-0.5	-6.8	-13.8

Table 4. Natural frequencies for beam model 2

Bending frequencies	**1th**	**2th**	**3th**	**4th**
Analytical [Hz]	3.262	20.440	57.232	112.151
Numeric No Damage [Hz]	3.419	21.387	59.693	116.440
Dif. Analytical x Num %	+4.8	+4.6	+4.3	+3.8

Table 5. Natural frequencies for beam model 3

Bending frequencies	**1th**	**2th**	**3th**	**4th**
Analytical [Hz]	5.400	34.100	95.400	186.900
Numeric No Damage [Hz]	5.664	33.879	88.929	161.010
Dif. Analytical x Num %	+4.9	-0.7	-6.7	-13.8

Table 6. Natural frequencies for beam model 4

Bending frequencies	**1th**	**2th**	**3th**	**4th**
Analytical [Hz]	9.800	61.300	171.700	336.500
Numeric No Damage [Hz]	10.240	63.062	171.950	325.120
Dif. Analytical x Num %	+4.5	+2.9	+0.1	-3.4

Table 7. Natural frequencies for beam model 5

Bending frequencies	1th	2th	3th	4th
Analytical [Hz]	13.000	81.800	228.900	448.600
Numeric No Damage [Hz]	13.628	82.836	221.870	410.630
Dif. Analytical x Num %	+4.8	+1.3	-3.1	-8.4

After validating the finite element models based on the Euler-Bernoulli frequency values, the same structure was simulated by applying the damage. Both the undamaged model and the damage model were discretized with more than ten thousand finite elements, which ensure a good convergence in the values of the natural frequencies.

Table 8. Variation of the natural frequencies of model 1 after inserting the damage

Bending frequencies	1th	2th	3th	4th
Numerical No Damage [Hz]	16.991	101.64	266.79	483.02
Numerical with Damage [Hz]	16.965	101.63	266.60	482.86

Table 9. Variation of the natural frequencies of model 2 after inserting the damage

Bending frequencies	1th	2th	3th	4th
Numerical No Damage [Hz]	3.419	21.387	59.693	116.44
Numerical with Damage [Hz]	3.418	21.387	59.682	116.43

Table 10. Variation of the natural frequencies of model 3 after inserting the damage

Bending frequencies	1th	2th	3th	4th
Numerical No Damage [Hz]	5.664	33.879	88.929	161.01
Numerical with Damage [Hz]	5.655	33.876	88.867	160.95

Table 11. Variation of the natural frequencies of model 4 after inserting the damage

Bending frequencies	1th	2th	3th	4th
Numerical No Damage [Hz]	10.240	63.062	171.95	325.12
Numerical with Damage [Hz]	10.231	63.061	171.86	325.05

Table 12. Variation of the natural frequencies of model 5 after inserting the damage

Bending frequencies	**1th**	**2th**	**3th**	**4th**
Numerical No Damage [Hz]	13.628	82.836	221.87	410.63
Numerical with Damage [Hz]	13.611	82.831	221.73	410.51

When inserting the damage, it was possible to observe a variation of the natural frequencies. The damage in each beam model was generated in such way that when the domain was subdivided damaged region presented greater energy variation. After some analyses it was possible to verify that all models presented similar results (Figures 4-8).

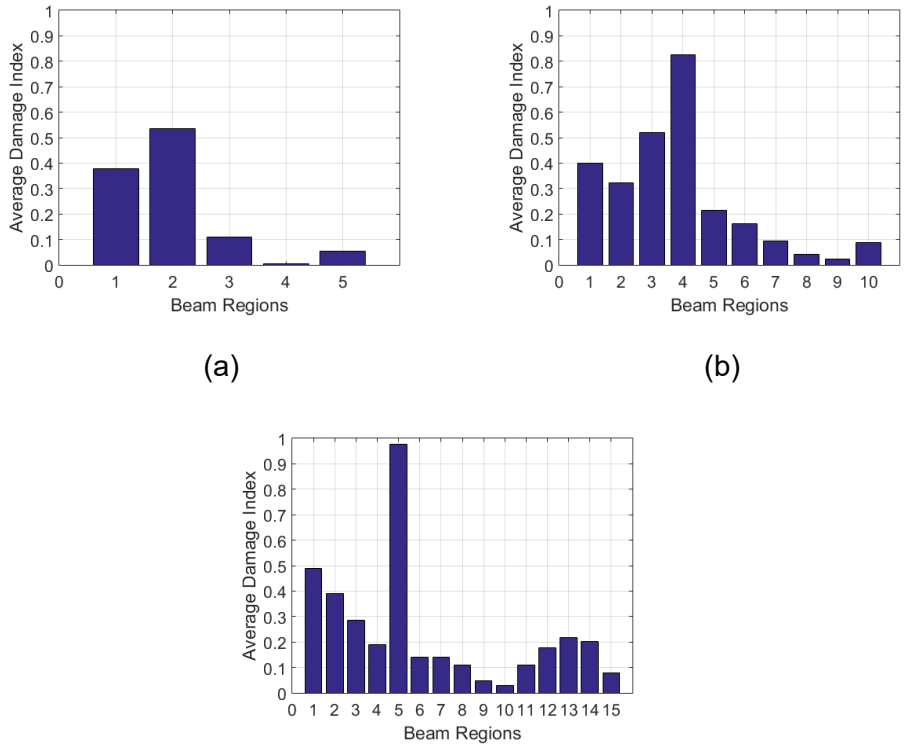


Figure 4. Average Damage Index for Beam model 1 with (a) 5 regions (b) 10 regions (c) 15 regions

In Figure 4 it is possible to identify the damage in regions where average damage index values are greater than 0.5. In the square section models, models 1, 3, 4 and 5, the results for all divisions were similar (Figures 4, 6, 7 and 8). Model 2 presented results different from the others, but it was also possible to identify regions where there was damage (figure 5).

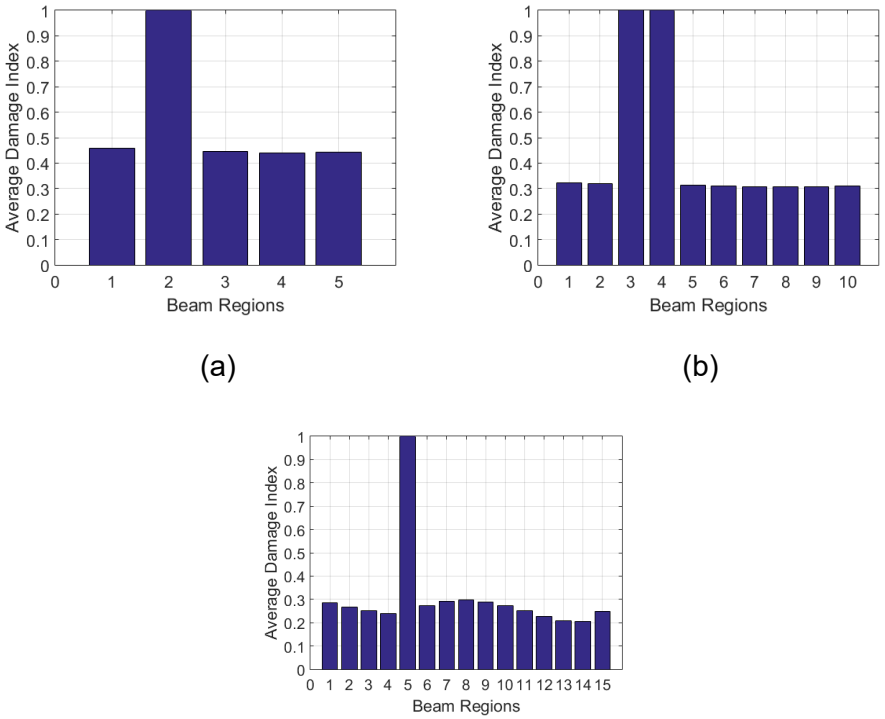


Figure 5. Average Damage Index for Beam model 2 with (a) 5 regions (b) 10 regions (c) 15 regions

This difference can be explained due to the fact that this model presents a different geometry from the others. While the other models had a square section and L / h ratio below 20, this model 2 has a rectangular section and L / h ratio of 50. The geometry imposed to model 2 approximates the present model to the Euler-Bernoulli model. This can be evinced by consulting the frequencies presented in table 4, whose differences between the numerical model and the analytical model were below 5%.

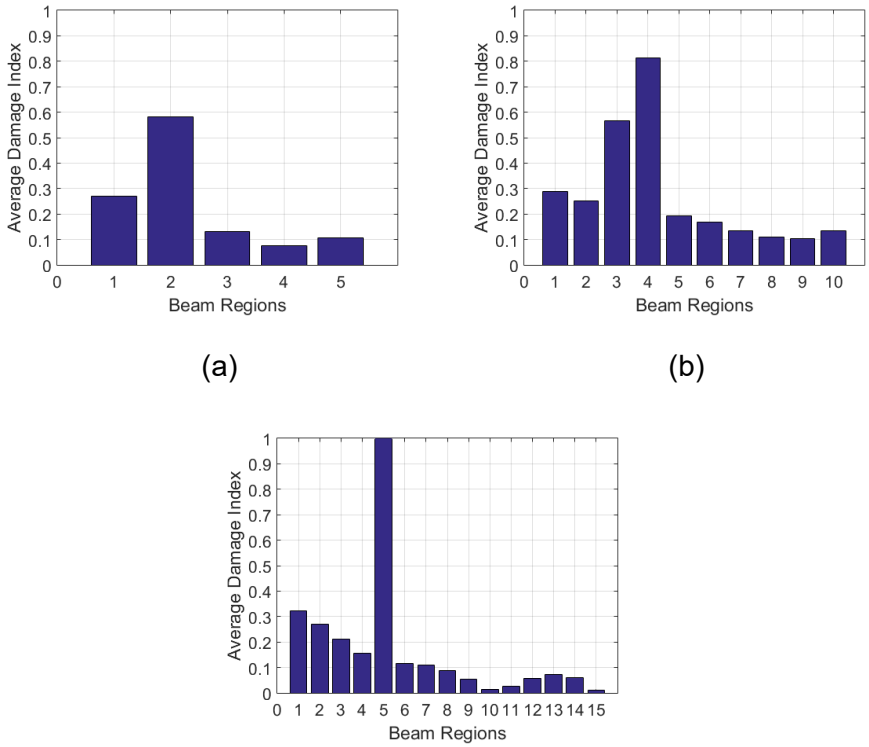
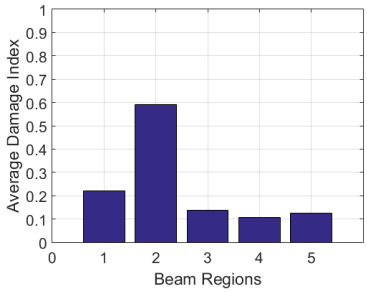
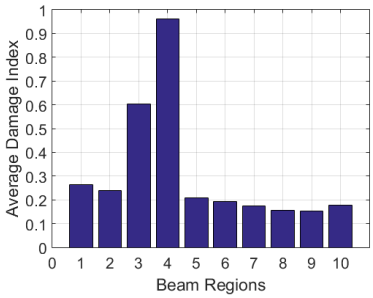


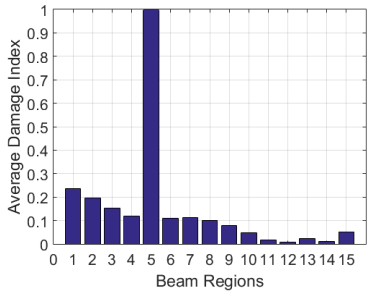
Figure 6. Average Damage Index for Beam model 3 with (a) 5 regions (b) 10 regions (c) 15 regions



(a)

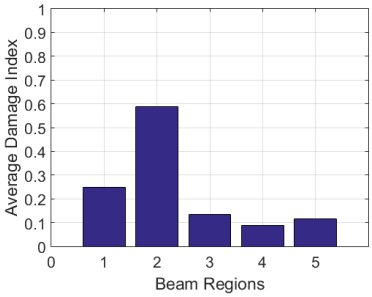


(b)

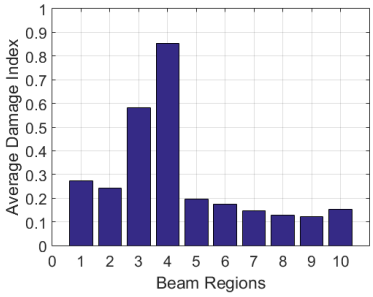


(c)

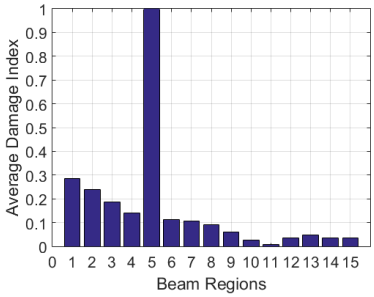
Figure 7. Average Damage Index for Beam model 4 with (a) 5 regions (b) 10 regions (c) 15 regions



(a)



(b)



(c)

Figure 8. Average Damage Index for Beam model 5 with (a) 5 regions (b) 10 regions (c) 15 regions

5. CONCLUSION

Although the method has shown the ability to identify the damage and locate it, the presented results are still preliminary. The present methodology must be improved in order to avoid the sensitivity of the model when increasing the number of modes as input. When increasing the number of normal modes, the proposed methodology fails in detecting the exact position of the damage. Furthermore, the methodology is able to detect damages that cause a great variation in the stiffness of the structure. Small damages are not identified and located by this method. Further investigations are in progress in order to improve the routine and review the formulation to overcome these issues regarding to the damage detecting.

ACKNOWLEDGEMENT

The authors would like to thank CAPES, CNPq - Brazilian Council for Research and Development - for the fellowships and FAPDF – Research Support Foundation of Brasília - for the research funding.

REFERENCES

1. **Pereyra, L. R., Osegueda, R. A., Carrasco, C., Ferregut, C. (1999). "**Damage Detection in a Stiffened-Plate Using Modal Strain Energy Differences" Conference on Nondestructive Evaluation of Aging Aircraft, Airports, and Aerospace Hardware II. Newport Beach, California

2. **N Hu, X Wang, H Fukunaga, ZH Yao, HX Zhang, e ZS Wu (2001)**. "Damage assessment of structures using modal test data". International Journal of solids and structures, 38(18):3111–3126.

3. **Otieno, A. W., Liu, P., Rao, V. S., Koval, L. R.(2000)**. "Damage Detection using Modal Strain Energy and Laser Vibrometer Measurements" Smart Structures and Materials 2000: Smart Structures and Integrated Systems, Norman M. Wereley, Editor, Proceedings of SPIE Vol. 3985.

4**. Yu, L., Cheng, L., Yam, L.H., Yan, Y.J., Jiang, J.S**. **(2007)**. "Experimental validation of vibration-based damage detection for static laminated composite shells partially filled with fluid". Composite Structures 79. 288–299.

5**. Trendafilova, Cartmell, M. P., Ostachowicz, W. (2008)**. "Vibration-based damage detection in an aircraft wing scaled model using principal component analysis and pattern recognition". Journal of Sound and Vibration 313. 560–566.

6**. Robert D Blevins**, **R Plunkett. (1980)**. "Formulas for natural frequency and mode shape."

7. **Stubbs, N. Kim, J. T.,(1995)** “Damage Detection in Offshore Jacket Structures from Limited Modal Information”. International Journal of Offshore and Polar Engineering 5. 58-66.

PERFORMANCE EVALUATION OF MICRO-TEXTURED CUTTING TOOLS IN DRY MACHINING OF INCONEL 718 USING FE SIMULATION

Eren KAYA, *erenkaya@anadolu.edu.tr* (1) Anadolu University, (2) Eskişehir Technical University, 26255, Eskişehir, Turkey

İrfan KAYA, *irfan_kaya@anadolu.edu.tr* (1) Anadolu University, (2) Eskişehir Technical University, 26255, Eskişehir, Turkey

ABSTRACT

This paper presents 2D FE simulation results of dry machining of Inconel 718 using micro-grooved cutting tools. FE model is validated by comparing the simulative results with reference experimental study. Mainly, influences of groove size and groove position on cutting force components, contact length and force ratio are investigated. The results of micro-grooved tools are compared with non-textured tool. These results showed that micro-grooved tools are effective in improving tribo-mechanical behaviors such as cutting force, feed force, contact length, and friction coefficient even in dry cutting. Furthermore, action mechanism of micro-grooves is discussed in detail.

Keywords: Textured cutting tool, Inconel 718, FEM modelling, Machining, Cutting force

1. INTRODUCTION

Super alloys were developed to meet demanding working conditions, especially at high temperatures. They are widely employed in various industries such as: aeroplane, bio-medical, metal processing, power plants, chemical and petrochemical, heat-treatment, and marine [Choudhury and El-Baradie, 1998]. Due to their unique qualities, super-alloys offer exceptional mechanical properties such as; high strength, strong oxidation resistance, creep resistance, thermal stability, thermal fatigue properties and relative lightness [Zhu et al., 2013]. Among Nickel-based superalloys, Inconel 718 is the most widely used and studied alloy. 50% weight of a jet engine is Inconel 718 [Ulutan and Özel, 2011]. But, machinability of Inconel 718 is quite challenging, due to its high temperature strength, work hardening tendency and low thermal diffusivity [Imran et al., 2014]. Its austenitic matrix, like stainless steels, is responsible for work hardening during machining. In addition, this alloy has affinity

to weld with the tool material, during high machining temperatures. Machinability of this alloy is worsened due to its tendency to form built up edge (BUE) and the presence of hard intermetallic compounds and abrasive carbides in their microstructure [Choudhury and El-Baradie, 1998]. Continuous and tough chips produced during machining are other factors negatively affect machining process. Frequent tool wear to due to high cutting forces, high cutting temperatures and BUE formation are considered to be the main limiting factor of machinability and process efficiency. Although there are substantial improvements in machine tools, cutting tools, machine control systems, cooling and lubrication technology, machining of superalloys is still leading to problems in terms of tool wear and surface integrity, which may cause very severe consequences in operating conditions [Ulutan and Ozel 2011]. Hereby, control of tool wear should be ensured through optimizing cutting forces and temperatures.

Tribological properties of cutting tools during machining process have been improved in many applications by employing surface texture patterns. Frequently, rectangular and square type micro-grooves were formed on rake and flank faces of cutting tools. Mostly applied fabrication methods for forming groove geometry are fiber laser machining [Su et al., 2017], wire electrical discharge machining (EDM) [Arulkirubakaran et al., 2016], femtosecond laser machining [Kawasegi et al., 2009], and micro grinding [Xie et al., 2012]. Arulkirubakaran et al. [2016] investigated effects of texture direction (parallel to chip flow, perpendicular to chip flow, and cross pattern) on various machinability parameters of turning process using micro grooved carbide tools. They found that textured tools can effectively reduce cutting force, cutting temperature and actual contact area. Among the investigated texture patterns, micro-grooves perpendicular to flow direction yielded the best results. Su et al. [2017] investigated machining performance of micro-grooved polycrystalline diamond tools in dry machining of Ti6Al4V. The results showed that frictional behaviors of the tool-chip interface and cutting forces of micro-grooved PCD tools were significantly reduced compared to those of the non-textured tools even in dry cutting conditions. These improvements were attributed to reduced tool-chip contact area. Kawasegi et al. [2009] studied effects of microscale and nanoscale texture patterns in machining of aluminum alloy A5052. The results revealed that cutting forces and amount of adhered material was decreased at cutting speeds above 420 m/min. It should also be noted that, textured cutting tools yielded larger shear angle, which eases machining process.

FEM simulations of surface textured cutting tools reported in literature were in a good agreement with experimental studies [Arulkirubakaran et al., 2016; Chen et al. 2013; Ma et al., 2015; Ma et al., 2016]. Chen et al. [2013] conducted a numerical study on orthogonal machining of Ti6Al4V with micro-textured cutting tools. They reported that cutting

temperatures can be effectively decreased with increase of texture rate. Ma et al. [2015] presented a 3D numerical simulation of microgroove textured cutting tools in dry machining of Ti6Al4V. The researchers assessed effects of geometrical micro-groove parameters. It was concluded that optimal groove with to depth ratio should exist between 10 and 16.

In addition to groove type textures, micro-hole geometries are also effective at yielding favorable tribological conditions. Lei at al. [2009] investigated performance of micro-pool lubricated carbide cutting tools in machining of mild steel. It was found that cutting forces were decreased between 10% and 30% and chip removal was eased with increased chip curl when using micro-pooled tools. Moreover, FE analysis results showed that micro-hole geometry did not decrease the mechanical strength of the tool. Ma et al. [2016] studied micro-hole textured cutting tools during machining of Ti6Al4V in 3D FE simulation. Effects of four different micro-hole parameters (diameter, diameter to depth ratio, edge distance, position pattern) on cutting forces and chip formation were investigated. It was reported that micro-holes on the rake face was very effective in reducing cutting force components and tool-chip contact length.

Among the textured tool studies conducted on high temperature alloys, most of the them concentrated on Titanium alloys. However, texture tool performance on other types of difficult to machine high temperature alloys should also be investigated, since machining demand of these alloys increasing rapidly. Recently, Sugihara et al. [2017] presented a study, which focuses on failure process of textured CBN tools during high speed machining of Inconel 718. In the study, three different groove patterns were generated on the flank faces of turning inserts using femtosecond laser machining. The results showed that CBN cutting tools with micro grooves orthogonal to cutting edge improved tool life by anchoring adhesion layer and preventing it from flaking.

The texture patterns generated on rake and flank faces of cutting tools have been found to successively increase various machinability characteristic. Although, number of studies focusing on surface texturing of cutting tools increasing recently, it was pointed out that optimal texture geometry, dimensions, and position may differ greatly depending on process parameters, cutting conditions, tool and workpiece materials [Sugihara et al., 2017]. To best of author's knowledge, there is no study concentrating on effects of surface texturing focusing on quantitative machinability characteristics such as cutting forces, when cutting Inconel 718.

In the present paper, performance of surface texture on rake face during dry cutting of Inconel 718 is investigated in 2D FE simulation using Deform 2D FE code [Deform-2D, 2014]. Validation of numerical results are ensured by comparing the simulative results and

experimental results. Effects of various micro-groove depth and position values on cutting forces, tool-chip contact length, and force ratio are investigated during simulations aiming to understand surface texturing behavior in machining of Inconel 718. By implementing successful optimizations on surface texture, minimization of cutting forces and temperatures as well as more favorable tribological properties seem possible. Hence, in turn, reducing energy consumption and tool wear would be possible. The authors also aim to contribute to research, design and application of the textured cutting tools.

2. FEM MODEL VALIDATION

FEM model validation is ensured by comparing simulative results with reference experimental results [Devillez et al., 2007]. Devillez et al. [2007] investigated cutting forces and wear of uncoated and various coated carbide cutting tools during dry cutting of Inconel 718. During experiments longitudinal turning of tube workpiece is ensured with uncoated carbide tools, referenced as TCMW16T304H13A, without chip-breaker geometry and a rake angle of α=0. Their experimental machining parameters were same as present simulation (cutting speed *Vc*=50 m/min and feedrate *f*=0.1 mm/rev). Comparison of cutting forces of the reference study and the simulation model is presented in Table 1. It can be seen that cutting force and feed force results are in good agreement with experimental study.

3. SIMULATION PROCEDURE

FEM model of the orthogonal process is developed using Deform 2D© FEM software, where plane strain assumption together with thermo-mechanical analysis was performed [Deform-2D, 2014]. Constant shear model was employed with a constant shear friction factor of μ=0.6. Implicit updated Langrangian FE algorithm (transient state simulation) along with continuous remeshing technique is used, where distorted mesh is substituted by new one. Initial and the deformed mesh structure of the FE model is shown in Figure 1. Each simulation is carried out until a cutting length of 5 mm is completed, which is equal to a cutting time of 6 ms.

Table 1. Comparison between experimentally measured and numerically obtained results

	Experimental	*Simulation*	*Error (%)*
Cutting Force (N)	500	457	0,086
Feed force (N)	255	238	0,067

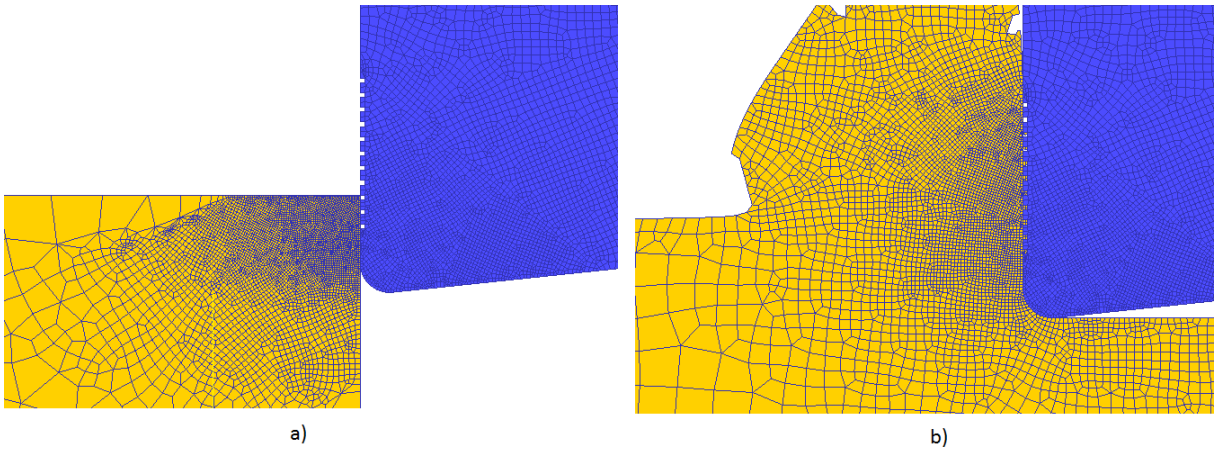


Fig. 1 Tool and workpiece mesh structures for grooved tool (groove size of 5μm and edge distance of 40 μm) a) Initial mesh structure b) Distorted mesh structure

Constant cutting speed of *Vc*=50 m/min and feedrate of *f*=0.1 mm/rev are employed during all simulations. Total of seventeen cutting simulations are conducted. Sixteen of these belong to textured tools with different texture geometries (four different groove sizes and four different groove positions for each size). Simulation of regular (non-textured) tool is ensured for comparison as well. After the simulations, the obtained results are as follows: mean cutting forces (Fv), mean feed forces (Ff), force ratio, and tool-chip contact length.

Workpiece

The investigated workpiece material is Inconel 718, which is modelled with plastic behavior. Mechanical and thermal properties of the workpiece employed in FE simulations are taken from Deform 2D library, given in Table 2 [Deform-2D, 2014]. Since machining process involves large strains, very high strain rates and quite high temperatures, it is not easy to predict plastic flow stress during machining. In order to simulate thermo-visco-plastic behavior of the material under these variables, Johnson-Cook constitutive material model is employed which considers temperature, strain and strain rate influences [Johnson and Cook, 1983]. It can be expressed as follows:

$$\sigma = [A + B\varepsilon^n] + \left[1 + C ln\frac{\dot{\varepsilon}}{\dot{\varepsilon}_0}\right][1 - \left(\frac{T - T_0}{T_{melt} - T_0}\right)^m] \quad (1)$$

where the components of the equation used in this study [Klocke et al., 2013] and their notation is given Table 2.

Table 2. Johnson Cook parameters and mechanical properties for Inconel 718 [Klocke et al., 2013; Deform-2D, 2014]

Notation	Property	Value
A	*Initial yield stress*	1485 MPa
B	*Hardening modulus*	904 MPa
C	*Strain rate dependency coefficient*	0.015
$\dot{\varepsilon}_0$	*Reference strain rate*	0.001 s^{-1}
n	*Work-hardening exponent*	0.777
T_0	*Ambient temperature*	20 °C
T_{melt}	*Melting temperature*	1300 °C
m	*Thermal softening coefficient*	1,689
ρ	*Density*	8190 kg m^{-3}
α	*Thermal expansion coefficient*	1.3 10^{-5} (at 20 °C)
E	*Young's modulus*	217 GPa (at 20 °C)
v	*Poisson's ratio*	0.30

The workpiece dimensions are 8 mm in length and 1 mm in height. The bottom side of the workpiece is fixed in y (feed) direction. Cutting speed simulation between tool and workpiece is ensured by horizontal movement of the workpiece in x axis at specified cutting speed. The workpiece is meshed with 10 000 quadrilateral elements and 10 500 nodes. In order to increase prediction accuracy of the simulation, four different mesh windows with different relative mesh sizes are generated. Relative size of the finest mesh window, defined around texture region, and coarsest mesh window, defined around bottom part of the work piece, are 0.001 and 0.05 respectively.

Cutting Tool

Micro-groove geometry parameters play a very important role in performance of texture effects. Thus, a better understanding of groove geometry influences during orthogonal cutting of Inconel 718 is aimed in this paper. For this purpose, effects of groove size and groove position are studied. Four different groove sizes perpendicular to chip flow, ranging from 5 to 30 μm, are generated on the rake face of the cutting tool, namely T1, T2, T3, T4. For each groove size, four different groove positions, namely P1, P2, P3 and P4, are generated. These texture positions are grouped regarding the first groove distance from the tool tip. Groove parameters and notation of all the tools investigated in present study are shown in Table 3. It should be noted that, all the sharp edges are rounded off with small radii range from 2.5 to 7.5 μm to facilitate numerical simulation.

Table 3. Microgroove parameters and notations of the investigated tools

Tool No	*Texture Position*	*Groove Depth (μm)*	*Groove Width (μm)*	*Groove Pitch (μm)*	*Distance From Edge(μm)*	*Tool Notation*
1	1	5	5	15	40	T1-P1
	2	5	5	15	140	T1-P2
	3	5	5	15	190	T1-P3
	4	5	5	15	220	T1-P4
2	1	10	10	25	40	T2-P1
	2	10	10	25	170	T2-P2
	3	10	10	25	210	T2-P3
	4	10	10	25	265	T2-P4
3	1	20	20	45	40	T3-P1
	2	20	20	45	170	T3-P2
	3	20	20	45	210	T3-P3
	4	20	20	45	265	T3-P4
4	1	30	30	65	40	T4-P1
	2	30	30	65	160	T4-P2
	3	30	30	65	210	T4-P3
	4	30	30	65	245	T4-P4
0	Non-textured					T0

The cutting' tools height and width dimensions are both 2 mm and edge radius is rβ=30 μm. The rake angle and clearance angle values are 0° and 6° respectively. Side view representations of the first texture position (P1) of the four different tool groove sizes are presented in Figure 2.

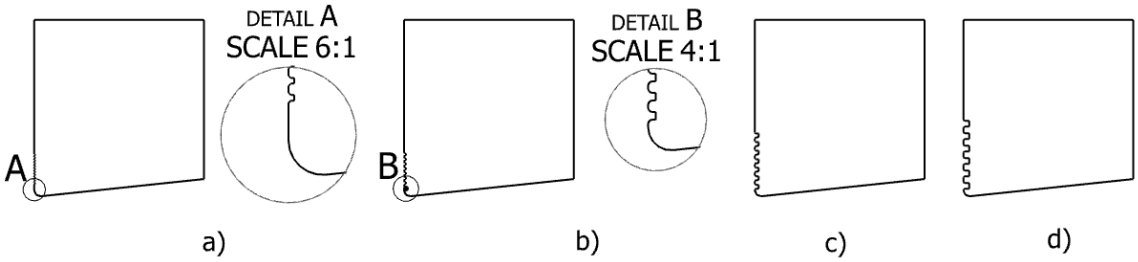


Fig. 2 Side view of the textured tools; a)T1-P1 and detailed view (detail A) b)T2-P1 and detailed view (detail B) c)T3-P1 d)T4-P1

The material of the cutting tool is uncoated tungsten carbide (WC). Mechanical and physical properties of the cutting tool are given in Table 4. The cutting tool, modelled as rigid geometry, is meshed with 5000 quadrilateral elements. Similar to workpiece meshing, 3

different mesh density windows are generated. The finest mesh windows is defined at texture region in order to simulate mechanical effects of tool texture accurately.

4. RESULTS AND DISCUSSION

In order to investigate effects of groove size and groove position, following results are evaluated: cutting force (Fv), feed force (Ff), and tool chip contact length. Fv and Ff are calculated as average force values of the related simulation. Another presented result is cutting force ratio (Fv/Ff). As rake angle is zero, cutting force ratio corresponds to mean friction coefficient at the tool-chip interface according to analytical modelling of chip removal mechanics of metal cutting [Shaw and Cookson, 1984]. Cutting force ratio was employed for predicting tool wear and yielded a good agreement with experimental results [Choudhury and Kishore, 2000]. Determination of optimum cutting parameters and insert coating when cutting Inconel 718 was successfully conducted taking the cutting ratio into consideration [Devillez et al., 2007].

Effects of Groove Size

Mean cutting force and feed force results for each groove size is shown in Figure 3. Mean forces are calculated by averaging same groove sized tools' force results of four texture positions. For example, Fv for T1 is calculated by averaging T1P1, T1P2, T1P3, and T1P4. Error bars demonstrate standard deviation of the force means. Force values of the non-textured tool (T0) is plotted as well. Compared to non-textured tool, a force reduction of 13% and 26% is performed by T1 for Fv and Ff, respectively. When the groove size increases from 5 to 20 μm, both force components increase gradually for T2 and T3, but still lower than T0. This increase reaches a plateau between T3 and T4. Cutting force and feed force of the largest groove are still lower than non-textured tool, about %5 lower for both components. According to these result, optimal groove size should be 5 μm or below for obtaining lowest cutting force results. Regarding maximum groove size, grooves larger than 20 μm seem to lose effectiveness.

Table 4. Mechanical and physical properties of WC tool (Deform-2D 2014)

Notation	Property	Value
E	*Young's modulus*	650 GPa
ρ	*Density*	15,700 kg m^{-3}
v	*Poisson's ratio*	0.25
α	*Thermal expansion coefficient*	9.1 10^{-6}
c	*Heat capacity*	15 J $°C^{-1}$
K	*Thermal conductivity*	59 W m^{-1} $°C^{-1}$

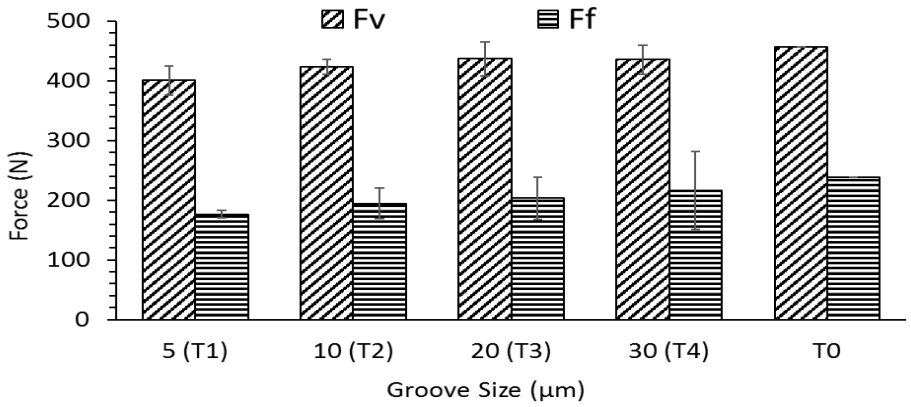


Fig. 3 Cutting force and feed force results of T0 and mean results of T1, T2, T3, and T4

Mean contact length and force ratio results for each groove size is shown in Figure 4. Here, error bars demonstrate standard deviation of the groove means for four different groove sizes. Mean results are calculated in same way with force components calculation. Contact length results for all groove sizes are lower than that of non-textured tool. Minimum contact length was observed when cutting with T2 (21% lower than non-textured tool). T1, T3 and T4 displayed similar results regarding contact length. These results suggest that all investigated groove sizes displayed favorable results in terms of contact length. Groove size of 10 µm yielded optimal contact length performance.

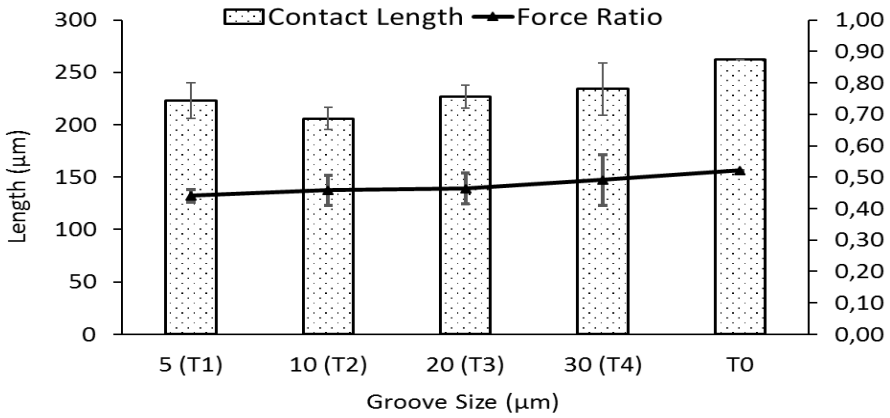


Fig.4 Contact length and force ratio results of T0 and mean results of T1, T2, T3, and T4

Variation of force ratio is shown in Figure 4. It is clear that, cutting force ratio values for each micro-groove size are less than that of the regular tool, which means textured tools will most probably perform better tribological behaviors. Force ratio value displays an increasing trend with increased groove size. It should be noted that minimum force ratio (0.44) was observed when cutting with 5 µm groove sized tools.

Effects of Texture Position

In Figure 5, Mean cutting force and mean feed force results of P1,P2,P3 and P4 of all groove sizes is shown. All texture positions of T1 (smallest groove size) is excluded from position mean force calculations. For example, Fc for P1 is calculated by averaging T2P1, T3P1, and T4P1, while T1P1 is plotted separately. Because, force results of T1 was completely distinct from other groove sizes. Hence, its position results are included separately to emphasize its distinct results. Force values of the non-textured tool (T0) is plotted as well. Error bars show standard deviation of the force means of T2, T3, and T4. Compared to non-textured tool, mean P1 result of T2, T3 and T4 yielded increased cutting force components (about 12% in feed force and about 2% cutting force). However, there is a sharp decrease in both force components at P2 and there is even more decrease at P3. Among the investigated positions, mean P3 force component results of T2, T3, T4 are at minimum (compared to regular tool about 10% reduced cutting force and about 27% lower feed force).

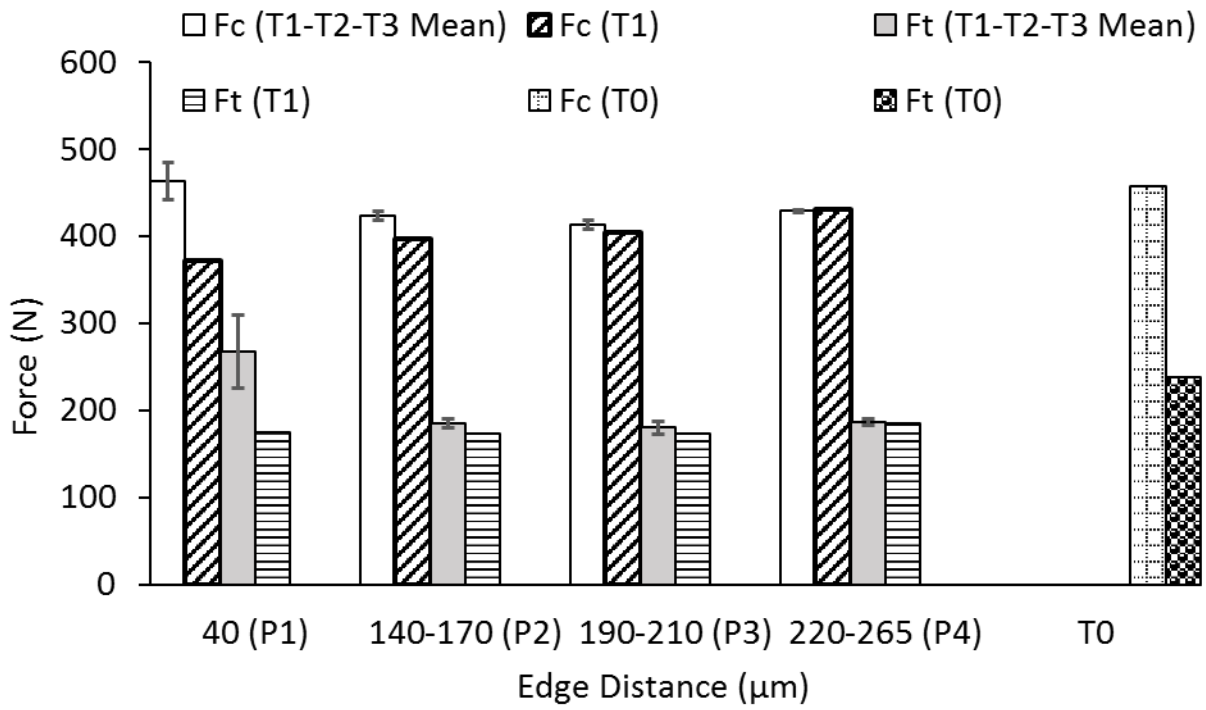


Fig. 5 Cutting force and feed force results of T0, T1 and position means of T2, T3, and T4

The reason of increased cutting and feed force results at P1 is attributed to existence of micro-grooves in sticking zone at tool chip interface. As suggested by Ma et al. [2016], micro grooves appear to play two important roles in machining process. First, they split the tool-chip contact area, which is normally long and continuous, into intermittent divisions. However, intimate contact still may be present inside of the grooves depending on the cutting conditions and texture geometry. Second, micro-grooves at tool chip interface behave like

micro cutters as chip flows over the rake face. This results in highly localized pressure and curling of micro-chips into the microgrooves, which in turn causes contact of chip onto groove valleys. Above described two roles, causes micro-grooves influence cutting performance in two distinct ways: (1) positive effect because of reduced tool-chip contact length, (2) negative effect because of high localized resistance to chip flow. Both of these two effects may exist at a rate, which depends on cutting conditions, groove size and groove position. According to cutting conditions of this simulation, it is concluded that increased cutting force results of groove position P1 (edge distance lower than uncut chip thickness) happened due to increased sticking effect. The result of this increase is the residue chip in micro-grooves as seen in Fig. 6a. In Figure 6, effective strain of regular tool and that of chip residues in micro-grooves for T3P1 and T3P2 are shown. It can be seen that effective strain of chip residues near cutting tip are relatively low. Direction of the chip flow and normal to shear stress ratio around edge region is probably responsible for this result.

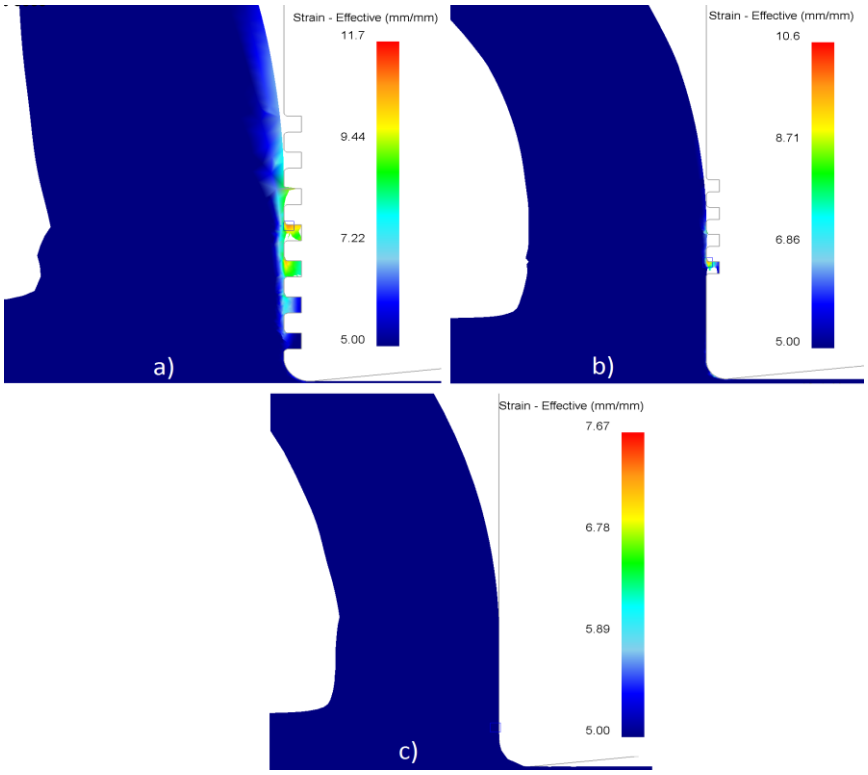


Fig. 6 Effective strain distribution during chip removal with textured tools and regular tool a) T3P1 b) T3P2 c) Regular tool

Regarding T1, cutting force versus texture position relationship is different. In case of T1 (minimum groove size), minimum cutting force components are obtained at P1 (compared to T0, 19% decreased cutting force and 26% decreased feed force). Force reducing effect of micro-grooves decreased when texture distance from tool edge is increased and this effect reaches to minimum level at P4. Different behavior of T1 from other groove sizes is attributed

its size. Similar results was reported by Kawasegi at al. [2009]. Probably, grove depth of T1 is not enough to create sticky chip residue effect on plastic flow of the chip at sticking zone. However, as the groove size increases, existence of grooves parallel to chip flow in the zone lower than uncut chip thickness seems to create negative effects in terms of cutting force components. According to these results, optimal edge distance should be higher than uncut chip thickness for T2, T3, and T4. For T1, this distance should be 40 µm or lower.

Figure 7 shows variation of contact length and force ratio for different texture positions. Force ratio and contact length values are calculated by averaging related results of four different groove sized tools (T1,T2,T3, and T4). Error bars demonstrate standard deviation of the means of T1, T2, T3 and T4 results. Results show that edge distance of 40 µm yielded largest contact length (5% larger than regular tool). This finding resulted from formation of chip residues touching groove valleys in micro-groove geometries. As seen in Fig. 6a and Fig. 6b, chip flow forms residues in grooves close to tool edge; whereas, it is observed that, chip flows over groove peaks at the upper grooves. This outcome is attributed to non-linearity of stresses on rake face of the cutting tool. With present analytical models, it is assumed that shear stress is constant in seizure region, whereas the normal stress is assumed to be at maximum at the tip of the tool. Most probably, high normal to shear stress ratio in seizure region gives raise to chip residues in grooves close to tool edge.

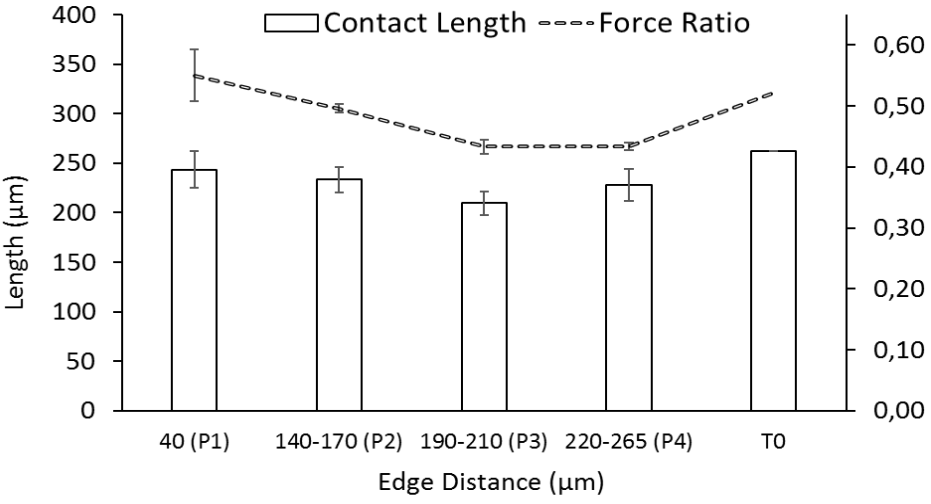


Fig.7 Contact length and force ratio results of different edge distance means (position means of T1,T2,T3, and T4)

Mean contact length increases with increased edge distance and reaches its minimum value at P3 (17% lower than regular tool) where edge distance is between 190 and 210 µm. Error bars at P2, P3 and P4 show that contact length among different groove sizes does not vary significantly, when edge distance is larger than uncut chip thickness.

Utilization of force ratios (Ff/Fv) for monitoring tool wear was proposed by some studies and yielded accurate results especially when predicting flank wear [Choudhury and Kishore, 2000]. Variation of force ratio with increased edge distance is shown in Figure 7. Here, error bars show standard deviation of the means of T1, T2, T3 and T4 results. Maximum force ratio, which is nearly equal to that of regular tool, is observed at edge distance of 40 µm (P1). This ratio decreases when edge distance increases and reaches its minimum value at P3. It should be noted that variation trend of contact length and force ratio are very similar. Figure 8 shows the relationship between contact length and force ratio. According to correlation analysis, a positive relation is observed between contact length and force ratio ($r>0.75$). It should also be noted that there is an agreement between contact length and force components. These results show that optimal edge distance should be between 190 and 210 µm to obtain most favorable tribological conditions under investigated cutting parameters. However, as described previously, any feedrate change will result in altered uncut chip thickness, which in turn alter length of seizure region. In such case, it is presumed that optimal groove position will change.

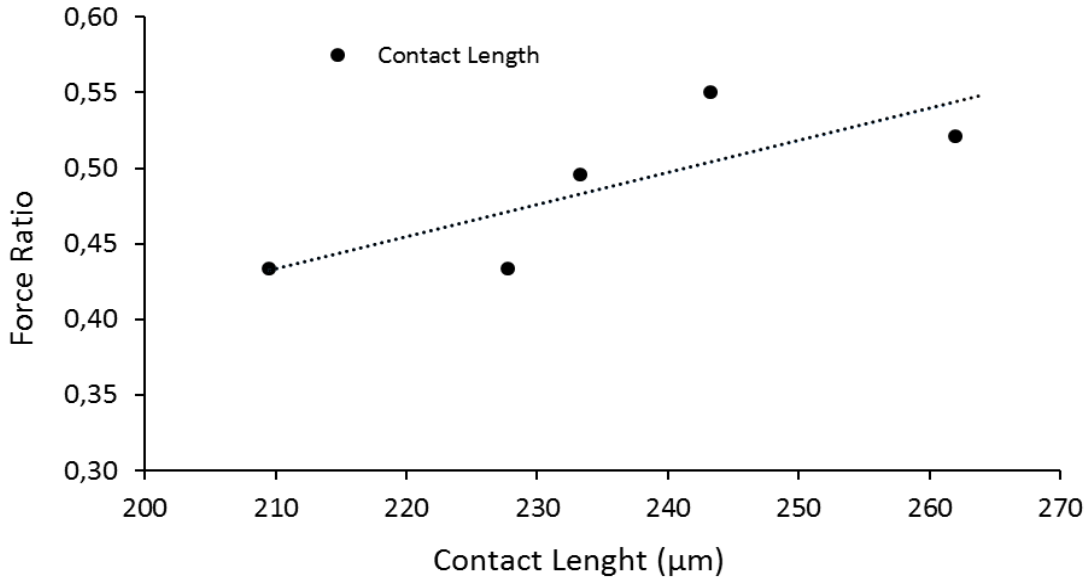


Fig. 8 Relationship between contact length and force ratio

5. CONCLUSIONS

Surface texturing of cutting tools during metal cutting have been reported to yield favorable tribological conditions, such as decreased cutting forces, coefficient of friction, contact length and less tool wear. In this paper, influences of surface texture on cutting force components, contact length, and force ratio during machining of Inconel 718 is investigated using FE simulation. Total of sixteen different micro-groove geometries (four different texture positions

for four different micro-groove sizes) are generated on rake face of cutting tool. Optimal groove size and texture position parameters are investigated under cutting speed of *Vc*=50 m/min and feedrate of *f*=0.1 mm/rev. After seventeen simulations, fallowing conclusions are made:

- Micro-grooves on the rake face of the cutting tool are effective in reducing cutting forces, contact length and force ratio.
- Force components of all investigated groove sizes are lower than those of non-textured tool. Among the investigated groove sizes, minimum cutting and feed force is obtained when machining with minimum grooved sized tool (5 μm).
- In reducing tool-chip contact area, the most effective groove size is 10 μm. While minimum force ratio is yielded by groove size of 5 μm.
- Except for the groove with minimum size, lowest cutting force components are obtained when the edge distance is between 190 and 210 μm. In case of 5 μm groove sized tool, minimum cutting force and feed force is observed when the edge distance is minimum (40 μm). Increase of this distance results in increased force components.
- Minimum contact length and force ratio are obtained when the edge distance is between 190 and 210 μm.
- For groove sizes larger than 5 μm, minimal edge distance resulted in negative consequences in terms of force components, force ratio and contact length. This is attributed to negative effect of grooves, as chip residue formation in groove geometries are seen in grooves close to tool tip. These residues create highly localized resistance to chip flow. It is presumed that optimal groove distance from edge should be more than length of seizure region.

ACKNOWLEDGEMENTS

The authors would like to thank SFTC, and FIGES Engineering A.Ş for their support with Deform 2D.

REFERENCES

1. **Arulkirubakaran, D., Senthilkumar, V. and Kumawat, V., (2016),** "Effect of micro-textured tools on machining of Ti–6Al–4V alloy: an experimental and numerical approach", International Journal of Refractory Metals and Hard Materials, Vol.54, pp 165-177.

2. **Chen, Z. M., Zhang, J. F., Feng P. F. and Wu, Z. J., (2013),** “A simulation study on the effect of micro-textured tools during orthogonal cutting of Titanium alloy Ti-6Al-4V”, Applied Mechanics and Materials, Vol.281, p. 389-394.

3. **Choudhury, I. and El-Baradie, M., (1998),** "Machinability of nickel-base super alloys: a general review", Journal of Materials Processing Technology, Vol.77, No.1-3, pp 278-284.

4. **Choudhury, S. K. and Kishore, K. K., (2000),** "Tool wear measurement in turning using force ratio", International Journal of Machine Tools and Manufacture, Vol.40, No.6, pp 899-909.

5. **Deform-2D (2014),** "Version 11 User Manual", STFC, Columbus, Ohio State, USA.

6. **Devillez, A., Schneider, F., Dominiak, S., Dudzinski, D. and Larrouquere, D., (2007),** "Cutting forces and wear in dry machining of Inconel 718 with coated carbide tools", Wear, Vol.262, No.7, pp 931-942.

7. **Imran, M., Mativenga, P. T., Gholinia A. and Withers, P. J., (2014),** "Comparison of tool wear mechanisms and surface integrity for dry and wet micro-drilling of nickel-base superalloys", International Journal of Machine Tools and Manufacture, Vol:76, pp 49-60.

8. **Johnson, G. R. and. Cook, W. H, (1983),** “A constitutive model and data for metals subjected to large strains, high strain rates and high temperatures”, Proceedings of the 7th International Symposium on Ballistics, The Netherlands.

9. **Kawasegi, N., Sugimori, H., Morimoto, H., Morita, N. and Hori, I., (2009),** "Development of cutting tools with microscale and nanoscale textures to improve frictional behavior", Precision Engineering, Vol.33, No.3, pp 248-254.

10. **Klocke, F., Lung D. and Buchkremer, S., (2013),** "Inverse identification of the constitutive equation of Inconel 718 and AISI 1045 from FE machining simulations", Procedia CIRP 8, pp 212-217.

11. **Lei, S., Devarajan, S. and Chang, Z., (2009),** "A study of micropool lubricated cutting tool in machining of mild steel", Journal of Materials Processing Technology, Vol.209, No.3, pp 1612-1620.

12. **Ma, J., Duong, N. H and Lei, S., (2015),** "3D numerical investigation of the performance of microgroove textured cutting tool in dry machining of Ti-6Al-4V", The International Journal of Advanced Manufacturing Technology, Vol.79, No.5-8, pp 1313-1323.

13. **Ma, J., Ge, X., Qiu, C. and Lei, S., (2016),** "FEM assessment of performance of microhole textured cutting tool in dry machining of Ti-6Al-4V", The International Journal of Advanced Manufacturing Technology, Vol.84, No.9-12, 2609-2621.

14. **Shaw, M. C. and Cookson, J., (1984),** Metal cutting principles, Clarendon press Oxford.

15. **Su, Y., Li, Z., Li, L., Wang, J., Gao, H. and Wang, G., (2017),** "Cutting performance of micro-textured polycrystalline diamond tool in dry cutting", Journal of Manufacturing Processes, Vol.27, pp 1-7.

16. **Sugihara, T., Nishimoto, Y. and Enomoto, T., (2017),** "Development of a novel cubic boron nitride cutting tool with a textured flank face for high-speed machining of Inconel 718", Precision Engineering, Vol.48, pp 75-82.

17. **Ulutan, D. and Ozel, T., (2011),** "Machining induced surface integrity in titanium and nickel alloys: A review", International Journal of Machine Tools and Manufacture, Vol.51, No.3, pp 250-280.

18. **Xie, J., Luo, M.J., He, J.L, Liu, X.R and Tan, T.W., (2012),** "Micro-grinding of micro-groove array on tool rake surface for dry cutting of titanium alloy", International Journal of Precision Engineering and Manufacturing, Vol.13, No.10, pp 1845-1852.

19. **Zhu, D., Zhang, X. and Ding, H., (2013),** "Tool wear characteristics in machining of nickel-based superalloys", International Journal of Machine Tools and Manufacture, Vol.64, pp 60-77.

FINITE ELEMENT ANALYZING THE EFFECT OF CRACK ON STRESS AND STRAIN IN HONEYCOMB STRUCTURE FROM ABS POLYMER MATERIALS

Bekir YALÇIN, *bekiryalcin@sdu.edu.tr* S. Demirel University, 32260, Isparta, Turkey

Berkay ERGENE, *berkayergene@sdu.edu.tr* S. Demirel University, 32260, Isparta, Turkey

ABSTRACT

Advanced technology requires new light materials, efficient structures and also new manufacturing methods. A typical conventional cellular example is the regular honeycomb structure produced by additive manufacturing. After doing new researches about fracture behaviour of honeycomb structure, the honeycomb structures with the three different rib thicknesses of 1 mm, 1.5 mm and 2 mm were designed, and then ABS material for structures were selected to use in finite element analyses (FAE). Also, the crack was created on structures, and then 2-D FAE were carried out for un-cracked and the cracked regular honeycomb structure under tensile forces. Finally, the results were interpreted with respect of stress values and strain concentration areas, effect of crack on stress-strain distributions and the crack tip opening through y axis. As results, the equivalent stresses (σ_{vm}) increase with a decrease in rib thickness and the crack in honeycomb structures leads to an increase in stresses and heterogeneous distribution of the stresses on the closest rib and rib joint to crack. In addition, the heterogeneous stresses distribution in the cracked honeycomb structure gives information about not to be the possible crack advance at lay on continuous patch in structure and but the crack advance will be in possible tortuous patch.

Keywords: Fracture behaviour, Honeycomb structure, Tensile forces

1. INTRODUCTION

Today, polymers play a very important role in many field and applications. They have been used in many application due to lightweight, excellent optical properties, good electric and thermal insulators, and easier and less expensive to make a final product. Polymers are mainly categorized as thermoplastics, thermosets and elastomers. Generally, thermoplastics solidify when they are cooled. These materials regain the ability to “flow”, when they are heated. On the other hand, thermosetting polymers solidify by a chemical curing process. The thermo-setting materials stiff, brittle and lose the ability to flow” even after reheating. Also, a common characteristic of elastomeric materials is that the glass transition

temperature is much lower than room temperature. So, their ability to “flow” is lost after they are vulcanized [Osswald and Menges, 2010; Calhoun and Peacock, 2006]. Some industrial applications of polymers can be followed: Polystyrenes have been mainly used to manufacture for the mass-produced transparent articles, thermoformed packaging, foamed packaging, thermal insulation products; polycarbonate for helmets, eyeglass lenses, CD’s, hockey masks, bulletproof windows, blinker lights, head lights; Polypropylenes for such as suitcases, tubes, engineering application (fiberglass-reinforced), housings for electric appliance; phenolics for heat-resistant handles for pans, irons and toasters, electric outlets; Polybutadiene for automotive tires (blended with natural rubber and styrene butadiene rubber), golf ball skin; polyamide for bearings, gears, bolts, skate wheels, pipes, fishing line, textiles, ropes; Polyurethane elastomer for roller skate wheels, sport arena floors, ski boots, automotive seats (foamed), shoe soles (foamed), etc. [Osswald and Menges, 2010].

Generally, plastics have been formed by conventional methods of injection, extrusion and blowing. Nowadays in industry, additive manufacturing has been introduced to a manufacturing method with layer upon layer from polymer, metal and ceramic based materials depending on time. Additive manufacturing method was classified by ASTM F42 standard [Lboro, 2012] that some of them such as selective laser sintering (SLS), multi jet melting (MJF), material jetting (MJ), digital light processing (DLP) and photopolimerization methods are suitable to manufacture from plastic materials [Lboro, 2012]. Also, near net shape plastic product having complex shapes, auxetic and honeycomb structures can be manufactured by these methods. In this context, the honeycombs of hexagonal cell structure are characterized by considerable rigidity in shear, high crushing stress, almost constant crushing force, long stroke, low weight and relative insensitivity to local loss of stability [Kumar et al, 2003]. The applications produced from honeycomb structure follow: Air stairs, overhead storage bins, passenger flooring, wing assembly, wing to body fairing, landing gears doors and leg fairing, elevators, acoustic leaning panels, engine access doors, compressor fairing for aircraft; fuselage panel section, flying control surfaces for satellite for fighter aircraft; solar panels, reflector antennae, satellite structures for satellite; energy absorber, driver protection, ceiling panels, connection archway, external doors for train wagon; a-pillar, front header, front side rail, upper roof for automotive; ventilation panels for electromagnetic waves [Hexcel, 2017; Global, 2017].

According to some literature surveys, the honeycomb core structure are classically manufactured with expansion, corrugation, router bit type cutting methods [Aydıncak, 2007], in addition, the additive manufacturing methods become applicable to manufacture the honeycomb cell structures [Barner, 2015]. Application areas for additive manufacturing are followed as particularly in the areas of architecture, fashion, molding tools, bio and medical

engineering. With the exploration of new materials and techniques, which provide better material properties, additive manufacturing will play a big role in all kind of products in future. Especially, for weight reduction there are large potentials [Berger et al, 2013]. Panda [Panda, 2015] carried out design and development of cellular structure for additive manufacturing. He found out that the relative density increases with decreasing the cell size and thickness at cellular structure, the compressive strength increases with an increase in relative density. The mechanic of cellular structures is different from the isotropic materials. Also, Wierzbicki [Wierzbicki, 1983] has proposed to estimate cellular structure strength with Wierzbicki model which was given in Eq. I.

$$\frac{\sigma}{\sigma_s} = 3.25 \left(\frac{\rho}{\rho_s}\right)^{1.7} \quad (1)$$

In Eq. 1, σ_s and ρ_s are the strength and density of solid material, respectively. Also, σ and ρ are the strength and density of regular hexagon honeycomb structure. In order to understand the mechanic of honeycomb structure, some equations were followed [John, 2017]: When the cells are regular hexagons, then then $\theta=30°$ and h=l, the relative density is expressed with Eq. 2;

$$\frac{\rho}{\rho_s} = \left(\frac{2}{\sqrt{3}}\right)\frac{t}{l} \quad (2)$$

As can be seen in Fig. 1, t is rib thickness, h and l is length of rib for cell of regular honeycomb in Eq. 2. The elastic modulus of regular honeycomb through y axis (E_y) and shear modulus (G_{xy}) can be obtained by the following equation 3 and 4.

$$\frac{E_y}{E_s} = \left(\frac{4}{\sqrt{3}}\right)\left(\frac{t}{l}\right)^3 \quad (3)$$

$$\frac{G_{xy}}{E_s} = \left(\frac{1}{\sqrt{3}}\right)\left(\frac{t}{l}\right)^3 \quad (4)$$

The poisson's ratio ($\nu_{xy}=\nu_{yx}$) can be written for regular honeycomb structure in Eq. 5. In Eq. 5, θ is the angle between h and l.

$$\nu_{xy} = \left(\frac{\cos^2\theta}{\left(\frac{h}{l}+\sin\theta\right)\sin\theta}\right) \quad (5)$$

Finally, the fracture toughness (K_{IC}) of regular honeycomb structure was expressed in Eq. 6 [John, 2017]. Where, σ_f is the fracture strength of solid material.

$$K_{IC} = 0.3\,\sigma_f\sqrt{\pi l}\left(\frac{t}{l}\right)^2 \quad (6)$$

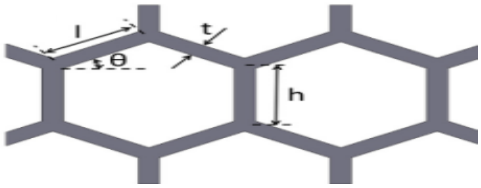


Fig. 1. The dimensional definition for regular honeycomb structure.

In this study, the effect of crack inside the regular honeycomb structure on stress and strain was analyzed by modelling of finite elements. After doing literature researches, the finite element models of regular honeycomb structure were created in drawing program for ABS polymer based materials. In analyses, three different rib thickness of 1 mm, 1.5 mm and 2 mm were assigned to the cell of honeycomb structure, then the stress analyses were carried out under tension loads. The normal stresses, shear stress, von-Mises stresses, strain and displacement values were obtained from the un-cracked and cracked regular honeycomb structures. Finally, the results were interpreted with respect of stress and strain concentration areas, effect of crack on stress-strain distributions and the crack tip opening through y axis in honeycomb structure.

2. MATERIALS AND METHODS

2.1 Finite Elements Modelling

Firstly, the materials and the cell size of regular honeycomb were respectively determined as a solid ABS material which has elasticity modulus of 2200 MPa, poisson's ratio of 0.35, density 1.05 g/cm^3, h=l=5.2 mm after doing literature survey [Ingrole et al, 2017]. Also, the rib thickness (t) and angle (θ) between h and l were assigned to the 1 mm, 1.5 mm, 2 mm and 30^o , respectively. Afterwards, the honeycomb model was designed by design program

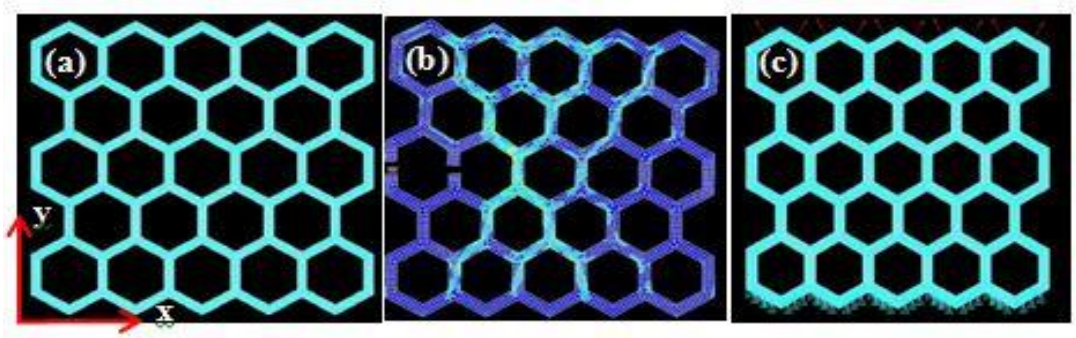


Fig. 2. a) The honeycomb model, b) the cracked honeycomb model c) mesh structure and boundary condition

m and then was exported to the finite element based program (Fig 2-a). The crack was created on the left of honeycomb structure which was shown in Fig 2-b. Subsequently, the elastic modulus (E) and density (ρ) of honeycomb structure used in analyses depending t of 1mm, 1.5 mm and 2 mm were respectively calculated as 36.127 MPa, 121.929 MPa, 289.019 MPa and 0.233 g/cm^3, 0.349 g/cm^3, 0.466 g/cm^3 by using Eq. 2 and 3 which were accepted in literature for mechanic of honeycomb cellular structures [John, 2017]. The honeycomb structure from ABS material was homogeneously meshed, in addition, the bottom of the honeycomb structure was fixed as ancastre, and then the tension stress of 0.05 MPa was applied to top of honeycomb structure as boundary condition which can be seen Fig. 2-c. In this state, the 2-D FAE were carried out for un-cracked and cracked regular honeycomb structures under tension loads. The normal stresses of σ_x, σ_y and shear stress of τ_{xy}, von-Mises stress of σ_{vm}, strain of ε_x and ε_y, displacement values of Δl_x and Δl_y , and finally the crack tip opening values were obtained from the analyses. Moreover, the results were commented in relation to the effect crack on stresses, strains, displacement and stress concentration on the honeycomb structure.

3. RESULTS

3.1 Stress Results

To understand the effect of crack on stress, strain and displacement in honeycomb structure, the finite element analyses were conducted. Some of σ_x, σ_y, τ_{xy}, σ_{vm}, ε_x, ε_y, Δl_x and Δl_y values were obtained from the analyses. Firstly, the normal stresses of σ_x, σ_y and shear stresses of τ_{xy} occurred in the analyses of honeycomb structure were shown in Fig. 3 and Fig. 5. According to the Fig. 3, similar tendency about the effect of crack on σ_x and σ_y are obtained. A decrease in rib thickness causes an increase in stresses for each honeycomb structure. The maximum stresses of σ_x for the rib thicknesses of 1 mm, 1.5 mm and 2 mm for un-cracked structure were obtained as 4.154 MPa, 1.88 MPa, 1.107 MPa and σ_y are 3.38 MPa, 1.759 MPa and 1.082 MPa, respectively. On the other hand, σ_x for the rib thicknesses of 1 mm, 1.5 mm and 2 mm in cracked honeycomb structure were obtained as 8.958 MPa, 4.254 MPa and 2.411 MPa, σ_y are 9.028 MPa, 4.331 MPa and 2.624 MPa, respectively. It can be seen clearly that the normal stresses in the cracked structure are higher than those of un-cracked structure. Also, while the compression stresses through x axis are higher than those of y axis for each structure, the tensile stresses in y axis are higher than those of x axis for all honeycomb structure. This phenomenon may cause the fatigue failure in rib joint and rib body. The tendency of σ_x and σ_y for the un-cracked and cracked honeycomb structures were shown in Fig 3-a, b.

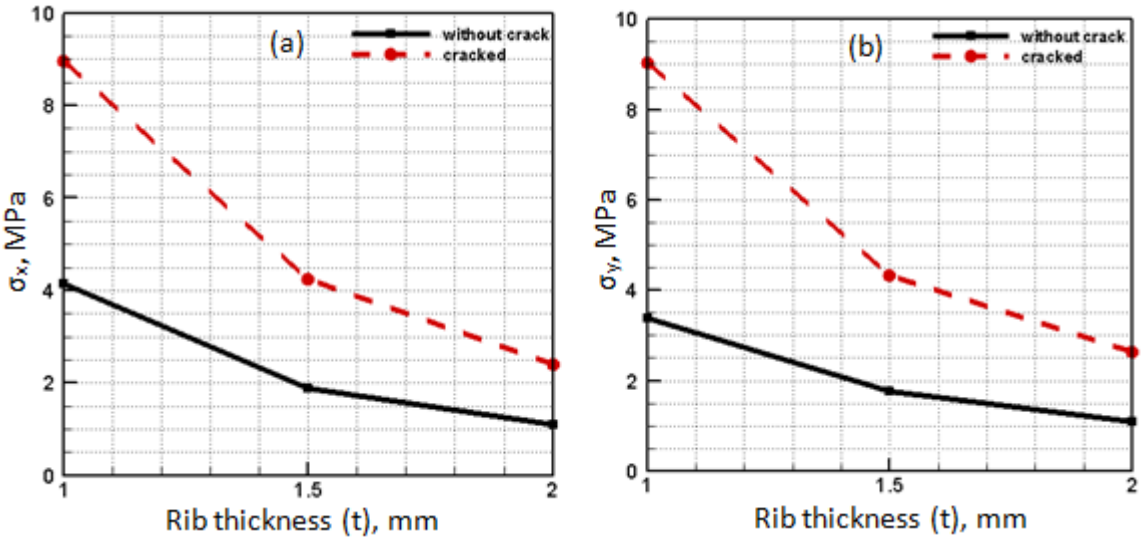


Fig. 3. The tendency of σ_x (a) and σ_y (b) for the un-cracked and cracked honeycomb structures

Moreover, the maximum stress concentrations and the normal stress distributions of σ_x and σ_y for each structure was given in Fig 4. While the maximum stress of σ_x occurred as compression of -4.154 MPa in rib joint, the maximum σ_y was shown as tension of 3.38 MPa for un-cracked honeycomb which can be seen in Figs 4-a, b. According to the Fig 4-b, the maximum tension stress of 3.38 MPa and compression stress of -2.637 MPa through y axis occurred in same rib, this state can be commented as critic stress concentration for beginning of the possible initial crack in un-cracked structure. The inferable result can be achieved with relation to be failure on rib (2 numbered) occurred both compression and the tension stresses which can be seen in Fig. 4-b. Fig. 4 shows the maximum σ_x and σ_y for rib thickness of 1 mm in the un-cracked and the cracked honeycomb structures.

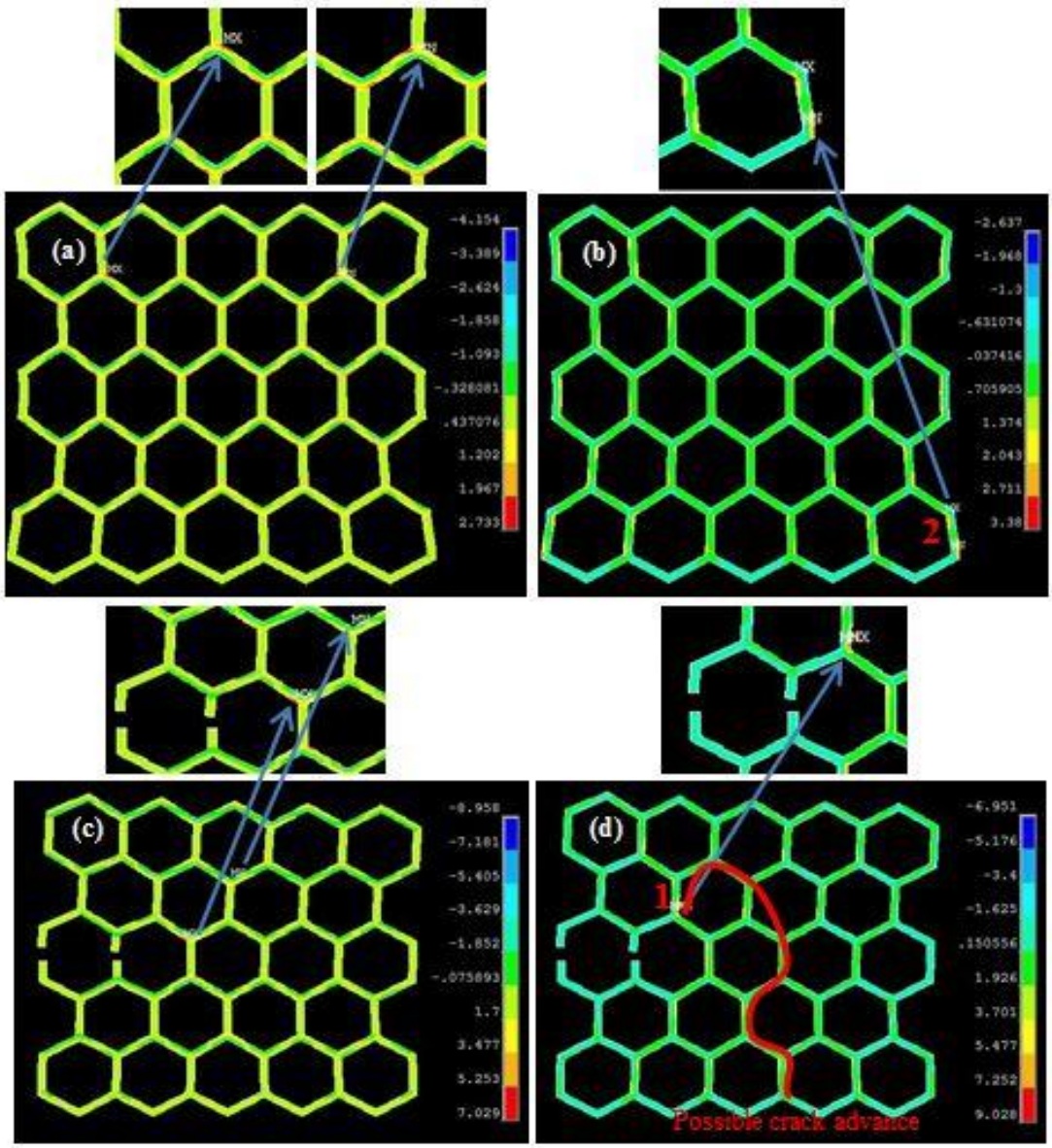


Fig. 4. a) The maximum σ_x distributions, b) the maximum σ_y distributions for rib thickness of 1 mm in un-cracked honeycomb structure; c) The maximum σ_x distributions, d) the maximum σ_y distributions the cracked honeycomb structure.

As can be seen Fig 4-c, d, more important results about stress distributions were obtained from analyses. Hence, the crack in honeycomb structure increases the σ_x and σ_y values and also the maximum stress occurred in rib joint through x and y axis. Moreover, the maximum stress concentration occurred on the closer rib and rib joints to the crack in the cracked structure than that of un-cracked structure. Specially, the maximum tension of 9.028 MPa and compression of -6.951 through y axis occurred on the nearest rib joint at the cracked cellular structure which can be seen in Fig 4-d. This may initiate the possible damage as the

fatigue failure on the nearest rib joint which is numbered as 1 in Fig. 4-d. In addition, σ_y occurred on the cracked structure has more affect than σ_x. Because, the normal stresses focused on the same rib and rib joint for both un-cracked and the cracked honeycomb structures.

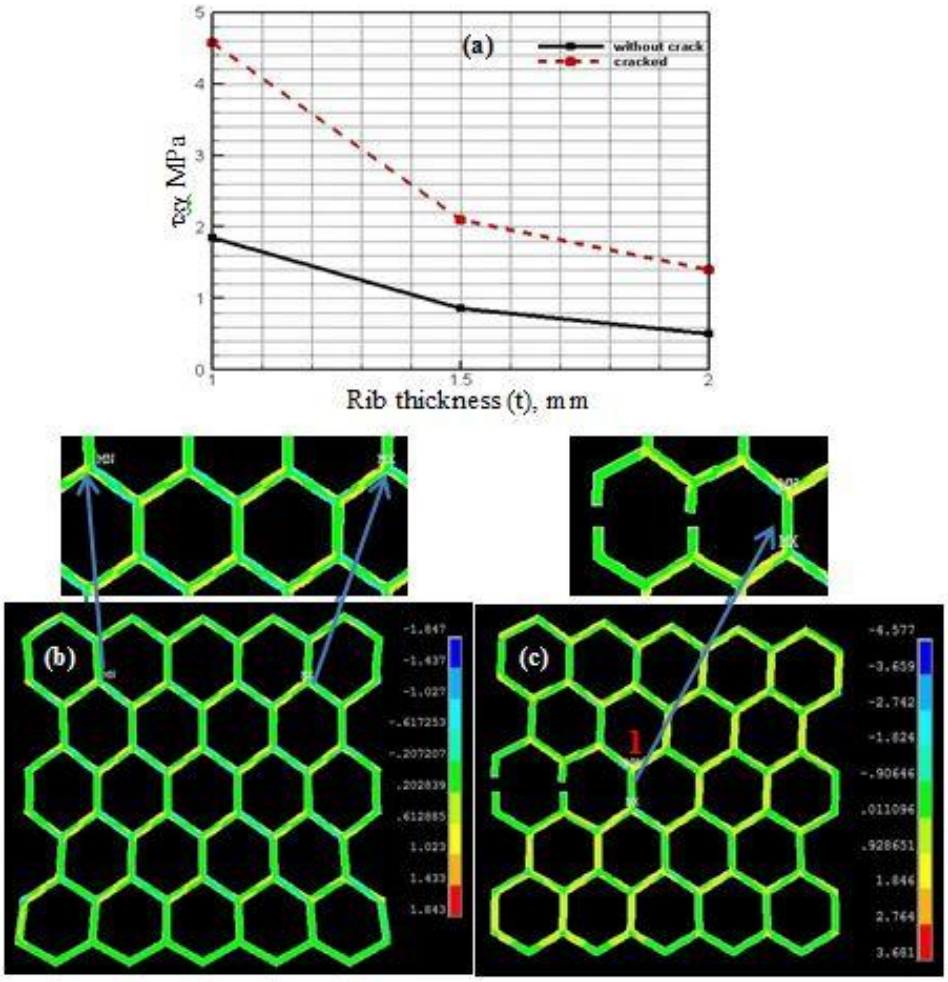


Fig. 5. a) Shear stresses, $\tau_{xy,}$ b) distributions of the shear stresses for un-cracked (b) and the cracked structures (c), t: 1 mm.

The similar trend in shear stresses with normal stresses was obtained that the highest effect of decreasing the rib thickness from 1.5 mm to 1 mm which can be seen in Fig. 5-a. It can be interpreted that when the rib thickness decreased from 2 mm to 1.5 mm in the un-cracked structure, the shear stress increased around 68%, the trend was obtained as 114% from 1.5 mm to 1 mm. Also, If the rib thickness decreased from 2 mm to 1.5 mm in the cracked

structure, the shear stress increased around 50%, the trend was obtained as 117% from 1.5 mm to 1 mm. Namely, increasing trend in shear stress for the cracked honeycomb structure is higher than that of un-cracked honeycomb structure. While, the maximum shear stresses occurred in further cellular joints of the un-cracked structure, those were observed in the closest rib and rib joints to crack for the cracked structure. Therefore, the possible crack advance may initiate the nearest ribs. It can be commented that the strength of rib joints play a very important role for the crack propagation. When examined Fig. 4-d and Fig. 5c., the typical crack advance in the cracked structure doesn't lay on x axis, but the crack advance will be in possible tortuous patch by starting from the "1" point. In one investigation [Schmidt and Fleck, 1999], the crack starts the large bridging zone and then advances around the ligaments. Schmidt and Fleck [Schmidt and Fleck, 2001], mentioned that the crack propagation in regular honeycomb structure doesn't lay on continuous patch, but the crack advances on sinuous patch. Also they impressed that the crack growth behaviour depends on the cell wall materials and geometric properties of honeycomb structures. The equivalent stress (σ_{vm}) obtained from analyses was given in Fig. 6.

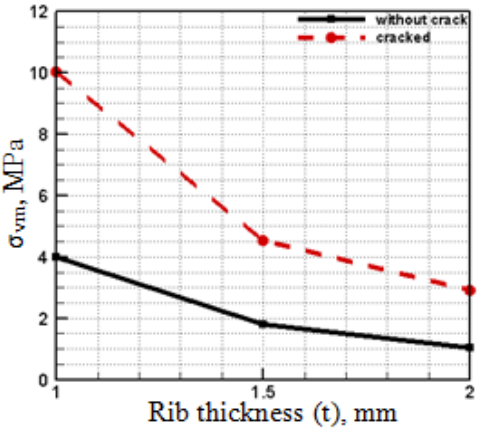


Fig. 6. The equivalent stress (σ_{vm}) obtained from analyses

Finally, the equivalent stresses obtained by resulting with normal and shear stresses from analyses possess a similar trend for honeycomb structure. So, the maximum σ_{vm} for t of 2 mm for un-cracked and the cracked structures were obtained around 1.041 MPa and 2.913 MPa; σ_{vm} for t of 1.5 mm as 1.815 MPa and 4.535 MPa, σ_{vm} for t of 1 mm as 3.989 MPa and 10.035 MPa, respectively. Hence, the maximum occurred on the smallest rib thickness of 1mm. Andrews and Gibson [Andrews and Gibson, 2001] reported that crack results a strong sensitive to the cell size. Furthermore, around 1.79 times increase in σ_{vm} took place in t of 2 mm in the cracked structure, for t of 1.5 mm as 1.49 times and for t of 1 mm as 1.51 times according to the un-cracked honeycomb structure. The depending the results, the highest

equivalent stress occurred on the smallest rib thickness of 1 mm in the cracked structure and un-cracked honeycomb. Therefore, the stress distributions of σ_{vm} for each structure having t of 1mm were in Fig. 7. According to Fig. 7-a, while the maximum σ_{vm} occurred on the closest rib joint to crack tip in the cracked structure, it was observed on the rib joint in second cellular under top of un-cracked structure. When interpreted Fig. 7-a, the stresses is heterogeneously distributed and the stresses concentrated on cellular near the end of crack. This state gives information about not to be the possible crack advance at lay on continuous patch. On the other hand, Fig 7-b exhibits the distributions of σ_{vm} in the un-cracked structure. The homogeneous the maximum at rib joints were obtained in un-cracked structure and the stresses decrease from rib joint to the center of rib. The stresses in the cracked structure are higher than those of the un-cracked structure which can be seen in Fig. 7.

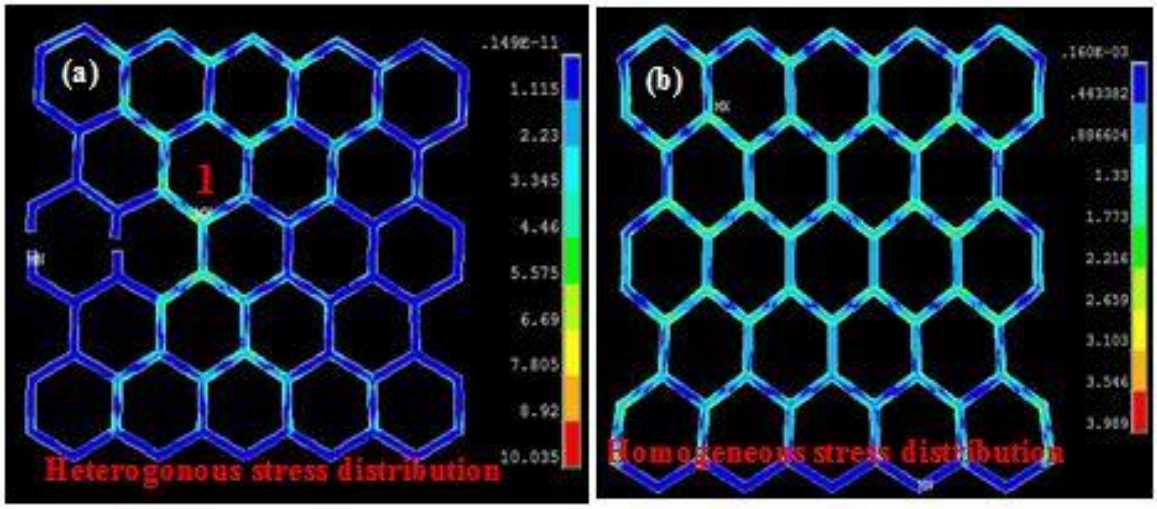


Fig. 7. Equivalent stress (σ_{vm}) distributions a) the cracked honeycomb structure, b) un-cracked honeycomb structure.

3.2 Strain and Displacement Results

The displacements and strains obtained from the analyses were given in Figs 8-10. According to Fig. 8-a, the displacement values (Δl_x) through x axis for the cracked honeycomb structure having t of 1 mm, 1.5 mm and 2 mm were respectively obtained as shortening of 2.519 mm, 0.201 mm and 0.033 mm. Furthermore, the values of Δl_x for un-cracked honeycomb structure were obtained as shortening of 5.661 mm, 0.586 mm and 0.122 mm from analyses, respectively. So, the honeycomb structure did not show auxetic structure behaviour due to shortening through x axis. There is an important result that the un-cracked structure possess higher displacement than that of the cracked structure through x axis which can be seen Fig. 8-a. Hence, the crack is obstacle more displacement through x axis of honeycomb structure. On the other hand, while the displacement values (Δl_y) through

y axis of the cracked honeycomb structure in t 1 mm, 1.5 mm and 2mm were obtained as elongation of 7.823 mm, 0.910 mm and 0.216 mm, Δl_y values of the un-cracked honeycomb structure were obtained as elongation of 3.999 mm, 0.476 mm and 0.114 mm, respectively. This state can be seen in Fig. 8-b. The Δl_y values are higher than Δl_x values for the cracked honeycomb structure; in addition, the crack leads to higher displacements in y axis. The reason of this can be interpreted that the crack tip opening with perpendicular tensile forces leads more displacement through y axis. Therefore, the crack tip opening were determined, it can be seen in Fig 9. Jin et al. [Jin et al, 2014] emphasized that the racks are dangerous due to crack tip stress concentration.

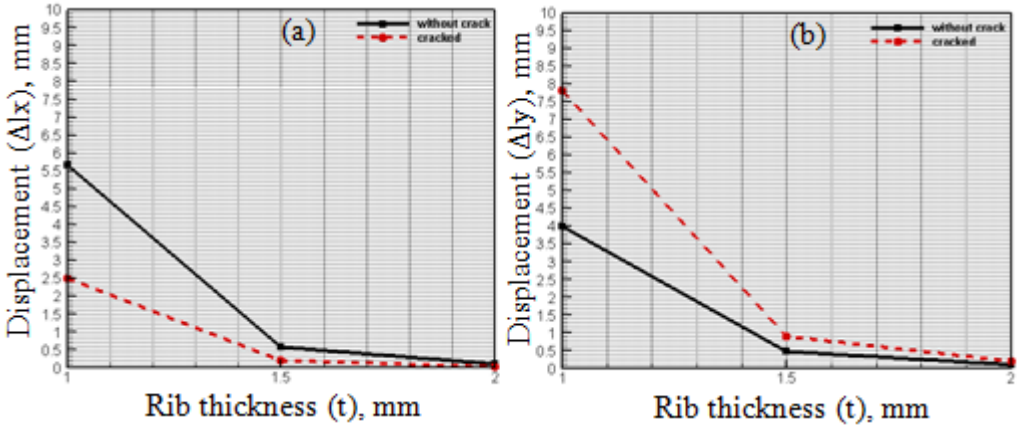


Fig. 8. Displacement through x axis (a), through y axis (b).

Fig. 9 shows the crack tip opening values at the beginning tip of crack under tension load in the cracked honeycomb structure. According to Fig. 9, the crack tip opening values are on y axis 22.968 mm, 2.671 mm and 0.632 mm for t of 1 mm, 1.5 mm and 2 mm, respectively. The biggest displacement in beginning tip of crack through y axis was seen in the rib thickness of 1 mm. This result is compatible with stress results in the cracked structure.

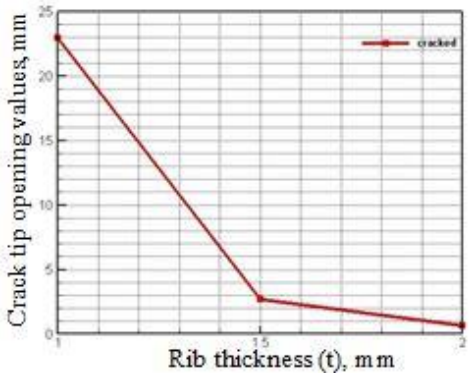


Fig. 9. Crack tip opening values through y axis.

It is known that the strain is named as deformation ratio (%), in addition, ε_x is qualified as shrinkage or shortening (%) through x axis and ε_y as elongation (%) under tension forces through y axis in this study. The strains of ε_x and ε_y were given in Fig 10. According to Fig 10-a, the values of ε_x in the cracked honeycomb structure for t of 1 mm, 1.5 mm and 2 mm were obtained as 4.929 %, 0.372 % and 0.057 %. Also, the values of ε_x in the un-cracked honeycomb structure for t of 1mm, 1.5 mm and 2 mm were obtained as 11.090%, 1.080% and 0.214%. It is obviously that the honeycomb structure doesn't show the auxetic behaviour due to shrinkage in dimension of x axis under tension load. Also, the crack didn't allow shrinkage as much as un-cracked honeycomb. On the other hand, the elongations (ε_y) in for each honeycomb structure were detected on y axis. The crack leads to more ε_y value than the un-cracked honeycomb structure. As similar to displacement values, the crack tip opening under tensile forces causes increasing the ε_y values in the cracked honeycomb structure.

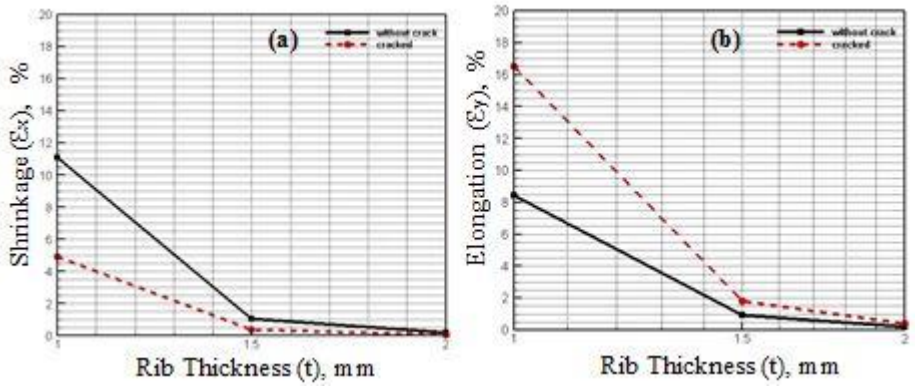


Fig. 10. Strain values on x axis, ε_x (a), on y axis, ε_y (b)

4. CONCLUSIONS

In this study, the finite element analyses were carried to determine the effect of crack on stress, strain and displacement in honeycomb structure from ABS polymer based materials. Some following results can be drawn;

- Firstly, the equivalent stresses (σ_{vm}) increase with a decrease in rib thickness in honeycomb structure.
- σ_{vm} distributed heterogeneously to the cracked honeycomb structure, in addition, the maximum σ_{vm} occurred on the closest rib and rib joint to crack tip. On the other hand, the homogeneous σ_{vm} distributed to the un-cracked structure.
- The σ_{vm} values in the cracked honeycomb structure are higher than those of the un-cracked honeycomb structure. For example, around 1.79 times increase in σ_{vm} took

place for t of 2 mm in the cracked structure, for t of 1.5 mm as 1.49 times and for t of 1 mm as 1.51 times according to un-cracked regular honeycomb structure.

- σ_{vm} concentrated on the cell near the end of crack in analyses (Fig. 7). This state gives information about not to be the possible crack advance at lay on continuous patch in honeycomb structure and but the crack advance will be in possible tortuous patch. This result is compatible with literature surveys [Schmidt and Fleck, 1999; Schmidt and Fleck, 2001].
- There is important result that the un- cracked structure possesses higher displacement (shortening) than that of the cracked structure through x axis. For example, the shortening of 5.661 mm in the un-cracked honeycomb structure and the shortening of 2.519 mm in the cracked structure were obtained for t of 1 mm from analyses.
- Also, the crack leads more elongation through y axis than un-cracked honeycomb structure. For instance, the elongation of 7.823 mm in the cracked honeycomb structure and the elongation of 3.999 mm in un-cracked honeycomb structure were obtained.
- Finally, the maximum crack tip opening under tension load in the cracked honeycomb structure were shown. The crack tip opening values increase with a decrease in rib thickness. For example, the maximum crack tip opening of 22.968 mm was obtained in the cracked honeycomb structure, t of 1 mm.

REFERENCES

1. **Osswald, T.A. and Menges, G. (2010),** Material science of polymers for engineers, 3rd Edition, Hanser Publishers, Munich.
2. **Calhoun, A. and Peacock, A. (2006),** Polymer chemistry – properties and applications, Hanser Publishers, Munich.
3. **Lboro, (2017),** Standard Terminology for Additive Manufacturing Technologies. The 7 categories of Additive Manufacturing. http://www.lboro.ac.uk/research/amrg/about/the7categoriesofadditivemanufacturing/ , Last access date: 19.12.2017
4. **Kumar D., Chawla A., Mukherjee S., Nakatani T., Ueno M. (2003),** "Prediction of Crushing Behaviour of Honeycomb Structures", International Journal of Crashworthiness,vol.8,no.3,pp.229-235.
5. **Hexcel, (2017),** HEXCEL Corp. Web Site, http://www.hexcel.com/Markets/ Last access date: 10.12.2017

6. **Global, (2017),** Global Spec Web Site. http://www.globalspec.com Last access date: 15.12.2017
7. **Aydıncak, I. (2007),** "Investigation of Design and Analyses Principles of Honeycomb Structures", MsC Thesis, Middle East Technical University, Aerospace Engineering Department,196 p, Ankara, Turkey.
8. **Barner, S. (2015),** "Mechanical Properties of Additive Manufactured Honeycomb Structures", MsC Thesis, Clemson University, Department of Mechanical Engineering, Master of Science in Mechanical Engineering, 110 p, USA.
9. **Berger, U., Hartmann, A., Schmid, D. (2013),** "Additive fertigungsverfahren –Rapid Prototyping", Rapid Tooling-Rapid Manufacturing.
10. **Panda, B.N. (2015),** "Design and Development of Cellular Structure for Additive Manufacturing.", MsC Thesis, National Institute of Technology, Master of Technology in Industrial Design, India.
11. **Wierzbicki, T. (1983),** "Crushing Analysis of Metal Honeycombs", International Journal of Impact Engineering Vol.1.2 pp. 157-174.
12. **John, (2017),** Mechanics of honeycomb. http://www.mse.mtu.edu/~drjohn/my4150/honey/h1.html Last access date: 12.01.2018
13. **Ingrole, A., Hao, A., Liang, R. (2017),** "Design and Modeling of Auxetic and Hybrid Honeycomb Structures for In-Plane Property Enhancement", Materials and Design. vol. 117 ,pp. 72–83.
14. **Schmidt I., Fleck N.A. (1999),** "Fracture Toughness of Honeycombs", Metal Foams and Porous Metal Structures, pp. 387-390.
15. **Schmidt, I., Fleck, N.A. (2001),** "Ductile Fracture of Two Dimensional Cellular Structures", International Journal of Fracture. vol. 111,pp. 324-342.
16. **Andrews E.W., Gibson I.J. (2001),** "The Influence of Cracks, Notches and Holes on The Tensile Strength of Cellular Solids", Acta Materialia. vol. 49, pp. 2975–2979.
17. **Jin M.Z., Zhao T.F., Chen C.Q. (2014),** "The Effects of Micro-Defects and Crack on The Mechanical Properties of Metal Fiber Sintered Sheets", International Journal of Solids and Structures vol. 51, pp. 1946–1953.

.

LITERATURE-BASED IDENTIFICATION OF BEHAVIOURAL MODULES FOR SOCIAL ROBOTS USING DESIGN STRUCTURE MATRIX

İlayda ÖZER, ilay2006@*hotmail.com* Atilim University, 06830, Ankara, Turkey

Zühal ERDEN, *zuhal.erden@atilim.edu.tr* Atilim University, 06830, Ankara, Turkey

ABSTRACT

Design of platform-based modular social robot families is important in order to quickly meet a diversity of needs regarding these types of robots. This paper describes a method for designing social robot families using behavioral modules. In this study, the tasks and behaviors of a group of social robots are compiled by using the literature and the relationships between the physical elements required for these behaviors are grouped by Design Structure Matrix method and social robot modules are identified. Within the scope of the study, some of these modules were designed and manufactured and physical models were developed.

Keywords: Platform-based robot family, modular robot, social robot, design structure matrix, behavioural module

1. INTRODUCTION

Robotic systems are becoming more and more popular in many fields such as defense industry, manufacturing, agriculture, healthcare and medical applications, industrial automation, and service systems. The use of modular design approaches in the design and production of robotic systems allows robots to be developed quickly and economically to meet changing customer needs. This approach requires companies to design robotic systems towards increasing their product variety. Product variety in robot design can be accomplished by developing platform-based robotic systems which form robot families. One may consider robot families as a special case of product families in mass customization [Tseng and Jiao, 2001]. A product family refers to a set of similar products that are derived from a common platform and yet possesses specific features/functionalities to meet particular customer requirements [Jiao et al., 2007]. In the platform-based modular design approach, robots to be used for different tasks can be designed by combining appropriate

modules on a common platform. One of the areas where this design approach can be used is social robots. A social robot is an autonomous or semi-autonomous robot that interacts or communicates with humans by following the behavioural norms expected by the people with whom the robot is intended to interact [Bartneck and Forlizzi, 2004]

Important application areas of social robots include health and/or elderly care, education and recreation practices, various tasks in the home or workplace environment, and various social and individual needs in public areas such as shopping centers, museums, government buildings, hospitals, parks. It is important to use a platform-based modular design approach that can quickly respond to different needs and expectations in the design of social robots that find such a wide application area.

As part of an undergraduate research project, the aim of this work is to determine and symbolically represent behavioral modules for a group of social robots in order to contribute to the design of platform-based social robot families. For this purpose, various tasks for a group of social robots in the literature perform have been studied and their behavioral characteristics are determined. The elements of social robots to perform these tasks are listed and the relationships among these elements are defined and grouped by using Design Structure Matrix method [Browning, 2001]. As a result of this clustering, 14 behavioural modules are defined and symbolically represented. Then, some of these modules are designed and manufactured, so as to physically develop a demonstrative social-robot family model in the laboratory.

The remaining part of this paper is organized as follows; Section 2 provides a brief literature review on social robot studies. Section 3 explains the identification and representation of behavioural modules for a group of social robots in the literature, using 3D Design Structure Matrix. Section 4 presents the design of a demonstrative social robot family using the behavioural modules. Finally, discussion and conclusion regarding this work is given in Section 5

2. LITERATURE SURVEY ON SOCIAL ROBOTS

Social robots are used to interact with humans with fully or semi-autonomous features to assist them in their daily routines to make life much easier. Nowadays, one of the requirements in robotics is to develop partner robots for assisting people in a living or working environment. Such robots that can guide people while communicating appropriately with them have been extensively researched. There are different socially serving robot types in that case for disabled patients, elderly people, waiter purposed robots, guide robots, hosting robots, therapy assisting robots and the others type. It is evident that the need for

social robots will increase gradually when considering the living conditions of today and tomorrow. Social robots not only make life easier, but they also play a role as a friend or helper. Social robots with a wide range of applications can be examined under the following groups according to the researches in the literature:

Waiter Robots/Service Robots/Guide Robots: These robots are used for service in places like hotels, restaurants, coffee shops and offices; as well as for guidance in places like museums, supermarkets, shopping centers and similar places. Waiter robots are designed for taking orders and organizing food serving for customers in a restaurant. These robots exhibit behaviors such as meeting customers, greetings, responding to questions, taking orders, describing directions, and serving. As examples of these robots Pepper (Lafaye et al., 2014) is a service robot working in a fast food restaurant that makes a pizza. CERO (Severinson-Eklund et al., 2003) is a robot who works and serves as an assistant. Guide robots can assist a person who needs help for social life in the indoor or outdoor. An example is a museum tour guide robot, called Minevra (Thrun, et al., 2000), which introduces the information for in the areas of social, political, cultural, scientific, and military history. XAVIER has the identity of a building guide robot which can accept commands to travel to different offices in the building, broadcasting camera images as it travels. A number of intelligent service robots have been developed to guide a building for visitors. (Simmons et al., 2000). NTU-I is an outdoor tour guide robot, which is constructed to provide autonomous guiding services on the campus of a university. Its goal is to provide educational content to university visitors in order to augment their university experience. (Chiang et al., 2008)

Robots working as patient caregivers: These robots help the elderly, children with disabilities, people living alone and with disabilities in homes or hospitals. These robots were made for purposes such as identifying the health conditions of the sick building and the elderly, helping them to walk, using regular medication, and the like. As an example of robots in this group; Pearl (Breazeal, 2002) is a robot nurse that measures blood pressure, pulse and sugar levels of patients. The Care-O-bot (Kittmann et al., 2015) is used as an assistant robot, helping patients to build up.

Entertainment Robots: These are toy-like social robots that address both big and small, play fun games, sing songs, tell stories. They are also robots that provide training for children with disabilities. As an example of robots in this group; eMuu and Muu2 (Bartneck and Forlizzi, 2004) robot is a smart robot used in the home. It is used for entertainment purposes in home environments. Leonardo (Stiehl and Breazeal, 2004) robot is an entertainment robot that does not move, but speaks and recognizes. AIBO (Hegel, et.al., 2007) is a robot inspired by robot dogs.

Assistant Robots: These robots are used in homes and workplaces. These robots are robots that people learn smartly to make things easier. Examples of what they do are: to make reminders, to set up phone connections, to send incoming messages, to check household electricity works, to detect and feel the emotional state of the person using this robot, to know what his owner likes and to behave accordingly. As an example of robots in this group; PaPeRo (Fong, et al., 2003) can live with people and help them in daily life. Vacuum Cleaning-A (Fink, et al., 2012) is a house cleaning robot. Assistant robots are assist human beings, typically by performing a job that is dirty, dull, distant, dangerous or repetitive, including household chores. They typically are autonomous and/or operated by a built-in control system, with manual override options.

In this study, characteristics of the above-mentioned groups derived from the literature are used to develop and conceptually describe several behavioral modules for social robots. The following section explains the methodology for identification of these behavioural modules using Design Structure Matrix method.

3. IDENTIFICATION OF BEHAVIOURAL MODULES FOR A GROUP OF SOCIAL ROBOTS

In order to identify the behavioral modules of social robots, the method applied in this study can be summarized as follows; Four different social robot scenarios have been developed for module determination study by using the basic working principles and application areas of social robots examined in the literature. Then, behaviors required to perform the robot tasks in these social robot scenarios to perform their duties are evaluated and the physical elements that have to be found in the robots are determined in order to obtain these behaviors. Then possible interactions among the physical elements are investigated. In the next phase of the study, interactions between the elements in the social robots that will perform the tasks specified in the above scenarios were determined using the Design Structure Matrix method (Browning, 2001). Using these interactions, physical elements are clustered so as to form behavioural modules. Details of each step for this methodology is given below:

The following social robot scenarios are developed for module identification in this study;

Home Monitoring Robot: In this scenario, a robot that can be integrated with an intelligent home system is considered. The robot checks the food items in the refrigerators and orders new ones, if any of them is about to finish. The robot also sends information to the security units by detecting gas leakage, smoke and similar dangerous situations that may occur in the house.

Patient Follow-up Robot: In this scenario, the robot measures the blood pressure, pulse, and fever of the patient and sends information to his / her relatives and doctor.

Entertainment Robot for Kids: In this scenario, the robot performs tasks such as showing movies to children, telling stories, playing games, and allowing parents to participate in these games remotely.

Assistant Robot: This robot is used to move household items, sweep or clean the required places, and can be remotely controlled when necessary.

At this stage of the method, the physical elements that can fulfill the robot behaviors required for the created scenarios are determined by using the literature. Relationships between these elements are shown by the Design Structure Matrix (Browning, 2001) model using four different interaction types defined in (Sosa et al., 2003) as structural, energy, signal and material. In this model, structural interaction represents physical connection for transferring loads and forces. Energy interaction shows heat energy, vibration energy, electrical energy, or noise. Signal interaction is used for transferring control signals from one component to another component. Finally, material interaction represents transferring air, oil, fuel, or water. Interaction between elements in the implementation of this method is expressed in (Helmer et al., 2010) by energy, signal, material dependencies and the fact that the two elements are spatially interdependent. These four types of interactions are coded as "+2", "+1", "0", "-1" and "-2", which are shown in Table 1 with their meanings.

Table 1. Interaction Types and Codes (Helmer et al., 2010)

Interaction Code	Explanation of Interaction Code
+2	Interaction and adjacency between the elements are necessary for functionality.
+1	Interaction is necessary but not adjacency.
0	No affect to each other.
-1	Refrain from interaction for functionality.
-2	Refrain from interaction and also from adjacency.

In the present study, 45 physical elements are extracted from the literature survey on social robots such that they can be used to fulfill the behaviors of social robots described in the above scenarios. Then, the interactions between these elements are represented in a DSM using the above scale. As an example, Figure 1 depicts part of the DSM structure for the interactions among 14 physical elements.

	Processor	Distance Sensor	Motor 1	Motor Driver 1	Wheel	Mechanism	Motor 2	Motor Driver 2	GSM	GPS	Touch Screen	Speaker	Loudspeaker	Database
Processor		1		1				1	-2	-2	1	1	1	2
Distance Sensor 1	1													
Motor 1				1	2				-1			-1		
Motor Driver 1	1		1											
Wheel 1			2											
Mechanism							2							
Motor 2						2		1	-1					
Motor Driver 2	1						1							
GSM 1	-2		-1				-1							
GPS	-2		-1				-1							
Touch Screen	1													
Speaker	1		-1											
Loudspeaker	1													
Database 1	2													

Figure 1. DSM representation of interactions between some physical elements for social robot behaviours.

Behavioural modules required for the social robot scenarios in this study were developed by grouping the interactions between the physical elements in the Design Structure Matrix. A total of 12 behavioral modules and their schematic representations are developed in this study. A brief description of each behavioural module is given below. Schematic representations for the Tracking Module and the Load Transport Module are given in Figure 2 and Figure 3, respectively, as example representations.

1. Tracking Module: This module allows a robot to acquire the behavior of following a person or an object. It is composed of a processor with an embedded software, a distance sensor, a motor driver, a motor and wheels. The distance data from the distance sensor in the module is processed to obtain distance information between the robot and the object to be tracked. Based on this information, commands are provided by the processor to enable the motor to operate as desired. The schematic representation of the tracking module is given in Figure 3.

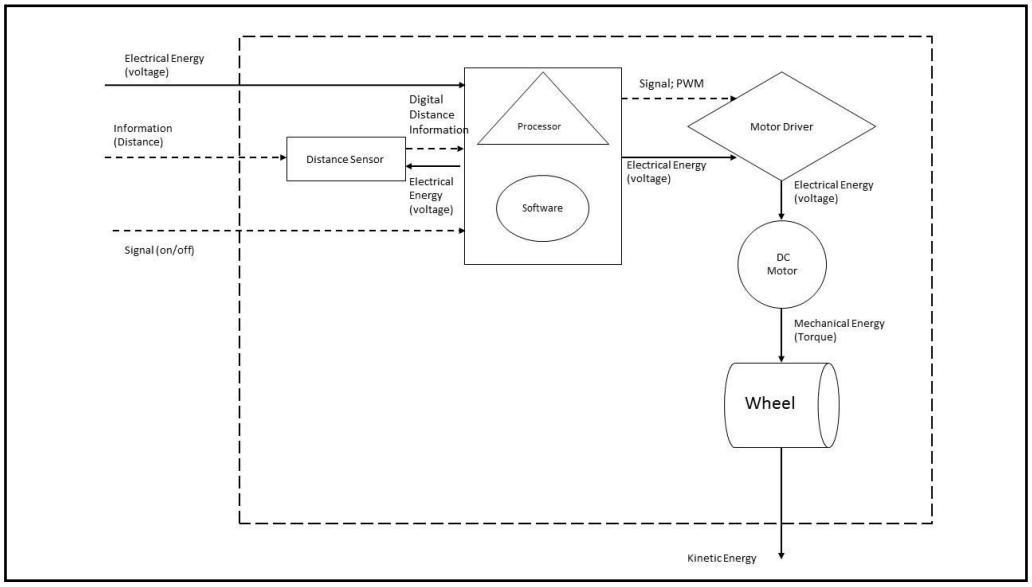


Figure 2. Schematic representation of Tracking Module.

2. Transportation Module: This module allows a robot to move an object from one place to another. It consists of a processor, weight sensor, motor, motor driver and a suitable mechanism. The data from the weight sensor in this module conveys the weight information of the load to be carried by the robot. Using this information, the processor calculates how much the motor will rotate and the necessary commands are sent to the motor driver. The desired load is carried by the mechanism. Figure 3 depicts schematic representation of the transportation module.

3. Firefighting Module: This module allows a robot to call the fire department in case of a fire in an environment. It consists of a processor, GSM and GPS. The processor sends the calling command to the GSM, with an input fire command. Then, the position information of the fire zone is reported by the processor using GSM.

4. Entertainment Module: This module allows a robot to entertain children by singing, playing music, telling stories, playing films. There is a processor, a touch screen, a speaker and a microphone. It is activated by selecting one of the options presented on the touch screen. With the outgoing command of the processor, the desired option is realized.

5. Health Module: This module allows a robot to regularly check people for health conditions. It consists of a processor, a pulse sensor, a blood pressure sensor, a sugar measuring sensor, a sensor for measuring fever, a screen and a buzzer. All data received from these sensors is sent to the processor and compared with acceptable levels. If the measured data is within the acceptable limits, it is reflected on the screen. Otherwise, the buzzer starts emitting sound to give a warning and this means that the person should visit a doctor.

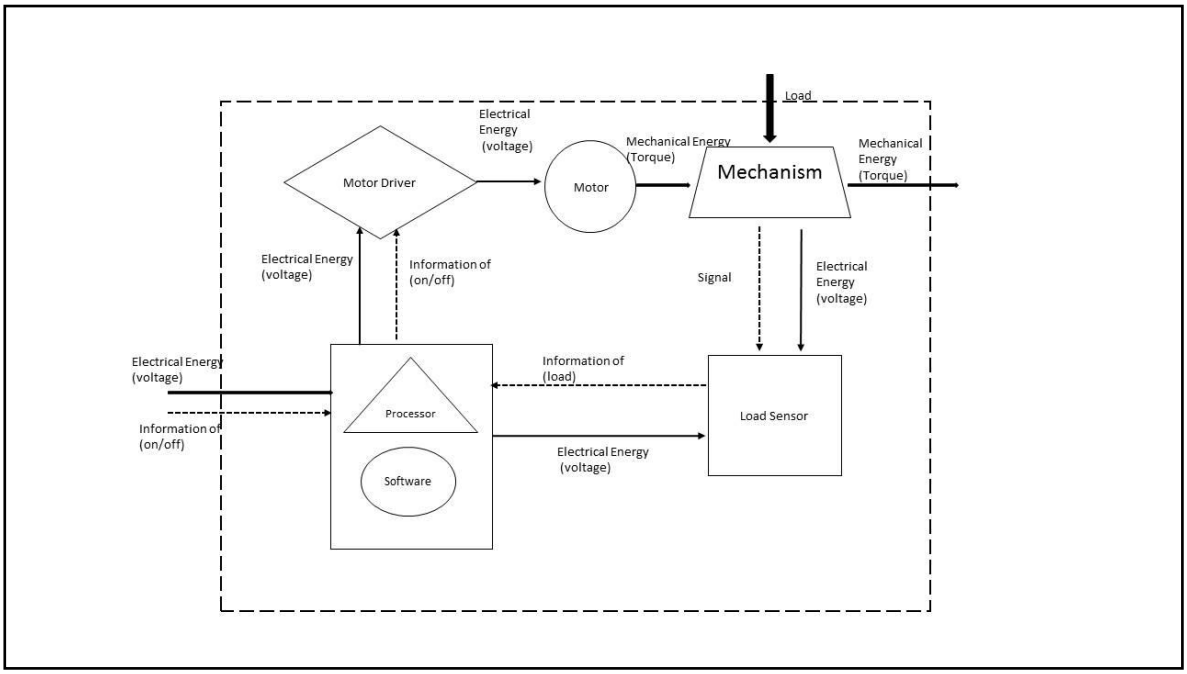


Figure 3. Schematic representation of transportation module

6. Motion Module: This module is used for a robot to move from one place to another. It consists of a processor, motor and motor driver, and wheels. With the command from the processor, the motor driver allows the motor to run and the robot moves to the desired point.

7. Collision avoidance module: This module is used to prevent a robot from crashing into obstacles during its motion. This module is composed of a processor, distance sensors, motor, motor driver and wheels. Information about an obstacle detected by the distance sensor is sent to the processor and the robot is allowed to change its path.

8. Carbon monoxide detection module: This module controls the level of carbon monoxide in the environment. It consists of a processor, a gas sensor and a buzzer. The information from the gas sensor is transmitted to the processor. If any gas leakage is detected, then it produces a buzzer warning.

9. Cleaning Module: This module allows a robot to clean the environment. It consists of a processor, a motor, a motor driver, a cleaning motor and a container. The motor runs with the command from the processor, garbage is collected by the help of a cleaning motor and transferred to the container.

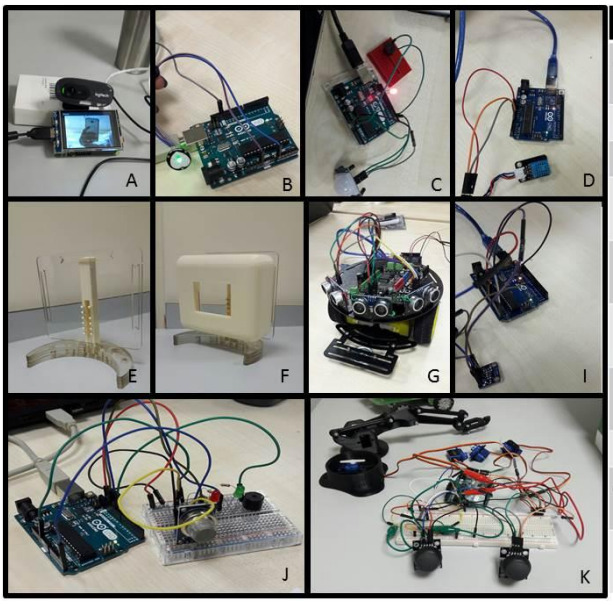
10. Communication Module: This module allows a robot to communicate with other electronic devices. It consists of a processor, X-bee module and GSM. The processor is activated by the incoming command and sends the information to the operator via the X-bee module. This information is also sent by GSM to the user of the robot.

11. Security Module: This module is designed to provide home security. It consists of a processor, motion sensor, camera, joystick and GSM. The information from the motion sensor and the information from the camera are inspected to check whether there is any security problem. This information is controlled by the processor. Remote control is provided by the joystick. If any security problem is detected, either police or houseowner is called.

12. Fire Extinguishing Module: This module allows a robot to intervene in case of fire in the house. It consists of a processor, motor, motor drive, pipe and pump, container. The instruction given by the processor helps to extinguish the fire by using the pipe and the pump with the water in the container. The control of the pipe and the pump takes place with the engine. With the command coming from the processor, the motor driver is actuated and the first intervention of the fire occurs.

4. PHYSICAL IMPLEMENTATION

In the next phase of this study, some of the above-mentioned behavior modules are designed, manufactured and physically implemented in the laboratory. Since this research is conducted at the undergraduate level, the simplest modules were physically realized because of the limited budget and manufacturing possibilities. Platform design has been realized and technical drawings have been prepared and manufactured. In addition, the necessary elements for the modules were purchased, necessary software was prepared in practice and connections were made. In Figure 4, manufacturing and assembly works related to the physical model of this robot are given.



Letter	Equipments
A	Usb Camera with Rasberry pi and screen
B	Pulse Sensor with Arduino Uno
C	PIR Sensor with Arduino Uno
D	Humidity sensor with Arduino Uno
E	The skeleton part of the modular robot Design
F	The implementation part of the modular robot Design
G	The obstacle avoidance of the modular robot
I	Light sensor with Arduino Uno
J	Robotic arm of the modular robot
K	MQ-2 gas detection sensor with Arduino Uno

Figure 4. Manufacture and assembly of modules for physical implementation

The devices shown in Figure 4 are the equipment that will form the modules. Details of these equipments will be explained below. The equipment shown with the letter A will be used in the security module, and the image will be captured with the USB camera and processed by the Raspberry Pi processor to be transferred to the Raspberry Pi screen. The equipment shown with the letter B measures the heart rhythm with the pulse sensor and reflects it on the screen with the Arduino Uno processor. This information is for health check and it will be used for the health module. The equipment shown with letter C detects the presence of movement with the PIR sensor and processes the resulting data with the Arduino Uno processor. This equipment, which will be used for the safety module, gives a buzzer warning when there is any movement. The equipment shown with the letter D operates with the Arduino Uno by measuring the humidity of the environment with a humidity sensor. This information will be used for the security module. Structural parts shown with E and F are the parts forming the main platform where the robot modules will be placed. The equipment shown with the letter G is the equipment that will allow the modular robot to avoid obstacles. It detects the distance with the HC-SR04 ultrasonic sensor on it and processes it with the Romeo V2 card. The Romeo V2 processor card sends commands to make the robot run away. This equipment is designed as a hijacking module. The equipment indicated by the letter I is controlled by the Arduino Uno operator command with information from the light sensor. This information will be used in the security module. The equipment shown with the letter J is robotically cabled. The module will be used by the robot in a transport module for transport from one cistern to another. The equipment indicated by the letter K is used to check whether the fire inside the house is being controlled by the Arduino Uno operator of the information received by the gas sensor. This equipment will be used for the fire module.

In Figure 5, the design of the main platform is shown as a solid model. In this design, Arduino Mega and Rasberry Pi processor cards will be placed into the platform. Raspberry Pi screen is located in the middle part in the shape of a rectangle. All modules will be connected to this main platform.

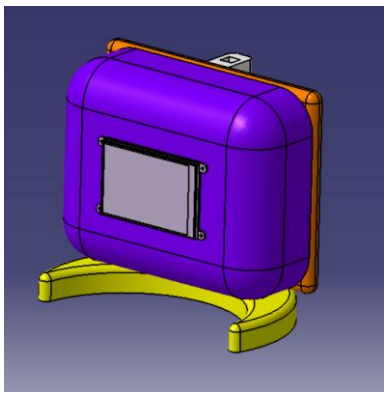


Figure 5. Solid model of the robot platform

5.CONCLUSION

Today's rapid technological developments show that social robots are inevitably involved more and more in our daily lives. The design of social robot families that can respond to different needs or be used in different applications is considered as an important research topic. This paper explains a study on the identification of behavioral modules for social robots based on the information obtained from the literature, by using the Design Structure Matrix (DSM) . The behaviors required for the generated robot scenarios are defined, and the relationships among the physical elements that enable robots to perform these behaviors are defined and grouped. Some of these behavioral modules are designed and manufactured in the laboratory. It was assessed that this work, conducted with a literature-based sampling, would contribute to the future development of a general systematic method for the design of social robot families.

ACKNOWLEDGEMENTS

The authors would like to thank to Yiğit Bulgur, Sevra Erşimşek, M. Raşit Ilgaz, Y. Taha Kılınç, H. Berkay Tanyeli, Ayhan Yelli and Mediha Zubari for their valuable contribution in this research.

REFERENCES

1. **Bartneck, C.,and Forlizzi, J., (2004)**, A design-centred framework for social human-robot interaction. Proc. *13th IEEE International Workshop on Robot and Human Interactive Communication, RO-MAN 2004.* pp. 591-594)
2. **Breazeal, C., (2000),** "Proto-conversations with an anthropomorphic robot", *Robot and Human Interactive Communication, 2000. RO-MAN 2000. Proceedings. 9th IEEE International Workshop on* (pp. 328-333). IEEE.
3. **Browning, T. R., (2001),** Applying the design structure matrix to system decomposition and integration problems: a review and new directions. *IEEE Transactions on Engineering Management*, 48(3), pp. 292-306.
4. **Chiang, K. H., Tseng, S. H., Wu, Y. H., Li, G. H., Lam, C. P., & Fu, L. C. (2008),** "Multisensor-based outdoor tour guide robot NTU-I", *SICE Annual Conference, 2008* (pp. 1425-1430). IEEE.

5. **Fink, J., Mubin, O., Kaplan, F., & Dillenbourg, P., (2012),** "Anthropomorphic language in online forums about Roomba, AIBO and the iPad", *Advanced Robotics and its Social Impacts (ARSO), 2012 IEEE Workshop on* (pp. 54-59). IEEE.
6. **Fong, T., Nourbakhsh, I., & Dautenhahn, K., (2003),** "A survey of socially interactive robots", *Robotics and autonomous systems*, *42*(3-4), pp. 143-166.
7. **Hegel, F., Lohse, M., Swadzba, A., Wachsmuth, S., Rohlfing, K. and Wrede, B., (2007),** "Classes of Applications for Social Robots: A User Study", *Proceedings of the 16th IEEE International Symposium on Robot and Human Interactive Communication* (RO-MAN 2007, pp.938-943.
8. **Helmer, R., Yassine, A., and Meier, C., (2010),** "Systematic module and interface definition using component design structure matrix", *Journal of Engineering Design*, 21(6), pp. 647-675.
9. **Jiao, J., Simpson, T. W. and Siddique, Z., (2007)**, Product Family Design and Platform-Based Product Development: A State-of-the-Art Review. *Journal of Intelligent Manufacturing*, 18(5), pp.5-29.
10. **Kittmann, R., Fröhlich, T., Schäfer, J., Reiser, U., Weißhardt, F., & Haug, A., (2015),** "Let me introduce myself: I am Care-O-bot 4, a gentleman robot", *Mensch und computer 2015–proceedings*, pp. 223-232.
11. **Lafaye, J., Gouaillier, D., and Wieber, P. B., (2014),** "Linear model predictive control of the locomotion of Pepper, a humanoid robot with omnidirectional wheels", Proceedings of the *14th IEEE-RAS International Conference on Humanoid Robots (Humanoids),* pp. 336-341.
12. **Severinson-Eklundh, K., Green, A., and Hüttenrauch, H., (2003),** "Social and collaborative aspects of interaction with a service robot", *Robotics and Autonomous systems*, *42*(3-4), pp. 223-234.
13. **Simmons, R., Fernandez, J. L., Goodwin, R., Koenig, S., and O'sullivan, J. (2000),** "Lessons learned from Xavier", *IEEE Robotics & Automation Magazine*, 7(2), 33-39.
14. **Stiehl, W. D., & Breazeal, C., (2004),** "Applying a "somatic alphabet" approach to inferring orientation, motion, and direction in clusters of force sensing resistors", *Intelligent Robots and Systems, 2004.(IROS 2004). Proceedings. 2004 IEEE/RSJ International Conference on* (Vol. 3, pp. 3015-3020). IEEE.
15. **Thrun, S., Beetz, M., Bennewitz, M., Burgard, W., Cremers, A. B., Dellaert, F., Fox, D., Hahnel, D., Rosenberg, C., Roy, N., Schulte, J. and Schulz, D. (2000).** Probabilistic algorithms and the interactive museum tour-guide robot minerva. *The International Journal of Robotics Research*, *19*(11), 972-999.
16. **Tseng, M. and Jiao, J. ,(2001),** *Mass Customization*. Handbook of Industrial Engineering, Gaviel Salvendy (Ed.), Wiley, New York.

LAY-UP DESIGN OPTIMIZATION FOR THE LOADED-CARRYING TUBULAR STRUCTURE MADE OF ORTHOTROPIC COMPOSITE

Sergey SHEVTSOV, *sergnshevtsov@gmail.com* South Center of Russian Academy, 344006, Rostov on Don, Russia

Igor ZHILYAEV, *zhilyaev@mail.com* South Center of Russian Academy, 344006, Rostov on Don, Russia

Natalia SNEZHINA, *snezhina@gmail.com* Don State Technical University, 344006, Rostov on Don, Russia

Jiing-Kae WU, *jiingkae.wu@gmail.com* National Kaohsiung University of Science and Technology, 81157, Kaohsiung City, Taiwan R.O.C.

ABSTRACT

The main requirements for high loaded composite structures experiencing the forces and torques with varied intensity and orientation, are the specified mechanical stiffness to prevent the inadmissible deformations and some structural failure. Examples of these structures are aircraft spars, stringers, wing panels etc. Usually, such parts are manufactured using reinforced composites with orthotropic structural symmetry, which provides the best combination of mechanical stiffness, strength and weight parameters. This paper considers a cantilevered long tube-like composite structure with varied cross-section that is manufactured by winding of glass fiber unidirectional tape. The operational loads include the bending forces, which cause the beam deflections along the directions of maximum and minimum stiffness of the tube, and also distributed torque causing the twist deformations. To increase the stiffness of the structure, hence to reduce the strain energy and peak von Mises stress the search of the best lay-up scheme and its angles is performed. The wall thickness, lay-up scheme, and the total number of layers are assumed as unchanged along the tube, whereas its mechanical properties are considered as homogenized and depending on the lamina properties and its lay-up scheme only. This search is performed by using the finite element model of the structure for three different, and most critical load scenario. The choice of the pseudo-optimal solution is made on the basis of an expert decision that excludes from the consideration of the solution with sharply degraded indicators at least at one load scenario.

Keywords: Structural optimization, composite structures, lay-up design

1. INTRODUCTION

The glass/carbon fiber composites are widely used in the design of various aircraft and rotorcraft components such as stringers, the spars of the rotor blades, the stiffened panels of the wings and stabilizers, which have predominantly a thin-walled geometry and are made of composite laminates that most often are adopted as orthotropic. The main requirements for these parts are the specified dynamic and endurance properties to provide the aerodynamic quality and reliability of the aircraft assembly at the different flight conditions with limited part weight [Baker et al. 2004]. Most of these parts are manufactured by laying-up or winding of the unidirectional lamina and curing in closed molds or autoclaves where the parts are exposed to the controlled pressure and temperature according to the predetermined laws.

The rapid growth of composite applications in aircraft and rotorcraft industries, the very complex mechanical behavior of anisotropic composite materials require new structural strength, rigidity, modeling, optimization and failure prediction methods using virtual testing analysis method, which is a concept with several attributes and is to be understood as the simulation of aircraft structure [Taylor, 2004; Ostergaard et al., 2011]. In the survey paper [Rao, 2015] the main milestones of development of the optimization and its applications in aircraft systems design, especially, in the context of the composite structures, are considered. According to the concept, which is present here, a full workflow process of the composite structures optimization consists of the following three phases:

- Free size or topology optimization;

- Detailed design: ply-bundle sizing with ply-based FE (finite element) modeling;

- Detailed design: Ply stacking sequence optimization.

During the second and third phases the composite plies with the different orientation are chosen and shuffled to determine the optimal stacking sequence for the given design optimization problem while satisfying some additional manufacturing constraints. As outlined in the article [Gillet, 2010], such a composite structure optimization involves a large number of both the design variables and the objectives. As a result, designers must consider only a restricted set of parameters among the most influential. In this paper the author uses the following parameters of optimized laminates: mass per unit area of an elementary plate, the compliance of elementary plate, and the stiffness of a composite plate experienced by the uniform pressure. The stacking sequence, total number of plies and prepreg materials are accepted as the design variables, whereas the mass and the total number of layers are constrained. It was established that the ply orientation seems to have a significant influence on the most common mechanical criteria (mass, rigidity, etc.). Using a more refined orientation set can improve the mechanical performance when accounting for intralaminar

stresses, or for laminates made of a few anisotropic plies. In most engineering applications, when there are a sufficient number of plies, it is entirely warranted to restrict the layers' orientations to a limited number of predefined values. The similar technologies and appropriate soft tools are developing and improving by the leaders of aircraft industry such as e.g. Altair Engineering GMBH [Zhou, 2011].

Because the dynamic behavior of the aircraft structures at the operating conditions when the structures work at the loading that is below the strength limits is very important, many investigations are devoted to the study of composites at the elastic conditions. The main assumptions, which should be used at the modeling such the elastic phenomena, were formulated in the early fundamental work [Zang & Evans, 1988]. These assumptions include: (i) The results obtained assume that the composite material may be modeled as a single phase anisotropic homogeneous continuum. This assumption is adequate for the elastic constants, provided sufficient consideration is given to the interface but is unlikely to apply to strength properties. (ii) There is a representative volume element whose mechanical properties are equal to the average properties of the particular composites. (iii) The constituent materials are linearly elastic and homogeneous, but in general anisotropic. (iv) Linearity of the stress-strain relations is assumed to hold for the composite material.

Most of investigations that have been implemented in this area use the finite element modeling for solving the forward structural mechanics problem combined with some optimization algorithms based on the soft computing concepts, e.g., genetic algorithm [Herencia et al., 2008; Satheesh et al., 2008; Gyan et al., 2012], shuffled Frog-Leaping (SFL) algorithm [Mohan Rao & Lakshmi, 2012] for lay-up sequence optimization of laminate composite structures. However, there are no theorems to prove that a soft algorithm ensures the achievement of a single global optimum. Therefore, some researchers use analytical approaches to optimize the simplest composite systems [Oktem & Soares, 2011] or empirical methods for more complex ones [Kaleemulla & Siddeswarappa, 2010, Metiche & Masmoudi, 2013].

Some works are devoted to the optimization of composite structures subjected to aeroelastic or hydraulic dynamic loading. The common part of such works is the subtask of simulating aeroelastic actions on a composite structure. In particular, the paper [Guo et al., 2003] examined phenomenon of bend-torsion coupling rigidity for achieving an optimal design of a composite wing with a maximum flutter speed. In order to ensure an effective way to achieve an optimal lay-up, two optimization approaches have been investigated. In the first approach, the flutter speed was set in the objective function directly. In the second approach, optimization was carried out to minimize an objective function containing the torsional and coupling rigidities rather than flutter speed. Kalavalapally and co-workers [Kalavalapally, 2006] solving a multidisciplinary optimization problem for a lightweight torpedo model

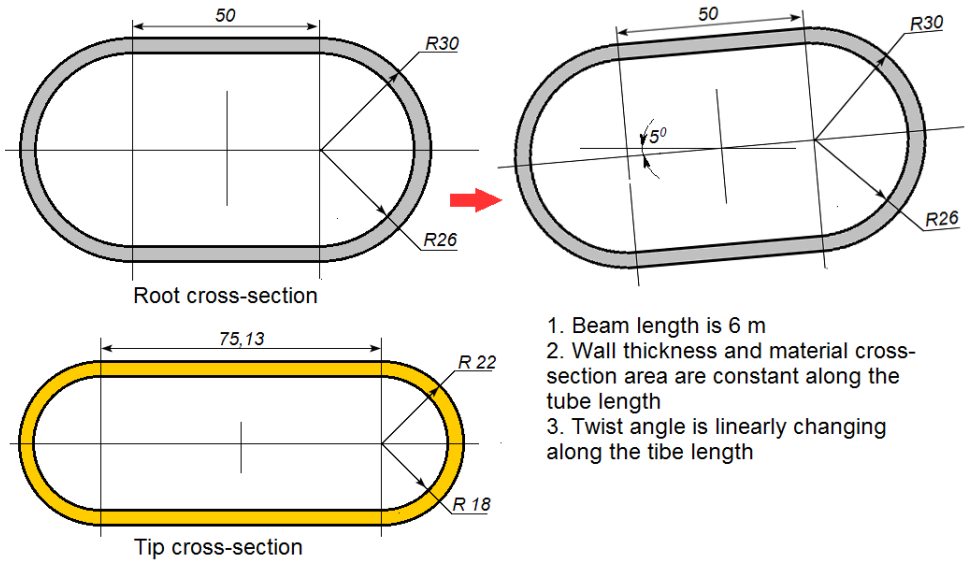
subjected to underwater explosions, observed that the composite torpedo model is stronger and lighter than the metallic design when subjected to an underwater explosions at a given standoff distance. The paper [Oganesyan et al., 2016] presented the numerical method and results of the structural optimization of the mounting zones of wind turbine blades to diminish and flatten the stress distribution at the action of the extremely stressed wind load on the blade, which has the stiff carbon/epoxy composite skin and less stiff lightweight core body. When composite structure with complex shape is studied, its CAD model needs to be used for the virtual aerodynamic testing by the means of FE tools. The main objective of the paper [Shevtsov et al., 2017] is the optimization of wall thickness and lay-up sequence of shell-like cowling made of the transversely isotropic composite. The used approach assumed conversion of the CAD model of the cowling surface to the FE representation, then its wind tunnel testing simulation at the different orientation of airflow to find the most stressed mode of flight that uses at the formulation of the loading pressure conditions for the forward problem of structural mechanics. The optimization problem used the global strain energy calculated within the optimized shell as the objective, whereas the total weight of the optimized part wad considered as design constraint.

The important conclusion that can be made taking into account the surveyed works is multiobjective nature of most composite optimization problems. Such a conclusion can be made on the base of present paper, which is broken onto several parts. First, we present a brief description of the optimized composite structure, which is the tube-like cantilever slender beam experiencing distributed bending and torsion forces. Then we determine the elastic properties of laminates used in the modeled tube. We start from the mechanical properties of reinforcing fibers and epoxy resin, then we determine the properties of the unidirectional lamina and, finally, the laminate properties. Our optimization approach contains three sequential stages. The preliminary stage is based on the consideration of the angular distribution of all engineering constants of laminates. This analysis allows us to choose the enough small set of "candidate" lay-ups, which should be used at the modeling of the mechanical response of the studied structure at three different load scenarios. The "candidates" of next, higher level are appointed for the final dynamic test, which includes applying full load to the better structures and gives us the possibility to make the expert decision about final choice of quasi-optimal structure. However, this final choice can be made only taking into account of manufacturing and other constraints.

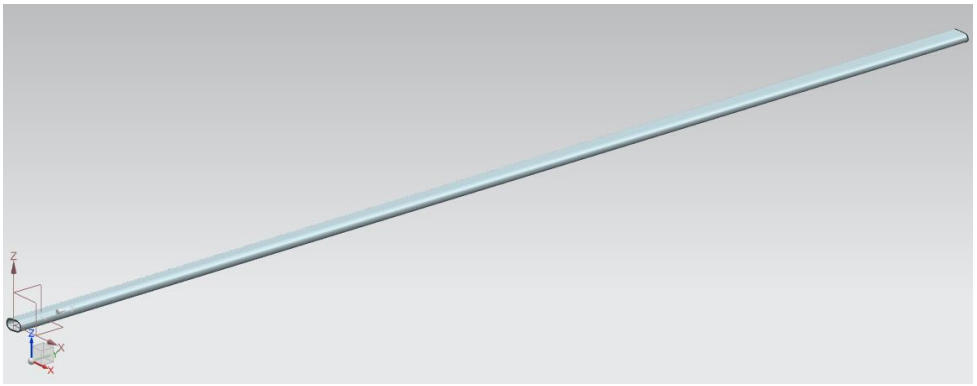
2. MODELED STRUCTURE: GEOMETRY AND OPERATING CONDITIONS

The composite beam studied in this research is a slender tubular structure with optimizing prepreg lay-up sequence. Its cross-section is comprised of two straight stripes and two half-circles, each of them is made of eight laminated layers (see Fig. 1), that is similar to studied

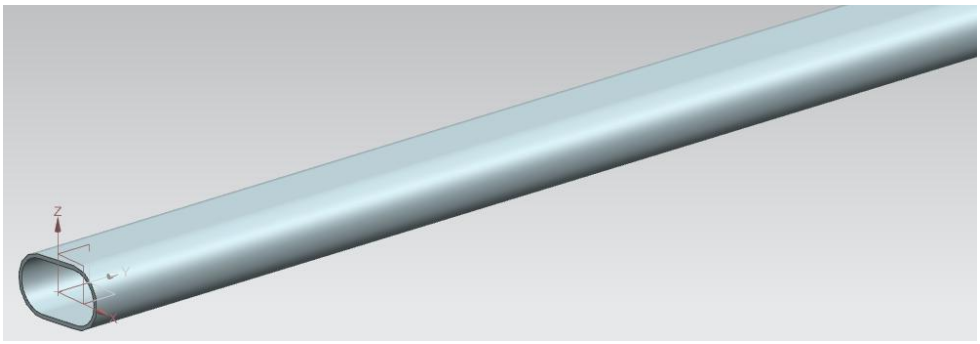
in [Hodges, 2006]. The CAD model of the structure was built by using NX CAD (Siemens ®) capabilities, then converted into the Structural Mechanics Comsol Multiphysics environment.



(a)



(b)



(c)

Fig. 1. Sketch of the beam cross-section (a), 3D view of the CAD model and magnified view on the cross-section of optimizing structure

In order to define the external loads and structural anisotropy of the laminate, the curvilinear coordinate systems ($\mathbf{e}_1$, $\mathbf{e}_2$, $\mathbf{e}_3$) have been intended on the external surface of the tube. To do this, we used a diffusion method which solves Laplace's equation $\Delta U = 0$ and computes the vector field as $-\nabla U$. The boundary conditions were set as follows: on the internal surface $U_{\text{int}} = 1$, $U_{out} = 1$ on the outer surface, and $-\mathbf{n} \cdot \nabla U = 0$ on the end faces. The normal to the surface is assigned as $\mathbf{e}_1 = -\nabla U / \left| -\nabla U \right|$. The second component is the unit vector parallel to

the beam longitudinal axis, and third unit vector $\mathbf{e}_3$ is normal to the plane $(\mathbf{e}_1, \mathbf{e}_2)$. The curvilinear coordinates are presented in Fig. 2.

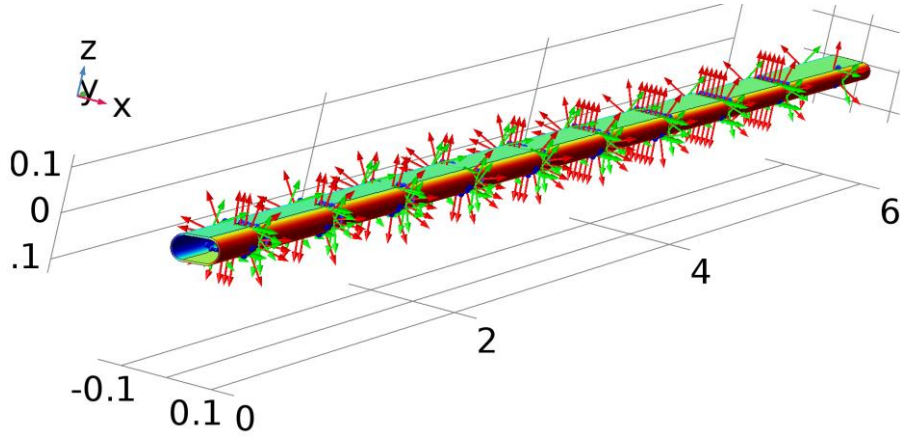


Fig. 2 Curvilinear local coordinate systems on the beam surface

The root end face is fixed $(u, v, w) = 0$, where u, v, w are the displacements along the global axis x, y and z, respectively. Three different external loads can be applied alternately or together:

$$F_{tors} = \begin{cases} 0 \cdot \mathbf{e}_1 \\ 0 \cdot \mathbf{e}_2 \\ 10^4 \cdot H(x - 3{,}1) \cdot \mathbf{e}_3 \end{cases} \quad (1)$$

$$F_{bend} = \begin{cases} 0 \cdot \xi \\ 70 \cdot yload \cdot \eta \\ 45 \cdot zload \cdot \zeta \end{cases} \quad (2)$$

In Equation (1) for the twisting load $H(x, \delta x)$ is the smoothed step-function with the coordinate of step x and smoothing width δx. The bending force F_{bend} is defined by the components in the global coordinate system whose unit vectors are (ξ, η, ζ) and by the parameters $yload, zload$, which can take alternatively or together having the values 0 and (or) one.

The FE mesh has been constructed for the given geometry as swept mesh (see Fig. 3) consists of 128,893 domain elements, 37,959 boundary elements, and 1,350 edge elements. The number of degrees of freedom solved for is 625,409.

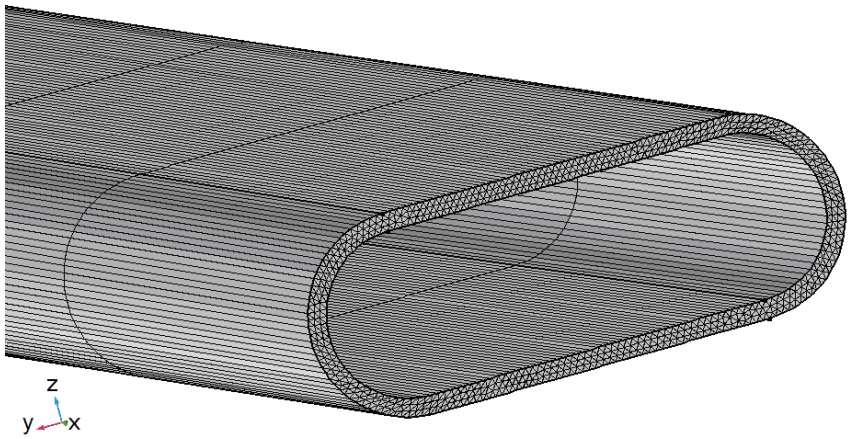


Fig. 3. FE mesh used at the mechanics problem

3. DETERMINATION OF LAMINA PROPERTIES

All numerical and experimental studies have been implemented for glass fiber reinforced epoxy based prepreg VPS-7. Initially, the properties of the fibers and resin, which was accepted as isotropic, have been studied experimentally using testing machines Galdabini. The samples of resin and bundles of the fibers were experienced by tensile forces with strain monitored by extensometers. During these experiments the following elastic moduli have been obtained (see Table 1).

Table 1. Mechanical properties of composite constituents

Components	Young module, GPa	Poisson ratio	Shear module, GPa
Glass fibers	87.5 (longitudinal)	$\nu_{12}=\nu_{13}=0.255$	$G_{12}=G_{13}=2.594$
Epoxy resin	2.55	0.364	0.94 (calculated)

The properties of unidirectional lamina, which has transversely isotropic symmetry, were determined both numerically and experimentally for the samples with laying-up scheme $(+30^0;-30^0)_s$ and fiber volume fraction V_f=0.534. In order to determine the parameters inaccessible through the experimental test, we used the mixing rule and FE modeling by Abaqus capabilities [**Barbero, 2013, Ha et al., 2010**]. The values of found properties are shown in Table 2, where bold numbers denote the most reliable values, which have been used in the follow-up investigation. These values have been used for determination of elastic moduli of laminates of chosen structures.

Table 2. Mechanical properties of lamina

Elastic module	Determination method		
	Experiment	Mixing rule	FE modeling
E_1, MPa	**49500±2500**	**49000**	**48090**
E_2, MPa	6000±500	5500	**8042**
ν_{12}	**0.315±0.015**	**0.31**	**0.299**
ν_{23}	NA	NA	**0.459**
G_{23}, MPa	2600±200	2000	**2758**
G_{12}, MPa	NA	NA	**2847**

Remark: Index 1 corresponds to the longitudinal ply orientation (along the fibers), whereas index 2 - to the transversal ply orientation

4. DETERMINATION OF ELASTIC MODULI FOR LAMINATES

In order to diminish formation of the residual stress and strains, which can arise during cure, we use only 8-layers symmetric balanced laminates in our investigation. All used schemes of lamina stacking are shown in Fig. 4 with their designations.

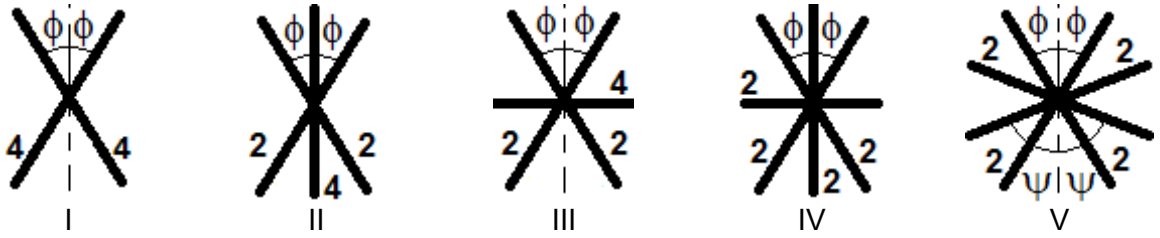


Fig.4. Used schemes of lamina stacking

For each lay-up scheme the elastic moduli were determined independently by two methods: by the finite element method and on the base of the classical laminates theory. The last one proposes the following relationships for the elastic moduli of laminate

$$\overline{E}_x = \frac{1}{a_{11}H}; \quad \overline{E}_y = \frac{1}{a_{22}H};$$
$$\overline{G}_{xy} = \frac{1}{a_{66}H}; \qquad (3)$$
$$\overline{\nu}_{xy} = -\frac{a_{12}}{a_{11}}; \quad \overline{\nu}_{yx} = -\frac{a_{12}}{a_{22}}$$

where indices x, y correspond to the longitudinal and transversal directions of laminate, respectively, $a_{i,j}, i = 1,2,6$ are the elements of {a} matrix [**Gibson, 1994, Voyiadjis & Kattan, 2005**], and H is the laminate thickness.

The FE model for determining of elastic moduli simulated the experimental tests according to the standards ASTM D 3039-95 and ASTM D 5379-93 with the numerical methods for the

accurate identification of the modules described in [**Chinchan, 2014**]. All modules are averaged by integration along the lines where the pure tensile or shear occur (see Fig.5).

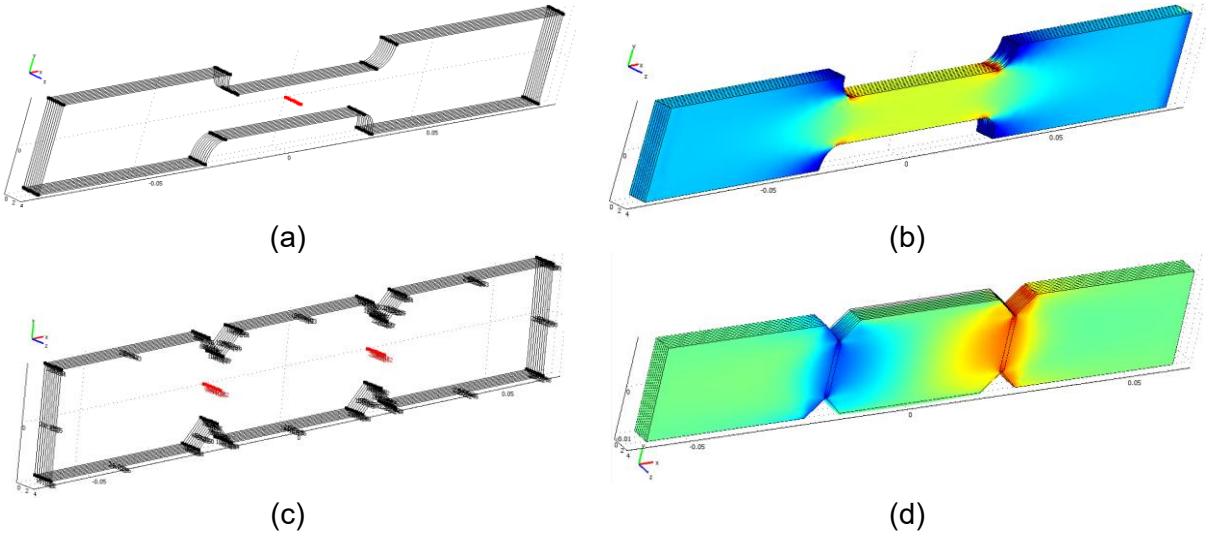


Fig.5. Geometry (a, c) and postprocessing results (b, d) of models simulating the mechanical tests ASTM D 3039-95 "Test Method for Tensile Properties of Polymer Matrix Composite Materials" (a, b) and ASTM D 5379-93 "Test Method for Shear Properties of Composite Materials" by V-Notched Beam Method" (c, d)

Geometry of the FE models consists of 8 separated layers, each of which is characterized by its orientation of lamina. Numerical calculation of elastic modules has been implemented for all lay-ups (see Fig. 4) with the step $\Delta\phi=10^0$ of lamina orientation. Both moduli calculation methods have been demonstrated a good correspondence, but FE method provides higher accuracy at the calculation of the Poisson ratios. Some examples of obtained results are shown in Fig. 6. Each point on these plots at the chosen angle ϕ (or ϕ and ψ for the scheme V) represents the values of effective elastic moduli for the laminate with given lay-up. Note that according to the homogenization hypothesis this laminate is considered as the solid body with uniform structure.

On the next stage of investigation the angular dependencies of the effective moduli were investigated. In order to avoid the significant reduction of the structural rigidity in some directions these dependencies should not have sharp drops, corresponding to these directions. Some examples of such angular dependencies are shown in Fig. 7. These dependencies have been used for the preliminary selections of the "candidates" lay-ups, which have been further used to test them in mechanical testing of the optimized slender structure.

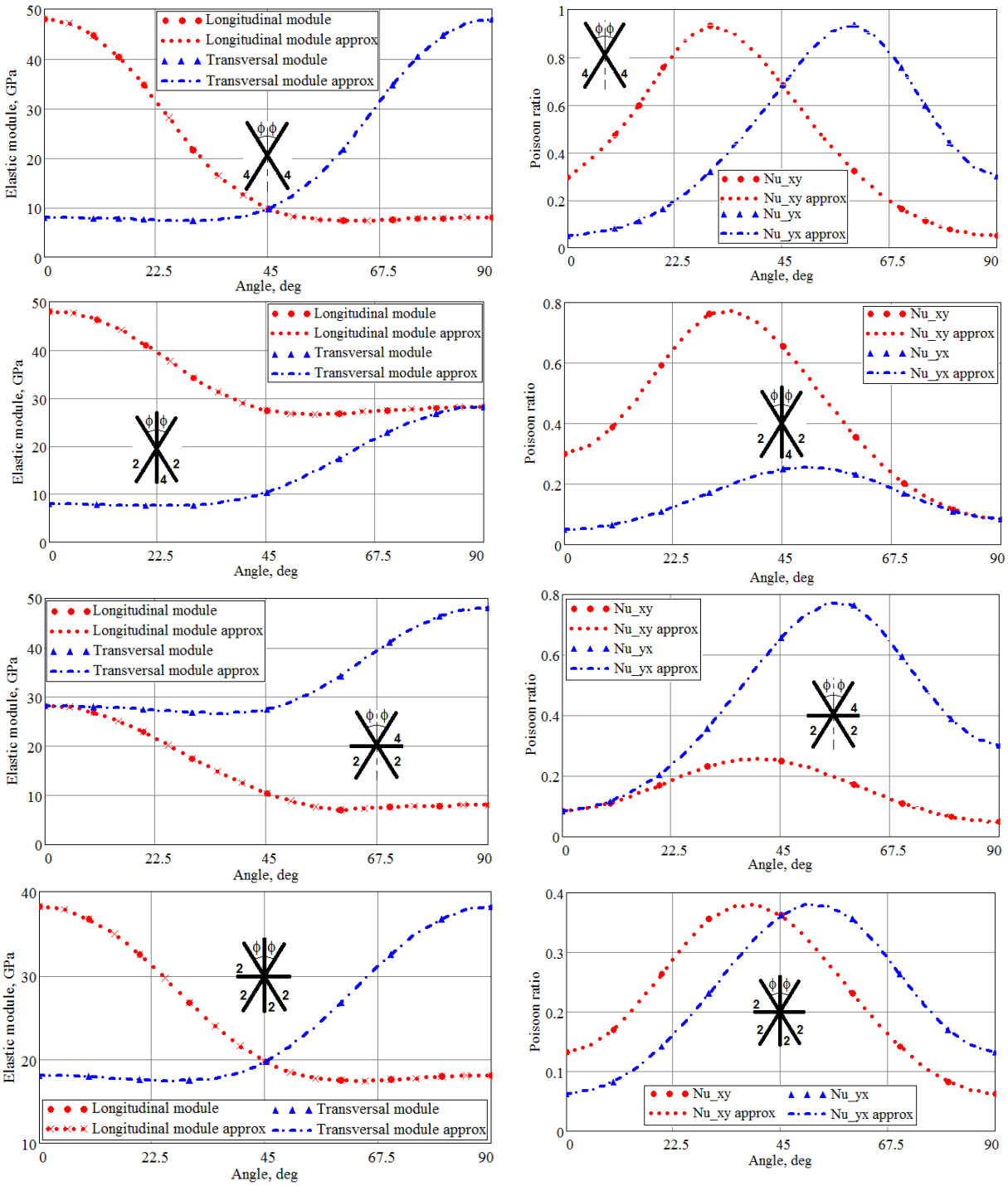


Fig.6. Some examples of longitudinal, transverse elastic modulus and Poisson ratios dependencies on the lay-up angles for the laminate stacking I, II, III, IV (see Fig. 4)

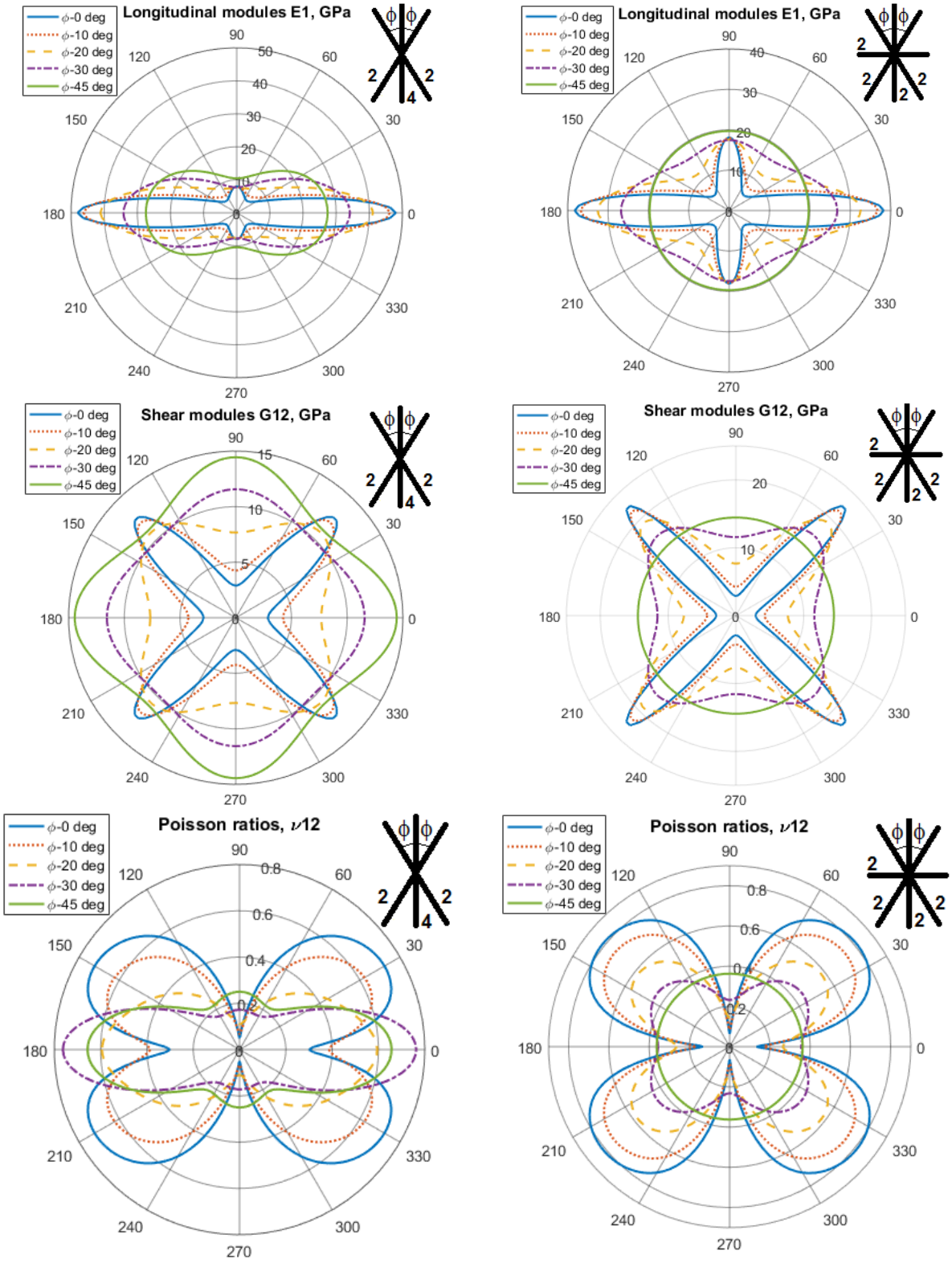


Fig. 7. Angular dependencies of the longitudinal, shear modules and in-plane shear ratio for the lay-ups II (left) and IV (right) (see Fig. 4)

4. MECHANICAL TESTING OF STRUCTURE WITH DIFFERENT LAMINATE STACKING

The mechanical testing of the structure with different lay-ups and ply stacking angles has been implemented using FE model (see Figs. 1 - 3) by using three aforementioned types of static bending and torsion loading. These loads were applied separately; for each load scenario the total strain energy, the maximum and averaged von Mises stress, two end deflections and torsion angles on the free face of the beam tip were calculated. Results of these testing were used for the refinement of the "candidates" list by selection of lay-ups that provide the minimum strain energy, bending and torsion deformation.

Moreover, these results demonstrated two very interesting and important features. First, we found that sensitivity of both maximum and averaged von Mises stress to the structural symmetry of orthotropic material is sufficiently less comparing to the total elastic strain energy. Second result is the practically independent response of the structure on the twisting load of the lay-ups II, III and IV. The reason for this is the practical identity of the shear modulus of these lay-up schemes at the same lamina angular orientation.

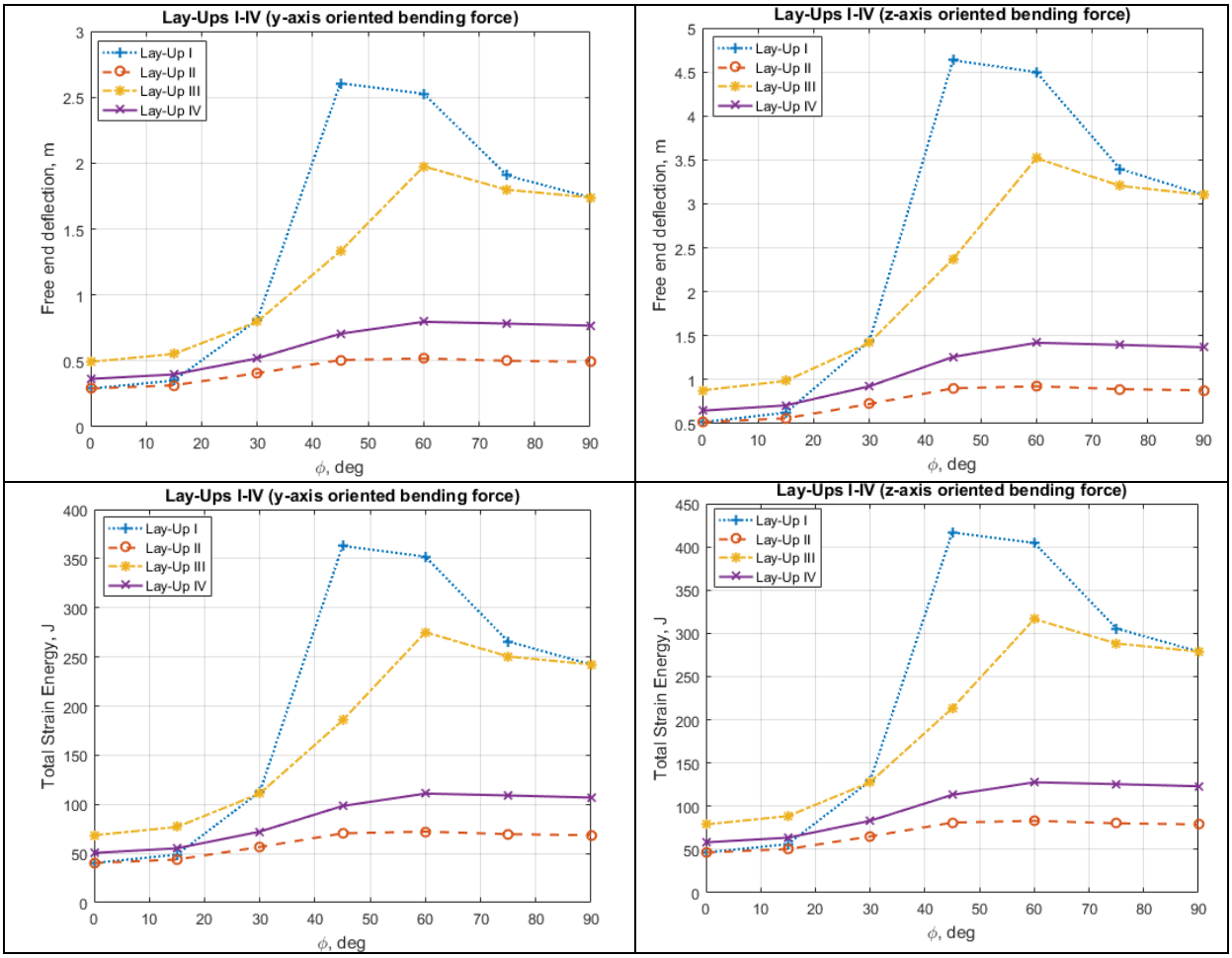


Fig. 8. Some dependencies of maximum deflections and total strain energy of the loaded beam

5. PSEUDO-OPTIMAL CHOICE OF THE BETTER LAY-UPS

On the final stage of investigation, the optimizing structure made of the preferred lay-ups "candidates" has been loaded by three systems of forces: bending by the distributed forces oriented along y and z axes, and twisting torque applied to the external surface. Figure 9 demonstrates the results of implemented quasi-optimization study, where the different responses of the "candidate" structures are shown. These responses include total strain energy, the maximum bending deflections and objective, which is accepted in the normalized dimensionless form

$$Obj = \theta/6 + \max(v_b) + \max(w_b)/1.5 \tag{4}$$

where θ is the torsion angle, and v_b, w_b are the beam tip deflections along the y and z, respectively. Naturally, the definition of such objective function and weights of its components has a significant element of arbitrariness. Therefore the total strain energy, the beam deflections and torsion angle were also monitored during the optimization process along with the objective function determined by Equation (4). During the optimization process the forward structural mechanics problem has been called by the built-in gradient-free Nelder-Mead optimizer.

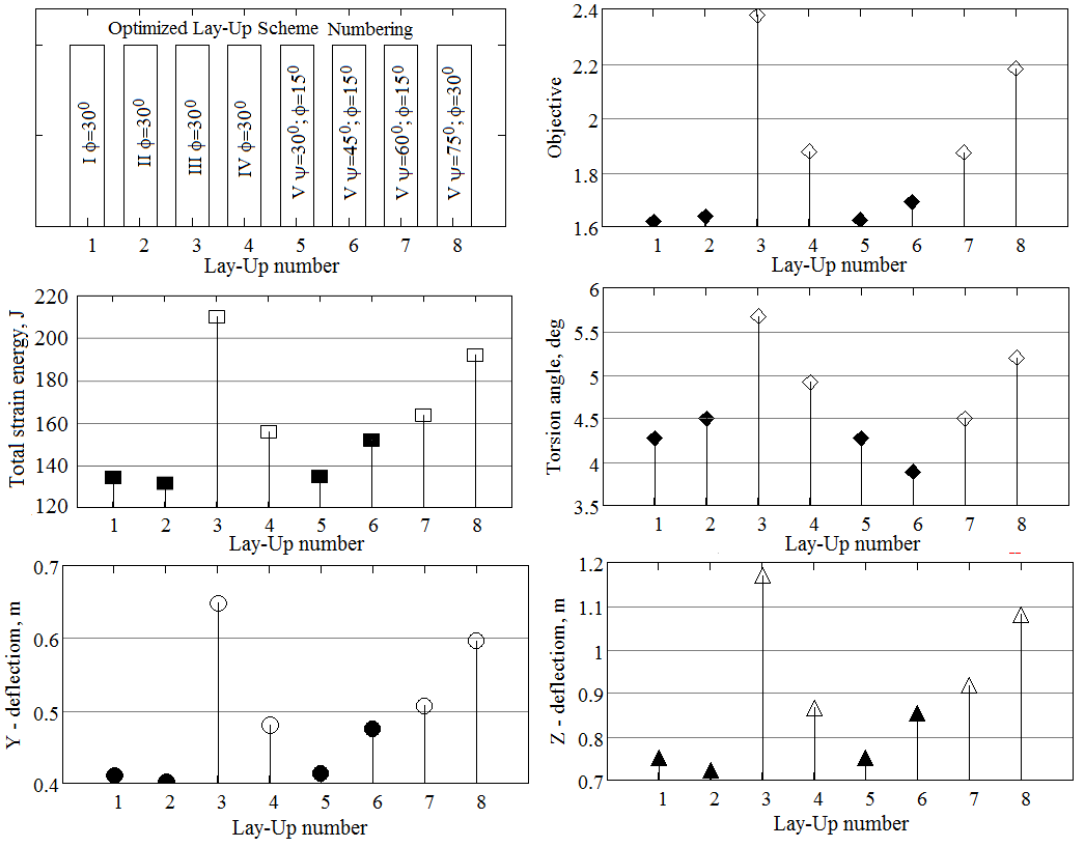


Fig. 9. Comparison the better lay-ups for the optimizing structure (stems with the filled symbols correspond to the preferred lay-ups)

The used approach requires many tedious calculations, but allows us to obtain the visual substantial representation about chosen composite lay-ups for optimizing structures, and can be expanded to the composite structures with every number of arbitrarily oriented unidirectional layers.

6. CONCLUSIONS

This paper presents the method and solution of the problem of lay-up optimization for a cantilevered long tube-like composite structure with varied cross-section that is manufactured by winding of glass fiber unidirectional tape. In order to optimize this structure we use the assumption of effective elastic moduli for multilayered composite, which were determined by the finite element modeling and by the laminate theory. The operational loads included the bending forces, which cause the beam deflections along the directions of its maximum and minimum stiffness, and also the distributed torque causing the torsion deformations. To increase the stiffness of the structure, hence, to reduce the total strain energy and peak von Mises stress, the search of the better lay-up scheme and its angles is performed. This search is implemented stepwise: by the analysis of all moduli angular distributions using the dependencies of these moduli on the lay-up angles for the different schemes of lay-up stacking. The final choice of the pseudo-optimal solution is made on the basis of an expert decision that excludes from the consideration of the solutions with sharply degraded structural rigidity at least at one load scenario.

ACKNOWLEDGEMENT

This work is implemented in the framework of the state mission for the South Scientific Center of Russian Academy of Science, project No. AAAA-A16-116012610052-3 and it was supported by the Russian Foundation for the Basic Research (Grants 15-08-99849 and 16-58-52013 MNT_a).

REFERENCES

1. **Baker, A., Dutton, S. & Kelly, D., (2004),** Composite Materials for Aircraft Structures, AIAA Inc., Reston, Virginia.

2. **Ostergaard, M.G., Ibbotson, A.R., Le Roux, O. and Prior, A.M., (2011),** "Virtual testing of aircraft structures", CEAS Aeronaut. Journal, Vol. 1, pp 83-103.

3. **Taylor, J.E., (2000),** "A Formulation for Optimal Structural Design with Optimal Materials". In: Topology Optimization of Structures and Composite Continua, Ed. by G.I. Rozvany. and N. Olhoff, Kluver Academic Publishers, Dordrecht, Boston, London, pp 49-55.

4. **Rao, J.S., (2015),** "Advances in Aero Structures", Proc. of ICOVP-2015 Conference, Guwahati, India, pp 20.

5. **Gillet, A., Francescato, P. and Saffre, P., (2010),** "Single- and Multi-objective Optimization of Composite Structures: The Influence of Design Variables", Journal of Composite Materials, Vol. 44, No. 4, pp 457-480.

6. **Zhou, M., Fleury, R. and Kemp, M., (2011),** "Optimization of Composite: Recent Advances and Application", www.altairproductdesign.com, pp 14.

7. **Zhang, W.C. and Evans, K.E., (1988),** "Numerical Prediction of the Mechanical Properties of Anisotropic Composite Materials", Computers & Structures, Vol. 29, No. 3, pp 413-422.

8. **Herencia, J.E., Hatfka, R.T., Weaver, P.M. and Friswell, M.I., (2008),** "Lay-Up Optimization of Composite Stiffened Panels using Linear Approximations in Lamination Space", AIAA Journal, Vol. 46, No.9, pp 2387-2391.

9. **Satheesh, R., Naik, G.N. and Ganguli, R., (2010),** "Conservative Design Optimization of Laminated Composite Structures Using Genetic Algorithms and Multiple Failure Criteria", Journal of Composite Materials, Vol. 44, No. 3, pp 369-387.

10. **Gyan, S., Ganguli, R. and Naik, G.N., (2012),** "Damage-tolerant design optimization of laminated composite structures using dispersion of ply angles by genetic algorithm", Journal of Reinforced Plastics and Composites, Vol. 31, No. 12, pp 799-814.

11. **Mohan Rao, A.R. and Lakshmi, K. (2012),** "Optimal design of stiffened laminate composite cylinder using a hybrid SFL algorithm", Journal of Composite Materials, Vol. 46, No. 24, pp 3031-3055.

12. **Oktem, A.S. and Soares, C.G., (2011),** "Higher order theory based Fourier analysis of cross-ply plates and doubly curved panels", Journal of Composite Materials, Vol. 46, No. 21, pp 2675-2694.

13. **Kaleemulla, K.M., and Siddeswarappa, B., (2010),** "Influence of Fiber Orientation on the In-plane Mechanical Properties of Laminated Hybrid Polymer Composites", Journal of Reinforced Plastics and Composites, Vol. 29, No. 12, pp 1900-1914.

14. **Metiche, S. and Masmoudi, R., (2013),** "Analysis and design procedures for the flexural behavior of glass fiber-reinforced polymer composite poles", Journal of Composite Materials, Vol. 47, No. 2, pp 207-229.

15. **Guo, S.J., Bannerjee, J.R.; Cheung, C.W., (2003),** "The effect of laminate lay-up on the flutter speed of composite wings", Proc. of the Institution of Mechanical Engineers, Part G: Journal of Aerospace Engineering, Vol. 217, No.3, pp 115-122.

16. **Kalavalapally, R., Penmetsa, R. and Grandhi, R., (2006),** " Multidisciplinary optimization of a lightweight torpedo structure subjected to an underwater explosion", Finite Elements in Analysis and Design, Vol.43, pp 103-111.

17. **Oganesyan, P., Zhilyaev, I., Shevtsov, S., and Wu, J.-K. (2016),** " Optimized Design of the Wind Turbine's Composite Blade to Flatten the Stress Distribution in the Mounting Areas". In: The Latest Methods of Construction Design, Ed. V. Dynybyl, Springer, Heidelberg, New York, Dordrecht, London, pp 335-341.

18. **Shevtsov, S., Zhilyaev, I., Oganesyan, P. and Axenov V., (2017),** "Optimization of wall thickness and lay-up for the shell-like composite structure loaded by non-uniform pressure field", AIP Conf. Proc., Vol. 1798, pp 0200144-1-10.

19. **Hodges, D.H., (2006),** Nonlinear Composite Beam Theory, AIAA, Inc., Reston, Virginia.

20. **Barbero E.J., (2013),** Finite Element Analysis of Composite Materials Using Abaqus, CRC Press, Boca Raton, London, New York

21. **Ha, S.K., Huang, Y., Han, H.H. and Jin, K.K., (2010),** "Micromechanics of Failure for Ultimate Strength Predictions of Composite Laminates", Journal of Composite Materials, Vol. 44, No. 20, pp 2347-2361.

22. **Gibson, R.F., (1994),** Principles of Composite Materials Mechanics, McGraw-Hill, Inc., Detroit, Michigan.

23. **Voyiadjis, G.Z. and Kattan, P.I., (2005),** Mechanics of Composite Materials with MATLAB, Springer, Berlin, Heidelberg, New York.

24. **Chinchan, L., Shevtsov, S., Soloviev, A. and Huang, J.-P. (2014),** In: Advanced Materials, Springer, Cham, pp 201-222.

NUMERICAL SIMULATION OF LATERAL JET IN A SUPERSONIC MISSILE USING COMPUTATIONAL FLUID DYNAMICS

Efe C. DAĞLI, *e211986@metu.edu.tr* Middle East Technical University, 06800, Ankara, Turkey

M. Halûk AKSEL, *aksel@metu.edu.tr* Middle East Technical University, 06800, Ankara, Turkey

ABSTRACT

Missiles need control mechanisms for maneuverability during the flight. Conventional method for missile control is deflecting control surfaces. However at low dynamic pressures control surfaces lose their effectiveness. An alternative method for missile control is side jet control. The ejection of jet in a direction perpendicular to missile axis causes a force in the reverse direction, therefore agile movement of the missile. In this study, effect of side jet control on missile aerodynamic performance and flow physics will be investigated using Computational Fluid Dynamics (CFD).

Keywords: Lateral jet control, Computational Fluid Dynamics, Numerical simulation

1. INTRODUCTION

Side jet control has advantages over conventional control systems such as still being effective at low dynamic pressures (at low speeds or higher altitudes), fast response time, high maneuver capability, etc. Although implementing side jet control system on a missile results in a complex flow domain, effects of side jet on the overall missile aerodynamic characteristics should be examined. In CFD studies, validation plays a crucial role. First, two equation turbulence models have been used and results are compared with experiment. Then mesh independency study have been conducted. Eventually, experimental data of a generic supersonic missile model from the literature using pressure coefficient results at different sections of missile geometry compared with the results of CFD solution. Then flow domain is examined with contours of current CFD solution and compared with the images from the experiments in the literature.

2. CFD CALCULATIONS

Side jet impinging in a supersonic free-stream results in very complex flow physics. Method (CFD solver, grid size, turbulence models, boundary types, etc.) should be validated in order to prove that it is adequate for solving jet and free-stream flow interaction. For validation, experimental studies conducted by wind tunnel facilities should be taken as a reference. The experiment used in this study, provides pressure coefficient distribution on missile body in the presence of side jet. If pressure coefficient distribution calculated numerically is in agreement with experimental results it shows that our method solves flow physics well enough. Experimental model is a generic missile geometry which has a diameter of 40 milimeters (D) and consists of a cylindrical body with 3.2D length, cone shaped nose with a length of 2.8D and a flare after-body with 3D length with a base diameter of 1.66D. The jet is located at a distance of 4.3D from the missile nose tip at the 180 degree roll angle indicating the top part of the missile in the circumferential direction. Also jet axis and missile axis are perpendicular to each other [Gnemmi, 2008]. Geometry of the experimental model and the sign convention for the roll angle are presented in Figure 1. On the surface of the experimental model, there exist pressure orifices for pressure measurements beginning from the nose and continuing on cylindrical body and flare in the longitudinal direction. There are three sets of pressure orifices at roll angles of 180°, 150° and 120°. In Table 1, properties of jet and free-stream flows are given.

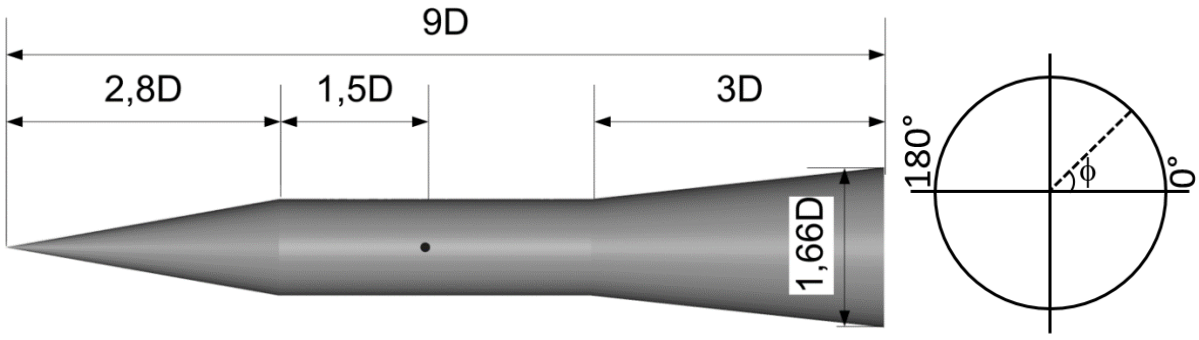


Figure 1 Dimensions of Experimental Model and Roll Angle Definition

Table 1 Boundary Conditions of Validation Study

Free-stream Flow	Jet Flow
M = 2.8	M = 1
P_{amb} [Pa] = 20793.2	R_{0J} = 100
T_{amb} [K] = 108.96	

For CFD solutions, commercial CFD solver ANSYS Fluent have been used. Far-field and mass inlet boundary conditions are used for the free-stream and jet flows, respectively, to simulate the flow field as in the literature [Krishnan, 2016], [Ağsarlıoğlu, 2011]. For pressure far-field, Fluent requires static pressure, static temperature and Mach number which are given in Table 1. For mass flow inlet, Fluent requires static pressure, total temperature and mass flow rate. In Table 1, R_{0J} is given which is defined as the strength of the jet and it is calculated by dividing total pressure of the jet flow by the static pressure of the free-stream flow. In the reference, jet flow temperature and the type of the fluid are not clearly emphasized [Gnemmi, 2008]. Therefore, the working fluid is assumed as air and its temperature is taken to be equal to the temperature of the free-stream flow. Therefore, static pressure and the total temperature of the jet flow should be calculated using isentropic relations which are given as follows, since both are required for full definition of mass flow inlet boundary condition.

$$\frac{P_0}{P} = \left[1 + \frac{\gamma-1}{2} M^2\right]^{\frac{\gamma}{\gamma-1}} \quad (1)$$

$$\frac{T_0}{T} = 1 + \frac{\gamma-1}{2} M^2 \quad (2)$$

Another input required by the mass flow inlet boundary condition is the mass flow rate which is calculated by the following formula,

$$\dot{m} = \rho V A_{jet} \quad (3)$$

Density of the jet flow should be calculated using ideal gas relation and the velocity of the jet is equal to the speed of sound. Formulas for calculating these parameters are given below,

$$P = \rho R T \quad (4)$$

$$a^2 = \gamma R T \quad (5)$$

2.1 Turbulence Models

At this point, different turbulence models have been employed for solving the flow domain. Using the same grid, different CFD runs have been completed using k-ε Realizable and k-w SST models. Both models use 2 equations for turbulence modeling. Pressure coefficient results at 180° roll angle which means a line crossing the missile surface in longitudinal direction which is also crossing the jet from the center of it are presented in Figure 2 together

with experimental data. In the comparison of different turbulence models, the same grid have been used. In the meshing process, y+ value has been kept around 1 in order to resolve boundary layer accurately.

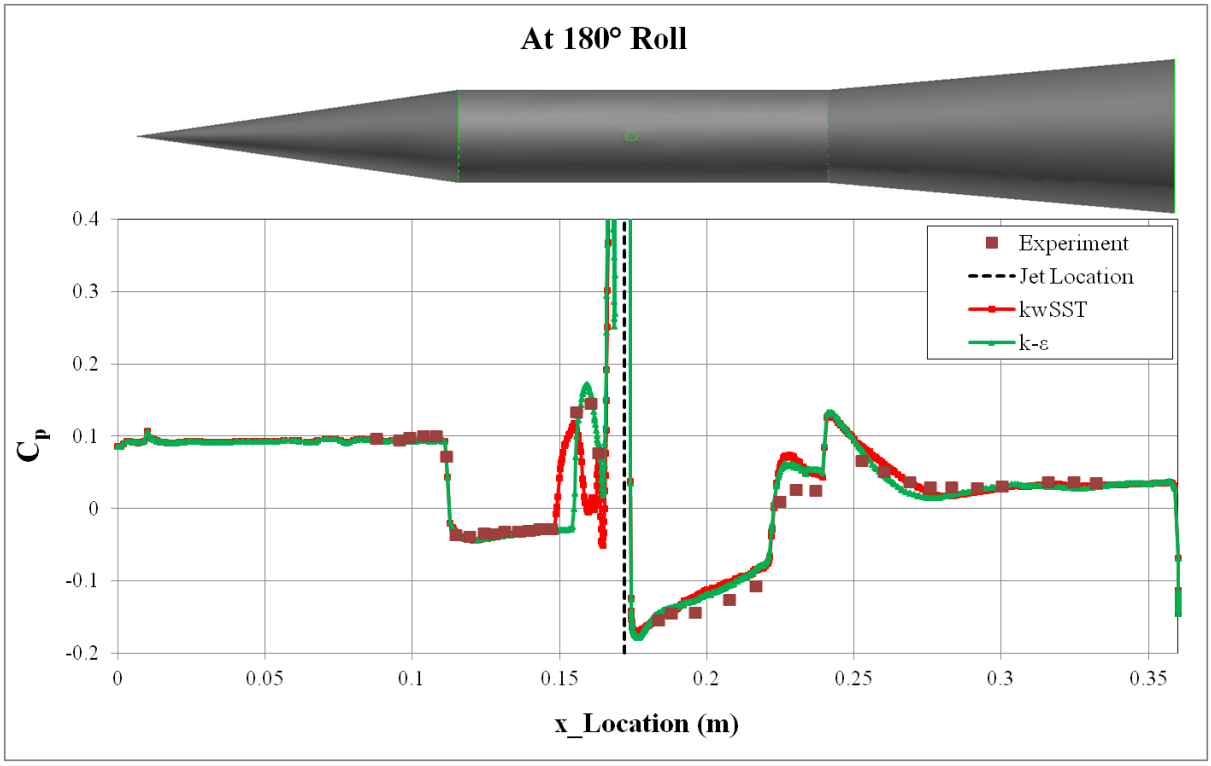


Figure 2. Comparison k-ε Realizable and k-w SST Turbulence Models

From Figure 2, one can say that k-ε Realizable turbulence model determines the pressure distribution more accurate than k-w SST turbulence model. This fact can be noticed at the separation region which is located before the jet location around 0.16 m along x-axis. It is concluded that, use of k-ε Realizable SST turbulence model is appropriate in this study for turbulence modeling.

2.2 Grid Independency

The flow domain is meshed using unstructured grid which consists of tetrahedral and hexahedral elements with the help of Gambit and TGrid softwares, both are commercially available by ANSYS. Generated grid is given in the Figure 3 and Figure *4*.

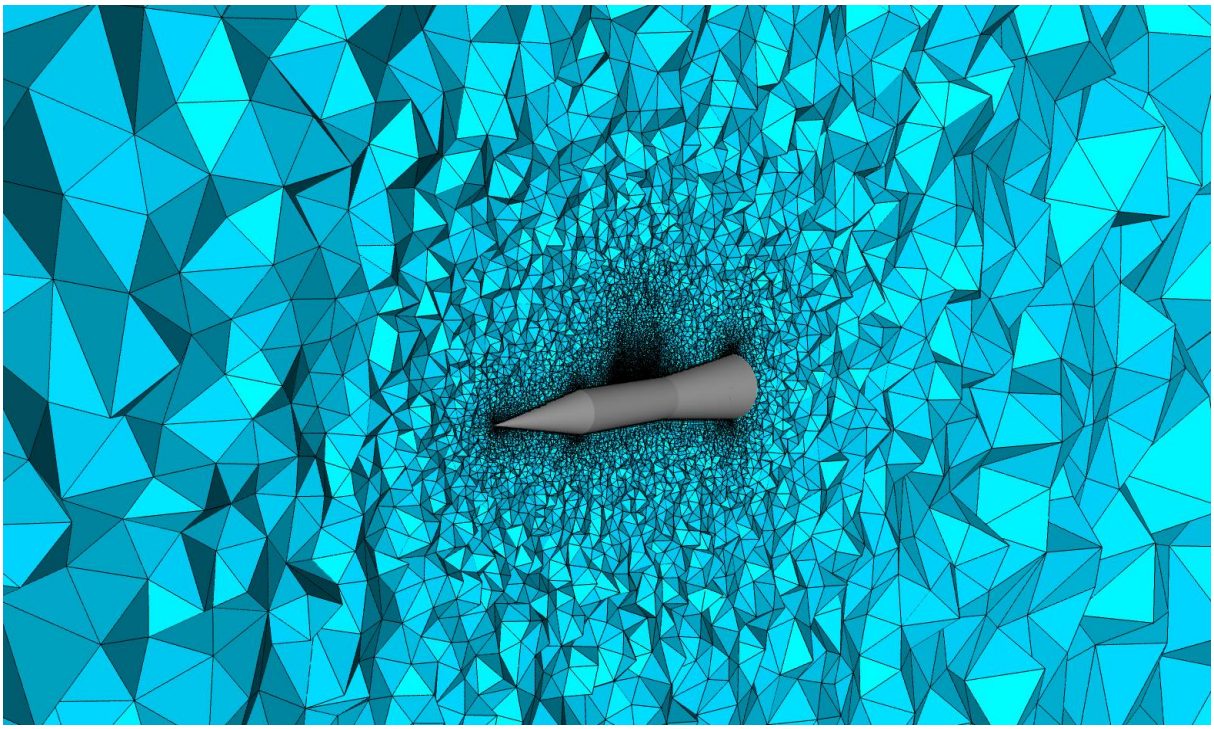


Figure 3. Generated Mesh for Validation Study

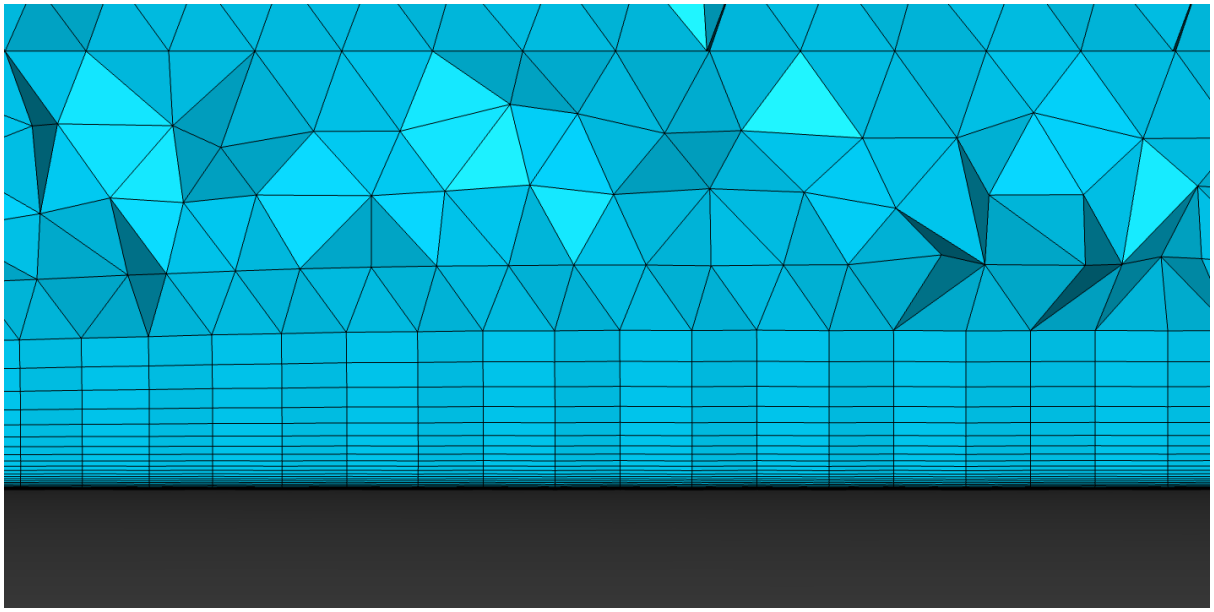


Figure 4. Boundary Layer Mesh for Validation Study

For mesh independency study, different mesh sizes have been constructed and to be able to check convergence. Variation of normal force and pitching moment coefficients for different mesh sizes have been compared with the result of the mesh having the largest number of cells. Normal force and pitching moment coefficients are selected for mesh independency check because this study will mainly focus on the normal force and pitching moment caused by the side jet. Results are presented in Figure 5, 6 and in Table 2.

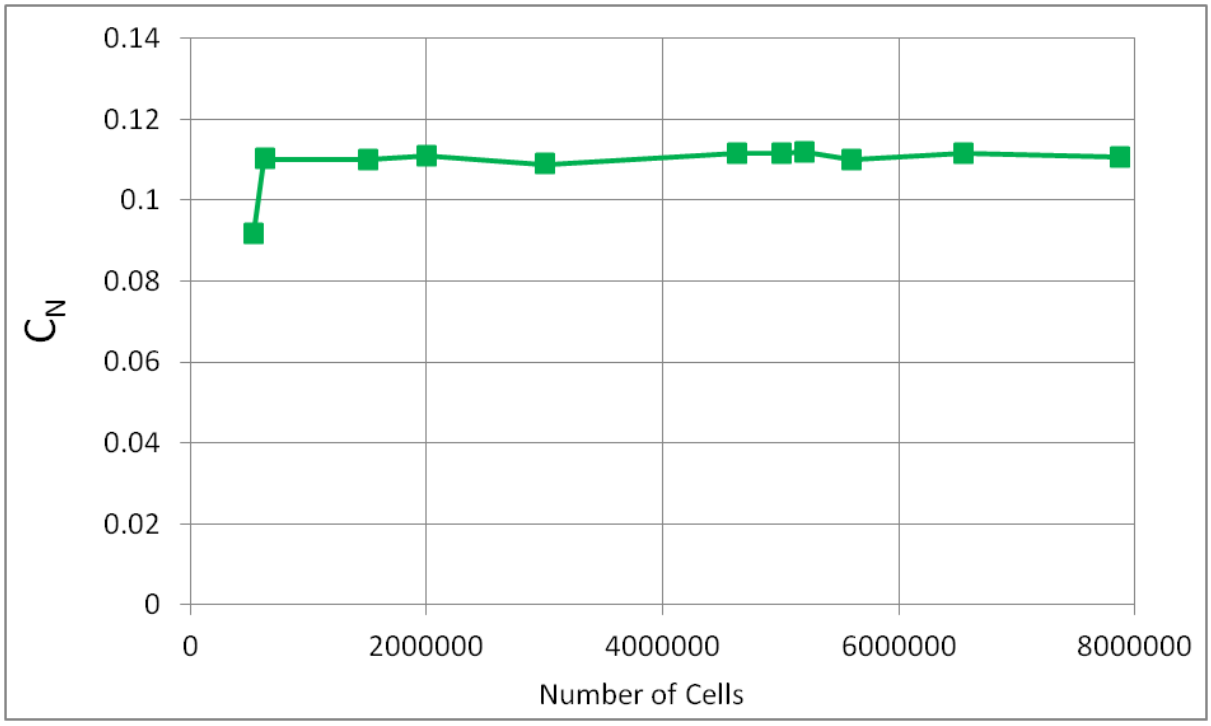


Figure 5. Normal Force Coefficients for Different Sizes of Grids

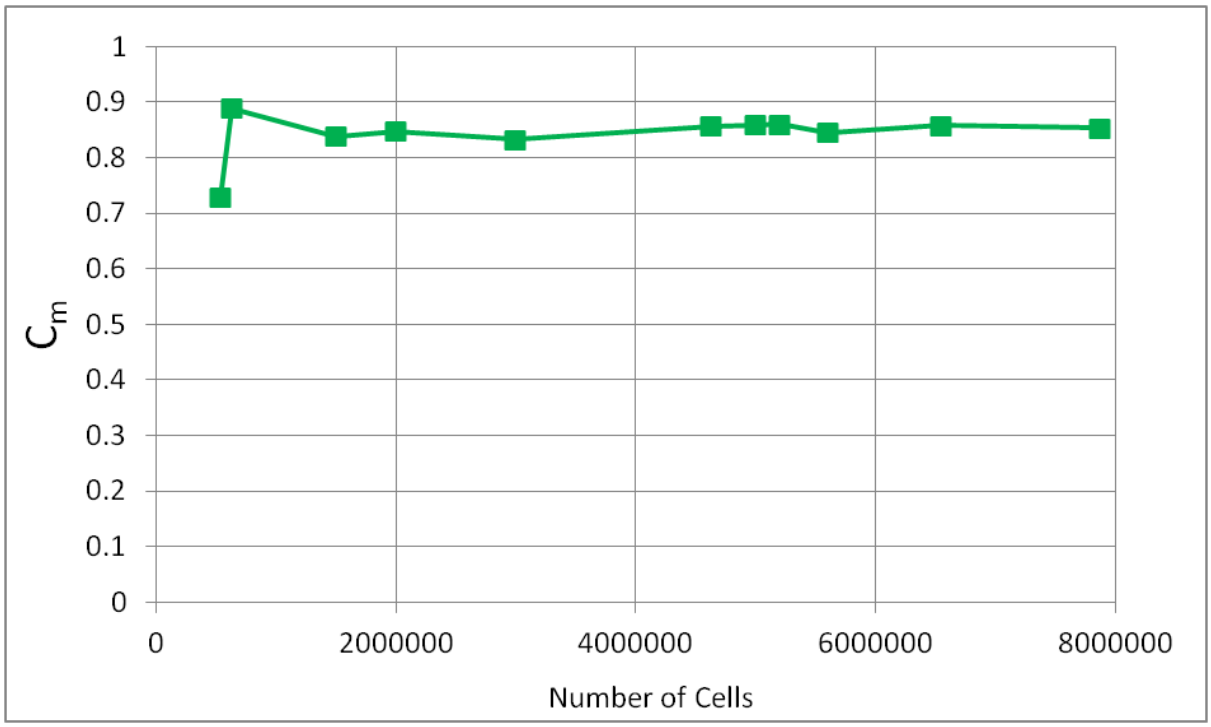


Figure 6. Pitching Moment Coefficients for Different Sizes of Grids

Table 2. Results of Grid Convergence

Number Of Cells	C_N	C_m	ΔC_N (%)	ΔC_m (%)
5,4 x 10^5	0.09183	0.72882	-17.05	-14.55
6,3 x 10^5	0.11020	0.88861	-0.45	4.18
1,5 x 10^6	0.11011	0.83849	-0.53	-1.70
2,0 x 10^6	0.11104	0.84764	0.31	-0.62
3,0 x 10^6	0.10895	0.83221	-1.58	-2.43
4,6 x 10^6	0.11148	0.85622	0.70	0.38
5,0 x 10^6	0.11169	0.85892	0.89	0.70
5,2 x 10^6	0.11191	0.86017	1.09	0.85
5,6 x 10^6	0.11012	0.84586	-0.52	-0.83
6,6 x 10^6	0.11152	0.85747	0.74	0.53
7,9 x 10^6	0.11070	0.85296		

According to Figure 5 and Figure 6, it can be observed that results are in good agreement with each other. In Table 2 which is the tabulated version of Figure 5 and 6, change of normal force and pitching moment coefficients for different mesh sizes are calculated with respect to result of the mesh having the largest number of cells which has almost 8 million cells. From Table 2, one can observe that convergence has been obtained starting with a grid size of 4.6 million cells.

3. RESULTS

In this section, results are given and examined in detail.

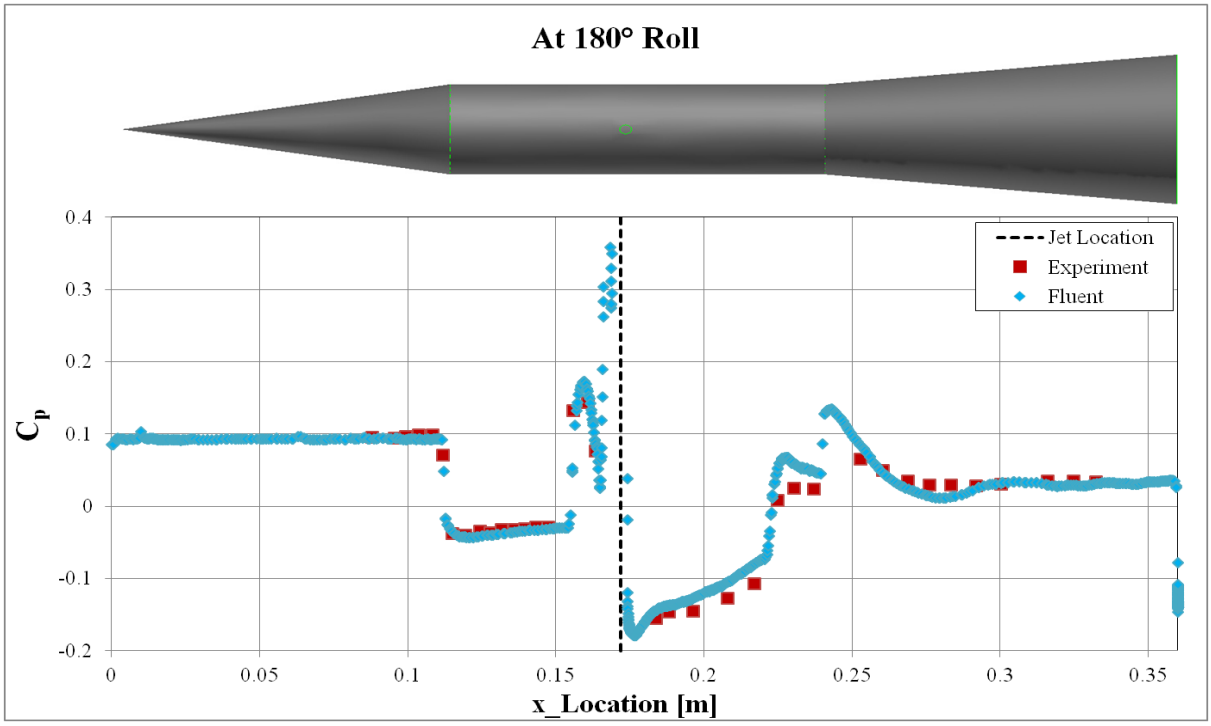


Figure 7. Pressure Coefficient Distribution at ϕ=180°

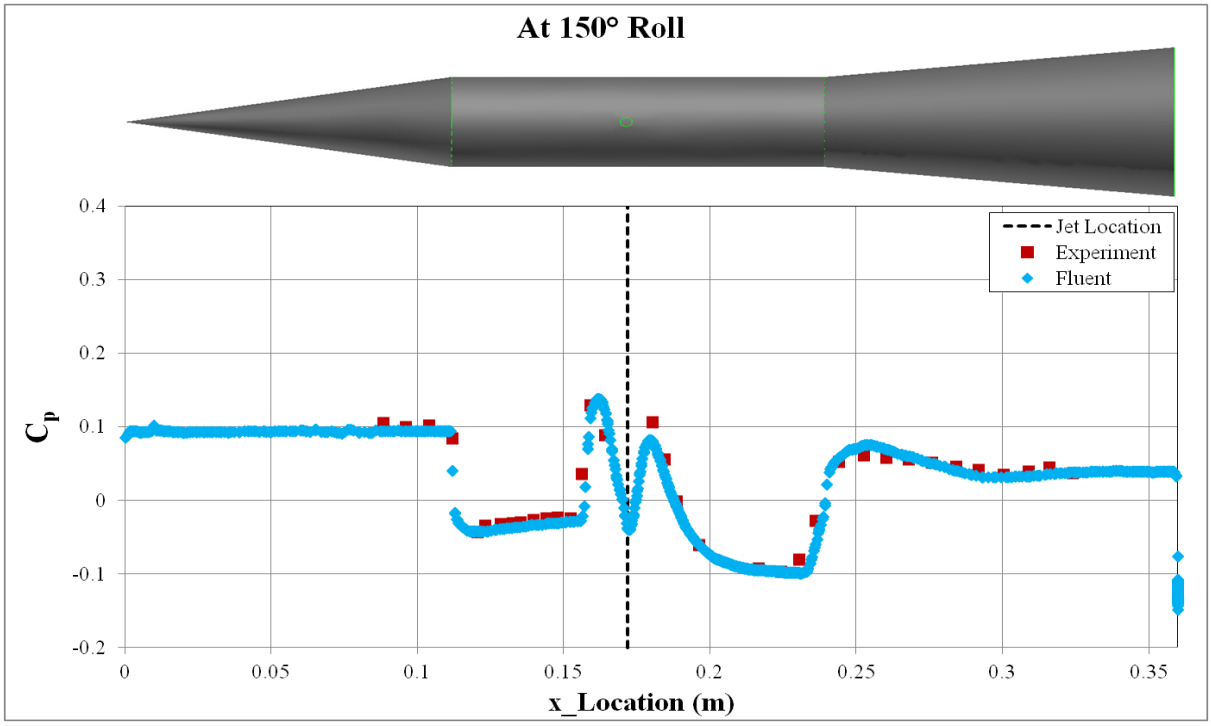


Figure 8. Pressure Coefficient Distribution at ϕ=150°

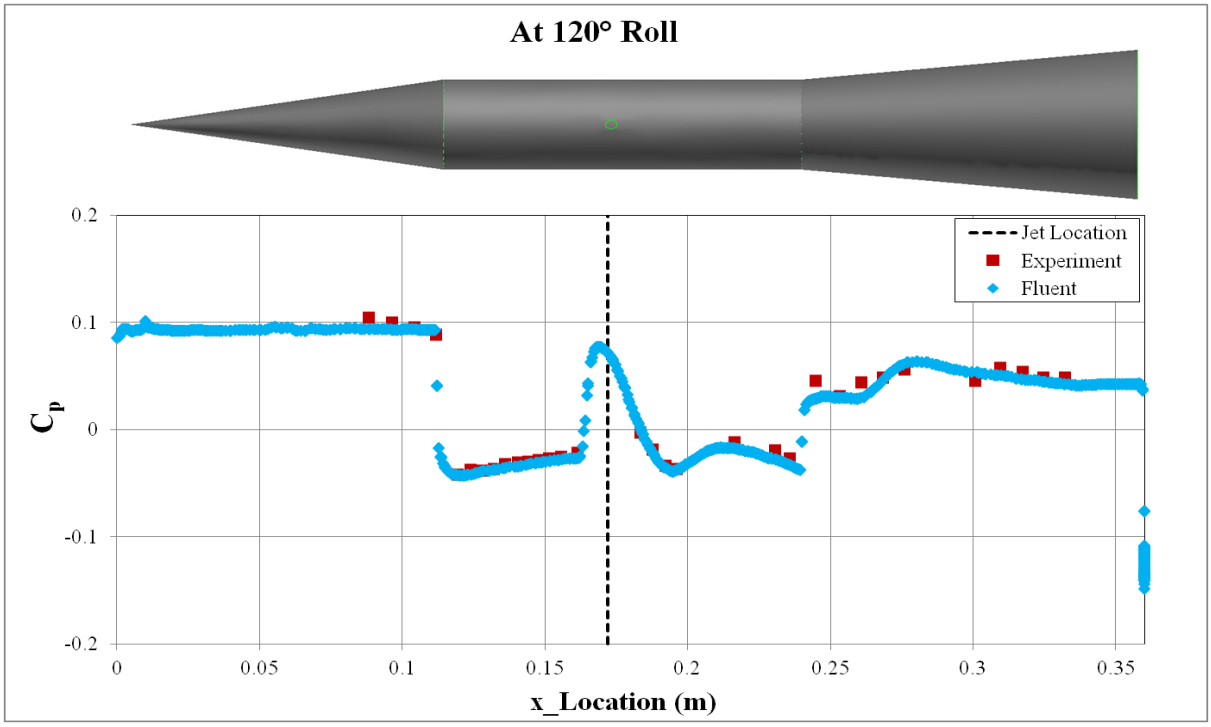


Figure 9. Pressure Coefficient Distribution at ϕ=120°

In Figure 7, 8 and 9, pressure coefficient results are given together with experimental results for 180°, 150° and 120° roll angles for the finest grid. CFD results shows a good agreement

with experimental data except for small inconsistencies. At x < 0.15 m, where jet does not expected to affect the pressure distribution, experimental and CFD data are almost identical for the three roll angles. At 0.15 m < x < 0.17 m where sudden pressure rise occurs due to jet flow, the variation of the pressure coefficient in the experiment and CFD shows a good agreement with each other for 180° and 150° roll angles. At 0.17 m < x < 0.22 m which is the wake region due to jet flow, experimental and CFD pressure distributions shows a similar behavior. For 0.22 m < x < 0.24 m, there are little differences between results especially for 180° roll angle where recompression shock occurs. In general, CFD solves flow and finds pressure coefficient distribution correctly with respect to experimental results except for some differences. After making numerical comparison between experiment and CFD, contours are obtained for observing the flow in detail which are presented in Figure 10.

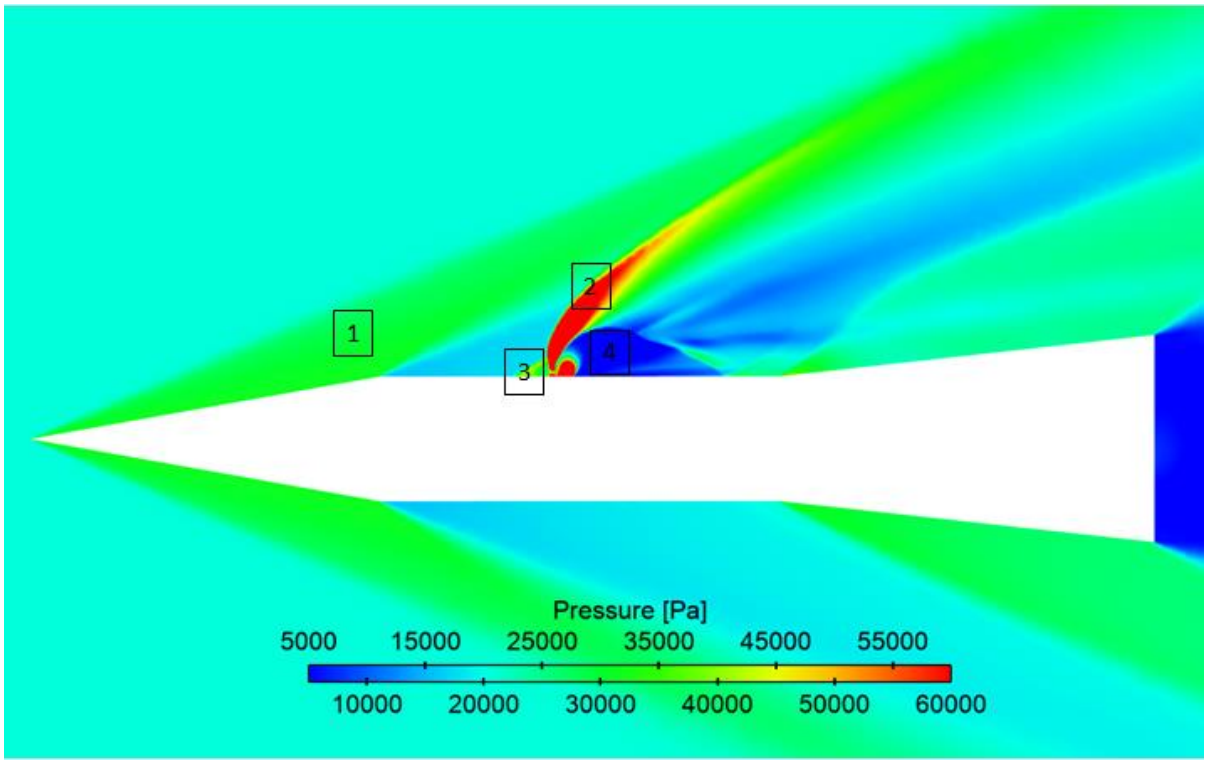


Figure 10. Pressure Contour at Symmetry Plane

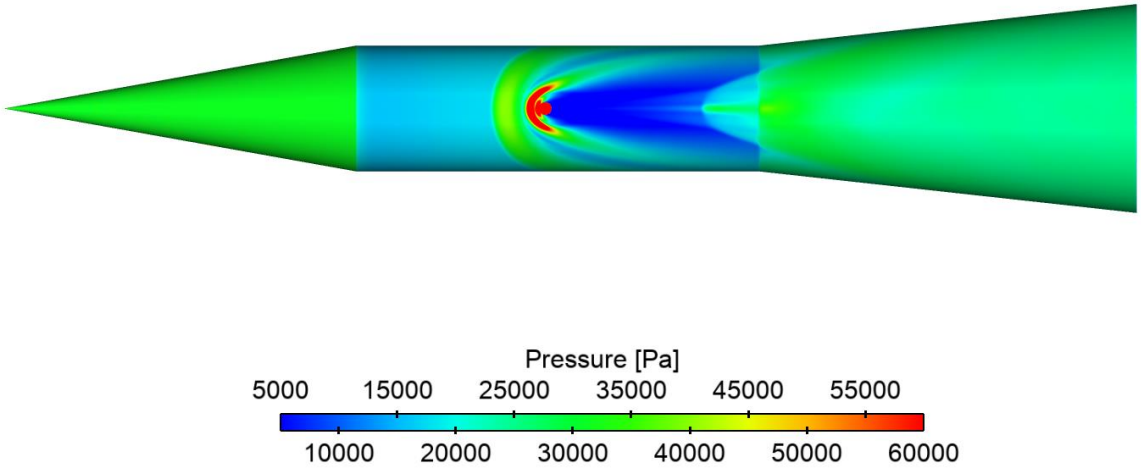


Figure 11. Surface Pressure Distribution around Jet Exit

Pressure distribution around the model is given in Figure 10. In this figure, body bow shock which occurs due to interaction of nose of the experimental model with the free-stream flow indicated as 1, jet bow shock which occurs due to interaction of jet and free-stream flows signed indicated by 2 and separation due to sudden pressure rise due to jet indicated by 3 and wake region which occurs after jet indicated by 4 can be observed clearly from pressure contours.

In the Figure 11 pressure distribution on the surface of experimental model is given. Local pressure rise due to jet flow can be observed before the jet location which has a shape like a bow on the surface. Also behind the jet, the wake region is visible in the surface pressure contours. In Figure 12, Mach number distribution is presented, while a photograph of the experiment which is taken by the Schlieren Image Technique [Stahl, 2009] is given in Figure 13. The aim is to observe flow phenomena around side jet and determine whether CFD solves flow accurately or not.

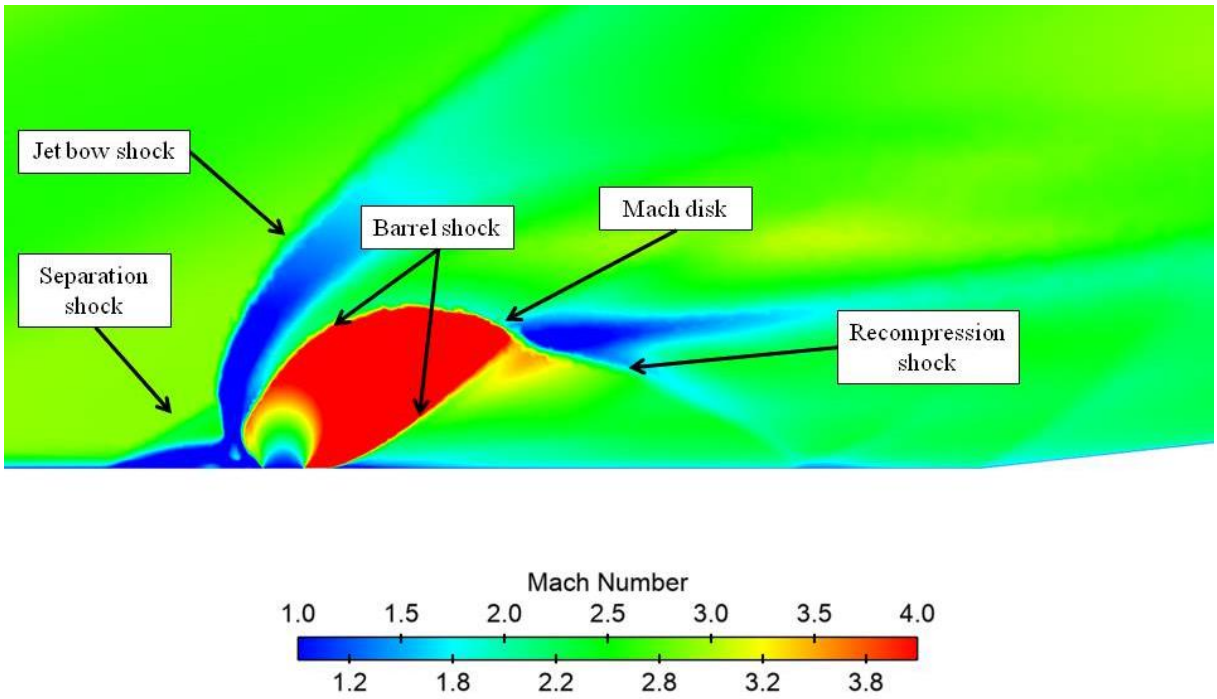


Figure 12. Mach Number Contour at Symmetry Plane

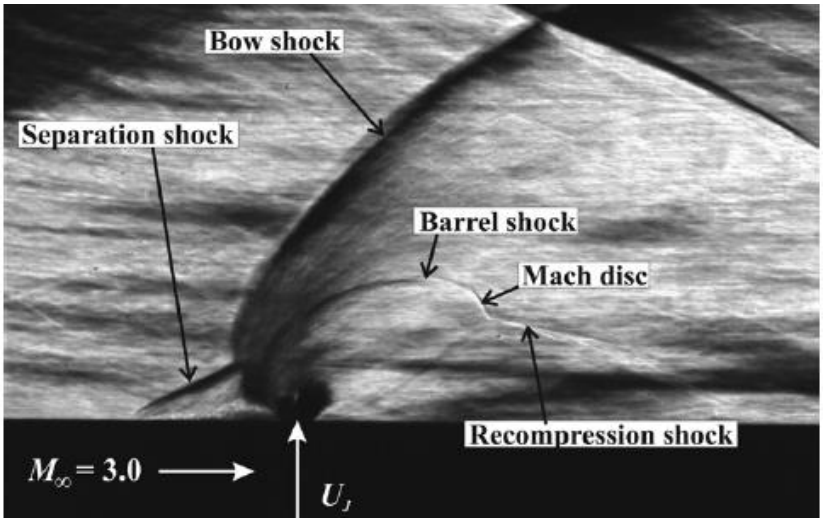


Figure 13. Schlieren Image of Jet Domain

Figure 12 show a very good agreement with each other. Therefore it can be concluded that CFD solves flow domain very well. Separation region which is visible in both figures are caused by the high adverse jet pressure. Jet bow shock can be easily noticed in the flow domain since before the shock velocity of flow is Mach 2.8 which is the velocity of free-stream flow. At the downstream of the jet bow shock, flow velocity drops drastically, which is, in general, a characteristic behavior of shocks. Jet plume becoming ‘an obstacle’ to the free-stream flow and jet bow shock occurs. Barrel shock occurs due to under-expansion of high pressure jet plume and this region terminates with the Mach disk occurrence.

4. ACKNOWLEDGEMENT

We thank Roketsan for supporting this research.

REFERENCES

1. **Gnemmi, P., Adeli, R. and Longo, J., (2008),** "Computational Comparisons of the Interaction of a Lateral Jet on a Supersonic Generic Missile", AIAA Atmosph. Fl. Mech. Con. and Exh., Hawai, pp. 1–9.

2. **Krishnan, S., Jouhari, A. K. and Balu, R., (2016),** "Numerical Simulation of Lateral Control Jets of an Interceptor Missile," *Int. J. Res. Eng. Technol.*, pp. 189–193.

3. **Ağsarlıoğlu, E., (2011),** "Numerical Investigations of Lateral Jets for Missile Aerodynamics", M. Sc. Thesis , METU Mech. Eng. Dept., Ankara.

4. **Stahl, B., Emunds, H. and Gülhan A., (2009)** "Experimental Investigation of Hot and Cold Side Jet Interaction with a Supersonic Cross-Flow," *Aerosp. Sci. Technol.*, vol. 13, pp. 488–496.

DESIGN AND COLD FLOW EXPERIMENTAL PROCEDURE OF A PINTLE INJECTOR

Berksu ERKAL, *berksu.erkal@tubitak.gov.tr* The Scientific & Technical Research Council of Turkey – Defense Industries Research & Development Institute TUBITAK-SAGE, P.K 16 Mamak, 06261 Ankara, Turkey

Bülent SÜMER, *bülent.sümer@tubitak.gov.tr* The Scientific & Technical Research Council of Turkey – Defense Industries Research & Development Institute TUBITAK-SAGE, P.K 16 Mamak, 06261 Ankara, Turkey

M. Haluk AKSEL, *aksel@metu.edu.tr* Middle East Technical University, 06800, Ankara, Turkey

ABSTRACT

An injector, which is the main component of the liquid rocket engine, has major effects on liquid rocket engine's mission. Pintle injector has two major effects on the engine performance. Although, for other types of injectors need more than one injector for the chamber, single pintle injector can cover entire chamber itself. This makes the pintle injector cheaper to manufacture and launch. Secondly, it has the ability to throttle by controlling the area at injection gaps. In this study, a design methodology is developed for a pintle injector. Following this methodology, a 750 N pintle injector is designed and then analyzed by computational fluid dynamics (CFD) analysis to predict the cone angle. Finally, the injector is manufactured and cold flow tests with air and water are conducted to validate the cone angle found by the analysis. Moreover, cone angles are measured with high-speed shadowgraphy system and Sauter mean diameter is measured by Phase Doppler Particle Analysis (PDPA) system.

Keywords: Injector, Pintle Injector, Computational Fluid Dynamics

1. INTRODUCTION

A pintle injector is a variable area injector, which controls the injection area of one or two propellants, to give throttling ability to a bipropellant liquid rocket engine (LRE). Early applications started with primitive geometries at TRW and gained experience by Apollo Lunar Module Descent Engine having a pintle injector controlling both propellants' injection area

[Dressler, 2000]. Moreover, Dressler states that more than 60 different pintle engine designs completed hot fire tests in thrust engines ranging from 5 lbf to 65000 lbf and no combustion instability is recorded. Designing and manufacturing a LRE is expensive and time consuming. Cost of the space missions is a major problem for governments and companies. A geostationary launch may cost up to 55000 $/kg and this leads space industry to change something major like reconsidering a pintle injector [Mercieca, 2017]. In contrast to the other types of injectors, pintle injector is easy to manufacture and design and this simplicity makes it valuable among others to work on. Recent studies about pintle injectors are commonly based on cold flow tests. Bedard has designed a throattable liquid oxygen-liquid methane (LOX-LCH4) thrust chamber and performed both cold and hot flow tests for the chamber [Bedard, 2012]. The design had a hole type pintle injector and they stated that reservoir for the fluid effects the uniformity of the flow. Son et al. studied a moveable pintle design and they stated the geometrical parameters effecting spray characteristics [Son, 2017]. They also conducted a numerical study about the centrally controlled injector to investigate combustion characteristics [Yoon,2017]. Cheng et al. derived a theoretical correlation to predict the spray cone angle and validated his correlation with numerical and experimental work [Cheng,2017]. Sakaki et al. introduced a hot wire test for ethanol/LOX combustion in a rectangular combustor and they stated that C* efficiency is highly effected when oxidizer is fed from center [Sakaki,2017]. This study aims to have a tool for designing a pintle injector and ready to be analyzed and tested. The tool gives the geometry and mesh to be analyzed and experimental investigation is still going on.

2. DESIGN METHODOLOGY

There have been several types of pintle injectors ranging from hole type pintle injector to planar pintle injector [Dressler, 2000]. Some may serve as a constant thrust injector, while others may have the ability of throttle. For this study, throttling is the major concern, thus the geometry given in Figure 1 is selected as the base geometry for the design. The parameters given in figure are:

D_p	=	pintle support thickness
D_t	=	pintle tip diameter
L_{aod}	=	actual opening distance
L_{tod}	=	tracing opening distance
t_{ag}	=	thickness of annular gap
t_{pg}	=	pintle gap thickness
α	=	pintle angle

θ = shadow angle

A MATLAB code is prepared as the design tool and all the parameters given in Figure 1 are the variables of this tool and easily changeable.

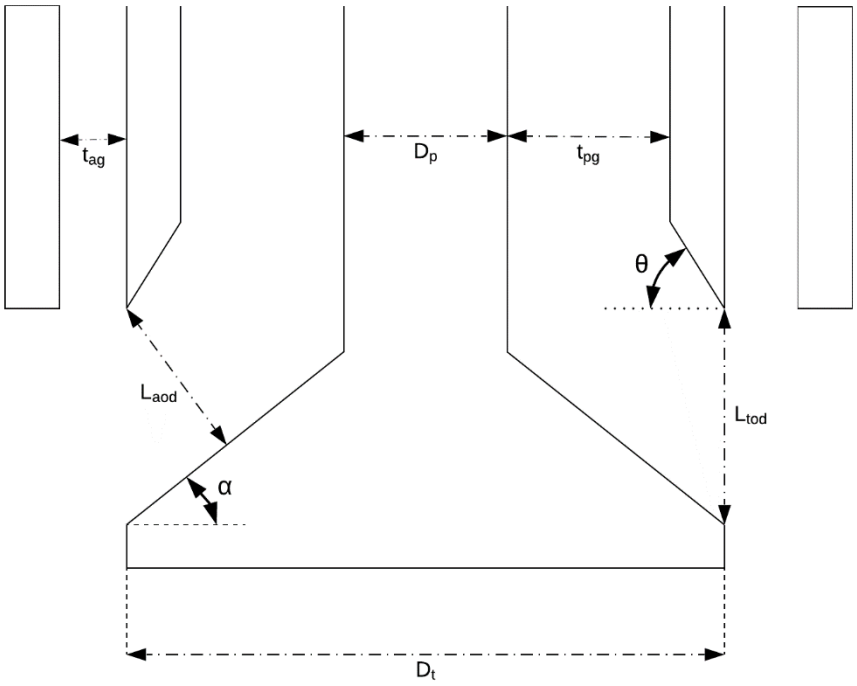


Figure 1 Base Geometry for the Design Tool

The code basically gets mission requirements as input. The mission requirements are defined as thrust profile, chamber pressure, throttle ratio, size constraints and Oxidizer/Fuel (O/F) ratio. The tool is coupled with the NASA's computer program Chemical Equilibrium with Applications (CEA), thus at this step it uses CEA to obtain specific impulse value for the given propellant inputs. Then, it uses (1) to obtain mass flow rates of fuel and oxidizer where T is thrust, $\dot{m}$ is mass flow rate, I_{sp} is specific impulse and g is gravitational acceleration . At the next step, pintle tip diameter, which is always the sum of pintle support diameter and pintle gap thickness, is estimated. From continuity, the injection velocity is calculated and if the result is higher than the speed of sound, this step is repeated. The same procedure applies to the inner flow. Geometrical parameters such as pintle angle, shadow angle and pintle support diameter are estimated and the inner flow injection velocity is calculated. If the velocity is higher than speed of sound, estimation process is repeated. At the end of the MATLAB part of the tool, a mesh is prepared for the Computational Fluid Dynamics (CFD) analysis. CFD analyses are then carried out manually. The methodology is given in Figure 2.

$$T = \dot{m} I_{sp} g \quad (1)$$

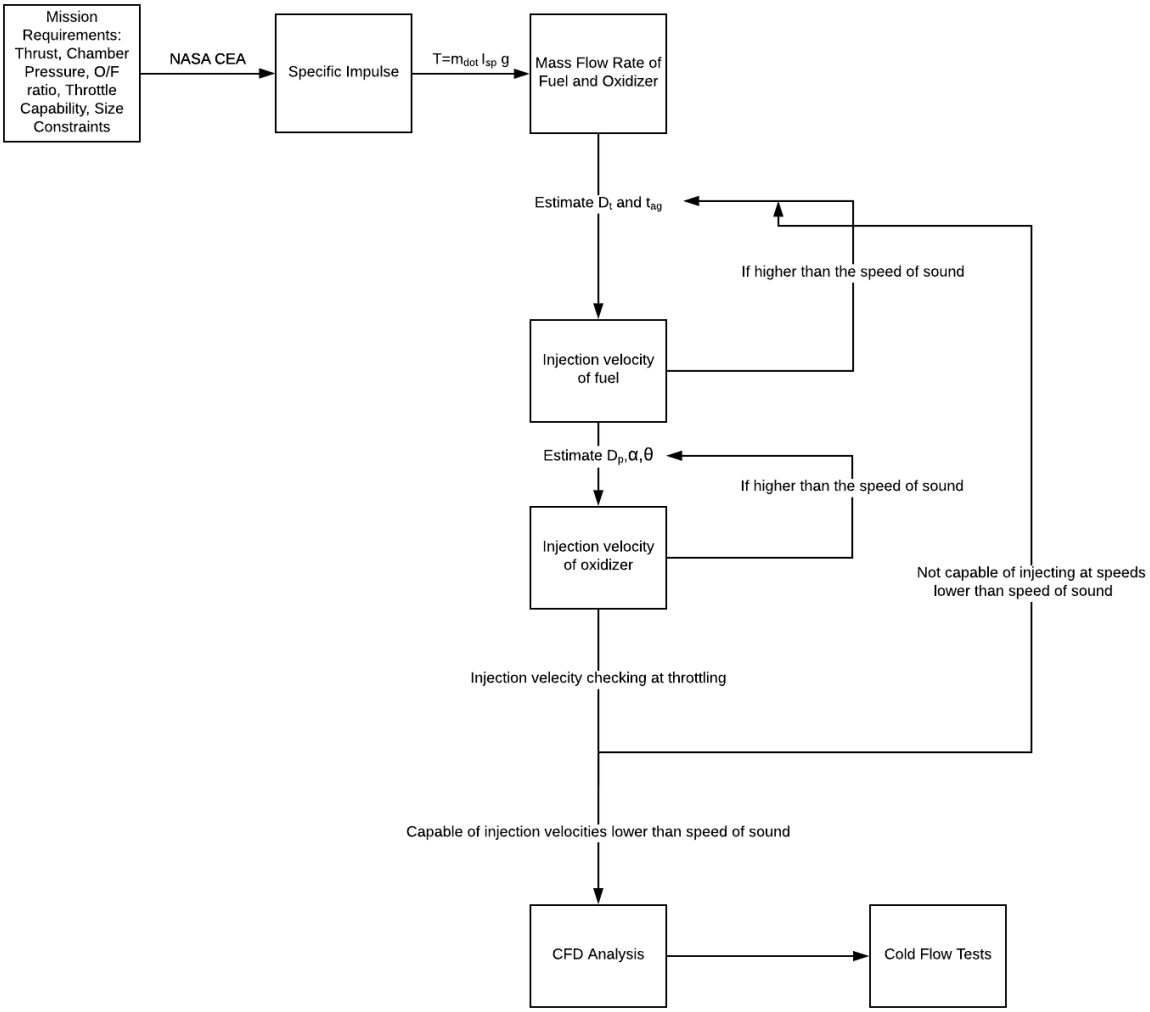


Figure 2 Design Methodology for a Pintle Injector

To validate the tool, a geometry, which is chosen from the Son's work, is given as input and CFD analysis is carried out for this specific geometry [Son, 2017]. The spray angle is estimated as 52.61° by using the given correlations. The analyses are performed with ANSYS FLUENT software. Volume of Fluid (VOF) model is used with fixed a time step of $1x10^{-6}$ s. Air is supplied from the annular gap, while water is supplied through the pintle gap. The flow is assumed to be adiabatic with no body force and surface tension and axisymmetric 2D analysis is performed with 46600 cells. The spray angle was found as 53.42° from the CFD analysis and assumed to be a satisfactory by considering numerical errors during experiments and CFD analysis. The phase volume fraction at 16 ms is shown in Figure 2.

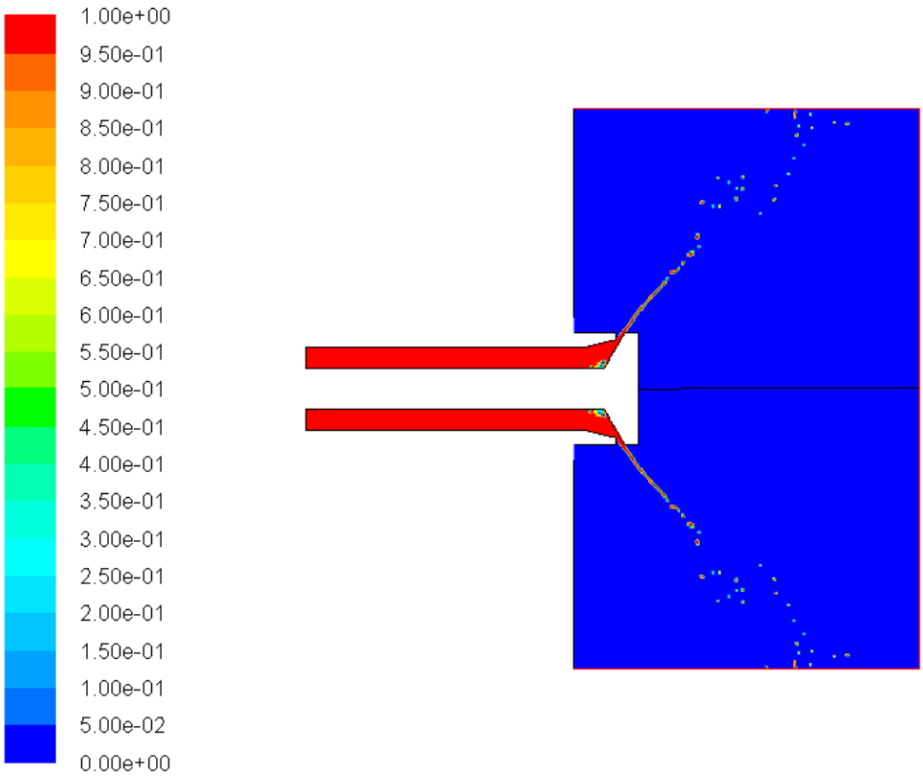


Figure 2 Phase Volume Fraction at t = 16 ms

There exists another important design point which is the reservoir design affecting the flow characteristics of the spray dramatically. This problem is also stated by Bedard et al and some different geometries and corresponding flow distributions are represented (Bedard, Feldman, Rettenmaier, & Anderson, 2012). A similar study is carried and new geometries are designed to be tested. The main problem of the low quality flow distribution is caused by the asymmetrical air or water inlets to the related reservoirs. The designed geometries are given for two different designs in Figure 3 and Figure 4.

For the first reservoir design, both water and air inlets are perpendicular to the main flow at the pipe region. This design is not sufficient for having a symmetrical spray distribution at the tip of the pintle. For the second design, water inlet is positioned at the entrance of the pipe region and a symmetrical water flow is obtained at the entrance of the pipe region. However, the mounting of the pintle has changed at the pipe region for this configuration. Mounting of pintle is satisfied by a star shaped geometry which affects the flow characteristics at the pipe region. The designs are manufactured and tested and test results are discussed at the next section.

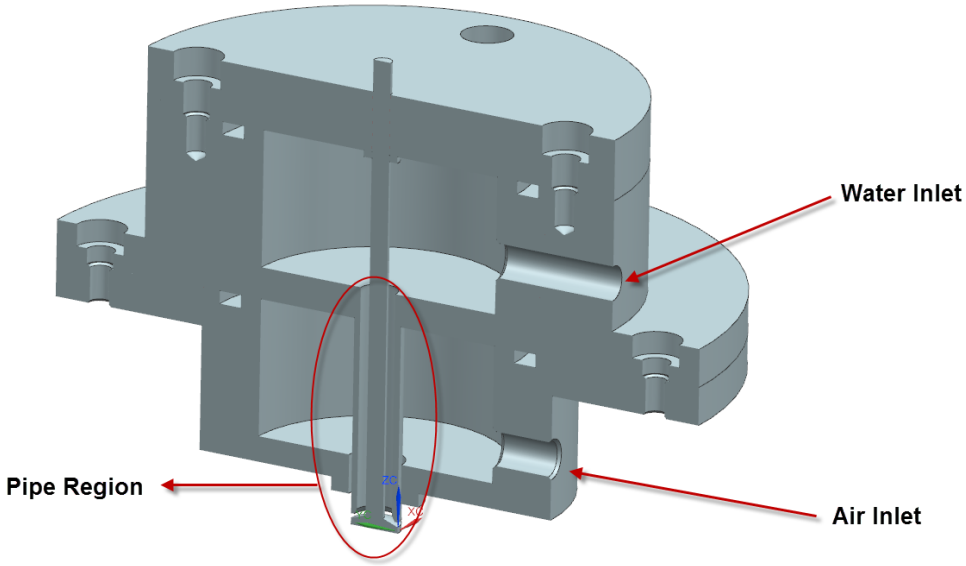


Figure 3 First Reservoir Design Geometry

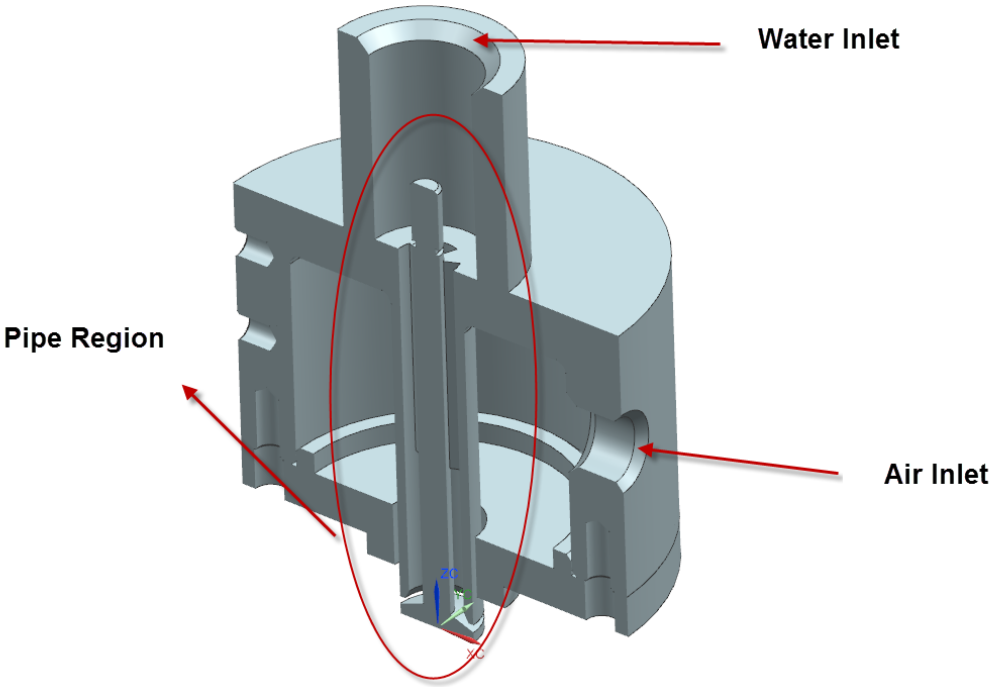


Figure 4 Second Reservoir Design Geometry

3. EXPERIMENTAL WORK

The experimental setup is given in Figure 5. Water is stored in a high-pressure water tank and it is supplied to the injector. Air is supplied from a dry air tube. While supplying the water and air, the mass flow rate and pressure at the injector is measured by a data acquisition system.

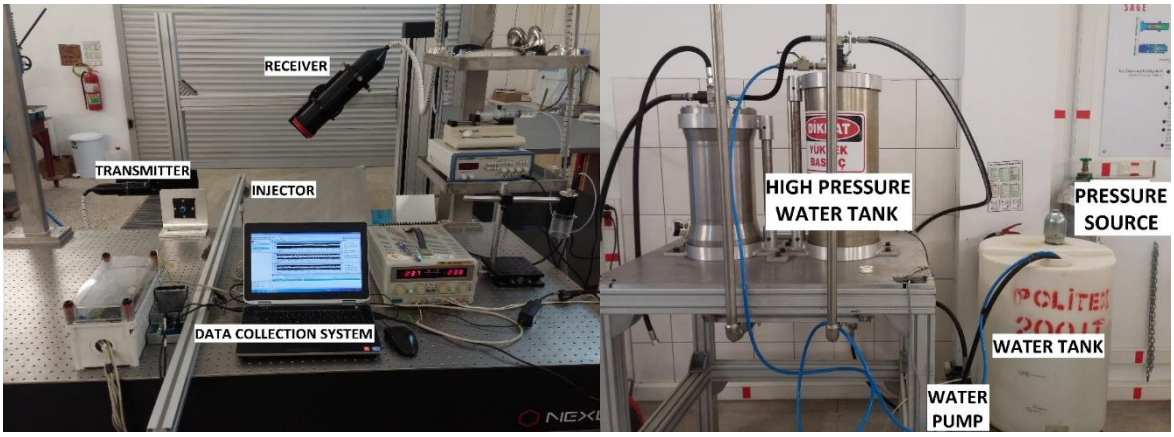


Figure 5 Experimental Test Setup

A high-speed camera is used with a shadowgraphy system to measure the cone angle. 5000 frames per second are captured and post processed with a MATLAB code. This code evaluates the cone angle for each image and calculates a mean angle for them.

Two designs are tested individually, however; both have problems with the spray pattern due to different reasons. First design has both asymmetrical inlet for water and air. Moreover, the mechanical tolerances of the injector are not at the desired condition. These problems lead flow pattern to be asymmetric. Thus, a well-defined test procedure is not applied during the test of the first design. 10 lt/min of water and 400 lt/min of air are used for the first design. The half cone angle is calculated as 44.7°. A shadowgraphy image of the test is given in Figure 6 where non-symmetric pattern is easily observed. The same flow rates are applied for the second design. Mechanical tolerances are also a problem for this design. However, the main problem is the mounting logic of the pintle to the pipe region. The half cone angle is calculated manually because of the undesired flow pattern shown in Figure 7. Since both flow patterns are unsatisfactory, no more test is conducted.



Figure 6 Spray Pattern in the First Design



Figure 7. Spray Pattern in the Second Design

4. CONCLUSION

A pintle injector design procedure is discussed and a validation case is selected from Son's study [Yoon,2017] for the pipe region. First CFD analysis are carried out and the obtained spray cone angles are in close agreement with the experiments. However, reservoir design is not discussed in their study, although it has an importance for the spray pattern in the pintle injector. For this reason, two different reservoirs are designed and tested. However, none of them manage to have the desired flow patterns. The reasons for this undesired flow pattern are inaccurate mechanical tolerances, mounting of the pintle close to injection point and non-symmetrical inlets. For the future work, a third design will be tested. Moreover, 'Phase Dopler Particle Analysis' will be conducted to obtain Sauter Mean Diameter and velocity distrubitions. In addition to eliminate the mechanical tolerance problems, a linear motor will be used to move pintle.

REFERENCES

1. **G. A. Dressler and J. M. Bauer. (2000)**, "TRW Pintle Engine Heritage and Performance Characteristics," in AIAA, Redondo Beach, CA.
2. **E. J. Mercieca. (2017),** "Spray Characteristics in Gas/ Liquid Pintle Injection," TU Delft, Delft.
3. **M. Bedard, T. W. Feldman, A. Rettenmaier and W. Anderson. (2012),** "Student Design/Build/Test of a Throttleable LOX-LCH4 Thrust Chamber," in 48th AIAA/ASME/SAE/ASEE Joint Propulsion Conference & Exhibit, Atlanta Georgia.
4. **M. Son, K. Radhakrishnan and J. Koo., (2017),** "Design Procedure of a Movable Pintle Injector for Liquid Rocket Engines," JOURNAL OF PROPULSION AND POWER, vol. 33, no. 4, pp. 858-869.
5. **M. Son, K. Radhakrishnan, Y. Yoon and J. Koo., (2017),** "Numerical study on the combustion characteristics of a fuel-centered pintle injector for methane rocket engines," Acta Astronautica, vol. 135, pp. 139-149.
6. **P. Cheng, Q. Li, S. Xu and Z. Kang., (2017)**, "On the prediction of spray angle of liquid-liquid pintle injectors," Acta Astronautica, vol. 138, pp. 145-151.
7. **K. Sakaki, H. Kakudo, S. Nakaya, M. Tsue, K. Suzuki, R. Kanai, T. Inagawa and T. Hiraiwa., (2017)**, "Combustion Characteristics of Ethanol/Liquid-Oxygen Rocket-Engine Combustor with Planar Pintle Injector," JOURNAL OF PROPULSION AND POWER, vol. 33, no. 2, pp. 514-521.

CFD SIMULATION OF TRAIN FIRE IN THE ISTANBUL METRO TUNNEL

M. İlter BİLGE, *ilter.bilge@meconyapi.com* Middle East Technical University, 06800, Ankara, Turkey

Haluk AKSEL, *aksel@metu.edu.tr* Middle East Technical University, 06800, Ankara, Turkey

ABSTRACT

This research thesis presents the simulation of a fire scenario in the tunnel of the Marmaray Metro Line by the use of Fire Dynamics Simulator (FDS) Computational Fluid Dynamics (CFD) Software. The main goal of the simulation is to determine the efficiency of the emergency ventilation system in case of a mid-train fire in the metro tunnels and investigate the ways to develop the safety degrees in underground metro tunnels.

On site measurements are carried out for the selected fire scenarios in the tunnel network and measured values are used as boundary conditions to the CFD simulation.

Keywords: Metro Tunnel, CFD, Fire Simulation

1. INTRODUCTION

The World's population is growing rapidly, and as the cities expand, the demand for public transportation is increasing. Increasing traffic problems in major cities force the municipalities to use railway systems in order to solve the problem. Underground transportation systems seem to be the best solution to solve the transportation problems in growing cities.

One of the most critical problems in underground systems are tunnel fires. Although the materials used in tunnels and train cars are fire rated, accidents involving fire and smoke cannot be prevented which causes numerous casualties as well as immense economic losses. The best way to fight fires in tunnels is to activate the tunnel ventilation system and remove the combustion products from the tunnel thus create a safe evacuation path for the passengers. Without adequate tunnel ventilation, smoke and heat tends to stay in the enclosed area and threatens the lives of hundreds of passengers and prevents the fire fighters to access the fire location.

In order to create a smoke free path for the passengers, the smoke has to be pushed to the opposite direction of evacuation path. Therefore, tunnel ventilation systems have to be designed and engineered with great care and detailed analysis has to be carried out to predict the smoke movement in the tunnels and stations.

Emergency ventilation systems operate in case of a fire caused by malfunction of a train component or a baggage fire inside the station and assists the passengers for evacuation. In this case the smoke extract fans start to operate and try to keep the evacuation routes in tenable conditions. This study investigates the emergency operation of the metro system, namely the Tunnel Ventilation System which is activated due to a fire case at the middle of the train by making use of Computational Fluid Dynamics.

1. 1 Description of Marmaray Metro Tunnel

Marmaray is the Metro Line that connects the European and Asian sides of Istanbul, the World's 6th most populated city. 1.387 meters of the tunnel is under the water and the deepest part is 60m below the sea level. The metro line is composed of 5 metro stations and corresponding tunnels. Tunnels are in twin-bore, single track arrangement in other words every track is on a separately bored tunnel. Within the tunnel, cross passages are located in every 200m in order to help passengers cross from one track to the other in case of an emergency scenario. The system started operation in October 2013 and currently carries about 200.000 passengers every day.

The passengers are required to walk to the nearest station by using the walkways located on both sides of the track in case of a train failure in the tunnel. Therefore, smoke evacuation is crucial in this metro system since there is no escape shafts in the tunnel.

A 1D simulation on Subway Environmental Simulation Software (SES) was carried out for different fire scenarios and the Tunnel Ventilation Fans were selected to operate at 144 m3/s flowrate with three fans are operational at each station. This study was carried out by AECOM, Tunnel Ventilation Group from USA, and the fan flow rates were verified by on-site measurements. Saccardo Nozzles were installed at both ends of the tube, namely Yenikapı and Ayrılık Çeşmesi Stations in order to direct the flow to the required tunnel sections. The fans are fully reversible, which means that the fans can exhaust or supply air depending on the location of the fire and the train.

At the cross-over locations where the two tunnels connect and the tunnel area increases by a factor of more than 2, Jet-Fans are utilized to direct the smoke towards the extract direction. Without the Jet-Fans it is not possible to reach the critical velocity in this area due to the drastic increase of tunnel area.

There are two tunnels each occupied with a single track, and the height of the tunnel is 6.2 meters. The cross section area of each tunnel is 33.26 m^2.

2. ON SITE MEASUREMENTS

Subway Environmental Systems (SES) is a widely used software in underground transportation systems and an analysis was carried out by the designer of the Marmaray Tunnel Ventilation System for different fire scenarios in the tunnel. Tunnel Ventilation Fans and Over Track Exhaust Fans were selected according to the calculated critical velocities as a result of the SES analysis. The equipment and systems were installed in parallel to the design values. It is very important to check if the system is operating according to the design values during commissioning of the Tunnel Ventilation System. In order to verify the design values obtained by SES simulations, on site cold flow tests were carried out inside the tunnels for various different fire scenarios.To measure the air velocity, alternative measurement tools such as vane anemometer, hot wire anemometer and Pitot tube are available. Since the cross sectional area is large, and velocity fluctuations occur along the measurement plane, a grid system that covers the entire tunnel cross-section have to be utilized and measurements need to be taken simultaneously.

The grid system was designed with reference to ASHRAE Fundamentals 2013, Chapter 36 [Ashrae_2013] on Measurement and Instruments. To account for the effect of wall friction and the decrease of velocity near the tunnel walls, the log-Tchebycheff (log-T) method was adopted, and the locations of the measurement points were selected accordingly. Five diameters have been chosen with six locations on each circle positioned every 60˚ as seen in the following figure. This arrangement allowed a measurement grid of 30 points. Pitot tubes were manufactured in accordance with Figure 1.

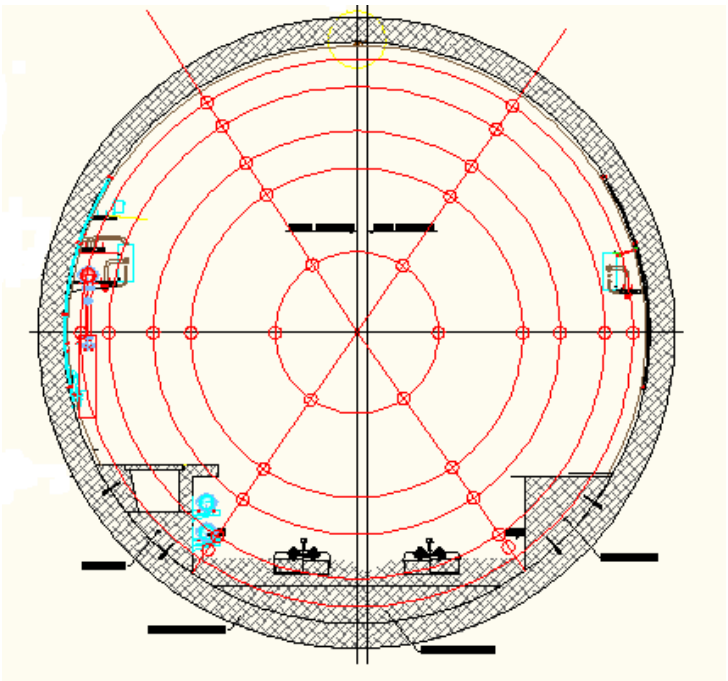


Figure 1. Measurement Locations on Tunnel Cross-Section for 30 Point Layout

A steel platform with wheels (Test Rig) was constructed in order to mount the pitot tubes, which are each 3m long. The heavy platform gave the rigidity to resist the vibrations from the oncoming flow.

The tubes were connected to the Test Rig by nuts and bolts, the rigid platform was moved to the test location with the help of track wheels mounted. Brake pads were also installed to stop the test rig after it is positioned at the correct location. The total and static pressure was measured by separate tubes mounted back to back.

The data acquisition system composed of 6 wireless pressure transducers which transferred the differential pressure data to 4-20mA signal and transferred the measured data to the TESTO computer software each 20 seconds. The current values in mA were then converted back to pressure values in Pa with the help of the software. A different pressure value was obtained for each the 6 Pitot tubes and average velocity was calculated by making use of Bernoulli's Equation.

The differential pressure readings from the pitot tubes were collected with six differential pressure transmitters (Dwyer 610 series low differential pressure transmitter) and transferred to PC unit using the Testo Software. By using the simplified form of Bernoulli's Equation velocity values were calculated.

$$P_t - P_s = \frac{\rho v^2}{2} \tag{1}$$

In this equation Pt and Ps (Pa) are total and static pressures measured by the pitot tubes, v is the air velocity (m/s) and, ρ is the density of air (kg/m3) which is read from the psychometric chart after the measurements of temperature and humidity. The velocity values were recorded continuously and averaged to determine the air flow rate inside the tunnel. Temperature and humidity values were measured to determine the density of the air in each test. Entire test set up can be seen in Figure 2.

The velocity around the train is much higher compared to the velocity inside the tunnel since the cross-sectional area is less. Velocity at the walkway next to the train is also measured by a Dwyer Series Pitot Tube and Testo 435-4 digital manometer in order to check that the velocity is below 11m/s and the escape routes are safe for passengers.



Figure 2. Test Set-up

3. 1 Measurement Results

The measurements are carried out at 7 different locations of the tunnel, with emergency ventilation system operating in each fire scenario. These locations are determined by the tunnel ventilation authorities as the most critical locations of the tunnel network.

The measured volume flow rates and velocities are compared with the values computed in the SES Simulations. Different scenarios at different locations are numbered from T1/4 to T8/4. As a result of the measurements, average velocities inside the incident tunnels were calculated for each scenario as summarized in the Table 1.

In conclusion, the air velocity in the tunnel in emergency case is acceptable for all seven scenarios since the measured velocities are within the measurement tolerance limits or greater than the design velocities. This is deemed adequate for tunnel safety by the local authorities since the values required by the SES Simulation is verified. However, since the design is based on the 1D Subway Environmental Systems simulation, the design velocities may not be satisfactory in a real fire case where the flow is dominated by buoyancy and this situation will be investigated by making use of 3D Computational Fluid Analysis in this study with the help of Fire Dynamics Simulator.

Therefore, the measured air velocity of 3.80m/s at the tunnel inlet is used as input parameter to the CFD simulation. Average cross-passage velocity is measured as 4.24m/s directed from the non-incident tunnel to the incident tunnel. This value is also used as an input parameter to the simulation.

Table 1. Measured Tunnel Air Velocities

Emergency Scenario	Scenario Location	Design Velocity (m/s)	Measured Velocity (m/s)
T1/4	Yedikule Station	3,51	5,11
T2/4	Yenikapı-Yedikule	2,39	3,21
T2/6	Yenikapı-Yedikule	3,82	4,12
T4/4	Yenikapı-Sirkeci	3,41	3,44
T5/4	Üsküdar-Sirkeci	3,07	2,95
T7/4	Ayrılık Çeşmesi-Üsküdar	3,38	3,80
T8/4	Ayrılık Çeşmesi-Üsküdar	2,30	2,59

3. FIRE SIMULATION BY FIRE DYNAMICS SIMULATOR

Fire Dynamics Simulator is used in this thesis due to its reliability and widespread use in fire involved scenarios. The software is specifically developed for fire applications.

The geometry in this thesis is composed of a 5 car train and a tunnel. It was assumed that the train stopped inside the tunnel at the station entrance and the fire was initiated at the middle of the third train car. Although trains are programmed to stop at stations in emergency situations, it is not rare to see passengers using emergency brakes and causing the trains to stop inside the tunnel such as the case with the Zurich Metro Fire [Carvel_2004]. The fire is located at the bottom of the front car and it is assumed to be growing with time up to the value of 20MW. The boundary conditions are obtained from on-site measurements and applied to the simulation.

Two sets of simulations are studied in this thesis and results are compared. The only difference between the two simulations is that in the first simulation Tunnel Ventilation Fans are activated at 120th second whereas the fans are not activated throughout the simulation in the second case.

3. 1 Geometry

The geometry is composed of the train and the tunnel and it is modeled in SolidWorks 2015 software and imported to Fire Dynamics Simulator. The curved structures such as the tunnel roof were modeled as small rectangular pieces since FDS supports only rectangular geometries.

In order to investigate the smoke spread clearly, a computational domain of 250m is used in the simulation. 45m of tunnel upstream of the train is also modeled in order to account for the hydrodynamic entry length of the air inside the tunnel. The tracks and wheels are not modeled, since they will have a small effect on the accuracy of the solutions, but they will increase the computational time significantly. Only one cross passage is modeled in the geometry since the other doors are far away from the incident location, and their doors will remain closed.

The train modeled is Hyundai Rotem which is currently being used in Istanbul Metro Lines. The width of the train is 3m, the height is 4.4m and the length of each train car is 22.5m. The entire train geometry is composed of 5 cars which add up to a total of 112.5m. Complicated geometry features such as windows, doors, and wheels are not model since they will not have a significant effect on the temperature and velocity distribution inside the tunnel. The train area is 22.26 m^2 and the train is immobilized inside the tunnel. The air movement inside the train is of small interest and doesn't have a very important contribution to the temperature distribution at the walkways and therefore entire train is modeled as a solid object with adiabatic boundary conditions. Specific damage to the train cars such as broken windows or collapsed compartments were not included in the simulations. Throughout the study, the train dimensions remained the same since it is difficult to predict such behaviour. The full scale 3D model of the train and tunnel can be seen in Figure 3.

3. 2 Meshing and Boundary Conditions

CFD softwares have the potential to develop more accurate results as the mesh is refined; however, the calculations require large amoung of computational time therefore the mesh has to be optimized for accuracy and computation duration.

For a simulation involving buoyant plumes, a measure of how well the flow field resolved is defined by the non-dimensional expression of D*/ Δx where Δx denotes the size of a mesh cell and D* denotes the characteristic fire diameter defined by the following equation as [Mcgratan_2013]:

$$D^* = \left(\frac{\dot{Q}}{\rho_\infty c_p T_\infty \sqrt{g}}\right)^{\frac{2}{5}} \quad (2)$$

Where,
$\dot{Q}$ = Total Heat Release Rate of Fire (kW)
ρ_∞= Ambient Air Density kg/m3)
c_p = Specific Heat of Air (kJ/kg*K)
T_∞ = Ambient Air Temperature (K)
g = acceleration caused by gravity (m/s^2)

The ratio of D* to ∆x is used to evaluate how fine the mesh is in the simulation. The greater the ratio, the more resolved the fire is. A ratio between 4 and 16 gives satisfactory results according to the verification reports of FDS [Nureg_2006]. But increasing the D*/ Δx increases the computational time drastically therefore excessive refinement of the mesh need to be avoided. By inputting the parameters for the current problem, with the nominal heat release rate of 20MW, the D* value is calculated as 3.18m for the given heat release

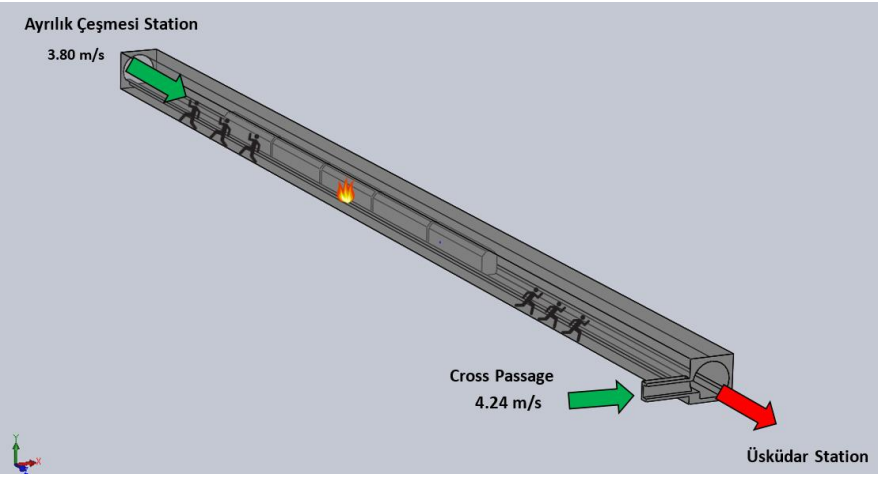


Figure 3. CAD Model of Tunnel and Train

rate, therefore Δx , nominal size of the mesh has to be selected accordingly. The mesh in FDS is obtained by discretizing the domain in x, y and z directions. The nominal edge lengths for optium mesh size after the mesh optimization is selected as x=0.34m, y= 0.35m, z = 0.36mThe following image shows the cross-section view of the used mesh and the orientation of x,y,z directions.

Appropriate boundary conditions are essential in obtaining meaningful numerical solutions. Tunnel inlet velocity is determined by on-site measurements, along with the inlet velocity at the cross passage entrance and these values are directly applied to the simulation. The fire is initated at t=0s, and the fans are operated at t=120s since the activation of fire alarm and ventilation system requires some time. Tunnel outlet is determined as zero gage pressure. Tunnel and train walls are modeled with no slip boundary conditions and they are assumed to be adiabatic. Other heat transfer options could be adpoted for the tunnel walls but this is not a bad apprximation since the tunnel linings are made of thick concrete material. Investigation of this assumption can be a subject of future research. This assumption also considers the worst case scenario since the heat transfer through the outer boundaries are neglected. Therefore, there will be no heat loss to the surrounding and all the thermal energy will be kept in the tunnel.

Table 2. Boundary Conditions

Description	**Boundary Condition Type**	**Value**
Tunnel Inlet	Velocity Inlet	3.80 m/s, 24,1 C^o
Cross Passage Inlet	Velocity Inlet	4.24 m/s, 24,1 C^o
Tunnel Walls	Stationary wall	Adiabatic, No Slip
Train Walls	Stationary Wall	Adiabatic, No Slip
Tunnel Outlet	Pressure Outlet	0 Gage Pressure

The initial temperautre inside the tunnel was set to 24,1^{0}C in accordance with site measurements and the supplied air temperautre was set to the same temperature. During the second simulation, the same boundary conditions are used except the inlet velocities. For the case without fan activation, the velocity inlets are defined as pressure outlets during the set up of the simulation.

3. 3 Modeling of Fire

The fire starts with the ignition and grows consuming the available fuel until it reaches the fully developed stage. Therefore, the growth of the fire from 0 to 20MW needs to be modeled in the simulation. A good approximation is to use a T-squared method where the heat release rate is assumed to be growing proportionally with the square of time. This is one of the most valid approximations since the initial growth period is nearly always accelerating. The following equation defines the fire heat release rate of a growing fire:

$$\dot{Q} = \alpha \cdot t^2 \tag{3}$$

Where $\dot{Q}$ (kW) is the fire heat release rate, $\alpha\ (kW/s^2)$ is the growth factor and t(s) is the time elapsed after the start of the fire i.e. ignition. The latest version of NFPA204 classifies

fires according to their growth factors. A fire with growth factor of 187W/s2 is very fast, 46,9 W/s2 is fast, 11.7 W/s2 is medium and 2.9 W/s2 is a slowly growing fire. The following graph shows the growth rates for different fire growth factors.

The fire is modeled at the bottom and two sides of the thrid train car at the mid-section. In previous fire cases it is seen that the flammable hydraulic fluid, or the wires located under the train might be the cause of the fire initiation. The fire can grow underneath the train since enough flammable materials are available. Therefore, the burning area is modeled to be at the bottom part of and two sides of the middle car.

The heat release rate of the fire follows the t-squared approximation and reaches a maximum value of 20MW, and a fire area of 12m^2 is selected to represent the fire source distributed evenly on the bottom and sides of the train. Therefore, a maximum heat release rate of 1666,7 kW/m^2 is defined for the burning surface area. The heat release rate starts from 0 kW/ m^2 at the start of the simulation and reaches to its maximum value at t=650 seconds. Spread of fire is not modeled for simplicity and it is assumed that the fire location remains the same throughout the simulation. Heptane is used as the source of fuel since it is a generic hydrocarbon fuel defined in Fire Dynamics Simulator. However, the soot yield value is updated as 0.117 kg/kg.

5. SIMULATION RESULTS

Contours of temperature are obtained at different times at a height of 1.80m from the walkway level. The passengers will be evacuating the fire zone through the walkways therefore the temperature on the walkways need to be evaluated carefully during the evacuation period. The temperature inside the tunnel increases with height due to the buoyancy effect of the hot air, therefore in order to see the worst case scenario, the height of 1.80m is selected as the measurement plane height.

Results are given with 60 second intervals in order to easily observe the temperature behavior inside the tunnel. Temperature scale of minimum temperature of 30^0C to maximum temperature of 80 ^{o}C is used for all plots for ease of comparison of temperatures at different times.

Two different scenarios are plotted. In the following figures, the first snapshot is taken from the scenario with fan operation starting at t=120s and the second snapshot is taken from the scenario with no fan operation. During the check for tenability criteria, it is important that the temperatures at the walkways and the cross-passage remain below 600^{o}C throughout the evacuation time.

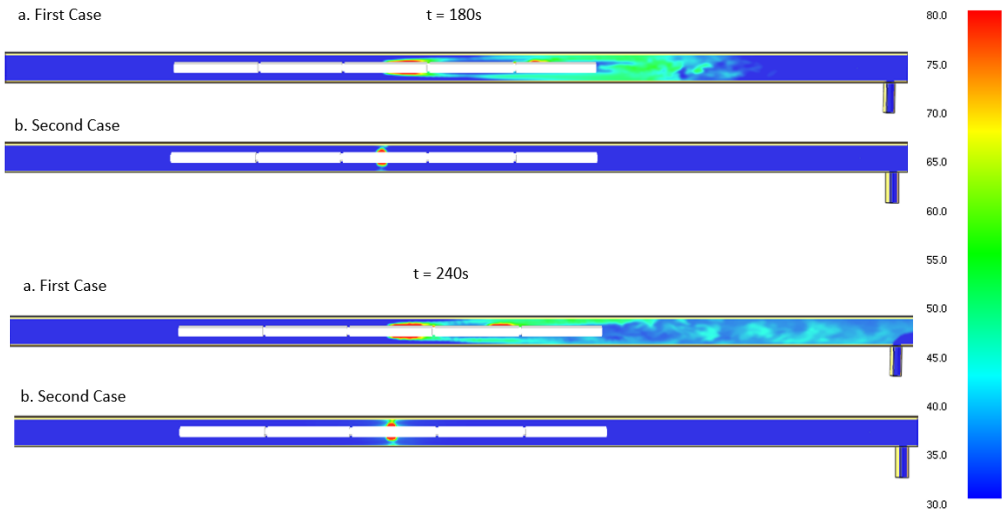


Figure 4. CAD Model of Tunnel and Train Temperature Distribution at the End of Third and Fourth Minute – a. with fan operation at t=120 seconds, b. with no fan operation

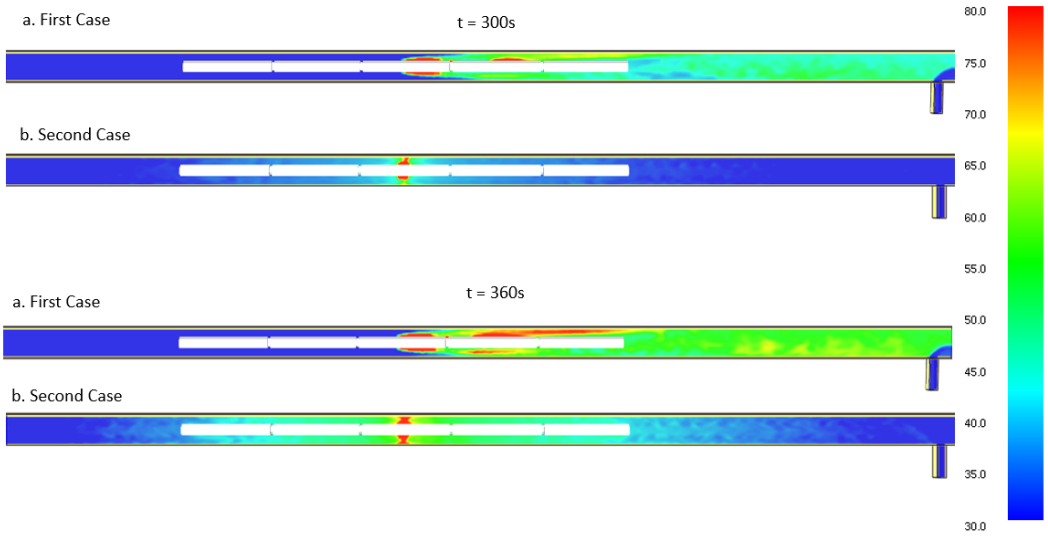


Figure 5. Temperature Distribution at the End of Fifth and Sixth Minute – a. with fan operation at t=120 seconds, b. with no fan operation

The simulation is carried for 650 seconds and the temperature plots are obtained as depicted in the above figures for both of the cases. It is observed that during the first two minutes no significant temperature rise is observed since the heat release rate of the fire is very low. This is the reason why emergency alarm is delayed and fan operation starts 2 minutes into the simulation in the first case. It is understood that both case 1 and case 2 have advantages over each other but the optimum scenario needs to be decided in order to be applied in train fire scenarios. Fire heat release rate increase proportionally to the square of time, therefore

the temperatures in the tunnel increase drastically as the simulation time increases for both simulation results.

In case one, passengers in the first three train cars can evacuate easily without any significant threat however since the smoke is directed to the downstream, passengers at remaining two train cars are subject to gasses with combustion products. The passengers at the last two cars need to either cross the fire zone to evacuate the tunnel through the upstream direction into the station, or they need to walk 80 meters downstream and evacuate through the cross passage within the first 6 minutes.

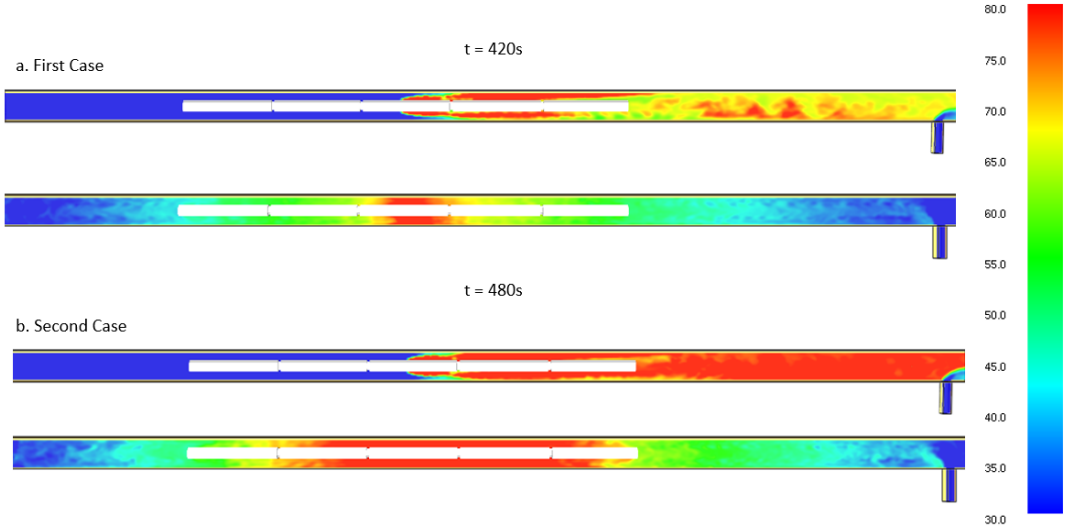


Figure 6. Temperature Distribution at the End of Seventh and Eighth Minute – a. with fan operation at t=120 seconds, b. with no fan operation

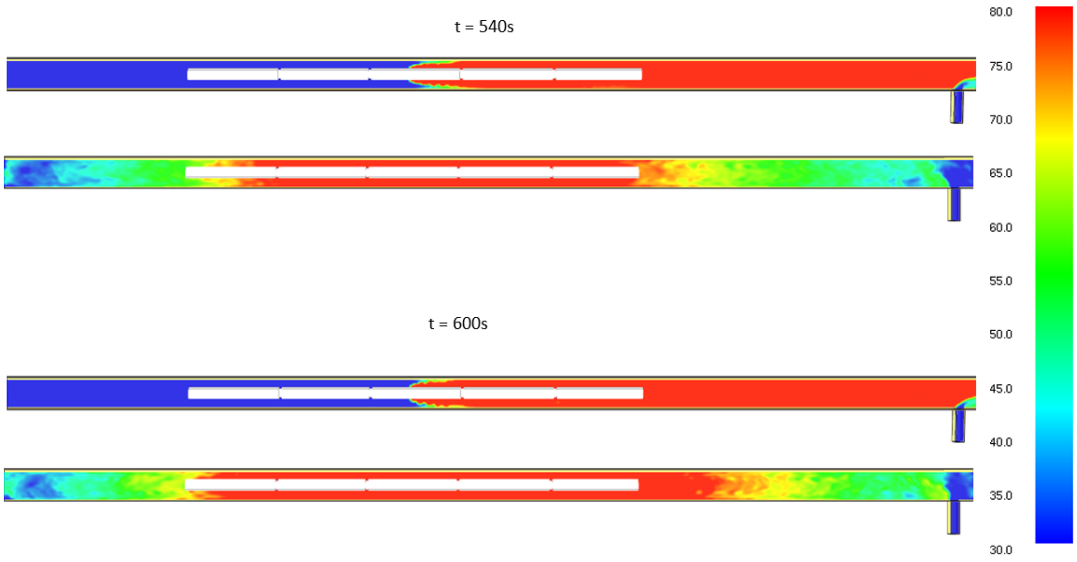


Figure 7. Temperature Distribution at the End of Ninth and Tenth Minute – a. with fan operation at t=120 seconds, b. with no fan operation

Whereas in the second case passengers have extra minutes to evacuate the tunnel but since backlayering is not prevented, high temperatures are seen both at the upstream and downstream of the fire zone thus possibly creating minor injuries, or threatening the lives of the last evacuees. To be able to clearly compare the tenability of two cases, in the FDS Simulation, thermocouples are located over the walkway at a height of 1.80m with 5m spacing in between them. The temperatures are measured every second and the data was recorded. Temperature values were averaged over 10 seconds in order to avoid rapid fluctuations and the results for 6th and 7th minute were plotted in the below figures. The red line shows the limit of T=60 C^0 and it is assumed that tenable conditions no longer exits above this value. In the below figures Case 1 represents the case with Tunnel Ventilation System operation whereas Case 2 represents the scenario without the fan activation. The fire is located at the 105th meters inside the tunnel and cross-passage is located at the 235th meter.

The graph clearly shows that during the 6th minute, ventilation inside the tunnel prevents backlayering and keeps the upstream direction at low temperaturesa, however the temperatures at the downstream side reach to high values since the entrained fresh air disturbs the stratified smoke later and causes it to descend below the height of 1.80m. On the other hand without the fan activation it is observed that the hot gasses stick to the ceiling and no temperature hazard is present at human height. Hot gasses move symmetrically to the upstream and downstream sides.

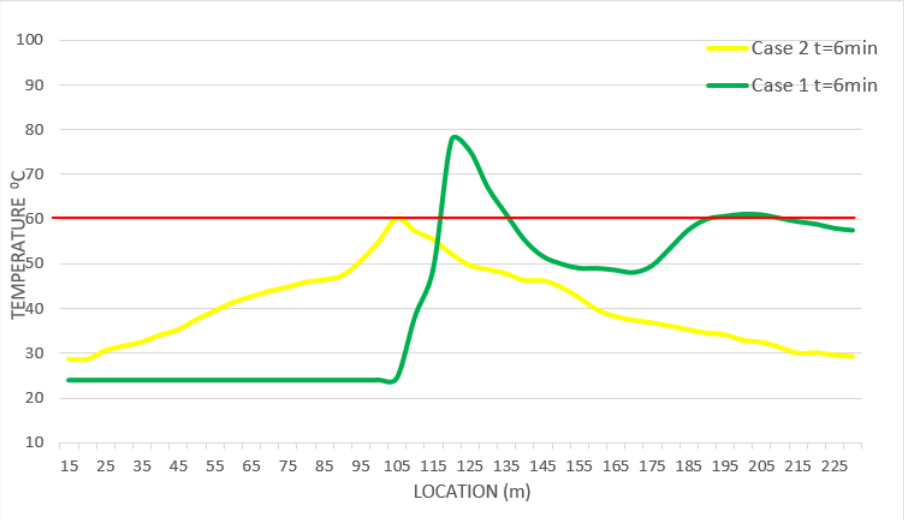


Figure 8. Comparison of Walkway Temperature Distribution With and Without TVS Operation

5. CONCLUSION

The most critical case in tunnel fires is the fire in the middle of the train and this situation was investigated for the Ayrılıkçeşme Station of the Marmaray Metro Line. Two cases were investigated, in the first case, the Tunnel Ventilation System was operated during the detection of fire as planned in the SES Fire Scenario whereas in the second case, ventilation systems were not activated throughout the simulation.

The ventilation direction is determined in SES simulations as directed from the Ayrılıkçeşmesi Station towards the tunnel and the velocity is above the critical velocity. Therefore with the activation of the Tunnel Ventilation System, the front three train cars are cleared from smoke and hot gasses but the ventilation pushes the combustion products to the downstream side of the train and remaining three train cars and the walkways are subject to untenable environments. After the fan operation, it is observed that no backlayering occurs, i.e, the passengers at the upstream side of the fire can self-evacuate easily through the walkway and into the Ayrılıkçeşmesi Station. It is seen that after the sixth minute both temperature and visibility criterions are failed, therefore the lives of passengers remaining at the downstream side of the fire are threatened after the sixth minute.

On the other hand, if the fans are not operated, the hot gasses tend to stack at the upper layers and do not threaten the evacuation during the first seven minutes. Therefore compared to the first case, passengers have an extra 80-90 seconds before the temperature limits are exceeded. It is also important to note that visibility limit is never exceeded for this case since the hot gasses remain at the upper parts of the tunnel.

The adiabatic heat transfer assumption on the tunnel walls has also an effect on the temperature plots and it can be said that the temperature values would be lower in a real fire case due to the heat transfer through the tunnel walls thus tenability time would increase slightly.

Tunnel Ventilation Systems are very efficient during end train and front train fires, and they provide tenable environments for passengers if they are operated in the right manner, on the other hand during the mid-tunnel fire cases it is observed that TVS has an adverse effect to the ventilation and the fans should not be operated until evacuation at both upstream and downstream side is completed.Previous accidents show that improvements are required to prevent loss of lives in Metro Train Fires. Following improvements can be made in order to further increase the safety degree in case of Tunnel Fires in Underground Metro Systems:

- Informing passengers about evacuation scenarios by signs or TV screens in the train cars.
- Carrying out frequent fire drills to train the personnel

- Installation of Safe Rooms on the walkways between cross-passages

Applying transverse ventilation instead of longitudinal ventilation throughout the tunnel network.

REFERENCES

1. **Ashrae, (2013) "**Ashrae Handbook: Fundamentals." Chapter 3, pp 812

2. **Carvel, R.O (2004) "**Fire Size In Tunnels", ", M. Sc. Thesis , Heriot-Watt University Civil Engineering Richard Oswald Carvel BSc, Edinburgh.

3. **McGratan, K (2013)** "Fire dynamics simulator technical reference guide", *NIST,* Vol. 1, pp 175.

4. **Nureg (2006) "**Verification and Validation of Selected Fire Models for Nuclear Power Plant Applications" Vol. 1.

CARTESIAN MESH GENERATOR WITH ADAPTATION TO BOUNDARY LAYER

Merve ÖZKAN, *merve.ozkan@tubitak.gov.tr* TÜBİTAK SAGE, 06261, Ankara, Turkey

Özgür Uğraş BARAN, *ubaran@metu.edu.tr* Middle East Technical University, 06800, Ankara, Turkey

M. Halûk AKSEL, *aksel@metu.edu.tr* Middle East Technical University, 06800, Ankara, Turkey

ABSTRACT

A new mesh generator, which is developed for producing body-fitted boundary layer mesh, is presented. The generated mesh is composed of prismatic, tetrahedral and pyramid cells with Cartesian core mesh. Triangular prismatic mesh generator is derived from an open source code SUMO, and the customized prismatic mesh generator allows building high quality meshes near solid boundaries for the calculation of viscous flow. The Cartesian core mesh is generated staring from the surface mesh located at the outermost layer of prismatic boundary layer mesh. The connection between the boundary layer and the Cartesian core mesh is provided by filling the gap between pyramid and tetrahedral volume elements. The tetrahedral volume elements are generated by an open source Delaunay tetrahedralization program, TetGen. In this study, the boundary layer mesh and Cartesian mesh generation modules are developed and all of the sub-mesh generation modules are integrated to achieve the new mesh generator.

Keywords: Computational fluid dynamics, Mesh Generation

1. INTRODUCTION

In Computational Fluid Dynamics (CFD), mesh generation plays an important role on the solution quality. For complex geometries, mesh generation becomes cumbersome to deal with, especially at the boundary layer. For boundary layer, the mesh should provide smooth transition between volume elements to handle high gradients at the viscous flow zone, which is mainly provided by prismatic elements. The Cartesian mesh, on the other hand, is preferred over other types of meshes due to the high quality interior cells. Also, Cartesian

mesh generation is fast and mesh size distribution from large to small cell sizes are straightforward.

In this study, a mesh generation method, which produces pentahedral-prismatic meshes near the solid boundaries and a Cartesian core mesh connected by Tetrahedral and Pyramid volume elements, is presented. The method is constructed using prismatic grids at the solid walls to provide boundary layer solution. Cartesian grids at the core are preferred over other types of meshes because it is known that hexahedral mesh gives more accurate calculations [Owen, 1998]. Also, the generation of the hexahedral mesh with an octree based algorithm is very fast. Cartesian grids are popular due to its performance and feasibility in computer memory even for complex geometries. Cartesian mesh can be generated automatically and provides simple flux formulations. The main drawback of Cartesian mesh is the incapability of body conforming adaptation in the vicinity of the domain boundaries, also at the locations where the boundary layer mesh should be provided [Wang, 1998]. In literature, two different methods are used for the boundary layer of the Cartesian mesh. The most used one is the cut cell approach, where the cells at the boundary of the surface mesh of the geometry surface are cut according to several possibility of polyhedral shape in order to be conformed to body surface. In three-dimensional domain, the cutting process requires lots of calculations and the cost of the mesh generation increases, which results in an inefficient mesh to have accurate results. One of the main drawbacks of this process is the huge number of cells, especially when required first layer thickness for boundary layer calculations is small.

Our approach requires modification at the boundary layer for smooth transition of mesh from surface mesh to boundary layer mesh. By this way, the cost of cutting the boundary cells are eliminated and irregularly shaped volume cells at the boundary layer is replaced by high quality prismatic cells. A new boundary layer generation method is explained in this paper.

2. METHOD

Mesh generation algorithm requires an initial surface mesh as a-priori. A couple of different surface mesh formats are accepted including standard CGNS file format with triangular mesh. A very simple initial surface mesh that will be used is given in Figure 1.

A quick overview of the mesh generation process can be explained as follows: Firstly, pentahedral/prismatic mesh is generated by expansion of the surface mesh into the flow domain. Then, Cartesian mesh is generated encapsulating the boundary layer mesh. Between the Cartesian mesh and boundary layer mesh, intersection hexahedrons are eliminated. Then, the void between hexahedrons and prismatic cell is filled with pyramids

and tetrahedral volume elements. The connection process between the hexahedral cells and the prismatic layer is not given in this article.

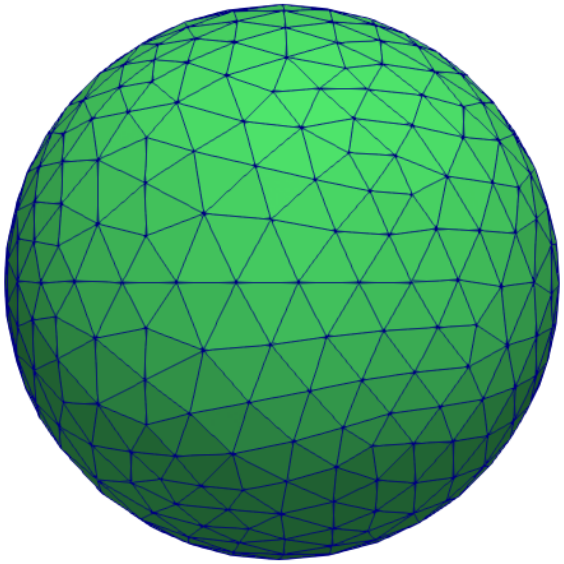


Figure 1. The Surface Mesh (Test Geometry 1)

2.1 Prismatic Boundary Layer Mesh Generation

At high Reynolds numbers, the boundary layer becomes very thin at the vicinity of the solid wall. The viscous forces cause the delay of the fluid. Viscous flow near the wall is called boundary layer flow. For viscous flow simulations, the solution at the boundary layer is an integral part of the solution. Due to no-slip boundary conditions, large velocity gradients are observed in the vicinity of the wall with the highest gradient being at the wall. These gradients are smaller in the direction parallel to the wall. Therefore, for successful simulation of the boundary layer flow and computational efficiency, very thin cells are required next to the wall. Also, the orthogonality is important for boundary layer simulation, since nearly all turbulence models use the wall function. Besides, the quadrilateral mesh provides better orthogonality [Kallinderis et al., 1998].

In this study, the prismatic mesh generation to achieve boundary layer grid is obtained by employing a customized version of prismatic mesh generation subroutines from an open source code called SUMO [Eller, 2009]. SUMO code includes a boundary layer generation library which uses prismatic layers on the surface mesh. The boundary layer library of the SUMO is extracted from the general code. The new customized boundary layer mesh generator has minimum dependencies to the original code. This simplification is carried out for keeping the final mesh generation code as simple as possible.

During the viscous mesh generation process, firstly, a prismatic envelop layer is generated from the triangular surface mesh. Within the envelop layer and the surface mesh, the pentahedral layers are generated according to the properties of the mesh given in the configuration file. The configuration file contains properties of the boundary layer mesh, including first layer thickness, growth ratio and number of prismatic layers. The growth of the prismatic layer is applied along the surface normal of the surface mesh. Accordingly, relatively fast prismatic layer generation is obtained and similarity between prismatic layers is achieved for all regions of the geometry [Tomac and Eller, 2004]. The envelop layer of the boundary layer mesh is, then, used by the Cartesian mesh generator for estimating the refinement level of the mesh as it will be discussed in the proceeding sections. The boundary layer mesh generated around the example geometry is shown in Figure 2.

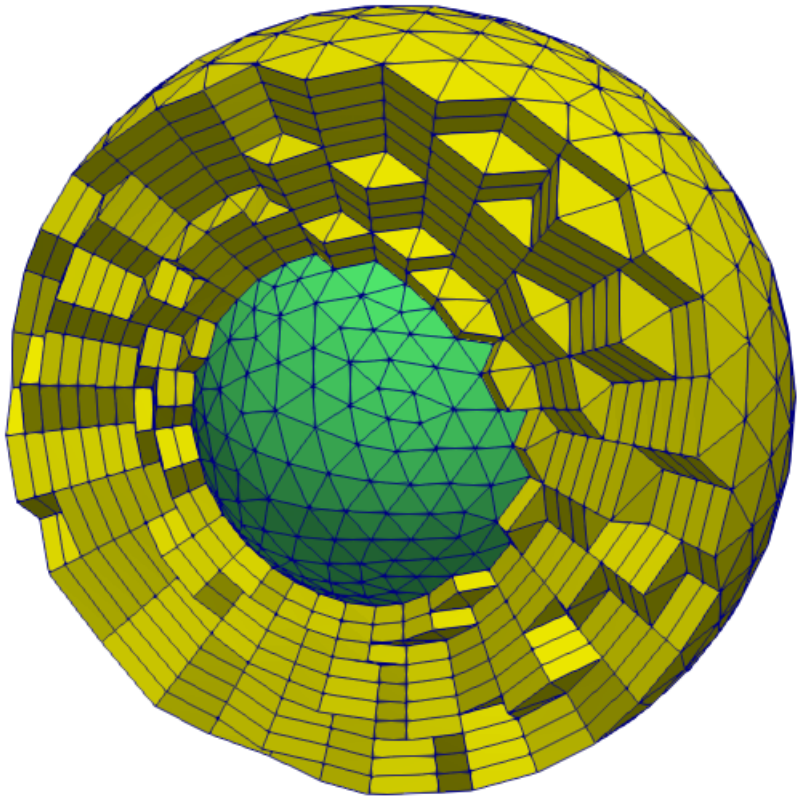


Figure 2. The Pentahedral Mesh

2.2. Cartesian Mesh Generation Process

The Cartesian mesh generator build on a very fast Octree based algorithm in this study. In Octree algorithm, a refinement criterion to capture the geometry must be introduced. This

criterion specifies the size of the smallest cells of the tree at a given location. In our study, the criterion is selected as the size of the side length of the triangular mesh face of the last layer of prismatic mesh, which composes the envelope layer. First the largest cell, that contains the geometry, is generated. Then, the cell is divided into eight child cells recursively. The division continues until the criterion for the local smallest cell size is reached [Owen, 1998].

The most important feature of the Octree algorithm is the possibility of access to the all children cells from the root cell. The relationship between the root cell and the child cells are provided by the parent-to-cell relationship. The parent cell is the cell that undergoes division to produce eight child cells. Also, the neighbors can be the child cells of the same parent or another parent. Neighbor relationship is never stored. If a neighbor cell is to be reached, a traverse starting from the root cell is required. This approach allows a very compact data structure with minimal information being stored about a cell.

“Root Cell”, as mentioned earlier, is the biggest cell that encapsulates the geometry. The length of the side of the root cell is given in the configuration file by the user. The root cell edge length should be given according to geometry to be meshed. The length should enclose the whole geometry. If the size of root cell is not sufficient, then an inappropriate mesh around the geometry would be created and there would be intersections of mesh and the geometry. A factor of safety should be considered as for the decision of the size of the root cell.

After creating the root cell, the decision of division of a child cell is made by comparing the edge size of the triangle of the envelop layer of prismatic mesh and the size of the smallest child cell. The division is called refinement and the refinement level is equal to the number of divisions from the root cell to the finest child cell. The refinement level is found by using the following equation.

$$\text{Refinement Level} = \log_2(2\text{xRoot Edge Length} / \text{Criterion Length}) \quad (1)$$

For fast generation of cell and for a compact memory footprint, the data stored in each cell object is limited to

- refinement level of the cell (integer)
- binary coordinates of the cell (3 integers)
- the information of child cells if they have children. (any case one pointer)
- the status of the cell

Refinement level is the division number of root cell to the smallest computational cell. Binary coordinates of the cells are integers. Giving integer number to the cells is applied by a binary shift operation. When the root cell is divided into eight child cells, the refinement level increases by one and bits are shifted by one digit to the left and binary coordinates of each cell are given accordingly. This operation is applied recursively for each children cell if necessary. From a parent cell, the child cells are accessible; however, access from the child cell to parent cell is not possible.

Therefore, the information about

- nodal coordinates
- parent and neighbor cells
- center coordinates of the cell

are not stored at the cell object to achieve a very compact data structure.

The status of a cell is the type of the cell indicating the location of the cell in the solution domain, whether the cell is in the computational domain or outside of the domain, or intersecting with the domain / prismatic cells. The second group of cells will be removed after marking. An algorithm is responsible from the refinement and marking neighbors of the cutcells with certain cell diffusion. In this process, the size criterion of the smallest cell plays an important role in case of a possible leak of computational cells into the prismatic layers.

After marking of the incells is completed, coordinates of cells can be found from the following equation starting from the Root Cell.

$$\text{Coordinate of Cell} = \text{Coordinate of Root Cell} + (\text{Location of Cell} / 2^{\text{Refinement Level}})\text{x}(\text{Side Length of Root Cell}) \quad (2)$$

Also, the center coordinates of the cells can be found by using the node coordinates and volumetric geometry of the cube.

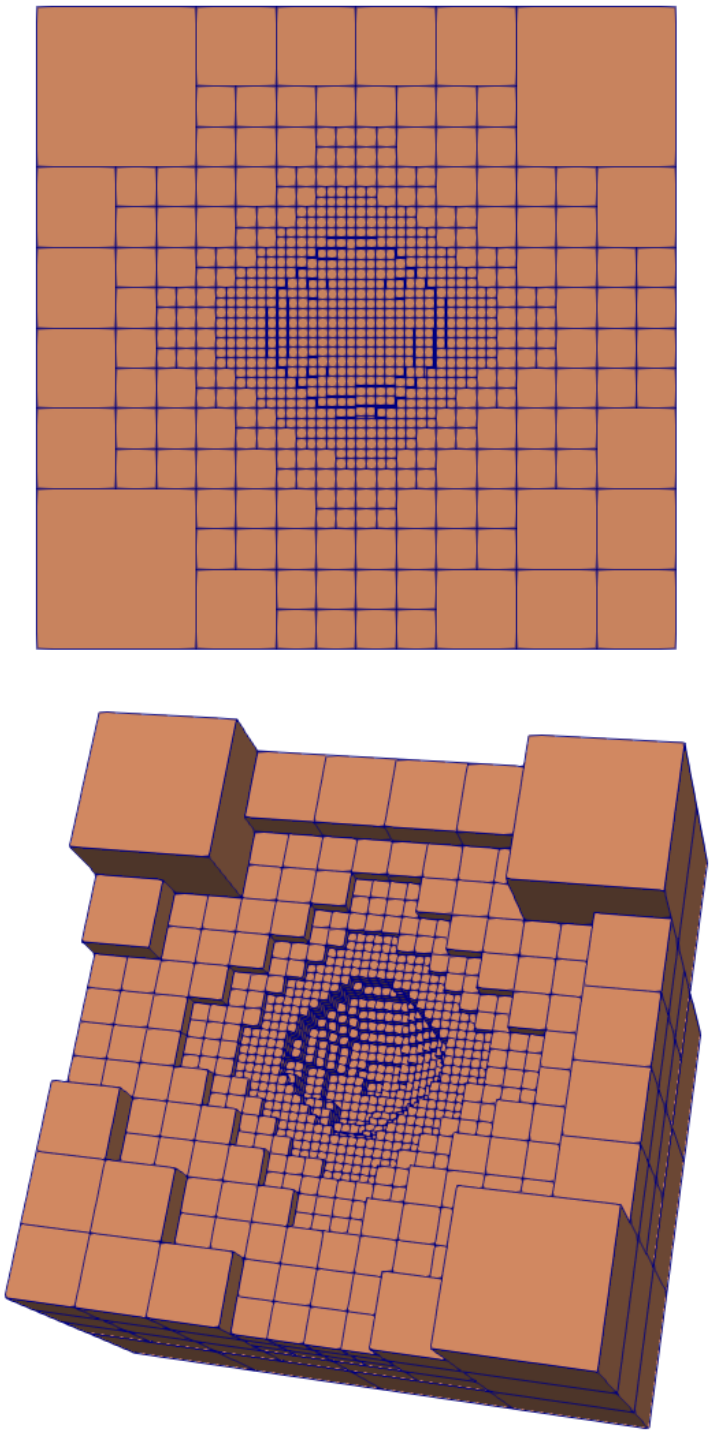


Figure 3. The Cartesian Mesh

The computational cells are marked according to their cell status. The cells, which cut the geometry and the prismatic mesh layer cannot be used as computational cells where the flow data is stored and transferred. Therefore, a seed cell is introduced after the refinement. The seed cell marks its neighbor's recursively and seeks for the cells which are at the boundary of the computational domain where the envelope surface of the prismatic mesh starts.

Reaching the boundary, the marking of the seed cell stops, and the unmarked cells, i.e. cutcells, are omitted from the computational domain. The marked cells that are not cutting the outer surface of the prismatic mesh layer, are called incells. The marking is done by finding the neighbor cell and mark them by the same type as the marked cell itself. An example view for the Cartesian mesh is shown in Figure 3 for the test geometry shown in Figure 1.

The nodes of the cells are generated through another octree based data structure derived from cell octree. It can be observed that the refinement level of the cells in cell-octree is one less than that of nodes of each cell in node-octree, since every cell has 8 corners. Therefore, for each cell, eight nodes are generated with the refinement level of one increment of the refinement level of the cell. Node-octree data structure contains node number starting from zero and continues until all nodes are numbered. To eliminate nodes with the same space coordinates, if a node has child nodes, in other words the cell of the node has child cells, this node does not numbered, instead it is numbered with the number of the node with greatest refinement level and same coordinates in the domain. The space coordinates of the nodes are found by using the following equation.

$$\text{Node Coordinate} = \text{NodeID} \times (2 \times \text{Root Cell Edge Length} / 2^{\text{Refinement Level} - 1}) + (\text{Root Cell Center} - \text{Root Cell Edge Length}) \quad (3)$$

2.3. Pyramid Elements

Pyramids elements are filling elements between tetrahedral and Cartesian grids, connected to hexahedrons only. Since Cartesian grids have square face and tetrahedral volume elements have triangular faces, the connection between them must be made with a geometry that has both square and triangular faces. The algorithm for pyramid elements is embedded in the Cartesian mesh generator algorithm; and therefore the pyramids are generated following the Cartesian mesh generator.

2.4. Tetrahedral Mesh

Tetrahedral volume elements are generated in between the pyramid filling elements and the prismatic layer. Tetrahedral cells provide the connectivity between the prismatic and Cartesian meshes.

Tetrahedra are generated by utilizing the open source mesh generator, TetGen, which is a very robust tetrahedralization program using Delaunay tetrahedralization algorithm. [Si, 2013] TetGen is written in C++ similar to the Cartesian and prismatic mesh generators; hence it is relatively easy to embed into main mesh generation algorithm. The generation of triangulation is fast and efficient, takes a little more than a minute to create triangulation with Delaunay algorithm for 1 million points with 234.47 Mb heap memory [Si, 2007]. TetGen can detect the boundary of a surface mesh and generate the tetrahedral volume elements covering the surface mesh.

The size of the tetrahedral volume elements can be controlled by the user according to the desired mesh configuration. The code also provides mesh refinement at certain locations of the geometry. Besides, the mesh quality can be looked up by giving the appropriate commands to the code. Mesh statistics can be printed [Si, 2007].

2.5. Test Geometries

2.5.1. Sphere (Test Geometry 1)

The surface mesh given in Figure 1, boundary layer mesh given in Figure 2 and Cartesian mesh given in Figure 3 are combined together in Figure 4. The gap between the Cartesian mesh and the boundary layer mesh is to be filled with pyramid and tetrahedral volume elements.

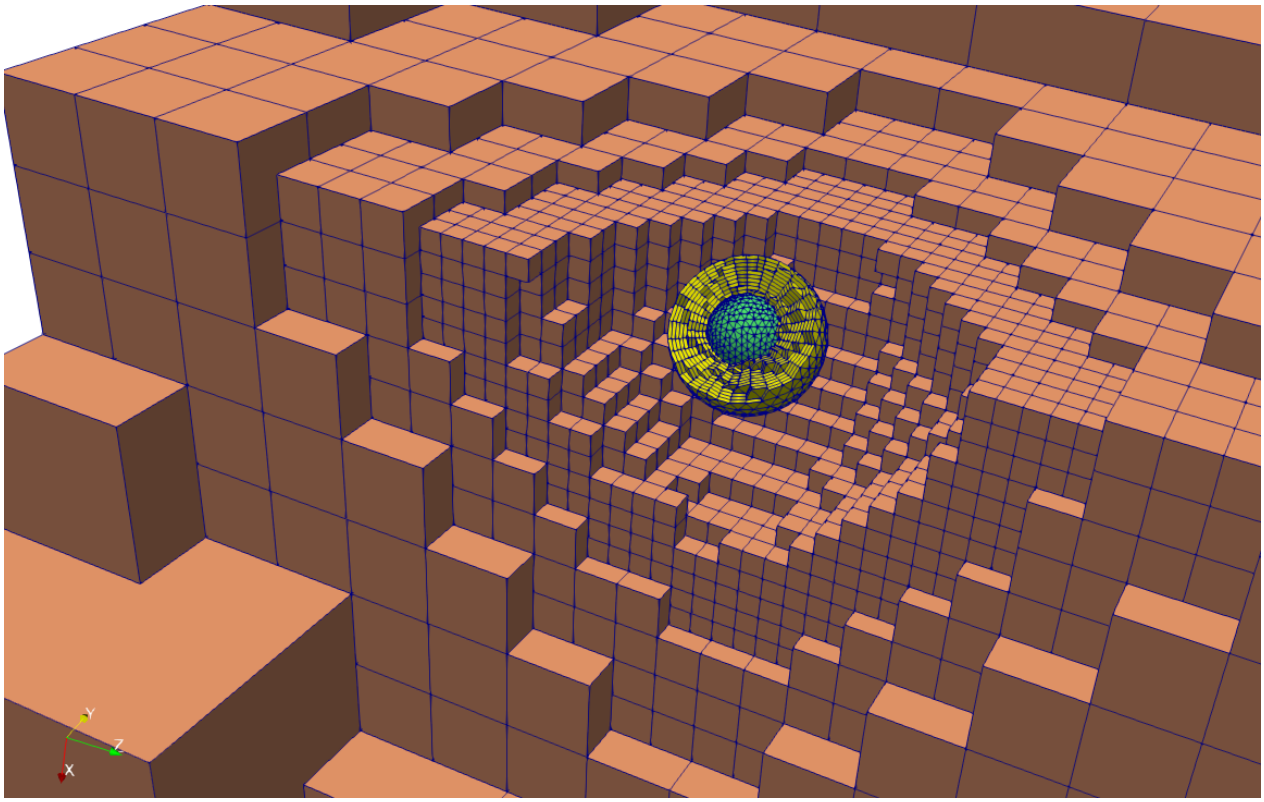


Figure 4. Surface Mesh - Pentahedral Mesh - Cartesian Mesh

2.5.2. NACA 0012 (Test Geometry 2)

Another test case is provided for the boundary layer and Cartesian mesh generators other than the sphere geometry. The airfoil geometry given in Figure 5 with a triangular surface mesh is used as the initial mesh. The boundary layer mesh generated around this test case is given in Figure 6. In Figure 6, a close up of the boundary layer mesh is also given. As seen in the figure, the layers of prismatic elements grow normal to the surface. In Figure 7, the Cartesian mesh generated around airfoil geometry is given with boundary layer mesh. As it is observed from the figure, the triangle size at the expanded layer is compatible with the Cartesian mesh size, which allows a smooth transition from the wedge cells to hexahedral cells.

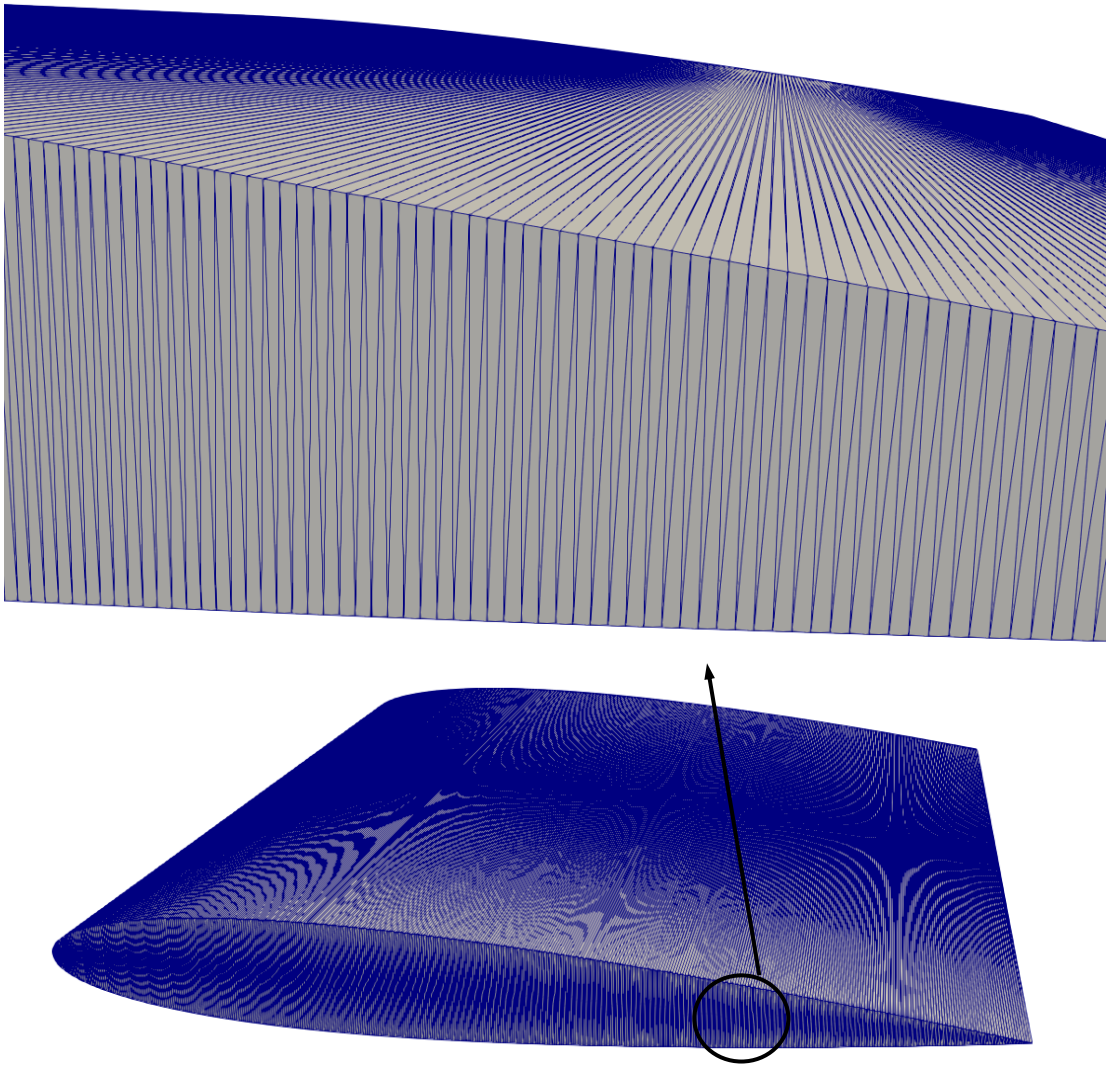


Figure 5. NACA 0012 Triangular Surface Mesh

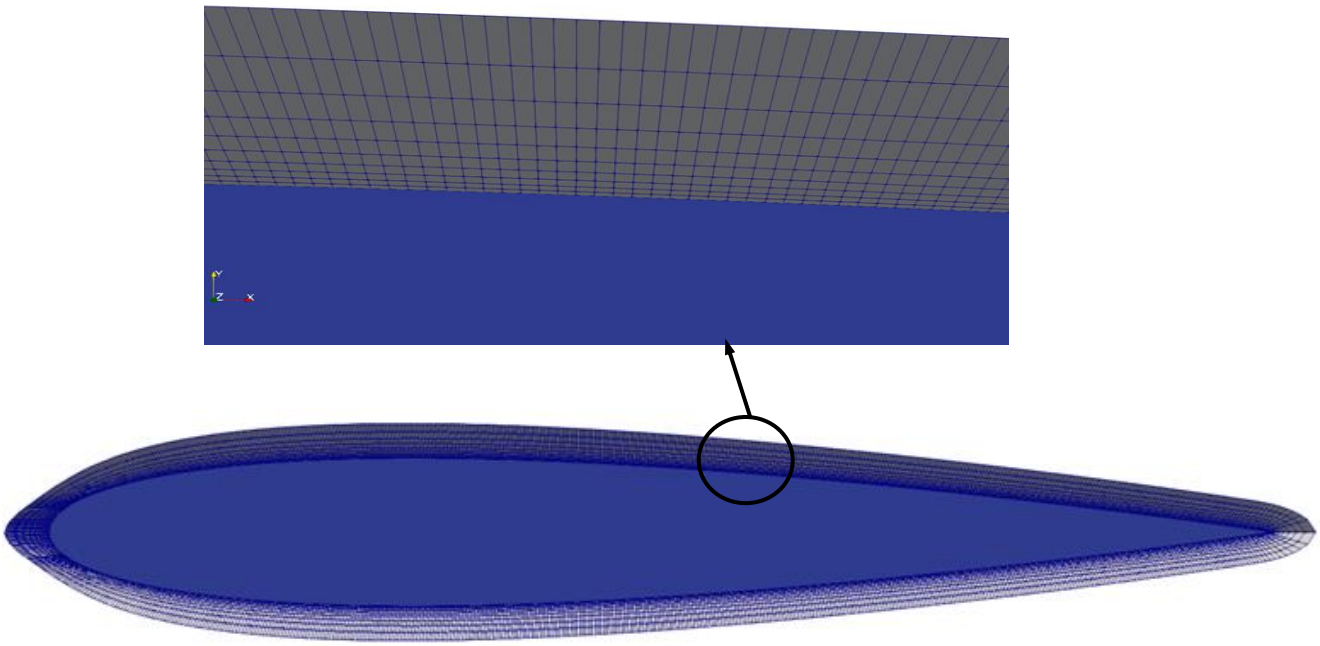


Figure 6. NACA 0012 Pentahedral Mesh

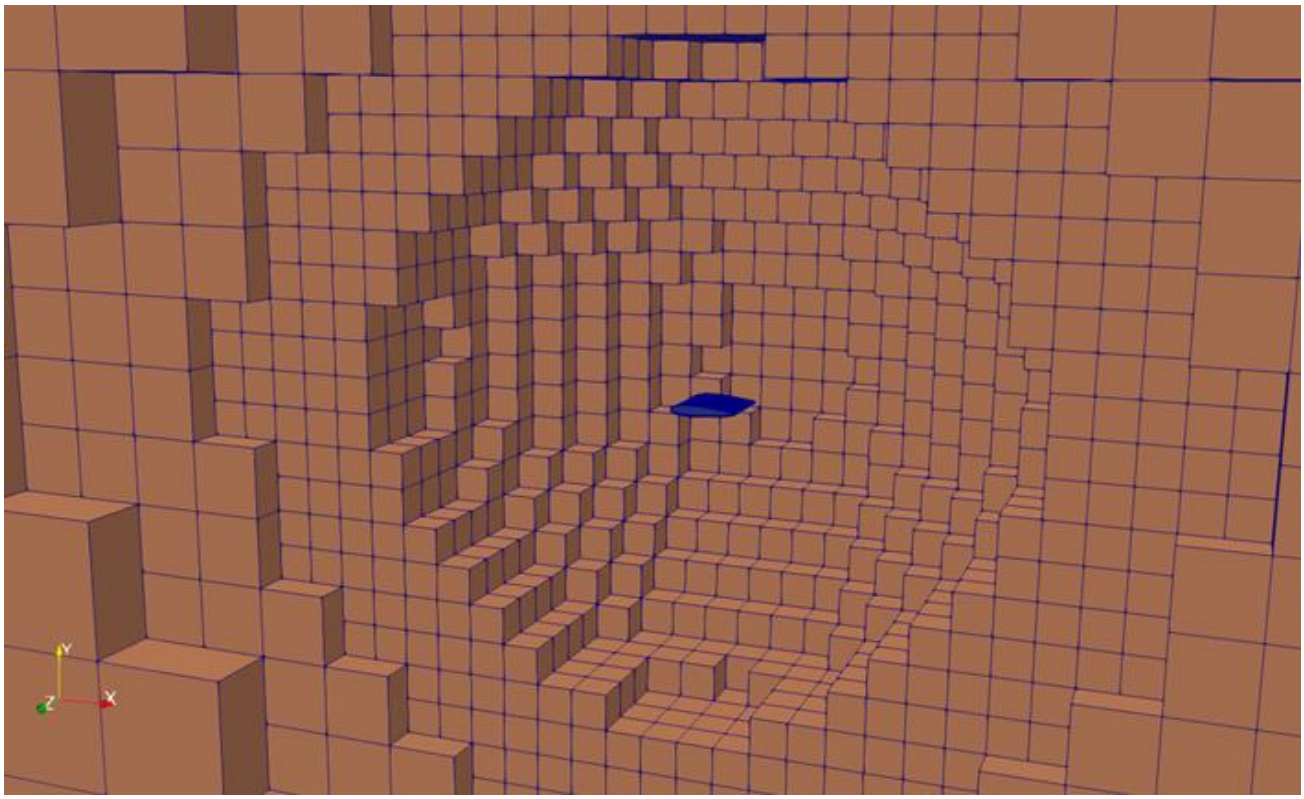


Figure 7. NACA 0012 Cartesian and Pentahedral Mesh

3. CONCLUSION

Algorithm of a Cartesian mesh generator with body-fitted boundary layers and mixed type cells is presented in this study. Different open source mesh generator codes are customized and merged with the in house hexahedral mesh generator. First, boundary layer mesh generator part of SUMO is stripped from the main source and restructured to be utilized in our software. This source is coupled with in-house Cartesian mesh generator and the open source Delaunay based tetrahedralization program, TETGEN. In this paper, the new mesh generator is presented as an alternative to the cutcell approach. The new mesh generator is very efficient in terms of computer resources, which can generate a million cell mesh less than a minute in a single processor. Afterwards, this hybrid mesh generator is integrated to the customized version of open source solver SU2.

ACKNOWLEDGEMENT

The authors acknowledge the support of this research by TÜBİTAK (The Scientific and Technological Research Council of Turkey) Project No. 114M590.

REFERENCES

1. **Owen, S. J. (1998)**, “A Survey of Unstructured Mesh Generation Technology”, Proceedings, 7th International Meshing Roundtable.
2. **Wang, Z. J. (1998),** “A Quadtree-based Adaptive Cartesian/Quad Grid Flow Solver for Navier-Stokes Equations” Computers & Fluids, 27(4), 529-549.
3. **Schlichting, H. (1979)**, Boundary-Layer Theory (7th Ed.). McGraw-Hill Book Company, New York.
4. **Kallinderis, Y., Khawaja, A., & Mcmorris, H. (1996)**, “Hybrid Prismatic/Tetrahedral Grid Generation for Viscous Flows around Complex Geometries”, AIAA Journal, 34(2), 291-298.
5. **Eller, D. (2009),** Sumo – aircraft geometry and surface modeling tool, https://www.larosterna.com/sumo.html
6. **Si, H. (2013)**, TetGen: A Quality Tetrahedral Mesh Generator and 3D Delaunay Triangular User’s Manual.
7. **Si, H. (2007, April 17)**, TetGen: Features. Retrieved from http://wias-berlin.de/software/tetgen/features.html

8. **Tomac, M. and Eller, D. (2014)**, “Towards Automated Hybrid-prismatic Mesh Generation”, Procedia Engineering, 82, 377-389.

EXPERIMENTAL AND NUMERICAL INVESTIGATION OF COAXIAL PRESSURE SWIRL INJECTORS

Onur BARAN, onur.baran@metu.edu.tr, Research Engineer, TÜBİTAK SAGE, 06261, Ankara, Turkey

Yusuf ÖZYÖRÜK, yusuf.ozyoruk@ae.metu.edu.tr, Professor, Department of Aerospace Engineering, Middle East Technical University, 06800, Ankara, Turkey

ABSTRACT

To investigate the spray characteristics of liquid-liquid coaxial injector, numerical analysis and cold flow tests have been performed. Research is planned to carry out by changing recess length and outer injector's type as well as injection pressures. For inner injector of coaxial swirl injector closed-end type injector is used, whereas for outer injector open-end type is used. Tests are performed with high speed camera to determine the spray cone angles. Phase Doppler Particle Analyzer (PDPA) is used to characterize spray characteristics. Two dimensional velocity profile is obtained for both separately and together for inner and outer injectors. Also, Sauter Mean Diameters (SMD) is found for each case. So far, as a test results when both inner and outer injectors are supplied spray cone angle of outer injector decreases and cone angle of inner injector increase and they merge at some point.

Keywords: Coaxial Pressure Swirl Injector, Phase Doppler Particle Analyzer (PDPA), Volume of Fluid (VOF), Sauter Mean Diameter (SMD)

1. INTRODUCTION

Prediction of spray cone angle and droplet size distributions are crucial for design and improvement in Liquid Rocket Engines. Previous studies showed that recess length in coaxial pressure swirl atomizers significantly effects spray characteristic of the injector [1]. To improve the present knowledge on effects of recess length and to see the effects of outer injector type on spray characteristic in coaxial pressure swirl atomizers, this study have been

performed. RD-0110 rocket engine's injector are used with different recess lengths and different outer injectors.

Firstly, injector of a Russian rocket RD-0110 is investigated. Spray characteristic at design and off-design conditions are obtained by using PDPA and high speed camera. Inner injector, open-end swirl injector and closed-end swirl injectors are shown in **Error! Reference source not found.** respectively. Open-end and closed-end type outer injectors are investigated to observe change in spray characteristics.

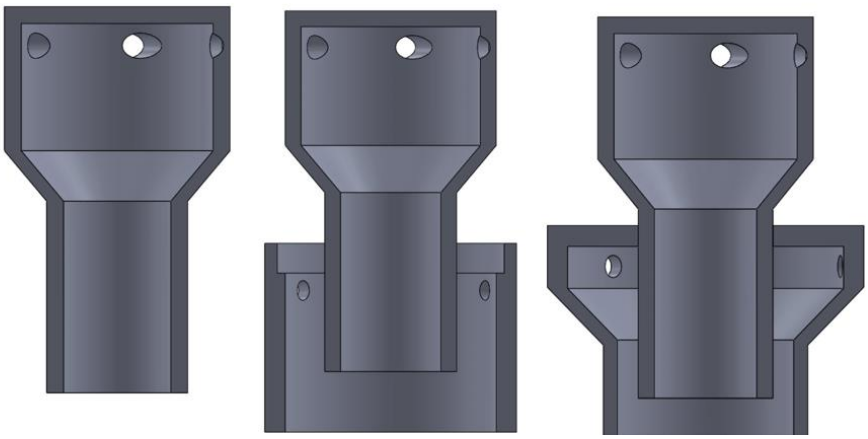


Figure 1. a) Inner Injector b) Open-end Coaxial Injector c) Closed-end Coaxial Injector

2. NUMERICAL ANALYSES

Before the test and CFD analysis performed, analytical and empirical relations are used in the literature to obtain approximate spray cone angles. Flow number and discharge coefficient are calculated using flow properties and geometrical properties of the injector. Area ratio between air core and the K (empirical area ratio) and air core area ratio to orifice nozzle area is calculated with using empirical constants. Then spray cone angle is estimated as below equations. [1].

$$FN = \frac{\dot{m}}{\sqrt{\rho . \Delta P}} \qquad Eq(1)$$

$$c_d = \frac{\dot{m}}{A_0 . \sqrt{2 . \rho . \Delta P}} \qquad Eq(2)$$

$$\mathrm{K} = \frac{A_t}{D_s D_o} \qquad Eq(3)$$

$$X = 1 - \frac{4.FN}{\pi.\sqrt{2}.D_o^2} \qquad Eq(4)$$

$$\sin(\Theta) = \frac{\left(\frac{\pi}{2}\right) c_d}{K(1+X)} \qquad Eq(5)$$

Also, as a rough estimate the total velocity is calculated with an assumption that there is no friction losses in the swirl injector and the angular momentum of the flow inside the swirl chamber [2].

$$V_{tot} = \sqrt{\frac{2\Delta p}{\rho}} \qquad Eq(6)$$

Firstly, designed reservoirs are analyzed to make sure flow are distributed equally to tangential inlets of the injectors. In reservoir analysis, mass flow is given from inlet and pressure outlet is given as boundary conditions for inlet and outlet respectively. Pressure based solver is used as solver and both laminar and k-omega sst models are used respectively in simulations. It is seen that both models give same results. Steady-state calculation is done and mass flows is obtained as it can be seen from below velocity distribution figure.

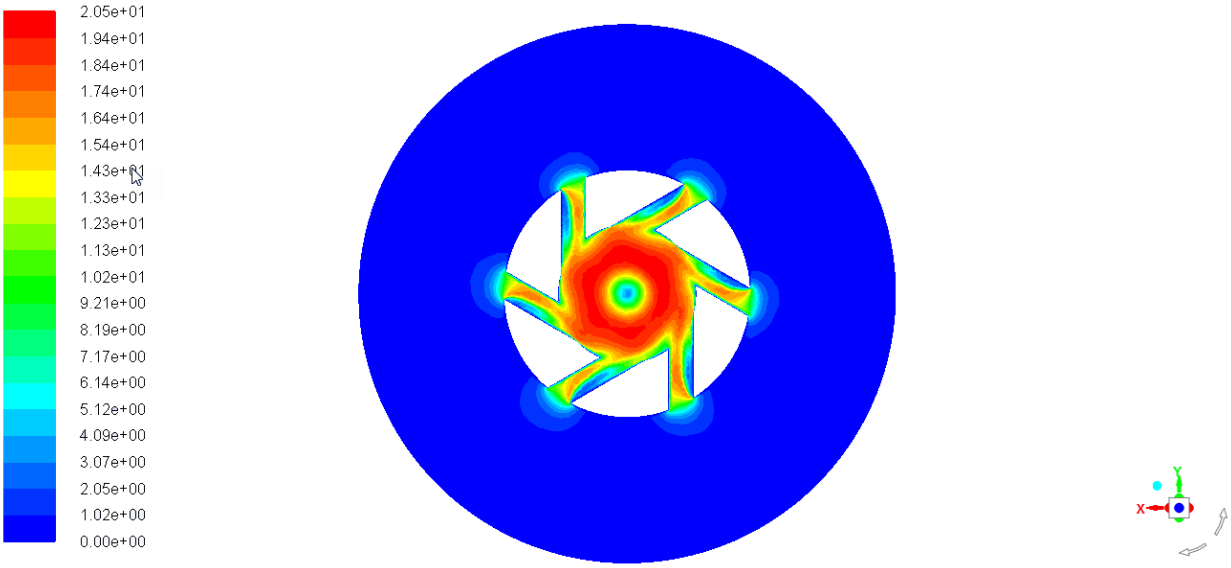


Figure 2. Velocity of Flow at Tangential Inlets

After the uniform flow and equally disturbed mass flows through tangential inlets are proved by CFD analyses, RD-0110 injector with water reservoirs are manufactured and tests are performed.

Two-phase, unsteady flow fields of inner and outer injectors are computed separately and together using volume of fluid method via ANSYS-FLUENT software. Change of spray cone angle is observed with analysis results. Two and three dimensional computational fluid dynamics analyses have been performed. CFDs are repeated to observe mesh independency of the solutions. Boundary conditions of the inner injector are shown in Fig.3.



Figure 3 Boundary conditions of the inner injector

2D axisymmetric VOF is solved for inner injector at 0.15 kg/s mass flow rate. Analysis gives very close results for spray cone angle measured by high speed camera and velocities measured with PDPA. For 0.15 kg/s mass flow rate volume fraction of water in injector resulting spray is shown in Fig. 4.

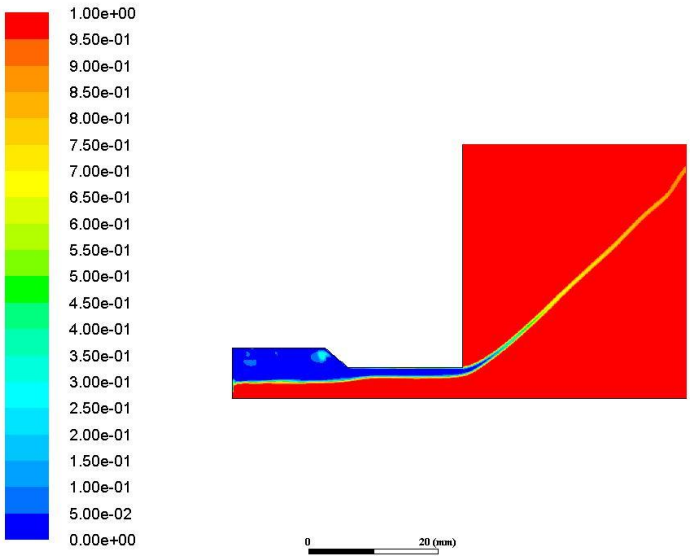


Figure 4. Water Phase for 0.15 kg/s Mass Flow Rate.

3. EXPERIMENTAL SETUP AND TECHNIQUES

The tests have been carried out at the cold flow test facility at TUBITAK SAGE. In modeling both propellant and oxidizer, water is used because of safety reason in the facility and ease of supply. Two centrifugal water pumps are used to supply constant mass flow to injectors' reservoir. Pumps received the water from 2 m^3 water tank. Using on such a scale water tank enabled to investigate many points on the spray without interrupting the test. High response absolute pressure transducers are placed in the reservoir inlets to measure pressure drop of the injectors. Water filters are employed to prevent possible contaminants to block the tangential inlets and needle valves are used to adjust mass flow rates. Two turbine type flow meters are used to measure incoming mass flow rates coming though the inner and outer injectors. Pressure transducers have %0.5 error margin whereas flowmeters have %1. Data from flowmeters and pressure transducers are collected with data acquisition system. Data acquisition system and PDPA system are shown in Figure 5.

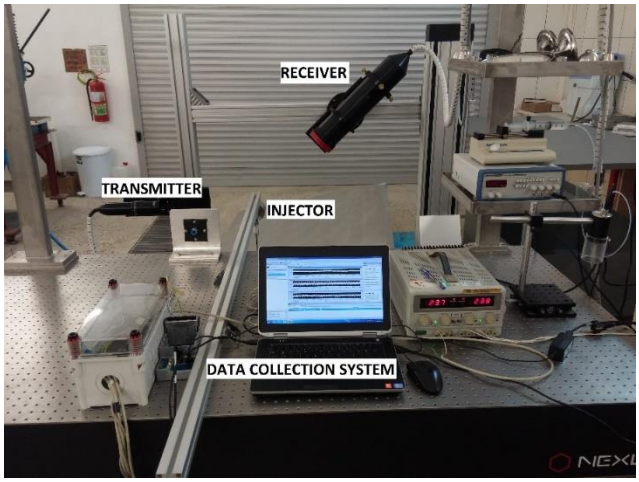


Figure 5. PDPA and DAQ System.

Tests are first conducted for the inner injector. For three different mass flow rates spray cone angles and measured pressure drop across the injector are shown in Table 1. High speed camera is used in spray visualization. The model of the camera is Photron SA 1.1, capable of recording images at 576*768 pixel with 20000 frame per second rate. For accurate determination of the spray cone angle, an image processing code to measure spray cone angle (by edge detecting) at every frame is developed.

It is seen that spray cone angles measured from tests are very close to the results obtained from VOF analysis.

Table 1. Inner Injector Test Results.

	Mass Flow Rate (kg/s)	**Pressure Drop (Bar)**	**Spray Cone Angle (Degree)**
Test 1	4.68	1.400	73.02
Test 2	6.00	2.258	77.82
Test 3	9.105	5.009	79.51

Resulting spray for test 1, test 2 and test 3 is shown in Figure 6 below.

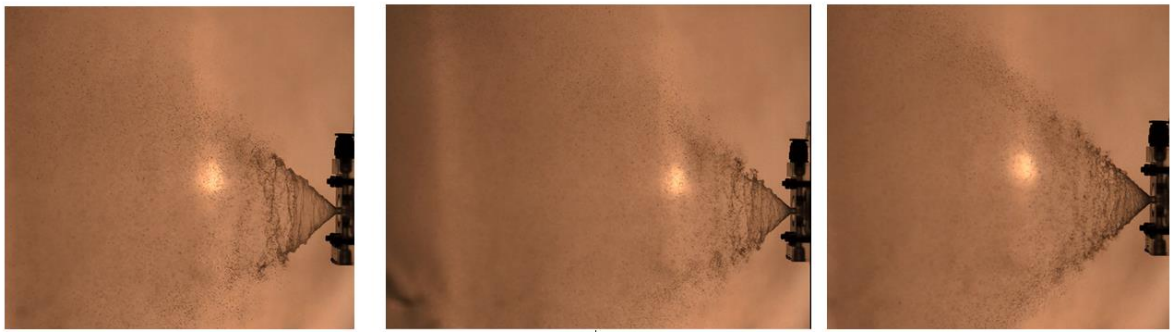


Figure 6. **a)** Test 1 **b)** Test 2 **c)** Test 3

In RD-0110 rocket injector's inner and outer injectors have 6 and 4 tangential inlets respectively. In order to make sure flows which come to those inlets are uniform and, mass flow rates are equally separated to tangential inlets for both injectors, reservoir is designed and analyzed to inspect mass flow rates of tangential inlets. Cross section of the reservoirs and injectors is given in Figure 7.

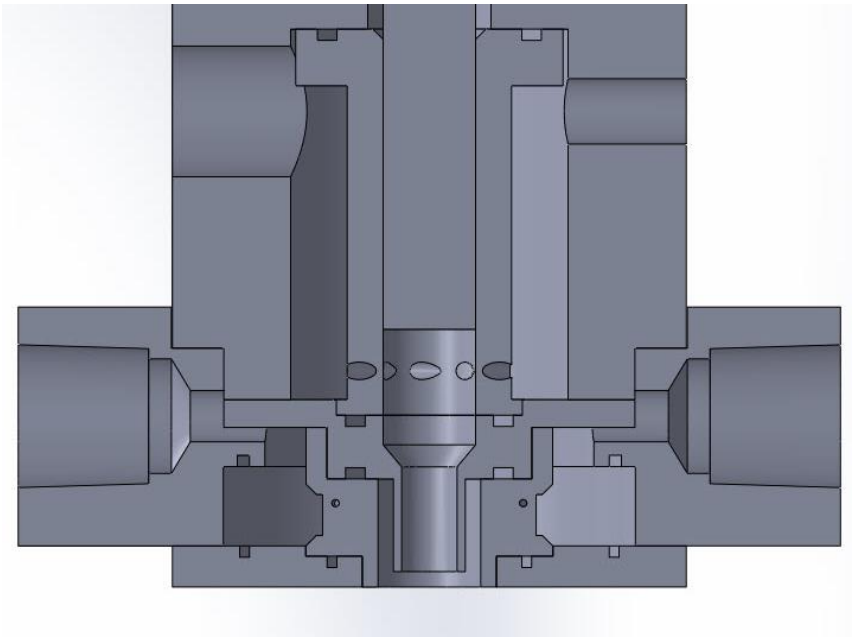


Figure 7. Cross Section of Reservoir and RD-0110 Injector.

Also, tests are performed for both inner and outer injector at the same time. Resulting hollow cone spray from outer injector is shown in Figure 8.

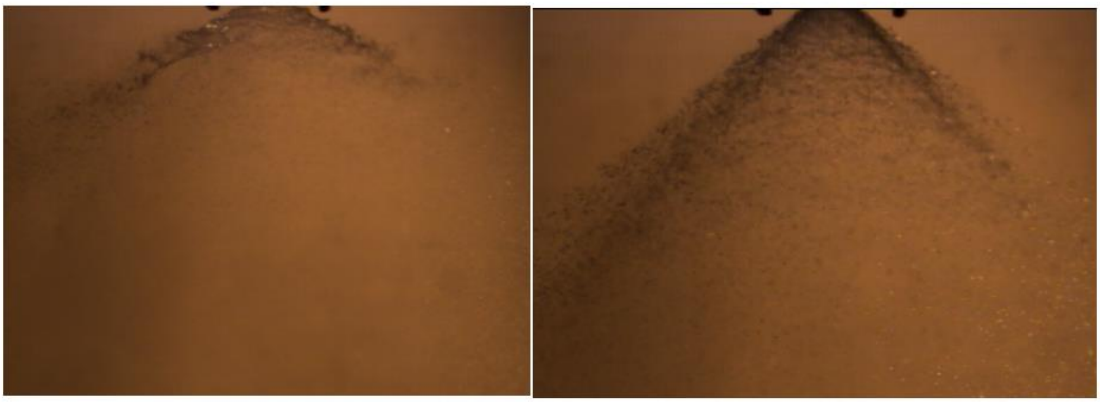


Figure 8. a) Spray from outer injector **b)** Spray from both injector

Further tests will be performed to invesitgate particle velocity and size of the merged spray of coaxial injector.

REFERENCES

1. **D. Kim, J.-H. Im, Y. Yoon and V. G. Bazarov,** "Effect of Recess on the Spray Characteristics of Liquid-Liquid Swirl Coaxial Injectors," *JOURNAL OF PROPULSION AND POWER,* vol. 23, no. 6, 2007.

2. **D. B.-N. A. P. P. Pedro Teixeira Lacava,** "Design Procedure and Experimental Evaluation of Pressure-Swirl Atomizer," in *International Congress of The Aeronautical Sciences*, 2004.

3. **H. F. V. N. V. G. B. Jose N. Hinckel,** "CFD Analysis of Swirl Atomizers," in *44th AIAA/ASME/SAE/ASEE Joint Propulsion Conference & Exhibit*, Hartford, 2008.

UNSTEADY SOLUTION OF 2D CONVERGING-DIVERGING NOZZLE USING LINEARIZED HARMONIC METHOD

Arash KARSHENASS, *arash.karshenass@metu.edu.tr* Middle East Technical University, 06800, Ankara, Turkey

O. Uğraş BARAN, *ubaran@metu.edu.tr* Middle East Technical University, 06800, Ankara, Turkey

M. Haluk AKSEL, *aksel@metu.edu.tr* Middle East Technical University, 06800, Ankara, Turkey

ABSTRACT

The aim of this study is to develop a model for applying harmonic method into periodic problems without concerning geometry and mesh complexity. So, a 2D inviscid, subsonic flow through a converging-diverging nozzle is studied with a harmonically-alternating back pressure as boundary condition with definite frequency and amplitude. Steady state solution is obtained by time averaged back pressure and coupled with harmonic solver, which is based on linearized Euler methods to solve perturbation effects. Harmonic and steady-state solutions are consolidated to achieve time-accurate solution.

Keywords: CFD, frequency, linearized, harmonic

1. INTRODUCTION

Dependency of aerospace and aeronautic industries on Computational Fluid Dynamics (CFD) analysis is unavoidable. In recent years it has been advancing significantly than ever thanks to growth of available computation power. However, the demand for computational resources with even higher capabilities still exist, followed by complicated mathematical methods to deal with more complex physical phenomena. Although, current status of computers is acceptable for nearly all of steady problems in CFD, it is often insufficient for complex unsteady problems in industrial design process. This issue is more outstanding when it comes to turbomachinery and aeroelasticity studies where required calculations soar due to interaction of several physical events on each other, needing simultaneous solutions. As an example, [McMullen,

2003] has reported that a study had done in 2001 at U.S. Department of Energy Defense Programs with contribution of Stanford University on time-accurate unsteady analyzes over a turbine and a compressor in a massively-parallel computer with 750 CPUs, Table 1. According to execution times, it is obvious that these methodologies are not applicable to industrial applications. One way to overcome this problem is to adopt improved, and usually more complicated, mathematical methods that require less processes of calculation, instead of looking for more computation power to use.

Unsteady solutions inside passages of a turbomachine is periodic both in time and space. It is possible to define periodic boundaries for space in steady solutions to truncate a row into a single passage for periodicity but it is not applicable in unsteady solutions. Therefore, unsteady Euler equations must be solved within whole passages by employing established time-accurate algorithm in CFD. Additionally, repeating rotor-stator configuration cause the solution within domain varies periodically in time, Figure 1. However, these periodic solutions cannot be achieved quickly in time-accurate manner but an initial transient solution must be run out to lead to periodic ones. It means that required number of time-steps of transient part is significantly large compared to those for a period of solution, about 95% [Mitchell, 1995; Yao et al., 2001]. Hence, massive part of process is associated with this useless transient part and consequently is an inefficient method. On the other hand, it is possible to represent governing equations in a more suitable form by temporal periodic essence. In this periodic approach, new form of equations with temporal periodic nature can be solved in the frequency domain rather than time domain which have steady form and consequently makes it possible in turbomachinery to truncate a row into a single passage for its spatial periodicity. In periodic approach, Fourier series (as trigonometric interpolant) is used to represent the solution in time with the aim of eliminating the time-dependent parameters in governing equations and obtaining perturbed solution from time-independent perturbed equations that only rely on frequency. While number of governing equations which have to be solved simultaneously increase two or three times, the method benefits from lower computational cost since time marching calculations are avoided.

Generally, there exist three methods in periodic approach for solving compressible flow equations in frequency domain, time-linearized, nonlinear (Deterministic-Stress) [Adamczyk and Goldstein, 1978] and full harmonic balance [Hall et al., 2002 and Giles,1992],.

Table 1: Details of the time-accurate study

Unit	Blade Rows	Grid Points	Execution Time (days)
Turbine	9	94 million	500
Compressor	23	N.A.	1300

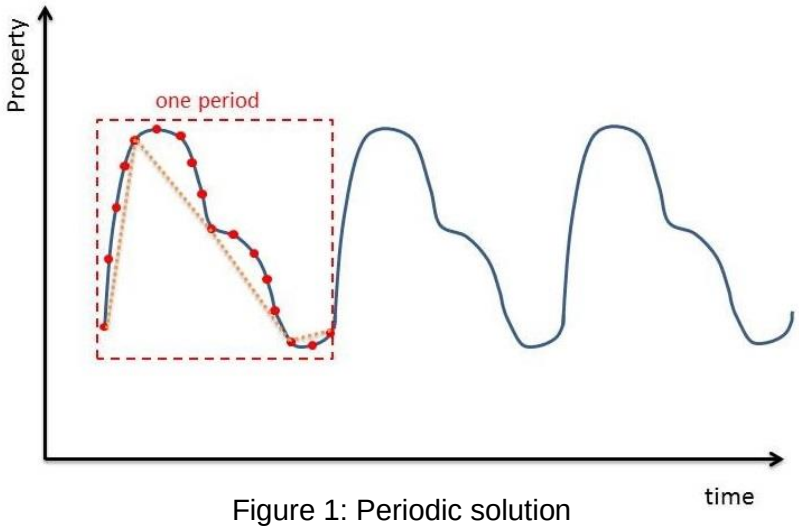


Figure 1: Periodic solution

All these methods are based on separation of unsteady periodic solution into a mean solution plus perturbed harmonic solution(s) about the values of mean solution.

In time-linearized method, only one disturbance with specific frequency is considered. Note that due linearization, flow must be free from shocks due to nonlinear nature of shocks in order to have exact results. If there exists a shock in problem (steady), perturbed solution cannot predict high details in shock. Furthermore, magnitude of perturbed solution should be sufficiently small compared to mean solution for having linear behavior. Since time-linearized method is linear, it is possible to use superposition to sum multiple distortions with different frequencies, which are solved separately. [Casper and Verdon, 1981] and [Verdon and Casper, 1984] applied time-linearized method into potential flow for linear cascades. Following that, [Hall, 1987] and [Gundevia, 2015] applied the method into Euler equations and [Lindquist, 1992] into Navier-Stokes equations. All these studies, are based on JST method for convective flux calculations by introducing artificial viscosity. In the previous study, [Karshenass et al., 2017], the method was applied into Euler equations for an inviscid, transonic Quasi-1D nozzle. Result shows that despite the simple geometry, the system of perturbed harmonic equations cannot be solved by upwind or averaging methodologies without adding artificial viscosity. However, flux vector splitting (FVS) can undertake it.

2. PROBLEM SUMMARY

The aim of this study is to develop a model for applying time-linearized harmonic method into 2D periodic problems. To do that, steady and perturbed compressible flow is solved within a 2D transonic converging-diverging nozzle, Figure 2. Source of periodic pattern is harmonically-alternating back pressure with known a priori frequency and amplitude as periodic boundary condition. Following that, the problem is decomposed into a steady-state solution and a harmonic perturbed solution, which can be combined for obtaining unsteady solution;

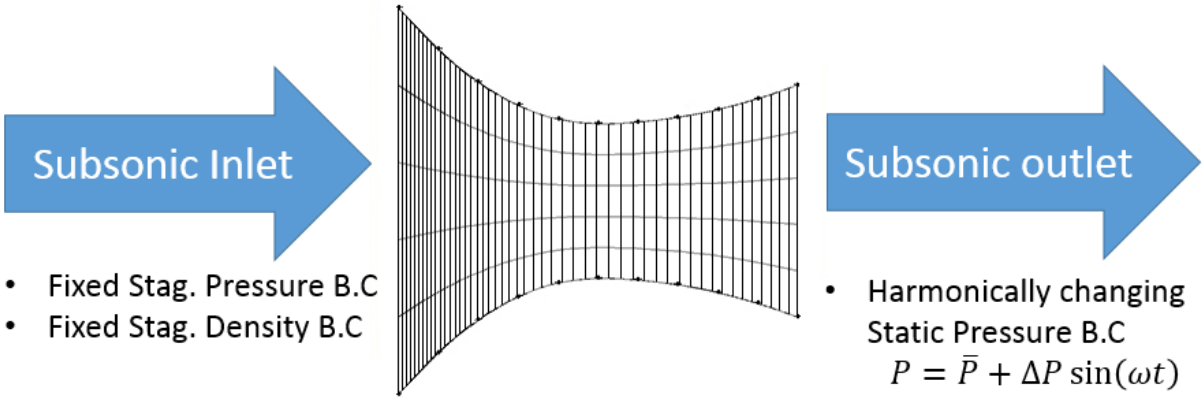


Figure 2 Geometry and mesh structure of nozzle

Hence, steady-state accelerating techniques can be applied in both steady and perturbed solutions. Steger-Warming FVS method is adopted for calculating convective fluxes.

Outlet static pressure of nozzle varies harmonically in time as $P = \bar{P} + \Delta P \sin(\omega t)$ where ω is angular frequency and ΔP is the amplitude of variation from mean value $\bar{P}$. In order to have subsonic flow through nozzle, boundary values are set as $P_{stag,inlet} = 1.75\ MPa,\ T_{stag,inlet} = 300\ K,\ \bar{P} = 1.55,\ \Delta P = 0.007 MPa$ and $\omega = 1$.

3. METHODOLOGY

Unsteady 2D Euler equation without external forces in integral form is:

$$\frac{\partial}{\partial t}\int_{\Omega} W d\Omega + \int_{A} F dA = 0 \quad \& \quad W = \begin{bmatrix} \rho \\ \rho u \\ \rho v \\ \rho E \end{bmatrix} \quad \& \quad F = \begin{bmatrix} \rho(\vec{V}.\vec{n}) \\ \rho u(\vec{V}.\vec{n}) + Pn_x \\ \rho v(\vec{V}.\vec{n}) + Pn_y \\ \rho H(\vec{V}.\vec{n}) \end{bmatrix} \tag{1}$$

Where W and F are conservative variables and fluxes respectively.

As the first assumption, unsteady variables are the sum of mean plus perturbed variables;

$$W_{(x,y,t)} = \bar{W}_{(x,y)} + \tilde{W}_{(x,y,t)} \tag{2}$$

Similarly, unsteady fluxes are the are the sum of mean plus perturbed variables;

$$F_{(x,y,t)} = \bar{F}_{(x,y)} + \tilde{F}_{(x,y,t)} \tag{2}$$

Parameters with “bar” and “tilde” over them are mean and perturbed parts respectively, while those without any notation above them are the unsteady ones. Thus:

$$\frac{\partial}{\partial t}\int_{\Omega} \left(\bar{W}_{(x,y)} + \tilde{W}_{(x,y,t)}\right) d\Omega + \int_{A} \left(\bar{F}_{(x,y)} + \tilde{F}_{(x,y,t)}\right) dA = 0 \tag{3}$$

As the second assumption, mean solution is considered as the steady solution. From steady Euler equation without external forces we have:

$$\frac{\partial}{\partial t}\int_{\Omega}\bar{W}_{(x,y)}d\Omega+\int_{A}\bar{F}_{(x,y)}dA=0 \tag{4}$$

Subtracting Equation 4 from Equation 3, we get:

$$\frac{\partial}{\partial t}\int_{\Omega}\tilde{W}_{(x,y,t)}d\Omega+\int_{A}\tilde{F}_{(x,y,t)}dA=0 \tag{5}$$

For simplicity, $\tilde{W}_{(x,y,t)}$ and $\tilde{F}_{(x,y,t)}$ are replaced by $\tilde{W}$ and $\tilde{F}$ at the rest.

Additionally it is assumed that the perturbed solution has a linear effect on problem (F changes linearly from $\bar{F}$ when W varies from $\bar{W}$). Since, fluxes are functions of conservative variables, $F=F_{(W)}$, it is possible to obtain F from $\bar{F}$ using Taylor Series.

$$F=\bar{F}+\left.\frac{dF}{dW}\right]_{\bar{W}}\tilde{W}=\bar{F}+\frac{d\bar{F}}{d\bar{W}}\tilde{W}\rightarrow\tilde{F}=\frac{d\bar{F}}{d\bar{W}}\tilde{W} \tag{6}$$

Thus:

$$\frac{\partial}{\partial t}\int_{\Omega}\tilde{W}d\Omega+\int_{A}\bar{J}\tilde{W}dA=0 \tag{7}$$

Where:

$$\bar{J}=\frac{d\bar{F}}{d\bar{W}}=\begin{bmatrix}\frac{d\bar{F}_1}{d\bar{W}_1} & \frac{d\bar{F}_2}{d\bar{W}_1} & \frac{d\bar{F}_3}{d\bar{W}_1} & \frac{d\bar{F}_4}{d\bar{W}_1}\\ \frac{d\bar{F}_1}{d\bar{W}_2} & \frac{d\bar{F}_2}{d\bar{W}_2} & \frac{d\bar{F}_3}{d\bar{W}_2} & \frac{d\bar{F}_4}{d\bar{W}_2}\\ \frac{d\bar{F}_1}{d\bar{W}_3} & \frac{d\bar{F}_2}{d\bar{W}_3} & \frac{d\bar{F}_3}{d\bar{W}_3} & \frac{d\bar{F}_4}{d\bar{W}_3}\\ \frac{d\bar{F}_1}{d\bar{W}_4} & \frac{d\bar{F}_2}{d\bar{W}_4} & \frac{d\bar{F}_3}{d\bar{W}_4} & \frac{d\bar{F}_4}{d\bar{W}_4}\end{bmatrix}\quad \bar{W}=\begin{bmatrix}\bar{\rho}\\ \bar{\rho}\bar{u}\\ \bar{\rho}\bar{v}\\ \bar{\rho}\bar{E}\end{bmatrix}\quad \tilde{W}=\begin{bmatrix}\tilde{\rho}\\ \bar{\rho}\tilde{u}+\tilde{\rho}\bar{u}\\ \bar{\rho}\tilde{v}+\tilde{\rho}\bar{v}\\ \bar{\rho}\tilde{E}+\tilde{\rho}\bar{E}\end{bmatrix}\quad \bar{F}=\begin{bmatrix}\bar{\rho}\left(\vec{\bar{V}}.\vec{n}\right)\\ \bar{\rho}\bar{u}\left(\vec{\bar{V}}.\vec{n}\right)+\bar{P}n_x\\ \bar{\rho}\bar{v}\left(\vec{\bar{V}}.\vec{n}\right)+\bar{P}n_y\\ \bar{\rho}\bar{H}\left(\vec{\bar{V}}.\vec{n}\right)\end{bmatrix} \tag{8}$$

Outlet boundary condition is defined as $P=\bar{P}+\Delta P\sin(\omega t)$ which has a harmonic pattern. Note that $\bar{P}$ part of back pressure is satisfied with steady-state solution and consequently what remains for the perturbed part is $\tilde{P}=\Delta P\sin(\omega t)$, a pure harmonic pattern. As a consequence of having harmonic boundary condition with specified frequency, perturbed variables along nozzle will inherit the same pattern with the same frequency but different amplitude and phase angle. Any harmonic function (with limited domain) can be represented by Fourier series, thus $\tilde{W}$ can be represented as:

$$\tilde{W}_{(x,y,t)}=\sum_{n=1}^{\infty}\hat{W}_{(x,y)_n}e^{i\omega tn} \tag{9}$$

Where:

$$\widehat{W} = \widehat{W}_r + i\widehat{W}_i = \begin{bmatrix} \widehat{W}_1 \\ \widehat{W}_2 \\ \widehat{W}_3 \\ \widehat{W}_4 \end{bmatrix} = \begin{bmatrix} \widehat{W}_{1r} + i\widehat{W}_{1i} \\ \widehat{W}_{2r} + i\widehat{W}_{2i} \\ \widehat{W}_{3r} + i\widehat{W}_{3i} \\ \widehat{W}_{4r} + i\widehat{W}_{3i} \end{bmatrix}$$

Having boundary condition with pure harmonic pattern in form of $\sin(\omega t)$, only the first harmonic term vanish in Fourier Series and the rest become zero (Except the average term which is used in steady-state solution). Consequently, Equation 9 is simplified to:

$$\widetilde{W}_{(x,y,t)} = \widehat{W}_{(x,y)} e^{i\omega t} \tag{10}$$

Subtotaling the new definition of $\widetilde{W}$ into Equation 7, adding a pseudo-time term, separating real and imaginary parts and temporal and spatial discretization, result in:

$$\begin{aligned} d\widehat{W}_r &= \left(-\omega \widehat{W}_i + \frac{\sum \bar{J} \widehat{W}_r dA}{\Omega} \right) d\tau \\ d\widehat{W}_i &= \left(\omega \widehat{W}_r + \frac{\sum \bar{J} \widehat{W}_i dA}{\Omega} \right) d\tau \end{aligned} \tag{11}$$

Decomposing each of these equations, 8 ODE equations will be obtained that need to be solved simultaneously; continuity real and imaginary, x-momentum real and imaginary, y-momentum real and imaginary and finally energy real and imaginary. After obtaining real and imaginary parts of $\widehat{W}$, which is the perturbed solution in frequency domain, $\widetilde{W}$ can be obtained as:

$$\widetilde{W} = \left|\widehat{W}\right| e^{i(\omega t + \varphi)} \quad \& \quad \left|\widehat{W}\right| = \sqrt{\widehat{W}_r{}^2 + \widehat{W}_i{}^2} \quad \& \quad \varphi = \tan^{-1}\left(\frac{\widehat{W}_i}{\widehat{W}_r}\right) \tag{12}$$

Finally, imaginary part of $\widetilde{W}$ can be summed up with $\bar{W}$ to W which is the unsteady solution.

References

1. McMullen, M. S. (2003), “The application of non-linear frequency domain methods to the Euler and Navier-Stokes equations”, Ph.D. thesis, Citeseer.
2. Mitchell, B. E. (1995), “Direct computation of the sound generated by subsonic and supersonic axisymmetric jets”,
3. Yao, J.A. et al. (2001), “Development and validation of a massively parallel ow solver for turbomachinery flows”, Journal of Propulsion and Power, Vol. 17, No. 3, pp 659-668.
4. Adamczyk, J. and Goldstein, M. (1978), “Unsteady ow in a supersonic cascade with subsonic leading-edge locus”, AIAA Journal, Vol. 16, No. 12, pp 1248-1254
5. Hall, K.C. et al (2002), “Computation of unsteady nonlinear flows in cascades using a harmonic balance technique”, AIAA journal, Vol. 40, No. 5, pp 879-886

6. Giles, M. (1992), “An approach for multi-stage calculations incorporating unsteadiness”, ASME International Aerodynamics and Aeroelasticity of Turbomachines, pp 183-193
7. Casper, J.R. and Verdon, J.M. (1981), “Numerical treatment of unsteady subsonic flow past an oscillating cascade”, AIAA, Vol. 19, No. 12, pp 1531-1539
8. Verdon, J.M. and Casper, J.R. (1984), “A linearized unsteady aerodynamics analysis for transonic cascades”, Journal of Fluid Mechanics, No. 149, pp403-429
9. Hall, K.C. (1987), “A linearized Euler analysis of unsteady flows in turbomachinery”, Ph.D. Thesis, Massachusetts Institute of Technology.
10. Gundevia, R. (2015), “Application of Linear and Non-Linear Harmonic Methods for Unsteady Transonic Flow”, M.Sc. Thesis, University of California, Irvine
11. Lindquist, D. R. (1992), “Computation of unsteady transonic flowfields using shock capturing and the linear perturbation Euler equations”, Ph.D. Thesis, Massachusetts Institute of Technology.
12. Karshenass, A. and BARAN, O.U. and AKSEL, M.H. (2017), “Unsteady solution of quasi-1D nozzle using linearized harmonic method”, 9th Ankara International Aerospace Conference (AIAC)

AUTHORS INDEX

AUTHORS	Paper ID (Page)
ABBASI Tohid	U18-SI6(919)
ACAR B. Serpil	SA6(113)
AHMADINIA Omid Farid	U18-117(527), U18-118(539)
AKBULUT Güray	U18-SI3(775)
AKKÖK Metin	U18-65(549)
AKKUŞ Gökçe	U18-76(277)
AKSEL M. Haluk	U18-55(457), U18-46(469), U18-49(479), U18-51(495), U18-45(517)
AKSOY Şükrü Taha	U18-85(261)
AKTAŞ Umut	U18-43(145)
ALTAN Mihrigül	U18-20(247)
AMEL Hoda	U18-97(163)
ANFLOR Carla Tatiana Mota	U18-42(385)
ARSLAN Turan	SA7(131)
ATAHAN Ali Osman	SA1(47), SA5(97), SA7(131)
AY Feridun	U18-21(727)
AYBARÇ Uğur	U18-19(593)
AYDIN Erman	U18-23(615)
AYDIN Mehmet	U18-2(603)
AYKAN Emre	U18-27(695)
BADAY Şehmus	U18-SI1(881)
BAL Burak	U18-69(569)
BALTACIOĞLU Furkan	U18-38(31)
BARAN Onur	U18-54(509)
BARAN Özgür Uğraş	U18-51(495), U18-45(517)
BARUT Zeki Mert	U18-43(145)
BEDIZ Bekir	U18-57(319)
BİLGE M. İlter	U18-49(479)
BİLGİÇ Furkan	U18-SI12(973)
BUDAK Erdem İnanç	U18-67(217)
BÜYÜK Murat	SA1(47), SA5(97)
CARNEIRO Sergio	U18-42(385)
CRNJAC Marina	U18-11(3)
ÇAKAN Betül Gülçimen	U18-79(685)
ÇAKIR F. Hayati	U18-SI13(855)

AUTHORS	Paper ID (Page)
ÇAKIR Mustafa Cemal	U18-79(685)
ÇAKIRGÖZ İsmail	U18-19(593)
ÇALIN Recep	U18-117(527), U18-118(539)
ÇAVDAR Kadir	U18-30(737)
ÇELENK Oktay	U18-21(727), U18-30(737)
ÇETİN Barış	U18-69(569)
ÇETİN Muzaffer	U18-86(713)
ÇİÇEK Süleyman	U18-SI17(1011)
ÇOĞUN Can	U18-SI2(761)
DAĞLI Efe C.	U18-55(457)
DALAK Kağan	U18-19(593)
DEMIR Burkay Yılmaz	U18-43(145)
DEMİRCİ Emre	U18-56(673)
DOMINGUES Allan	U18-42(385)
DONDER Abdulhamit	U18-25(355)
DURMUŞ Ali	U18-30(737)
EKİCİ Merve	U18-SI6(919)
EKMEKCİ Bülent	U18-SI5(787), U18-SI8(803)
EKMEKCİ Nihal	U18-SI5(787), U18-SI8(803)
ENSARİOĞLU Cihat	U18-79(685)
EPSİLELİ Ercan	SA5(97)
ER Ümit	U18-SI12(973)
ERDEM Oğuz	U18-SI2(761), U18-SI14(863)
ERDEN Zühal	U18-91(429)
ERGENE Berkay	U18-36(415)
ERKAL Berksu	U18-46(469)
EROĞUL Osman	U18-67(217)
ERSOY Kıvılcım	U18-7(169)
ESAT Volkan	SA3(81)
EYERCİOĞLU Ömer	U18-SI9(831), U18-SI10(843)
GANDAŞ Sinan	U18-21(727)
GIBBONS Gregory J	U18-97(163)
GÖRGÜLÜARSLAN Recep Muhammet	U18-84(199), U18-85(261)
GÖV Kürşad	U18-SI9(831), U18-SI10(843)
GÜNGÖR Kaan	U18-19(593)

AUTHORS	Paper ID (Page)
GÜRBÜZ Hüseyin	U18-SI1(881), U18-SI11(945)
GÜRER Batuhan	SA3(81)
GÜRGEN Selim	U18-SI13(855)
GÜRÜN Hakan	U18-117(527)
GÜZELİPEK Özgücan	U18-76(277)
HAMARAT, İbrahim	U18-SI1(881)
HATİPOĞLU Uğur	U18-66(653)
HİMMETOĞLU Selçuk	SA2(61)
ISA Mohammed A.	U18-113(297)
İLBAY Kadir	U18-SI17(1011)
JOUDI Javad	U18-117(527), U18-118(539)
KACAR İlyas	U18-SI4(897)
KAFKAS Fırat	U18-SI11(945)
KALAMAN Sudi	U18-SI8(803)
KAMBER O. Saban	U18-SI14(863)
KARATAŞ Çetin	U18-40(577)
KARSHENASS Arash	U18-45(517)
KAŞ Mustafa	U18-SI15(989)
KAYA Duran	U18-118(539)
KAYA Eren	U18-13(399)
KAYA İrfan	U18-13(399)
KAYNAK Yusuf	U18-SI15(989), U18-SI16(999), U18-SI17(1011)
KHAN Shaheryar A.	U18-114(309)
KILIÇ Sadık Engin	U18-96(345)
KILIÇ Süleyman	U18-SI4(897)
KITAY Özhan	U18-SI15(989), U18-SI16(999)
KOÇ Barış	U18-7(169)
KONUKSEVEN E. ilhan	U18-25(355)
KOSKU PERKGÖZ Nihan	U18-21(727)
KOSUMCU Sadık İnan	U18-84(199)
KOVAN Volkan	U18-SI7(935)
KÖKSAL Aybars Feyzi	U18-85(261)
KÖLÜK Hüseyin	U18-79(685)
KURUCUOĞLU Kenan	SA1(47)
KUŞHAN M. Cemal	U18-SI13(855)

AUTHORS	Paper ID (Page)
KÜÇÜKTÜRK Gökhan	U18-117(527),U18-118(539)
LATIFINAVID Masoud	U18-25(355)
LAZOĞLU Ismail	U18-112(285), U18-113(297), U18-114(309)
LUO Tzuo-Liang	U18-73(335)
MALAYOĞLU Uğur	U18-76(277)
MEÇO Halim	U18-69(569)
MEHMERT Patrick	U18-80(233)
MLADINEO Marko	U18-11(3)
MOZTARZADEH Hadi	U18-97(163)
MURPHY Mark F.	U18-SI5(787)
MUSTAFA S. Shahid	U18-112(285)
NALBANT Muammer	U18-23(615)
NAMLU Ramazan	U18-121(375)
NESLİ Şafak	U18-SI15(989)
ORAK Mahir Gökhan	U18-65(549)
ORAK Sezan	U18-SI13(855)
OSMAN Khaled Ali	U18-96(345)
ÖPÖZ Tahsin T.	U18-SI5(787), U18-SI8(803)
ÖREN Soner	U18-SI3(775)
ÖRNEK Murat	SA5(97)
ÖZEL Tuğrul	U18-78(185)
ÖZER İlayda	U18-91(429)
ÖZEREN EMRE	U18-20(247)
ÖZKAN Merve	U18-51(495)
ÖZTÜRK Fahrettin	U18-SI4(897)
ÖZYÖRÜK Yusuf	U18-54(509)
PATEL Kaushalendra	U18-78(185)
PENG Ta-Jen	U18-73(335)
PEREME Michel	U18-80(233)
POYRAZ Özgür	U18-SI3(775)
REİS Murat	U18-79(685)
SAFARIAN Asghar	U18-40(577)
SANTOS Tharcísio	U18-42(385)
SARIKAYA Hüseyin	U18-26(633)
SERİN Gökberk	U18-84(199)

AUTHORS	Paper ID (Page)
SETH Sampan	U18-97(163)
SEVİK Cem	U18-21(727)
SEVİM Umur Korkut	SA7(131)
SHAH Chirayu H.	U18-78(185)
SHAH Harshal N.	U18-78(185)
SHEVTSOV Sergey	U18-35(441)
SMALLEY Grace	SA6(113)
SNEZHINA Natalia	U18-35(441)
SOFUOĞLU M. Alper	U18-SI13(855)
SOLAKOĞLU Ezgi Uğur	U18-SI3(775)
SOYUSİNMEZ Tuğrul	U18-76(277)
SUBAŞI Mehmet	U18-40(577)
SÜMER Bülent	U18-46(469)
ŞAHİN Mevlüt	U18-SI4(897)
ŞAHİN Murat	U18-63(557)
ŞEKER Ulvi	U18-96(345), U18-117(527), U18-118(539), U18-SI11(945)
ŞİMŞİR Caner	U18-121(375)
TAI Chung-Yu	U18-73(335)
TAŞCIOĞLU Emre	U18-SI14(863), U18-SI15(989), U18-SI17(1011)
TEZEL Tuğçe	U18-SI7(935)
TOPAL Eyüp Sabri	U18-SI7(935)
TURNACILAR Tarkan	U18-85(261)
TÜZEMEN Cansinem	U18-SI3(775)
UĞUZ Agah	U18-79(685)
ULUTAN Mustafa	U18-SI12(973)
URUNGA Candaş	U18-29(367)
USLAN İbrahim	U18-SI2(761)
ÜNAL Ramazan	U18-38(31)
ÜNÜVAR Ali	U18-26(633)
ÜNVER Hakkı Özgür	U18-84(199), U18-96(345)
VEZA Ivica	U18-11(3)
WU Jiing-Kae	U18-35(441)
YALÇIN Bekir	U18-36(415), U18-27(695)
YAMAN Kemal	U18-86(713)

AUTHORS	Paper ID (Page)
YASA Evren	U18-7(169)
YAŞAR Hamidullah	U18-SI5(787), U18-SI8(803)
YENİ Harun	U18-79(685)
YENİKAYA Gökhan	U18-66(653)
YENİKAYA Sibel	U18-66(653)
YERLİTAŞ Mustafa	U18-69(569)
YILDIRIM Bora	U18-86(713)
YILDIZ Ali Rıza	U18-53(665), U18-56(673)
YILDIZ Betül S.	U18-52(157)
YILMAZ Bülent	U18-95(15), U18-63(557)
YILMAZ Oğuzhan	U18-SI6(919), U18-SI15(989)
YILMAZ Okan Deniz	U18-121(375)
YILMAZ Volkan	U18-96(345)
YİĞİT I. E.	U18-114(309)
YÜCEL Ayhan Öner	SA7(131)
ZHILYAEV Igor	U18-35(441)